Douglas H. Werner
Do-Hoon Kwon *Editors*

Transformation Electromagnetics and Metamaterials

Fundamental Principles and Applications

Springer

Transformation Electromagnetics and Metamaterials

Douglas H. Werner · Do-Hoon Kwon
Editors

Transformation Electromagnetics and Metamaterials

Fundamental Principles and Applications

Springer

Editors
Douglas H. Werner
The Pennsylvania State University
University Park, PA
USA

Do-Hoon Kwon
University of Massachusetts Amherst
Amherst, MA
USA

ISBN 978-1-4471-4995-8 ISBN 978-1-4471-4996-5 (eBook)
DOI 10.1007/978-1-4471-4996-5
Springer London Heidelberg New York Dordrecht

Library of Congress Control Number: 2013937602

Printed on acid-free paper

Springer is part of Springer Science+Business Media (www.springer.com)

To my wife Pingjuan L. Werner, without whose support this book would not have been possible

Douglas H. Werner

To my family

Do-Hoon Kwon

Preface

The subject of this book is the newly emerging area of research known as transformation electromagnetics and the associated metamaterials technology for designing and realizing devices that can control the behavior of electromagnetic waves (including light) in ways that have not been conventionally possible. The fundamental principle behind transformation electromagnetics has been known for decades, but it was only recently formalized in 2006 and subsequently established as a powerful design tool for microwave and optical engineers. Combined with the development over the past decade of the state of the art in metamaterials technology, which allows for realizing practical engineered materials having inhomogeneous and anisotropic parameters, transformation electromagnetics provides designers with an unprecedented flexibility in device shapes and functionality. The technique is credited with numerous novel device designs, most notably invisibility cloaks. In this book, a comprehensive treatment has been compiled from a group of leading scholars and researchers throughout the world on the subject, from the fundamental theoretical principles to application examples realized using the state of the art in metamaterials technology, encompassing a wide range of the electromagnetic spectrum.

Transformation electromagnetics has led to designs that enable novel wave-material interaction properties such as invisibility cloaks, flat aberration-free lenses, photonic integrated systems on a chip, low-profile highly directive antennas, and a host of other remarkable devices. On the theoretical side, the following questions will be addressed: "Where does transformation electromagnetics come from?", "What are the general material properties derived from different classes of coordinate transformations?", "What are the limitations and challenges of device realizations?", and "What theoretical tools are available to make the coordinate transformation-based designs more amenable to fabrication using currently existing technologies?" The comprehensive theoretical treatment is complemented by a broad range of design examples as well as experimental measurements of fabricated metamaterial-enabled transformation electromagnetics devices in various spectral regimes with applications ranging from radio frequencies, through the terahertz and infrared, to visible wavelengths. The applications encompass invisibility cloaks, gradient-index lenses in the microwave and optical regimes, negative-index superlenses for sub-wavelength resolution focusing, flat lenses that

produce highly collimated beams from an embedded antenna or optical source, beam concentrators, polarization rotators and splitters, perfect electromagnetic absorbers, and many others. This edited volume is intended to serve as an authoritative reference to the fast-evolving and exciting research area of transformation electromagnetics/optics, its application to the design of revolutionary new devices and their associated metamaterial realizations. We hope that this book will be an indispensable resource for graduate students and researchers in academia as well as professionals in the optical/microwave device industries.

This book comprises a total of 14 invited chapters contributed from leading experts in the field of transformation electromagnetics and metamaterials. Many color illustrations have been included throughout the book, which supply the reader with an important visual aid to understanding transformation electromagnetics. A brief summary of each chapter is provided as follows. Chapter 1 presents quasi-conformal coordinate transformations with an emphasis on their application to the design of lenses. Benefits of the proposed approach as well as considerations for minimizing aberrations and for extending to three-dimensional applications are discussed. Chapter 2 covers transformation optics applications to cloaking, lensing, and radiation problems. Various designs ranging from invisibility cloaks to flat focusing lenses and beam control devices as well as some envisioned metamaterial realizations are provided. Chapter 3 introduces the theory of metasurface transformation along with corresponding anisotropic impedance-modulated metasurface design techniques. Examples are presented where planar surface waves are transformed into surface waves with arbitrarily curved wavefronts. Potential realization approaches based on resonant patch elements are provided. Chapter 4 reviews the various methods to simplify the design of transformation optics devices. The effects of different coordinate transformations on the complexity of medium parameters while achieving the same overall device functionality are investigated. Approximations to the exact medium parameters and numerical optimizations of device designs are also discussed. Chapter 5 describes the creation of illusion effects using transformation optics and metamaterials. It is shown that the electromagnetic response of a physical space containing real objects can be converted into a virtual space containing illusion objects. Chapter 6 investigates the interactions between invisibility cloaks and anti-cloaks in two and three dimensions. Effects of permittivity mismatch, vacuum gap, and approximate double-positive medium implementations on cloaking and field-restoring capabilities are presented. The trade-offs between absorption and scattering from the sensor cloaking perspective are discussed. Chapter 7 presents a discrete coordinate transformation methodology that provides an all-dielectric approach for device designs. Several antenna designs including a flat reflector, a flat lens, and a zone plate Fresnel lens are presented and numerically analyzed. Realization methods are discussed and a prototype of the carpet cloak is demonstrated. Chapter 8 considers devices for achieving highly directive radiation designed via the transformation electromagnetics approach and their experimental demonstration. Several transformations that lead to simplified medium parameters without sacrificing the beam-collimating performance are introduced and validated through metamaterial

realizations. Chapter 9 proposes a spherical core–shell structure for creating a virtual aperture from a physically smaller aperture enclosed within the shell. The performance of free-space arrays as well as conductor-backed arrays are evaluated analytically using Ricatti–Bessel functions. The effects of loss on the beamwidth and transmission coefficient are studied. Chapter 10 reviews the recent progress on the theory and fabrication of invisibility cloaks at optical wavelengths. In addition to the fundamental magneto-dielectric cloaks, non-magnetic optical cloaks and carpet cloaks are discussed and their fabrication and experimental characterization in the optical regime are reported. Chapter 11 discusses experimental methods for characterizing invisibility cloaks at microwave frequencies. Quantitative characterization of scattering is defined in terms of scattering cross sections. Parallel-plate waveguide measurements, rectangular-waveguide measurements, free-space measurements, antenna pattern measurements, and polarizability measurements are described. Chapter 12 presents broadbanding techniques for transformation optics-derived invisibility cloaks incorporating passive and active elements. For passive techniques, the trade-offs between the invisibility gain and bandwidth are analyzed. The authors demonstrate that active non-Foster metamaterials offer a potential pathway toward extremely broadband, almost dispersionless cloaking operation. Chapter 13 develops a rigorous anisotropic representation for metamaterials comprising spatially dispersive periodic arrays of passive inclusions. It is shown that a spatially dispersive permittivity and a spatially dispersive inverse transverse permeability characterize the fundamental Floquet modes of the array. Analytical and numerical examples are presented for two- and three-dimensional arrays that confirm the theoretical results. Chapter 14 presents three antenna applications based on transformation electromagnetics together with the associated metamaterial design, fabrication, and experimental validation. Creation of highly directive radiation from a localized source, a method for achieving directive azimuthal patterns from vertical radiation, and a device that generates isotropic radiation from a directive source are investigated theoretically and validated experimentally.

We are indebted to the authors of the 14 chapters for the quality work that was contributed. Indeed, their contributions define this book. In addition, each contributor's prompt and efficient communication with us over the year-long period of this book project is deeply appreciated. Finally, we gratefully acknowledge the editorial assistance provided by the following members of The Pennsylvania State University Computational Electromagnetics and Antennas Research Lab during the preparation of this book: Jeremy A. Bossard, Donovan E. Brocker, Philip P. Calderone, Chad Z. Welsh, Clinton P. Scarborough, and Jeremiah P. Turpin.

Douglas H. Werner
Do-Hoon Kwon

Contents

Chapter 1
Quasi-Conformal Approaches for Two and Three-Dimensional Transformation Optical Media

Nathan Landy, Yaroslav Urzhumov and David R. Smith

Abstract Transformation optical design is generally complicated by the requirement for highly anisotropic and inhomogeneous constituent materials. Quasi-conformal mappings have appeared as an attractive subset of the general transformation optics method because they only require isotropic, dielectric-only materials. In this chapter, we examine the quasi-conformal method as it applies to transformation optics and show that while it does significantly ease the burden of material design and fabrication, it may also create severely aberrant behavior unless caution is taken. We also show how to extend the method to three dimensions, and examine the performance of an optic designed with the quasi-conformal method.

1.1 Introduction

One of the great benefits of transformation optics (TO) as a design paradigm is its ability to solve complicated inverse scattering problems with a minimum of computational difficulty. The primary tool of TO—the coordinate transformation—provides an extremely intuitive, visual approach to managing electromagnetic waves that enable entire classes of complex electromagnetic devices to be designed almost effortlessly. The TO approach consists essentially of two steps. First, a coordinate transformation is applied that accomplishes some desired conceptual distortion of space; the distribution of the electromagnetic fields within

N. Landy (✉) · Y. Urzhumov · D. R. Smith (✉)
Center for Metamaterials and Enhanced Plasmonics,
Duke University, Durham, NC 27708, USA
e-mail: nathanlandy@gmail.com

D. R. Smith
e-mail: drsmith@ee.duke.edu

D. H. Werner and D.-H. Kwon (eds.), *Transformation Electromagnetics and Metamaterials*, DOI: 10.1007/978-1-4471-4996-5_1,

that space is likewise distorted. Second, the form invariance of Maxwell's equations is employed to determine the specification of a hypothetical medium that performs the exact same operation on the electromagnetic field as the transformation. In what has become well known as the standard algorithm for TO media, the relationship between the constitutive tensors in the original (unprimed) and transformed (primed) frames has the form [1]:

$$\varepsilon' = \frac{\mathbf{A}\varepsilon\mathbf{A}^T}{|\mathbf{A}|} \quad \mu' = \frac{\mathbf{A}\mu\mathbf{A}^T}{|\mathbf{A}|}. \tag{1.1}$$

A is the Jacobian matrix that relates the coordinates between the two frames, or

$$\mathbf{A} = \begin{bmatrix} x'_x & x'_y & x'_z \\ y'_x & y'_y & y'_z \\ z'_x & z'_y & z'_z \end{bmatrix}. \tag{1.2}$$

For compactness, we represent the differentiation of coordinates with subscripts. The TO approach provides two major benefits: it simplifies the electromagnetic design process, and provides insight enabling the creation of novel devices. In typical TO practice, a domain is first selected where wave propagation is simply described—the virtual domain—which is then transformed to the more complex physical domain. In this way, the wave propagation and scattering properties can be easily described in the virtual domain, oftentimes analytically, and the equivalent properties in the physical domain are immediately established from the transformation. Equation (1.1) provides the prescription that enables the transformation to be realized in an actual medium.

The material distributions that arise from (1.1) are generally complex, being inhomogeneous and anisotropic in both $\boldsymbol{\varepsilon}$ and $\boldsymbol{\mu}$; nevertheless, the form-invariance of Maxwell's equations guarantees that these distributions will fully reproduce the field deformations corresponding to the coordinate transformation. Although a powerful design tool, the TO algorithm provides no insight whatsoever as to any physical implementation of these material distributions. In addition, it can be inferred from (1.1) that extreme deformations of space will call for equally extreme material parameters through the dependency on the Jacobian of the coordinate transformation.

In general, the complex TO designs cannot be implemented with naturally occurring materials. Naturally occurring materials do not offer an easy means of achieving arbitrary, controlled gradients in the constitutive tensor elements, and are not generally able to satisfy the extreme ranges often needed in TO designs (such as very large values, values near zero—or even negative parameters [2]). Artificially structured metamaterials (MMs) have become recognized as a means of implementing TO designs, since MMs can be fashioned to display a much wider range of effective medium properties, including both electric and magnetic response with arbitrary anisotropy. Moreover, MMs can access the extreme values needed in TO designs.

Unfortunately, MMs are able to achieve these extreme ranges usually by virtue of introducing a geometrical resonance that couples to the impinging electromagnetic fields. The use of resonant elements typically entails significant losses due to absorption, as well as a reduction in the operating bandwidth due to the large frequency dispersion. Resonant MMs become especially problematic as designs are scaled to higher frequencies, where dissipation due to resistive losses in metals increases. Thus, while MMs can in principle be used to implement TO designs, those implementations may not represent practical realizations.

For the above reasons, much of the active research in TO in recent years has focused on the introduction of approximations in the TO specification to achieve more practical TO devices, including those that will scale toward infrared and visible wavelengths. In this chapter, we explore one particular subset of optimized, planar transformations known as quasi-conformal mappings (QCM). Under certain restrictions, QCM may be used to achieve particular two-dimensional (2D) TO designs that require only positive dielectrics and can therefore be implemented with non-resonant, dielectric MMs. By virtue of their relative design simplicity, quasi-conformal TO (QCTO) media have already been demonstrated across the electromagnetic spectrum, from the microwave [3–6] up to infrared and even visible wavelengths [7–10]. Experiments have also shown that the all-dielectric method may be extended in some fashion to three-dimensional devices [11–15].

Our aim in this chapter is to critically examine both the benefits and limitations of the QCM method for both 2D and 3D TO-derived devices. In 2D, we show that the implementation of QCTO inevitably involves approximations to the final material specification, and that these approximations can reduce performance in the final device. At the same time, this methodology drastically reduces the burden of fabrication and design while retaining key aspects of wave propagation in the transformed medium.

To demonstrate the benefits of this method in 3D, we introduce a QCTO-modified optic (a flattened Luneburg lens) and examine it using the standard metrics of lens performance. By virtue of this optic, we show that isotropic, dielectric-only implementations of QCTO devices are inherently approximate and that performance degrades significantly when certain conditions are violated. As an alternative, we show how QCTO affords us extra flexibility in material design such that we can regain much of the performance lost in an isotropic design without a significant increase in design complexity.

1.2 Conformal Subset of Transformation Optics

The physical field within a TO device is determined by the specific coordinate transformation that, in turn, determines the distribution of constitutive parameters throughout a volume. In most instances, however, the field distribution within the volume of the device is of no consequence per se; only the fields on the boundaries of the device are relevant, since the function of most optical devices is to relate a

set of output fields on one port or aperture to a set of input fields on another port or aperture. From the TO perspective, then, device functionality is determined by the properties of the coordinate transformation at the boundaries of the domain. Since there are an infinite number of transformations that have identical behavior on the boundary, there is considerable freedom to find a transformation that is "optimal" in the sense that it maximizes a desired quantity, such as isotropy.

A coordinate transformation produces a mapping between points in two domains. The constitutive parameters that result from a general mapping can be determined from (1.1). It is instructive to restrict our attention to two-dimensional (2D) mappings of the form $\mathbf{x}' = [x'(x, y), y'(x, y)]$, for which the permittivity tensor can be written as

$$\varepsilon' = \frac{\varepsilon}{|\mathbf{A}|}\begin{bmatrix} x'^2_x + x'^2_y & x'_x y'_x + x'_y y'_y & 0 \\ x'_x y'_x + x'_y y'_y & y'^2_x + y'^2_y & 0 \\ 0 & 0 & 1 \end{bmatrix}, \tag{1.3}$$

and similarly for the permeability tensor. The 2D mapping is useful for configurations in which the fields are constrained to propagate within the plane, and are polarized either transverse electric (TM^Z, or TE^Z where the magnetic or electric field are perpendicular to Z, respectively)

For the reasons explained below, it is preferable to deal with isotropic media. Here, we derive the necessary and sufficient conditions for the TO medium to be isotropic, and give a simple geometric interpretation of such transformations. The formal requirement for in-plane medium isotropy is that the two principal values (eigenvalues) of the in-plane portions of the tensor in (1.3) be equal to each other. Suppose one starts from a medium that is isotropic in the virtual frame, that is, the tensor $\boldsymbol{\varepsilon}$ on the r.h.s of (1.3) is a scalar. Then the requirement of isotropy simplifies to the condition that the matrix on the r.h.s of (1.3) is proportional to the unit matrix $\mathbf{I}$, multiplied by an overall scalar factor. The general Eq. (1.1) then reduces to

$$\varepsilon' = \varepsilon\frac{\mathbf{A}\mathbf{A}^T}{|\mathbf{A}|} \quad \mu' = \mu\frac{\mathbf{A}\mathbf{A}^T}{|\mathbf{A}|} \tag{1.4}$$

where $\mathbf{A}$ is a 2D Jacobian matrix defined in the same way as the 3D matrix in (1.2). In general, any Jacobian matrix A can be written in the form $\mathbf{A} = \mathbf{U}\boldsymbol{\Lambda}$, where U is an orthogonal 2×2 matrix (such that $\mathbf{U}^{\mathrm{T}} = \mathbf{U}^{-1}$) and $\boldsymbol{\Lambda} = \mathrm{diag}[a_1, a_2]$ is a diagonal matrix. The geometric interpretation of this decomposition is that any coordinate transformation can be seen locally as a combination of a rotation (given by orthogonal matrix $\mathbf{U}$) and a stretching along two orthogonal directions, with the stretch factors corresponding to the eigenvalues (a_1, a_2) of the diagonal matrix $\boldsymbol{\Lambda}$. The matrix $\mathbf{A}\mathbf{A}^{\mathrm{T}}$ in Eq. (1.4) thus has the form $\mathbf{U}\boldsymbol{\Lambda}^2\mathbf{U}^T$. The necessary and sufficient condition for this matrix to be proportional to a unit matrix is that $a_1 = a_2$, making $\boldsymbol{\Lambda}$ and $\boldsymbol{\Lambda}^2$ both proportional to $\mathbf{I}$. In geometric terms, this means that the transformation must stretch the coordinates isotropically.

A second-rank tensor that is proportional to a unit matrix retains the property of isotropy regardless of the choice of orientations of the local coordinate system. Therefore, from (1.3) we arrive at the conditions that must be satisfied by the transformation functions in order to yield a locally isotropic medium in the point $(x,\ y)$. We can obtain these conditions directly by requiring that the two eigenvalues of the matrix $\mathbf{AA}^T$ be equal. Since the eigenvalue equation is quadratic for 2D matrices, the two eigenvalues are equal if and only if the discriminant of that quadratic equation is zero. The discriminant takes the form

$$\left|\mathbf{AA}^{\boldsymbol{T}}\right| = \left(\left(x'_x - y'_y\right)^2 + \left(x'_y + y'_x\right)^2\right)\left(\left(x'_x + y'_y\right)^2 + \left(x'_y - y'_x\right)^2\right), \tag{1.5}$$

Thus, requiring the equality of two eigenvalues necessitates either a pair of conditions:

$$\begin{aligned} x'_x &= y'_y \\ x'_y &= -y'_x, \end{aligned}' \tag{1.6}$$

or another pair of conditions:

$$\begin{aligned} x'_x &= -y'_y \\ x'_y &= y'_x, \end{aligned} \tag{1.7}$$

which corresponds to a transformation that includes a reflection. These two pairs of conditions are well known as the Cauchy-Riemann conditions for holomorphic and antiholomorphic functions, respectively. From now on, we eliminate antiholomorphic maps, as they introduce an unwanted flip of the grid. Thus, the conformal maps considered here are generated by holomorphic functions.

In geometrical terms, one can define the conformal map as a transformation that preserves the angles between intersecting curves and aspect ratio of the resulting curvilinear grid. Consider a locally orthogonal coordinate system, the simplest example of which is a Cartesian system. The coordinate lines of a Cartesian system form a rectangular grid, as shown in Fig. 1.1 (left). Under a conformal map, the transformed coordinate system remains locally orthogonal, and angles formed by any two curves intersecting at any given point in one coordinate system are conserved in the transformed coordinate system.

By differentiating (1.6) and noting that mixed partial derivatives commute, we see that the primed coordinates satisfy Laplace's equation, or

$$\nabla^2 \mathbf{x}' = 0. \tag{1.8}$$

Conversely, any transformation that satisfies (1.8) everywhere will be conformal, so that Laplace's equation can be employed to obtain maps that satisfy certain boundary conditions numerically.

The constitutive parameters that correspond to conformal maps are much easier to implement physically than the general TO media. To illustrate this point

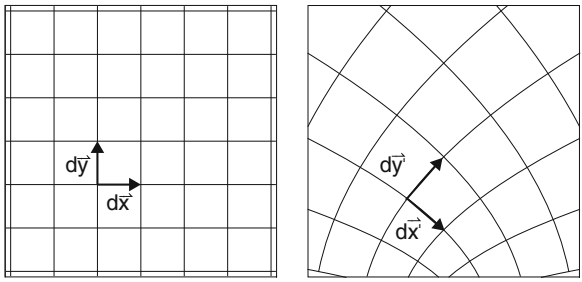

Fig. 1.1 Depiction of a conformal transformation. Lines of constant x and y (virtual domain coordinates) are shown in each domain

explicitly, we insert (1.6) into (1.4), and find that the constitutive parameters take the form

$$\varepsilon = \mu = \text{diag}\left[1, 1, |\mathbf{A}|^{-1}\right], \tag{1.9}$$

where diag[] indicates a diagonal matrix. Interestingly enough, by merely requiring that the in-plane tensors ε and μ are isotropic, we have simultaneously obtained that these tensors are equal to a unity matrix. This is, of course, not a coincidence: one can show that upon a general transformation, the two principal values of the constitutive tensors $\boldsymbol{\varepsilon}$ (or $\boldsymbol{\mu}$) are multiplied by factors $f = a_1/a_2$ and $1/f = a_2/a_1$, respectively; these factors are the eigenvalues of the matrix $\mathbf{A}\mathbf{A}^T/|\mathbf{A}|$. Eliminating transformation anisotropy thus leads to $f = 1$ and simultaneously—without any additional restrictions—to unity matrices in the in-plane part of the ε and μ tensors.

The TO media that are of the form (1.9) are often described as "isotropic" and "dielectric-only"; however, the use of these terms with respect to (1.9) and conformal transformations requires some qualification. The in-plane components of the constitutive tensors corresponding to the conformal mapping are identically unity. Nevertheless, such a transformation can be implemented with isotropic dielectrics if the polarization of the fields is restricted in the medium. With this restriction in place, the incident field only "sees" the relevant material components. In this case, the full transformation could be obtained with an isotropic dielectric if the electric field is constrained to be parallel to the z-axis (so that the magnetic field is transverse to the z-axis or, TM^z polarization).

The TO media implementing conformal maps therefore benefit from both being locally isotropic and non-magnetic, the latter being true for TM^z polarization devices only. The μ_z component that becomes relevant for TE^z polarization waves can be made equal to unity only in the very special and restrictive case of area-preserving maps[16]. Eliminating the need for magnetic response in TO devices is particularly beneficial for high-frequency (THz and optical) designs, where natural materials with magnetic properties are practically nonexistent, and magnetic metamaterials tend to exhibit non-negligible dissipation and dispersion.

The benefits of isotropy of the conformal transformation media deserve a separate discussion. On one hand, isotropic media are more abundant in nature than anisotropic ones, where they exist both as amorphous (disordered) molecular

media as well as crystals of the cubic crystal system. However, electromagnetic anisotropy is not such an exotic property in natural crystalline media, and, in fact, it can be easily found at optical frequencies in molecular crystals of lower than cubic symmetry. An example of using naturally anisotropic media for non-conformal TO can be found, for instance, in references [17, 18], which exploited the natural anisotropy of calcite to realize variations of a cloaking transformation.

It should be noted, however, that anisotropic dielectrics, such as calcite, require the electric field to be polarized transverse to the optical axis, and thus cannot be used when this polarization does not correspond to the desired mode of operation. Moreover, the indices of calcite are fairly low (indices of 1.66 and 1.49 for the extraordinary mode and ordinary mode, respectively), limiting the range of indices that can be accessed and therefore limiting the possible distortion induced by the transformation.

On the other hand, when designers turn to radio-frequency electromagnetic metamaterials in order to obtain properties not available in natural crystals, creating weak or even extreme anisotropy becomes readily achievable. In fact, anisotropic metamaterials can be more easily manufactured and in some cases offer lower loss tangents than their isotropic counterparts [19]. Medium isotropy, however, becomes indispensable when three-dimensional designs are considered, where propagating fields cannot be decoupled into pure TE and TM modes. In general, anisotropic media exhibit birefringence, that is, simultaneous propagation of two waves with different dispersion relations (the ordinary and extraordinary waves). In a later section, we explain how the concept of conformal transformation optics can be extended both rigorously and approximately into three dimensions, where the benefits of medium isotropy and carefully designed anisotropy are instrumental for the design of well-behaving electromagnetic devices.

1.3 Conformal Mappings and Complex Analysis of the Helmholtz Equation

Although a restrictive set of transformations, conformal mappings have particular value for 2D systems in that—as described above—the corresponding materials can be realized using isotropic dielectrics. Isotropic dielectrics can be low loss, even at infrared and visible wavelengths, and thus conformal maps are an attractive subset of TO transformations for optical devices. Even more importantly, isotropic media do not introduce birefringence, thus avoiding the issue of coupled multimode propagation. In relation to the design of electromagnetic devices, the term optical conformal mapping was coined to describe this approach [20]. We follow the development in [20] for this section.

Consider the fields in an inhomogeneous but isotropic dielectric. We constrain all variations of materials and fields to the x–y plane. With the assumption that the magnetic field lies within the plane, we can obtain a scalar wave equation for the non-vanishing component of the electric field:

$$\nabla \times \nabla \times E_z = -\varepsilon k_0^2 E_z \tag{1.10}$$

Applying the vector identity $\nabla \times \nabla \times \mathbf{F} = \nabla(\nabla \cdot \mathbf{F}) - \nabla^2 \mathbf{F}$ and assuming all field are invariant in z, Eq. (1.10) reduces to

$$\nabla^2 E_z + \varepsilon k_0^2 E = 0, \tag{1.11}$$

Defining the complex coordinate $z = x + iy$ and its complex conjugate $\bar{z} = x - iy$ (z is not to be confused with the out-of-plane z direction), we can further define the derivatives

$$\partial_z = \frac{1}{2}\left(\partial_x - i\partial_y\right) \quad \partial_{\bar{z}} = \frac{1}{2}\left(\partial_x + i\partial_y\right) \tag{1.12}$$

The Laplacian operator can be expressed in terms of the complex variables as

$$\nabla^2 = \left(\partial_{xx} + \partial_{yy}\right) = 4\partial_{z\bar{z}} \tag{1.13}$$

and the scalar Helmholtz equation can be written as

$$\left(4\partial_{z\bar{z}} + \varepsilon k_0^2\right) E_z = 0 \tag{1.14}$$

Suppose we can define a mapping $z' = x' + iy'$ that is explicitly independent of $\bar{z}$, i.e., $\partial_{\bar{z}} z' = 0$. Using (1.12), this condition simply becomes a restatement of the Cauchy-Riemann equations (1.5). Then we also have $\bar{z}' = \bar{z}'(\bar{z})$. Applying the chain rule we rewrite the differentials in (1.14) as

$$\partial_{z\bar{z}} = \left|\frac{dz'}{dz}\right| \partial_{z'\bar{z}'} \tag{1.15}$$

and the Helmholtz equation (1.14) can be written in the primed coordinates as

$$\left(4\left|\frac{dz'}{dz}\right| \partial_{z'\bar{z}'} + \varepsilon k_0^2\right) E_z = 0. \tag{1.16}$$

This last equation can be conveniently rewritten as

$$\left(4\partial_{z'\bar{z}'} + \varepsilon' k_0^2\right) E_z = 0 \tag{1.17}$$

where

$$\varepsilon' = \varepsilon |dz'/dz|^{-1}. \tag{1.18}$$

Therefore we can interpret the Helmholtz equation in distorted coordinates as the Helmholtz equation in Cartesian coordinates with an inhomogeneous dielectric loading. The optical conformal map can thus be seen as a special case of the general TO formulation, whereby the transformation is lumped into only one material parameter. Equation (1.17) is a special case of Maxwell's equations in curvilinear coordinates, and (1.18) is a special case of (1.1).

It should be pointed out that the success of the conformal mapping approach assumes the constrained 2D nature of the wave propagation, resulting in the scalar Helmholtz equation. With the restriction in polarization, an inhomogeneous, isotropic permittivity distribution (1.18) is all that is needed to achieve the transformation.

We note that the wave equation for TE^z polarization in a homogeneous dielectric is

$$\nabla^2 H_z + \varepsilon k_0^2 H_z = 0 \tag{1.19}$$

We might be led to believe that the conformal mapping could be perfectly implemented with an isotropic dielectric for both TM^z and TE^z polarizations. However, the wave equation in an inhomogeneous dielectric takes the form

$$\nabla \times \left(\varepsilon(x,y)^{-1} \nabla \times H_z\right) = -k_0^2 H_z, \tag{1.20}$$

which does not reduce to (1.19) unless we can ignore the spatial variation in ε. To implement this transformation properly, we would be forced to use μ. We will explore this validity of this approximation in a later section.

The use of complex analysis renders the effort of discovering conformal transformations a trivial matter. Leonhardt [20] proposed a simple mapping to create an all-dielectric cloak using this method. Others have found conformal mappings that act as collimators for point sources [21]. Nevertheless, the limitations of the optical conformal technique are two-fold. First, while finding conformal maps is straightforward, there is no straightforward algorithm to find a map that gives a desired device performance. Second, and perhaps more importantly, conformal transformations imply the transformation of all space. If we desire our device to fit within a finite region, we must truncate the mapping in such a way that we retain the desired functionality. This is by no means guaranteed; it has been shown that simply terminating the dielectric distribution makes the cloak described by Leonhardt highly visible [22], for example. To make sure our device functions correctly, we must impose certain boundary conditions on our governing differential equations. As we demonstrate in the next section, the imposition of boundary conditions drastically limits the applicability of purely conformal mapping

1.4 Extending Conformal Transformation Optics: Quasiconformal Mappings

The Riemann mapping theorem states that any simply connected domain may be conformally mapped to the unit disk. In essence, it guarantees that we can find a conformal map between any two domains by mapping each of them to each other through a mapping to the unit disk. However, as we discussed previously, much of the power of TO is determined by the transformation at the boundary of the

domain. For instance, we might require that our transformation does not introduce reflections or change the direction of a wave entering or exiting our transformed domain. These conditions introduce additional restrictions to our transformation [23]. The most straightforward way to satisfy these conditions is to stipulate that the coordinates are the same as free space on the boundary of our transformed domain (Dirichlet boundary conditions). At the very least, we should require that each side of our physical region is mapped to the same corresponding boundary in the virtual domain. Mathematically, we assign a vertex to the intersection of each arc in our physical domain, as shown in Fig. 1.2. We then stipulate that each of these vertices is mapped to a corresponding vertex in the virtual domain.

This extra constraint severely limits the scope of conformally equivalent domains. Specifically, once the sides of the quadrilateral domain have been specified, the region can only be mapped to another quadrilateral that shares the same conformal module. The conformal module M is simply the aspect ratio of the differential rectangle corresponding to a set of orthogonal coordinates. If the domain is rectangular, then M is the aspect ratio of the entire domain.

Another concern relates to the boundary conditions directly. While Dirichlet boundaries are ideal for most purposes, they may be incompatible with our requirement of orthogonality at all points in the mapped domain. If we simultaneously specify $x'(x)$ and M at the boundary, the problem becomes over-determined and we are not guaranteed that the mapping will be orthogonal at the boundary [24]. Instead, we require a combination of Dirichlet and Neumann boundaries to simultaneously fix the geometry of the transformed domain and maintain orthogonality on the boundary.

The Dirichlet component of the boundary conditions appear when we state that each arc in physical space corresponds to an edge in the virtual space, as shown in Fig. 1.2. Formally, we state that

$$\begin{aligned} x &= 0 \text{ on edge } D'A' \text{ and } x = L \text{ on edge } B'C' \\ y &= 0 \text{ on edge } A'B' \text{ and } x = L \text{ on edge } C'D' \end{aligned} \tag{1.21}$$

The Neumann component determines the position of the coordinate lines not specified by (1.21) and guarantees orthogonality on the boundary. The orthogonality condition on the other boundaries may be rewritten as

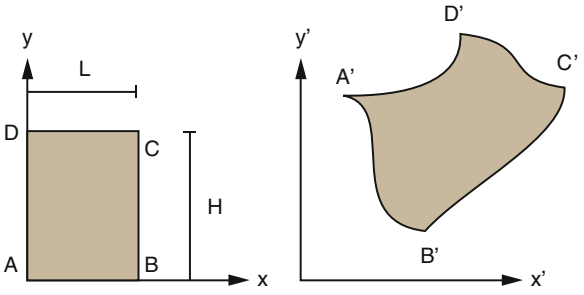

Fig. 1.2 Mapping between a rectangle Q and a quadrilateral domain R. The generalized quadrilateral R consists of four Jordan arcs and represents the physical domain. The vertices (A, B, C, D) in Q are mapped to vertices (A′, B′, C′, D′) in R, as shown to the right

$$\begin{aligned} \nabla_{\mathbf{x}'} x \cdot \mathbf{n} &= 0 \quad \text{on} \quad y = 0, H \\ \nabla_{\mathbf{x}'} y \cdot \mathbf{n} &= 0 \quad \text{on} \quad x = 0, L \end{aligned} \tag{1.22}$$

where $\mathbf{n}$ is the normal to the boundary curve. This formulation of the boundary conditions in terms of gradients in the physical space will be useful for our numerical solution process later. The important thing to note at this point is that the Neumann boundary condition allows coordinate lines to slide along the boundary to ensure orthogonality. This deviates from the normal Dirichlet specification and aberrations may result depending on the severity of the deviation.

We now return to our discussion of the conformal module. What happens when two domains do not share the same conformal module? We can consider the effect through an example using the tools of TO. We wish to map a given region of space onto a region that has a perturbation introduced, in this case a bump that protrudes into the domain from below, as shown on the right of the Fig. 1.3. This configuration has become known as the carpet cloak. If it is assumed that the lower boundary will correspond to a perfect electric conductor, then the mapping represents the design of a "cloak" that removes the effect of the perturbation from the reflecting surface [25].

For simplicity, we assume that the dimensions of the physical domain are one by one in arbitrary units. Note that the conformal modules for the two domains are not the same; for the case shown in Fig. 1.3, the conformal module of the physical domain is approximately $M = 0.68$. We have intentionally made the physical domain distortion large to create a substantially different conformal module and aid in visualization of the process. To compensate for the mismatch in conformal modules, we first map our virtual domain to an intermediate domain having the same conformal module as the physical domain. The simplest way to do this is with a uniform dilation of the form $y' = My$. We can then conformally map this intermediate domain onto the physical domain with a conformal transformation, so

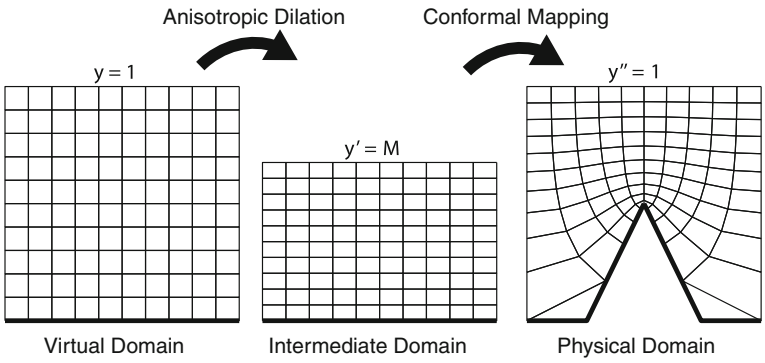

Fig. 1.3 Depiction of the quasi-conformal mapping using intermediate transformations. Lines of constant x and y (virtual domain coordinates) are shown in each domain. The *thick black line* represents a PEC boundary in each domain

that the functional dependence of the final transformed coordinates may be written as $\mathbf{x}'' = \mathbf{x}''(\mathbf{x}'(\mathbf{x}))$.

We can now consider the effect of the multiple transformations on the material parameters. The combined dilation and conformal mapping produce material tensors of the form:

$$\varepsilon'' = \mu'' = \mathrm{Diag}\left[M^{-1}, M, (M|\mathbf{A}_c|)^{-1}\right], \tag{1.23}$$

where $|\mathbf{A}_c|$ is the Jacobian of the conformal transformation between the intermediate and physical domains. For an assumed TM^z polarization, the conformal module provides an immediate measure of the anisotropy of the TO medium, as well as its required magnetic response, since $M = \sqrt{\mu_y/\mu_x}$. Written in terms of x'' and y'', (1.6) becomes

$$\begin{aligned} M x''_x &= y''_y \\ M y''_x &= -x''_y \end{aligned} \tag{1.24}$$

So that (1.8) becomes

$$M^{-2}\mathbf{x}''_{xx} + \mathbf{x}''_{yy} = \mathbf{0}. \tag{1.25}$$

The solution to this vector equation is the quasi-conformal (QC) map. The QC map minimizes the anisotropy of mappings between domains of differing modules [25]. In general, there is no closed-form solution to (1.25), and it must be calculated using a numerical approach. Historically, iterative methods [24, 26] were used. Since M is not known a priori, it must be calculated at each solution step and inserted into the discretized governing equations. Alternatively, the domains may be approximated by polygons and the mapping may be computed analytically via Schwarz-Christoffel transformations [27].

It is possible to simplify circumvent the issue of calculating M by reformulating the problem in terms of its inverse. Noting that the inverse of a conformal map is conformal, we can write:

$$\begin{aligned} x_{x''} &= M y_{y''} \\ M y_{x''} &= -x_{y''} \end{aligned} \tag{1.26}$$

Following the steps between (1.6) and (1.8), we find that we recover the vector Laplacian for the inverse problem:

$$\nabla^2_{\mathbf{x}'}\mathbf{x} = 0. \tag{1.27}$$

Since the inverse mapping is independent of M, it behooves us to calculate the inverse mapping and use (1.26) to determine M in a single step. The forward transformation and material parameters can then be calculated in a post-processing step. This can be done iteratively, as before, or in a single step using PDE solution software based on the finite element method [28]. We used the latter method for all

the mappings shown. Explicitly, we solved (1.27) subject to the boundary conditions (1.21) and (1.22) in the physical domain using the commercial software suite COMSOL.[1]

Returning to (1.23), we see that the cost of the QC map is immediately clear; the in-plane material tensor elements are no longer equal to each other. However, it is generally the case that small deformations of space create small perturbations to the conformal module of the physical domain. Li and Pendry [25] suggested that the small anisotropy be ignored in this case. Specifically, if we define local indices of refraction along the principle axes of the transformation according to

$$n_x = \sqrt{\mu_y \varepsilon_z} \quad n_y = \sqrt{\mu_x \varepsilon_z}, \tag{1.28}$$

the geometric average of these quantities is simply

$$n = \sqrt{\varepsilon_z} = (M|\mathbf{A}_c|)^{-1/2}. \tag{1.29}$$

To implement this transformation without magnetic materials, we set the in-plane tensor components to unity and use (1.29) for the out-of-plane component. We see that the resulting material parameters are simply those of an isotropic in-plane dilation $\mathbf{x}'' = \sqrt{M}\mathbf{x}'$:

$$\varepsilon'' = \mathrm{Diag}\left[1, 1, (M|\mathbf{A}_\mathbf{c}|)^{-1}\right] \tag{1.30}$$

All of the limitations of the isotropic approximation can be understood in terms of these intermediate transformations. Instead of correcting the aspect ratio of the virtual domain through anisotropic stretching, we have simply isotropically dilated the virtual domain. This is shown schematically in Fig. 1.4. Assigning the physical domain a side length of one, we see that the virtual domain now has a horizontal extent of $M^{-1/2}$ and a vertical extent of $M^{1/2}$. The intermediate transformation uniformly dilates virtual domain by another factor of $M^{1/2}$, and this region is then conformally mapped to the physical domain. Note that neither the aspect ratio nor the area of the virtual domain is the same as the physical domain.

We are now in a position to discuss the limitations of QC mapping compared with the general TO formulation. Any deviation from the strict TO prescription may result in a number of undesired wave propagation properties, or aberrations.

Even when properly implemented with the anisotropic material properties of (1.23), the QC map requires Neumann boundary conditions that allow coordinate lines to "slip" along the boundary of the transformed domain. This can lead to aberrations, since resulting material parameters are not those of free-space. In general, however, this type of error is small and can be mitigated by increasing the

[1] COMSOL is a multi physics simulation suite based on the finite element method (FEM). In addition to multiple physics models (e.g., electromagnetics), COMSOL allows the user to choose from a number of classical PDE models—including Laplace's equation. COMSOL also allows the user to generate new physics models or modify existing templates; a feature we exploit in Sect. 1.8.

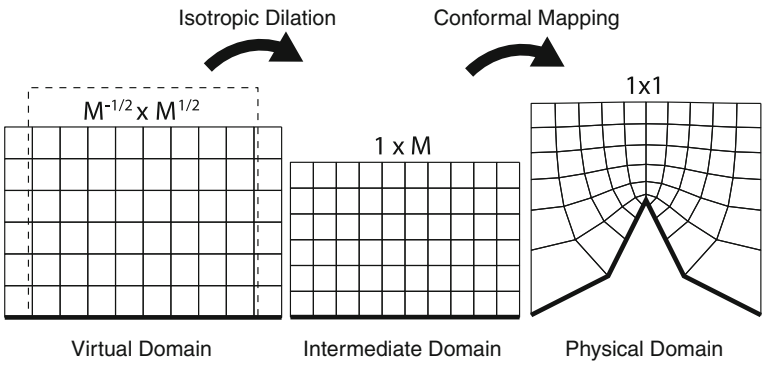

Fig. 1.4 Depiction of the effective transformation when the anisotropy in the domain is neglected. The dimensions of each domain are shown on the *top*. The *dashed square* around the virtual domain depicts the desired domain size compared to the effective size

size of the transformation domain. We will see the effect of slipping quantitatively when we study a QCM-derived optic.

A more significant problem arises from the isotropic approximation represented by the material prescription in (1.30). Since the virtual and physical domains are no longer the same size, the transformations no longer result in a strictly TO medium; instead, the resulting distributions of material parameters are only approximately correct, and will introduce a number of aberrations. The aberrations that result from the QC approximation will clearly depend on the severity of the transformation; larger deformations of space will inevitably result in larger changes in the module. However, even small changes in the module can disrupt the functionality of a QC device; it has been shown that carpet cloaks are always rendered visible when anisotropy is neglected, regardless of the size of the perturbation [29].

Despite its limitations, the QC method has found many applications. For example, those aberrations that might be manifest in ray-tracing analyses [29] can be obscured when the device is of the order of the wavelength of operation so that diffractive effects dominate device behavior. This is a common situation at microwave frequencies, and the QC method may be applied to flatten conventional dielectric lens—and parabolic reflector—antennas without significant loss in performance [30–32]. Alternatively, the method can be used to reshape antenna radiation patterns by reshaping the boundary of a domain containing the antenna [33].

We could also mitigate aberrations introduced by the QC method by exploiting extra degrees of freedom that might exist in the design. For instance, as we have shown, the QC map is required when the conformal module of the physical and virtual domains are not the same. This situation is typically the case for the carpet cloak, whereby the boundaries of the cloak intercept free space on three sides of the domain. But there may be other cases where the boundary conditions are less severe. We will demonstrate how this can be used via example.

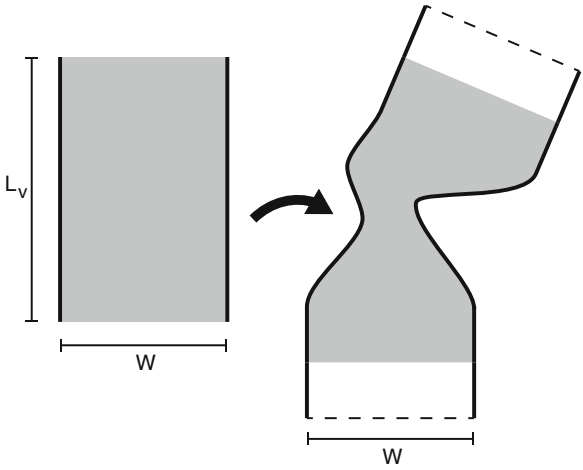

Fig. 1.5 Conformal mapping applied to a waveguide bend. A rectangle is mapped to a distorted waveguide on the *right*. The height of the rectangle is chosen such that it shares the same conformal module as the bent domain

Consider a metallic waveguide operating in the TE_{10} mode, as shown in Fig. 1.5. Inserting a kink or a bend in this waveguide will, in general, cause reflections. We could use TO to map this distorted region to a straight one and restore performance [34, 35]. However, we note that there is some ambiguity when we define our transformation; how long is our virtual domain? Theoretically, we could choose any length we wanted and performance would be unchanged up to a phase shift in the wave exiting the transformed region. We may as well set the length of the virtual domain to be equal to the conformal module of our physical domain. When we do this, the transformation becomes strictly conformal and we may use a dielectric-only implementation without cost [36, 37]. The calculation is straightforward; we first calculate the QC map numerically using an arbitrary length virtual domain. We can then calculate M according to (1.26). With this knowledge we simply make the substitution $dy \rightarrow Mdy$ to effectively scale our virtual domain. We will revisit this technique in the later sections to help alleviate some of the aberrations that appear in optics modified with QCTO.

1.5 Reshaping the Luneburg Lens with Quasiconformal Mappings

While the carpet cloak provides a good platform to demonstrate the functionality and simplicity of the quasi-conformal technique, it is not very interesting from an applications standpoint. Fortunately, other proposed TO designs are amenable to QC optimization. One of the more compelling of these designs is the modified Luneburg lens proposed by Schurig [38]. The Luneburg lens is one implementation of a family of spherically symmetric gradient index lenses that perfectly focuses images of concentric spherical surfaces onto one another in the geometric optics limit. The Luneburg lens is a perfect optical instrument, as defined in the ray

limit, focusing rays with no aberrations of any order. Typically, the radius of one of these spheres is taken to infinity so that parallel rays are imaged to points on the surface of the Luneburg lens. The most well-known (and simplest) index distribution was derived by Rolf Luneburg in 1944 [39]:

$$n(r) = \sqrt{2 - \left(\frac{r}{a}\right)^2} \quad 0 \leq r \leq a, \tag{1.31}$$

where n is the index of refraction, $r$is the radial coordinate, and a is the radius of the lens.

While the Luneburg lens can produce a perfect image, it has the key disadvantage that the image is spread over a spherical surface; any attempt to image onto a planar surface—as would be needed for most detector arrays—would result in extreme field curvature aberration. Schurig demonstrated that TO could be used to map a portion of the spherical image surface onto a flat one, thereby creating a flat focal plane without introducing any aberrations. Schurig's proposed transformation exhibited all of the aforementioned limitations of MM-enabled TO design, in particular requiring both anisotropic permittivity and permeability with relatively extreme ranges of values.

Given its advantages for imaging, the Luneburg lens represents a useful challenge for QC techniques, since an all-dielectric implementation could serve as a superior optical device. Kundtz and Smith [4] made use of the transformation illustrated in Fig. 1.6, in which the virtual space consists of the unperturbed Luneburg lens index distribution. In this 2D realization of the Luneburg, it is desired that the physical space be a quadrilateral, with one side corresponding to the flattened Luneburg. The virtual space is then distorted, bounded on the top, left, and right by straight lines, while the lower boundary is conformal to the curve of the lens, as shown in Fig. 1.6. The index distribution of the Luneburg is then inserted into the virtual space, where it multiplies the QCTO material distribution,

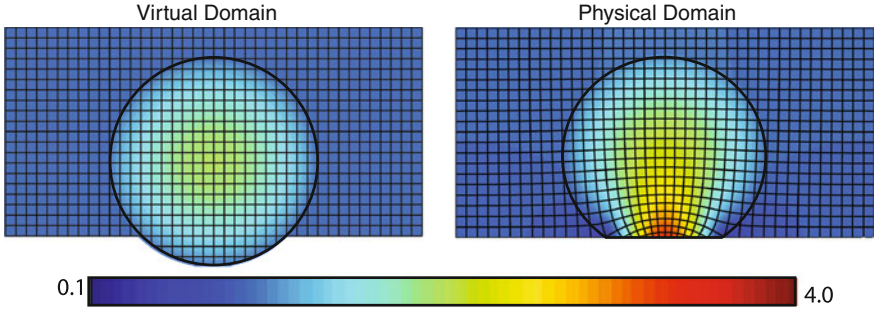

Fig. 1.6 Depiction of the QC transform for the Luneburg lens flattened for a 90° field-of-view in 2D. The *red shaded* region indicates the extent of the lens in the mapped rigions. (*left*) Virtual domain lens geometry showing lines of constant x and y and the Luneburg dielectric distribution. (*right*) Physical domain geometry showing lines of constant x and y and the transformed dielectric distribution. The *scale bar* on the *bottom* indicates the color scaling of the dielectric

and the inverse transformation used to flatten the Luneburg. Since it is assumed that a detector will terminate the fields on the flattened side, the same "slipping" boundary conditions can be applied on the lower edge as were used for the carpet cloak and (1.25) solved to determine the QC grid.[2] This same "flattening" procedure may be applied to other GRIN devices, such as the Maxwell fisheye lens [6], and can also be used as a method to correct field curvature in conventional optical systems [40].

The first implementation of the flattened Luneburg was performed at microwave frequencies using cut-wire dipoles to achieve the desired gradient index structure [4]. Recently, a similar design has been demonstrated in the infrared [10], showing the versatility of the QCTO technique.

While possibly of use for planar, chip-scale devices, the 2D lens has limited utility. An initial approach to extend the QCTO methodology to three dimensions was to take the 2D dielectric distribution from a QC transform and revolve it around an axis of symmetry [11, 12, 41]. However, as we show in the subsequent sections, this method does not produce a medium that corresponds to the correct transformed material parameters.

We begin by considering a quasiconformal transformation in the plane as depicted in Fig. 1.6, which we have determined using the tools of Sect. 1.4. We will assume that the deformation of the module is negligible $(M \approx 1)$ or that we have scaled the virtual domain to enforce the conformal condition as discussed at the end of the last section.[3]

In part, the simplicity of the QCTO method arises from the reduced dimensionality of the problem. The question then naturally arises: Can this simplicity be retained for other systems that exhibit some form of invariance? For instance, since many optical systems are rotationally symmetric about an optical axis, i.e., $\partial_\varphi = 0$, it is natural to apply the conformal mapping procedure in the $\rho - z$ plane, as depicted in Fig. 1.7. This procedure is slightly more involved than the Cartesian case because of the complications of working in cylindrical coordinates [38, 42].

We begin by considering our 2D mapping. Our coordinate transformation will be of the form:

$$\begin{aligned} \rho' &= \rho'(\rho, z) \\ \phi' &= \phi \\ z' &= z'(\rho, z) \end{aligned} \quad , \tag{1.32}$$

The Jacobian of the coordinate transformation is then

[2] Rigorously, the slipping boundary condition should be applied to all boundaries as specified in the last section. However, there is little practical difference between this and Dirichlet boundary conditions on the boundaries that are removed from the perturbation.

[3] We will explore the impact these methods have on lens performance in Sect. 1.7.

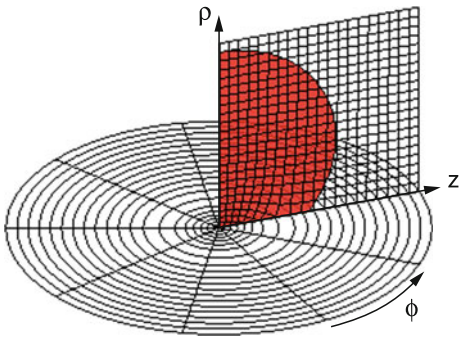

Fig. 1.7 Physical domain representation of the conformal mapping for the Luneburg Lens in the $\rho' - z'$ plane. The transformation is axially symmetric, so $\phi' = \phi$

$$\mathbf{A}_c = \begin{bmatrix} \rho'_\rho & 0 & \rho'_z \\ 0 & 1 & 0 \\ z'_\rho & 0 & z'_z \end{bmatrix}. \tag{1.33}$$

Following the procedure in Sect. 1.2 and making the substitutions $x \to \rho$ and $y \to z$, we find the transformed material parameters have the form:

$$\varepsilon'_c = \mu'_c = \text{Diag}\left[1, (|\mathbf{A}_c|)^{-1}, 1\right], \tag{1.34}$$

where $|\mathbf{A}_c|$ is now understood to be the Jacobian of the conformal transformation in the $\rho - z$ plane. While the material prescription is complete at this point, we pause to highlight a subtlety of working in non-Cartesian coordinate systems. The material parameters that we have derived are expressed in a coordinate basis. This is not the typical basis used to express physical quantities. To illustrate the complications this causes, consider the ϕ basis vector:

$$\varphi = \rho^{-1}(-\mathbf{x}\sin\phi + \mathbf{y}\cos\phi). \tag{1.35}$$

It is clear that ϕ is not normalized, implying that the material response of (1.34) will have a different physical meaning depending on the position in the mapped space. In particular, the in-plane components of (1.34) will require a nonvanishing response although they are expressed as unity in this basis. However, (1.35) suggests that we can convert to a unit basis through the change-of-basis matrix:

$$\mathbf{A}_{cu} = \text{Diag}[1, \rho, 1] \tag{1.36}$$

and back to a coordinate basis with:

$$\mathbf{A}_{uc} = \mathbf{A}_{cu}^{-1} = \text{Diag}\left[1, \rho^{-1}, 1\right] \tag{1.37}$$

To determine the resulting material parameters, we first use (1.37) to transform from the traditional unit basis into a cylindrical coordinate basis. In the coordinate basis, we perform our coordinate transformation (1.34) and then return to our (now transformed) unit basis with (1.36). We can therefore express the total transformation operator as:

$$\mathbf{A}_T = \mathbf{A}_{cu'}\mathbf{A}_c\mathbf{A}_{uc}, \tag{1.38}$$

or,

$$\mathbf{A}_T = \begin{bmatrix} \rho'_\rho & 0 & \rho'_z \\ 0 & \frac{\rho'}{\rho} & 0 \\ z'_\rho & 0 & z'_z \end{bmatrix}. \tag{1.39}$$

We can now use (1.1) to find that the transformed material parameters are:

$$\varepsilon = \boldsymbol{\mu} = \mathrm{Diag}\left[\frac{\rho}{\rho'}, \frac{1}{|\mathbf{A}_c|}, \frac{\rho'}{\rho}\right]. \tag{1.40}$$

As in the Cartesian case, the parameters are orthogonal; however, for the cylindrical case the in-plane tensor components are no longer those of free-space. The factor of ρ/ρ' arises from the fact that the differential volume element in cylindrical coordinates is a function of ρ. The transformed material parameters must compensate for this extra dilation of space between the virtual and physical coordinates. Additionally, the material parameters are orthotropic in cylindrical coordinates, which mean the principle axes are not constant but vary circumferentially. We have therefore not simplified our system by much, as we still require six material responses to implement this transformation, and we certainly cannot implement this transformation solely with a dielectric. However, as we shall see, this transformation is amenable to certain simplifying approximations.

1.6 Eikonal Approximations for Uniaxial Transformations

The Luneburg lens design is based on geometric optics, and it is natural to work within this framework when we consider the modified lens. In this regime, electromagnetic waves take the form of plane waves with spatially varying phase contours. At each point in space, these waves obey a local dispersion equation that is equivalent to that of a homogeneous medium. We begin by discussing the dispersion relation for the azimuthally uniaxial material of the previous section. Maxwell's Equations for time-harmonic fields take the usual form:

$$\nabla \times \mathbf{E} = j\omega\mu_0\mu\boldsymbol{H} \quad \nabla \times \mathbf{H} = -j\omega\varepsilon_0\varepsilon\boldsymbol{E} \tag{1.41}$$

We make the assumption that the fields can be written as

$$\begin{aligned} \mathbf{E} &= \mathbf{E}_0(\mathbf{r})e^{-jk_0\psi(\mathbf{r})} \\ \mathbf{H} &= \mathbf{H}_0(\mathbf{r})e^{-jk_0\psi(\mathbf{r})} \end{aligned}. \tag{1.42}$$

This is a "quasi-plane wave," where the spatial variation of phase is decoupled from that of the field amplitude. Inserting this form for the fields and defining $k \equiv \nabla\psi$, we find

$$\begin{aligned} \mathbf{k} \times \mathbf{H_0} - c_0\varepsilon_0\boldsymbol{\varepsilon}\mathbf{E}_0 &= -\frac{1}{ik_0}\nabla \times \mathbf{H}_0 \\ \mathbf{k} \times \mathbf{E}_0 + c_0\mu_0\boldsymbol{\mu}\mathbf{H}_0 &= -\frac{1}{ik_0}\nabla \times \mathbf{E}_0 \end{aligned} \tag{1.43}$$

Taking the limit $k_0 \to \infty$, the right-hand side of Eq. (1.43) go to zero and we recover the form of Maxwell's Equations in a homogeneous medium. A more rigorous discussion of the applicability of this approximation is given in [43, 44] Combining (1.43) in this limit yields:

$$\mathbf{k} \times \left(\boldsymbol{\mu}^{-1}(\mathbf{k} \times \mathbf{E}_0)\right) + \varepsilon\mathbf{E} = 0. \tag{1.44}$$

Making the definition $K_{ik} = \varepsilon_{ijk}k_j$, we can recast (1.44) as an operation on the electric field:

$$\left(\mathbf{K}\mu^{-1}\mathbf{K} + \varepsilon\right)\mathbf{E} = 0 \tag{1.45}$$

For a nontrivial solution to exist, Eq. (1.45) must have zero determinant. Enforcing this condition yields the local dispersion relation for our medium. In general, this task is complicated by the general anisotropy of $\boldsymbol{\varepsilon}$ and $\boldsymbol{\mu}$ [45], but it is greatly simplified in our case, where we constrain the material parameters to be uniaxial; i.e., of the form:

$$\begin{aligned} \boldsymbol{\mu} &= \mathrm{Diag}\left[\mu, \mu, \mu_z\right] \\ \varepsilon &= \mathrm{Diag}[\varepsilon, \varepsilon, \varepsilon_z]. \end{aligned}, \tag{1.46}$$

We find that the dispersion relation is a bi-quadratic equation that factors into two (nominally independent) modes:

$$\left(\frac{k_x^2 + k_y^2}{\mu\varepsilon_z} + \frac{k_z^2}{\mu\varepsilon} - 1\right)\left(\frac{k_x^2 + k_y^2}{\mu_z\varepsilon} + \frac{k_z^2}{\mu\varepsilon} - 1\right) = 0. \tag{1.47}$$

Since our system is diagonal in a cylindrical basis, we convert to cylindrical coordinates in (1.47) by making the substitution $(\mathrm{x}, \mathrm{y}, \mathrm{z}) \to (\mathrm{p}, \mathrm{z}, \varphi)$ to find:

$$\left(\frac{k_\rho^2 + k_z^2}{\mu\varepsilon_\phi} + \frac{k_\phi^2}{\mu\varepsilon} - 1\right)\left(\frac{k_\rho^2 + k_z^2}{\mu_\phi\varepsilon} + \frac{k_\phi^2}{\mu\varepsilon} - 1\right) = 0. \tag{1.48}$$

It is important to emphasize that the components of $\mathbf{k}$ do not correspond to the solutions to Maxwell's equations in cylindrical coordinates. Rather, they are simply the projections of the Cartesian wave vector onto a cylindrical basis, i.e.,

$$\begin{aligned} k_\rho &= k_x \cos(\phi) + k_y \sin(\phi) \\ k_\phi &= k_y \cos(\phi) - k_x \sin(\phi). \end{aligned} \tag{1.49}$$

These modes form uniaxial ellipsoidal surfaces in k-space that are equivalent to the extraordinary mode of a uniaxial dielectric. Unlike a uniaxial dielectric, however, there will not in general be an ordinary mode corresponding to anisotropic material. This form is only valid when two components of the constitutive tensors are equal in the eigenbasis of the material. For TO media, the TE and TM modes are identical since $\boldsymbol{\varepsilon} = \boldsymbol{\mu}$.

At this point, we note that the dispersion relation does not depend directly on the optical properties of the material. Rather, the relation is determined solely by the indices of refraction of the wave propagating along each of the principle axes of the material tensors. We label these unique indices

$$n_{\perp,TE} = \sqrt{\varepsilon_{||}\mu} \quad n_{\perp,TE} = \sqrt{\varepsilon\mu_{||}} \quad n_{||} = \sqrt{\varepsilon\mu}, \tag{1.50}$$

where the subscripts indicate whether the electric field (TE) or magnetic field (TM) is transverse to the optical axis. The subscripts $(\perp)$ and $(||)$refer to quantities perpendicular or parallel to the optical axis (z or ϕ in the examples above). Since Eq. (1.50) only specifies these three parameters for the four unique components of $\boldsymbol{\varepsilon}$ and $\boldsymbol{\mu}$, we are free to specify one of these material components to be equal to an arbitrary value α if we make appropriate substitutions to the other components. For instance, if we set $\mu' = \alpha$, then the other components become (in the cylindrical case):

$$\varepsilon' = \frac{\varepsilon\mu}{\alpha} \quad {\varepsilon_\phi}' = \frac{\varepsilon\mu_\phi}{\alpha} \quad \mu'_\phi = \alpha\frac{\mu_\phi}{\mu}. \tag{1.51}$$

In order to minimize the number of magnetic elements in our eventual design, we should choose $\alpha = \mu = 1$. This flexibility is general to uniaxial magneto-dielectric media, but for our TO-derived design, this approximation also retains the degeneracy of the dispersion relation so that waves of both polarizations follow the same trajectory in the medium.

The above procedure illustrates the great benefit of the QC method for 3D TO. While the material parameters derived directly from the TO algorithm are not particularly simple (three required magnetic responses), the symmetries of the mapping permit us to make a subsequent approximation that greatly reduces the complexity of the problem (one required magnetic response) [46].

This approximation is especially appropriate for the transformed Luneburg lens, since the original dielectric distribution was derived under geometric optics considerations. Using the techniques that we have developed in this and the preceding sections, we can determine the 3D reduced-parameter set for a flattened lens with 90° field of view, as shown in Fig. 1.8.

It is interesting to note that the only nonvanishing magnetic response (μ'_ϕ) is bounded between zero and unity throughout the transformed lens. Diamagnetic responses such as these can be implemented in a broadband fashion with

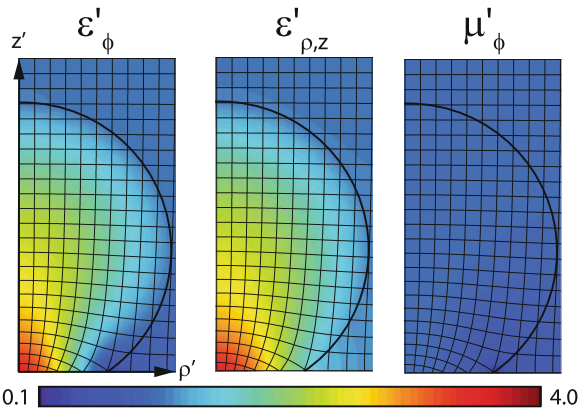

Fig. 1.8 Reduced-parameter material distribution for a flattened Lunburg lens. The other two components of μ' are unity

metamaterials, as shown in [47, 48], holding out the possibility of creating a transformed lens that operates over a wide band of frequencies. However, the lens as depicted does require $n_{||} = \sqrt{\varepsilon'_{\rho,z}} < 1$, which limits the possible performance of any implementation over a given frequency band due to causality. To circumvent this limitation, the background dielectric distribution could be raised, as suggested for the 2D carpet cloak in [25], and implemented in the carpet cloak and flattened Luneburg in [3] and [10], respectively. The Luneburg case is especially interesting since the Luneburg dielectric distribution itself may be altered according to [49] or [50] to provide a higher background dielectric for the transformation, as demonstrated by [5]. In this manner, the transformed Luneburg could still be coupled to free space without introducing refractive aberrations.

At this point, we have introduced a number of approximations to the general TO specification. Since lenses have well-defined metrics of performance, we can test the effectiveness of the QC mappings as well as our material approximations by evaluating the performance of these lenses. In the remaining sections of this chapter we will use a variety of numerical techniques to judge the effectiveness of these lenses.

1.7 The Hamiltonian Method

Ray-tracing is a useful tool for optically large problems in which diffraction effects may be ignored. Additionally, ray-tracing may be formulated in the language of Hamiltonian optics, and it may be possible to glean some insight into the performance of devices based upon the symmetries that they might possess.

We begin by considering each ray of light as a particle that follows a trajectory that satisfies the Hamiltonian

$$H(p_j, q_j) = 0. \tag{1.52}$$

The parameterized ray trajectory q_i (τ) is found by numerically integrating Hamilton's equations:

$$\begin{aligned} \dot{q}_i &= \frac{\partial H}{\partial p_i} \\ \dot{p}_i &= \frac{\partial H}{\partial q_i}. \end{aligned} \tag{1.53}$$

In Cartesian coordinates, the Hamiltonian is simply the local dispersion relation, and the conjugate momenta are simply the components of the normalized wave-vector **k**. Straightforward algorithms exist for ray-tracing in general impedance-matched media [51] and uniaxial media specifically [43]. However, we wish to exploit the symmetry of our system by performing our integration in cylindrical coordinates. We accomplish this by finding the Hamiltonian that preserves the form of Hamilton's equation [52]:

$$H = \frac{p_\rho^2 + p_z^2}{n_\perp^2} + \frac{p_\phi^2}{n_\perp^2 \rho^2}. \tag{1.54}$$

where we have used the indices of refraction along the principle axes of the material as defined by (1.50) and assumed degeneracy in the dispersion relation. This form of the Hamiltonian is important for two reasons. From Hamilton's equations we see that the coordinates are cyclic in ϕ:

$$\dot{p}_\phi = -\frac{\partial H}{\partial \phi} = 0. \tag{1.55}$$

so that p_ϕ is conserved along a ray. This implies that we can categorize rays based upon their initial angular momentum. Rays with zero angular momentum $\left(p_\varphi(0) = p_\varphi(\tau) = 0\right)$ obey a reduced Hamiltonian of the form

$$H = \frac{p_\rho^2 + p_z^2}{n_\perp^2}, \tag{1.56}$$

which is simply the Hamiltonian of a ray in an axially symmetric isotropic medium. The implication here is that the flattened Luneburg lens can be properly implemented with an isotropic dielectric only at normal incidence.

Extreme care must be taken in the numerical integration of (1.53), since the mapping itself is determined numerically. In the absence of a closed-form solution for the mapping, we must rely on an intelligent interpolation scheme to retrieve the material values and their spatial derivative as required by (1.53).

Fortunately, COMSOL provides us with the spatial derivatives of all solved quantities. However, these are derivatives in the virtual domain, and we require them in the physical domain for our ray-tracing.

From the chain rule, we see that

$$\partial_{i'} = \left(\partial_{i'} x^i\right)\partial_i = \mathbf{A}\partial_i. \tag{1.57}$$

With these quantities calculated on a regular grid, we can then use Hermite-cubic interpolation [42] to determine these quantities anywhere to high precision. We expect even higher accuracy could be achieved by using the same mesh and interpolation functions that are used internally by COMSOL.

In our study, we considered four distinct lenses based on two different transformations. The first transformation is based on the traditional QC mapping where the conformal module between domains is not preserved. The second transformation is based on the conformal (C) mapping where we have adjusted the height of the virtual domain to preserve the conformal module. From each of these transformations we construct two different lenses; one anisotropic, based on the proper transformed material equations, and one isotropic, which mimics the proper material parameters at zero field angle as shown by (1.56).

Figure 1.9 shows the root-mean-square (RMS) spot size for four different lens constructions: C isotropic and anisotropic and QC isotropic and anisotropic. At normal incidence (zero field angle), $p_\phi = 0$ and the ray paths for the anisotropic and isotropic lenses are degenerate. However, aberrations do appear in the lenses derived from the QC mapping. These aberrations are related to our neglection of in-plane anisotropy, as discussed in Sect. 1.4.

At normal incidence, all the rays pierce the top boundary of the cylindrical transformation domain without refractive aberration since $\mathbf{n} \times \mathbf{k} = 0$. Therefore, we can ignore the slight material inhomogeneity at this boundary as well as the isotropic scaling that occurs in the quasi-conformal approximation. However, we

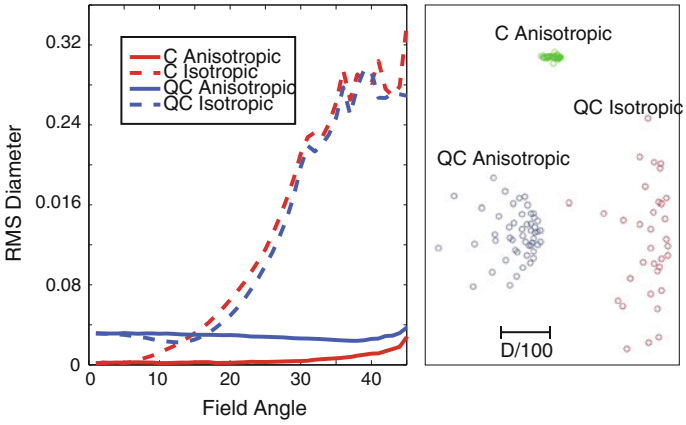

Fig. 1.9 *Left*—Spot Size comparison of various flattened luneburg lenses calculated with numerical ray-tracing. The spot size at each angle is the RMS average of 100 incident rays. *Right*—Spot diagrams at 30° for (*top*, *green*) a conformal, anisotropic lens, (*left*, *blue*) a conformal, anisotropic lens, and a (*right*, *red*) isotropic lenslens

cannot neglect the error induced by neglecting anisotropy. As we showed previously, the material anisotropy allowed us to stretch the mapped region to fit in the transformation domain. Without this stretching transformation, the Luneburg lens is no longer circular in the virtual domain. Instead, it will appear compressed along one axis. This leads to the nonvanishing spot at zero field angle.

Up to approximately 5°, the isotropic lens configurations are essentially identical to their anisotropic counterparts. However, we see that the isotropic lens performance drops dramatically for larger field angles. By comparison, the anisotropic lenses show consistent performance across the specified field of view. The conformally mapped lens shows the smallest spot size up to about 44°. At this point, a significant number of rays are now intercepting the domain from the side where the mismatch has been increased by scaling the virtual domain. This aberration could be reduced by increasing the lateral extent of the transformation domain, which would thereby increase the size of the optic.

The isotropic variants of lenses clearly show the largest aberrations for large field angles. We can clearly visualize the source of these aberrations by plotting the ray trajectories for anisotropic and isotropic lens variants as shown in Fig. 1.10. Rays that lie in the plane of the chief ray and the optical axis (meridional rays) are focused identically in both cases, as these are the rays with zero angular momentum. However, we see a dramatic difference in performance when we plot rays in an orthogonal plane that contains the chief ray. This is the sagittal plane, and these rays have maximum angular momentum. Only the anisotropic lens properly focusses in this case. Sagittal rays in the isotropic case appear to be focused to a point above the nominal focal plane so that the lens exhibits

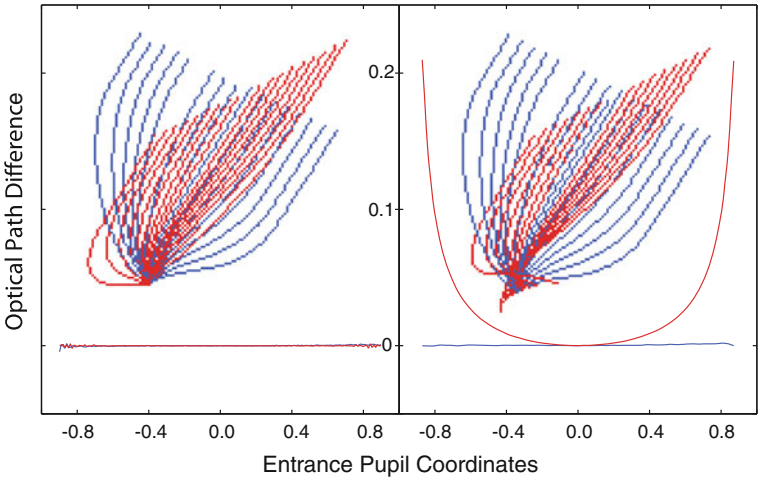

Fig. 1.10 OPD plots across the sagittal and meridional planes an anisotropic (*left*) and isotropic (*right*) lens. Inset are traces of rays in the meridional plane and sagittal plane. The sagittal rays and OPD are *red*, and the meridional rays and OPD are *blue*

astigmatism. Similar results were shown qualitatively in [46] for all three lenses and in [41] for the isotropic case.

We can connect these results to those of traditional optical lens design by calculating the optical path difference (OPD) for our rays. The optical path length (OPL) is simply the change in the eikonal across the path of each ray. From the definition of the eikonal, we then have:

$$OPL = \psi(\mathbf{r}_1) - \psi(\mathbf{r}_0) = \int_{\mathbf{r}}^{\mathbf{r}_1} \mathbf{k} \cdot d\mathbf{l}. \tag{1.58}$$

The OPD is calculated by subtracting the OPL of the chief ray from the OPL of all other rays. The OPD is plotted in Fig. 1.10 for both sagittal and tangential rays. As expected, the meridional rays have virtually no OPD in either case. However the sagittal rays in the isotropic case show an OPD plot that is symmetric about the optical axis. This is indicative of astigmatism, as previously mentioned.

Similar ray-tracing analysis may be performed for the carpet cloak [41]. Unsurprsingly, the revolved, all-dielectric implementation of the cloak fails to operate effectively at all angles of incidence. Interestingly, an extruded version of the all-dielectric carpet cloak appears to mitigate these aberrations to some extent [53, 54]. However, this technique may have some application, especially in designs with restricted incident angles. For instance, alternative cloaking designs—such as the conformal map introduced by Leonhardt [20] are only designed to work at one angle of incidence. If this structure is revolved around the axis parallel to this angle, performance is not diminished, as shown in [55].

1.8 Full-Wave Verification of Eikonal-Limit Designs

Ray-tracing is strictly valid only in the limit of vanishing wavelength. However, lenses are often used in situations where the aperture is only a few wavelengths across. In this regime, diffractive effects must be considered explicitly. Various models (physical optics, geometrical theory of diffraction) can account for these effects with increasing accuracy, but, to our knowledge, only full-wave numerical solvers can handle these effects in conjunction with the complicated gradients and anisotropy of TO-derived materials. Full-wave simulations also allow us to test the effects of the eikonal approximation that we made to the transformation.

The full-wave simulation of optically large, three-dimensional objects is a formidable task. For example, the finite element method (FEM) requires at least a few nodal points per wavelength to resolve gradients in electromagnetic fields. Memory requirements thus scale with the volume of the simulation domain.

Fortunately, these requirements can be drastically reduced for problems with azimuthal invariance, such as the lens considered above. We first expand the fields in a Fourier series in ϕ:

$$\begin{aligned}\mathbf{E} &= \sum_{m=-\infty}^{\infty} \mathbf{E}_m(\rho, z)e^{jm\phi} \\ \mathbf{H} &= \sum_{m=\infty}^{\infty} \mathbf{H}_m(\rho, z)e^{jm\phi}\end{aligned} \tag{1.59}$$

The orthogonality of the series permits us to solve for the fields associated with each mode individually. Moreover, we can make the substitution $\partial_\varphi \rightarrow jm$ in Maxwell's equations so that the problem is reduced to finding the 2D field pattern for each mode. This allows us to solve M small 2D problems sequentially instead of one large one.

To simulate a plane wave incident on the lens, we decompose the incident fields as in (1.59). The decomposition is facilitated by the introduction of the auxiliary vector potentials A and F to represent the two distinct polarizations of the incident wave (magnetic field or electric field transverse to the z-axis, respectively) [56]. For instance, an incident wave making an angle θ_i from the z-axis with the electric field in polarized in y may be expressed as

$$\begin{aligned}E_\rho &= \frac{-E_0}{k_0\rho\sin\theta_j}e^{jk_0\cos\theta_j}\sum_{m=-\infty}^{\infty} j^{1-m}J_m\left(k_0\rho\sin\theta_j\right)e^{jm\phi} \\ E_\phi &= E_0 e^{jk_0\cos\theta_j}\sum_{m=-\infty}^{\infty} J'_m\left(k_0\rho\sin\theta_j\right)e^{jm\phi}.\end{aligned} \tag{1.60}$$

In practice, the series must be truncated at some maximal wavenumber M. From the asymptotic form of Bessel functions, the series may be truncated without significant error when [57]

$$M = \text{ceil}[k_0\rho_{\max}\sin\theta_i] + 6, \tag{1.61}$$

where ceil[] is the integer ceiling operator. With these tools in place, we can now investigate the performance of our lenses. For each lens, we simulate an incident plane at 30° off-normal for apertures ranging from five to thirty wavelengths in diameter. Our performance metric is the spot size that encompasses 84 % of the energy in the focal plane, the same amount of energy contained in the primary lobe of a non-aberrated Airy disk. Use of this metric enables quick comparison between our lenses and the expected diffraction-limited performance of a lens with the same aperture and focal length.

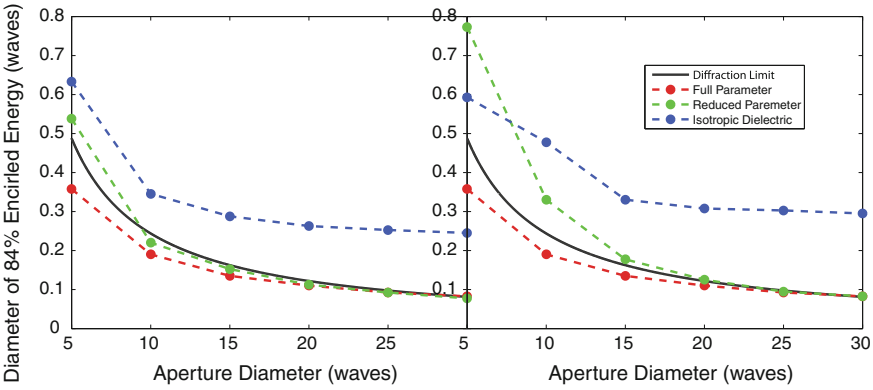

Fig. 1.11 Comparison of spot sizes for various lenses using FEM. *Left*—TE^z incidence. *Right*—TM^z incidence

In our study, we looked at three lenses derived from the same conformal transformation.[4] The first lens uses the full-parameter implementation given by (1.48). For this case, we also set the virtual-domain Luneburg material distribution to be

$$\varepsilon_L = \mu_L = \sqrt{2 - r^2}, \tag{1.62}$$

so that the lens performance is identical for both polarizations of the incident wave.

The second lens uses the eikonal approximation of (1.49). As opposed to the first lens, the Luneburg distribution is entirely dielectric so as to maintain the minimum amount of magnetic coupling in the design. Since this design is based on a high frequency approximation, we expect inferior performance as compared to the full transformation for small apertures, and then we expect it to approach the performance of the full transformation as the aperture size is increased. Additionally, we expect some difference in performance for the two polarizations of the incident wave.

The final lens represents an isotropic, dielectric-only implementation. Since this implementation neglects the anisotropy of the transformation, we expect it to show the worst performance for all aperture sizes. Additionally, we expect the spot size to asymptote to the nonzero value corresponding to the RMS size given by the ray-tracing analysis of the previous section.

The simulation results are plotted in Fig. 1.11. For comparison, we also plot the expected diffraction-limited spot diameter, given by

[4] Unlike in ray-tracing, we found no significant difference between the strictly conformal—and the quasi-conformal mapped—lenses since the RMS spot size of both lenses lies below the diffraction limit in the simulated range of aperture sizes.

$$D = 2.44\lambda f/\# \tag{1.63}$$

where $f/\# = f/D = 1/2$ is the f-number of the untransformed Luneburg lens. As expected, the full-parameter lens shows superior performance for all simulated aperture sizes. In fact, the spot size is a bit smaller than one would expect from (1.62), though both curves show the same behavior at short wavelengths.

At long wavelengths, the reduced-parameter and isotropic lenses have substantially degraded performance in comparison to the full-parameter implementation. However, the reduced-parameter implementation quickly regains performance as the aperture size is increased, so that by the time $D = 25\lambda$, the reduced parameter curve is practically indistinguishable from the full-parameter curve. On the other hand, the performance of the isotropic curve quickly asymptotes to a nonzero value as predicted by our previous ray tracing analysis.

Lens performance in the five- to ten-wavelength range is difficult to understand since the scale of material variation is of the order of the free-space wavelength. From simulations, it appears that the main performance limiting factor is reflections in the lens interior where the material variations are the most rapid; these reflections spread energy over the focal plane so that the diameter of 84 % encircled energy is larger than we would expect from qualitative examination of the spot diagrams in Fig. 1.12.

While the short-wavelength behavior of the reduced-parameter lens is diffraction limited, the spot diagram shown in Fig. 1.12 clearly differs from expected Airy disk. The full-parameter lens shows the same behavior at all frequencies; the

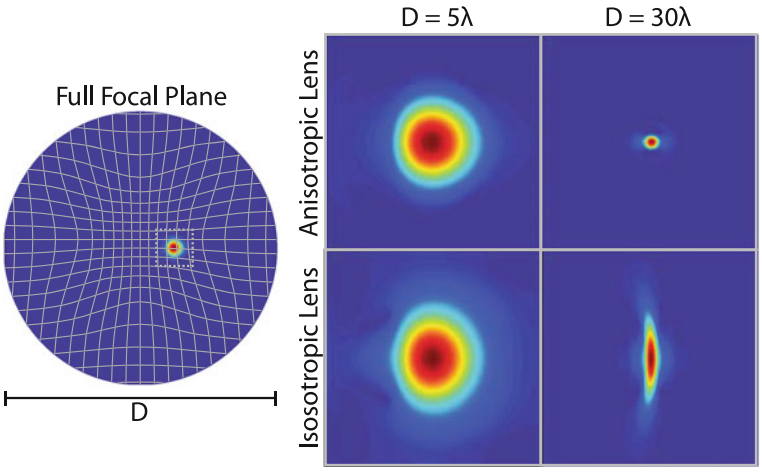

Fig. 1.12 Intensity plotted in the focal plane of each lens. (*Left*) Intensity over the full focal plane for a five wavelength, reduced parameter-set lens. A virtual domain grid is overlaid to show distortion in the focal plane. The *dotted gray square* indicates the relative dimensions of the spot diagrams on the right. (*right*, *top*) spot diagrams for the reduced-parameter lens for apertures of five and thirty wavelengths. (*right*, *bottom*) spot diagrams for the isotropic, dielectric-only lens at the five and thirty wavelengths

distortion in the spot is due to the mapping itself. This is unsurprising in light of the Neumann boundary conditions we enforced when generating the map. In the focal plane, the lines of constant ρ (virtual coordinates) are distorted to guarantee orthogonality in the mapping. To illustrate this distortion, we plot the virtual coordinates in the physical focal plane in Fig. 1.12. We see that an image near the center is demagnified, whereas an image toward the edge is slightly magnified. Additionally, an image of our 30° incident plane wave is compressed vertically, as we saw in our full-wave simulation previously. The only way to circumvent this problem is to specify the virtual domain points directly as done in [38].

1.9 Summary

In this chapter, we have discussed the QCM technique as it applies to the design of transformation optical devices. We have shown that the primary benefit of this technique is the reduction of complexity in the derived material parameters; only one material response is required in two dimensions, and three distinct responses are required in three dimensions. However, the quasi-conformal method does come at some cost. As we have demonstrated, the method is inherently approximate, and aberrations may manifest unless care is taken to mitigate them using the techniques that we have developed.

References

1. Pendry JB, Schurig D, Smith DR (2006) Controlling electromagnetic fields. Science 312:1780–1782. doi:10.1126/science.1125907
2. Schurig D, Pendry JB, Smith DR (2007) Transformation-designed optical elements. Opt Express 15:14772–14782
3. Liu R, Ji C, Mock JJ, Chin JY, Cui TJ, Smith DR (2009) Broadband ground-plane cloak. Science 323:366–369. doi:10.1126/science.1166949
4. Kundtz N, Smith DR (2010) Extreme-angle broadband metamaterial lens. Nat Mater 9:129–132. doi:10.1038/Nmat2610
5. Hunt J, Kundtz N, Landy N, Nguyen V, Perram T, Starr A, Smith DR (2011) Broadband wide angle lens implemented with dielectric metamaterials. Sensors-Basel 11:7982–7991. doi:10.3390/S110807982
6. Hunt J, Jang G, Smith DR (2011) Perfect relay lens at microwave frequencies based on flattening a maxwell lens. J Opt Soc Am B 28:2025–2029
7. Valentine J, Li JS, Zentgraf T, Bartal G, Zhang X (2009) An optical cloak made of dielectrics. Nat Mater 8:568–571. doi:10.1038/Nmat2461
8. Gabrielli LH, Cardenas J, Poitras CB, Lipson M (2009) Silicon nanostructure cloak operating at optical frequencies. Nat Photonics 3:461–463. doi:10.1038/Nphoton.2009.117
9. Gharghi M, Gladden C, Zentgraf T, Liu YM, Yin XB, Valentine J, Zhang X (2011) A carpet cloak for visible light. Nano Lett 11:2825–2828. doi:10.1021/Nl201189z
10. Hunt J, Tyler T, Dhar S, Tsai YJ, Bowen P, Larouche S, Jokerst NM, Smith DR (2012) Planar, flattened Luneburg lens at infrared wavelengths. Opt Express 20:1706–1713

11. Ma HF, Cui TJ (2010) Three-dimensional broadband ground-plane cloak made of metamaterials. Nat Commun 1:21. doi:10.1038/Ncomms1023
12. Ma HF, Cui TJ (2010) Three-dimensional broadband and broad-angle transformation-optics lens. Nat Commun 1:124. doi:10.1038/Ncomms1126
13. Fischer J, Ergin T, Wegener M (2011) Three-dimensional polarization-independent visible-frequency carpet invisibility cloak. Opt Lett 36:2059–2061
14. Ergin T, Fischer J, Wegener M (2011) Three-dimensional invisibility carpet cloak at 700 nm wavelengths. In: 2011 Conference on lasers and electro-optics (Cleo)
15. Ergin T, Stenger N, Brenner P, Pendry JB, Wegener M (2010) Three-dimensional invisibility cloak at optical wavelengths. Science 328:337–339. doi:10.1126/science.1186351
16. Xu HY, Zhang BL, Yu TY, Barbastathis G, Sun HD (2012) Dielectric waveguide bending adapter with ideal transmission: practical design strategy of area-preserving affine transformation optics. J Opt Soc Am B 29:1287–1290
17. Zhang BL, Luo, YA, Liu XG, Barbastathis, G (2011) Macroscopic invisibility cloak for visible light. Phys Rev Lett 106:Artn 033901. doi:10.1103/Physrevlett.106.033901
18. Chen XZ, Luo Y, Zhang JJ, Jiang K, Pendry JB, Zhang SA (2011) Macroscopic invisibility cloaking of visible light. Nat Commun 2:176. doi:10.1038/Ncomms1176
19. Urzhumov Y, Chen WC, Bingham C, Padilla W, Smith DR (2012) Magnetic levitation of metamaterial bodies enhanced with magnetostatic surface resonances. Phys Rev B 85:054430. doi:10.1103/Physrevb.85.054430
20. Leonhardt U (2006) Optical conformal mapping. Science 312:1777–1780. doi:10.1126/science.1126493
21. Turpin JP, Massoud AT, Jiang ZH, Werner PL, Werner DH (2010) Conformal mappings to achieve simple material parameters for transformation optics devices. Opt Express 18:244–252
22. Urzhumov YA, Kundtz NB, Smith DR, Pendry JB (2011) Cross-section comparisons of cloaks designed by transformation optical and optical conformal mapping approaches. J Opt-Uk 13:024002. doi:10.1088/2040-8978/13/2/024002
23. Rahm M, Cummer SA, Schurig D, Pendry JB, Smith DR (2008) Optical design of reflectionless complex media by finite embedded coordinate transformations. Phys Rev Lett 100:063903. doi:10.1103/Physrevlett.100.063903
24. Thompson JF, Soni Bk, Weatherill NP (1999) Handbook of grid generation. CRC Press, Boca Raton
25. Li JS, Pendry JB (2008) Hiding under the carpet: a new strategy for cloaking. Phys Rev Lett 101:203901. doi:10.1103/Physrevlett.101.203901
26. Knupp P, Steinberg S (1994) Fundamentals of grid generation. CRC Press, Boca Raton
27. Tang LL, Yin JC, Yuan GS, Du JL, Gao HT, Dong XC, Lu YG, Du CL (2011) General conformal transformation method based on Schwarz-Christoffel approach. Opt Express 19:15119–15126
28. Chang Z, Zhou XM, Hu J, Hu GK (2010) Design method for quasi-isotropic transformation materials based on inverse Laplace's equation with sliding boundaries. Opt Express 18:6089–6096
29. Zhang BL, Chan T, Wu BI (2010) Lateral shift makes a ground-plane cloak detectable. Phys Rev Lett 104:233903. doi:10.1103/Physrevlett.104.233903
30. Tang WX, Argyropoulos C, Kallos E, Song W, Hao Y (2010) Discrete coordinate transformation for designing all-dielectric flat antennas. Ieee T Antenn Propag 58:3795–3804. doi:10.1109/Tap.2010.2078475
31. Kong FM, Wu BII, Kong JA, Huangfu JT, Xi S, Chen HS (2007) Planar focusing antenna design by using coordinate transformation technology. Appl Phys Lett 91:253509 10.1063/1.2826283
32. Mei ZL, Bai J, Cui TJ (2011) Experimental verification of a broadband planar focusing antenna based on transformation optics. New J Phys 13:063028. doi:10.1088/1367-2630/13/6/063028

33. Garcia-Meca C, Martinez A, Leonhardt U (2011) Engineering antenna radiation patterns via quasi-conformal mappings. Opt Express 19:23743–23750
34. Roberts DA, Rahm M, Pendry JB, Smith DR (2008) Transformation-optical design of sharp waveguide bends and corners. Appl Phys Lett 93:251111. doi:10.1063/1.3055604
35. Rahm M, Roberts DA, Pendry JB, Smith DR (2008) Transformation-optical design of adaptive beam bends and beam expanders. Opt Express 16:11555–11567
36. Landy NI, Padilla WJ (2009) Guiding light with conformal transformations. Opt Express 17:14872–14879
37. Ma YG, Wang N, Ong CK (2010) Application of inverse, strict conformal transformation to design waveguide devices. J Opt Soc Am A 27:968–972
38. Schurig D (2008) An aberration-free lens with zero F-number. New J Phys 10:115034. doi:10.1088/1367-2630/10/11/115034
39. Luneburg RK, Herzberger M, Brown University. Graduate School (1944) Mathematical theory of optics. Providence, R.I
40. Smith DR, Urzhumov Y, Kundtz NB, Landy NI (2010) Enhancing imaging systems using transformation optics. Opt Express 18:21238–21251
41. Driscoll T, Lipworth G, Hunt J, Landy N, Kundtz N, Basov DN, Smith DR (2012) Performance of a three dimensional transformation-optical-flattened Luneburg lens. Opt Express 20:13262–13273
42. Birchenhall C (1994) Numerical recipes in C—the art of scientific computing. Econ J 104:725–726
43. Sluijter M, de Boer DKG, Braat JJM (2008) General polarized ray-tracing method for inhomogeneous uniaxially anisotropic media. J Opt Soc Am A 25:1260–1273
44. Sluijter M, de Boer DKG, Urbach HP (2009) Ray-optics analysis of inhomogeneous biaxially anisotropic media. J Opt Soc Am A 26:317–329
45. Damaskos NJ, Maffett AL, Uslenghi PLE (1982) Dispersion-relation for general anisotropic media. Ieee T Antenn Propag 30:991–993
46. Landy NI, Kundtz N, Smith DR (2010) Designing three-dimensional transformation optical media using quasiconformal coordinate transformations. Phys Rev Lett 105:193902. doi:10.1103/Physrevlett.105.193902
47. Magnus F, Wood B, Moore J, Morrison K, Perkins G, Fyson J, Wiltshire MCK, Caplin D, Cohen LF, Pendry JB (2008) A d.c. magnetic metamaterial. Nat Mater 7:295–297. doi:10.1038/Nmat2126
48. Wood B, Pendry JB (2007) Metamaterials at zero frequency. J Phys-Condens Mat 19:Artn 076208. doi:10.1088/0953-8984/19/7/076208
49. Gutman AS (1954) Modified luneberg lens. J Appl Phys 25:855–859
50. Morgan SP (1958) General solution of the luneberg lens problem. J Appl Phys 29:1358–1368
51. Schurig D, Pendry JB, Smith DR (2006) Calculation of material properties and ray tracing in transformation media. Opt Express 14:9794–9804
52. Jacob Z, Alekseyev LV, Narimanov E (2007) Semiclassical theory of the Hyperlens. In: 2007 Conference on Lasers & electro-optics/quantum electronics and laser science (Cleo/Qels 2007), Vols 1–5, pp 2095–2096
53. Halimeh JC, Ergin T, Mueller J, Stenger N, Wegener M (2009) Photorealistic images of carpet cloaks. Opt Express 17:19328–19336
54. Ergin T, Halimeh JC, Stenger N, Wegener M (2010) Optical microscopy of 3D carpet cloaks:ray-tracing calculations. Opt Express 18:20535–20545
55. Urzhumov Y, Landy N, Smith DR (2012) Isotropic-medium three-dimensional cloaks for acoustic and electromagnetic waves. J Appl Phys 111:053105. doi:10.1063/1.3691242
56. Balanis CA (1989) Advanced engineering electromagnetics. Wiley, New York
57. Andrease MG (1965) Scattering from bodies of revolution. Ieee T Antenn Propag 13:303–310

Chapter 2
Transformation Electromagnetics for Cloaking, Lensing, and Radiation Applications

Do-Hoon Kwon, Qi Wu and Douglas H. Werner

Abstract The transformation electromagnetics technique provides a powerful tool to electromagnetic and optical designers by offering a blueprint for creating novel devices that feature a variety of unconventional wave-material interaction properties. Combined with the recent advances in metamaterials technology, the coordinate transformation-based design methodology paves the way to realizing devices that perform entirely new functions or traditional functions in different geometrical configurations that are advantageous in practical applications. Here, transformation electromagnetics techniques are applied to the design of invisibility cloaks, lenses, beam controllers, and antennas. Each device design is illustrated with an example, including the associated specifications and performance expectations. For the two-dimensional embedded antenna application, a microwave metamaterial design is also presented.

2.1 Introduction

In 2006, transformation optics (TO) or transformation electromagnetics [1, 2] was introduced as a technique to control and manipulate interaction between electromagnetic fields and materials, offering an unprecedented degree of flexibility. This was enabled through the application of coordinate transformations in space from a simple, known electromagnetic phenomenon to a novel, envisioned wave-material

D.-H. Kwon
Department of Electrical and Computer Engineering, University of Massachusetts Amherst, Amherst, MA 01003, USA
e-mail: dhkwon@ecs.umass.edu

Q. Wu · D. H. Werner (✉)
Department of Electrical Engineering, Pennsylvania State University, University Park, PA 16803, USA
e-mail: dhw@psu.edu

D. H. Werner and D.-H. Kwon (eds.), *Transformation Electromagnetics and Metamaterials*, DOI: 10.1007/978-1-4471-4996-5_2,

interaction characteristic. In the context of TO, a coordinate transformation is interpreted as inhomogeneous and anisotropic compression and stretching of constituent materials. This "material interpretation" [3] is based on the form invariance of Maxwell's equations under coordinate transformations. The exact medium parameters that will physically realize the new phenomena in the transformed space are completely specified by the coordinate transformation definition.

Since its introduction, the TO technique has attracted a significant amount of interest both in the physics and engineering communities. The most significant contributing factor was the design [2] and experimental demonstration in the microwave regime [4] of invisibility cloaks. Since magnetic responses of natural materials are weak at optical wavelengths, a reduced set of medium parameters that do not require magnetic materials and optical cloak designs utilizing dielectric materials alone have been reported as ways to achieve the necessary electric response [5, 6]. Various properties of invisibility cloaks have been investigated such as the effect on an embedded source [7], induced surface voltages on a cloak's inner surface [8], sensitivity of cloak performance to medium parameter variations [9] and loss [10], and energy transport velocities [11]. Spatial variations of the ideal cloak parameters and use of engineered dispersion have been proposed to extend the bandwidth. Furthermore, coordinate transformations in non-Euclidean space were suggested as a possible pathway to overcoming the bandwidth limitation of Euclidean cloaks [12].

The original cloak was designed for three-dimensional (3D) spherical shell and two-dimensional (2D) cylindrical shell geometries. However, the TO design technique does not limit the shape of a cloak to these geometries. For example, 2D cloak designs of elliptic annular cross sections have been reported [13, 14]. Starting with the 2D square cloak [15], a variety of 2D polygonal annular cloak designs were presented [16, 17]. In addition, 2D cloaks having inner and outer cloak boundaries that are not geometrically similar were considered in Refs. [18–20], including an elliptic annular cloak having a uniform thickness [18].

The class of coordinate transformations used in cloak designs have the property that they are continuous across the cloak's outer boundary. Devices derived from such a class of transformations are inherently invisible to outside observers and thus cannot change the fields external to them. In Rahm et al. [21], a new class of transformations that allows discontinuities along device boundaries was introduced. An "embedded" coordinate transformation allows novel interactions between devices and waves with a great degree of flexibility. For example, 2D reflectionless beam shifters and splitters were presented in Rahm et al. [21]. Reflectionless beam bends [22] and waveguide bends [23, 24] have also been designed. 2D beam expander designs have been reported [25], but their performances were found to suffer due to reflections from the exit interface, which become larger as the expansion ratio increases. To overcome the impedance mismatch issue, a 3D beam expander that is reflectionless for a normal plane wave illumination and has a significantly improved impedance match for oblique illuminations was introduced in Emiroglu and Kwon [26].

Lenses represent one of the most fundamental of all optical devices, where traditional design approaches typically involve finding the appropriate curved interfaces of a constant-permittivity medium. In addition to the lens boundary profile, the TO technique allows the medium parameters of the lens to be used to achieve further design flexibility. TO lenses that convert diverging waves originating from an embedded source into a collimated beam or highly directive radiation, forming an image at infinity, were presented in Refs. [22, 27, 28]. For external electromagnetic sources, 2D focusing lenses with flat interfaces have been designed [22]. A simple compression of the coordinate along the lens axis was applied to change the profile or thickness of a curved-surface lens [29].

In 2000, Pendry showed that a flat homogeneous, isotropic material slab having relative effective permittivity and permeability values simultaneously equal to –1 operates as a perfect lens [30] that is capable of forming an image of the source beyond the conventional half-wavelength diffraction limit. This super resolution is the main driving force behind the research on negative-index materials (NIMs) and their metamaterial realizations. It was observed that the perfect lens can be interpreted as a TO device by employing a negative slope between the original and the transformed coordinates. The negative refraction phenomenon was experimentally verified in both the microwave [31] and optical [32] regimes. The flat perfect lens configuration was extended to cylindrical designs in Yan et al. [33]. Novel devices exploiting negative-index constituent media such as the anti-cloak [34], superscatterer [35], and superabsorber [36] have been reported. A class of coordinate transformations involving NIM constituent media result in "folded geometries" [37, 38]. For a scatterer outside of a cylindrical folded geometry, embedding a complementary anti-object inside the folded space led to the idea of cloaking-at-a-distance [39]. In addition, by using a complementary medium together with a restoring medium in a folded geometry, an illusion optics device can be designed, where an electromagnetic signature of a physical object can be replaced by that of a different object [40].

The TO technique has also been applied to radiation problems by antennas and arrays. In Kwon and Werner [41], the idea of cloaked antennas was proposed to restore the intended impedance and radiation characteristics of an antenna in a scattering environment. A TO medium for a 2D non-uniform circular array was designed and the array was shown to behave the same as a linear array [42]. The inverse function was demonstrated in Kwon [43], where a TO medium-embedded linear array of sources was designed to have the same scanning capability as a circular array operating in free space. An ultradirective radiation pattern was predicted from a line source by transforming a circular wavefront into a planar wavefront [44] and was subsequently validated by experiment [45]. Using a folded geometry, it was shown that the exact radiation pattern of a monopole antenna above a ground plane (*i.e.* vertically polarized maximum radiation at the horizon) can be reproduced by an embedded monopole inside a recess, such that there is no physical structure present above the ground plane [46].

Typical transformation media are comprised of magneto-dielectric materials with inhomogeneous and anisotropic parameters. Such complex medium

characteristics as well as the associated frequency dispersion are the main challenges to realizing practical TO-based devices. To alleviate difficulties associated with magnetic materials and narrow bandwidths of synthesized metamaterials, quasi-conformal TO (QCTO) was introduced, which is based on quasi-conformal coordinate transformations [47]. In QCTO, transformed grids in 2D are numerically generated such that the average anisotropy introduced by the transformation is minimized. If the anisotropy is low, the medium can be accurately approximated by an isotropic medium with a spatially varying index of refraction. Under a transverse electric (TE) polarization, the QCTO medium becomes non-magnetic, which can be realized using gradient index dielectric media. QCTO media can also have a significantly wider bandwidth compared with typical TO media. Using the QCTO technique, a ground plane cloak (or carpet cloak) design was presented and a broadband characteristic was predicted [47]. The cloaking function and broad operational bandwidth were validated by experiment in the microwave [48] and optical [49] regimes. The QCTO technique has been applied to change the shapes of lenses [50, 51], flatten a parabolic reflector [52], and obtain customized directive radiation patterns from an embedded isotropic radiator [53].

Several review articles are available on the TO and QCTO techniques [54–56]. Interested readers are referred to these papers and the references therein. This chapter presents basic TO and QCTO principles and their applications to cloaking, lensing, and radiation problems. The organization of this chapter is as follows. In Sect. 2.2, the two coordinate transformation-based design techniques are reviewed. Section 2.3 presents 2D invisibility cloak designs. Flat focusing lenses and beam control devices such as benders, splitters, polarization rotators, and expanders are treated in Sect. 2.4. Section 2.5 presents TO applications to antennas. Planar photonic device designs based on the QCTO technique are presented in Sect. 2.6. Finally, Sect. 2.7 provides a summary and conclusions.

2.2 Coordinate Transformation-Based Design Techniques

2.2.1 General Transformations for Magneto-Dielectric Media

The transformation optics/electromagnetics technique is built upon two key observations: (1) Maxwell's equations retain the same format under coordinate transformations in space, *i.e.* they are form-invariant under coordinate transformations [57], and (2) Maxwell's equations interpreted in different coordinate systems are equivalent to changing the medium parameters in the constitutive relationships [3]. An overview of the device design method based on coordinate transformations is presented in Cartesian coordinates, but the approach is valid in general non-orthogonal coordinate systems as well.

Consider a set of time-harmonic electric and magnetic fields **E** and **H** at an angular frequency ω in a Cartesian (x, y, z) coordinate system. Adopting the $e^{j\omega t}$ time convention, the fields satisfy Maxwell's curl equations

$$\nabla \times \mathbf{E} = -j\omega\boldsymbol{\mu}\mathbf{H},\ \nabla \times \mathbf{H} = j\omega\boldsymbol{\varepsilon}\mathbf{E} \tag{2.1}$$

at any source-free point. In (2.1), the constitutive relationships

$$\mathbf{B} = \boldsymbol{\mu}\mathbf{H}, \mathbf{D} = \boldsymbol{\varepsilon}\mathbf{E} \tag{2.2}$$

have been used to relate the two field intensities to the electric and magnetic flux densities **D** and **B** in terms of the electric permittivity tensor $\boldsymbol{\varepsilon}$ and the magnetic permeability tensor $\boldsymbol{\mu}$.

Figure 2.1 illustrates the TO design approach using a simple coordinate transformation to change the propagation path of a plane wave. Figure 2.1a depicts a plane wave propagating in the $+x$ direction, together with three ray paths. From the original Cartesian (x, y, z) system, consider a transformation to the (x', y', z') system described by

$$x' = x'(x, y, z),\ y' = y'(x, y, z),\ z' = z'(x, y, z). \tag{2.3}$$

An example of the transformed system is illustrated in Fig. 2.1b, where the original space is warped in the $-y$ direction in the region around $x' = 0$. All three ray paths in Fig. 2.1a follow constant-y paths in the original system. These straight lines are mapped to curved contours in the (x', y', z') system, which the ray paths in the deformed system will also follow, as shown in Fig. 2.1b.

Since Maxwell's equations are form-invariant under coordinate transformations, the two curl equations in the transformed system may be written as

$$\nabla' \times \mathbf{E}' = -j\omega\boldsymbol{\mu}'\mathbf{H}',\ \nabla' \times \mathbf{H}' = j\omega\boldsymbol{\varepsilon}'\mathbf{E}'. \tag{2.4}$$

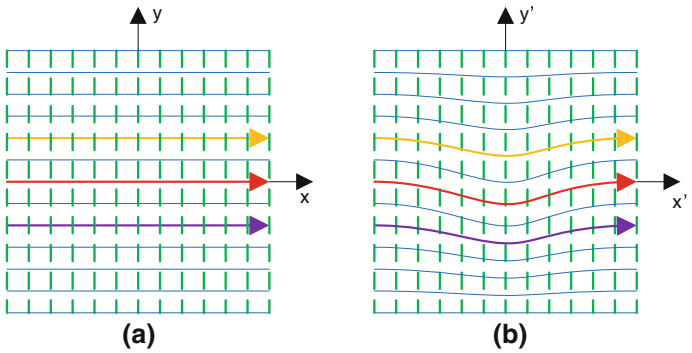

Fig. 2.1 An example coordinate transformation describing deformation of ray paths. **a** Three parallel rays in free space in the original Cartesian system. **b** Deformed ray paths following the transformed grid lines

Let the coordinate transformation be described by the 3 × 3 Jacobian matrix **A** defined as

$$\mathbf{A} = \begin{bmatrix} \partial x'/\partial x & \partial x'/\partial y & \partial x'/\partial z \\ \partial y'/\partial x & \partial y'/\partial y & \partial y'/\partial z \\ \partial z'/\partial x & \partial z'/\partial y & \partial z'/\partial z \end{bmatrix}. \tag{2.5}$$

Both field and medium quantities in the (x', y', z') system are related to their respective counterparts in the (x, y, z) system. Specifically, the medium tensor parameters, $\boldsymbol{\mu}'$ and $\boldsymbol{\varepsilon}'$, are related to $\boldsymbol{\mu}$ and $\boldsymbol{\varepsilon}$ in the original space by the following expressions [3, 57]

$$\boldsymbol{\mu}' = \frac{\mathbf{A}\boldsymbol{\mu}\mathbf{A}^T}{\det \mathbf{A}}, \; \boldsymbol{\varepsilon}' = \frac{\mathbf{A}\boldsymbol{\varepsilon}\mathbf{A}^T}{\det \mathbf{A}}. \tag{2.6}$$

In addition, the fields in the transformed system are given in terms of the fields in the original system via [57]

$$\mathbf{E}' = (\mathbf{A}^{-1})^T\mathbf{E}, \; \mathbf{H}' = (\mathbf{A}^{-1})^T\mathbf{H}. \tag{2.7}$$

A single electromagnetic phenomenon (e.g. plane wave propagation in free space in Fig. 2.1) may be described by either set of Maxwell's equations (2.1) or (2.4). Here, (2.4) allows an alternative interpretation different from describing the same phenomenon in a deformed space. The left-hand sides of the two equations in (2.4) still represent curl operations on the two field quantities, while the right-hand sides are multiplication of fields by medium tensors. Therefore, the set of Maxwell's equations given in (2.4) are equally valid in any coordinate system, not just the (x', y', z') system. If (2.4) is interpreted in a different coordinate system, say the original (x, y, z) system, it now describes a new electromagnetic phenomenon. Furthermore, the electric and magnetic medium specifications that are needed to realize this new phenomenon in the original space are represented by (2.6). This is known as the "materials interpretation" [3] of the coordinate transformation.

The materials interpretation allows electromagnetic phenomena envisioned in the transformed space to be realized in real space using the "transformation media" specified by (2.6). Hence, designing an electromagnetic/optical device that performs a given novel function reduces to finding an appropriate coordinate mapping that realizes it in the transformed space. This process provides device designers with an unprecedented control over wave-material interactions.

2.2.2 *Quasi-Conformal Transformation for Dielectric Media*

The construction of transformation media for the TO designs discussed above normally require anisotropic and inhomogeneous metamaterials with extreme parameters, which give rise to narrow bandwidths and high intrinsic losses arising from the resonant properties of inclusions [54]. One way to reduce material

complexities is to employ QC transformations, which can minimize the anisotropy of the constitutive materials, allowing all-dielectric implementations [47]. This approach was first introduced by Li and Pendry [47] for designing carpet cloaks, which have subsequently been experimentally demonstrated in both the microwave and optical wavelength regimes [48, 49, 58–61]. Thereafter, a variety of functional devices, including transformed Luneburg lenses, flat antennas, and zone plates, have been proposed and developed to provide enhanced performance when compared with their conventional counterparts [50, 53, 62–65]. To implement such QCTO designs, nearly-isotropic gradient index (GRIN) materials with a broad bandwidth and low losses can be utilized, leading to practical devices for a variety of applications [66–70].

The QC transformations can be employed to design many TO devices whose geometries do not contain sharp boundaries. Such mappings are numerically generated orthonormal grids, which can be implemented through a variety of different techniques [71]. For instance, QC mappings can be obtained with the aid of grid generation theory by using the Poisson transform algorithm [72, 73]. It has been shown that such mappings could also be found by solving the inverse Laplace's equation together with sliding boundary conditions [74]. These mappings approximately satisfy the Cauchy-Riemann equations, and can be regarded as possessing all the properties of a conformal mapping for the purposes of the TO approach [75–78]. In fact, the QC transformation can be exactly conformal if the original and transformed spaces have the same conformal module [79].

Consider a 2D transformation in the x–y plane, where the coordinate is invariant in the z-direction. Under these conditions, the Jacobian matrix reduces to a simpler form given in (2.8):

$$\mathbf{A} = \begin{bmatrix} \frac{\partial x'}{\partial x} & \frac{\partial x'}{\partial y} & 0 \\ \frac{\partial y'}{\partial x} & \frac{\partial y'}{\partial y} & 0 \\ 0 & 0 & 1 \end{bmatrix} \tag{2.8}$$

Based on the general TO design equations provided above, the resulting permittivity and permeability tensors become

$$\boldsymbol{\varepsilon}' = \frac{\varepsilon_0}{\det(\mathbf{A})} \begin{bmatrix} \left(\frac{\partial x'}{\partial x}\right)^2 + \left(\frac{\partial x'}{\partial y}\right)^2 & \frac{\partial x'}{\partial x}\frac{\partial y'}{\partial x} + \frac{\partial x'}{\partial y}\frac{\partial y'}{\partial y} & 0 \\ \frac{\partial y'}{\partial x}\frac{\partial x'}{\partial x} + \frac{\partial x'}{\partial y}\frac{\partial y'}{\partial y} & \left(\frac{\partial y'}{\partial x}\right)^2 + \left(\frac{\partial y'}{\partial y}\right)^2 & 0 \\ 0 & 0 & 1 \end{bmatrix} \tag{2.9}$$

$$\boldsymbol{\mu}' = \frac{\mu_0}{\det(\mathbf{A})} \begin{bmatrix} \left(\frac{\partial x'}{\partial x}\right)^2 + \left(\frac{\partial x'}{\partial y}\right)^2 & \frac{\partial x'}{\partial x}\frac{\partial y'}{\partial x} + \frac{\partial x'}{\partial y}\frac{\partial y'}{\partial y} & 0 \\ \frac{\partial y'}{\partial x}\frac{\partial x'}{\partial x} + \frac{\partial x'}{\partial y}\frac{\partial y'}{\partial y} & \left(\frac{\partial y'}{\partial x}\right)^2 + \left(\frac{\partial y'}{\partial y}\right)^2 & 0 \\ 0 & 0 & 1 \end{bmatrix} \tag{2.10}$$

It has been demonstrated that the QC mapping technique minimizes the anisotropic factor and produces coordinate transformations that approximately satisfy the Cauchy–Riemann conditions given in (2.11) [63, 64].

$$\frac{\partial x'}{\partial x} = \frac{\partial y'}{\partial y}; \ \frac{\partial y'}{\partial x} = -\frac{\partial x'}{\partial y} \tag{2.11}$$

For a TE-polarized wave with electric field normal to the plane of propagation, an effective average refractive index can be defined as

$$n' = \frac{\sqrt{n'_{xx} n'_{yy}}}{\sqrt{\varepsilon_0 \mu_0}} = \frac{\sqrt[4]{\mu'_{xx} \mu'_{yy}} \sqrt{\varepsilon'_{zz}}}{\sqrt{\varepsilon_0 \mu_0}} = \sqrt{\frac{\varepsilon'_{zz}}{\varepsilon_0}} = \frac{1}{\sqrt{\det(\mathbf{A})}} \tag{2.12}$$

As a result, the TO medium possesses non-magnetic and isotropic material parameters, facilitating their implementation and applications in practical devices.

Most of the common QC mappings define a transformation between an arbitrary geometry to a rectangle. As an example, Fig. 2.2a, b illustrate the mapping between a rectangular region with a circular protrusion in the original space and a rectangular domain in the transformed space. After specifying the source domain and choosing four points (A, B, C, and D) to be mapped to the rectangle corners (A′, B′, C′, and D′), the remaining boundary points in the original space are mapped to the four edges of the rectangle to define the boundary conditions. Note that assignment of corners to the QC transformation is critical to obtaining a design with practical material parameters. Either dense or sparse grid lines will result if a corner is mapped onto a straight line in the original domain due to the orthogonality requirement. With a transformation where the corners of the rectangle do not map to a hard corner in the original domain, the material parameters generally possess extremely high or low values. As a result, the geometry in the original domain is perturbed, if necessary, to create corners for assignment to the destination corners.

The orthogonality of the grids can be quantified by measuring the angle θ between two edges of each cell. The distribution of the angle parameter is demonstrated in Fig. 2.2c for the grids shown in (a). It is noticed that the mesh grids created by the QC mappings possess strong orthogonality within the entire transformation domain, indicating that the anisotropy of the medium has been minimized. The effective parameters of the transformation medium are found from the equations provided above. By assuming a TE-polarized wave, the TO devices can be characterized by the spatial distribution of refractive index. Figure 2.2d shows the resulting gradient refractive index profile for this transformation.

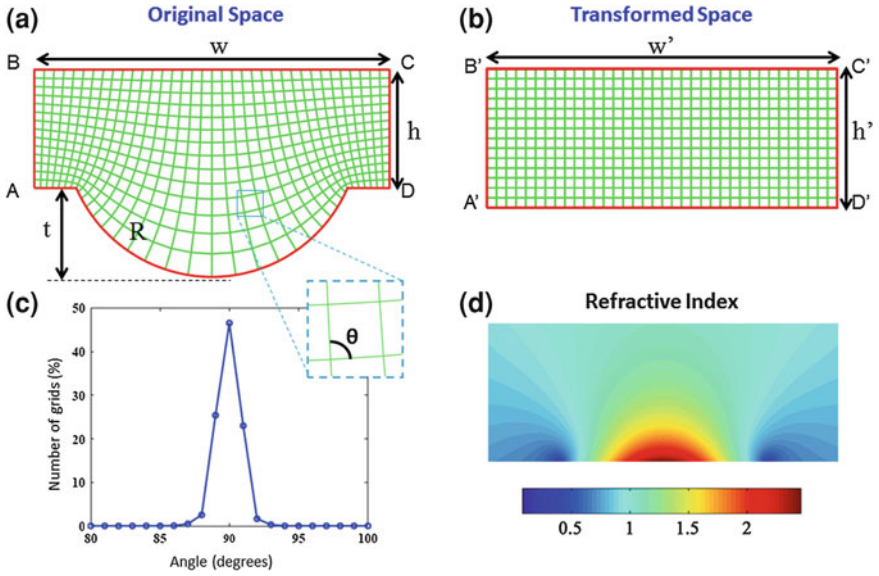

Fig. 2.2 A QC mapping transforms a rectangular domain with a circular protrusion in the original space into a rectangular domain in the transformed space. The resulting spatial grids from the mapping are illustrated by *green lines* in (**a**) and (**b**). The *bottom* surface of the *circle* in (**a**) is mapped into a straight segment along the bottom surface of the *rectangle* in (**b**). The distribution of degrees between two edges in each grid of the original space (**c**). The refractive index profile for this QC transformation (**d**). The interior region of the domain in the original space consists of free space

2.3 Electromagnetic Invisibility Cloaks

2.3.1 2D Annular Cloaks

The original 2D invisibility cloak [80] was designed and validated for a circular annular shape. Cross sections of cloaks are not limited to a circular annulus, however, which is not a very convenient geometry from a practical viewpoint. Other cloak geometries can be obtained using appropriate coordinate transformations that involve non-circular cross sections in the original system. Here, designs for an eccentric elliptic annular cloak [13] and a constant-thickness cloak for elliptical cloaked regions [18] are presented.

An eccentric elliptic annular cloak is defined by the inner and outer boundaries of ellipses with centers that are not co-located. Such geometries are conveniently treated in a special coordinate system (q_1, q_2, q_3) defined in terms of Cartesian coordinates (x, y, z) as

$$(q_1, q_2, q_3) = \left(\sqrt{\left(\frac{x - q_1 x_c}{a}\right)^2 + \left(\frac{y - q_1 y_c}{b}\right)^2}, \tan^{-1} \frac{(y - q_1 y_c)/b}{(x - q_1 x_c)/a}, z \right). \quad (2.13)$$

Figure 2.3a illustrates the (q_1, q_2, q_3) system. Constant-q_1 contours are a family of ellipses with a constant axial ratio b/a, whereas a family of constant-q_2 radial lines extend from the origin O. It is noted that the (q_1, q_2, q_3) system is not an orthogonal coordinate system. For any given q_1, the center of the ellipse is located at $(x, y) = (q_1 x_c, q_1 y_c)$.

To create an annular cloak, we transform the elliptic cylindrical region $q_1 \leq s$ ($s > 1$) in the original system into an annular region $1 \leq q_1' \leq s$ in the transformed system, i.e.,

$$(q_1', q_2', q_3') = \left(1 + \frac{s-1}{s} q_1, q_2, q_3\right), \; 0 \leq q_1 \leq s; \quad (2.14)$$

$$(q_1', q_2', q_3') = (q_1, q_2, q_3), \; q_1 > s. \quad (2.15)$$

The transformed (q_1', q_2', q_3') coordinate system is illustrated in Fig. 2.3b. The coordinate origin O is mapped into the shaded region of elliptic cross section ($q_1' \leq 1$). Moreover, the transform (2.14) is continuous across the outer cloak boundary $q_1 = q_1' = s$.

The medium parameters of the cloak are obtained in terms of the design parameter s and the coordinate system definitions. In this study, the unit vectors are defined along the coordinate axes via

$$\hat{q}_i = \frac{\partial \mathbf{r}/\partial q_i}{|\partial \mathbf{r}/\partial q_i|}, \; \hat{q}_i' = \frac{\partial \mathbf{r}'/\partial q_i'}{|\partial \mathbf{r}'/\partial q_i'|}; \; i = 1, 2, 3, \quad (2.16)$$

where $\mathbf{r} = \hat{x}x + \hat{y}y + \hat{z}z$ and $\mathbf{r}' = \hat{x}x' + \hat{y}y' + \hat{z}z'$ are position vectors in the original and transformed coordinates, respectively. Expressed in the (q_1', q_2', q_3') system, the elements of the relative permittivity tensor $\boldsymbol{\varepsilon}'$ are computed following the standard procedure in Pendry et al. [2] and found to be

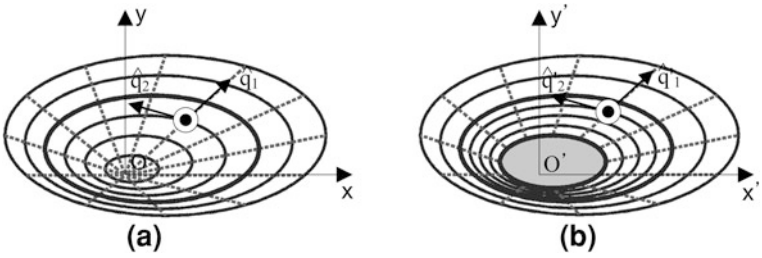

Fig. 2.3 Coordinate systems for the eccentric elliptic annular cloak design. **a** The original system. **b** The transformed system. Reprinted with permission from Kwon and Werner [13]. Copyright 2008, American Institute of Physics

$$\begin{aligned}\varepsilon'_{11} &= \frac{1}{\hat{q}_3 \cdot \hat{q}_1 \times \hat{q}_2} \frac{q'_1 - 1}{q'_1},\ \varepsilon'_{12} = \varepsilon'_{21} = -\frac{\hat{q}_1 \cdot \hat{q}_2}{\hat{q}_3 \cdot \hat{q}_1 \times \hat{q}_2}, \\ \varepsilon'_{22} &= \frac{1}{\hat{q}_3 \cdot \hat{q}_1 \times \hat{q}_2} \frac{q'_1}{q'_1 - 1},\ \varepsilon'_{33} = \hat{q}_3 \cdot \hat{q}_1 \times \hat{q}_2 \left(\frac{s}{s-1}\right)^2 \frac{q'_1 - 1}{q'_1}.\end{aligned} \tag{2.17}$$

The relative permeability tensor $\boldsymbol{\mu}'$ is identical to $\boldsymbol{\varepsilon}'$ and all remaining tensor elements are equal to zero. These parameters can be interpreted conveniently in the Cartesian (x, y, z) system as the constituent medium specification for the cloak. This conversion is achieved by way of another coordinate transformation from $(q'_1,\ q'_2,\ q'_3)$ to (x, y, z) using an appropriate Jacobian matrix, which is expressed in terms of the unit vectors defined in Fig. 2.3. Specifically, the Cartesian medium tensor $\boldsymbol{\varepsilon}$ is given by

$$\boldsymbol{\varepsilon} = \sum_{i=1}^{3} \sum_{j=1}^{3} \frac{\varepsilon'_{ij} \hat{q}'_i (\hat{q}'_j)^T}{\left|\hat{q}'_3 \cdot \hat{q}'_1 \times \hat{q}'_2\right|}, \tag{2.18}$$

where each unit vector is written as a column vector and the superscript T denotes the transpose operator.

The cloaking performance is numerically tested using COMSOL Multiphysics. Figure 2.4 shows snapshots of the $\hat{z}$-directed total magnetic field in the x–y plane when a plane wave in a transverse magnetic (TM) polarization with its propagation direction making a $-60°$ angle with the $+x$ axis illuminates an elliptic perfect electric conducting (PEC) cylinder. The magnetic field amplitude of the incoming plane wave is 1 A/m. The semi-axes of the cylinder are equal to $a = 0.1$ m and $b = 0.05$ m. Its center is located at $(x_c, y_c) = (0.025\text{ m}, 0.025\text{ m})$. The frequency of the time-harmonic incident wave is 4.0 GHz, so that the scatterer measures 2.67λ and 1.33λ along the major and minor axes, respectively. The design parameter s is set to 2, so that the outer elliptic boundary of the cloak measures $5.33\lambda \times 2.66\lambda$, centered at (0.05 m, 0.05 m). Inner and outer boundary positions of the cloak are indicated by black contours in Fig. 2.4. Figure 2.4a shows the total field when a bare PEC cylinder scatters the incoming plane wave. Scattered waves are generated in every direction. A strong standing wave pattern is created in the backscattering direction and a shadow is cast in the forward direction. In Fig. 2.4b, the scatterer is enclosed within the cloak and subject to the same incident plane wave. It is observed that the incident field is guided around the scatterer and recovered unperturbed at any point outside the cloak. The scatterer and cloak geometries as well as the incident field do not possess any mirror or rotational symmetry. At the design frequency, the cloak is capable of hiding the enclosed region when illuminated from any direction, which is supported by the numerical simulation results.

The second non-circular annular cloak design that will be considered is comprised of a uniform-thickness coating around an elliptic cylinder [18]. Consider a cylinder to be cloaked having an elliptic cross section S (its boundary denoted by ∂S) with semi-axes a and b centered at the origin. In order to design a uniform-thickness cloak,

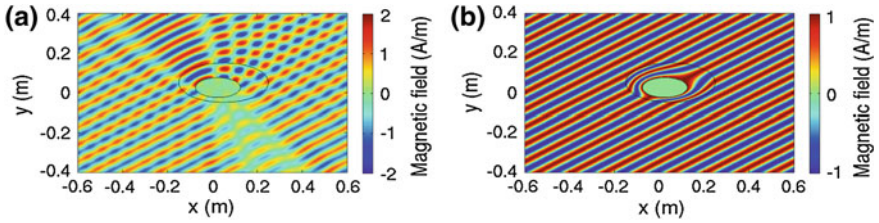

Fig. 2.4 Snapshots of the total magnetic field for a 2D eccentric elliptic annular cloak due to an elliptic conducting cylinder subject to a plane wave illumination. **a** Bare conducting cylinder exposed to incoming plane wave. **b** The same cylinder enclosed by the cloak

it is convenient to define a new coordinate system outside ∂S, where one coordinate measures the shortest distance to ∂S. Inside ∂S, a system similar to (2.13) can be used. Hence, a composite (q_1, q_2, q_3) coordinate system is defined as

$$(q_1, q_2, q_3) = \left(\sqrt{\left(\frac{x}{a}\right)^2 + \left(\frac{y}{b}\right)^2}, \tan^{-1}\frac{y/b}{x/a}, z \right), \; q_1 \leq 1, \tag{2.19}$$

$$(q_1, q_2, q_3) = \left(\sqrt{(x - x_s)^2 + (y - y_s)^2} + 1, \tan^{-1}\frac{y_s/b}{x_s/a}, z \right), \; q_1 > 1. \tag{2.20}$$

In (2.20), at any point (x, y) in the x–y plane outside ∂S, (x_s, y_s) is the closest point on ∂S. In other words, a line through (x_s, y_s) that is normal to the elliptic boundary ∂S passes through (x_s, y_s). Outside ∂S $(q_1 > 1)$, q_1 is the distance between (x, y) and (x_s, y_s) plus one, and q_2 takes the value of q_2 at (x_s, y_s).

The composite coordinate system is illustrated in Fig. 2.5a. The two types of systems join at ∂S, which is indicated by a dash-dot line. In $q_1 > 1$, constant-q_1 (solid) curves are no longer ellipses. Constant-q_2 (dashed) contours are line segments originating from O having a slope discontinuity at $q_1 = 1$. Both inside and

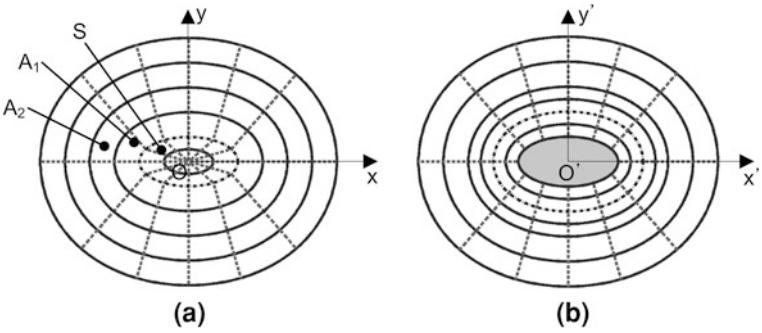

Fig. 2.5 Composite coordinate system for designing a uniform-thickness cloak. **a** The original system. **b** The transformed system. Reprinted with permission from Kwon and Werner [18]. Copyright 2008, American Institute of Physics

outside ∂S, the unit vectors defined along the coordinate directions are found from (2.16).

With the coordinate system definitions in place, a proper transformation needs to be determined. Let the cloak fill the region of uniform thickness T from $\partial S\,(q_1 = 1)$. Suppose this annular cloak is composed of a union of two annular regions A_1 and A_2 having thicknesses T_1 and T–T_1, respectively. These two annular regions are illustrated in Fig. 2.5a. We introduce a transformation that maps S to A_1 and $A_1 + A_2$ to A_2. Then, $S + A_1 + A_2$ in the original (q_1, q_2, q_3) system is mapped into $A_1 + A_2$ in the transformed $(q_1',\ q_2',\ q_3')$ system so that the intended cloaked region S is completely excluded. The transformed coordinate system is illustrated in Fig. 2.5b with the inner and outer cloak boundaries indicated by thick solid contours. For a point $(x, y) \in S$ in the original system and the associated transformed point $(x', y') \in A_1$ in the transformed system, mapping S into A_1 is realized using

$$\left(q_1', q_2', q_3'\right) = (1 + T_1 q_1, q_2, q_3). \tag{2.21}$$

Note that the origin $O\,(q_1 = 0)$ is transformed to $\partial S\,(q_1' = 1)$ and $\partial S\,(q_1 = 1)$ is mapped to the interface between A_1 and A_2 $(q_1' = 1 + T_1)$. Using the unit vectors and the mapping (2.21), the scale factors Q_i in the direction of $\hat{q}_i'$ can be computed [2]. Subsequently, in A_1, the elements of $\boldsymbol{\varepsilon}'$ in the (q_1', q_2', q_3') system are found to be

$$\begin{aligned}
\varepsilon_{11}' &= \frac{1}{\hat{q}_3 \cdot \hat{q}_1 \times \hat{q}_2} \frac{\rho_s\left(q_1' - 1\right)}{\left[\rho_s + \left(q_1' - 1\right)\right]\sqrt{x_s^2 + y_s^2}},\ \varepsilon_{12}' = \varepsilon_{21}' = -\frac{\hat{q}_1 \cdot \hat{q}_2}{\hat{q}_3 \cdot \hat{q}_1 \times \hat{q}_2}, \\
\varepsilon_{22}' &= \frac{1}{\hat{q}_3 \cdot \hat{q}_1 \times \hat{q}_2} \frac{\left[\rho_s + \left(q_1' - 1\right)\right]\sqrt{x_s^2 + y_s^2}}{\rho_s\left(q_1' - 1\right)},\ \varepsilon_{33}' = \hat{q}_3 \cdot \hat{q}_1 \times \hat{q}_2 \frac{\rho_s\left(q_1' - 1\right)\sqrt{x_s^2 + y_s^2}}{T_1^2\left[\rho_s + \left(q_1' - 1\right)\right]}
\end{aligned} \tag{2.22}$$

where ρ_s is the radius of curvature of the constant-q_1 curve at (x_s, y_s). All remaining tensor elements are equal to zero. For (x, y) in $A_1 + A_2$ and (x', y') in A_2, only the coordinate q_1 needs to be transformed. One possible transformation for mapping $A_1 + A_2$ into A_2 is

$$\left(q_1', q_2', q_3'\right) = \left(1 + T_1 + \frac{T - T_1}{T}(q_1 - 1), q_2, q_3\right). \tag{2.23}$$

From (2.23), it is recognized that $\partial S\ (q_1 = 1)$ is mapped to the boundary between A_1 and A_2 $(q_1' = 1 + T_1)$, making the overall transformation continuous across $q_1 = 1$. The outer boundary of the cloak $(q_1 = 1 + T)$ is mapped onto itself, so that the cloak boundary becomes a reflectionless interface. The permittivity tensor parameters in A_2 are found to be

$$\begin{aligned}
\varepsilon_{11}' &= \frac{T - T_1}{T} \frac{\rho_s + (q_1 - 1)}{\rho_s + \left(q_1' - 1\right)},\ \varepsilon_{22}' = \frac{T}{T - T_1} \frac{\rho_s + \left(q_1' - 1\right)}{\rho_s + (q_1 - 1)}, \\
\varepsilon_{33}' &= \frac{T}{T - T_1} \frac{\rho_s + (q_1 - 1)}{\rho_s + \left(q_1' - 1\right)}
\end{aligned} \tag{2.24}$$

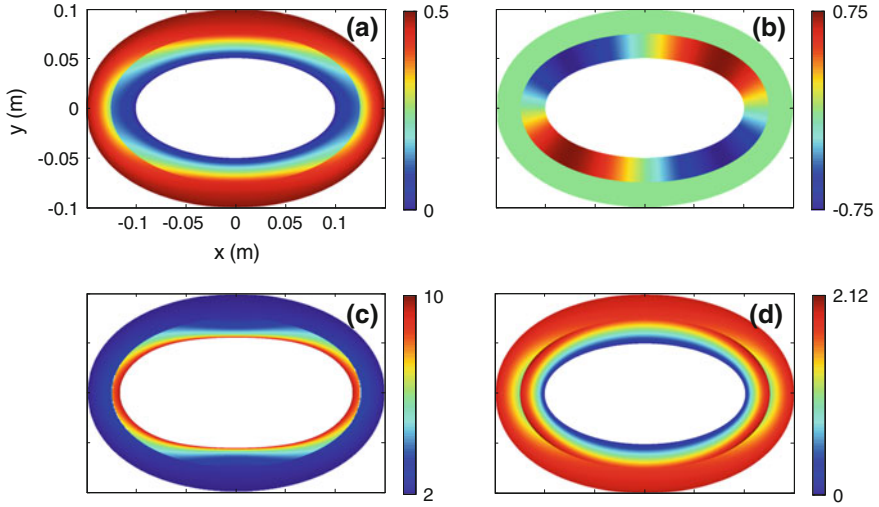

Fig. 2.6 Medium tensor elements for the example 2D uniform-thickness cloak. **a** ε'_{11}. **b** ε'_{12}. **c** ε'_{22}. **d** ε'_{33}. In (**a**), (**b**), and (**d**), the *color legends* indicate the minimum and maximum values of the corresponding parameter. In (**c**) the high-value approaches infinity and the color scale is clipped at 10

corresponding to a diagonal tensor in the (q'_1, q'_2, q'_3) system. The medium parameters in the Cartesian (x, y, z) system are computed using (2.18) in terms of appropriate unit vectors from (2.16) and the medium parameters (2.22) and (2.24) expressed in the transformed system.

Next the uniform-thickness cloak design will be validated numerically by considering a specific example of an elliptic PEC cylinder with $a = 0.1$ m and $b = 0.05$ m. This elliptic PEC cylinder is then assumed to be coated by a cloak designed with thickness parameters $T_1 = 0.025$ m and $T = 0.05$ m. Figure 2.6 shows the associated medium parameters for this design. The cloak medium is inhomogeneous and anisotropic. Furthermore, the parameters are discontinuous across the A_1–A_2 interface. In Fig. 2.6c, the tensor element in the circumferential direction (ε'_{22}) approaches infinity along the inner boundary of the cloak ∂S.

At 12 GHz, suppose that the PEC cylinder is illuminated by a TM-polarized plane wave propagating in the direction $(\hat{x} + \hat{y})/\sqrt{2}$, making a +45° angle with the $+x$ axis. At this frequency, the elliptic scatterer measures $8\lambda \times 4\lambda$ in the two axes and the cloak thickness is $T = 2\lambda$. Figure 2.7 shows snapshots of the $\hat{z}$-directed magnetic field distribution. The cloak boundaries and the A_1–A_2 interface are indicated by black contours. When directly exposed to the incoming wave, the PEC cylinder creates scattered fields in every direction as shown in Fig. 2.7a. When a cloak having the permittivity and permeability tensor parameters presented in Fig. 2.6 is applied, then there is no scattering and the incident field is recovered everywhere outside the cloak as shown in Fig. 2.7b.

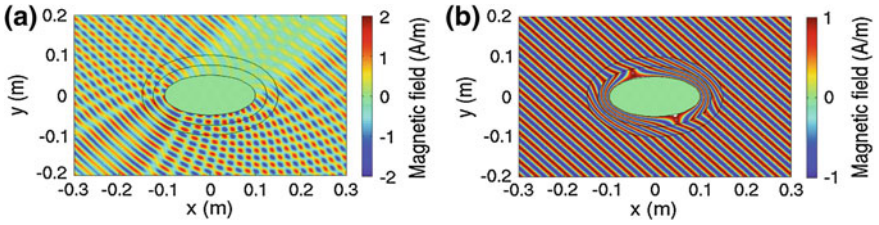

Fig. 2.7 Snapshots of the total magnetic field distributions for a PEC cylinder subject to a plane wave illumination. **a** The conducting cylinder without a cloak. **b** The cylinder enclosed by the uniform-thickness cloak

Both the eccentric elliptic and uniform-thickness cloaks are generalizations of the original circular annular cloak that allow more flexible shapes for the cloaked region as well as the cloak itself. When design parameters are chosen such that the cloaked region has a circular cross section and the cloak is a circular annulus, the medium parameters should reduce to those of the circular annular cloak. For example, let the uniform-thickness cloak parameters be chosen as $b = a$ and $T_1/T = a/(a+T)$. These lead to $\rho_s + (q_1' - 1) = \rho'$ and $\rho_s = \sqrt{x_s^2 + y_s^2} = a$. Hence, under these conditions the cloak parameters (2.22) and (2.24) will reduce to

$$\varepsilon_{11}' = \frac{\rho' - a}{\rho'},\ \varepsilon_{22}' = \frac{\rho'}{\rho' - a},\ \varepsilon_{33}' = \left(\frac{a+T}{T}\right)^2 \frac{\rho' - a}{\rho'}, \tag{2.25}$$

which are the parameters of a circular annular cloak [80] with inner and outer radii equal to a and $a + T$ in the 2D cylindrical $(q_1',\ q_2',\ q_3') = (\rho',\ \phi',\ z')$ coordinate system.

2.3.2 Electromagnetic Cloaking of Antennas

Modern commercial and military applications, such as for communications and radar purposes, often require multiple antennas operating in close proximity to one another at high power levels. For antennas on large, complex mounting platforms, blockage can create a deep shadow in the forward direction of a scatterer. For closely located multiple antennas, mutual coupling in the near-field range can significantly alter both impedance and radiation characteristics from their ideal parameters in free space.

Electromagnetic cloaking provides a novel approach for shielding an antenna's radiation and impedance responses from surrounding mounting structures or other antennas operating in close proximity. For a collection of narrowband antennas that are physically and electrically close to one another, it is desired that each antenna transmits and receives with the same pattern and input impedance as it would have in free space. This can be achieved by designing a cloaking radome

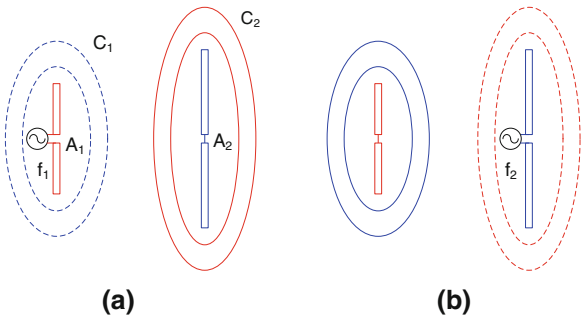

Fig. 2.8 Two antennas A_1, A_2 for operation at frequencies f_1, f_2 enclosed by two narrowband cloaks C_1, C_2. **a** A_1 radiating at frequency f_1. **b** A_2 radiating at frequency f_2. Solid cloak boundaries indicate perfect cloaking, whereas dashed cloak boundaries signify the perfectly transparent condition. Reprinted with permission from Kwon and Werner [41]. Copyright 2008, American Institute of Physics

that becomes transparent at the operating frequency of the enclosed antenna, but performs perfect cloaking at the operating frequencies of all other neighboring antennas. Then, each antenna will transmit and receive as if all other antennas are not physically present over the narrow bandwidth of operation. Both radiation pattern and input impedance will be the same as the values associated with the ideal environment of free space.

Consider an example of two antennas, A_1 and A_2, operating in close proximity as illustrated in Fig. 2.8. Antenna A_1 is designed for narrowband operation around frequency $f = f_1$. Similarly, A_2 operates at $f = f_2$. A_1 is enclosed inside cloak C_1, which assumes the free space medium parameters at $f = f_1$, but becomes a perfect cloak at $f = f_2$. A reversed set of conditions apply to A_2 and C_2. In Fig. 2.8, perfect cloaking and perfect transparency are indicated by the solid and dashed contours, respectively. At $f = f_1$, A_1 cannot sense the presence of A_2 and C_2, and thus operates as if it were situated in free space. A similar situation occurs at $f = f_2$ for A_2.

The antenna shielding effect can be visualized using numerical analysis. Here, 2D line-dipole antennas are considered due to the prohibitive computational requirement of 3D antennas and cloaks. However, the observed phenomenon and conclusion in 2D should directly extend to 3D cases. A 2D line-dipole antenna is a time-harmonic equivalent of a 2D static line-dipole charge. Both antenna structure and excitation are uniform and infinite in one dimension. Consider line-dipole antennas of length 75 mm and 150 mm for A_1 and A_2, designed for operation at $f_1 = 2$ GHz and $f_2 = 1$ GHz, respectively. Their axes are aligned with the y-axis and the separation between them is 200 mm. For both antennas, the dipole width is equal to 0.3 mm and the gap between the two arms for excitation is equal to 0.75 mm. Figure 2.9 compares the z-directed total magnetic field distribution at $f = f_1$ for two different conditions on A_2 obtained using COMSOL Multiphysics. In the presence of an uncloaked A_2, Fig. 2.9a shows that both near- and far-zone fields are perturbed by the presence of A_2. In Fig. 2.9b, A_1 radiates in the presence

of a cloaked A_2. C_2 is an elliptic annular cloak with the semi-axes of the inner boundary equal to 0.05 m and 0.1 m, and those of the outer boundary given by 0.1 m and 0.2 m. The cloak parameters were obtained from (2.17) using appropriate coordinate system definitions. It is observed that both near- and far-zone fields are restored to the reference case of A_1 radiating by itself in free space.

The restoring effect of cloak C_2 on the radiation characteristics of A_1 can be quantified by comparing the 2D directivity patterns. The directivity D_{2D} is plotted with respect to the angle ϕ measured from the $+x$ axis in Fig. 2.10a for three different cases. When A_1 radiates in the presence of an uncloaked A_2, the radiation pattern is significantly distorted. In particular, the reduced field strength in the $+x$ direction seen in Fig. 2.9a results in directivity reduction at $\phi = 0$ in Fig. 2.10a from the reference case (solid blue). When C_2 encloses A_2, the directivity pattern is restored to that of A_1 in free space. The perturbed field in the near zone observed in Fig. 2.10a translates into modification of the input parameter of A_1 when A_2 is present nearby without C_2. Figure 2.10b compares the input admittance per unit length at the driving point of A_1 as a function of frequency. When A_1 radiates in the presence of the uncloaked A_2, both real and imaginary parts of Y_{in} deviate and oscillate around the curves associated with A_1 in free space. This is attributed to the well-known effect of mutual coupling between closely spaced antennas. However, when cloak C_2 encloses A_2, the input admittance is restored to the exact value associated with the reference configuration.

The antenna shielding illustrated with the two-antenna example can be extended to N antennas operating over N non-overlapping frequency bands. For an antenna A_i at frequency f_i ($i = 1,2,\ldots,N$), cloak C_i can be designed for enclosing A_i using dispersive constituent materials such that it works as a perfect cloak at f_j ($j \neq i$) and becomes transparent (*i.e.* assumes free-space medium parameters) at f_i. Shell-type electromagnetic cloaks based on the transformation electromagnetics technique are inherently narrowband due to the inevitably dispersive constituent materials [2]. Unlike for invisibility cloaks in the optical regime, narrowband antenna shielding in the microwave spectrum can exploit the frequency dispersion of materials to its advantage.

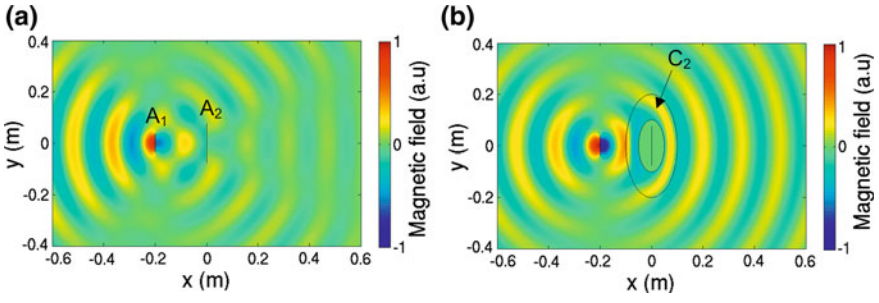

Fig. 2.9 Magnetic field distributions for antenna A_1 radiation at $f = f_1 = 2$ GHz. **a** A_1 radiates in the presence of an uncloaked A_2. **b** A_1 radiates in the presence of a cloaked A_2

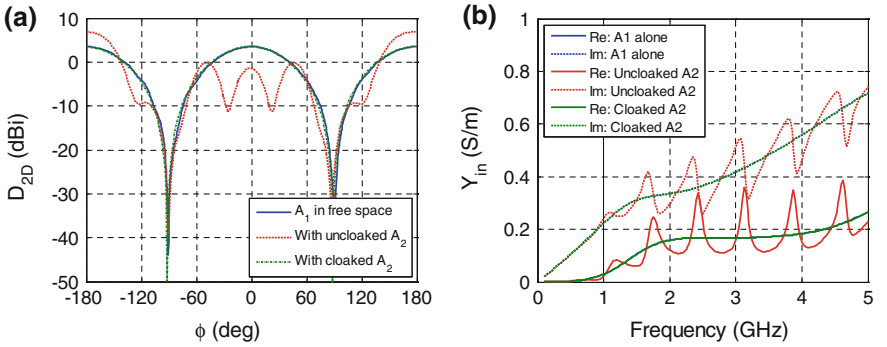

Fig. 2.10 Comparison of radiation and impedance characteristics of A_1 in different environments. **a** 2D far-field radiation patterns at the design frequency $f = f_1 = 2$ GHz. **b** The input admittance per unit length

The antenna cloaks may be designed and fabricated using existing metamaterials technology. Figure 2.11 illustrates a potential metamaterial realization which is based on printed circuit board (PCB) technology. For cylindrical antennas, a cloaking radome may take the shape of a long cylindrical shell with spherical shell end caps. Figure 2.11a shows one layer of the cylindrical shell radome composed of an array of interlocked PCB strips running in the radial and azimuthal directions, similar to the 2D microwave cloak reported in Schurig et al. [4]. As suggested in Fig. 2.11b, the unit cell walls can incorporate both electric and magnetic resonators.

For a multiple narrowband antenna environment involving N different frequency bands, each cloak C_i should satisfy conditions on the realized medium parameter values at N distinct frequencies. Designing appropriate resonant inclusions for this scenario would be challenging, nevertheless two design and

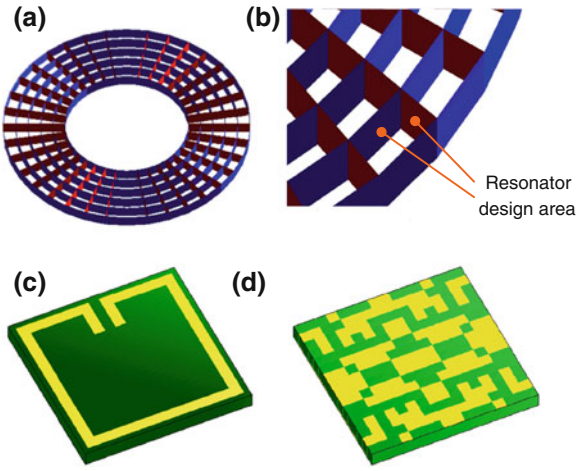

Fig. 2.11 Potential metamaterial realization of an antenna cloak. **a** One layer of a metamaterial cloak realized using PCB technology. **b** A detailed view of the metamaterial structure showing PCB walls for incorporating resonators. **c** Illustration of a ring resonator for magnetic response. **d** A GA-optimized patterned resonator surface. In (**c**) and (**d**), the *bright yellow* indicates a conductor trace or pixel

realization approaches are envisioned. The first approach is to incorporate multiple resonant inclusions. For example, for the two antenna configuration of Fig. 2.8, one face of a unit cell wall can incorporate a resonator of one size (Fig. 2.11c) while a resonator of different size can be designed into the other side. Dimensions of both resonators need to be jointly optimized in order to satisfy the necessary set of conditions at $f = f_1$ and $f = f_2$. For more antennas, additional resonators need to be included in the unit cell with their dimensions judiciously chosen to satisfy requirements at $f = f_i$ ($i = 1,2,\ldots,N$). The second approach is to use an optimization technique, such as the genetic algorithm (GA) [81], to determine the best size and shape of the resonator inclusions. This approach is more time-consuming and computationally demanding than the first method, but the GA optimization is capable of searching for the best unit cell configuration within a much larger design space. It can also lead to unconventional and non-intuitive designs that perform better than those based on intuition or trial-and-error approaches. One or both sides of each planar unit cell wall can be discretized into a collection of rectangular pixels, each of which may be determined by the GA to have metallization or not. A typical GA-optimized unit cell wall with pixelized metallization on one or both sides is shown in Fig. 2.11d.

2.4 Lenses and Beam Control Devices

Coordinate transformations employed for cloak designs use mappings that are continuous across the outer cloak boundary. In addition, there are other devices that are based on transformations having the same property such as a field concentrator [15] or a field rotator [82]. These devices are always invisible to an external illuminating field, *i.e.,* they do not change the field outside the device boundary. On the other hand, coordinate transformations having discontinuities at device boundaries, known as embedded transformations [21], can be utilized to achieve various novel wave transmission phenomena. Three types of device designs for novel beam propagation characteristics are described in this section.

2.4.1 Polarization Splitter and Rotator

Unlike in acoustics, coordinate transformation-based design approaches allow for novel optical devices that are associated with the vector nature of electromagnetic fields. For example, two different polarizations of a single beam may be manipulated independently of each other by defining a separate coordinate mapping for each polarization; or a transformation can be designed to alter the polarization state of a propagating field. Here, a 2D polarization splitter and a beam polarization rotator [83] are presented.

In 2D configurations where both media and fields do not vary along the longitudinal (z) axis, electromagnetic fields of arbitrary polarization can be decomposed into a set of two decoupled modes, TE and TM, with reference to the longitudinal direction. Since TE- and TM-mode fields interact with an independent set of tensor medium parameters, propagation of the fields associated with the two modes can be independently controlled via an appropriate set of permittivity and permeability tensor elements. Consider the two embedded transformations illustrated in Fig. 2.12, where two transformed (x', y', z') coordinate systems are defined over the cross section of $2w \times 2h$. For both transformed systems, the associated original system is defined in Cartesian (x, y, z) coordinates over the same cross section ($b_0 = c_0 = -h$, $b_3 = c_3 = h$). The polarization splitter is designed specifically for a 2D beam impinging on the device on the left face, propagating in the $+x$ direction, with the incident beam field essentially limited to the range $b_1 < y' < b_2$. The TE-mode fields are affected by the medium tensor parameters ε'_{zz}, μ'_{xx}, μ'_{xy}, μ'_{yx}, and μ'_{yy} of the device; while the TM-mode fields interact only with μ'_{zz}, ε'_{xx}, ε'_{xy}, ε'_{yx}, and ε'_{yy}. The transformed systems illustrated in Fig. 2.12 will shift the TE component in the $+y$ direction and the TM component in the $-y$ direction.

Three distinct regions are defined within the device, where their boundaries are indicated by thick red line segments given by $y' = y'_i(x)$ ($i = 0,1,2,3$). In region i ($i = 1,2,3$), let us define the transformation that changes only the y coordinate as

$$x' = x,\ y' = \frac{y_i - y_{i-1}}{b_i - b_{i-1}}(y - b_{i-1}) + y_{i-1},\ z' = z. \tag{2.26}$$

For both polarizations, the width of region 2 is kept uniform, *i.e.* $b_2 - b_1 = c_2 - c_1$. This constant width leads to a reflectionless property at the exit boundary of the device where $x' = w$. Regions 1 and 3 are either squeezed or expanded to make the device cross section fixed at $2w \times 2h$. From the complete transformation

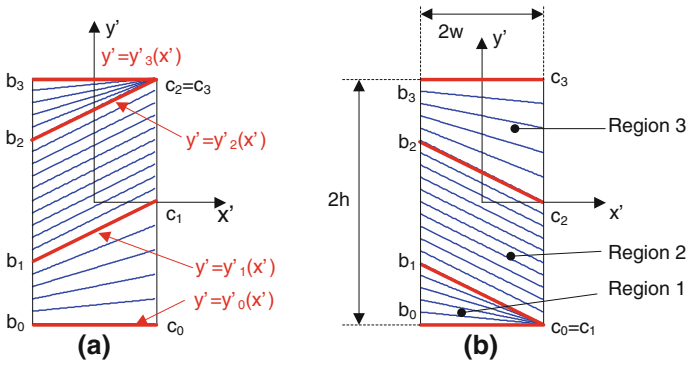

Fig. 2.12 Coordinate transformations for TE- and TM-mode polarization splitter design. **a** Transformation for the TE (to z) mode. **b** Transformation for the TM mode. Reprinted from Kwon and Werner [83]

definition (2.6) for the entire device, the Jacobian matrix can be computed and the resulting medium tensor parameters can be determined. Parameters ε'_{zz}, μ'_{xx}, μ'_{xy}, μ'_{yx}, and μ'_{yy} are determined from the mapping in Fig. 2.12a; whereas μ'_{zz}, ε'_{xx}, ε'_{xy}, ε'_{yx}, and ε'_{yy} are obtained from the mapping depicted in Fig. 2.12b.

The performance of the polarization splitter device can be numerically tested using an example design under a Gaussian beam illumination. Suppose we consider a design with $w = 0.1$ m and $h = 0.3$ m. On the input face, the values of b_1 and b_2 are set to $b_2 = -b_1 = 0.15$ m. On the exit face, $c_1 = 0$ and $c_2 = 0.3$ m are chosen for the TE mode and $c_1 = -0.3$ m and $c_2 = 0$ are selected for the TM mode. Figure 2.13 shows the parameters ε'_{zz}, μ'_{xx}, μ'_{xy}, and μ'_{yy} associated with the TE-mode fields. The TM-mode medium parameters μ'_{zz}, ε'_{xx}, ε'_{xy}, and ε'_{yy} are the same as the associated dual quantities in Fig. 2.13 after the following considerations are made: taking the mirror images of the color plots with respect to $y' = 0$ for all four parameters; additionally for ε'_{xy}, a negative sign should be added to μ'_{xy} in Fig. 2.13c. In region 3, it is noted that ε'_{zz} and μ'_{xx} diverge to infinity at a single point $(x', y') = (w, h)$ because it corresponds to a finite length ($x = w$, $h/3 \leq y \leq h$) in the original system. However, this is not a significant issue because the splitter is designed and positioned such that negligible beam field reaches this point.

In Fig. 2.14, the polarization splitter is under Gaussian beam illumination propagating in the $+x$ direction. In both polarizations, the frequency is 15 GHz and the minimum beam waist is equal to 0.05 m. The TE-polarized beam is shifted in the $+y$ direction while the TM-polarized beam is shifted in the $-y$ direction, without any reflections at the entry or exit boundaries at $x' = \pm w$.

Next, a beam polarization rotator is introduced, which is capable of changing the polarization state of a beam that passes through the device. Consider a cylindrical free space volume of length $2l$ and radius a as illustrated in Fig. 2.15a. For a 3D beam propagating in the $+z$ direction having the beam axis aligned with the z axis, it is desired that the polarization vector be rotated by an arbitrary, fixed

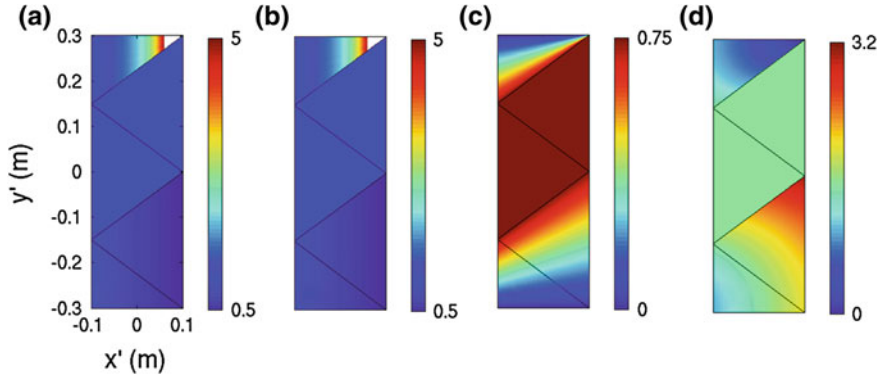

Fig. 2.13 TE-mode medium parameters for a 2D polarization splitter design with $w = 0.1$ m, $h = 0.3$ m, $b_2 = -b_1 = 0.15$ m, $c_1 = 0$, and $c_2 = 0.3$ m. **a** ε'_{zz}, **b** μ'_{xx}, **c** μ'_{xy}, **d** μ'_{yy}

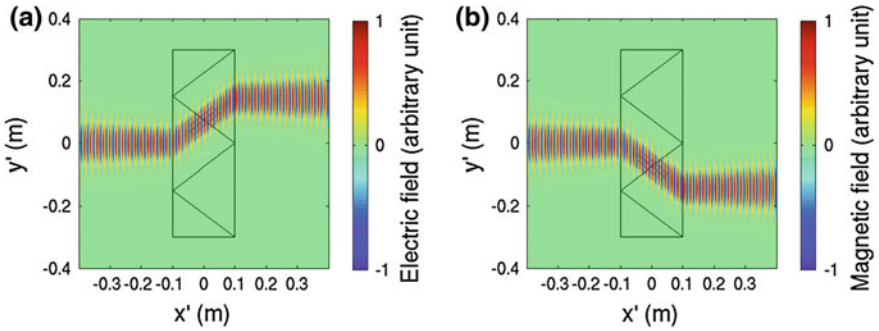

Fig. 2.14 Longitudinal field distribution for a 2D Gaussian beam illuminating the polarization splitter. **a** The electric field for a TE-polarized beam illumination. **b** The magnetic field for a TM-polarized beam illumination

angle α around its axis passing through the rotator. In the original (ρ, ϕ, z) and transformed (ρ', ϕ', z') circular cylindrical systems, this rotation can be achieved by changing only the circumferential coordinate via

$$\rho' = \rho,\ \phi' = \frac{\alpha}{2l}(z + l) + \phi,\ z = z'. \tag{2.27}$$

The transformed system is illustrated in Fig. 2.15b, where only the coordinate lines over the cylindrical shell are shown for clarity.

The Jacobian matrix and the resultant medium parameters are conveniently expressed in the cylindrical system. The medium tensor parameters of the polarization rotator are found to be

$$\varepsilon'_{\rho\rho} = \varepsilon'_{zz} = 1,\ \varepsilon'_{\phi\phi} = 1 + \left(\frac{\alpha}{2l}\rho'\right)^2,\ \varepsilon'_{\phi z} = \varepsilon'_{z\phi} = \frac{\alpha}{2l}\rho' \tag{2.28}$$

with all remaining elements of $\boldsymbol{\varepsilon}'$ and $\boldsymbol{\mu}'$ equal to zero. The parameters $\varepsilon'_{\rho\rho}$ and ε'_{zz} are unity, while the other two elements depend only on the radial coordinate ρ'.

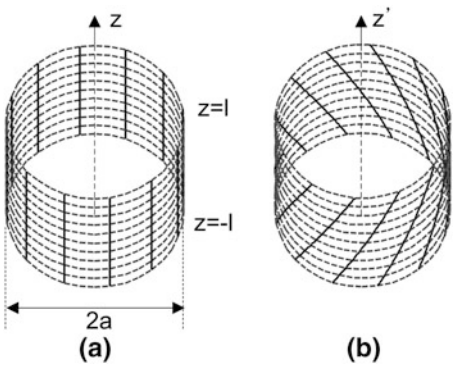

Fig. 2.15 Coordinate systems for a polarization rotator design. **a** The original system. **b** The transformed system. Reprinted from Kwon and Werner [83]

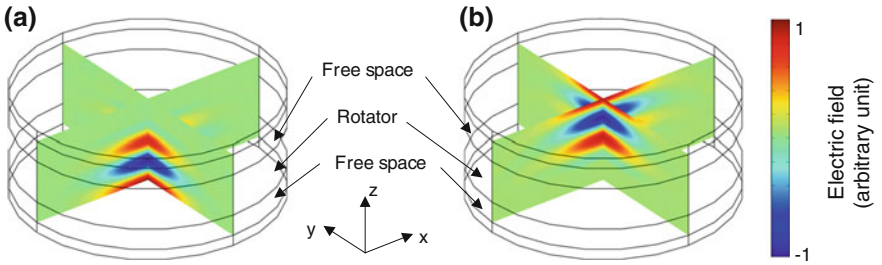

Fig. 2.16 Snapshots of the total electric field in the x–z and y–z planes. **a** E_x. **b** E_y. Reprinted from Kwon and Werner [83]

Consider an example design with the geometrical parameters $a = 0.15$ m, $l = 0.025$ m. The angle of rotation is set to $\alpha = \pi/2$ so that the two polarization states for a linearly polarized beam at the input and output of the rotator are orthogonal. At the time-harmonic frequency of 6 GHz, the rotator measures 6λ wide in diameter and λ in length. In the COMSOL simulation, a $\lambda/2$-thick free space volume was added to each side of the rotator. Finally, a thin perfectly matched layer was padded to the free space volumes to eliminate spurious numerical reflections. A linearly polarized Gaussian beam with the electric field in the $\hat{x}$ direction having a minimum waist of λ propagates in the $+\hat{z}$ direction and impinges on the rotator. Figure 2.16 shows snapshots of the components E_x and E_y of the total electric field $\mathbf{E} = \hat{x}E_x + \hat{y}E_y + \hat{z}E_z$ in the x–z and y–z planes. Comparing Fig. 2.16a and Fig. 2.16b, it is observed that the total electric field is $\hat{x}$-polarized when $z < -l$; non-zero E_y appears and grows as the beam propagates within the rotator when $-l < z < l$; and the field is completely $\hat{y}$-polarized beyond the exit face when $z > l$. Therefore, the polarization vector of the incident Gaussian beam is rotated by 90° passing through the device. Further inspection of the total electric field reveals that the device is reflectionless at both the input and output faces [83].

2.4.2 Flat Focusing Lenses

Lenses are one of the most fundamental and ubiquitous elements of optics. They are capable of forming an image of a source at any designed distance from the lens, including infinity. At microwave frequencies, lenses are used with antennas to convert diverging wavefronts into planar wavefronts to obtain highly directive radiation beams. Traditional lenses are made of homogeneous material, which reduces the design process to controlling the shape of the curved lens boundary. Transformation electromagnetics provides a novel approach to design devices that manipulate the shapes of propagating wavefronts through the inhomogeneous and/or anisotropic properties of the bulk materials. Here, 2D flat focusing lenses of rectangular [22] and trapezoidal [84] cross sections are presented.

A flat focusing lens can be obtained using a coordinate transformation that converts a curved, equal-phase surface in the original system into a planar surface in the transformed system. Consider a 2D radiation scenario having a circular arc of radius a centered at the origin as the equi-phase contour, as exhibited for example by a line source along the z axis. Figure 2.17a shows such an arc defined by $\rho = \sqrt{x^2 + y^2} = a$, $|\phi - \pi/2| \leq \Delta\phi$. One possible transformation to map this arc into a straight line segment is to first choose a section of a circle given by $\rho \leq a$, $y \geq g$ as illustrated in Fig. 2.17a and change only the y coordinate to arrive at a rectangular slab of width $2w$ and thickness l as shown in Fig. 2.17b, where $w = \sqrt{a^2 - g^2}$. Specifically, the transformation is given by

$$x' = x,\ y' = \frac{l}{\sqrt{a^2 - x^2} - g}(y - g) + g,\ z = z'. \tag{2.29}$$

Constant-x and -y line segments in the original system and the corresponding contours in the (x', y', z') system are shown in Fig. 2.17a and Fig. 2.17b, respectively. The arc $\rho = \sqrt{x^2 + y^2} = a$ is mapped to the line $y' = g + l$; the straight lower boundary $y = g$ remains unchanged. The associated medium tensor parameters are found to be

$$\begin{aligned} \varepsilon'_{xx} &= \frac{\sqrt{a^2 - x'^2} - g}{l},\ \varepsilon'_{xy} = \frac{x'(y' - g)}{l\sqrt{a^2 - x'^2}}, \\ \varepsilon'_{yy} &= \frac{1}{\sqrt{a^2 - x'^2} - g}\left[\frac{x'^2(y' - g)^2}{l(a^2 - x'^2)} + l\right],\ \varepsilon'_{zz} = \frac{\sqrt{a^2 - x'^2} - g}{l} \end{aligned} \tag{2.30}$$

and all remaining elements of the tensor $\boldsymbol{\varepsilon}' = \boldsymbol{\mu}'$ are equal to zero. For an example design that corresponds to choosing $w = 0.6$ m, $g = 0.4$ m, and $l = 0.1$ m, the four medium parameters relevant to the TE polarization are plotted in Fig. 2.18. Parameters μ'_{xx} and ε'_{zz} are equal to each other and they range from zero at $x' = \pm w$ to $(a - g)/l$ at $x' = 0$. The parameter μ'_{yy} diverges to infinity at $x' = \pm w$ because points $(x, y) = (\pm w, g)$ are stretched into line segments $x' = \pm w$, $g \leq y' \leq g + l$.

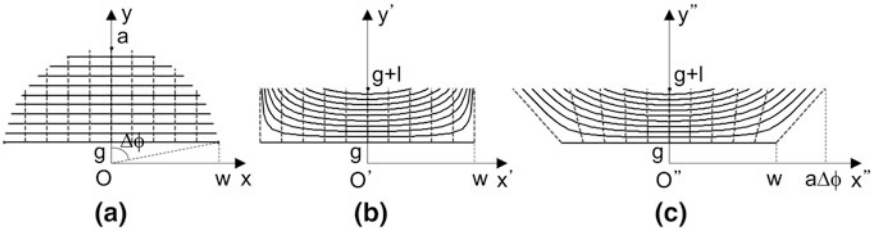

Fig. 2.17 Coordinate systems for flat focusing lens designs. **a** The original system. **b** The transformed system for a rectangular lens. **c** The transformed system for a trapezoidal lens. Reprinted from Kwon and Werner [84]

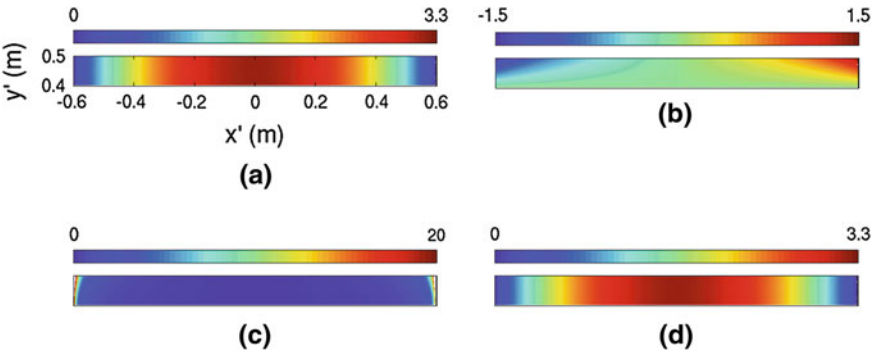

Fig. 2.18 The medium parameters of the *rectangular* lens design. **a** μ'_{xx}, **b** μ'_{xy}, **c** μ'_{yy}, **d** ε'_{zz}. The lens geometry is defined $w = 0.6$ m, $g = 0.4$ m, and $l = 0.1$ m. Reprinted with permission from Kwon and Werner [22]. Copyright 2008, Institute of Physics

Comparison of the coordinate systems in Fig. 2.17a and b reveals that the circular arc of length $2a\Delta\phi$ is mapped to a straight line segment of length $2w$, which causes reflections at the interface $y' = g + l$. In order to improve the impedance match at the exit boundary of a flat lens, it is desirable to map the arc length variable in the original free space to a straight boundary in the transformed space without any stretching or compression. Remembering that the interface $|x'| \leq w$, $y' = g$ needs to stay unchanged, a second set of transformations from the (x', y', z') to (x'', y'', z'') systems can be defined to smoothly transition the x'' variable from the x' coordinate at $y' = g$ to the arc length variable at $y' = g + l$ using

$$x'' = (1 - \alpha)x' + \alpha a \sin^{-1}\frac{x'}{a},\ y'' = y',\ z'' = z';\ \alpha = \frac{y' - g}{l}. \tag{2.31}$$

The transformed (x'', y'', z'') system is illustrated in Fig. 2.17c. Constant-x' lines are mapped into straight lines in the (x'', y'', z'') system. This causes the cross section of the flat focusing lens with an improved impedance match to have a trapezoidal shape.

The transformation for the trapezoidal lens design is completely specified by (2.29) and (2.31). The Jacobian matrix is obtained and the medium tensor parameters can be computed using (2.6). The medium parameters should be specified in the physical coordinates (x'', y'', z'') of the final device. This involves inversion of the mapping from (x, y, z) to (x'', y'', z''). Here, a numerical solution of the nonlinear equation relating x' and x'' in (2.31) is required. For the rectangular lens geometry shown in Fig. 2.18, a corresponding trapezoidal lens has been designed. The resulting medium parameters are shown in Fig. 2.19.

The performance of the rectangular and trapezoidal example lens designs in converting cylindrical wavefronts into planar wavefronts are evaluated numerically. For this purpose, TE-polarized 2D waves having angle-limited diverging wavefronts are numerically generated and used as illuminations upon the lens surface. Specifically, a $\hat{z}$-directed electric surface current is placed in the region

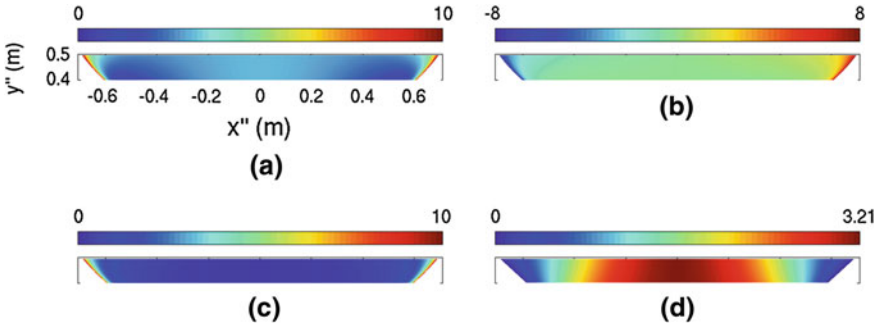

Fig. 2.19 Medium parameters of the *trapezoidal* lens design. **a** μ'_{xx}, **b** μ'_{xy}, **c** μ'_{yy}, **d** ε'_{zz}. The lens geometry is defined by $w = 0.6$ m, $g = 0.4$ m, and $l = 0.1$ m. Reprinted from Kwon and Werner [84]

$y'' < 0$ over a cylindrical surface of radius a_0 centered at the origin O'' having the following angle-dependent Gaussian current distribution:

$$\mathbf{J}_s(\phi'') = \hat{z}\, J_0 \exp\left[-\frac{(\phi'' + \pi/2)^2}{2\sigma_\phi^2}\right], \tag{2.32}$$

where J_0 is the strength of the surface current and the parameter σ_ϕ determines the angular spread of the current distribution. This surface current will generate converging cylindrical waves in the region $y'' < 0$ that converge at O''. Past the origin, they will become diverging cylindrical waves with maximum intensity at the angle $\phi'' = \pi/2$.

At a time-harmonic frequency of 4 GHz, the two flat lens designs are illuminated by the incident wave generated from (2.32) using $a_0 = 1$ m, $\sigma_\phi = 0.316$. The electrical dimensions of the lenses are $w = 8\lambda$ and $l = 1.33\lambda$. Figure 2.20 shows snapshots and magnitude distributions for the total electric field associated with the two lens designs. Figure 2.20a and Fig. 2.20c show that both lenses convert the circular wavefronts into planar wavefronts upon exit. The impedance match characteristics are demonstrated in Fig. 2.20b and Fig. 2.20d. In Fig. 2.20b, a small amount of rippling is observed below the exit boundary at $y' = g + l$. Since the incident wave is virtually zero at the two edges of the lens where $x' = \pm w$, no diffracted waves are generated. Therefore, the observed ripples are attributed to an impedance mismatch at $y' = g + l$. However, in Fig. 2.20d, no reflection is observed for the trapezoidal lens. Hence, the trapezoidal lens is capable of converting cylindrical waves into planar waves without reflection from both the entry and exit boundaries.

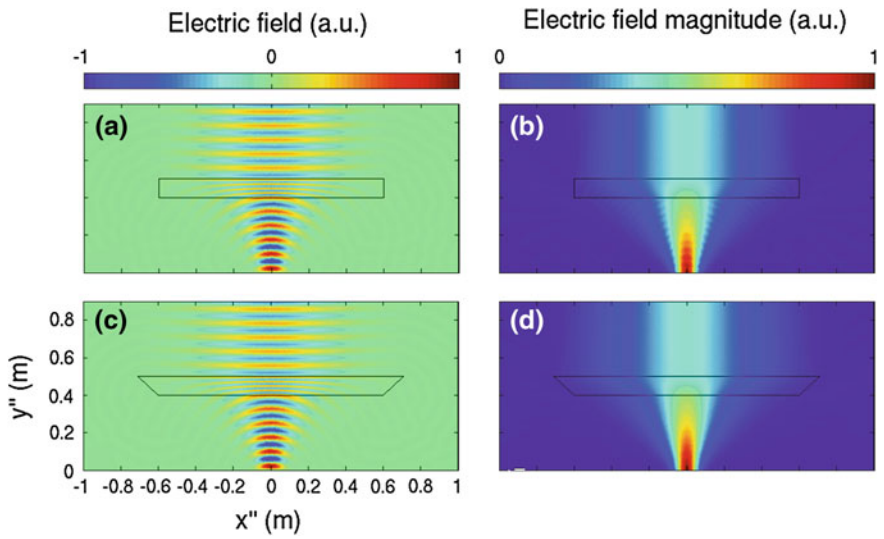

Fig. 2.20 Performance comparison of rectangular and trapezoidal lens designs. **a** A snapshot and **b** the magnitude of the electric field for the rectangular lens under an angle-limited Gaussian beam illumination. **c** A snapshot and **d** the magnitude of the electric field for the trapezoidal lens under the same Gaussian beam illumination

2.4.3 Beam Bends and Expanders

In Sect. 2.4.1, it was shown that the propagation axis of a beam could be shifted using a device based on an appropriate coordinate transformation. Additional devices that manipulate beam propagation characteristics can be obtained using the coordinate transformation technique. Here, designs for a 2D beam bend [22] and a 3D beam expander [26] are presented.

Coordinate transformations mapping Cartesian coordinates in the original system to cylindrical coordinates in the transformed system can result in a device that is capable of changing a beam's propagation direction. A 2D right-angle beam bender can be designed using the coordinate transformation depicted in Fig. 2.21. A square area defined by $0 \leq x \leq w$, $0 \leq y \leq w$ in Fig. 2.21a is mapped to a quarter section of a circle of radius w in Fig. 2.21b. Constant-x and -y lines are transformed into constant-ϕ' and -ρ' lines in the transformed cylindrical (ρ', ϕ', z') system, respectively. The resulting device will continuously change the direction of propagation of a $+\hat{x}$-propagating beam entering at the left interface in the clockwise direction so that a $-\hat{y}$-propagating beam exits at the bottom interface. Specifically, the transformation is given by

$$\rho' = y,\ \phi' = \frac{\pi}{2w}(w - x),\ z' = z. \tag{2.33}$$

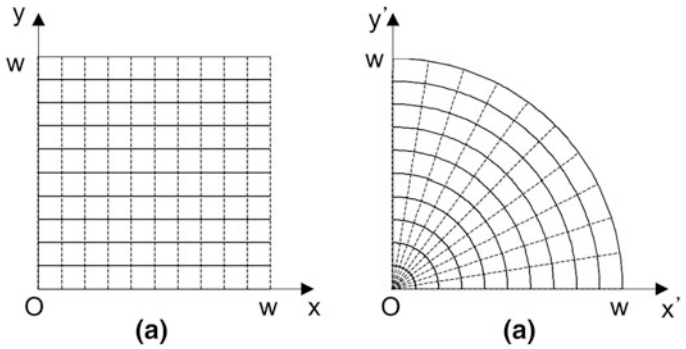

Fig. 2.21 Coordinate systems for a 2D right-angle beam bend design. **a** The original system. **b** The transformed system. Reprinted with permission from Kwon and Werner [22]. Copyright 2008, Institute of Physics

The Jacobian matrix and the resulting medium tensor parameters are conveniently expressed in the cylindrical coordinate system. For TE polarization, the associated medium parameters are found to be

$$\mu'_{\rho\rho} = \frac{2w}{\pi\rho'},\ \mu'_{\phi\phi} = \frac{\pi\rho'}{2w},\ \varepsilon'_{zz} = \frac{2w}{\pi\rho'}, \tag{2.34}$$

with all off-diagonal terms being equal to zero.

The performance of the right-angle bend device is tested using an example design with $w = 0.3$ m. At a time-harmonic frequency of 15 GHz, a TE-polarized 2D Gaussian beam propagating in the $+\hat{x}$ direction having the beam axis along $y' = 0.15$ m illuminates the bend. The minimum waist of the beam is equal to 0.05 m reached at $x' = 0.15$ m. In COMSOL, the incident beam was generated by an impressed magnetic surface current. The field snapshot in Fig. 2.22a shows that the direction of propagation is rotated by 90° and the beam exits the bend propagating in the $-\hat{y}$ direction. In addition, both the input and output interfaces are reflectionless, which is evidenced by the absence of ripples in the field magnitude distribution as shown in Fig. 2.22b.

For a propagating beam, a transformation that stretches the coordinate transverse to the beam axis leads to a beam expander design, as reported in [25]. 2D beam expander designs [25, 85] suffer from reflections from the device boundary due to an impedance mismatch that is attributed to the 2D nature of the transformations; only one coordinate in the transverse plane to the beam axis is stretched or compressed. A 3D beam expander can eliminate or significantly reduce the reflections by building the impedance match property into the design methodology.

For a beam propagating in the $+z$ direction having the beam axis coinciding with the z axis, consider a transformation between the original (ρ, ϕ, z) and the transformed (ρ', ϕ', z') cylindrical coordinate systems described in Fig. 2.23. Specifically, only the radial coordinate is changed between the two systems via

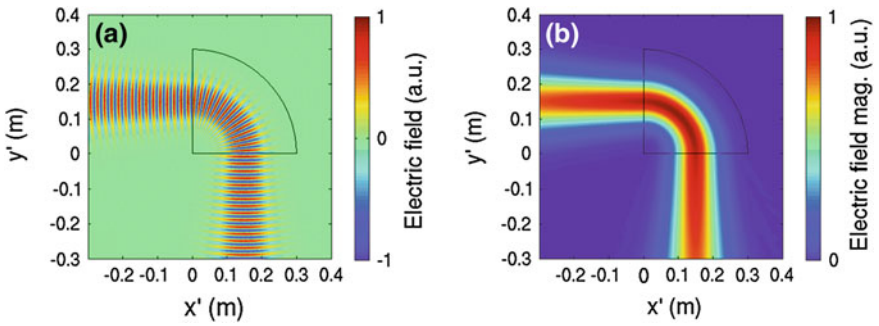

Fig. 2.22 Beam-bending performance of a right-angle bend for a 2D TE-mode Gaussian beam. **a** Snapshot of the total electric field. **b** The magnitude distribution. The boundary of the beam bend is indicated by the *black contour*

$$\rho' = \begin{cases} u(z)\rho, & -t < z < 0 \\ \rho, & \text{elsewhere} \end{cases}, \quad \phi' = \phi, \quad z' = z, \tag{2.35}$$

where t is the thickness of the expander and $u(z)$ describes the expansion in the $\hat{\rho}$ direction. For simplicity, we can choose a linear function of z as

$$u(z) = \frac{a-1}{t} z + a. \tag{2.36}$$

The constant a is an expansion factor in the radial direction at the exit boundary corresponding to $z' = 0$. A value less than unity for a results in a beam compressor. The Jacobian matrix $\mathbf{A}$ and the resulting medium tensor parameters are conveniently expressed in cylindrical coordinates. The medium tensors are found to be

$$\boldsymbol{\mu}' = \boldsymbol{\varepsilon}' = \begin{bmatrix} 1 + \left(\rho' u' / u^2\right)^2 & 0 & \rho' u' / u^3 \\ 0 & 1 & 0 \\ \rho' u' / u^3 & 0 & 1/u^2 \end{bmatrix} \tag{2.37}$$

when written in the (ρ', ϕ', z') system.

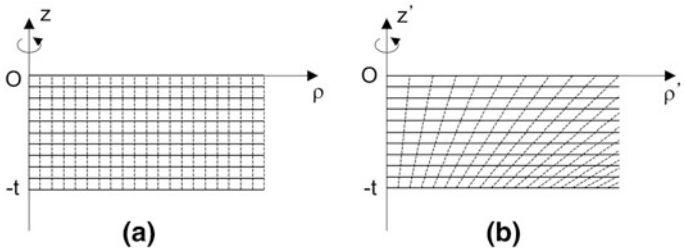

Fig. 2.23 Coordinate systems for the 3D beam expander design. **a** The original system. **b** The transformed system. Both systems are rotationally symmetric around the z axis. Reprinted with permission from Emiroglu and Kwon [26]. Copyright 2010, American Institute of Physics

Due to the inhomogeneous medium properties, numerical simulations of 3D beam expanders of practical electrical dimensions require a prohibitive amount of computational resources. Instead, the 3D design can be analytically tested using 2D Gaussian beams, where fields in free space and inside the device are expressed as a superposition of plane waves. To this end, first consider transmission and reflection of a $\hat{y}$-polarized plane wave by the expander. For an incident plane wave having the vector wavenumber $\mathbf{k}^i = \hat{x}k_x + \hat{z}k_z$ ($k_z = \sqrt{k^2 - k_x^2}$), the incident field, the reflected field in the region $z' < -t$, and the transmitted field in the region $z' > t$ can be written as

$$\mathbf{E}^i = \hat{y}E_0^i e^{-j(k_x x' + k_z z')},\ \mathbf{E}^r = \hat{y}E_0^r e^{-j(k_x x' - k_z z')},\ \mathbf{E}^t = \hat{y}E_0^t e^{-j\left(k_x' x' + k_z' z'\right)} \tag{2.38}$$

where $k_z' = \sqrt{k^2 - k_x'^2}$ for the transmitted field. The direction of propagation of the transmitted plane wave, which is specified by the vector wavenumber $\mathbf{k}^t = \hat{x}k_x' + \hat{z}k_z'$, is in general different from that of the incident plane wave due to the expansion operation. Inside the expander region ($-t < z' < 0$), both incident and reflected fields from the top boundary at $z' = 0$ are present. The associated field expressions are easily found from their respective counterparts in (2.38) via (2.7) as

$$\mathbf{E}^i = \left(\hat{y}\frac{1}{u} - \hat{z}\frac{u'y'}{u}\right)E_0^i e^{-j(k_x x'/u + k_z z')},\ \mathbf{E}^r = \left(\hat{y}\frac{1}{u} - \hat{z}\frac{u'y'}{u}\right)E_0^r e^{-j(k_x x'/u - k_z z')}. \tag{2.39}$$

The relationship between the wave vectors are found from the phase matching condition at $z' = 0$ to be

$$k_x' = \frac{k_x}{a}. \tag{2.40}$$

The relationships between the complex field amplitudes are obtained by enforcing the continuity of total tangential electric and magnetic fields. The reflection and transmission coefficients are found to be

$$R = \frac{E_0^r}{E_0^i} = \frac{k_z - k_z'}{k_z + k_z'},\ T = \frac{E_0^t}{E_0^i} = \frac{2k_z}{a\left(k_z + k_z'\right)}. \tag{2.41}$$

For normal incidence ($k_x = 0$), there is no reflection regardless of the expansion factor value a. This is the key difference from 2D expander designs, where a larger expansion factor leads to a larger amount of reflection.

Having the transmission and reflection properties of a plane wave propagating in an arbitrary direction established, characteristics of a 2D Gaussian beam propagating through the expander can be investigated using superposition. Specifically, consider a Gaussian beam propagating along the $+v$ axis in the u-v plane, which is a rotated version of the x–y plane by the angle α. Such a beam having a

minimum waist W_0 and an electric field amplitude E_0^i at the coordinate origin can be constructed from a spectrum of plane waves via the Fourier transform

$$E_y^i(u,v) = \frac{1}{2\pi}\int_{-\infty}^{\infty} \tilde{E}_y^i(k_u, v=0)e^{-j(k_u u + k_v v)}dk_u, \tilde{E}_y^i(k_u, v=0) = E_0^i W_0\sqrt{\pi}e^{-k_u^2 W_0^2/4}. \tag{2.42}$$

A rotation transformation from $(u,\ v)$ to $(x,\ z)$ leads to the field expression in $(x,\ z)$ given by

$$\begin{aligned} E_y^i &= \frac{1}{2\pi}\int_{-\infty e^{-j\alpha}}^{\infty e^{j\alpha}} \tilde{E}_y^i(k_x, z'=0)e^{-j(k_x x' + k_z z')}dk_x, \\ \tilde{E}_y^i(k_x, z'=0) &= \tilde{E}_y^i(k_u, v=0)\left(\cos\alpha - \frac{k_x \sin\alpha}{\sqrt{k^2 - k_x^2}}\right), \end{aligned} \tag{2.43}$$

where (2.43) represents a superposition of plane waves propagating in the direction given by $\mathbf{k}^i$. Hence, the associated reflected and transmitted fields can be similarly reconstructed by applying the reflection and transmission coefficients (2.41) to each plane wave, which results in

$$\begin{aligned} E_y^r &= \frac{1}{2\pi}\int_{-\infty e^{-j\alpha}}^{\infty e^{j\alpha}} R\tilde{E}_y^i(k_x, z'=0)e^{-j(k_x x' - k_z z')}dk_x, \\ E_y^t &= \frac{1}{2\pi}\int_{-\infty e^{-j\alpha}}^{\infty e^{j\alpha}} T\tilde{E}_y^i(k_x, z'=0)e^{-j\left(k_x' x' + k_z' z'\right)}dk_x. \end{aligned} \tag{2.44}$$

The integrals in (2.43) and (2.44) can be numerically evaluated. Fields within the expander are obtained from the untransformed field quantities.

Characteristics of the 3D beam expander can be investigated using an example 2D Gaussian wave illumination. Consider an expander design with the scaling factor $a = 2.5$ and thickness $t = 8\lambda$. Figure 2.24 shows the total electric field distribution in the x'-z' plane when a Gaussian beam with $W_0 = 4\lambda$ and $E_0^i = 1$ illuminates the beam expander at normal ($\alpha = 0$) and oblique ($\alpha = 20°$) incidence. For normal incidence, Fig. 2.24a and c show that the beam is expanded without any noticeable reflection from the device boundaries. For the oblique illumination, a small amount of reflection is visible in the form of magnitude fluctuations in the region $z' < 0$. A comparison with a 2D expander having the same scale factor confirms that 2D designs based on scaling only one coordinate suffer from a significant amount of reflections at the expander's exit boundary [26].

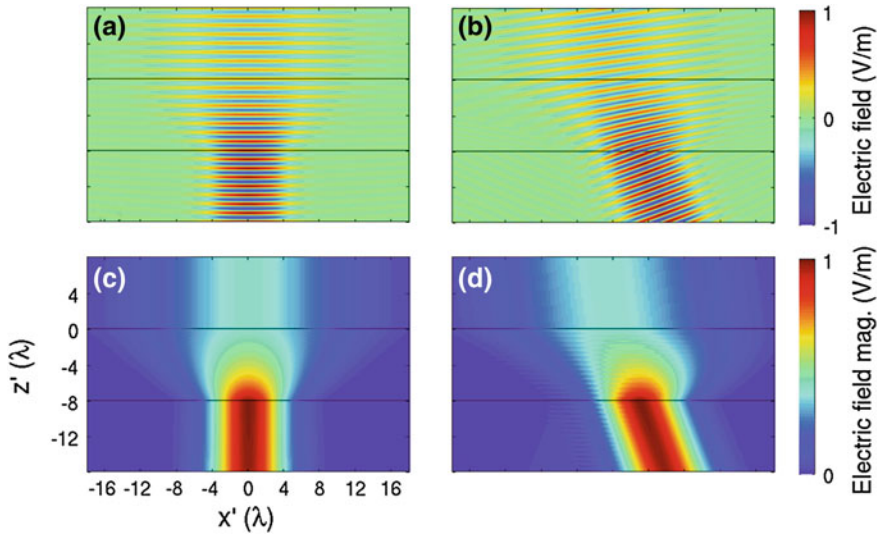

Fig. 2.24 The total electric field distribution in the $y' = 0$ plane for a 2D Gaussian beam incident upon a 3D beam expander. **a** A snapshot and **c** magnitude distributions under normal incidence. **b** A snapshot and **d** magnitude distributions under an oblique incidence with $\alpha = 20°$. The expander and beam parameters are $a = 2.5$, $t = 8\lambda$, and $W_0 = 4\lambda$

2.5 Applications to Antennas and Arrays

2.5.1 Antenna at a Virtual Location

If a volume containing electromagnetic sources undergoes a coordinate transformation, a new source distribution results. Quantitative changes of surface and line currents under coordinate transformations have been reported in [86]. In antenna applications, of particular interest is a change in the physical location of sources without changing the associated far-field radiation characteristics. Here, an embedded monopole antenna in a ground recess for conformal applications [46] is presented.

Consider a monopole antenna mounted above a ground plane as illustrated in Fig. 2.25a. It radiates a vertically polarized field with the maximum radiation at the horizon. It is desired that the same radiation characteristics be achieved using a completely flush geometrical configuration without any physical structure above the x–y plane. By creating a ground recess and moving the monopole below the x–y plane, a desired flush structure can be obtained, as illustrated in Fig. 2.25b. Specifically, the following coordinate transformation that maps the (ρ, ϕ, z) to the (ρ', ϕ', z') cylindrical system is introduced:

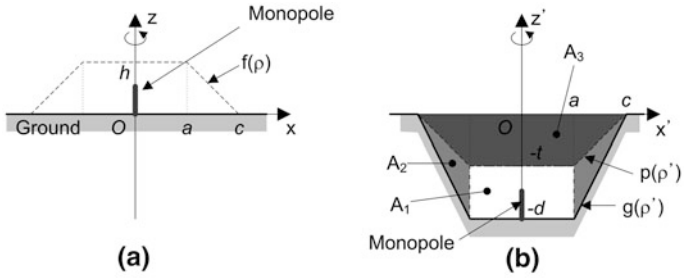

Fig. 2.25 Coordinate systems for a monopole antenna. **a** A monopole over a flat ground plane. **b** An embedded monopole in a ground recess. © 2010 IEEE. Reprinted, with permission, from Kwon [46]

$$\rho = \rho',\ \phi = \phi', z = \begin{cases} z', & z' \geq 0 \\ \frac{f(\rho)}{p(\rho')} z', & p(\rho') \leq z' \leq 0 \\ \frac{f(\rho)}{p(\rho') - g(\rho')} [z' - g(\rho')], & g(\rho') \leq z' \leq p(\rho') \end{cases} \tag{2.45}$$

The functions $f(\rho)$, $p(\rho')$, $g(\rho')$ are piecewise linear contours with respect to the radial coordinate as indicated in Fig. 2.25. The volume between $z = 0$ and $z = f(\rho)$ is mapped below the ground plane to the space between $z' = g(\rho')$ and $z' = p(\rho')$. The transformation in the range $p(\rho') \leq z' \leq 0$ is designed such that the overall transformation between z and z' is continuous. The continuity of the mapping guarantees that the resulting device is reflectionless at the free space interface where $z' = 0$. It also leads to a negative slope between z and z', resulting in a negative-index constituent material. This type of transformation is said to produce a folded geometry [37].

The medium parameters of the three regions A_1, A_2, and A_3 are computed from the Jacobian matrix of the transformation (2.45). The corresponding non-zero tensor elements are found to be

$$\varepsilon'_{\rho\rho} = \mu'_{\phi\phi} = \frac{h}{d-t},\ \varepsilon'_{zz} = \frac{d-t}{h} \tag{2.46}$$

in A_1,

$$\varepsilon'_{\rho\rho} = \mu'_{\phi\phi} = \frac{h}{d-t},\ \varepsilon'_{\rho z} = \varepsilon'_{z\rho} = \frac{dh}{(c-a)(d-t)},\ \varepsilon'_{zz} = \frac{d-t}{h} + \frac{d^2 h}{(c-a)^2 (d-t)} \tag{2.47}$$

in A_2, and

$$\varepsilon'_{\rho\rho} = \mu'_{\phi\phi} = -\frac{h}{t},\ \varepsilon'_{zz} = -\frac{t}{h} \tag{2.48}$$

in A_3. The transformation also moves the perfectly conducting boundary condition over $\rho \leq c$, $z = 0$ onto the slanted and bottom walls of the recess. The height of the monopole antenna is also scaled by a factor $(d - t)/h$ by the transformation.

It is noted that all media A_1, A_2, and A_3 are in general anisotropic, but homogeneous volumes. If the geometrical condition $h = t = d/2$ is chosen, then A_1 and A_3 become isotropic. Furthermore, A_1 is free space and the relative permittivity and permeability of A_3 are simultaneously equal to –1, which are those of a NIM superlens [30]. Hence, the design can be viewed as a finite-sized NIM superlens that forms an image of the monopole at the bottom of the recess at the original monopole location above the ground plane. The volume A_2 is an impedance matching block that eliminates diffraction from the edges of the finite superlens.

Consider a thin-wire monopole antenna of length $l = 0.235\lambda$ and radius of $\lambda/200$ at 3 GHz ($\lambda = 0.1$ m). Figure 2.26a shows a snapshot of the $\hat{\phi}$-directed magnetic field H_ϕ in a constant-ϕ plane. Next, an example ground recess is designed with the parameter values $a = \lambda$, $c = 2\lambda$, $h = t = \lambda/2$, and $d = \lambda$. These values correspond to region A_1 being free space and A_3 a NIM superlens. The parameters of A_2 relevant to the TM (to ρ) fields are given by

$$\varepsilon'_{\rho\rho} = \mu'_{\phi\phi} = 1,\ \varepsilon'_{\rho z} = \varepsilon'_{z\rho} = 1,\ \varepsilon'_{zz} = 2. \tag{2.49}$$

At the design frequency, Fig. 2.26b shows that the original monopole field distribution is reproduced away from the boundary at $z' = 0$, which will result in the original monopole and the embedded monopole having the same radiation pattern, with vertically polarized maximum radiation at the horizon. It is noted that a perfect reproduction of the radiation pattern is achieved using a finite NIM lens and impedance-matching volumes measuring only 4λ across and λ deep. When there is no embedding media in the same recess, Fig. 2.26c shows that the field

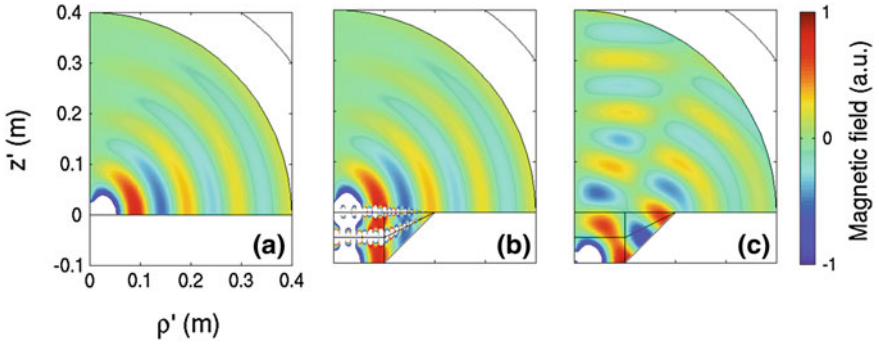

Fig. 2.26 Snapshots of the total magnetic field distribution of a thin-wire monopole antenna. **a** Monopole on a flat ground plane. **b** Monopole at the bottom of the recess enclosed by transformation media. **c** Monopole at the bottom of an air-filled recess. © 2010 IEEE. Reprinted, with permission, from Kwon [46]

distribution is significantly distorted. It is found that the maximum directivity deviates from the horizon ($\theta = 90°$) to $\theta = 61.6°$.

2.5.2 Microwave Metamaterials for a Virtual Line Source

A 2D equivalent of the virtual monopole discussed in the previous section is a virtual electric line source. As an intermediate step toward designing metamaterials for a 3D radiation configuration by a monopole, metamaterials for a virtual line source in a 2D configuration [87] are investigated.

Figure 2.27 shows cross sections in the x–y plane of the original (virtual) and transformed (physical) systems for an electric line source. It is desired that a 2D ground recess and embedding metamaterials be designed such that the physical line source in Fig. 2.27b radiate as if it is located above a flat ground plane as illustrated in Fig. 2.27a. Let us choose the same set of recess parameters as in Sect. 2.5.1, which are: $a = \lambda$, $c = 2\lambda$, $h = t = \lambda/2$, and $d = \lambda$. Following the same design procedure, the medium parameters of the four distinct volumes A_1–A_4 are computed. A_1 containing the physical source is free space, while the region A_4 is the NIM superlens. The parameters of the impedance matching blocks A_2/A_3 are equal to

$$\boldsymbol{\mu}' = \begin{bmatrix} 1 & \mp 1 \\ \mp 1 & 2 \end{bmatrix}, \quad \varepsilon'_{zz} = 1. \tag{2.50}$$

Here, metamaterials for A_4 and A_2/A_3 in the microwave frequency regime are designed, where formation of a virtual line source as well as reproduction of the radiation pattern associated with the virtual configuration are numerically tested and confirmed. The design frequency is chosen to be 10 GHz in the X band. The required metamaterials are based on doubly periodic arrangements of unit cells and fabrication using standard printed circuit technologies is targeted. For this purpose, the RT/duroid 5880 copper-clad laminates from Rogers Corporation of

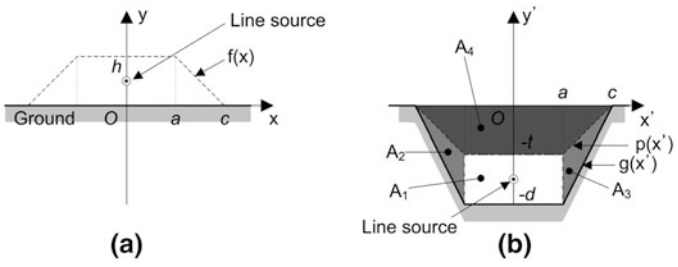

Fig. 2.27 Coordinate systems for a virtual line source design. **a** The original system. **b** The transformed systems. Both systems are uniform and infinite in the $\pm z$ directions. © 2012 IEEE. Reprinted, with permission, from Kwon and Emiroglu [87]

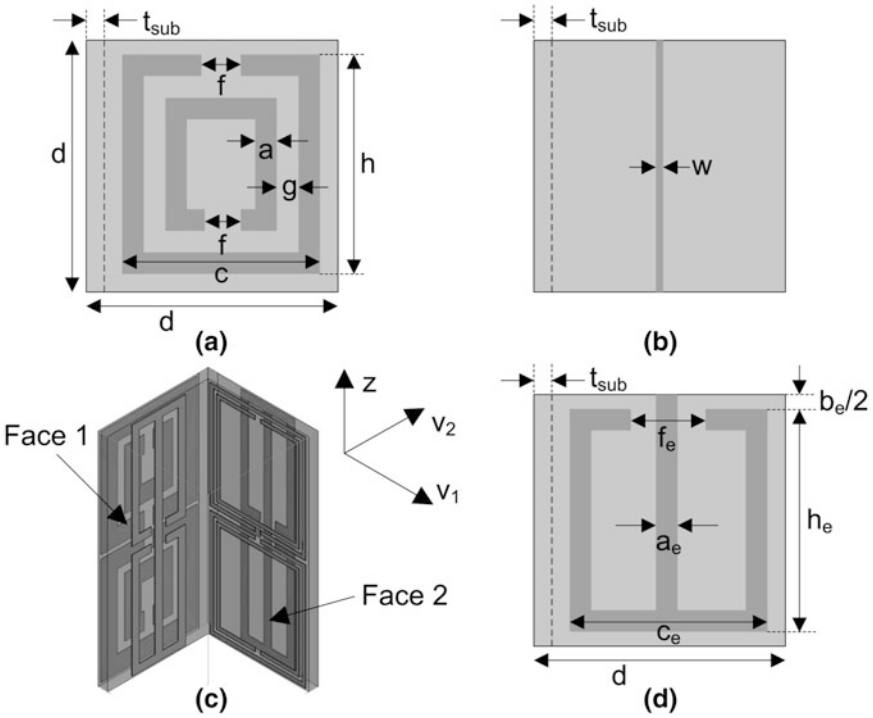

Fig. 2.28 Unit cell designs for the embedding media for a virtual line source. **a** The SRR and **b** wire faces of the NIM superlens A_4. **c** The unit cell for the impedance-matching block A_3. **d** The ELC face of the A_3 cell. © 2012 IEEE. Reprinted, with permission, from Kwon and Emiroglu [87]

thickness $t_{sub} = 0.254$ mm with 0.5-oz. (0.017-mm thickness) copper cladding were chosen to enable the unit cell designs for A_4 and A_2/A_3.

For the NIM superlens region A_4, a unit cell design is adopted that contains split-ring resonators (SRRs) [88] for realizing negative permeability and a copper strip for realizing negative permittivity. The SRR and copper strip sides of the unit cell walls are illustrated in Fig. 2.28a, b, where strips in dark gray indicate copper traces. Positions of the gaps in the SRR are chosen such that the bianisotropy resulting from magneto-dielectric coupling within the magnetic resonator is minimized. The geometrical parameters of the unit cell were numerically optimized to obtain $\mu = \varepsilon = -1$, or equivalently $n = -1$ and $z = 1$ in terms of the index of refraction n and the normalized impedance z (relative to free space). The optimized values obtained using Ansys HFSS are equal to $n = -0.999 - j0.035$, and $z = 1.015 + j0.0001$. The associate geometrical parameters are $a = 0.3$, $c = 2.6$, $d = 3.0$, $g = 0.15$, $h = 2.9$, $f = 0.38$, and $w = 0.0762$ (all dimensions in mm). It is found that the metamaterial has a negative index of refraction in the range 9.13–10.60 GHz. A medium parameter retrieval technique based on scattering parameters of the unit cell under periodic boundary conditions was employed [89].

For the impedance matcher A_3, the permeability tensor in the x–y plane can be diagonalized as

$$\boldsymbol{\mu}' = \begin{bmatrix} 1 & 1 \\ 1 & 2 \end{bmatrix} = [\,\mathbf{v}_1 \quad \mathbf{v}_2\,] \begin{bmatrix} \mu'_{11} & 0 \\ 0 & \mu'_{22} \end{bmatrix} \begin{bmatrix} \mathbf{v}_1^T \\ \mathbf{v}_2^T \end{bmatrix}, \tag{2.51}$$

where the column vectors $\mathbf{v}_1$ and $\mathbf{v}_2$ are eigenvectors of $\boldsymbol{\mu}'$ given by $\mathbf{v}_1 = [\,0.5257 \quad 0.8507\,]^T$ and $\mathbf{v}_2 = [\,-0.8507 \quad 0.5257\,]^T$, which are orthogonal to each other. In addition, the two eigenvalues are equal to $\mu'_{11} = 2.618$ and $\mu'_{22} = 0.382$. When written in the $(v_1, v_2, v_3 = z)$ coordinate system, which is the (x, y, z) system rotated around the z axis by +53.8°, the permeability tensor will be a diagonal matrix. Hence, a metamaterial unit cell of square cross section can be designed for realizing the diagonal permeability tensor. This can be achieved by incorporating a different pair of electric and magnetic resonators on the two orthogonal faces of the unit cell. Once the resonators are optimized to synthesize the permeabilities μ'_{11} and μ'_{22}, the unit cell can be rotated such that the normal vectors to the cell walls are aligned with $\mathbf{v}_1$ and $\mathbf{v}_2$. This approach to synthesizing reciprocal anisotropic medium parameters has been proposed by Rahm et al. [15].

Figure 2.28c illustrates the unit cell for A_3, comprising a pair of SRR and electronic L-C (ELC) resonators [90] on each face. The resonators on face 1 contribute primarily to μ'_{11} and ε'_{zz}; similarly, the resonators on face 2 are the main contributors to μ'_{22} and ε'_{zz}. However, the two sets of resonators need to be jointly optimized due to mutual coupling. The same ELC structure was used on both faces, while the SRRs on the two faces were allowed to be different. Hence, the geometrical parameters for one ELC and two SRRs were optimized to realize a desired set of values for μ'_{11}, μ'_{22}, and ε'_{zz}. The parameter values for the optimized design are listed in Table 2.1. The retrieved parameters using a plane wave having the magnetic field polarized along the v_1 axis were found to be $\mu'_{11} = 2.79 - j0.154$ and $\varepsilon'_{zz} = 1.116 - j0.232$. Simulation using an incident plane wave having a $\hat{v}_2$-polarized magnetic field resulted in the retrieved parameters $\mu'_{22} = 0.369 - j0.103$ and $\varepsilon'_{zz} = 0.955 + j0.016$. They are close to the target values $\mu'_{11} = 2.618$, $\mu'_{22} = 0.382$, and $\varepsilon'_{zz} = 1$. Finally, the unit cell for A_2 is a mirror-image structure of the optimized A_3 cell.

Table 2.1 Optimized geometrical parameter values for the unit cell of the impedance matcher A_3

ELC on both faces		SRR on face 1		SRR on face 2	
a_e	0.2	a	0.45	a	0.1
b_e	0.2	c	2.6	c	2.6
c_e	1.45	d	3.0	d	3.0
d	3.0	g	0.2	g	0.075
f_e	0.4	h	2.9	h	2.9
h_e	2.85	f	0.25	f	0.15

All dimensions are in mm.

The optimized unit cells for A_3 and A_4 were assembled for numerical analysis of the specified recess together with a free space area of $4\lambda \times 4\lambda$ above the $y' = 0$ plane using Ansys HFSS at 10 GHz. A line current was placed at $(x', y') = (0, -0.75\lambda)$, at a quarter wavelength above the bottom of the recess. The simulation domain is one cell height tall and tightly bounded in z from both directions by PEC boundary conditions. This configuration can be realized in practice using a parallel-plate waveguide simulator. For efficient analysis, a magnetic mirror symmetry condition was applied on the $x' = 0$ plane.

Figure 2.29 compares snapshots of the electric field distribution at the source current phase of 0 for three different radiation configurations. In Fig. 2.29a, the original configuration of a line source at $\lambda/4$ over a flat ground plane creates a well-known field distribution. When the line source is placed inside an air-filled recess at $\lambda/4$ above the bottom, the field distribution is distorted as shown in Fig. 2.29b. When the line source is embedded inside the optimized metamaterial structure, Fig. 2.29c shows that the original field distribution is almost completely restored except for a slight reduction in field strength due to conductor and dielectric losses in the metamaterials.

To quantitatively assess the effectiveness of the embedding metamaterial in restoring the far-field radiation patterns, Fig. 2.30 plots 2D directivity patterns for the same three configurations shown in Fig. 2.29. When the line source is placed in an empty recess, the radiation pattern is significantly distorted. In particular, the radiation intensity in directions close to the ground plane is significantly lower than that of the original configuration. It is observed that the embedding metamaterial restores the directivity pattern within approximately ± 1 dB of the ideal case.

Finally, the radiation efficiency has been predicted by simulation to be approximately 50%. Since the metamaterials used in this design incorporate highly resonant inclusions of both electric and magnetic types, reduction in radiation efficiency is expected due to conductor and dielectric losses. Considering that

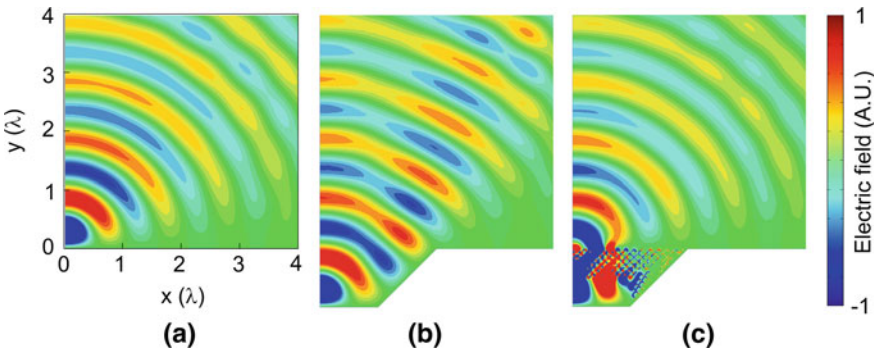

Fig. 2.29 Snapshots of the electric field distribution. **a** Original configuration. **b** Line source inside an air-filled recess. **c** Line source embedded in the metamaterial. All three *color plots* use the same range

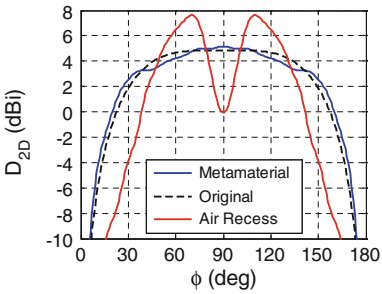

Fig. 2.30 Comparison of 2D directivity patterns for the three radiation configurations. © 2012 IEEE. Reprinted, with permission, from Kwon and Emiroglu [87]

practical NIMs typically exhibit significant losses, an overall reduction in radiation efficiency by 50% may not be a serious shortcoming in this metamaterial application to antennas incorporating NIM building blocks.

2.6 Planar Photonic Devices for Integrated Systems

There has been a growing interest in the development of integrated photonics systems as they are expected to play an increasingly important role in optical communications, imaging, computing, and sensing [91, 92]. Future advancement of this technology is critically dependent on an ability to develop miniaturized, functional photonic devices. By using the emerging transformation optics technique, a variety of practical optical components have been designed. As a result, a new type of photonic integrated circuit can be envisioned, which is comprised of a group of TO-based photonic components integrated with conventional optical and optoelectronic devices, including waveguides and photodetectors, on a common substrate [93].

Here, the TO building blocks are designed by using embedded QC transformations, which contain non-magnetic, dielectric-only materials. Therefore, they can be implemented with standard fabrication techniques, such as patterning air holes or rods on a silicon on insulator (SOI) platform, facilitating their application and integration into photonic systems [66, 67]. Moreover, such TO-based GRIN components can effectively steer light throughout the entire volume of the device, providing a dramatic improvement in the control of light compared to conventional GRIN optics with simple axial, radial, and spherical gradient profiles [63]. Since the QCTO approach is inherently two-dimensional, it is ideally suited for the design of planar photonic devices which manipulate the spatial propagation of light within a thin layer. As a result, the unprecedented design flexibility of transformation optics allows for the creation of a number of novel devices, such as a light source collimator, a waveguide coupler, and a waveguide crossing, which have broad applications in integrated photonic chips. Using the Finite-Difference

Time-Domain (FDTD) method, full-wave numerical simulations were performed to demonstrate the superior optical properties of these TO devices and their efficient integration with other components in an on-chip photonic system.

2.6.1 On-chip Light Source Collimator

A square TO quad-beam collimator was first designed by following the QC mapping illustrated in Fig. 2.31a. This transformation converts a circle into a square, where four equally distributed arcs are mapped in sequence onto the four sides of the square in the transformed domain. Consequently, an isotropically-radiating source at the center of the TO domain can be morphed into four highly collimated beams with planar equal-phase surfaces, propagating in the outward normal direction to each face of the device [22, 76]. When connected to silicon waveguides at its collimating surfaces, this TO component efficiently couples light emitted from a point source at the center of the device into each waveguide. As illustrated by Fig. 2.31a, the mesh grids created by the QC mappings possess strong orthogonality within the transformation domains, indicating that the anisotropy of the medium has been minimized.

The required effective parameters of the transformation medium can be calculated by following the general TO design equations [54]. For a TE-polarized wave with electric field normal to the plane of propagation, the TO devices can be characterized by the spatial distribution of refractive index. Figure 2.31b shows the GRIN profile of the collimator, which exhibits four-fold symmetry due to the transformation geometry and has a high index at each collimating surface. The highest refractive index found at the edge of the device can be adjusted by controlling the geometry and dimensions of the transformation domain. Therefore, the transformation is engineered such that the indices of the silicon waveguide and the QCTO element are mostly matched at the boundaries with an index of 3.4, leading to minimal reflection.

In order to characterize the performance of the TO collimator coupled with waveguides, full-wave numerical simulations were performed by using the FDTD method. As shown in Fig. 2.32a, the TO collimator connects four silicon waveguides at each collimating surface. The square collimator measures 7.5 μm on a side, while the width of each silicon waveguide is $t = 5$ μm. Figure 2.32b demonstrates the light intensity distribution excited by a point source with a wavelength of 1.5 μm, where the emitting light is smoothly guided inside the TO collimator before entering the connecting waveguides. Low reflections at the interface are evidenced by the fact that the interference fringes are fairly weak inside the TO collimator. FDTD simulations reveal that over 98% of the emitted energy is coupled into the waveguides through the TO collimator, demonstrating a high coupling efficiency and low insertion losses.

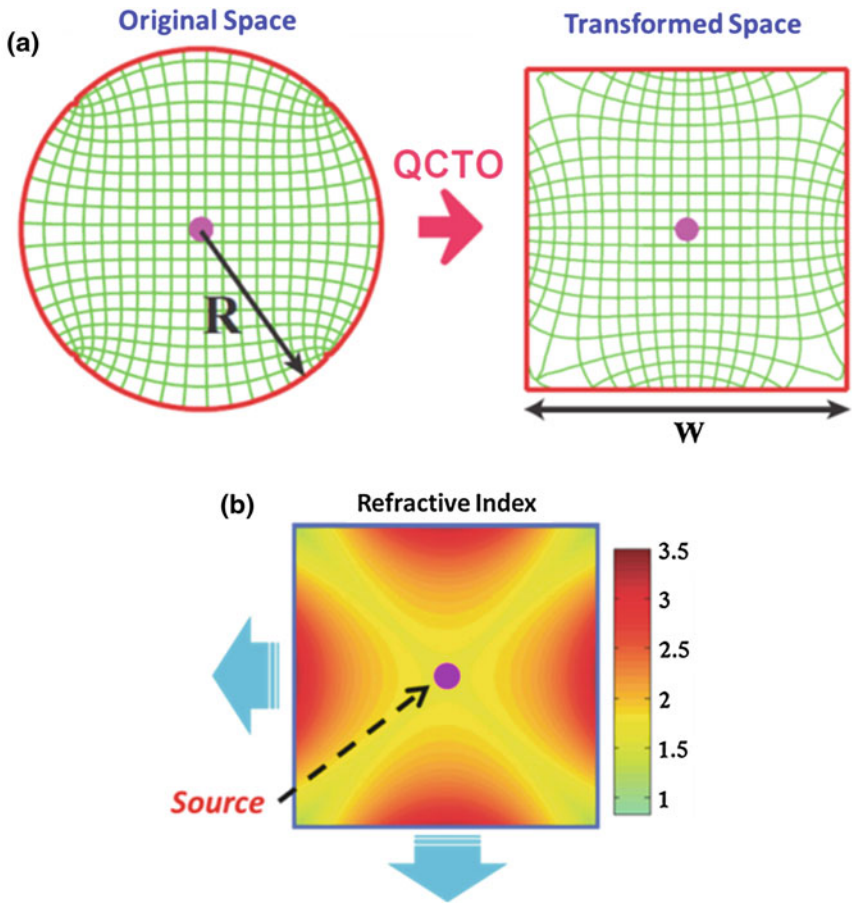

Fig. 2.31 **a** A QC mapping transforms a *circular region* in the original space into a *square region* in the transformed space. The resulting spatial grids and their inverse from the mapping are illustrated by *green lines* within the TO domains. **b** The refractive index profile of the resulting TO collimator. A line source indicated by the *dot* in the middle of the device can produce four collimated beams in directions normal to the faces of the square collimator

2.6.2 Compact Waveguide Adapters

The QC transformation technique can also be employed to design many other GRIN components with versatile functionalities, such as waveguide adapters. For instance, Fig. 2.33a illustrates another geometry transformation from a circle with radius R in the original space to a rectangle in the transformed space. Two additional flat protrusions with a width of w are chosen in order to facilitate orthogonal grid generation through QC mappings. In particular, the arcs on the top and bottom boundaries of the circular domain are mapped into two straight segments along the surfaces of the rectangular domain as shown by the solid red

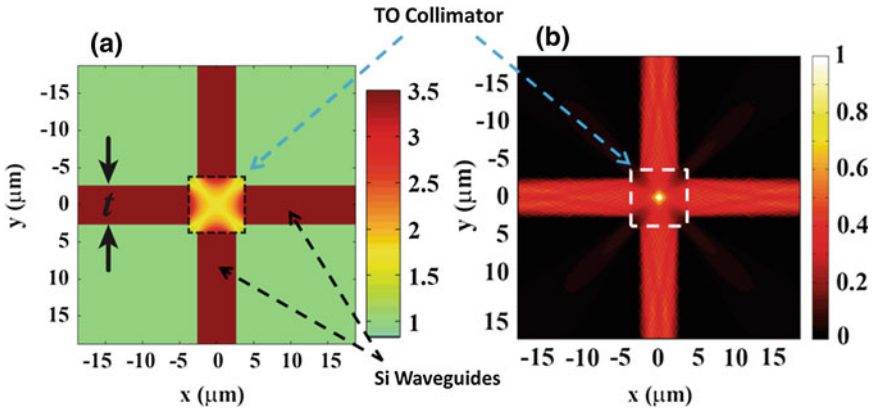

Fig. 2.32 **a** A quad-beam TO collimator connects four silicon waveguides. **b** The light intensity distribution excited by a point source at the center of the device demonstrates efficient coupling from the light source to all four waveguides. The wavelength of the light source is 1.5 μm

curves. When a point source is placed at the center of the original space in vacuum, the diverging cylindrical waves have equal-phase surfaces as concentric circles, including those curved boundaries in red. Since the circular arcs are mapped into straight lines in the new system, the emerging electromagnetic waves from these interfaces will have planar wave fronts, producing highly directive beams that can efficiently couple into neighboring components, such as optical waveguides. The resulting GRIN profile of the transformed domain is demonstrated in Fig. 2.33b, which possesses a mirror symmetry as indicated by the dashed line.

The transformation presented in Fig. 2.33 is employed here to design a waveguide coupler, which can connect different-sized optical waveguides by effectively converting the guided modes [94]. In contrast to a conventional coupler which requires a long adiabatically tapering section to reduce losses, the TO-based design approach leads to compact devices as the light propagation can be controlled effectively over the entire transformation medium. As shown in Fig. 2.34a, the TO coupler is comprised of two GRIN elements. The index distributions of both elements are obtained based on the QC mapping illustrated in Fig. 2.33. Due to the mirror symmetry of the refractive index profile in Fig. 2.33b, each element of the waveguide coupler consists of half of the transformation medium. Furthermore, the geometrical transformations are chosen so that the resulting TO coupler matches the size and refractive index of the waveguides at both the input and output surfaces. In this way, light carried by the input waveguide from the left is compressed into a narrow beam by the first element of the coupler before experiencing a subsequent expansion to match the size of the output waveguide.

Figure 2.34b demonstrates the performance of the coupling device, through which light is smoothly guided and coupled between two silicon waveguides of different size. Despite a small amount of reflective and scattered light, such a compact TO waveguide coupler provides a coupling efficiency with up to 95% transmission. It is interesting to note that the incident light is focused in the middle

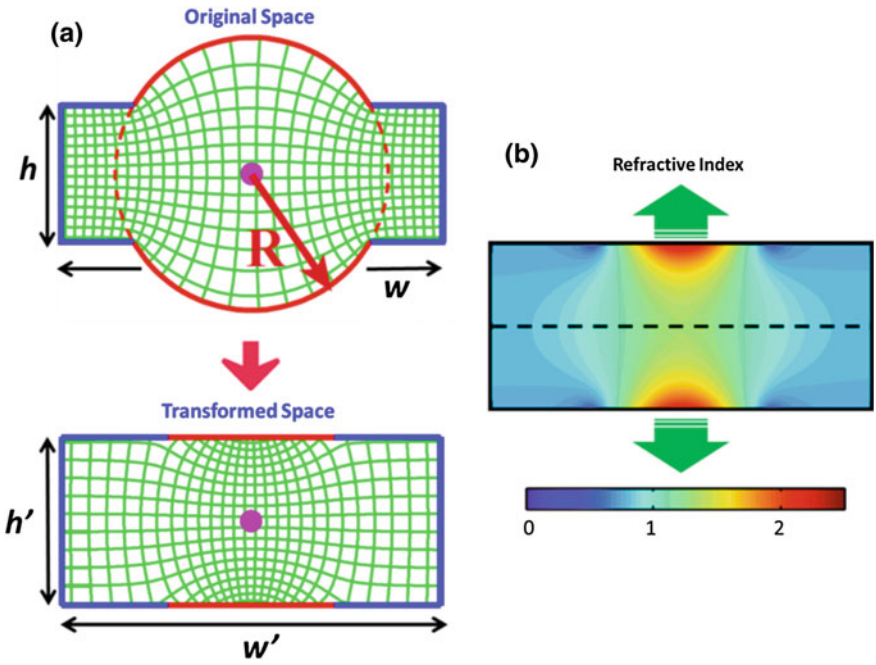

Fig. 2.33 **a** A QC mapping transforms a circular region with protrusions in the original space into a rectangle in the transformed space. The *top* and *bottom* surfaces of a circle are mapped into two straight segments along the surfaces of the rectangle (*solid red lines*). **b** The resulting refractive index profile of the transformed device. The TO device can generate two collimated beams in directions normal to the collimating faces indicated by the *arrows*

of the coupler, producing an enhanced electric field that is 5 times stronger than that in the input waveguide. As a result, this TO component, together with the associated waveguides, provides an integrated platform that is suitable for investigating light interaction with optical media, such as active and nonlinear materials.

Another essential component in integrated photonics is the waveguide crossing, which allows optical signals carried by waveguides to be routed and interconnected within a limited space, providing the possibility for high-density integration of optical devices in photonic circuits [91, 92]. In order to mitigate insertion loss and crosstalk at the intersections of optical waveguides, either a resonator or a mode expander type crossing device is needed [95, 96]. By applying an appropriate QCTO approach to engineer the GRIN profile of the device, a new type of waveguide crossing that can channel the light propagation throughout the transformation medium without any wave guiding structures was designed.

The same geometrical mapping illustrated in Fig. 2.33 can be used for the development of a waveguide crossing. Since light rays in both spaces must remain normal to the boundaries (solid red lines), the light will bend to pass through the origin in the physical space and exhibit a lateral shift when exiting the device [66]. Instead of assuming a vacuum in the virtual space as in most of the TO designs, we

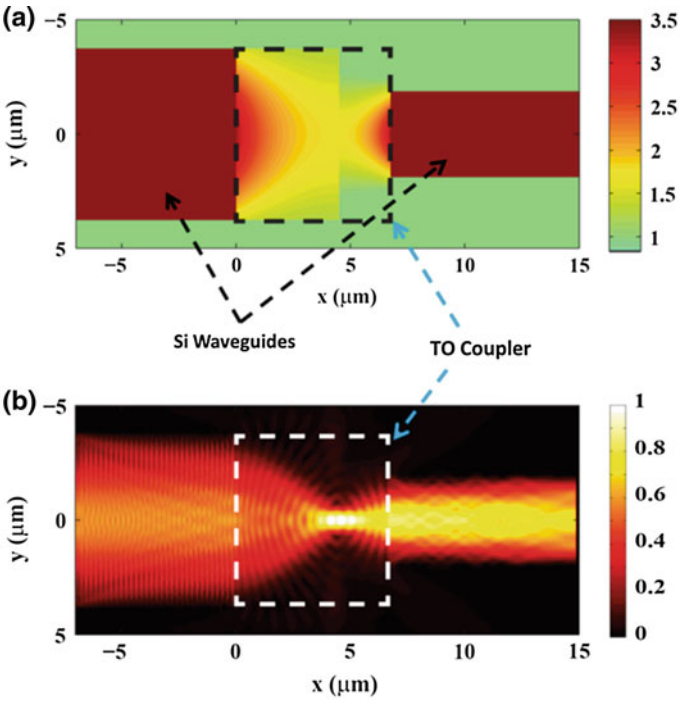

Fig. 2.34 **a** A TO-based GRIN waveguide coupler connects two silicon waveguides with a width of 7.5 μm and 3.75 μm, respectively. The coupler device, illustrated in the *black dashed* box, has a size of 7.5 μm by 6.7 μm. **b** Light intensity distribution obtained from FDTD simulations. Light from the input waveguide on the left couples well into the output waveguide through the TO coupler

assign a Maxwell fisheye lens with a radial GRIN distribution given in (2.52) to the circular region as shown in Fig. 2.35a, where R is the radius of the circular region and $0 \leq r \leq R$.

$$n(r) = \frac{2}{1 + \left(\frac{r}{R}\right)^2} \tag{2.52}$$

The resulting GRIN profile of the transformed medium is shown in Fig. 2.35b, where the center region within the dashed black box is truncated and employed as a crossing device.

To demonstrate the waveguide crossing behavior, the GRIN device is connected to two input and two output waveguides with reversed order on either side of the device as shown in Fig. 2.35c. The crossing device, illustrated by the black dashed box, has a size of 15 μm by 10 μm and a refractive index ranging from 2.0 to 3.4. All the connecting Si waveguides possess a width of 1.5 μm while the adjacent waveguides on each side of the device are separated by a distance of 3 μm. FDTD simulations were performed to illustrate the light crossing effects

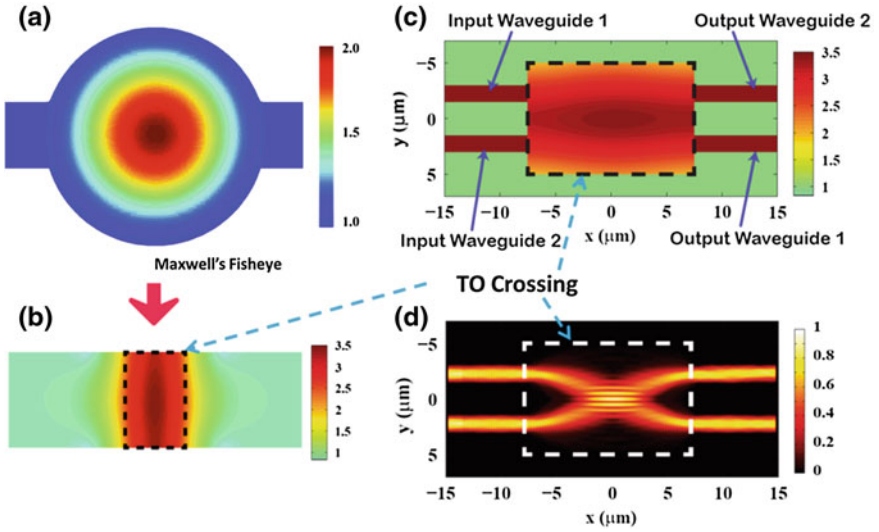

Fig. 2.35 **a** The refractive index profile of a Maxwell fisheye lens in a circular domain with protrusions in the original space. **b** The GRIN profile of the transformed rectangular region. **c** A TO waveguide crossing connects two silicon waveguides with a width of 1.5 μm on either side of the device. The crossing device, illustrated in the *black dashed box*, has a size of 15 μm by 10 μm. **d** Light intensity distribution obtained with both input waveguide 1 and 2 illuminated. Light from the input waveguide 1 and 2 bends down/up and couples efficiently into the corresponding output waveguides through the QCTO component. The wavelength is 1.5 μm

throughout the TO device. When both input waveguides are illuminated, as shown in Fig. 2.35d, the TO device provides the desired crossing performance by routing two beams into the corresponding output waveguides in an inverse order. Due to the imaging property of the Maxwell fisheye lens, the diffraction of light is compensated as the wave is focused right in front of the output waveguide and the lateral expansion of the beam is well confined within the GRIN region. Although some interference fringes can be observed at the intersection area of the two beams, the two optical signals are guided independently and couple into the output waveguides with transmission of over 98% in each case. By increasing the size of the TO crossing element and including more waveguide ports, it is possible to further extend the number of optical signals across the device and thereby further enhance the integration density of neighboring devices.

2.7 Conclusions

Novel device designs based upon the TO and QCTO techniques have been presented for invisibility cloaks, flat lenses, beam propagation manipulation devices, planar photonic devices, and antennas. For each design, the associated coordinate

transformation, parameters for the transformation media, example designs as well as predicted performance were shown. The device designs presented in this chapter represent only a small fraction of a host of applications that the TO technique can provide, with new functional features or traditional utilities in new form factors. As fabrication techniques mature for realizing anisotropic and inhomogeneous constituent media, TO-based devices will become viable options in practical applications.

Acknowledgments This work was partially supported by the NSF MRSEC program under grant number DMR-0820404. Kwon acknowledges the support by the ECE Department of UMass Amherst for this work.

References

1. Leonhardt U (2006) Optical conformal mapping. Science 312:1777–1780
2. Pendry JB, Schurig D, Smith DR (2006) Controlling electromagnetic fields. Science 312:1780–1782
3. Schurig D, Pendry JB, Smith DR (2006) Calculation of material properties and ray tracing in transformation media. Opt Express 14:9794–9804
4. Schurig D, Mock JJ, Justice BJ, Cummer SA, Pendry JB, Starr AF, Smith DR (2006) Metamaterial electromagnetic cloak at microwave frequencies. Science 314:977–980
5. Huang Y, Feng Y, Jiang T (2007) Electromagnetic cloaking by layered structure of homogeneous isotropic materials. Opt Express 15:11133–11141
6. Gaillot DP, Croenne C, Lippens D (2008) An all-dielectric route for terahertz cloaking. Opt Express 16:3986–3992
7. Zolla F, Guenneau S, Nicolet A, Pendry JB (2007) Electromagnetic analysis of cylindrical invisibility cloaks and the mirage effect. Opt Lett 32:1069–1071
8. Zhang B, Chen H, Wu B-I, Kong JA (2008) Extraordinary surface voltage effect in the invisibility cloak with an active device inside. Phy Rev Lett 100:063904
9. Ruan Z, Yan M, Neff CW, Qiu M (2007) Ideal cylindrical cloaks: perfect but sensitive to tiny perturbations. Phy Rev Lett 99:113903
10. Chen H, Wu B-I, Zhang B, Kong JA (2007) Electromagnetic wave interactions with a metamaterial cloak. Phy Rev Lett 99:063903
11. Chen H, Chan CT (2008) Time delays and energy transport velocities in three dimensional ideal cloaking devices. J Appl Phys 104:033113
12. Leonhardt U, Tyc T (2009) Broadband invisibility by non-Euclidean cloaking. Science 323:110–112
13. Kwon D-H, Werner DH (2008) Two-dimensional eccentric elliptic electromagnetic cloaks. Appl Phys Lett 92:013503
14. Nicolet A, Zolla F, Guenneau S (2008) Finite-element analysis of cylindrical invisibility cloaks of elliptical cross section. IEEE Trans Magn 44:1150–1153
15. Rahm M, Schurig D, Roberts DA, Cummer SA, Smith DR, Pendry JB (2008) Design of electromagnetic cloaks and concentrators using form-invariant coordinate transformations of Maxwell's equations. Photon Nanostruct Fundam Appl 6:87–95
16. Zhang J, Luo Y, Chen H, Wu B-I (2008) Cloak of arbitrary shape. J Opt Soc Amer B 25:1776–1779
17. Wu Q, Zhang K, Meng F, Li L (2008) Material parameters characterization for arbitrary N-sided regular polygonal invisible cloak. J Phys D 42:035408

18. Kwon D-H, Werner DH (2008) Two-dimensional electromagnetic cloak having a uniform thickness for elliptic cylindrical regions. Appl Phys Lett 92:113502
19. Nicolet A, Zolla F, Guenneau S (2008) Electromagnetic analysis of cylindrical cloaks of an arbitrary cross section. Opt Lett 33:1584–1586
20. Li C, Yao K, Li F (2008) Two-dimensional electromagnetic cloaks with non-conformal inner and outer boundaries. Opt Express 16:19366–19374
21. Rahm M, Cummer SA, Schurig D, Pendry JB, Smith DR (2008) Optical design of reflectionless complex media by finite embedded coordinate transformations. Phys Rev Lett 100:063903
22. Kwon D-H, Werner DH (2008) Transformation optical designs for wave collimators, flat lenses and right-angle bends. New J Phys 10:115023
23. Donderici B, Teixeira FL (2008) Metamaterial blueprints for reflectionless waveguide bends. IEEE Microw Wireless Comp Lett 18:233–235
24. Huangfu J, Xi S, Kong F, Zhang J, Chen H, Wang D, Wu B-I, Ran L, Kong JA (2008) Application of coordinate transformation in bent waveguides. J Appl Phys 104:014502
25. Rahm M, Roberts DA, Pendry JB, Smith DR (2008) Transformation-optical design of adaptive beam bends and beam expanders. Opt Express 16:11555–11567
26. Emiroglu CD, Kwon D-H (2010) Impedance-matched three-dimensional beam expander and compressor designs via transformation optics. J Appl Phys 107:084502
27. Jiang WX, Cui TJ, Ma HF, Zhou XY, Cheng Q (2008) Cylindrical-to-plane-wave conversion via embedded optical transformation. Appl Phys Lett 92:261903
28. Zhang JJ, Luo Y, Xi S, Chen HS, Ran LX, Wu B-I, Kong JA (2008) Directive emission obtained by coordinate transformation. Prog Electromagn Res 81:437–446
29. Roberts DA, Kindtz N, Smith DR (2009) Optical lens compression via transformation optics. Opt Express 17:16535–16542
30. Pendry JB (2000) Negative refraction makes a perfect lens. Phys Rev Lett 85:3966–3969
31. Shelby RA, Smith DR, Schultz S (2001) Experimental verification of a negative index of refraction. Science 292:77–79
32. Valentine J, Zhang S, Zentgraf T, Ulin-Avila E, Genov DA, Bartal G, Zhang X (2008) Three-dimensional optical metamaterial with a negative refractive index. Nature 455:376–380
33. Yan M, Yan W, Qiu M (2008) Cylindrical superlens by a coordinate transformation. Phy Rev B 78:125113
34. Chen H, Luo X, Ma H, Chan CT (2008) The anti-cloak. Opt Express 16:14603–14608
35. Yang T, Chen H, Luo X, Ma H (2008) Superscatterer: enhancement of scattering with complementary media. Opt Express 16:18545–18550
36. Ng J, Chen H, Chan CT (2009) Metamaterial frequency-selective superabsorber. Opt Lett 34:644–646
37. Lai Y, Zheng H, Zhang Z-Q, Chan CT (2011) Manipulating sources using transformation optics with 'folded geometry'. J Opt 13:024009
38. Leonhardt U, Philbin TG (2006) General relativity in electrical engineering. New J Phys 8:247
39. Lai Y, Chen H, Zhang Z-Q, Chan CT (2009) Complementary media invisibility cloak that cloaks objects at a distance outside the cloaking shell. Phys Rev Lett 102:093901
40. Lai Y, Ng J, Chen H, Han D, Xiao J, Zhang Z-Q, Chan CT (2009) Illusion optics: the optical transformation of an object into another object. Phys Rev Lett 102:253902
41. Kwon D-H, Werner DH (2008) Restoration of antenna parameters in scattering environments using electromagnetic cloaking. Appl Phys Lett 92:113507
42. Popa B-I, Allen J, Cummer SA (2009) Conformal array design with transformation electromagnetics. Appl Phys Lett 94:244102
43. Kwon D-H (2009) Virtual circular array using material-embedded linear source distributions. Appl Phys Lett 95:173503
44. Tichit P-H, Burokur SN, de Lustrac A (2009) Ultradirective antenna via transformation optics. J Appl Phys 105:104912

45. Tichit P-H, Burokur SN, Germain D, de Lustrac A (2011) Design and experimental demonstration of a high-directive emission with transformation optics. Phy Rev B 83:115108
46. Kwon D-H (2010) Transformation electromagnetic design of an embedded monopole in a ground recess for conformal applications. IEEE Antennas Wireless Propag Lett 9:432–435
47. Li J, Pendry JB (2008) Hiding under the carpet: a new strategy for cloaking. Phys Rev Lett 101:203901
48. Liu R, Ji C, Mock JJ, Chin JY, Cui TJ, Smith DR (2009) Broadband ground-plane cloak. Science 323:366–369
49. Valentine J, Li J, Zentgraf T, Bartal G, Zhang X (2009) An optical cloak made of dielectrics. Nat Mater 8:568–571
50. Kundtz N, Smith DR (2009) Extreme-angle broadband metamaterial lens. Nat Mater 9:129–132
51. Demetriadou A, Hao Y (2011) Slim Luneburg lens for antenna applications. Opt Express 19:19925–19934
52. Mei ZL, Bai J, Cui TJ (2011) Experimental verification of a broadband planar focusing antenna based on transformation optics. New J Phys 13:063028
53. Garcia-Meca C, Martinez A, Leonhardt U (2011) Engineering antenna radiation patterns via quasi-conformal mappings. Opt Express 19:23743–23750
54. Kwon D-H, Werner DH (2010) Transformation electromagnetics: an overview of the theory and applications. IEEE Antennas Propag Mag 52:24–46
55. Chen H, Chan CT, Sheng P (2010) Transformation optics and metamaterials. Nat Mater 9:387–396
56. Kuntz N, Smith DR, Pendry JB (2011) Electromagnetic design with transformation optics. Proc IEEE 99:1622–1633
57. Milton GW, Briane M, Willis JR (2006) On cloaking for elasticity and physical equations with a transformation invariant form. New J Phys 8:248
58. Gabrielli LH, Cardenas J, Poitras CB, Lipson M (2009) Silicon nanostructure cloak operating at optical frequencies. Nat Photon 3:461–463
59. Lee J, Blair J, Tamma V, Wu Q, Rhee S, Summers C, Park W (2009) Direct visualization of optical frequency invisibility cloak based on silicon nanorod array. Opt Express 17:12922–12928
60. Ma HF, Cui TJ (2010) Three-dimensional broadband ground-plane cloak made of metamaterials. Nat Commun 1:1–6
61. Ergin T, Stenger N, Brenner P, Pendry JB, Wegener M (2010) Three-dimensional invisibility cloak at optical wavelengths. Science 328:337–339
62. Ma HF, Cui TJ (2010) Three-dimensional broadband and broad-angle transformation-optics lens. Nat Commun 1:124
63. Kundtz NB, Smith DR, Urzhumov Y, Landy NI (2010) Enhancing imaging systems using transformation optics. Opt Express 18:21238–21251
64. Tang W, Argyropoulos C, Kallos E, Song W, Hao Y (2010) Discrete coordinate transformation for designing all-dielectric flat antennas. IEEE Trans Antennas Propag 58:3795–3804
65. Yang R, Tang W, Hao Y (2011) A broadband zone plate lens from transformation optics. Opt Express 19:12348–12355
66. Zentgraf T, Valentine J, Tapia N, Li J, Zhang X (2010) An optical "Janus" device for integrated photonics. Adv Mater 22:2561–2564
67. Hunt J, Tyler T, Dhar S, Tsai Y-J, Bowen P, Larouche S, Jokerst NM, Smith DR (2012) Planar, flattened Luneburg lens at infrared wavelengths. Opt Express 20:1706–1713
68. Bao D, Rajab KZ, Tang W, Hao Y (2012) Experimental demonstration of broadband transmission through subwavelength aperture. Appl Phys Lett 97:134105
69. Yang R, Tang W, Hao Y, Youngs I (2011) A coordinate transformation-based broadband flat lens via microstrip array. IEEE Antennas Wireless Propag Lett 10:99–102
70. Mei ZL, Bai J, Cui TJ (2010) Illusion devices with quasi-conformal mapping. J Electromagn Waves Appl 24:2561–2573

71. Mastin CW, Thompson JF (1984) Quasiconformal mappings and grid generation. SIAM J Sci Stat Comp 5:305–310
72. Ives DC, Zacharias RM (1989) Conformal mapping and orthogonal grid generation. J Propul Power 5:327–333
73. Thompson JF, Soni BK, Weatherill NP (1999) Handbook of grid generation. CRC Press, Boca Raton
74. Chang Z, Zhou X, Hu J, Hu G (2012) Design method for quasi-isotropic transformation materials based on inverse Laplace's equation with sliding boundaries. Opt Express 18:6089–6096
75. Turpin JP, Massoud AT, Jiang ZH, Werner PL, Werner DH (2010) Conformal mappings to achieve simple material parameters for transformation optics devices. Opt Express 18:244–252
76. Schmiele M, Varma VS, Rockstuhl C, Lederer F (2010) Designing optical elements from isotropic materials by using transformation optics. Phys Rev A 81:033837
77. Tang L, Yin J, Yuan G, Du J, Gao H, Dong X, Lu Y, Du C (2011) General conformal transformation method based on Schwarz-Christoffel approach. Opt Express 19:15119–15126
78. Ma YG, Wang N, Ong CK (2010) Application of inverse, strict conformal transformation to design waveguide devices. J Opt Soc Am A: 27:968–972
79. Landy NI, Padilla WJ (2009) Guiding light with conformal transformations. Opt Express 17:14872–14879
80. Cummer SA, Popa B-I, Schurig D, Smith DR, Pendry JB (2006) Full-wave simulations of electromagnetic cloaking structures. Phys Rev E 74:036621
81. Haupt RL, Werner DL (2007) Genetic algorithms in electromagnetics. Wiley, Hoboken, NJ
82. Chen H, Chan CT (2007) Transformation media that rotate electromagnetic fields. Appl Phys Lett 90:241105
83. Kwon D-H, Werner DH (2008) Polarization splitter and polarization rotator designs based on transformation optics. Opt Express 16:18731–18738
84. Kwon D-H, Werner DH (2009) Flat focusing lens designs having minimized reflection based on coordinate transformation techniques. Opt Express 17:7807–7817
85. Xu X, Feng Y, Jiang T (2008) Electromagnetic beam modulation through transformation optical structures. New J Phys 10:115027
86. Cummer SA, Kundtz N, Popa B-I (2009) Electromagnetic surface and line sources under coordinate transformations. Phys Rev A 80:033820
87. Kwon D-H, Emiroglu CD (2012) Two-dimensional metamaterial designs for line-source radiation from a virtual location. In: Proceedings of the 6th European conference on antennas and propagation, Prague, 26–30 March 2012, pp 1706–1710
88. Pendry JB, Holden AJ, Robbins DJ, Stewart WJ (1999) Magnetism from condcutors and enhanced nonlinear phenomena. IEEE Trans Microw Theory Tech 47:2075–2084
89. Smith DR, Schultz S, Markos P, Soukoulis CM (2002) Determination of effective permittivity and permeability of metamaterials from reflection and transmission coefficients. Phys Rev B 65:195104
90. Schurig D, Mock JJ, Smith DR (2006) Elecric-field-coupled resonators for negative permittivity metamaterials. Appl Phys Lett 88:041109
91. Lifante G (2003) Integrated photonics: fundamentals. Wiley, Chichester
92. Pollock CR, Lipson M (2003) Integrated photonics. Kluwer Academic Publishers, Norwell
93. Wu Q, Turpin JP, Werner DH (2012) Integrated photonic systems based on transformation optics enabled gradient index devices. Light Sci Appl 1:e38
94. Tichit P-H, Burokur SN, de Lustrac A (2010) Waveguide taper engineering using coordinate transformation technology. Opt Express 18:767–772
95. Johnson SG, Manolatou C, Fan S, Villeneuve PR, Joannopoulos JD, Haus HA (1998) Elimination of cross talk in waveguide intersections. Opt Lett 23:1855–1857
96. Bogaerts W, Dumon P, Thourhout D, Baets R (2007) Low-loss, low cross-talk crossings for silicon-on-insulator nanophotonic waveguides. Opt Lett 32:2801–2803

Chapter 3
Metasurface Transformation Theory

Enrica Martini and Stefano Maci

Abstract Metasurfaces constitute a class of thin metamaterials, which are used from microwave to optical frequencies to create new antennas and microwave devices. This chapter describes how to use transformation optics (TO) to create anisotropic modulated-impedance metasurfaces able to transform planar surface waves (SW) into a predefined curved-wavefront surface wave. In fact, the modulated anisotropic impedance imposes a local modification of the dispersion equation and, at constant operating frequency, of the local wavevector. The general effects of metasurface modulation are similar to those obtained by TO in volumetric inhomogeneous metamaterials, namely readdressing the propagation path of an incident wave; however, significant technological simplicity is gained.

3.1 Introduction

Metamaterials have found several applications in designing antennas and microwave components. These artificial materials can be formed by periodic arrangements of many small inclusions in a dielectric host environment, for achieving macroscopic electromagnetic or optical properties that cannot be found in nature. After about 10 years from the first pioneering works on metamaterials, the new concept of transformation optics (TO) has been introduced [1, 2], which establishes criteria to obtain a control on ray field paths within inhomogeneous anisotropic metamaterials. This control is achieved on the basis of macroscopic equivalent constitutive tensors of the anisotropic material. The TO methodology has been applied, for instance, to design invisibility cloaks, i.e., shells of anisotropic metamaterials capable of rendering any object within their interior cavities

E. Martini · S. Maci (✉)
Department of Information Engineering, University of Siena, Siena, Italy
e-mail: macis@dii.unisi.it

D. H. Werner and D.-H. Kwon (eds.), *Transformation Electromagnetics and Metamaterials*, DOI: 10.1007/978-1-4471-4996-5_3,

invisible to detection from outside [3, and references therein]. The technological difficulties in controlling the variation of the homogenized constitutive tensors of volumetric metamaterials, together with anisotropy and extreme parameters, complicate the engineering implementation of TO in practical devices.

Our main starting point is the observation that effects similar to addressing waves in *volumetric* media may be obtained by modulating the properties of a *metasurface* that supports surface waves (SW).

In analogy with metamaterials, metasurfaces are constituted by an arrangement of printed elements whose dimensions are smaller than the wavelength of the dominant wave phenomenon. In general, the resulting structure is periodic. We consider instead *aperiodic* metasurfaces. The aperiodicity is obtained by gradually modulating the geometry of the elements in contiguous cells. Macroscopically, this results in a modulation of the equivalent impedance of the metasurface, which produces a change of phase velocity and propagation path of the SW supported by the metasurface. In Ref. [4], this metasurface-driven wave-field transformation is synthetically referred to as "metasurfing". In the latter reference, this concept has been introduced without a coordinate transformation, treating only cases where an equivalent refraction index can be defined. The main objective here is instead to link a generic coordinate transformation to an anisotropic impedance supporting a curved-wavefront surface wave, whose phase is directly related to the transformation.

This chapter is organized as follows. Section 3.2 reviews the metasurface concept for both the isotropic and the anisotropic case. Emphasis is placed on the anisotropic case since we predict such a type of final output. Section 3.3 presents the formulation of the metasurface transformation theory. After a statement of the problem, this section introduces the local dispersion concept, and the conditions on the transformation parameters which allow for the fulfilment of the free-space wave equation for a given form of electric and magnetic potentials. The desired curved wavefront SW field distribution is obtained from these potentials. The anisotropic impedance tensor congruent with the above curved wavefront is obtained by matching the dispersion equation obtained via local transverse resonance with the dispersion equation associated with the transformed wavefront. The maximum error of this matching is evaluated by a rigorous closed form expression. Expressions of fields and impedance matching conditions at the boundary of the transformation domain are also provided. Section 3.4 specializes the theory to the case of conformal and nearly conformal transformations, which leads to the drastic simplification of isotropic boundary conditions and to the definition of an equivalent refractive index satisfying the Fermat's principle. Some numerical examples are presented in Sect. 3.5 and conclusions are drawn in Sect. 3.6. The chapter is completed by two Appendices: the first one (Appendix A) summarizes some useful TO formulas for 3D metamaterials and the second one (Appendix B) illustrates the derivation of the dispersion equation for anisotropic impedance boundary conditions.

3.2 Modulated Metasurfaces

A metasurface is a thin metamaterial layer characterized by unusual reflection properties of plane waves and/or dispersion properties of surface/guided waves. Metasurfaces may be distinguished as penetrable and impenetrable. A penetrable metasurface (sometimes called metafilm) consists of a planar distribution of small periodic elements in a very thin host medium. Its effective properties can be studied for instance by applying generalized sheet transition conditions (GSTCs) [5, 6] which allow one to characterize a metasurface in terms of an unambiguous anisotropic sheet impedance.

Impenetrable metasurfaces, which are those treated in this chapter, are realized at microwave frequencies through a dense periodic texture of small elements printed on a grounded slab with or without shorting vias. They can also simply consist of a dense distribution of pins on a ground plane [7]. This kind of metasurfaces has been used for realizing electromagnetic bandgap (EBG) surfaces or equivalent magnetic walls [8, 9]. Impenetrable metasurfaces can be characterized in terms of an anisotropic surface impedance tensor through the use of the pole-zero-matching method [10]. Absence of losses in the dielectric and in the metal implies that the surface *impedance* is actually a surface *reactance*. This is true for periodicities small in terms of a wavelength; larger periodicities may instead cause transfer of energy to higher order Floquet modes that may be effectively interpreted as a loss [10]. This case is not considered here.

The basic assumption in the conventional analysis of metasurfaces is the periodical distribution of the constituent elements. In a TO framework, we have to remove this assumption and to deal with an aperiodic element distribution. The aperiodicity is obtained by gradually changing the geometry of the elements in contiguous cells, while maintaining the period unchanged and very small in terms of a wavelength.

3.2.1 Isotropic Modulated Metasurface Reactance

The aperiodic metasurface is described by an equivalent homogenized model and characterized through a lossless *modulated metasurface reactance* (MMR) which imposes boundary conditions on the ratio between the average tangential components of the electric and magnetic fields. Whenever the elements exhibit a symmetric shape, the MMR is isotropic with respect to the direction of the wavevector of the supported mode; in this case, we denote the relevant MMR as isotropic-MMR (IMMR). An IMMR can be synthesized by using an appropriate technology that depends on the frequency range of operation. Figure 3.1 illustrates a practical realization of an IMRR in the microwave–millimetre wave frequency range, consisting of square or circular patches with different sizes printed on a grounded slab. The size of the elementary cell of the texture is assumed constant

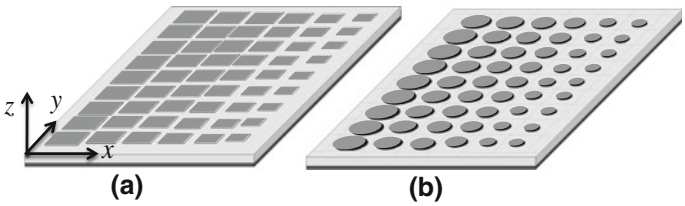

Fig. 3.1 IMMR at microwave frequencies consisting of small patches with variable sizes printed on a grounded slab. **a** *Rectangular patches* with variable side. **b** *Circular patches* with variable radius. The patches are positioned at the center of the unit cell, whose size is assumed uniform

throughout the surface and small in terms of a wavelength. The modulation of the IMMR is obtained through a smooth cell-by-cell variation of the patch dimension.

An effective IMMR is obtained by considering each constituent element of the metasurface as embedded in a locally uniform periodic structure. That is, we identify the local texture and the relevant value of reactance with those of a *periodic* texture which matches the local geometry.

Due to the small dimensions of the unit cell, we may assume that the IMMR exhibits an almost continuous variation, characterized by a *scalar* value $X_S(\rho)$ (here, ρ is the coordinate of the 2D observation point on the surface). This constitutes a quite reasonable approximation for printed patches with symmetric shapes. A scalar IMMR implies that the ratio between the average tangential electric and magnetic fields is equal to $jX_S(\rho)$; thus, the tangential fields are orthogonal and in quadrature of phase. This latter property is due to the fact that no energy can penetrate into the surface. A transverse magnetic (TM) SW has magnetic field transverse to the metasurface normal. Similarly, a transverse electric (TE) SW has electric field transverse to the metasurface normal. An inductive isotropic reactance $(X_S(\rho) > 0)$ supports a TM SW, while a capacitive isotropic reactance $(X_S(\rho) < 0)$ supports a TE SW. In both cases, the amplitude $k_t(\rho)$ of the transverse wavevector $\mathbf{k}_t(\rho) = k_t(\rho)\hat{\mathbf{k}}_t(\rho)$ is *independent* of the direction $\hat{\mathbf{k}}_t$. The dispersion equation for an ω-dependent inductive reactance X_S is

$$k_t(\rho) = k\sqrt{1 + (X_S(\rho)/\zeta)^2} \tag{3.1}$$

where ζ and k are the free space impedance and wavenumber, respectively. This dispersion equation is obtained by imposing the transverse resonance condition. It is apparent that k_t is larger than the wavenumber k of free space, i.e., the phase velocity is smaller than the speed of light; as a consequence, the wave equation imposes an exponential attenuation of the fields in the direction normal to the metasurface, with attenuation constant $v = kX_S/\zeta$. A typical behavior of the TM wave dispersion diagram (3.1) is shown in Fig. 3.2. It is apparent that, at a given frequency, larger patches (smaller gaps) support SW's with larger wavenumbers (smaller phase velocity) and vice versa.

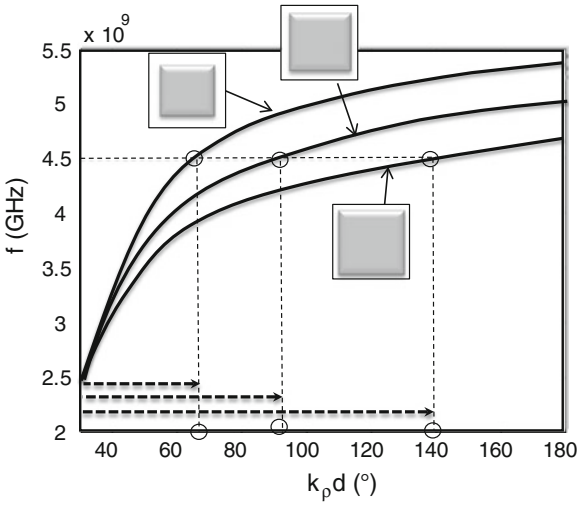

Fig. 3.2 Typical dispersion diagrams for TM-SW supported by a metasurface consisting of *square patches* of different sizes periodically printed on a grounded slab

Due to the presence of the grounded slab, the reactance X_S is actually dependent on k_t, so that (3.1) is an implicit form of the dispersion equation. In Ref. [11], a k_t-dependent reactance model is proposed. However, the dependence on k_t is often weak and does not modify the basic wave mechanism, except for a slight shift of the operational frequency. Although the above k_t-dependence may be introduced in the formulation presented in the following, we will not consider it in order to avoid formal complications, but it is understood that this assumption does not imply a loss of generality.

The modulation of the wave vector obtained through the IMMR produces a change of the phase velocity and propagation path of the SW supported by the metasurface. Let us understand this through the simple example illustrated in Fig. 3.3. Figure 3.3a shows a IMMR consisting of a uniform rectangular lattice of printed square patches modulated in size along x, with smaller sizes toward the center and larger sizes toward the periphery. The transverse wavenuber of the SW supported by the metasurface changes along x according to the dispersion diagram in Fig. 3.2. Assume that this metasurface is excited at a certain section $y = y_0$ with a TM surface *plane* wave, represented in Fig. 3.3 by a congruence of parallel wavevectors. As the wave progresses along y, the boundary conditions impose a local decrease of k_t at the center and an increase at the periphery. Correspondingly, the local phase velocity decreases at the periphery and increases at the center, thus producing a diverging wavefront. This forces the wavevector to modify its direction, so as to maintain its amplitude consistent with the dispersion (3.1) for the local reactance value. The opposite occurs when the patches are larger at the center and smaller at the periphery (Fig. 3.3b). The congruence of rays forms, in this case, a converging wavefront that may focus the field in a point. The propagation path of the ray field can be found by defining a local refraction index and invoking the Fermat's principle of minimum optical path.

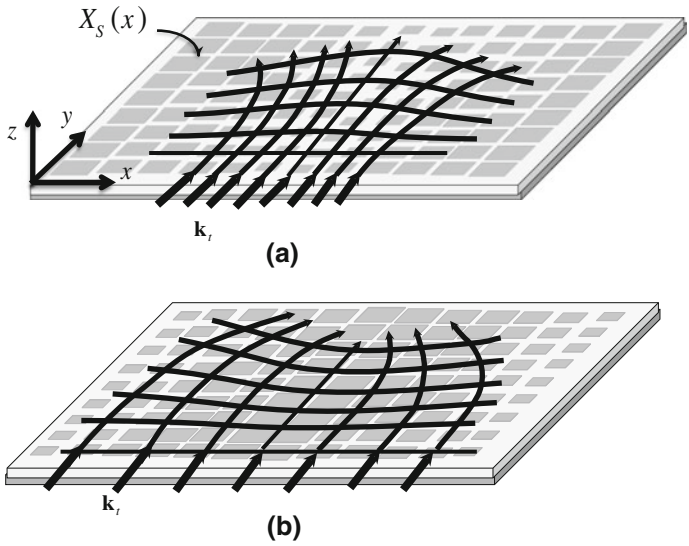

Fig. 3.3 Example of curved-wavefront SW supported by an IMMR. **a** Diverging rays. **b** Converging rays

The modulation of the surface reactance can therefore be used to guide the propagation and to shape the wavefront of SW's, with the objective of constructing engineering devices. In recent papers, Luneburg lenses based on this concept have been presented [12]. A similar lens designed by transmission line metamaterials is shown in Ref. [13]. A solution at terahertz and infrared frequencies is obtained in Ref. [14] by using surface plasmon polaritons on a graphene monoatomic layer, where the graphene conductivity is tuned by using static electric fields. Examples of Luneburg and Maxwell's fish eye lenses designed by metasurfaces are presented in Fig. 3.4 (from Ref. [4]).

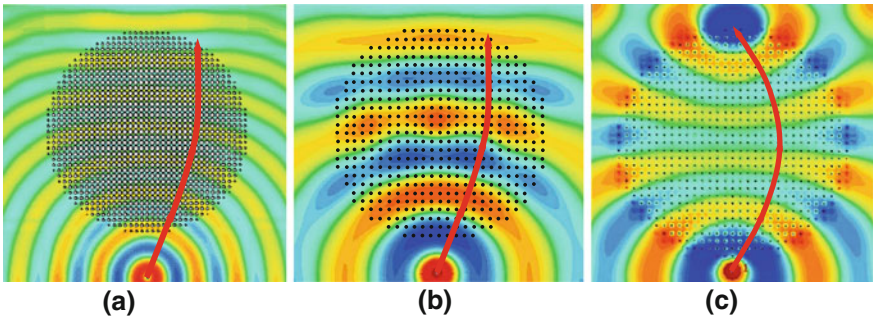

Fig. 3.4 Snapshots of the field and local wave–vector path in planar lenses designed with an IMMR. **a** Luneburg lens obtained by *circular* patches of variable size. **b** Luneburg lens realized by pins of different heights. **c** Maxwell's fish eye realized by pins (from Ref. [4])

IMMR can also be applied to the walls of horns; this application has been introduced in Ref. [15] to render the phase of the aperture field more uniform than in a conventional horn with the same size. Conversely, one can use an IMMR to reduce the horn dimensions when a uniform aperture phase is required.

The wavenumber modulation can also produce leaky-wave radiation. In Ref. [16] this is used for realizing spiral leaky-wave antennas.

3.2.2 Anisotropic Modulated Metasurface Reactance

An anisotropic metasurface (AMMR) impedance $\underline{\underline{Z}}$ located on the plane $z = 0$ imposes boundary conditions on the average tangential fields of the type $\mathbf{E}_t|_{z=0^+} = \underline{\underline{\mathbf{Z}}} \cdot (\hat{\mathbf{z}} \times \mathbf{H}_t)|_{z=0^+}$. The impedance tensor $\underline{\underline{\mathbf{Z}}}$ satisfies, in absence of losses, the anti-Hermitian condition $\underline{\underline{\mathbf{Z}}} = -\underline{\underline{\mathbf{Z}}}^{T*}$ [17], where superscript $T*$ denotes the transpose-conjugate operation. This condition derives from the absence of energy penetration into the surface. A particular, but very common case which satisfies this condition is a tensor of the form $\underline{\underline{\mathbf{Z}}} = j\underline{\underline{\mathbf{X}}}$, where $\underline{\underline{\mathbf{X}}}$ is a real symmetric tensor which admits real eigenvalues (i.e., principal values) and orthogonal eigenvectors (i.e., principal axes). The SW modes supported by a uniform tensor impedance surface are in general hybrid, i.e., neither pure TM nor TE. When both the eigenvalues of $\underline{\underline{\mathbf{X}}}$ are real positive numbers (which normally occurs in AMMR) the dominant SW (i.e., the SW without cut off frequency) exhibits a dominant TM contribution. After indicating with $\hat{\mathbf{k}}_t(\boldsymbol{\rho}) = \mathbf{k}_t/|\mathbf{k}_t|$ the direction normal to the SW wavefront, the tensor $\underline{\underline{\mathbf{X}}}$ can be conveniently represented in the basis $\hat{\mathbf{k}}_t$, $\hat{\mathbf{k}}_t^{\perp}$, where $\hat{\mathbf{k}}_t^{\perp} = \hat{\mathbf{z}} \times \hat{\mathbf{k}}_t$; i.e., $\underline{\underline{\mathbf{X}}} = X^{ee}\hat{\mathbf{k}}_t\hat{\mathbf{k}}_t + X^{hh}\hat{\mathbf{k}}_t^{\perp}\hat{\mathbf{k}}_t^{\perp} + X^{eh}\left(\hat{\mathbf{k}}_t^{\perp}\hat{\mathbf{k}}_t + \hat{\mathbf{k}}\hat{\mathbf{k}}_t^{\perp}\right)$. Through these components, the dispersion equation assumes the form

$$k_t = k\sqrt{1 + \bar{X}_s^2/\zeta^2};\ \bar{X}_s = \frac{1}{2\zeta X^{hh}}\left\{\left(\Delta - \zeta^2\right) + \sqrt{\left(\Delta - \zeta^2\right)^2 + 4X^{ee}X^{hh}\zeta^2}\right\} \quad (3.2)$$

where $\Delta = \det(\underline{\underline{\mathbf{X}}})$. With a good approximation (3.2) represents, at each frequency, an ellipse in the plane $(k_x, k_y) = (\mathbf{k}_t \cdot \hat{\mathbf{x}}, \mathbf{k}_t \cdot \hat{\mathbf{y}})$. The axes of this ellipse are aligned with the principal axes of the tensor $\underline{\underline{\mathbf{X}}}$ (see Appendix B).

An AMMR may be designed by using transmission-line (TL) metamaterials, as done in Ref. [18]. In this reference, TL metamaterials with arbitrary full tensors are introduced and characterized through a Bloch analysis. An AMMR may also be implemented by printed patches, provided a geometrical asymmetry is introduced in the periodic cell. Some geometries are proposed in Ref. [19] for realizing holographic antennas and in Ref. [20] to design circularly polarized isoflux antennas for space applications.

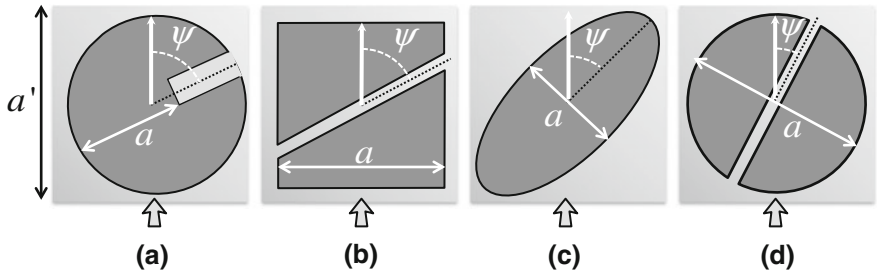

Fig. 3.5 Patch geometries for AMMR. Each geometry possesses two specific non-dimensional parameters *a/a'* and ψ that are considered for constructing the reactance maps. The *arrow* denotes the direction of SW propagation

Some examples are shown in Fig. 3.5. The solution of Fig. 3.5b has been suggested in Ref. [19], while Fig. 3.5d has been adopted in Ref. [20]. All the geometries exhibit two non-dimensional parameters a/a' and ψ which primarily affect the principal values and the principal axes of $\underline{\underline{\mathbf{X}}}$, respectively. The first parameter a/a' is the ratio between a characteristic length of the patch, a, and the side length of the periodic cell, a'. The larger the ratio a/a', the larger the area of the patch with respect to the unit cell area. Increasing this parameter implies increasing the magnitude of the principal values of the tensor $\underline{\underline{\mathbf{X}}}$. The second parameter is the angle ψ, which describes for instance the orientation of the slot in the geometries of Fig. 3.5b and d. This parameter influences mostly the orientation of the principal axes of the tensor. In any case, these principal axes are oriented along symmetry axes of the geometry.

Figure 3.6 shows the AMMR tensor components for the screw-head patch in Fig. 3.5d as a function of the two aforementioned parameters. These maps have been obtained by assuming the patch embedded in a periodic Cartesian lattice and applying a periodic method of moment (MoM) analysis for a limited but sufficiently high number of $(a/a',\ \psi)$ pairs. The pole-zero matching method [10] is then used to interpolate the results obtained in the $(a/a',\ \psi)$ plane.

3.3 Metasurface Transformation

3.3.1 Statement of the Problem

In the previous section, we have illustrated the possibility to readdress SWs by modulating a metasurface; in this section, we formalize this concept on the basis of TO. TO is a general mathematical tool allowing for the definition of inhomogeneous anisotropic metamaterials which create a controlled spatial wave-field distribution. The fundamental points of TO are summarized in Appendix A.

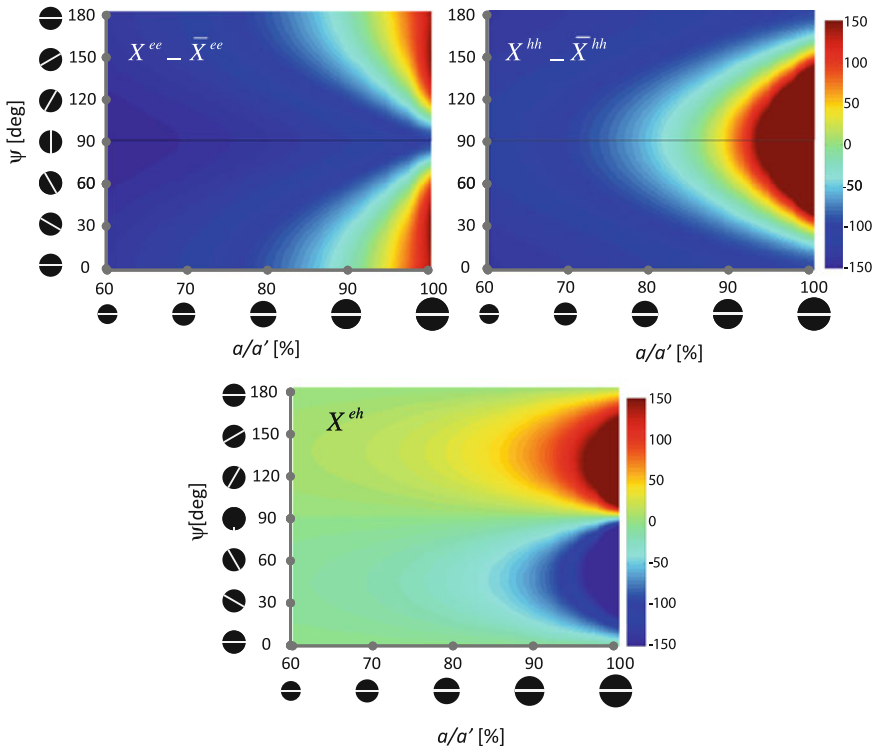

Fig. 3.6 Impedance maps (in ohms) of AMMR tensor components $X_{ee} - \bar{X}_{ee}$, $X_{hh} - \bar{X}_{hh}$, X_{eh}; where $\bar{X}_{ee}$, $\bar{X}_{hh}$ are average values around 300 Ohms (results from Ref. [20])

In order to extend TO theory to metasurfaces, let us consider two half-spaces: a "virtual" one, identified by a primed position vector $\mathbf{r}' = x'\hat{\mathbf{x}} + y'\hat{\mathbf{y}} + z'\hat{\mathbf{z}}, z' > 0$, and a "real" one, whose points are identified by an unprimed position vector $\mathbf{r} = x\hat{\mathbf{x}} + y\hat{\mathbf{y}} + z\hat{\mathbf{z}}$, $z > 0$. Both the position vectors are expressed in Cartesian coordinates and unit vectors of their respective spaces. To describe a given observation point in the two spaces, whenever useful for simplifying the formulas, we adopt the following alternative notations: $\{x, y, z\} \equiv \{x_1, x_2, x_3\}$, $\{x', y', z'\} \equiv \{x'_1, x'_2, x'_3\}$; $\hat{\mathbf{x}}, \hat{\mathbf{y}}, \hat{\mathbf{z}} \equiv \hat{\mathbf{x}}_1, \hat{\mathbf{x}}_2, \hat{\mathbf{x}}_3$, $\hat{\mathbf{x}}', \hat{\mathbf{y}}', \hat{\mathbf{z}}' \equiv \hat{\mathbf{x}}'_1, \hat{\mathbf{x}}'_2, \hat{\mathbf{x}}'_3$. Both half-spaces are filled by *free space*, whose intrinsic wavenumber is denoted by $k = \omega\sqrt{\varepsilon_0\mu_0}$; however, they have two *different boundary conditions* at $z' = 0$ and $z = 0$. We assume that the *virtual* space possesses boundary conditions described by a *uniform* scalar reactive ω-dependent surface impedance jX_S. In the *real* space, instead, we define at $z = 0$ two complementary surfaces S' and S, separated by a continuous line boundary ∂S, whose summation covers the entire plane (Fig. 3.7). Note that ∂S can also be a closed contour. In S', we assume the same uniform impedance boundary conditions described by the surface impedance jX_S. In S, we impose an AMMR characterized by an impedance tensor $\underline{\underline{\mathbf{Z}}}_S^{eq}(\boldsymbol{\rho}) = j\underline{\underline{\mathbf{X}}}_S^{eq}(\boldsymbol{\rho})$.

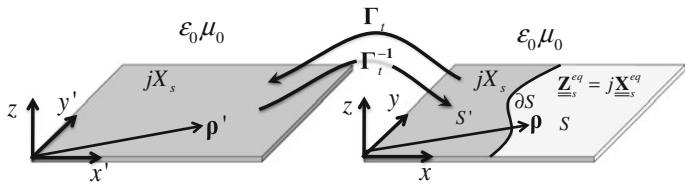

Fig. 3.7 Metasurface transformation geometry

We define a coordinate transformation from the real to the virtual space. This transformation leaves unchanged the z coordinate, so that we may write $\mathbf{r}' = \boldsymbol{\rho}' + z\hat{\mathbf{z}}$ and $\mathbf{r} = \boldsymbol{\rho} + z\hat{\mathbf{z}}$, with $\boldsymbol{\rho}' \equiv x'\hat{\mathbf{x}}' + y'\hat{\mathbf{y}}'$ and $\boldsymbol{\rho} \equiv x\hat{\mathbf{x}} + y\hat{\mathbf{y}}$. The two coordinates $\boldsymbol{\rho}$ and $\boldsymbol{\rho}'$ are related by a 2D transformation $\boldsymbol{\Gamma}_t$ with domain in $\boldsymbol{\rho}$ and codomain in $\boldsymbol{\rho}'$. $\boldsymbol{\Gamma}_t$ maps univocally any point of the real space to a point of the virtual space. Vice versa, the *inverse* transformation $\boldsymbol{\Gamma}_t^{-1}$ *maps the virtual space to the real space*. We also impose that the transformation is the identity in the region of space S':

$$\boldsymbol{\rho}' = \boldsymbol{\Gamma}_t(\boldsymbol{\rho}) : \{x, y\} \rightarrow \{x'(x, y), y'(x, y)\} \quad \text{in } S \tag{3.3}$$

$$\boldsymbol{\rho}' = \boldsymbol{\rho} \quad \text{in } S' \tag{3.4}$$

Finally, we assume that the transformation is continuous and differentiable at the boundary.

Having defined $\boldsymbol{\Gamma}_t$ as an identity in S', the virtual space coincides with the real space in S'. This allows one to interpret any wave in the *virtual* space as an incident field coming from the region S' of the *real* space. This trick is normally used in volumetric TO, for instance in cloaking problems. In fact our objective is to transform, through the AMMR, a plane SW coming from S' into a desired "curved wavefront SW" in S, which is the *inverse* mapping via $\boldsymbol{\Gamma}_t^{-1}$ of a plane-wavefront surface wave in the virtual-space. Reversely, a curved ray path of the curved-wavefront can be transformed by $\boldsymbol{\Gamma}_t$ in a rectilinear ray-path in the virtual space. (We note that several authors using TO invert the definition of "direct" and "inverse" transform with respect to the one used here)

It is useful to introduce the covariant and contravariant bases, denoted as $\{\mathbf{g}_i\}$ and $\{\mathbf{g}^i\}$, respectively. Covariant (contravariant) basis vectors are tangent (orthogonal) to the curves obtained in *the real space* by transforming the Cartesian axes of the virtual space through $\boldsymbol{\Gamma}_t^{-1}$:

$$\mathbf{g}_i = \partial\boldsymbol{\rho}/\partial x_i' = \sum\nolimits_{j=1,2} \partial x_j/\partial x_i' \hat{\mathbf{x}}_j \quad i = 1, 2 \tag{3.5}$$

$$\mathbf{g}^i = \nabla_t x_i' = \sum\nolimits_{j=1,2} \partial x_i'/\partial x_j \hat{\mathbf{x}}_j \quad i = 1, 2 \tag{3.6}$$

where $\nabla_t = \partial/\partial x\hat{\mathbf{x}} + \partial/\partial y\hat{\mathbf{y}}$ is the transverse gradient. Figure 3.8 shows covariant and contravariant bases for a transformation where ∂S is a straight line.

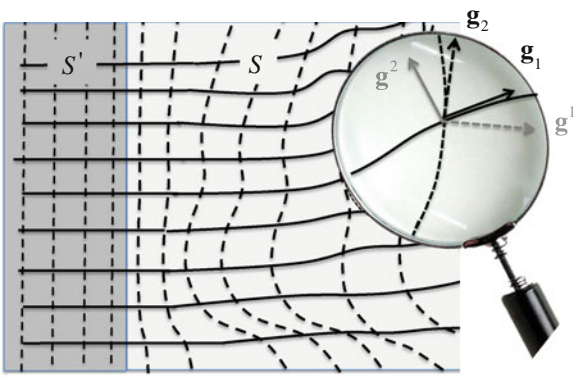

Fig. 3.8 Surface transformation *coordinate lines* and covariant and contravariant bases (in the zoomed view)

Covariant and contravariant bases can also be defined *in the virtual space* by referring to the direct transformation $\mathbf{\Gamma}_t$:

$$\boldsymbol{\gamma}_j = \partial \boldsymbol{\rho}' / \partial x_j = \sum\nolimits_{i=1,2} \partial x_i' / \partial x_j \hat{\mathbf{x}}_i' \tag{3.7}$$

$$\boldsymbol{\gamma}^j = \nabla_t' x_j = \sum\nolimits_{i=1,2} \partial x_j / \partial x_i{}' \hat{\mathbf{x}}_i' \tag{3.8}$$

The two couples of bases introduced are bi-orthogonal, namely $\mathbf{g}^i \cdot \mathbf{g}_j = \delta_{ij}$, $\boldsymbol{\gamma}^i \cdot \boldsymbol{\gamma}_j = \delta_{ij}$. The Jacobian tensor $\underline{\underline{\mathbf{M}}}_t$ of the transformation $\mathbf{\Gamma}_t$ and its inverse $\underline{\underline{\mathbf{M}}}_t^{-1}$ can be expressed in covariant and contravariant bases as

$$\underline{\underline{\mathbf{M}}}_t = \sum\nolimits_{i=1,2} \hat{\mathbf{x}}_i' \mathbf{g}^i = \sum\nolimits_{j=1,2} \boldsymbol{\gamma}_j \hat{\mathbf{x}}_j \tag{3.9}$$

$$\underline{\underline{\mathbf{M}}}_t^{-1} = \sum_{i=1,2} \mathbf{g}_i \hat{\mathbf{x}}_i' = \sum_{j=1,2} \hat{\mathbf{x}}_j \boldsymbol{\gamma}^j \tag{3.10}$$

3.3.2 Curved Wavefront Surface Wave

Consider a SW propagating in the virtual space, supported by the reactive uniform surface impedance jX_S. This SW propagates along a direction $\mathbf{k}' = k_x' \hat{\mathbf{x}}' + k_y' \hat{\mathbf{y}}'$ with a phase velocity less than the speed of light $\left(\sqrt{\mathbf{k}_t' \cdot \mathbf{k}_t'} > k\right)$ and exhibits an exponential attenuation along z. Since the coordinate transformation is the identity in S', the primed space is coincident with the real space in S'.

TM-SW or TE-SW are supported by $X_S > 0$ or $X_S < 0$, respectively, and can be derived through a vertical magnetic or electric potential, respectively, of the form

$$\begin{aligned}\mathbf{A}'(\boldsymbol{\rho}', z) &= A_z\hat{\mathbf{z}} \doteq I'_{TM}\hat{\mathbf{z}}\, e^{-j\mathbf{k}'_t\cdot\boldsymbol{\rho}'} e^{-z\sqrt{\mathbf{k}'_t\cdot\mathbf{k}'_t - k^2}} \\ \mathbf{F}'(\boldsymbol{\rho}', z) &= F_z\hat{\mathbf{z}} \doteq V'_{TE}\hat{\mathbf{z}}\, e^{-j\mathbf{k}'_t\cdot\boldsymbol{\rho}'} e^{-z\sqrt{\mathbf{k}'_t\cdot\mathbf{k}'_t - k^2}}\end{aligned} \tag{3.11}$$

where $I_{TM}{}'$ and $V_{TE}{}'$ are arbitrary constants. Consistency of (3.11) with boundary conditions $\mathbf{E}'_t\big]_{z'=0} = jX_S\hat{\mathbf{z}} \times \mathbf{H}'_t\big]_{z'=0}$ implies

$$\sqrt{\mathbf{k}'_t \cdot \mathbf{k}'_t} = k\sqrt{1 + (X_S/\zeta)^2} \quad \text{for TM - SW} \tag{3.12}$$

$$\sqrt{\mathbf{k}'_t \cdot \mathbf{k}'_t} = k\sqrt{1 + (\zeta/X_S)^2} \quad \text{for TE - SW} \tag{3.13}$$

In practical situations, the TM case is more important, since inductive AMMR are easier to implement. Therefore, in the following we will assume in *S'* the sole presence of a TM mode generated by the potential **A'.** TE case can be constructed in a similar manner.

Transformation Optics applied to (3.11) suggests us to construct magnetic and electric potentials in the real space in the form

$$\mathbf{A}(\boldsymbol{\rho}, z) = I_{TM}\hat{\mathbf{z}} e^{-j\mathbf{k}'_t\cdot\boldsymbol{\rho}'(\boldsymbol{\rho})} e^{-z\nu_z(\boldsymbol{\rho})} \tag{3.14}$$

$$\mathbf{F}(\boldsymbol{\rho}, z) = V_{TE}(\boldsymbol{\rho})\hat{\mathbf{z}} e^{-j\mathbf{k}'_t\cdot\boldsymbol{\rho}'(\rho)} e^{-z\nu_z(\boldsymbol{\rho})} \tag{3.15}$$

where $\boldsymbol{\rho}'(\boldsymbol{\rho}) \equiv \Gamma(\boldsymbol{\rho})$ is defined in (3.3). In (3.14), I_{TM} is an arbitrary constant to be set on the basis of the continuity conditions of the fields along ∂S, while V_{TE} in (3.15) is a slowly varying function of space. The phase term $\exp(-j\mathbf{k}'_t \cdot \boldsymbol{\rho}')$ in (3.14) and (3.15) describes in the real space a *curved wavefront*, obtained by distorting the planar one according to the transformation $\boldsymbol{\rho}' = \Gamma_t(\boldsymbol{\rho})$. The direction $\hat{l}(\boldsymbol{\rho})$ tangent to the wavefront satisfies the condition $\nabla_t\left(\mathbf{k}'_t \cdot \boldsymbol{\rho}'(\boldsymbol{\rho})\right) \cdot \hat{l} = \partial\left(\mathbf{k}'_t \cdot \boldsymbol{\rho}'\right)/\partial l = 0$. The local wavevector $\mathbf{k}_t$ can be therefore identified as

$$\begin{aligned}\mathbf{k}_t(\boldsymbol{\rho}) &= \nabla_t\left(\mathbf{k}'_t \cdot \boldsymbol{\rho}'(\boldsymbol{\rho})\right) = \nabla_t\left(k'_x x' + k'_y y'\right) \\ &= k'_x\nabla_t x' + k'_y\nabla_t y' = k'_x\mathbf{g}^1 + k'_y\mathbf{g}^2 = \underline{\underline{\mathbf{M}}}_t^T \cdot \mathbf{k}'_t\end{aligned} \tag{3.16}$$

Thus, the transformation rotates the Cartesian components of $\mathbf{k}'_t$ along the corresponding contravariant vectors in the real space. For instance, a SW propagating in *S'* with wavevector along $x = x'$, will continue in *S* with wavevector aligned with the contravariant vector $\mathbf{g}^1$, and with a local wavefront along $\mathbf{g}_2$ (see Fig. 3.8).

Before proceeding further, we emphasize that the potentials in (3.14) and (3.15) do not follow the usual TO transformation in z, that would simply replicate the z-dependent term in (3.11). In fact, in conventional TO, a 2D coordinate transformation that leaves the z-coordinate unchanged implies a variable compression (or expansion) along z, which modifies the value of the corresponding entries of the

constitutive tensors in the real space. In our problem, instead, we have assumed free space above the impedance surface. This imposes the condition $\mathbf{k}_t \cdot \mathbf{k}_t + k_z = k^2$, that implies an exponential decay in z with attenuation constant:

$$v_z = jk_z = \sqrt{\mathbf{k}_t \cdot \mathbf{k}_t - k^2} > 0 \tag{3.17}$$

where $\mathbf{k}_t$ is given in (3.16). However, in order to construct Maxwellian fields from the potentials (3.14) and (3.15), these potentials must satisfy the free-space wave equation, like $\nabla^2 A_z + k^2 A_z = 0$. It can be shown that this is true *in proximity of the surface* under certain conditions on the coordinate transformation. In order to find such conditions, we observe that

$$\nabla_t^2 A_z \approx (-\mathbf{k}_t \cdot \mathbf{k}_t - j\nabla_t \cdot \mathbf{k}_t) A_z + z e^{-zv_z}\, \chi(z, \rho) \tag{3.18}$$

where $\chi(z, \rho)$ is a smoothly varying function. Approaching the surface, the last term of (3.18) vanishes. Therefore, A_z approximately satisfies the wave equation $\nabla^2 A_z + k^2 A_z = 0$ with $\mathbf{k}_t \cdot \mathbf{k}_t + k_z = k^2$ when

$$|\nabla_t \cdot \mathbf{k}_t| \ll \mathbf{k}_t \cdot \mathbf{k}_t \tag{3.19}$$

This relationship can be cast in a form which explicitly highlights the parameters of the transformation, as will be shown in Sect. 3.4.

3.3.3 Local Dispersion Equation

As anticipated in the previous section, without loss of generality we refer in the following to an incoming TM-SW. As a consequence, the amplitude of the wavevector $\mathbf{k}_t'$ in the virtual space satisfies (3.12) for any propagation direction; this means that when the propagation direction changes, the tip of $\mathbf{k}_t'$ describes a circle of radius $k\sqrt{1 + (X_S/\zeta)^2}$ (Fig. 3.9a). On the other hand, according to (3.16) the tip of the wavevector $\mathbf{k}_t$ in the real space describes an ellipse (Fig. 3.9b). The expression of this ellipse is obtained by writing $\mathbf{k}_t' \cdot \mathbf{k}_t' = k^2 + k^2 (X_S/\zeta)^2$ in terms of $\mathbf{k}_t$ through (3.16); this leads to $\mathbf{k}_t \cdot \underline{\underline{\mathbf{M}}}_t^{-1} \cdot (\underline{\underline{\mathbf{M}}}_t^T)^{-1} \cdot \mathbf{k}_t = k^2 \left(1 + (X_S/\zeta)^2\right)$. The latter can be rewritten as

$$\sqrt{g}\, \mathbf{k}_t \cdot \underline{\underline{\boldsymbol{\alpha}}}_t \cdot \mathbf{k}_t = k^2 \left(1 + (X_S/\zeta)^2\right) \tag{3.20}$$

where

$$\underline{\underline{\boldsymbol{\alpha}}}_t(\boldsymbol{\rho}) = \frac{1}{\sqrt{g}} \underline{\underline{\mathbf{M}}}_t^{-1} \cdot \left(\underline{\underline{\mathbf{M}}}_t^T\right)^{-1} = \frac{1}{\sqrt{g}} \sum_{i,j=1,2} \hat{\mathbf{x}}_i \hat{\mathbf{x}}_j \left[\boldsymbol{\gamma}^i \cdot \boldsymbol{\gamma}^j\right] \tag{3.21}$$

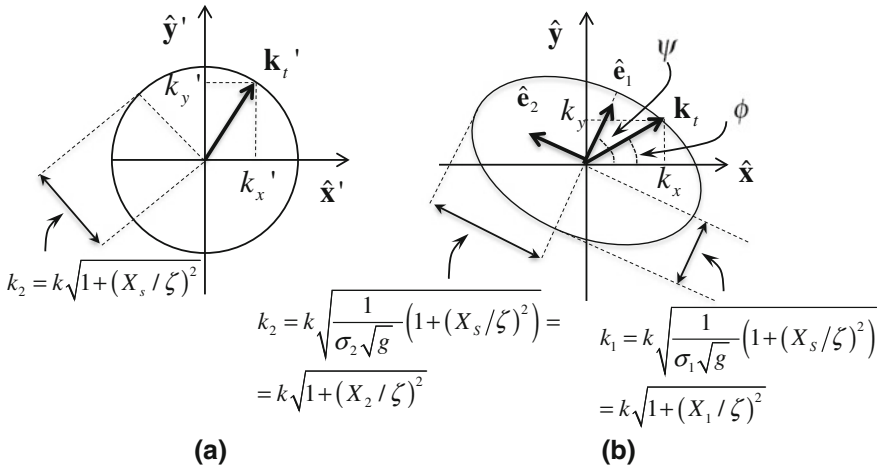

Fig. 3.9 **a** Representation of the wavevector in the (k_x', k_y') plane consistent with an isotropic boundary conditions (TM case). **b** Representation of the local wavevector in the (k_x, k_y) space corresponding to a curvilinear coordinate transformation and consistent with an anisotropic impedance boundary condition

and $\sqrt{g} = \hat{\mathbf{z}} \cdot (\boldsymbol{\gamma}^1 \times \boldsymbol{\gamma}^2) = [\hat{\mathbf{z}} \cdot (\mathbf{g}^1 \times \mathbf{g}^2)]^{-1}$. The tensor in (3.21) is coincident with the transverse component of the normalized constitutive tensors provided by TO (see Appendix A). Observing that $\sqrt{g} = |\boldsymbol{\gamma}^1||\boldsymbol{\gamma}^2| \sin\delta$, where δ is the angle between $\boldsymbol{\gamma}^1$ and $\boldsymbol{\gamma}^2$, one has $\det \underline{\underline{\boldsymbol{\alpha}}}_t = g^{-1}\left[|\boldsymbol{\gamma}^1|^2|\boldsymbol{\gamma}^2|^2 - \left(|\boldsymbol{\gamma}^1||\boldsymbol{\gamma}^2|\cos\delta\right)^2\right] = 1$.

The principal axes of the ellipse are aligned with the eigenvectors of $\underline{\underline{\boldsymbol{\alpha}}}_t$, i.e., along the unit vectors $\hat{\mathbf{e}}_i = \hat{\mathbf{e}}_i(\boldsymbol{\rho})(i = 1, 2)$. The angle ψ formed by $\hat{\mathbf{e}}_1$ with the Cartesian axis $\hat{\mathbf{x}}$ is given by

$$\psi = \tan^{-1}\left[\frac{1}{2\boldsymbol{\gamma}^1 \cdot \boldsymbol{\gamma}^2}\left(|\boldsymbol{\gamma}^2|^2 - |\boldsymbol{\gamma}^1|^2 + \sqrt{\left(|\boldsymbol{\gamma}^1|^2 - |\boldsymbol{\gamma}^2|^2\right)^2 + 4(\boldsymbol{\gamma}^1 \cdot \boldsymbol{\gamma}^2)^2}\right)\right] \tag{3.22}$$

so that $\hat{\mathbf{e}}_1 = \cos\psi\hat{\mathbf{x}} + \sin\psi\hat{\mathbf{y}}$, $\hat{\mathbf{e}}_2 = -\sin\psi\hat{\mathbf{x}} + \cos\psi\hat{\mathbf{y}}$. In the eigenvector basis, $\underline{\underline{\boldsymbol{\alpha}}}_t = \hat{e}_1\hat{e}_1\sigma_1 + \hat{e}_2\hat{e}_2\sigma_2$, where σ_n, the eigenvalues, may be written in the simple form

$$\sigma_{1,2} = \frac{1}{2}t \pm \sqrt{\left(\frac{1}{2}t\right)^2 - 1} \tag{3.23}$$

where the subscript 1 (3.2) is associated with the upper (lower) sign, and $t = \left(|\boldsymbol{\gamma}^1|^2 + |\boldsymbol{\gamma}^2|^2\right)/\sqrt{g}$ is the trace of $\underline{\underline{\boldsymbol{\alpha}}}_t$. Since $\det \underline{\underline{\boldsymbol{\alpha}}}_t = 1$, we have $\sigma_1\sigma_2 = 1$. The dispersion (3.20) can be therefore written in the equivalent form

$$k_1^2\sigma_1 + k_2^2\sigma_2 = k^2\left[1 + (X_S/\zeta)^2\right]\frac{1}{\sqrt{g}} \tag{3.24}$$

where $k_n = \mathbf{k}_t \cdot \hat{\mathbf{e}}_n$. From (3.24) it is seen that the semi-axes of the dispersion ellipse are

$$k_n = k\sqrt{\frac{1}{\sigma_n\sqrt{g}}\left[1 + (X_S/\zeta)^2\right]} \tag{3.25}$$

as depicted in Fig. 3.9.

3.3.4 Conditions on the Transformation

The above formulation is subjected to some conditions. First, the argument of the square root in (3.17) should be positive to avoid radiation. Second, as previously shown, the condition in (3.19) must hold so that the potentials A_z and F_z locally satisfy the free space wave equation. We express now these conditions in terms of the transformation parameters. From (3.24)

$$\mathbf{k}_t \cdot \mathbf{k}_t \geq k^2 \frac{1}{\sigma_{\max}\sqrt{g}}\left[1 + (X_S/\zeta)^2\right] \tag{3.26}$$

where $\sigma_{\max}$ is the maximum between σ_1 and σ_2. From (3.26), the nonradiating condition $\mathbf{k}_t \cdot \mathbf{k}_t \geq k^2$ becomes

$$\frac{\sigma_{\max}\sqrt{g}}{1 + (X_S/\zeta)^2} \leq 1 \tag{3.27}$$

Furthermore, (3.19) can be cast in a form which explicitly shows the transformation parameters. To this end, we note from (3.16) that

$$\nabla_t \cdot \mathbf{k}_t = k_x'\nabla_t \cdot \mathbf{g}^1 + k_y'\nabla_t \cdot \mathbf{g}^2 = k_x'\nabla^2 x' + k_y'\nabla^2 y' \tag{3.28}$$

The last term in (3.28) is maximized when the two vectors $\mathbf{k}_t'$ and $\nabla^2 x'\hat{\mathbf{x}}' + \nabla^2 y'\hat{\mathbf{y}}' = \nabla^2\boldsymbol{\rho}'$ are parallel. Thus, one has

$$|\nabla_t \cdot \mathbf{k}_t| \leq k\sqrt{1 + (X_S/\zeta)^2}\left|\nabla^2\boldsymbol{\rho}'\right| \tag{3.29}$$

The above tells us that $\nabla_t \cdot \mathbf{k}_t = 0$ when the transformation respects the Cauchy–Riemann conditions, the latter implying $\nabla^2\boldsymbol{\rho}' = 0$. Use of (3.29) and (3.26) in (3.19), leads to a condition only dependent on the coordinate transformation:

$$\frac{\left|\nabla^2 \boldsymbol{\rho}'\right| \sigma_{\max} \sqrt{g}}{k\sqrt{1+(X_S/\zeta)^2}} \ll 1 \tag{3.30}$$

The latter, can be approximated with a simpler expression, obtained by substituting $\sigma_{\max}$ with the average $\sqrt{\sigma_1 \sigma_2} = \sqrt{\det \underline{\underline{\boldsymbol{\alpha}}}_t} = 1$. This approximation loosens the inequality in (3.30) and leads to

$$\frac{\left|\nabla^2 \boldsymbol{\rho}'\right|}{|\nabla x'||\nabla y'| \sin \delta' k\sqrt{1+(X_S/\zeta)^2}} \doteq \tau \ll 1 \tag{3.31}$$

where δ' is the angle between $\nabla x'$ and $\nabla y'$. The non-dimensional parameter τ should be less than 10 % at any point of S. We observe that increasing X_S and decreasing wavelength renders both the conditions in (3.27) and (3.31) less restrictive. Strongly nonorthogonal transformations (small values of δ') render instead (3.27) and (3.31) more restrictive.

3.3.5 Determination of the Surface Tensor

When the transformation satisfies (3.31), the transverse fields may be derived from the potentials according to

$$\mathbf{E}_t = -jk\zeta \nabla_t \frac{\partial}{k^2 \partial z} A_z - \nabla_t F_z \times \hat{z} \tag{3.32}$$

$$\mathbf{H}_t = \frac{-jk}{\zeta} \nabla_t \frac{\partial}{k^2 \partial z} F_z + \nabla_t A_z \times \hat{z} \tag{3.33}$$

It is worth noting that, also if the incident wave is TM, both potentials are needed; indeed, the anisotropic surface impedance supports a hybrid mode (i.e., neither purely TM nor TE). Boundary conditions on S impose

$$\mathbf{E}_t]_{z=0} = j\underline{\underline{\mathbf{X}}}_S^{eq} \cdot (\hat{\mathbf{z}} \times \mathbf{H}_t)]_{z=0} \tag{3.34}$$

The tensor $\underline{\underline{\mathbf{X}}}_S^{eq}$ must be locally consistent with $\mathbf{k}_t$. In order to derive the dispersion equation, let us introduce the quantities

$$X_0^{TM} = -\zeta \sqrt{\mathbf{k}_t \cdot \mathbf{k}_t / k^2 - 1} \tag{3.35}$$

$$X_0^{TE} = \zeta \Big/ \sqrt{\mathbf{k}_t \cdot \mathbf{k}_t / k^2 - 1} \tag{3.36}$$

which are the characteristic reactances of z-transmission lines for TM and TE modes, respectively.

After inserting (3.14) and (3.15) into (3.32) and (3.33) and performing the derivatives, one finds

$$\mathbf{E}_t \approx -j\left(\mathbf{k}_t V_{TM} + \mathbf{k}_t^{\perp} V_{TE}\right) e^{-j\mathbf{k}_t'\cdot\boldsymbol{\rho}'} e^{-zv_z} \tag{3.37}$$

$$\mathbf{H}_t \approx -j\left(-\mathbf{k}_t^{\perp} I_{TM} + \mathbf{k}_t I_{TE}\right) e^{-j\mathbf{k}_t'\cdot\boldsymbol{\rho}'} e^{-zv_z} \tag{3.38}$$

where $\mathbf{k}_t^{\perp} = \hat{\mathbf{z}} \times \mathbf{k}_t$ and we have neglected the terms multiplied by z. The coefficients $V_{TM,TE}$ and $I_{TM,TE}$ are related through $-jX_0^{TM} I_{TM} = V_{TM}$ and $-jX_0^{TE} I_{TE} = V_{TE}$. The latter relations can be written in dyadic form as

$$\mathbf{E}_t = -j\underline{\underline{\mathbf{X}}}_0 \cdot (\hat{\mathbf{z}} \times \mathbf{H}_t) \tag{3.39}$$

where

$$\underline{\underline{\mathbf{X}}}_0 = X_0^{TM} \hat{\mathbf{k}}_t \hat{\mathbf{k}}_t + X_0^{TE} \hat{\mathbf{k}}_t^{\perp} \hat{\mathbf{k}}_t^{\perp} \tag{3.40}$$

and $\hat{\mathbf{k}}_t = \mathbf{k}_t/|\mathbf{k}_t|$, $\hat{\mathbf{k}}_t^{\perp} = \hat{\mathbf{z}} \times \hat{\mathbf{k}}_t$. Summing up (3.39) and (3.34) leads to

$$\left(\underline{\underline{\mathbf{X}}}_S^{eq} + \underline{\underline{\mathbf{X}}}_0\right) \cdot (\hat{\mathbf{z}} \times \mathbf{H}_t)\Big|_{z=0} = 0 \tag{3.41}$$

from which one obtains the following dispersion equation

$$\det\left[\underline{\underline{\mathbf{X}}}_S^{eq} + \underline{\underline{\mathbf{X}}}_0\right] = 0 \tag{3.42}$$

The tensor impedance $\underline{\underline{\mathbf{X}}}_S^{eq}$ is found by imposing the local matching of the dispersion equations in (3.42) with the one in (3.20). To this end, the first condition is that the principal axes of $\underline{\underline{\mathbf{X}}}_S^{eq}$ are aligned with the eigenvector basis $\hat{\mathbf{e}}_n (n = 1, 2)$ of $\underline{\underline{\boldsymbol{\alpha}}}_t$. By denoting as X_i the relevant eigenvalues, we assume therefore the form

$$\underline{\underline{\mathbf{X}}}_S^{eq} = X_1 \hat{\mathbf{e}}_1 \hat{\mathbf{e}}_1 + X_2 \hat{\mathbf{e}}_2 \hat{\mathbf{e}}_2 \tag{3.43}$$

In Appendix B, it is shown that the dispersion equation associated with (3.42) for a reactance tensor with principal axes along $\hat{\mathbf{e}}_n$ describes with excellent approximation an ellipse with axes aligned with the same unit vectors, and semi-axes equal to

$$k_n = k\sqrt{1 + (X_n/\zeta)^2} \tag{3.44}$$

The condition for approximating the dispersion equation in (3.42) through an ellipse is

$$f\left(\frac{X_1}{\zeta}, \frac{X_2}{\zeta}\right) = \frac{\left(\frac{X_1}{\zeta} - \frac{X_2}{\zeta}\right)^2 - \left(\sqrt{\frac{X_1}{X_2}} - \sqrt{\frac{X_2}{X_1}}\right)^2}{4\left(\frac{X_1}{\zeta} + \frac{\zeta}{X_1}\right)\left(\frac{X_2}{\zeta} + \frac{\zeta}{X_2}\right)} \ll 1 \tag{3.45}$$

The double argument function f is represented in Fig. 3.10 in a range of realizable impedance values. It is seen that in the range $X_1, X_2 \in (0.5\zeta, 2\zeta)$, it results $f < 3$ %. This means that the approximation is good in a wide range of impedance values.

Equations (3.44)–(3.25) provides the following expression for the eigenvalues X_n

$$\frac{X_n}{\zeta} = \sqrt{\frac{1}{\sigma_n \sqrt{g}} \left[1 + \left(\frac{X_S}{\zeta} \right)^2 \right]} - 1 \tag{3.46}$$

Equations (3.43) and (3.46) provide the desired representation of $\underline{\underline{\mathbf{X}}}_S^{eq}$ in terms of the parameters of the coordinate transformation.

3.3.6 Field Expression

The dispersion equation in (3.42) yields the following relationship between the coefficients in (3.37) and (3.38):

$$\frac{I_{TE}}{I_{TM}} = \frac{-X^{eh}}{(X^{hh} + X_0^{TE})} \doteq \xi^H(\mathbf{k}_t); \frac{V_{TE}}{V_{TM}} = \frac{X_0^{TE}}{X_0^{TM}} \xi^H(\mathbf{k}_t) \doteq \xi^E(\mathbf{k}_t) \tag{3.47}$$

where X^{hh} and X^{eh} are given in Appendix B. By using the coefficients ξ^H, ξ^E, and exploiting the relationships $-jX_0^{TM} I_{TM} = V_{TM}$ and $-jX_0^{TE} I_{TE} = V_{TE}$, (3.37) and (3.38) can be rewritten in a form which depends on the sole arbitrary constant I_{TM}

$$\mathbf{E}_t = -\left(\mathbf{k}_t + \xi^E \mathbf{k}_t^{\perp} \right) X_0^{TM} I_{TM} e^{-j\mathbf{k}_t' \cdot \rho'} e^{-z v_z} \tag{3.48}$$

$$\mathbf{H}_t = -j\left(-\mathbf{k}_t^{\perp} + \xi^H \mathbf{k}_t \right) I_{TM} e^{-j\mathbf{k}_t' \cdot \rho'} e^{-z v_z} \tag{3.49}$$

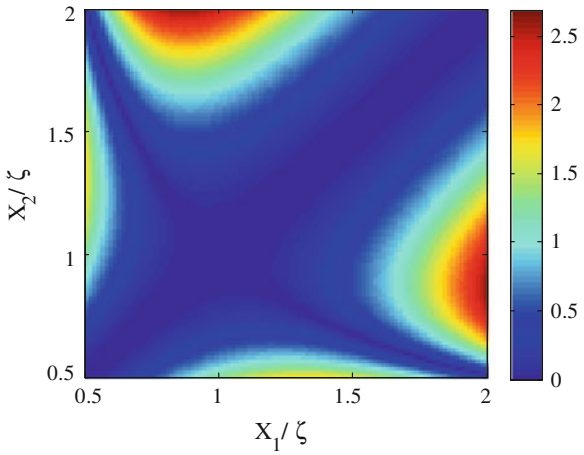

Fig. 3.10 Percent error in the approximation of the dispersion equation of an anisotropic surface impedance through an ellipse as a function of the reactance tensor eigenvalues normalized to the free-space impedance

where $\mathbf{k}_t = \underline{\underline{\mathbf{M}}}_t^T \cdot \mathbf{k}_t'$ and $v_z = \sqrt{\mathbf{k}_t \cdot \mathbf{k}_t - k^2}$. Normal components of the field can be found by imposing the condition of vanishing divergence of the total fields, thus leading to

$$E_z = -j\zeta \frac{\mathbf{k}_t \cdot \mathbf{k}_t}{k} I_{TM} e^{-j\mathbf{k}_t' \cdot \rho'} e^{-zv_z},\ H_z = -\frac{\mathbf{k}_t \cdot \mathbf{k}_t}{\zeta k} X_0^{TE} \xi^H I_{TM} e^{-j\mathbf{k}_t' \cdot \rho'} e^{-zv_z} \tag{3.50}$$

For practical realizable values of X_n in (3.46) the TM component is dominant with respect to the TE one. In fact, it can be seen that the coefficients ξ^H, ξ^E in (3.48) and (3.49) are usually much less than 1. Figure 3.11 presents the maximum value of the above coefficients with respect to the direction of $\mathbf{k}_t'$ in the range $X_1, X_2 \in (0.5\zeta, 2\zeta)$. It can be seen that the maximum values can be approximated by

$$\left|\xi^H\right|_{max} \approx 0.26\left(\frac{X_2 - X_1}{\zeta}\right);\ \left|\xi^E\right|_{max} \approx 0.13\left(\frac{X_2 - X_1}{\zeta}\right)\left(\frac{\zeta}{X_2} + \frac{\zeta}{X_1}\right) \tag{3.51}$$

For isotropic reactance tensors ($X_2 = X_1$), the two coefficients vanish, and one has a purely TM wave.

3.3.7 Impedance Matching Between Regions S' and S

In order to avoid reflection at the boundary ∂S between S and S', the tensor impedance in S should match the isotropic impedance imposed in S' along ∂S. This gives the matching condition

$$X_1 \hat{\mathbf{e}}_1 \hat{\mathbf{e}}_1 + X_2 \hat{\mathbf{e}}_2 \hat{\mathbf{e}}_2|_{\partial S} = X_S(\hat{\mathbf{e}}_1 \hat{\mathbf{e}}_1 + \hat{\mathbf{e}}_2 \hat{\mathbf{e}}_2) \tag{3.52}$$

The previous equation implies from (3.46)

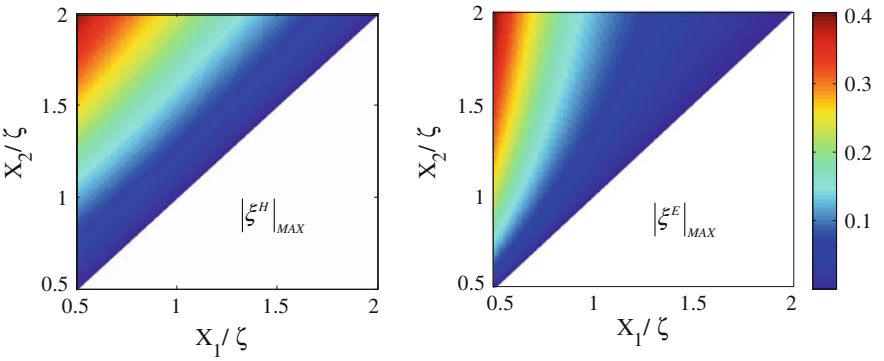

Fig. 3.11 Maximum values of the coefficients ξ^H, ξ^E in the plane X_1, X_2 in the region $X_2 > X_1$. Approximate expressions are given in (3.51)

$$\lim_{\boldsymbol{\rho}\to\partial S} \sigma_n \sqrt{g} = 1 \tag{3.53}$$

which means that at the boundary the coordinate transformation should match the identity transformation up to the first order. When (3.53) is satisfied one has at the boundary $\xi^{E,H}(\mathbf{k}_t) = 0$ and $\mathbf{k}_t = \mathbf{k}'_t$, thus obtaining

$$\mathbf{E}_t = -\mathbf{k}_t X_0^{TM} I_{TM} e^{-j\mathbf{k}'_t\cdot\boldsymbol{\rho}'} e^{-zv_z} \tag{3.54}$$

$$\mathbf{H}_t = j\mathbf{k}_t^{\perp} I_{TM} e^{-j\mathbf{k}'_t\cdot\boldsymbol{\rho}'} e^{-zv_z} \tag{3.55}$$

which is coincident with the incident wave provided that $I_{TM} = I_{TM}'$.

3.4 Conformal and Nearly Conformal Transformations

An arbitrary coordinate transformation results in a spatially inhomogeneous AMMR tensor. The final effect of bending the waves is, however, similar to that obtained in graded index media, mainly used for realizing lenses and optical devices. In the next subsections, we show that this situation rigorously corresponds to the case of a conformal coordinate transformation and it can be approximated with a nearly conformal coordinate transformation. This concept has been applied several times in the framework of volumetric 2D TO to simplify the engineering realization of TO-based devices [21–23].

3.4.1 Conformal Transformations

We start with the assumption that both the transformation Γ_t and its inverse are conformal, namely they satisfy the Cauchy–Riemann (CR) conditions. For the inverse transformation, these conditions are $\partial x/\partial x' = \partial y/\partial y'$, $\partial x/\partial y' = -\partial y/\partial x'$ which imply $\boldsymbol{\gamma}^1 \cdot \boldsymbol{\gamma}^2 = \nabla'_t x \cdot \nabla'_t y = 0$ and $\left|\nabla'_t x\right|^2 = \left|\nabla'_t y\right|^2$. As a consequence, the tensor $\underline{\boldsymbol{\alpha}}_t$ in (3.21) coincides with the identity ($\underline{\boldsymbol{\alpha}}_t \equiv \underline{\mathbf{I}}$) and the dispersion equation in (3.20) becomes:

$$\sqrt{\mathbf{k}_t \cdot \mathbf{k}_t} = \frac{k}{\left|\nabla'_t x\right|} \sqrt{1 + (X_S/\zeta)^2} \tag{3.56}$$

The latter is associated with an isotropic medium of equivalent refractive index

$$n_{\mathrm{eq}}(\rho) = \frac{\sqrt{1 + (X_S/\zeta)^2}}{\left|\nabla'_t x\right|} \tag{3.57}$$

From (3.12), this equivalent refractive index is locally supported by the isotropic surface reactance

$$\frac{X_{eq}}{\zeta} = \sqrt{\frac{1}{|\nabla_t' x|^2}\left[1 + (X_S/\zeta)^2\right] - 1} \tag{3.58}$$

We observe that when the transformation is conformal $\nabla_t'^2 x$ and $\nabla_t'^2 y$ vanish, $\nabla_t \cdot \mathbf{k}_t = 0$ and the condition (3.29) is always fulfilled; as a consequence, in this case A_z satisfies the wave equation close to the surface.

3.4.2 Nearly Conformal Transformations

Assume that $\sigma_1 \approx \sigma_2$, i.e., the two eigenvalues of $\underline{\underline{\boldsymbol{\alpha}}}_t$ are almost equal (in practice they can differ by up to 10 %). This condition is satisfied for a nearly conformal coordinate transformation, and allows us to approximate both the eigenvalues of $\underline{\underline{\boldsymbol{\alpha}}}_t$ with $\sigma_1 \approx \sigma_2 \approx \sqrt{\sigma_1 \sigma_2} = 1$. This approximation is the same suggested in Ref. [24] and used in Refs. [21–23] for 2D TO. The dispersion equation becomes

$$\sqrt{g}\,\mathbf{k}_t \cdot \mathbf{k}_t = k^2\left[1 + (X_S/\zeta)^2\right] \tag{3.59}$$

which identifies an equivalent refraction index equal to

$$n_{eq}(\boldsymbol{\rho}) = \sqrt{\frac{1 + (X_S/\zeta)^2}{\sqrt{g}}} = \sqrt{\frac{1 + (X_S/\zeta)^2}{|\nabla_t' x||\nabla_t' y| \sin\delta}} \tag{3.60}$$

where δ is the angle between $\nabla_t' x$ and $\nabla_t' y$. From (3.12), this equivalent refractive index is locally supported by the isotropic impedance

$$\frac{X_{eq}}{\zeta} = \sqrt{\frac{1 + (X_S/\zeta)^2}{|\nabla_t' x||\nabla_t' y| \sin\delta} - 1} \tag{3.61}$$

3.4.3 Fermat's Principle

In conformal as well as in nearly conformal transformations, the definition of an equivalent refractive index allows one to treat ray field problems by simply applying the Fermat's principle. According to this principle, rays paths follow extremal optical paths. The length of the curvilinear ray path connecting two points $\boldsymbol{\rho}_1$ and $\boldsymbol{\rho}_2$ is given by

$$s(\boldsymbol{\rho}_1, \boldsymbol{\rho}_2) = \int_{\boldsymbol{\rho}_1}^{\boldsymbol{\rho}_2} n_{eq}(\boldsymbol{\rho}) \mathrm{d}s = \int_{\boldsymbol{\rho}_1}^{\boldsymbol{\rho}_2} \sqrt{\frac{1 + (X_S/\zeta)^2}{\left|\nabla_t' x\right| \left|\nabla_t' y\right| \sin\delta}} \mathrm{d}s \tag{3.62}$$

In the real space, each ray is thus curved according to Fermat's principle while in the virtual space the path of each ray appears as a straight line. Equation (3.62) provides a powerful tool for tracing ray fields coming from a given source for an assigned coordinate transformation. However, it is worth noting that the use of an equivalent refractive index is not necessarily associated with a coordinate transformation, but in some canonical cases (e.g., Luneburg lenses, Maxwell's fish eyes) the refractive index variation law can be given in a closed form.

3.5 Numerical Examples

In this section, some examples of metasurface transformations are provided. The first coordinate transformation is defined with domain in the square surface $S = \{|x| < a/2, |y| < a/2\}$ and is given by

$$\boldsymbol{\rho}' = \Gamma_t(\boldsymbol{\rho}) \rightarrow \begin{cases} x' = x \\ y' = y - \dfrac{a}{8} \cos^2\left(\dfrac{\pi x}{a}\right) \cos^2\left(\dfrac{\pi y}{a}\right) \end{cases} \tag{3.63}$$

S' is the region complementary to *S*.

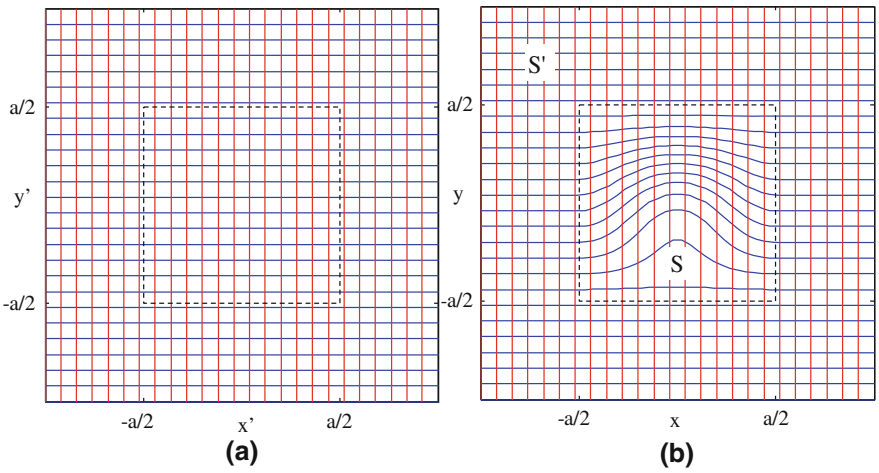

Fig. 3.12 **a** Virtual space (*codomain*). **b** Real space (*domain*) of the coordinate transformation in (3.63)

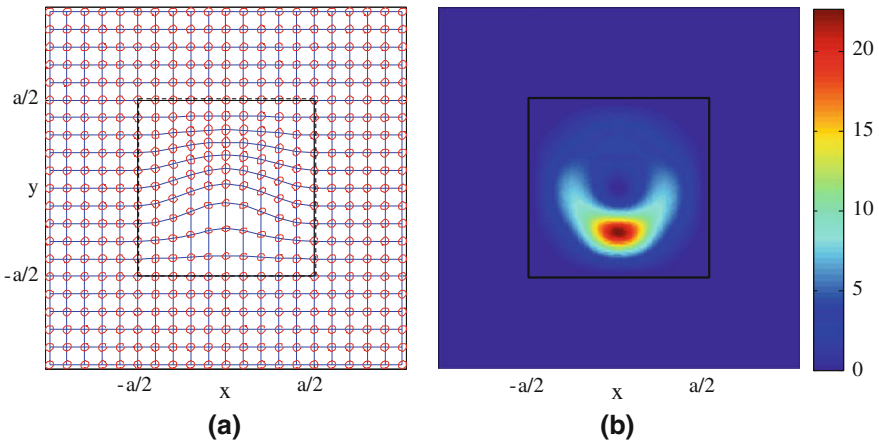

Fig. 3.13 Approximation of the local dispersion equation through AMMR for the transformation in (3.63). **a** Dispersion *ellipses*. **b** Maximum percent error made when reconstructing these dispersion *ellipses* though an AMMR

Fig. 3.14 Color plot of the parameter τ in (3.31) for the transformation in (3.63)

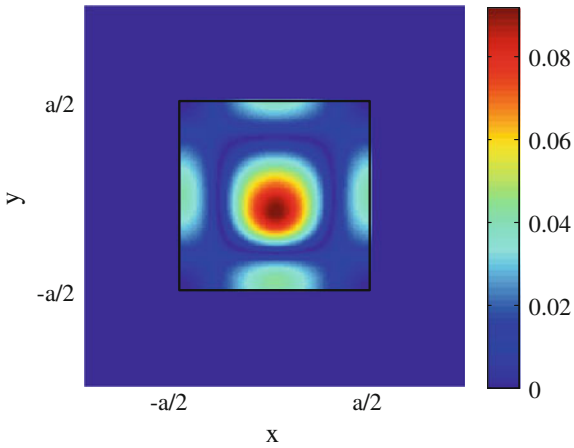

The inverse transformation distortes the square grid of the virtual space (x',y') into a curvilinear grid in the real space as shown in Fig. 3.12.

In constructing the impedance value, the region S' namely the region of unperturbed environment, has been assumed with reactance $X_S = \sqrt{3}\zeta$ so that $\sqrt{1 + (X_S/\zeta)^2} = 2$. Figure 3.13a shows the local dispersion ellipses (see Fig. 3.9) at sample points as calculated according to (3.20); Fig. 3.13b presents the maximum percent error (calculated through (3.45)) which is made when reconstructing the dispersion ellipses though an anisotropic equivalent surface impedance characterized by the equivalent tensor in (3.43) with principal values given by (3.46).

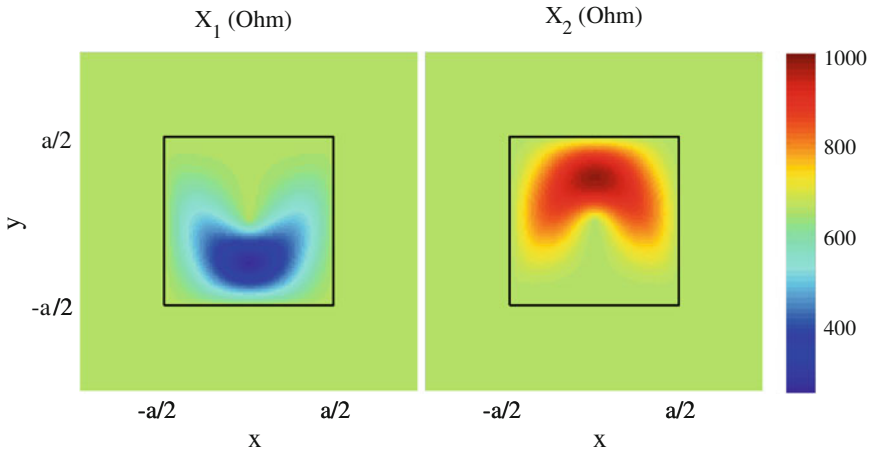

Fig. 3.15 Principal values of the AMMR tensor in the real space for the transformation in (3.63)

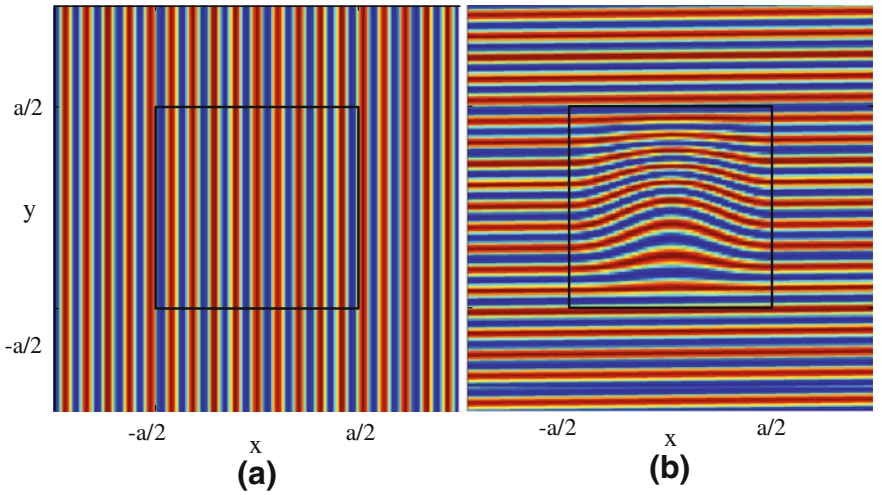

Fig. 3.16 Phase distribution for an incident SW traveling. **a** Along *x*. **b** Along *y*. The SW phase is not changed by the presence of the impedance surface in case **a,** namely the metasurface variation is invisible for the incident SW

Figure 3.14 shows the parameter τ defined in (3.31). Having this parameter small in the entire domain ensures the required condition on the smoothness of the coordinate transformation. In this specific case, it is seen that this parameter is less than 10 % throughout S.

Figure 3.15 shows the principal values of the reactance tensor. It is apparent that the reactance tensor smoothly reduces to the isotropic reactance X_S at the boundary of S, thus, ensuring the condition for impedance matching. The required

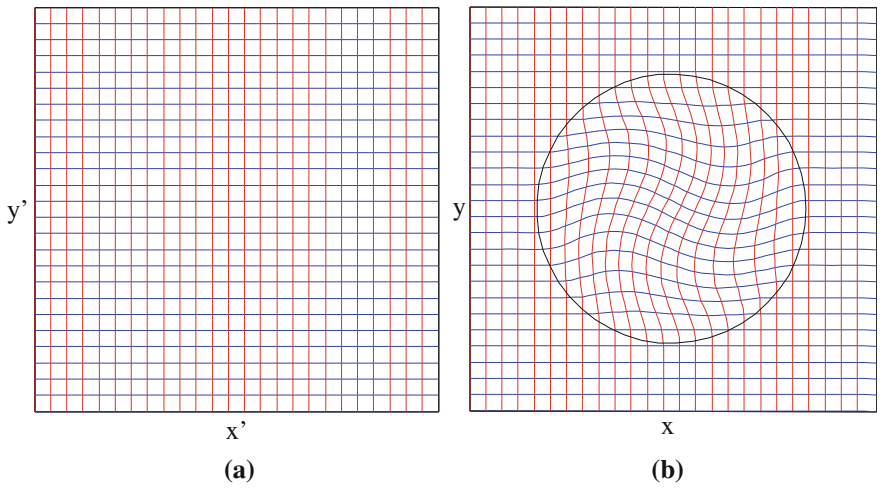

Fig. 3.17 **a** Virtual space (*codomain*). **b** Real space (*domain*) of the coordinate transformation in (3.64)

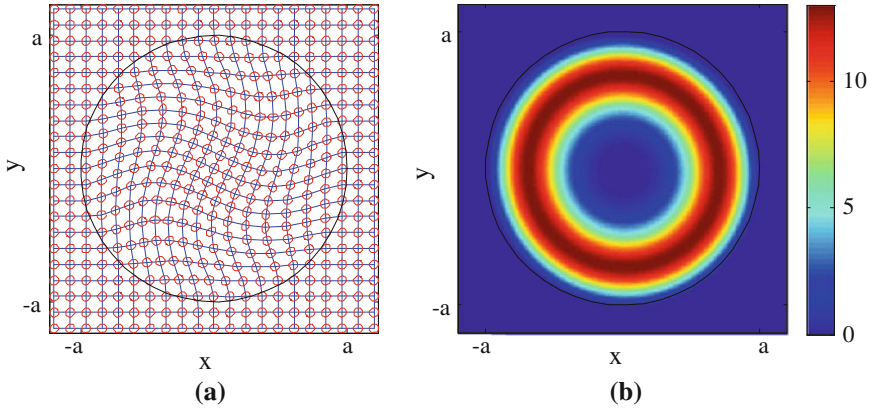

Fig. 3.18 Approximation of the local dispersion equation through AMMR for the transformation in (3.64). **a** Dispersion *ellipses*. **b** Maximum percent error made when reconstructing these dispersion *ellipses* though an AMMR

impedance values range from 0.8 ζ to 2.65 ζ, and are therefore realizable through metasurfaces consisting of printed patches. Figure 3.16 shows the phase distribution of the field associated with an incident SW traveling along x (16a) and with an incident SW traveling along y (16b). In the first case, no phase distortion occurs, namely the AMMR is practically invisible, while in the second case, the phase fronts are deformed according to the coordinate transformation.

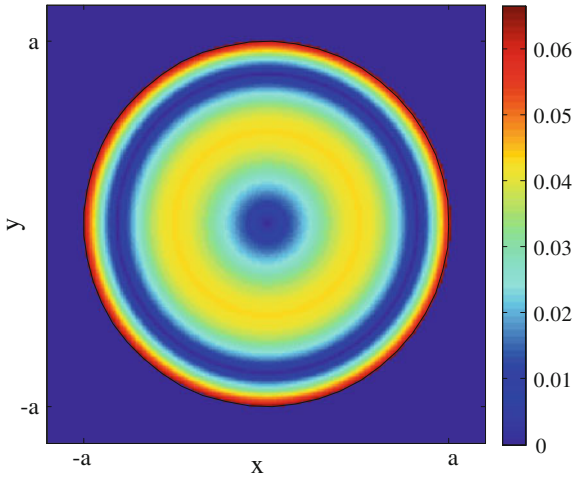

Fig. 3.19 Color plot of the parameter τ in (3.31) for the transformation in (3.64)

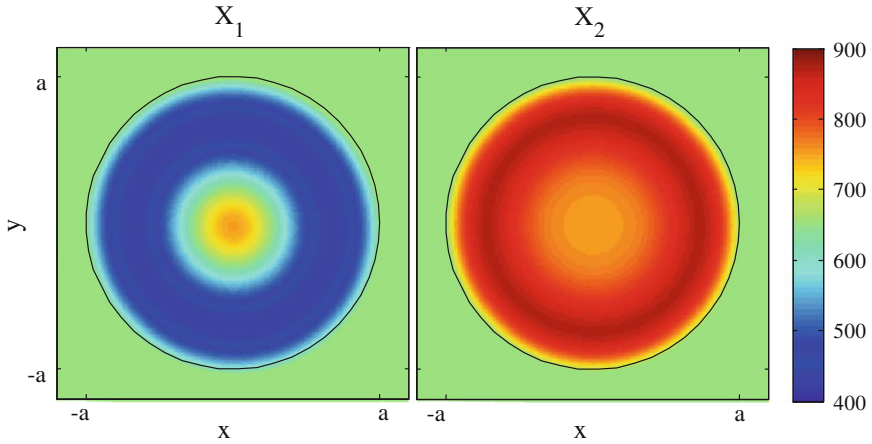

Fig. 3.20 Principal values of the AMMR tensor for the transformation in (3.64)

Consider now the transformation

$$\rho' = \Gamma'(\rho) \rightarrow \begin{cases} x' = x - \frac{1}{2}\left[\frac{a^2 - (x^2 + y^2)}{a^2}\right]^2 y \\ y' = y + \frac{1}{2}\left[\frac{a^2 - (x^2 + y^2)}{a^2}\right]^2 x \end{cases} \tag{3.64}$$

The regions S and S' are identified by the conditions $\rho < a$ and $\rho > a$, respectively. This coordinate transformation is illustrated in Fig. 3.17. The region S'

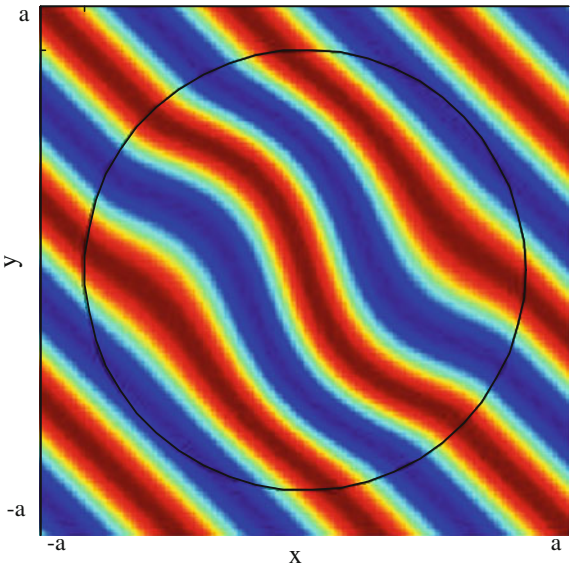

Fig. 3.21 Phase distribution for an incident SW propagating at an angle 45° with the x axis for the transformation in (3.64)

possesses reactance $X_S = \sqrt{3}\zeta$. Figure 3.18a shows the local dispersion ellipses according to (3.20) and Fig. 3.18b presents the maximum percent error on their approximation through an AMMR, calculated according to (3.45). Figure 3.19 shows the parameter τ in (3.31); as it can be seen, its value is smaller than 7 % throughout S. Figure 3.20 shows the distribution of the eigenvalues of the reactance tensor, which exhibit values ranging from ζ to 2.4 ζ. Finally, Fig. 3.21 shows the phase distribution for an incident SW propagating at an angle 45° with the x axis.

3.6 Conclusions

We have presented a theory of metasurface transformation which extends TO to control the wavefront of SW's through the use of modulated metasurface reactances. The phase of the SW field is varied according to a 2D coordinate transformation. It is therefore possible to choose the transformation so as to generate a desired curved wavefront. Here, we have derived the relationship between the transformation needed to obtain a given SW curved wavefront and the AMMR tensor able to support such SW wavefront. As expected, the MMR tensor is in general anisotropic, except for the case of nearly conformal transformations. As the outputs of the conventional TO approach are the metamaterial constitutive parameters able to perform a certain modification of the ray field path, here the outcomes are the components of the AMMR tensor.

In our treatment, we have not directly applied a 2D version of TO, since this would have implied a variable compression of the medium in the direction normal

to the surface, with a consequent inhomogeneity of the surrounding medium. In order to simplify the practical implementation, we have instead assumed a priori the presence of free space above the AMMR, and we have compensated this assumption by changing the principal values of the tensor. The process suggested here is not exact; however, we have individuated the parameters of the coordinate transformation that reveal the accuracy of the approximation and the condition to avoid radiation losses.

We have not addressed in this chapter, the problem of the practical synthesis and realization of the desired AMMR by using transmission line lumped elements or patches, except for the qualitative discussion given in Sect. 3.2.2. However, AMMR have been already proposed in literature, often in order to realize circularly polarized aperture fields. Thus, the process of synthesis and practical implementation of AMMR tensors is a subject which is now starting its maturation process. Also, we have not addressed the problem of ohmic losses. However, we can say that, since the elements are very small in terms of the wavelength, the currents are weak and the ohmic losses do not constitute a critical issue.

A.1 Appendix A Fundamentals of Transformation Optics

Let us consider Maxwell's equation in absence of sources in primed space (assumed for simplicity as free space)

$$\begin{aligned} \nabla \times \mathbf{E}' &= -j\omega\mu_0 \mathbf{H}' \\ \nabla \times \mathbf{H}' &= j\omega\varepsilon_0 \mathbf{E}' \end{aligned} \tag{3.65}$$

The observation point of this space, that will be denoted in the following as "virtual space" or "transformed space", will be identified by the vector $\mathbf{r}' = x'\hat{\mathbf{x}}' + y'\hat{\mathbf{y}}' + z'\hat{\mathbf{z}}'$. The physical space individuated by $\mathbf{r} = x\hat{\mathbf{x}} + y\hat{\mathbf{y}} + z\hat{\mathbf{z}}$ will be instead denoted as "real space". For simplicity, Cartesian coordinates have been chosen in both spaces. The real space is mapped to the virtual space by a 3D invertible transformation $\mathbf{\Gamma}$; conversely, the inverse transformation $\mathbf{\Gamma}^{-1}$ maps the virtual space to the real space

$$\mathbf{r}' = \mathbf{\Gamma}(\mathbf{r}) : \{x, y, z\} \rightarrow \{x'(x, y, z), y'(x, y, z), z'(x, y, z)\} \tag{3.66}$$

$$\mathbf{r} = \mathbf{\Gamma}^{-1}(\mathbf{r}') : \{x', y', z'\} \rightarrow \{x(x', y', z'), y(x', y', z'), z(x', y', z')\} \tag{3.67}$$

The coordinate transformation $\mathbf{\Gamma}$ is the one on which the TO process is based. Note that several authors interchange the definition of transformation and inverse transformation, so that the domain is the virtual space and the co-domain is the real space. On the basis of TO, Maxwell's equations in the real space are satisfied provided that the real space is filled with an inhomogeneous anisotropic medium characterized by tensors $\underline{\underline{\mu}}$ and $\underline{\underline{\varepsilon}}$ properly related to the coordinate transformation. Hence, Maxwell's equations in the real space are written as [25, 26]

$$\begin{aligned}\nabla \times \mathbf{E} &= -j\omega \underline{\underline{\boldsymbol{\mu}}} \cdot \mathbf{H} \\ \nabla \times \mathbf{H} &= j\omega \underline{\underline{\boldsymbol{\varepsilon}}} \cdot \mathbf{E}\end{aligned} \tag{3.68}$$

In (3.68), the nabla operator $\nabla = \frac{\partial}{\partial x}\hat{\mathbf{x}} + \frac{\partial}{\partial y}\hat{\mathbf{y}} + \frac{\partial}{\partial z}\hat{\mathbf{z}}$ acts on the Cartesian coordinates of the real space. The electric and magnetic fields are expressed as

$$\begin{aligned}\mathbf{E}(\mathbf{r}) &= \underline{\underline{\mathbf{M}}}^T(\mathbf{r}) \cdot \mathbf{E}'(\mathbf{r}'), \\ \mathbf{H}(\mathbf{r}) &= \underline{\underline{\mathbf{M}}}^T(\mathbf{r}) \cdot \mathbf{H}'(\mathbf{r}')\end{aligned} \tag{3.69}$$

where $\mathbf{r}' = \boldsymbol{\Gamma}(\mathbf{r})$ and the Jacobian tensor $\underline{\underline{\mathbf{M}}}$ is defined as

$$\begin{aligned}\underline{\underline{\mathbf{M}}}(\mathbf{r}) &= \left(\frac{\partial \mathbf{r}'}{\partial \mathbf{r}}\right) = \sum_{i,j=1,3} \frac{\partial x_i'}{\partial x_j} \hat{\mathbf{x}}_i' \hat{\mathbf{x}}_j \\ \underline{\underline{\mathbf{M}}}^{-1}(\mathbf{r}) &= \sum_{i,j=1,3} \frac{\partial x_j}{\partial x_i'} \hat{\mathbf{x}}_j \hat{\mathbf{x}}_i'\end{aligned} \tag{3.70}$$

In (3.70) for simplifying the notation we have redefined $\{x, y, z\} \equiv \{x_1, x_2, x_3\}$, $\{x', y', z'\} \equiv \{x_1', x_2', x_3'\}$; $\hat{\mathbf{x}}, \hat{\mathbf{y}}, \hat{\mathbf{z}} \equiv \hat{\mathbf{x}}_1, \hat{\mathbf{x}}_2, \hat{\mathbf{x}}_3$, and $\hat{\mathbf{x}}', \hat{\mathbf{y}}', \hat{\mathbf{z}}' \equiv \hat{\mathbf{x}}_1', \hat{\mathbf{x}}_2', \hat{\mathbf{x}}_3'$. In the following, we will use this latter indexed notation when needed within summation symbol. The permittivity and permeability TO tensors in (3.68) are related to the Jacobian tensors by the following equations

$$\frac{1}{\mu_0}\underline{\underline{\boldsymbol{\mu}}} = \frac{1}{\varepsilon_0}\underline{\underline{\boldsymbol{\varepsilon}}} = \underline{\underline{\boldsymbol{\alpha}}}\,;\ \underline{\underline{\boldsymbol{\alpha}}} = \det[\underline{\underline{\mathbf{M}}}]\underline{\underline{\mathbf{M}}}^{-1} \cdot \left(\underline{\underline{\mathbf{M}}}^T\right)^{-1} \tag{3.71}$$

The induced electric and magnetic fields are given by

$$\begin{aligned}\mathbf{D}(\mathbf{r}) &= \det(\underline{\underline{\mathbf{M}}})\underline{\underline{\mathbf{M}}}^{-1} \cdot \varepsilon_0 \mathbf{E}'(\mathbf{r}') \\ \mathbf{B}(\mathbf{r}) &= \det(\underline{\underline{\mathbf{M}}})\underline{\underline{\mathbf{M}}}^{-1} \cdot \mu_0 \mathbf{H}'(\mathbf{r}')\end{aligned} \tag{3.72}$$

Being the real space inhomogeneous, rays propagate there along curvilinear paths; these paths are mapped to straight lines in the virtual space. It is convenient to introduce covariant basis $\mathbf{g}_i = \partial \mathbf{r}/\partial x_i' = \sum_j \partial x_j/\partial x_i' \hat{\mathbf{x}}_j$ and contravariant basis $\mathbf{g}^i = \nabla x_i' = \sum_j \partial x_i'/\partial x_j \hat{\mathbf{x}}_j$ of the coordinate transformation $\boldsymbol{\Gamma}$, as well as covariant basis $\boldsymbol{\gamma}_j = \partial \mathbf{r}'/\partial x_j = \sum_i \partial x_i'/\partial x_j \hat{\mathbf{x}}_i'$ and contravariant basis $\boldsymbol{\gamma}^j = \nabla' x_j = \sum_i \partial x_j/\partial x_i{}' \hat{\mathbf{x}}_i'$ of the inverse coordinate transformation $\boldsymbol{\Gamma}^{-1}$. Figure 3.22 illustrates an example. Note that $\mathbf{g}_i, \mathbf{g}^i$ and $\boldsymbol{\gamma}_j, \boldsymbol{\gamma}^j$ are defined in the real space and in the transformed space, respectively. The two introduced bases are bi-orthogonal, namely $\mathbf{g}^i \cdot \mathbf{g}_j = \delta_{ij}, \boldsymbol{\gamma}^i \cdot \boldsymbol{\gamma}_j = \delta_{ij}$, and

$$\begin{aligned}\mathbf{g}^1 \times \mathbf{g}^2 &= \mathbf{g}_3/\sqrt{g} \quad \mathbf{g}_1 \times \mathbf{g}_2 = \mathbf{g}^3\sqrt{g} \\ \mathbf{g}^2 \times \mathbf{g}^3 &= \mathbf{g}_1/\sqrt{g}\,;\ \mathbf{g}_2 \times \mathbf{g}_3 = \mathbf{g}^1\sqrt{g} \\ \mathbf{g}^3 \times \mathbf{g}^1 &= \mathbf{g}_2/\sqrt{g} \quad \mathbf{g}_3 \times \mathbf{g}_1 = \mathbf{g}^2\sqrt{g}\end{aligned} \tag{3.73}$$

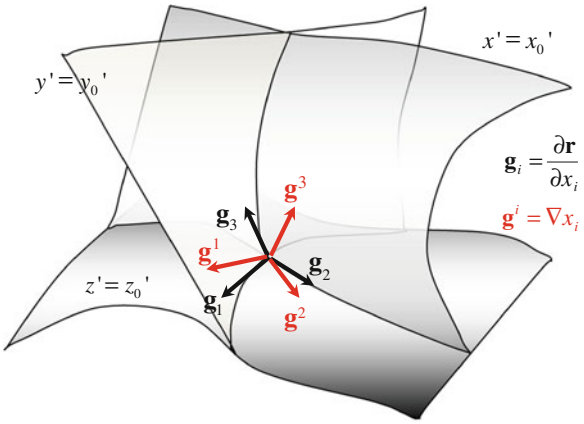

Fig. 3.22 Coordinate planes and coordinate lines in the real space as transformed from the cartesian planes and coordinates in the virtual space and covariant and contravariant bases

where $\det \underline{\underline{\mathbf{M}}} = 1/\sqrt{g}$. The Jacobian tensor, its inverse, and its determinant can be written in terms of covariant and contravariant basis as

$$\underline{\underline{\mathbf{M}}} = \sum_{i=1,3} \hat{\mathbf{x}}_i' \mathbf{g}^i = \sum_{j=1,3} \gamma_j \hat{\mathbf{x}}_j \tag{3.74}$$

$$\underline{\underline{\mathbf{M}}}^{-1} = \sum_{i=1,3} \mathbf{g}_i \hat{\mathbf{x}}_i' = \sum_{j=1,3} \hat{\mathbf{x}}_j \gamma^j \tag{3.75}$$

$$\det \underline{\underline{\mathbf{M}}} = \frac{1}{\sqrt{g}} = \mathbf{g}^3 \cdot \left(\mathbf{g}^1 \times \mathbf{g}^2\right) = \frac{1}{\mathbf{g}_3 \cdot (\mathbf{g}_1 \times \mathbf{g}_2)} = \gamma_3 \cdot (\gamma_1 \times \gamma_2) = \frac{1}{\gamma^3 \cdot (\gamma^1 \times \gamma^2)} \tag{3.76}$$

Using (3.74) in (3.69), and observing that the transpose operation in (3.69) swaps the order of the vectors in the dyads in (3.74), leads to

$$\mathbf{E}(\mathbf{r}) = \sum_{i=1,3} \mathbf{g}^i \left[\hat{\mathbf{x}}_i' \cdot \mathbf{E}'(\mathbf{r}')\right] \tag{3.77}$$

$$\mathbf{H}(\mathbf{r}) = \sum_{i=1,3} \mathbf{g}^i \left[\hat{\mathbf{x}}_i' \cdot \mathbf{H}'(\mathbf{r}')\right] \tag{3.78}$$

$$\mathbf{D}(\mathbf{r}) = \frac{1}{\sqrt{g}} \sum_{i=1,3} \mathbf{g}_i \left[\hat{\mathbf{x}}_i' \cdot \mathbf{D}'(\mathbf{r}')\right] \tag{3.79}$$

$$\mathbf{B}(\mathbf{r}) = \frac{1}{\sqrt{g}} \sum_{i=1,3} \mathbf{g}_i \left[\hat{\mathbf{x}}_i' \cdot \mathbf{B}'(\mathbf{r}')\right] \tag{3.80}$$

which identifies the electric and magnetic field Cartesian components in the virtual space with the covariant components of the fields in the real space. On the other

hand, the Cartesian components of the electric and magnetic inductions in the virtual space represent the contravariant components of the inductions in the real space.

The normalized tensors are indeed expressed through (3.71) and (3.75–3.76) as

$$\underline{\underline{\boldsymbol{\alpha}}} = \frac{1}{\sqrt{g}} \sum_{i,j=1,3} \hat{\mathbf{x}}_i \hat{\mathbf{x}}_j \left[\boldsymbol{\gamma}^i \cdot \boldsymbol{\gamma}^j \right] \tag{3.81}$$

We observe that for orthogonal transformations covariant vectors coincide with contravariant vectors.

The tensor $\underline{\underline{\alpha}}$ can be represented in the reference system identified by unit vectors $\hat{\mathbf{e}}_i$ aligned with its principal axes as follows

$$\underline{\underline{\boldsymbol{\alpha}}} = \hat{e}_1 \hat{e}_1 \sigma_1 + \hat{e}_2 \hat{e}_2 \sigma_2 + \hat{e}_3 \hat{e}_3 \sigma_3 \tag{3.82}$$

where σ_i are the principal values of $\underline{\underline{\alpha}}$. Note that the unit vectors $\hat{\mathbf{e}}_i = \hat{\mathbf{e}}_i(\mathbf{r})$ are in general space dependent. The dispersion equation for *local* plane waves propagating with $\mathbf{r}$-dependent wavevector $\mathbf{k} = k_x \hat{\mathbf{x}} + k_y \hat{\mathbf{y}} + k_z \hat{\mathbf{z}} = k_1 \hat{\mathbf{e}}_1 + k_2 \hat{\mathbf{e}}_2 + k_3 \hat{\mathbf{e}}_3$ ($k_i = \mathbf{k} \cdot \hat{\mathbf{e}}_i$) can be written as

$$k_1^2 \sigma_1 + k_2^2 \sigma_2 + k_3^2 \sigma_3 - k^2 \sigma_1 \sigma_2 \sigma_3 = 0 \tag{3.83}$$

where $k = \omega \sqrt{\varepsilon_o \mu_o}$ is the free-space wavenumber. We note that this equation is valid for both TE and TM modes with respect to one of the three axes; degeneration of TE/TM mode phase velocity in TO media was underlined in Ref. [27] with reference to a spherical cloak. For positive values of σ_i, (3.83) represents in the $\mathbf{k}$-space an ellipsoid with axes aligned with the principal axes $\hat{\mathbf{e}}_i$ and semi-axes given by $k\sqrt{\sigma_2 \sigma_3}$, $k\sqrt{\sigma_1 \sigma_3}$, $k\sqrt{\sigma_1 \sigma_2}$ along $\hat{\mathbf{e}}_1$, $\hat{\mathbf{e}}_2$, $\hat{\mathbf{e}}_3$, respectively. The coordinate- free expression of this ellipse is $\mathbf{k} \cdot \underline{\underline{\boldsymbol{\alpha}}} \cdot \mathbf{k} = k^2 \sigma_1 \sigma_2 \sigma_3$. (Fig. 3.23)

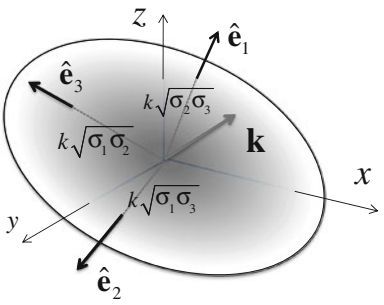

Fig. 3.23 Dispersion *ellipse* for a given constitutive parameter tensor

A.2 Appendix B -Dispersion Equation for an Anisotropic Tensor

To solve (3.41) in terms of $\sqrt{\mathbf{k}_t \cdot \mathbf{k}_t}$, we project $\underline{\underline{\mathbf{X}}}_S^{eq}$ along the basis $\hat{\mathbf{k}}_t$, $\hat{\mathbf{z}} \times \hat{\mathbf{k}}_t = \hat{\mathbf{k}}_t^{\perp}$, i.e.,

$$\begin{aligned}
&\underline{\underline{\mathbf{X}}}_S^{eq} = X^{ee}\hat{\mathbf{k}}_t\hat{\mathbf{k}}_t + X^{hh}\hat{\mathbf{k}}_t^{\perp}\hat{\mathbf{k}}_t^{\perp} + X^{eh}\left(\hat{\mathbf{k}}_t\hat{\mathbf{k}}_t^{\perp} + \hat{\mathbf{k}}_t^{\perp}\hat{\mathbf{k}}\right)_t \\
&X^{ee} = \hat{\mathbf{k}}_t \cdot (X_1\hat{\mathbf{e}}_1\hat{\mathbf{e}}_1 + X_2\hat{\mathbf{e}}_2\hat{\mathbf{e}}_2) \cdot \hat{\mathbf{k}}_t = \cos^2(\psi - \phi)X_1 + \sin^2(\psi - \phi)X_2 \\
&X^{hh} = \hat{\mathbf{k}}_t^{\perp} \cdot (X_1\hat{\mathbf{e}}_1\hat{\mathbf{e}}_1 + X_2\hat{\mathbf{e}}_2\hat{\mathbf{e}}_2) \cdot \hat{\mathbf{k}}_t^{\perp} = \sin^2(\psi - \phi)X_1 + \cos^2(\psi - \phi)X_2 \\
&X^{eh} = \hat{\mathbf{k}}_t \cdot (X_1\hat{\mathbf{e}}_1\hat{\mathbf{e}}_1 + X_2\hat{\mathbf{e}}_2\hat{\mathbf{e}}_2) \cdot \hat{\mathbf{k}}_t^{\perp} = \sin(\psi - \phi)\cos(\psi - \phi)(X_1 - X_2)
\end{aligned} \tag{3.84}$$

where $\cos\psi = \hat{\mathbf{e}}_1 \cdot \hat{\mathbf{x}}$, $\sin\psi = \hat{\mathbf{e}}_1 \cdot \hat{\mathbf{y}}$; $\cos\phi = \hat{\mathbf{k}}_t \cdot \hat{\mathbf{x}}$, $\sin\phi = \hat{\mathbf{k}}_t \cdot \hat{\mathbf{y}}$. An explicit expression of ψ is given in (3.22). The dispersion (3.41) can be therefore rewritten as

$$\det\left[\underline{\underline{\mathbf{X}}}_S^{eq} + \underline{\underline{\mathbf{X}}}_0\right] = \left(X^{ee} + X_0^{TM}\right)\left(X^{hh} + X_0^{TE}\right) - \left(X^{eh}\right)^2 = 0 \tag{3.85}$$

The latter equation can be simplified by exploiting the identities $X_0^{TE}X_0^{TM} = -\zeta^2$ and $X^{ee}X^{hh} - (X^{eh})^2 = \det\underline{\underline{\mathbf{X}}}_S^{eq} = X_1X_2$. This leads to

$$X^{ee}X_0^{TE} + X^{hh}X_0^{TM} + X_1X_2 - \zeta^2 = 0 \tag{3.86}$$

Solving (3.86) in terms of $\eta = \sqrt{\mathbf{k}_t \cdot \mathbf{k}_t/k^2 - 1} = -X_{TM}/\zeta = \zeta/X_{TE}$ provides

$$\sqrt{\mathbf{k}_t \cdot \mathbf{k}_t/k^2 - 1} = \frac{1}{2\zeta X_{hh}}\left\{\left(X_1X_2 - \zeta^2\right) + \sqrt{\left(X_1X_2 - \zeta^2\right)^2 + 4X_{ee}X_{hh}\zeta^2}\right\} \tag{3.87}$$

The above equation can be approximated by

$$\frac{\mathbf{k}_t \cdot \mathbf{k}_t}{k^2} \approx \left(\frac{\cos^2(\psi - \phi)}{1 + (X_1/\zeta)^2} + \frac{\sin^2(\psi - \phi)}{1 + (X_2/\zeta)^2}\right)^{-1} \tag{3.88}$$

which is an ellipse with the main axes aligned with the eigenvectors $\hat{\mathbf{e}}_1$, $\hat{\mathbf{e}}_2$ and semi-axes equal to $\frac{k_i}{k} \approx \sqrt{1 + (X_i/\zeta)^2}$. The maximum deviation of the approximation in (3.88) from (3.87) is exactly given by

$$\left|\frac{\mathbf{k}_t \cdot \mathbf{k}_t}{k^2}\left[\frac{\cos^2(\psi - \phi)}{1 + (X_1/\zeta)^2} + \frac{\sin^2(\psi - \phi)}{1 + (X_2/\zeta)^2}\right] - 1\right|_{MAX\ \phi} = \left|f\left(\frac{X_1}{\zeta}, \frac{X_2}{\zeta}\right)\right| \tag{3.89}$$

with

$$f\left(\frac{X_1}{\zeta},\frac{X_2}{\zeta}\right)=\frac{\left(\frac{X_1}{\zeta}-\frac{X_2}{\zeta}\right)^2-\left(\sqrt{\frac{X_1}{X_2}}-\sqrt{\frac{X_2}{X_1}}\right)^2}{4\left(\frac{X_1}{\zeta}+\frac{\zeta}{X_1}\right)\left(\frac{X_2}{\zeta}+\frac{\zeta}{X_2}\right)} \tag{3.90}$$

This relation has been obtained analytically by imposing a vanishing derivative of the error function with respect to $\psi-\phi$.

References

1. Pendry JB, Schurig D, Smith DR (2006) Controlling electromagnetic field. Science 312(5781):1780–1782
2. Leonhardt U (2006) Optical conformal mapping. Science 312(5781):1777–1780
3. Yaghjian A, Maci S (2008) Alternative derivation of electromagnetic cloaks and concentrators. New J Phys 10:1–29
4. Maci S, Minatti G, Casaletti M, Bosiljevac M (2011) Metasurfing: addressing waves on impenetrable metasurfaces. IEEE Antenn Wirel Pr 10:1499–1502
5. Holloway CL, Dienstfrey A, Kuester EF, O'Hara JF, Azad AK, Taylor AJ (2009) A discussion on the interpretation and characterization of metafilms/metasurfaces: the two dimensional equivalent of metamaterials. Metamaterials 3:100–112
6. Holloway CL, Kuester EF, Gordon JA, O'Hara J, Booth J, Smith DR (2012) An overview of the theory and applications of metasurfaces: the two-dimensional equivalents of metamaterials. IEEE Antenn Propag M 54(2):10–35
7. Silverinha MG, Fernandes CA, Costa JR (2008) Electromagnetic charactrerization of textured surfaces formed by metallic pins. IEEE T Antenn Propag 56(2):405–415
8. Kildal PS, Kishk A, Maci S (2005) Special issue in artificial magnetic conductors, soft/hard surfaces, and other complex surfaces. IEEE T Antenn Propag, 53(1), p 1
9. Sievenpiper D, Zhang L, Broas FJ, Alexopulos NG, Yablanovitch E (1999) High-impedance electromagnetic surfaces with a forbidden frequency band. IEEE T Microw Theory 47(11):2059–2074
10. Maci S, Caiazzo M, Cucini A, Casaletti M (2005) A pole-zero matching method for EBG surfaces composed of a dipole FSS printed on a grounded dielectric slab. IEEE T Antenn Propag 53(1):70–78
11. Luukkonen O, Simovski C, Granet G, Goussetis G, Lioubtchenko D, Raisanen AV, Tretyakov SA (2008) Simple and accurate analytical model of planar grids and high-impedance surfaces comprising metal strips or patches. IEEE T Antenn Propag 56(6):1624–1632
12. Bosiljevac M, Casaletti M, Caminita F, Sipus Z, Maci S (2011) Non-uniform metasurface luneburg lens antenna design. IEEE T Antenn Propagat 60(9):4065–4073
13. Pfeiffer C, Grbic A (2010) A printed, broadband luneburg lens antenna. IEEE T Antenn Propag 58(9):3055–3059
14. Vakil A, Engheta N (2011) Transformation optics using graphene. Science 332:1291–1294
15. Casaletti M, Caminita F, Maci S, Bosiljevac M, Sipus Z (2011) New type of horn based on variable metasurface. IEEE AP-S 2011:1048–1050
16. Minatti G, Caminita F, Casaletti M, Maci S (2011) Spiral leaky-wave antennas based on modulated surface impedance. IEEE T Antenn Propag 59(12):4436–4444
17. Hoppe J, Rahmats Samii Y (1995) Impedance boundary conditions in electromagnetics. Taylor and Francis, Washington pp 135–137
18. Gok G, Grbic A (2010) Tensor transmission-line metamaterials. IEEE T Antenn Propag 58(5):1559–1566

19. Fong BH, Colburn JS, Ottusch JJ, Visher JL, Sievenpiper DF (2010) Scalar and tensor holographic artificial impedance surfaces. IEEE T Antenn Popag 58(10):3212–3221
20. Minatti G, Maci S, De Vita P, Freni A, Sabbadini M (2012) A circularly-polarized isoflux antenna based on anisotropic metasurface. IEEE T Antenn Propag 60 (12)
21. Tang W, Argyropoulos C, Kallos E, Song W, Hao Y (2010) Discrete coordinate transformation for designing all-dielectric flat antennas. IEEE T Antenn Propag 58(12): 3795–3804
22. Yang R, Tang W, Hao Y (2011) Wideband beam-steerable flat reflectors via transformation optics. Antenn Wirel Pr 10:99–102
23. Yang R, Hao Y (2012) An accurate control of the surface wave using transformation optics. Opt Express 20(9):9341–9350
24. Li J, Pendry J (2008) Hiding under the carpet: a new strategy for cloaking. Phys Rev Lett 101(20):203901–203905
25. Yaghjian A, Maci S, Martini E (2009) Electromagnetic cloaks and concentrators. In: Capolino F (ed) Handbook of artificial materials. vol I phenomena and theory. ISBN: 978-1-4200536-2-2010
26. Martini E, Maci S, Yaghjian A (2011) Cloaking in terms of non-radiating cancelling currents. In: Galdi V (ed) Selected topics in metamaterials and photonic crystals. World Scientific, Singapore
27. Martini E, Maci S, Yaghjian A (2009) Characteristic wave velocities in spherical electromagnetic cloaks. New J Phys 11 113011 10.1088/1367-2630/11/11/113011

Chapter 4
Design for Simplified Materials in Transformation Electromagnetics

Steven A. Cummer

Abstract In this chapter we review some of the common methods used to simplify the design of transformation electromagnetics devices. One of the major challenges is the complexity of the needed material parameters, and a variety of analytical, numerical, and approximation techniques can be used to create devices that still perform well, although not ideally, but are much easier to fabricate. All of these techniques are a manifestation of the general concept that transformation electromagnetics designs are relatively robust to material perturbations.

4.1 Introduction

The power of transformation electromagnetics stems, in part, from its astonishing generality. Any imaginable manipulation of electromagnetic fields that can be described by a coordinate transformation—including dragging, stretching, twisting, or opening a hole—can be created by a specific electromagnetic material that spans the region of that transformation [1]. Deriving the properties of that electromagnetic material from the coordinate transformation is a mathematically straightforward operation [2].

The well-acknowledged downside of transformation electromagnetics is that the material properties that result from a given design are often very complex. For almost all interesting or useful transformations, these materials are strongly inhomogeneous and anisotropic [1]. Moreover, they usually require control over both the electric and magnetic properties (permittivity and permeability, respectively) of the material.

S. A. Cummer (✉)
Department of Electrical and Computer Engineering, Duke University,
Durham NC 27708, USA
e-mail: cummer@ee.duke.edu

D. H. Werner and D.-H. Kwon (eds.), *Transformation Electromagnetics and Metamaterials*, DOI: 10.1007/978-1-4471-4996-5_4,

These complexities of the resulting material parameters limit the practical realization of transformation electromagnetics devices. Nature has unfortunately provided us with very few materials in which the magnetic properties can be controlled. The story is similar for inhomogeneous or anisotropic materials. Consequently, the best hope for building functional transformation electromagnetics devices is to use engineered electromagnetic metamaterials. How to design an artificial metamaterial to achieve certain electromagnetic properties is a large field unto itself (metamaterials) and beyond the scope of this chapter. See [3, 4] for reviews of this topic.

The range of electromagnetic material properties that can be achieved through electromagnetic metamaterials is remarkable and includes strong anisotropy, inhomogeneity [5], and even negative values [6]. However, there are still substantial limits to the realizable properties, including frequency-dependence or dispersion when parameters are negative [7], and loss or absorption for materials with extreme values [8]. These and other practical limitations mean that even with the power of electromagnetic metamaterials, it remains a major challenge to fabricate a device based on a transformation electromagnetics design.

This challenge is well-demonstrated through the literature of electromagnetic cloaking [1]. The first experimental demonstration of a cloaking shell that deformed electromagnetic wavefronts to bend the energy around a central object [9] employed several approximations to simplify the material properties of a 2D device. These approximations reduced the device performance but dramatically simplified its design and fabrication. Improving the device would require fabrication of a device with control over more electromagnetic material parameters, and to date, no such improvement has been published.

These challenges in realizing the full, complicated set of electromagnetic material parameters needed for transformation electromagnetics devices has led to a recognition that constraints related to physical realizability need to be incorporated early into their design. The goal of this chapter is to describe some of the different techniques that have been employed in designing transformation electromagnetics devices for physical realizability. We describe herein three distinct techniques:

- Use degrees of freedom associated with the coordinate transformation itself to control the needed material parameters and improve device performance.
- Make approximations to a transformation electromagnetics design to gain material simplicity at the expense of device performance.
- Use optimization techniques that begin with transformation electromagnetics devices or designs to find realizable material properties that yield adequate device performance.

As shown in the sections below, these techniques span a wide range of approaches, including analytical to numerical, and exact to approximate. But they all have the same underlying goal: finding material properties based on transformation electromagnetics designs that can be more simply fabricated but still perform the desired function.

4.2 Controlling Material Properties Through Transformations

One of the more remarkable aspects of transformation electromagnetics is that there are usually many different coordinate transformations that can perform a specific job. For example, the spherical cloaking transformation maps the interior of a sphere to a spherical shell. The top panel of Fig. 4.1 illustrates how this transformation looks in mapping between physical space (defined with unprimed coordinates, $a<r<b$) to the virtual space (defined with primed coordinates, $0<r'<b$) in which the electromagnetic wave feels as though it is propagating. With these cloaking transformations, the fields that begin undistorted in the virtual space are compressed via mapping into an annulus ($a<r<b$) so that the fields in the virtual space do not interact at all with the physical space $r<a$. Thus any object hidden inside this interior space is effectively invisible to interrogation by electromagnetic waves.

To derive the material parameters of this cloaking shell, we need to explicitly specify the transformation between virtual and physical space. The constraints on this transformation are modest: $r=a$ must map to $r'=0$, so that an object inside $r<a$ is effectively removed or hidden; $r=b$ must map to $r'=b$, so that the medium outside the shell is unaffected; and the transformation should never involve $r<a$ or $r>b$ so that the wave fields are constrained to the spherical shell $a<r<b$. The transformation should also be single valued in r so that the fields at each position in physical space takes a single value, although the fields from a single point in virtual space r' may repeat at different values of r.

Interestingly, there are infinitely many coordinate transformations that satisfy these constraints. The original work on transformation electromagnetics [1] identified the linear cloaking transformation, namely

$$r=(b-a)\left(\frac{r'}{b}\right)+a, \tag{4.1}$$

and computed the resulting material parameters for the cloaking shell. This transformation is represented by the straight line in the top panel of Fig. 4.1 and is perhaps the simplest and most straightforward transformation that meets the constraints.

However, this is not the only transformation that satisfies the constraints listed above. One could use nonlinear transformations such as

$$r=(b-a)\left(\frac{r'}{b}\right)^2+a, \tag{4.2}$$

or

$$r=(b-a)\left(\frac{r'}{b}\right)^{1/2}+a, \tag{4.3}$$

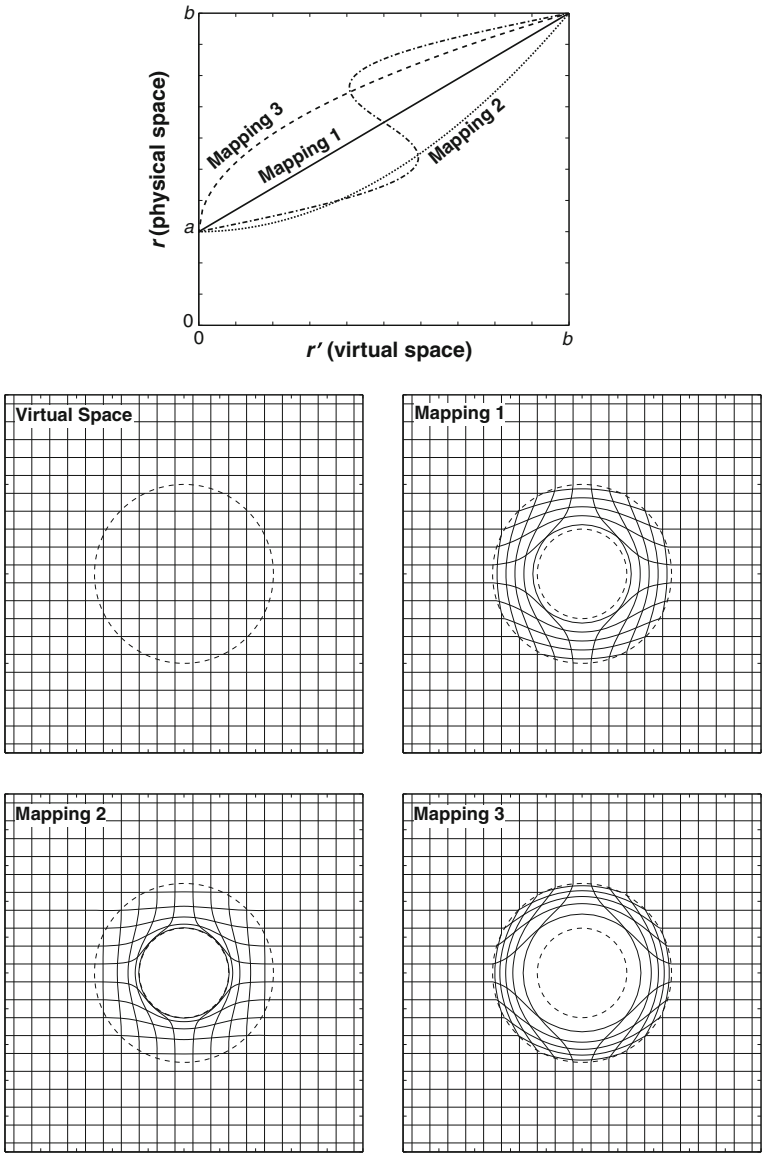

Fig. 4.1 Examples of different spherical cloaking coordinate transformations that satisfy the constraints discussed in the text and thus generate distinct electromagnetic cloaking shells

both of which are also shown in the top panel of Fig. 4.1. These transformations map the same regions of space but do it differently. The mapping labeled 2 in the figure squeezes a lot of the virtual space into a thin region near $r = a$. In contrast, the mapping labeled 3 in the figure maps very little virtual space into the region

near the interior of the cloaking shell, and instead puts most of the fields near the outer edge of the shell.

Even more complex mappings can be used. For example, the mapping

$$r' = \frac{b}{b-a}(r-a) + 0.3\sin\left(2\pi\frac{r-a}{b-a}\right) \tag{4.4}$$

satisfies all of the constraints listed above, as can be seen from the top panel Fig. 4.1. Note that this transformation is specified in an inverted form compared to the others (r' as a function of r instead of vice versa) so that it is very clearly a single valued function of r. Mappings that are multiple valued in r' typically result in negative electromagnetic material parameters in some locations. This makes them even more challenging to try to implement in practice, and unless there is a good reason, one should generally stay away from these kinds of transformations when designing transformation electromagnetics devices and materials. But theoretically they produce cloaking shells or other transformation electromagnetics devices that are just as functional as those from simpler transformations.

As mentioned above, each of these transformations maps the same region of space but in a different way. This is illustrated in the lower 4 panels of Fig. 4.1. The simple cartesian grid in the middle left panel represents the undistorted virtual space, although the outer boundary of the eventual transformation at $r' = b$ is marked. The linear mapping of Eq. 4.1 takes that cartesian grid and squeezes it into an annulus, as shown by the middle right panel of Fig. 4.1. Notice how the grid lines remain essentially uniformly spaced throughout the transformed shell; this reflects the linearity of the transformation.

The nonlinear transformations of Eqs. 4.2 and 4.3 are illustrated in the lower two panels of Fig. 4.1. The reader can see that these still map the virtual cartesian grid into an annulus. However, they do so nonuniformly that either squeezes more grid lines into the inner or outer portion of the cloaking shell. We do not illustrate the multivalued transformation because, frankly, it is confusing to look at.

The key point is that each one of these different transformations yields a theoretically ideal cloaking shell, but each would be composed of completely distinct material parameters because the resulting material parameters depend critically on the Jacobian (the matrix of first derivatives) of the transformation equation. This means that, generally, there are degrees of freedom in applying of transformation electromagnetics to create a particular device. This is quite remarkable. Until Pendry et al. [1], there was no theoretical set of material properties known that would act as a cloaking shell. After Pendry et al. [1], there were infinitely many of them.

Importantly, these degrees of freedom can be exploited to yield electromagnetic material property distributions with desirable properties. As discussed above, if the goal is to use transformation electromagnetics to design a device with relatively simple electromagnetic material properties, one should try to stay away from complex, multivalued transformations. But this still leaves many smooth, monotonic transformations with different gradients in different places that results in

different material parameters. How can this be exploited to simplify the material properties needed for a particular device?

One of the first efforts to exploit this concept used it to control the electromagnetic material properties at the outside boundary of the electromagnetic cloaking shell [10]. Specifically, this work addressed 2D cylindrical cloaking and found a transformation that produces material properties at the outer edge of the cloaking shell that are unchanged from the background medium (usually free space). This requires that the slope of the transformation, $\partial r/\partial r'$, be unity at the outer edge of the shell ($r = b$).

Referring back to the top panel of Fig. 4.1, one can see that a wide range of valid cloaking transformations can be imagined in which the slope at the outer edge ($r = r' = b$) is asymptotic to the $r = r'$ line. Employing a polynomial approach, and using the same notation as in the equations above, the particular transformation found in [10] is

$$r = \left[\frac{a}{b}\left(\frac{r'}{b} - 2\right) + 1\right] r' + a, \tag{4.5}$$

where it is required that $a/b < 0.5$ to make the transformation monotonic. This transformation becomes even more worthwhile when it is combined with the reduced parameter approximation (see Sect. 4.3.1), in which the impedance matched outer edge of the cloaking shell will reduce reflections from this interface (although not from the interior of the shell) even in an approximate, non-magnetic implementation suitable for optical frequencies.

Related 2D cylindrical cloaking work [11] has also considered a family of power law cloaking transformations defined by

$$r = (b - a)\left(\frac{r'}{b}\right)^n + a, \tag{4.6}$$

where n defines the polynomial order of the transformation. The specific cases of $n = 1$, $n = 2$ and $n = 0.5$ are given above in Eqs. 4.1–4.3, and the geometry of each of these transformations are illustrated in Fig. 4.1. For the ensuing discussion and to give the reader a sense of the electromagnetic material parameters that result from transformation electromagnetics theory, it would be useful to see the actual material parameter values. We consider here a 2D cylindrical scenario in which the cloaking shell inner radius $a = 0.5$ and the outer radius $b = 1$. Figure 4.2 plots the numerical values of the r, ϕ, and z components of the relative electric permittivity (or relative magnetic permeability, which is equal) as a function of radial position in the cloaking shell. Again the specific cases of $n = 1$, $n = 2$, and $n = 0.5$ are shown.

In all cases, the ϕ component tends to infinity at the inner edge of the shell, although this becomes more extreme as n gets smaller. The r component is always the inverse of the ϕ component, and thus tends to zero at the inner edge of the shell. The z component exhibits more complex variation with n, taking finite and nonzero values for a specific value of n which depends on the ratio b/a, but for

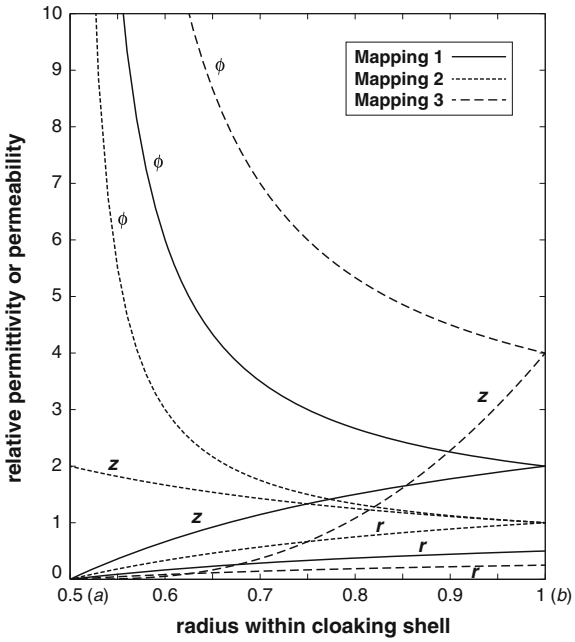

Fig. 4.2 Plot of the 2D cylindrical cloaking shell material parameters required for the different mappings shown in Fig. 4.1

other values of n the z component will be zero or infinite at $r = a$. These significant differences with n are again remarkable given that they are all members of a family of theoretically ideal cylindrical cloaking shells.

Notice the complexity of these material parameters. They take very extreme values (such as zero and infinity) in certain locations, and they have a very specific variation with position that, for ideal performance, must be realized in any attempt to fabricate a functioning device. The material is also extremely anisotropic in the sense that the components in the three coordinate directions must have very different values and thus must be controlled independently. This highlights the challenge of designing and fabricating transformation electromagnetics devices—it is difficult to conceive of an approach that would allow one to realize these parameters exactly in a fabricated material. Consequently, it also highlights the potential value of the subject of this chapter, namely techniques to simplify the material parameters needed for a particular design. For all practical purposes, simplifications are required to make a transformation electromagnetics device.

The actual performance of each of these cloaking shells was not what might have been expected, however. Interestingly, Zhang et al. [11] showed using numerical simulations, for transverse electric polarization and a perfectly electric conducting target, that the cloaking performance for these three different designs was not equal and varied significantly with n. Looking at Fig. 4.2, one might imagine that the $n = 2$ case would perform best because the cloaking shell parameters at the outer edge ($r = b$) are equal to free space. This presents a gentle gradient instead of a step change in the material parameters at the outer edge, and thus might make a lower reflection cloaking shell.

However, reality turns out to be opposite this expectation. The $n = 2$ case performs the worst, and the $n = 0.5$ case performs the best. Why, one might ask? The authors of Ref. [11] identify a critical scattering singularity at the inner edge of the cloaking shell. At this location, the conducting boundary condition requires that the axial electric field be zero. But a pure mapping of this z directed electric field from some general incident signal would not be identically zero at this location. This mismatch leads to scattering from the interior edge of the cloak. For this reason, mappings that direct most of the energy through the outer portion of the cloaking shell, such as $n = 0.5$, reduce the impact of this singularity and perform best in practice. In contrast, mappings that direct most of the energy through the inner portion, such as $n = 2$, lead to significant scattering and actually perform worse in practice.

Combining this result with the material parameters shown in Fig. 4.2 creates an interesting design trade-off. In general, the $n = 2$ material parameters are the least extreme of the three mappings considered. The values are closer to unity for more of the shell, and the large values of the ϕ component are more modest than for the other mappings. And the $n = 0.5$ parameters are the most extreme, with more large and small values and stronger anisotropy. Perhaps not surprisingly, it is mapping with the more extreme parameters that performs best in simulation. This is a manifestation of something that seems to occur commonly in transformation electromagnetics designs. Designs with more extreme material parameters can perform better, but are harder to physically realize. This trade-off between performance and physical realizability is discussed in detail in Sect. 4.2.2.

This raises another interesting and general issue that is one of the main points of this chapter. Although a large or infinite family of transformations may lead to equal and ideal performance in theory, in practice there may be subtle physical issues that lead to unequal performance when numerically simulated (which, after all, is a form of approximation) or physically realized (also an approximation). Exploring the entire design space of ideal transformations to find those that perform best, when accounting for the imperfections of fabrication, is a critical element of transformation electromagnetics design.

4.2.1 Conformal Transformations

A class of transformations that yields especially simple electromagnetic material properties is the so-called conformal transformation. These were first investigated in the context of electromagnetic cloaking [12, 13] and are described more broadly in [14, 15]. A conformal transformation is one of a special class of 2D transformations for which, when applied in the transformation electromagnetics formalism, results in isotropic (equivalently, scalar) electromagnetic material properties. This offers the hope of realizing the needed materials with conventional, isotropic dielectrics, albeit still generally requiring smoothly inhomogeneous properties.

Unfortunately, the constraints on transformations that make them strictly conformal are severe, which means that few devices can be realized as truly conformal devices. Analysis and simulations have shown that there are major challenges to applying a conformal approach to cloaking [16] although more limited devices, such as a cloaking shell that works for only one direction of incident wave, can be realized with this approach [17].

The value and applicability of conformal transformation concepts is dramatically increased when they are combined with approximations. Broadly speaking, this combination of conformal transformations (or nearly conformal transformations) and approximations is called the quasi-conformal approach [13, 14], and it is described in detail below in Sect. 4.3.2.

4.2.2 Near-Cloaking and Imperfect Device Design

It is well known that some of the most interesting transformation electromagnetics devices, such as cloaking shells, require some rather extreme material parameters to realize exactly [1], even if one explores the full space of possible transformations. This motivates the following question: can fabrication simplicity be improved if we design the device to be imperfect (but still good) from the outset?

Among the first to consider this possibility was Ref. [18], which considered a non-ideal cloak in the following sense. A perfect cylindrical or spherical cloak makes an object of radius $r = a$ that interacts with waves as if it had identically zero radius. What if instead a cloaking shell is designed to make that object of radius $r = a$ behave as though it had a small but nonzero size? This idea is appropriately called near-cloaking [19]. The scattering from this effectively shrunken object, while not zero, would still be reduced significantly and in a controlled way, and perhaps the resulting material parameters would be easier to fabricate. In a way, this approach acknowledges that the ultimate fabrication of a transformation electromagnetics device will be imperfect, and allows that imperfection to be accounted for in the theoretical design stage. The focus of Chen et al. [18] was on the manipulation of cloaking bandwidth, and they found that this concept could extend that bandwidth by a factor of 2–3.

A similar application of near-cloaking theory identified an explicit trade-off between the cloaking performance and the extremeness of the required electromagnetic parameters [20]. Cloaking of a 2D perfectly conducting cylinder or radius $r = a$ was considered under the target condition that the azimuthal component of the permittivity and permeability tensors be uniform throughout the cloaking shell. This condition cannot be satisfied by a perfect cloaking shell, but it can be satisfied by a near-cloaking transformation that shrinks the scattering object to an arbitrarily small but non-zero size. The parameter s denotes the multiplicative factor by which the object is effectively shrunk, for electromagnetic scattering purposes, by the cloaking shell. We call this the compression factor. For example, $s = 0.1$ shrinks the cylinder by a factor of 10. The outer radius of the

cloaking shell is defined as $r = b$, and consequently b/a is the ratio of the outer radius to the inner radius of the cloaking shell and thus defines the thickness of the shell.

For a 2D cylindrical cloaking shell, this work first required that the azimuthal (ϕ) component of permittivity and permeability have a constant value k throughout the entire cloaking shell. With only that constraint, one finds that k is determined by the compression and thickness parameters by

$$k = 1 - \frac{\ln s}{\ln b/a}. \tag{4.7}$$

The resulting electric permittivity components of the cloaking shell are, as a function of radius r, given by

$$\epsilon_\phi = k,\ \epsilon_r = k^{-1},\ \epsilon_z = s^2 k \left(\frac{r}{a}\right)^{2k-2}. \tag{4.8}$$

Note that the magnetic permeability components are the same. These expressions fully specify the cloaking shell material parameters in terms of its thickness b/a and its compression parameter s. In contrast to the ideal 2D cloaking shell parameters shown in Fig. 4.2, those for this near-cloaking shell have no singularities in any component.

Figure 4.3 summarizes the findings of this analysis. The top panel shows the variation of the components of the electric permittivity tensor (magnetic permeability is equal) through cloaking shells of different thickness, defined by the thickness parameter b/a, and different theoretical performance, defined by the compression parameter s. The critical finding is as follows. The thinner the cloaking shell, or the higher the compression parameter s, then the steeper the material gradients and the higher the maximum parameter values. Succinctly, better performing or thinner cloaks require more extreme electromagnetic material parameters. Intuitively, this is not a surprise. A thinner or better performing cloak requires more extreme bending or compression of the electromagnetic fields, which in turn must require more extreme material properties. Nevertheless it is valuable to have explicit expressions that illustrate that trade-off directly.

The right panels of Fig. 4.3 confirm that the cloaking performance is as expected as a function of compression parameter s. These full wave simulations show that for a compression factor of 0.1, the cloaking shell bends much of the incident field energy around the hidden interior, but the nonuniform wavefronts show that there is some scattering in most directions. For $s = 0.01$ in the bottom panel, the cloaking performance is much better as indicated by the smoother wavefronts implying less scattering. But recall that the top panel shows that this better performance comes at a cost of more complex material parameters, with larger maximum values and steeper gradients.

This study illustrates an important and general trade-off that exists in cloaking shells designed through transformation electromagnetics and perhaps more general devices as well. Specifically, there appears to be a trade-off between the

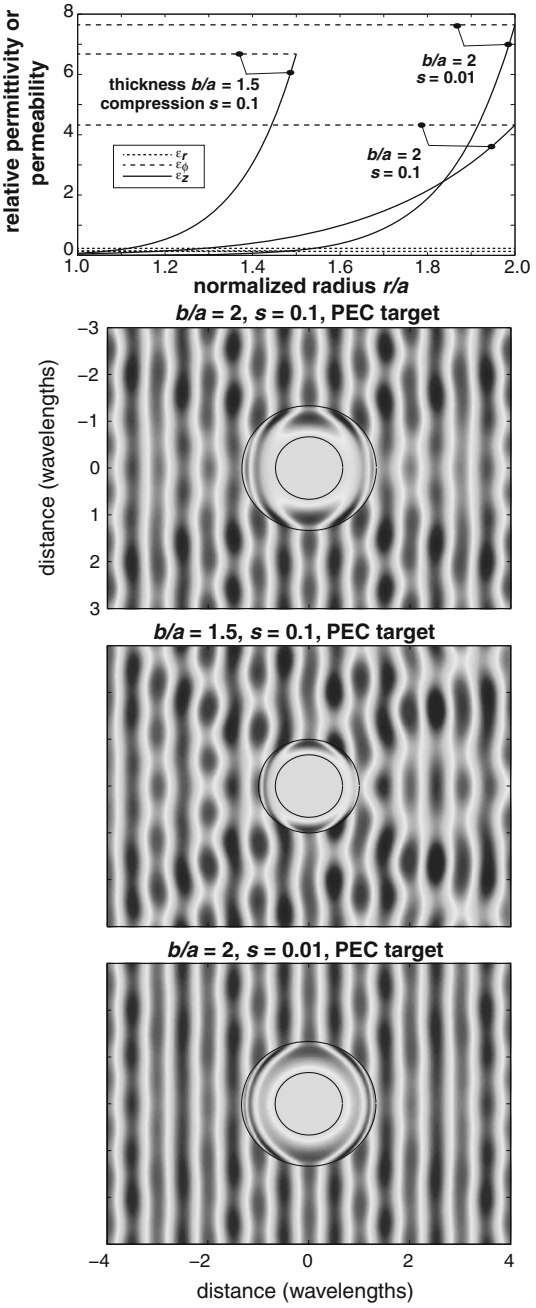

Fig. 4.3 Summary of material parameters (*top panel*) and performance simulations (*bottom panels*) of near-cloaking for different values of cloaking shell thickness and compression factor (adapted from Cummer et al. [20])

performance of a transformation electromagnetics device and the difficulty in physically realizing such a device due to the extreme electromagnetic material parameters required. Again, note how Fig. 4.3 shows that desirable properties of the cloaking shell, namely thinness (a small b/a) and good performance (a small s) both require more extreme material parameter values and gradients.

This complexity-performance trade-off is perhaps not a big surprise. But one powerful element of transformation electromagnetics is that it enables one to explore this tradeoff in the earliest stages of design, provided there is a way to parameterize the original coordinate transformation in terms of device performance.

4.3 Approximations to Transformation Electromagnetics Design

Another approach to designing transformation electromagnetics devices for physical realizability involves making approximations to the ideal design. When analytical approximations are made, in most cases the performance will no longer be theoretically ideal. However, ideal designs typically involve features such as perfectly smooth gradients that are challenging or impossible to realize in practice. Aiming for ideal performance may not always be a worthwhile goal, and if an approximation can be made that dramatically simplifies fabrication for a modest performance penalty, then often that trade-off is worth it.

The first insight into the value of approximations to transformation electromagnetics designs came from early numerical simulations of cloaking shell performance [21]. In addition to showing that numerical simulations confirmed that cloaking shells performed as expected based on transformation electromagnetics theory, this work analyzed the performance of stepwise approximations to the ideal continuous material parameters. It was shown that device performance, in this case scatter reduction, degraded smoothly as fewer and fewer uniform shells were used to approximate the ideal device. These simulations of performance of the continuous and step-wise approximate cloaking shells are shown in Fig. 4.4.

This work was the first to show that transformation device performance, in most cases, is relatively robust to perturbations. In other words, small changes to the material properties produce small, not large, changes to the performance. This opened the door to using a wide range of approximate and optimization techniques to enhance the ease of fabrication of transformation electromagnetics devices.

4.3.1 Reduced Material Parameters

One of the first approximations considered in the context of transformation electromagnetics is the so-called reduced parameter approximation [21]. Ideal transformation electromagnetics devices bend electromagnetic power flow in

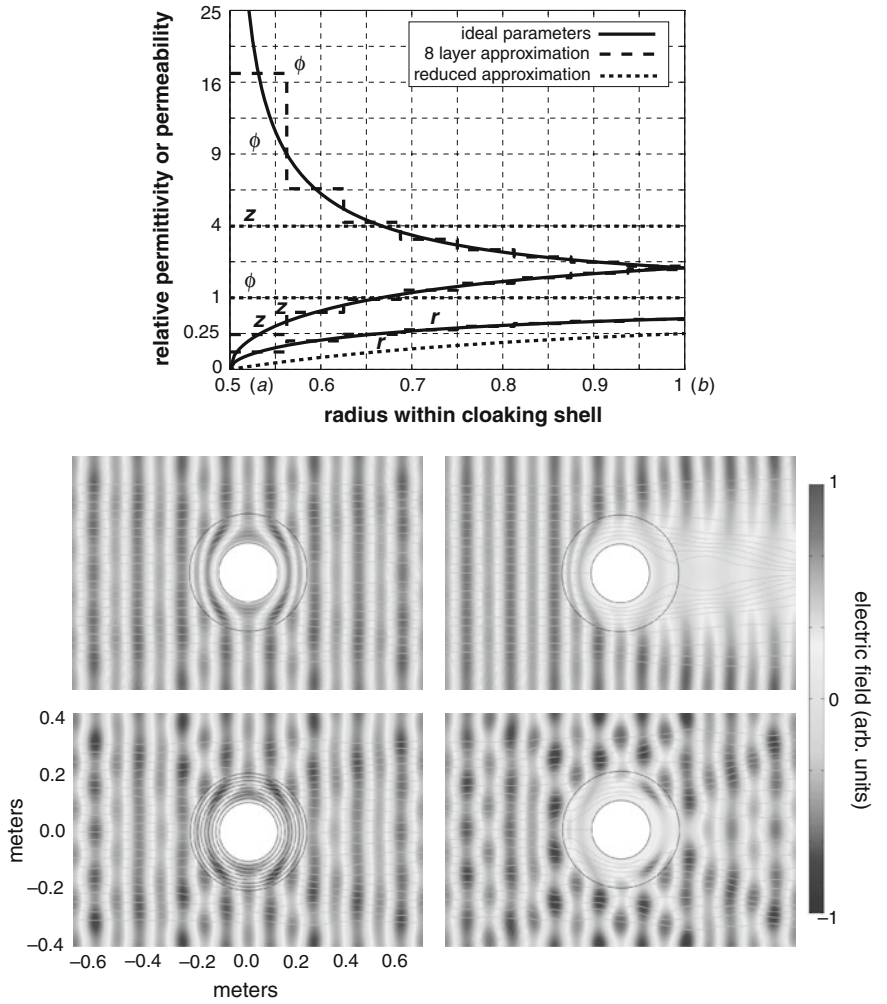

Fig. 4.4 Summary of material parameters (*top panel*) and performance simulations (*bottom panels*) of ideal cloaking shells, and lossy and stepwise approximations to ideal cloaking shells (adapted from Cummer et al. [21])

prescribed directions and do so in a completely reflectionless fashion. Meeting both of these goals is a challenge because it requires the ability to control electric permittivity and magnetic permeability in the material. As noted previously, magnetic permeability is often a significant challenge to control because of the lack of natural materials with a strong magnetic response. If one requires only that power flow follows the desired paths, but allows that reflections might occur during that process, then only the refractive index need be controlled in the material, and not the wave impedance. The reduced parameter approximation does

this by setting the new, reduced magnetic permeability μ_{red} to unity, to facilitate possible material fabrication. To maintain the refractive index profile in the material, one then needs to assign a new, reduced electric permittivity that is given simply by $\varepsilon_{red} = \varepsilon\mu$.

Simulations in Ref. [21] showed that the reduced parameter approximation could yield devices that exhibited the basic physics of the original and ideal transformation electromagnetics device, although with less than ideal performance. The reduced parameter approximation found successful application in the first experimental demonstration of electromagnetic cloaking at microwave frequencies [9]. This effort involved a two-dimensional metamaterial device that controlled the radial magnetic permeability and the vertical electric permeability so that the refractive index profile (but not the wave impedance) of the ideal cloaking shell was matched. Measurements of this reduced parameter material confirmed the basic physics of the transformation electromagnetics design, namely that the wavefronts and energy flow were bent around the cloaked object in the way dictated by the coordinate transformation itself. And although the cloaking performance was not perfect, this work is widely regarded as the first successful experimental demonstration of transformation electromagnetics.

Other efforts have applied the reduced parameter approximation to design transformation electromagnetics devices that, while not perfect, are functional and dramatically simpler to fabricate than unapproximated designs. The effort described in Sect. 4.2 to create a cloaking shell with a reflectionless outer boundary [10] also employed this reduced parameter approximation to make a cloaking shell design that could be fabricated from non-magnetic materials [22].

4.3.2 The Quasi-Conformal Approximation

The so-called quasi-conformal approximation [13] combines multiple approximations and typically results in isotropic, permittivity-only designs that are particularly straightforward to fabricate. Section 4.2.1 described the concept of conformal transformations, which is a class of transformations that result in especially simple material parameters. However, strictly conformal transformations can be applied to a very limited set of transformation electromagnetics devices. Building on previous work showing that approximations in the transformation electromagnetics procedure can still result in functional devices [21], Ref. [13] described the concept of quasi-conformal, or almost conformal, transformations.

The concept is relatively simple. While few transformations can be implemented in a strictly conformal sense, far more transformations can be implemented in a transformation that is not too far from conformal. Reference [13] describes one approach by which a particular transformation can be optimized in an iterative manner to minimize the anisotropic components of permittivity and permeability in a resulting transformation electromagnetics device. The particular device they

applied this approach to is the so-called carpet cloak or reflecting plane cloak, in which a scattering object residing on or near a reflecting surface can be hidden by a shell placed over the object.

The degree to which a reflecting plane cloak can be approximated by an isotropic design is a function of several elements of the transformation. Most importantly, the size of the shell needs to be significantly larger than the volume that is hidden. However, if this constraint is met, then the anisotropic or off-diagonal components of the material properties can be many times smaller than the single on-diagonal component. Thus to a good approximation, the anisotropic part of the material properties can be discarded, dramatically simplifying device fabrication. In the case analyzed in [13], for a cloaking shell that is approximately 30 times the area of the object to be hidden, an optimized transformation yielded a maximum anisotropy factor (the ratio of the refractive indexes in the two principal axis directions) of only 1.04.

As was discussed in Sect. 4.2.1 on conformal transformations, Ref. [13] also employ the reduced parameter approximation (see Sect. 4.3.1) to convert the design to fully non-magnetic materials. The result is an isotropic, dielectric-only design of a functional transformation electromagnetics device. This concept was experimentally demonstrated at microwave frequencies using a metamaterial realization of the needed isotropic dielectric material shell [5]. It was later demonstrated at optical frequencies as well [23, 24]. It should be mentioned that a quasi-conformal design of the ground-plane cloak requires a material with dielectric constants both above and below the background material. This presents a challenge for cloaking in air, in which smaller dielectric constants can only be realized in a narrowband sense. These experiments thus demonstrated the concept in higher dielectric background materials so that the relative permittivity in the cloaking shell never drops below unity. Another successful demonstration of a transformation electromagnetics device designed with the quasi-conformal approximation is a flattened version of the Luneburg lens [25].

As successful as the quasi-conformal approach has been, it is important to note that it cannot be applied to all transformation electromagnetics devices. For example, there is no way to make a two- or three-dimensional free space cloaking transformation (see Sect. 4.2) close to conformal [17]. Care and creativity are required to conceive of useful devices that can be implemented with this approach. It should also be mentioned that there are approaches other than that described in [13] for finding an optimal quasi-conformal transformation given the transformation boundaries [14].

4.4 Optimized Transformation Electromagnetics Devices

The last technique we will discuss in this chapter is numerical optimization. This idea again hinges on the notion that transformation electromagnetics designs are relatively robust to perturbations in the material parameters. For example, let us

begin with the finding shown above in Fig. 4.4 that an 8-layer stepwise approximation to a continuous transformation electromagnetics cloaking shell still performs reasonably well [21]. One might then ask, is there a different 8-layer material configuration that performs even better?

The first effort to apply optimization to transformation electromagnetics design in this sense is described in [26], which we summarize here. That work posed the following problem: given a shell composed of n discrete layers of homogeneous but anisotropic material for which there may be limits on the numerical parameter values in each shell, what configuration of shells gives the best cloaking performance? As for most optimization problems that involve a relatively large number of unknowns, a suitable initial guess is critical to finding a good solution. Transformation electromagnetics provides exactly the needed initial guess.

Figure 4.5 summarizes some of the promising results from the 2D analysis in [26]. This work considered the case of a cloaking shell with a thickness equal to 10% of the radius of the hidden interior region. The initial solution in all cases is the ideal, continuous cloaking shell defined by the mapping in Eq. 4.1. Then this continuous shell is approximated in staircase fashion by a fixed number of layers in which the material parameters are completely uniform but still anisotropic. The upper and middle left panels of the figure schematically show this cloaking shell divided into 9 and 3 regions, respectively, and a 100 layer approximation was also considered.

The bottom panel shows the scattering width of the cloaked object as a function of scattering angle as computed from numerical simulations of the layered structure. This metric quantifies the scattered field strength of the cloaked object. It is clear that the cloaking performance improves as the accuracy of the layered approximation increases, although it does not increase very quickly because of the interior scattering singularity mentioned above at the end of Sect. 4.2. The simulated fields for the 9 layer case shown in the upper right panel confirm this, as some scattering is evident from the irregular wave fronts.

In Ref. [26] it was asked whether better performance could be obtained from a small number of layers using optimization. Beginning with the parameters of the 3 layer approximation, an iterative optimization routine was run in which the parameters of these three, uniform, anisotropic layers were altered to find the combination that minimized the forward scattering from the cloaked object. And, it turns out, a cloaking shell composed of 3 optimized anisotropic layers can perform much better than even the 100 layer approximation for this particular problem. The bottom panel shows that this optimized 3 layer cloak can reduce the effective size of the object by more than 30 dB, compared to 10–15 dB for the staircase approximation of the ideal parameters. The middle right panel shows the full wave simulated fields of a plane wave interacting with this optimized cloak. Essentially no scattering is observed.

Perhaps even more interesting are the results of applying optimization with constraints on the resulting material properties. Controlling magnetic permeability in transformation electromagnetics designs is one of the major challenges because there are so few magnetic materials in nature. For this reason non-magnetic

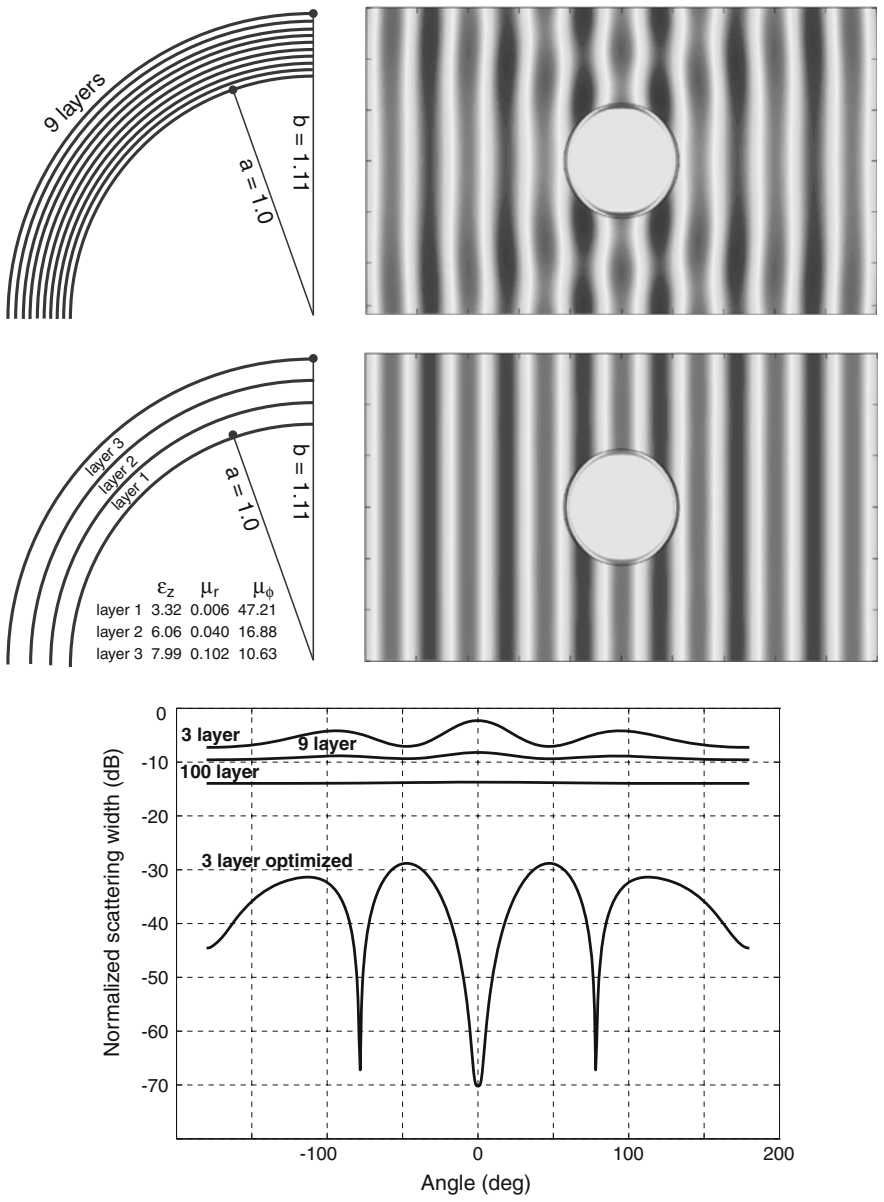

Fig. 4.5 Conceptual illustration and performance simulation of cloaking with optimized anisotropic layers, showing that numerical optimization and few layers can lead to a better-performing design than a many-layered simple approximation of the continuous ideal cloaking shell material parameters (adapted from Popa and Cummer [26])

transformation electromagnetics designs of substantial interest. As described in Sect. 4.3.1 above, one approach is to approximate the design using reduced parameters in which the magnetic permeability is renormalized to unity. This often results in significantly reduced performance, but optimization can restore much of that lost performance.

The top panel of Fig. 4.6 shows how this happens. The solid line illustrates, for reference, the scattering for a 3 layer approximation of an ideal cloaking shell. There is modest scatter reduction but 3 layers is not generally enough for a staircase approximation to perform well. The wide-dashed line shows the scattering for that same 3 layer approximation to which the reduced parameter approximation (see Sect. 4.3.1) has been applied. This reduced cloak has the significant property that it is composed of completely nonmagnetic materials, which makes it easier to fabricate. Although there are angles for which scattering is low, the scattering is in general substantial from the object surrounded by the 3 layer reduced cloak. In this case the reduced approximation is not especially good despite its advantages for fabricatibility.

However, this can be improved with optimization. Reference [26] takes this 3 layer reduced cloak as a starting point for a numerical optimization that forces the magnetic permeability of each layer to remain unity and also constrains the maximum relative permittivity of any component of any layer to be less than 10. This second condition is again imposed to help make the materials more physically feasible. The scattering performance of the 3 layer, nonmagnetic, optimized cloaking shell is shown by the fine-dashed line in Fig. 4.6. As the reader can see, scattering over all angles is reduced by more than 10 dB, and the overall performance is better than either of the other 3 layer approximations, despite still being nonmagnetic. The middle panel shows for illustration purposes the field distribution for an incident uniform plane wave interacting with this optimized 3 layer cloak, with the nearly unperturbed wavefronts confirming the good cloaking performance.

The table at the bottom of the figure shows the numerical values for the 3 layer reduced cloak and for the 3 layer optimized cloak. The numerical parameters are comparable in magnitude but do change substantially after optimization. These two designs are approximately equal in fabrication complexity, but optimization results in dramatically improved performance.

Other efforts to apply optimization to transformation electromagnetics designs have yielded similarly promising results. Similar layered optimization but for oblique incidence on cylindrical structures has also shown that scatter reduction and fabrication simplicity can be improved through optimization [27]. In Ref. [28] a somewhat different approach of topology optimization was applied to find configurations of standard dielectric materials (isotropic and permittivity above unity). Interesting dielectric configurations are found that can substantially reduce electromagnetic scattering in a narrow bandwidth over a range of incident angles. Related work for acoustic wave cloaking showed that narrowband cloaking can be achieved through the optimal placement of scattering cylinders [29].

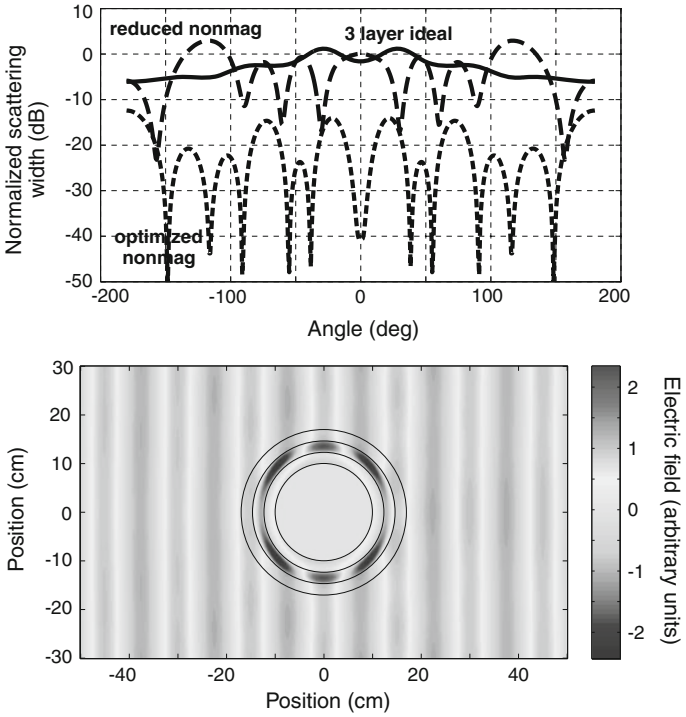

	Reduced 3 Layer			Optimized Nonmagnetic		
Layer	μ_z	ε_r	ε_ϕ	μ_z	ε_r	ε_ϕ
1	1.000	0.064	5.900	1.000	0.100	4.490
2	1.000	0.400	5.900	1.000	1.380	9.990
3	1.000	0.800	5.900	1.000	0.700	0.890

Fig. 4.6 Material parameters and performance simulation of cloaking with optimized anisotropic layers, showing that numerical optimization with constraints on the parameters, in this case requiring the layers to be nonmagnetic, can result in a simple but high performance cloaking shell (adapted from Popa and Cummer [26])

Although these latter two examples do not yield designs that are based on transformation electromagnetics, they are based on the application of optimization to a device that was originally conceived and designed using the transformation approach. Collectively, these results show the promise of using transformation electromagnetics for an initial design, and then applying optimization to create a device that meets constraints for physical realizability and performance.

4.5 Summary

In this chapter we have reviewed many of the methods commonly used to simplify the design of transformation electromagnetics devices. One of the major challenges in the field remaining is that the complexity of the needed material

parameters is very high, and fabricating such materials is correspondingly difficult. However, it is generally true that transformation electromagnetics designs are relatively robust to material perturbations. Consequently, one has the ability to trade reduced performance for simpler electromagnetic material parameters. The methods described in this chapter are a variety of analytical, numerical, and approximation techniques that enable some control over that trade-off, and that can be used to create devices that still perform well, although not perfectly. These simplifications have been used in most experimental demonstrations of transformation electromagnetics devices to date, and it is likely they will continue to be used heavily as the field of transformation electromagnetics transitions from initial experimental demonstrations to practical, functional devices.

References

1. Pendry JB, Schurig D, Smith DR (2006) Controlling electromagnetic fields. Science 312:1780–1782
2. Schurig D, Pendry JB, Smith DR (2006) Calculation of material properties and ray tracing in transformation media. Opt Express 14:9794–9804
3. Padilla WJ, Basov DN, Smith DR (2006) Negative refractive index metamaterials. Mater Today 9:28
4. Caloz C (2009) Perspectives on EM metamaterials. Mater Today 12(3):12–20
5. Liu R, Li C, Mock JJ, Chin jY, Cui TJ, Smith DR (2009) Broadband ground-plane cloak. Science 323:366
6. Shelby RA, Smith DR, Schultz S (2001) Experimental verification of a negative index of refraction. Science 292(5514):77–79
7. Pendry JB, Holden AJ, Robbins DJ, Stewart WJ (1999) Magnetism from Conductors and Enhanced Nonlinear Phenomena. IEEE Trans Microw Theory Tech 47(11):2075–2084
8. Güney DÖ, Koschny T, Soukoulis CM (2009) Reducing ohmic losses in metamaterials by geometric tailoring. Phys Rev B 80(12):125129. doi:10.1103/PhysRevB.80.125129
9. Schurig D, Mock JJ, Justice BJ, Cummer SA, Pendry JB, Starr AF, Smith DR (2006) Metamaterial electromagnetic cloak at microwave frequencies. Science 314:977–980
10. Cai W, Chettiar UK, Kildishev AV, Shalaev VM, Milton GW (2007) Nonmagnetic cloak with minimized scattering. Appl Phys Lett 91:111105
11. Zhang L, Yan M, Qiu M (2008) The effect of transformation order on the invisibility performance of a practical cylindrical cloak. J Opt A 10(9):095001. doi:10.1088/1464-4258/10/9/095001
12. Leonhardt U (2006) Optical conformal mapping. Science 312:1777–1780
13. Li J, Pendry JB (2008) Hiding under the carpet: A new strategy for cloaking. Phys Rev Lett 101:203901
14. Landy NI, Padilla WJ (2009) Guiding light with conformal transformations. Opt Express 17(14):872. doi:10.1364/OE.17.014872
15. Turpin JP, Massoud AT, Jiang ZH, Werner PL, Werner DH (2010) Conformal mappings to achieve simple material parameters for transformation optics devices. Opt Express 18:244. doi:10.1364/OE.18.000244
16. Urzhumov YA, Kundtz NB, Smith DR, Pendry JB (2011) Cross-section comparisons of cloaks designed by transformation optical and optical conformal mapping approaches. J Opt 13(2):024002. doi:10.1088/2040-8978/13/2/024002

17. Urzhumov Y, Landy N, Smith DR (2012) Isotropic-medium three-dimensional cloaks for acoustic and electromagnetic waves. J Appl Phys 111(5):053105. doi:10.1063/1.3691242
18. Chen H, Liang Z, Yao P, Jiang X, Ma H, Chan CT (2007) Extending the bandwidth of electromagnetic cloaks. Phys Rev B 76:241104. doi:10.1103/PhysRevB.76.241104
19. Kohn RV, Onofrei D, Vogelius MS, Weinstein MI (2010) Cloaking via change of variables for the Helmholtz equation. Commun Pur Appl Math 63:973–1016. doi:10.1002/cpa.20326
20. Cummer SA, Liu R, Cui TJ (2009) A rigorous and nonsingular two dimensional cloaking coordinate transformation. J Appl Phys 105(056):102
21. Cummer SA, Popa BI, Schurig D, Smith DR, Pendry J (2006) Full-wave simulations of electromagnetic cloaking structures. Phys Rev E 74(3):036,621, doi: 10.1103/PhysRevE.74.036621.
22. Cai W, Chettiar UK, Kildishev AV, Shalaev VM (2007) Optical cloaking with metamaterials. Nature Photon 1:224–227. doi:10.1038/nphoton.2007.28
23. Valentine J, Li J, Zentgraf T, Bartal G, Zhang X (2009) An optical cloak made of dielectrics. Nature Mater 8:568–571. doi:10.1038/nmat2461
24. Gabrielli LH, Cardenas J, Poitras CB, Lipson M (2009) Silicon nanostructure cloak operating at optical frequencies. Nature Photon 3:461–463. doi:10.1038/nphoton.2009.117
25. Kundtz N, Smith DR (2010) Extreme-angle broadband metamaterial lens. Nature Mater 9:129–132. doi:10.1038/nmat2610
26. Popa BI, Cummer SA (2009) Cloaking with optimized homogeneous anisotropic layers. Phys Rev A 79:023806
27. Zhang B, Wu BI (2010) Cylindrical cloaking at oblique incidence with optimized finite multilayer parameters. Opt Lett 35:2681–2683
28. Andkjaer J, Sigmund O (2011) Topology optimized low-contrast all-dielectric optical cloak. Appl Phys Lett 98:021112
29. Garcia-Chocano VM, Sanchis L, Diaz-Rubio A, Martinez-Pastor J, Cervera F, Llopis-Pontiveros R, Sanchez-Dehesa J (2011) Acoustic cloak for airborne sound by inverse design. Appl Phys Lett 99:074102. doi:10.1063/1.3623761

Chapter 5
Creating Illusion Effects Using Transformation Optics

Yun Lai, Jack Ng and C. T. Chan

Abstract In this chapter, we show how to create illusion effects using metamaterials. We will see that a passive metamaterial device can be designed such that when it is placed next to or covering an object, the scattered fields of the object and the device together will be changed to be exactly the same as the scattered fields due to another object. Simply put, we can turn an object optically and stereoscopically into another one. For instance, an apple can be made to look like a banana. If we make a measurement of the electromagnetic fields at the designed working frequency, there is no way to distinguish optically between the true object and the illusion. The theory on realizing such an optical illusion effect is called *illusion optics*. Invisibility can be regarded as a special case of the illusion effect, in which the object is turned optically to a volume of free space. A metamaterial does not need to encircle the object to create the illusion effect. Furthermore, if we use this method to implement invisibility, the "cloaked" object will not be blinded by the cloak as in the cases of normal invisibility cloaks. The design of illusion optics is based on the replacement of optical spaces, where the material parameters are determined using the technique of transformation optics. One unique route to achieve illusion effects is to employ the idea of "complementary media". Materials designed using "complementary media" typically contain negative refractive index components, and no extreme constitutive parameters values are needed. Slight variations of the scheme can create a variety of interesting illusion effects. For example, we can make an object appear larger in size, rotated, or located at other positions. Illusion optics may lead to some plausible applications, such as

Y. Lai
School of Physical Science and Technology, Soochow University, Suzhou, China
e-mail: laiyun@suda.edu.cn

J. Ng · C. T. Chan (✉)
Department of Physics, Hong Kong University of Science and Technology, Hong Kong, China
e-mail: phchan@ust.hk

J. Ng
e-mail: jack@ust.hk

D. H. Werner and D.-H. Kwon (eds.), *Transformation Electromagnetics and Metamaterials*, DOI: 10.1007/978-1-4471-4996-5_5, © Springer-Verlag London 2014

small or reduced form-factor optical devices that exhibit the same optical functions as much larger instruments or even "super-absorbers" that can absorb significantly more than their geometric cross-sections.

5.1 Metamaterials

In this chapter, we will examine how negative index metamaterials can create illusion effects. In the 1960s, Veselago proposed that some exotic optical phenomena, such as negative refraction, may occur in "abnormal" materials with simultaneously negative permittivity and permeability [1]. While negative permittivity can be found in natural materials, negative permeability is much more difficult to obtain. It is even more difficult for both to be negative at the same frequency. Hence, negative refraction remained largely an academic curiosity until artificial magnetism was proposed [2] and realized experimentally [3, 4]. To date, advances in research on *metamaterials* have paved the way for realizing new materials with nearly arbitrary values of permittivity and permeability tensor components at various frequencies. Even position dependent, anisotropic, tunable, and reconfigurable material parameters can be designed and made. Such advances enable us to realize not only negative and zero refractive indexes, but also more exotic and intriguing effects such as invisibility and illusion.

Metamaterials are typically composed of an array of man-made subwavelength metallic resonators embedded in a dielectric medium. For such an inhomogeneous media, the components of permittivity and permeability tensors are effective material parameters obtained conceptually and operationally through the process of homogenization. As one of the key metamaterial properties needed to realize "illusion optics" is negative refractive index, we show in Fig. 5.1 the most straightforward method to obtain a negative refractive index, as first proposed by

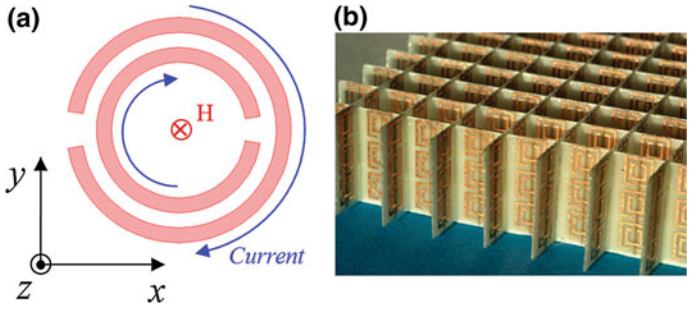

Fig. 5.1 **a** Schematic illustration of a double split ring resonator that has a controllable response to the magnetic field in the z direction. **b** A double negative metamaterial composed of split ring resonators and wires that was used to experimentally demonstrate negative refraction [3]

Pendry et al. [2] and Smith et al. [3, 4]. In this design, artificial permeability is achieved using a double split ring resonator structure, in which the oscillating electric currents with opposite phases in the two split rings provide a controllable response to the magnetic field in the z direction, as shown in Fig. 5.1a. The resonant response to the time varying change of magnetic flux results in a susceptibility that can be out of phase with the driving field, giving the possibility of a negative response. If the response of the individual resonator is strong enough and if the density of such resonators inside the embedding medium is sufficiently high, we can obtain negative permeability. Negative permittivity is obtained using metallic wires of a finite length that have a resonant response to external electric fields. If the system parameters are designed such that a negative response to both of the electric and magnetic fields occurs at the same frequency range, a pass band with negative group velocity is obtained, and as long as the resonators are subwavelength, the metamaterial can be described by effective negative permittivity and permeability values.

It is difficult to scale the structures realized by Smith et al. as shown in 5.1 down to infrared and optical frequencies. Absorption of the metallic components will also compromise the performance at high frequencies. However, with rapid advances in nanotechnology fabrication techniques [5, 6] and new ideas such as loss compensation [7], metamaterials with nearly arbitrary values of constitutive parameters, and high frequency operation have become an achievable goal. In this chapter, we will not consider how to realize such metamaterials in detail, but instead we will focus on how to use metamaterials to create arbitrary optical illusions, assuming that metamaterials of arbitrary permittivity and permeability with negligible loss at a single frequency can be achieved. In most of the simulations presented here, metamaterials with small losses on the order of 10^{-4} have been used to ensure good illusion effects. Readers interested in the design and realization of metamaterials may refer to some important works listed in the references. We also note at the outset that the theory of illusion optics applies in both two dimensions and three dimensions. However, all of the simulations shown below are for two-dimensional examples as three-dimensional simulations are too demanding on computation resources. Furthermore, all of the cloaking and illusion effects discussed below only work at a narrow band of frequencies, where the bandwidth is limited by the frequency dispersion of the metamaterial.

5.2 Transformation Optics as a Design Tool

It has long been recognized that some wave equations are from invariant under coordinate transformations, with a correspondence between the transformed space geometry and the new material properties. However, such correspondence was previously used as a mathematical technique to solve wave equations, and the physical implication of such a correspondence was not fully explored. Part of the reason that such as a correspondence was not exploited is because the parameters

of the new material after transformation often become anisotropic, inhomogeneous, and exhibit extreme values not found in natural materials. However, this difficulty has been overcome by the emergence of metamaterials which paved the way for the introduction of the idea of transformation optics.

The concept of *transformation optics* has been proposed based on the form invariance of the Helmholtz equation and Maxwell's equations under coordinate transformations [8, 9]. It quickly became one of the most useful theories in the design of metamaterial applications and enabled the exotic wave manipulation effects that were previously thought to be impossible.

To see how transformation optics works, let us consider Maxwell's equations at a particular frequency ω :

$$\nabla \times \mathbf{E} + i\omega\boldsymbol{\mu}\mathbf{H} = 0,\ \nabla \times \mathbf{H} - i\omega\boldsymbol{\varepsilon}\mathbf{E} = 0, \tag{5.1}$$

in which $\boldsymbol{\varepsilon}(\mathbf{x})$ and $\boldsymbol{\mu}(\mathbf{x})$ are the permittivity and permeability tensors. Now if we do a coordinate transformation by applying a mapping from $\mathbf{x}$ to $\mathbf{x}'$, i.e., $\mathbf{x}' = \mathbf{x}'(\mathbf{x})$, then the form of Maxwell's equations in the new coordinate $\mathbf{x}'$ is preserved, i.e.,

$$\nabla \times \mathbf{E}' + i\omega\boldsymbol{\mu}'\mathbf{H}' = 0,\ \nabla \times \mathbf{H}' - i\omega\boldsymbol{\varepsilon}'\mathbf{E}' = 0, \tag{5.2}$$

in which the new electromagnetic fields are expressed as

$$\mathbf{E}'(\mathbf{x}') = \left(\mathbf{A}^{\mathrm{T}}\right)^{-1}\mathbf{E}(\mathbf{x}),\ \mathbf{H}'(\mathbf{x}') = \left(\mathbf{A}^{\mathrm{T}}\right)^{-1}\mathbf{H}(\mathbf{x}), \tag{5.3}$$

and the new parameters in the transformed space are

$$\boldsymbol{\varepsilon}'(\mathbf{x}') = \mathbf{A}\boldsymbol{\varepsilon}(\mathbf{x})\mathbf{A}^{\mathrm{T}}/\det(\mathbf{A}),\ \boldsymbol{\mu}'(\mathbf{x}') = \mathbf{A}\mu(\mathbf{x})\mathbf{A}^{\mathrm{T}}/\det(\mathbf{A}), \tag{5.4}$$

where $\mathbf{A}$ is the Jacobian matrix with components $A_{ij} = \partial x_i'/\partial x_j$.

The most important information in the above analysis is that every solution of the Maxwell equations (either a propagating beam of light in free space or decaying evanescent waves in metals) in the original space [$\mathbf{E}$ and $\mathbf{H}$ in Eq. (5.1)] is mapped to a corresponding solution in the transformed space [$\mathbf{E}'$ and $\mathbf{H}'$ in Eq. (5.2)]. We now have a recipe to "glue" the light rays to the coordinate system, as long as we transform the material parameters correspondingly according to Eq. (5.4). This is illustrated pictorially in Fig. 5.2 in two dimensions, in which a beam is bent after transformation, while from the coordinate mapping point of view, the beam is simply trying to follow those coordinates that correspond to its original path in the original space. The parameters of the transformed space are obtained in Eq. (5.4). And the electromagnetic fields in the two spaces are related by Eq. (5.3).

We note that Eqs. (5.1–5.4) do not depend on the choice of reference coordinates. In Fig. 5.2, we may use cylindrical coordinates instead of Cartesian coordinates, but as long as the mapping is fixed, the physical nature of the original and new solutions would not be changed. For instance, if a surface (or a curve in two dimensions) is fixed (the blue line in Fig. 5.2) during the transformation, then we

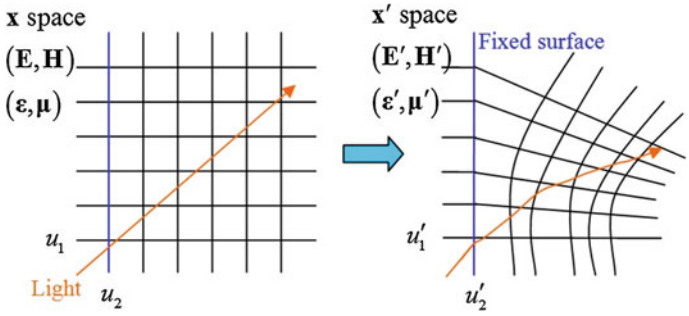

Fig. 5.2 The *left* panel shows a ray of light propagating in free space. The *right* panel shows the ray propagating in transformed space. The theory of transformation optics establishes a *mapping* of the trajectory of light between the original space and the transformed spaces and the material parameters that are needed to perform the coordinate transformation

can choose to use the reference coordinate systems (u_1, u_2) and $\left(u_1', u_2'\right)$ before and after transformation (shown in Fig. 5.2), in which the fixed surface can be described as $u_1 = u_1' = c$. On the fixed surface, the Jacobian matrix elements $A_{ij} = \partial u_i'/\partial u_j$ have $\partial u_1'/\partial u_2 = 0$ and $\partial u_2'/\partial u_2 = 1$, since each point on $u_1 = c$ is mapped to the same point on $u_1' = c$. Substituting into Eq. (5.3), we find that $E_2' = E_2$ and $H_2' = H_2$, indicating that the tangential field components on the fixed surface are unchanged after transformation. This is an important point that is useful in many transformation optics devices as it assures that there is no reflection on the fixed surface boundary.

5.3 Complementary Media

As a simple example, we consider the coordinate transformation $x' = -x$ (for $-d < x < 0$) and $y' = y$, $z' = z$. This transformation corresponds to a "folding" of space [10, 11]. The Jacobian matrix for this transformation can be written as $\mathbf{A} = \begin{pmatrix} -1 & 0 & 0 \\ 0 & 1 & 0 \\ 0 & 0 & 1 \end{pmatrix}$. From Eq. (5.4), the parameters of transformed space are obtained as $\boldsymbol{\varepsilon}'(x', y', z') = -\boldsymbol{\varepsilon}(x, y, z)$ and $\boldsymbol{\mu}'(x', y', z') = -\mu(x, y, z)$. From Eq. (5.3), we obtain the following interesting relations: $\begin{pmatrix} E_x'(x', y', z') \\ E_y'(x', y', z') \\ E_z'(x', y', z') \end{pmatrix} = \begin{pmatrix} -E_x(x, y, z) \\ E_y(x, y, z) \\ E_z(x, y, z) \end{pmatrix}$ and $\begin{pmatrix} H_x'(x', y', z') \\ H_y'(x', y', z') \\ H_z'(x', y', z') \end{pmatrix} = \begin{pmatrix} -H_x(x, y, z) \\ H_y(x, y, z) \\ H_z(x, y, z) \end{pmatrix}$.

If the original space is free space, i.e. $\varepsilon = 1$, $\mu = 1$, then the transformed space is a slab with material parameters $\varepsilon = -1$ and $\mu = -1$ as shown in Fig. 5.3a. Such

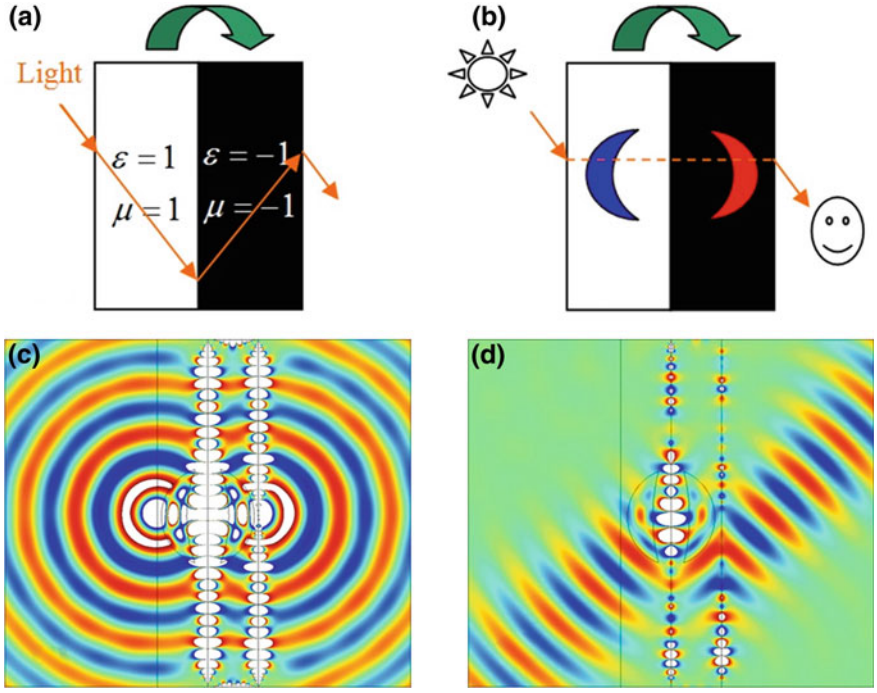

Fig. 5.3 **a** The operation of a perfect lens (a flat slab with $\varepsilon = \mu = -1$) can be explained using the concept of complementary media. The $n = -1$ perfect lens slab optically cancels the space of a slab of air of the same thickness, effectively moving the source closer to the observer and hence enabling higher resolution. **b** An inhomogeneous slab (shown pictorially as a *blue* crescent in a *white* background) can be optically canceled by a complementary media slab shown pictorially as a *red* crescent in a *black* background. The wave propagates as if some space has disappeared. The effect of passing a wave through the complementary media is numerically demonstrated in **c** for a point source and in **d** for a Gaussian beam. In both cases, we note that the wave propagates as if the complementary media pair removes some space

a slab forms the so called "perfect lens", which is capable of not only demonstrating negative refraction [1], but also achieving a perfect image beyond the different limit, as was pointed out by Pendry [12].

If the original space is not free space, but is inhomogeneous or contains objects, then the transformed space is slab composed of mirror images of the objects with negative parameters as compared with those in the original space, as shown in Fig. 5.3b. Such a slab is called the "*complementary media*" [13, 14] of the original space. The notion of complementary media was actually introduced before transformation optics, but the unusual behavior of such media can be explained elegantly using the language of transformation optics. Interestingly, although the original slab and its complementary media slab are inhomogeneous, they are still capable of achieving good imaging effect as illustrated in Fig. 5.3c, where we show that a point source on the left surface of the original slab gives a point image

on the right surface of the complementary media slab even though there are "objects" inside the slabs that can potentially lead to scattering. Actually, the complementary media slab is capable of copying arbitrary electromagnetic field values as well as their momentum from the left surface of the original slab to its right surface. To demonstrate this, we show in Fig. 5.3d a Gaussian beam incident on the left surface of the original slab as it tunnels to the right side of the complementary media slab and continues to propagate in its original direction.

The above exotic behaviors of complementary media can be explained physically by space operations. From the point of view of transformation optics, complementary media slabs are formed by the operation of folding space. During the folding, the folding line (surface) is always fixed. According to our previous analysis, the tangential field components on the fixed surface are unchanged; therefore the boundary conditions between the complementary media slab and the original slab are always satisfied by the two solutions that are mapped to each other in the original and transformed spaces. Thus, the electromagnetic fields on the other side of original slab are also mapped to the other side of the complementary media slab. This leads to an interesting and intriguing consequence: the complementary media slab serves the function of cancelling the original slab of space. The canceled space can be simply removed from the system when we consider the fact that wave propagation and waves would go through the canceled space as if it did not exist at all. This can be used to explain the operation of a perfect lens. A perfect lens (a slab of $\varepsilon = \mu = -1$) of thickness d is capable of optically cancelling spaces on either or both sides. The total thickness of the canceled slab spaces is also d. The observer is, hence, moved a distance $2d$ closer to the light sources, and as a result, the resolution is increased. By using the space cancellation concept, it is straightforward to understand the results shown in Fig. 5.3c, d. The space cancellation function is so powerful that a lot of illusion tricks can emerge, as will be shown later. However, we should emphasize that space cancellation (and therefore complementary media) alone does not imply invisibility. To achieve invisibility, we need to make a certain domain behave optically as if it has $\varepsilon = \mu = 1$. Light will have phase accumulation when it travels through an invisible domain. On the other hand, a complementary medium cancels space, and therefore, waves travel through it without phase change. An incident beam at oblique incidence will also be shifted as it passes through a complementary medium. What a complementary medium can do is remove the identity of any object inside. For example, independent of the size, shape, and composition of the embedded objects shown in the Fig. 5.3c, d, a pair of complementary media will give exactly the same scattered wave. The outside observer can tell that some space is missing, but the identity of the objects inside the folded space is not detectable. We will see later that if we add some additional "restoring media" to the complementary media to compensate for the missing phase, i.e., restore a region of illusion free space, we can achieve invisibility.

5.4 Invisibility Cloaks

In the pioneering works of transformation optics, the concept of *invisibility cloaks* has been proposed to illustrate the power of the method [8, 9]. Such invisibility cloaks are sometimes compared to Harry Potter's cloak, which possesses the "magical" effect of making objects or people invisible from all observation angles. However, we should note that thus far such invisibility cloaks can only operate in a narrow frequency range due to the limits of metamaterial dispersion. Moreover, the cloaked object is also "blind", i.e., it cannot see light from the outside world.

The design of invisibility cloaks are based on space operations using transformation optics. As shown in Fig. 5.4a, light in free space travels in straight lines, as long as gravity is not considered. In order to achieve the effect of cloaking, one proposed method is to bend the light such that it goes around a domain (encircled by the red curve). The light then exits from the other side with the original momentum as if it passes through a piece of free space, as shown in Fig. 5.4b. The shell that bends the light is the invisibility cloak. It can be created by expanding a dot (red dot in Fig. 5.4a) in free space within a circle of free space (dashed curve in Fig. 5.4a) using transformation optics. As a result, the original space within the

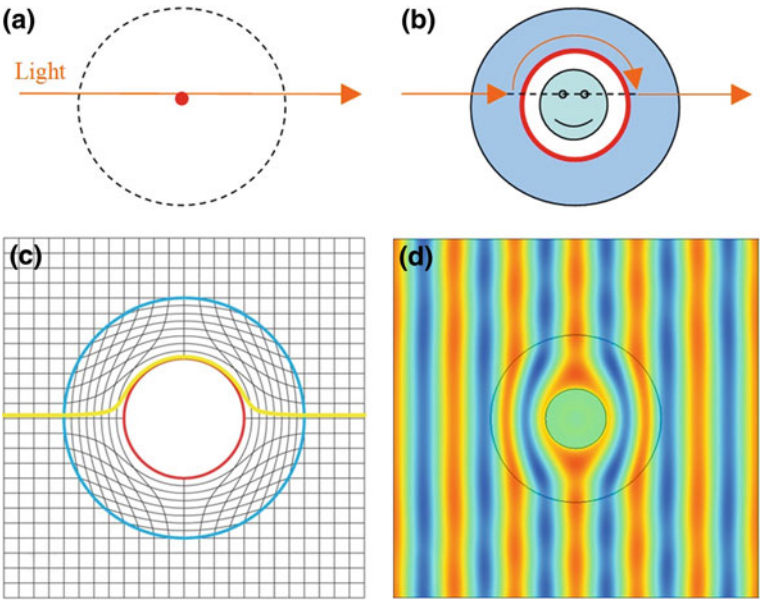

Fig. 5.4 **a** Light passing through free space. The *dotted line* represent the virtual boundary of a circle. **b** Light passing through a circular invisibility cloak obtained by expanding the *red* dot in free space into the circle marked by the solid *red* line. **c** The coordinate transformation corresponding to the invisibility cloak introduced by Pendry et al. **d** Numerical demonstration of the cloaking effect, where waves bend around the cloaked region. Any object placed inside the cloaked region will not cause scattering

circle is squeezed into a shell with a hidden space that light does not enter, as shown in Fig. 5.4c. On the other hand, the outer circle (blue curve in Fig. 5.4c) is a fixed surface on which the boundary conditions are automatically satisfied. This indicates that there would be no reflection or refraction under any incident waves for this device. Invisibility is therefore achieved with a hidden space inside which we can hide an object from being observed.

We note that similar coordinate transforms have been applied to the conductivity equation by Greenleaf et al. [15]. They proved that an object enclosed within a shell of anisotropic conductivities can escape detection by electrical impedance tomography, and the mathematical transformation ("blow up" transform) employed is the same as the transformation used in obtaining electromagnetic invisibility cloaks.

In Fig. 5.4d, we show a two-dimensional example of a cylindrical invisibility cloak. In this case, it is more convenient to use cylindrical coordinates in which the Jacobian matrix can be written as:

$$\mathbf{A} = \begin{pmatrix} \frac{\partial r'}{\partial r} & \frac{\partial r'}{r\partial \theta} & 0 \\ \frac{r'\partial \theta'}{\partial r} & \frac{r'\partial \theta'}{r\partial \theta} & 0 \\ 0 & 0 & 1 \end{pmatrix}, \tag{5.5}$$

where (r', θ') denotes the space coordinate in the cloak and (r, θ) denotes the coordinate in the original circular space. Here we take the simple "blow up" mapping of $r' = (b-a)\frac{r}{b} + a$ and $\theta' = \theta$, in which a and b denote the inner and outer radius of the invisibility cloak. The corresponding parameters for invisibility cloaks are obtained from Eq. (5.4) as $\varepsilon'_r = \mu'_r = \frac{b-a}{b}\frac{r}{r'}$, $\varepsilon'_\theta = \mu'_\theta = \frac{b}{b-a}\frac{r'}{r}$ and $\varepsilon'_z = \mu'_z = \frac{b}{b-a}\frac{r}{r'}$. Here, $\left(\varepsilon'_z, \mu'_r, \mu'_\theta\right)$ corresponds to TE polarization (electric field in z direction) and $\left(\varepsilon'_r, \varepsilon'_\theta, \mu'_z\right)$ corresponds to TM polarization (magnetic field in z direction). Figure 5.4d shows a plane wave with TE polarization incident on the cloak from the left. The invisibility cloak has $a = 0.5\lambda_0$ and $b = 1.4\lambda_0$. It is clearly seen that such a cloak indeed does not scatter incident waves and has thus achieved invisibility.

Realizing such a cloak is by no means straightforward because it is difficult to find suitable materials for constructing the perfect invisibility cloak, which requires some components of the permittivity and permeability tensors to go to zero or infinity. As a result, reduced parameters have been used in the first experiment by D. Schurig et al. [16], in which the effective refractive index, i.e., $\sqrt{\varepsilon_z\,\mu_r}$ and $\sqrt{\varepsilon_z\,\mu_\theta}$, are maintained as the original parameters, while the impedance matching is ignored. Plane wave patterns in this experiment have proven the cloaking effect.

While the full invisibility cloak is capable of achieving invisibility at all observation angles, it is usually very demanding on metamaterials and difficult to realize. If, however, only observation angles in a half space above a reflection plane are considered, the requirement on metamaterials can be greatly reduced. This is because in the case of a reflection geometry the hidden space can be

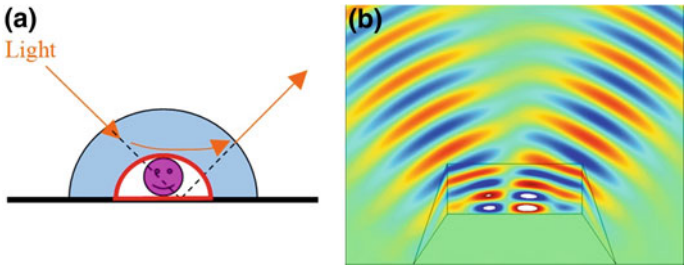

Fig. 5.5 **a** Schematic picture demonstrating the operation of a carpet cloak. **b** Numerical demonstration of the cloaking effect of a carpet cloak under a Gaussian beam incident from the *top left* and being reflected back

obtained by expanding from a surface instead of from a point. Such a cloak is called a *carpet cloak*, as shown in Fig. 5.5a. In Fig. 5.5b, we show the numerical demonstration of a carpet cloak under a Gaussian beam incident from the top left. It is seen that the field pattern appears as though the Gaussian beam is reflected back from a flat surface, resulting in a good cloaking effect. The original carpet cloak [17] employs a quasi-conformal mapping, which reduces the anisotropy to a minimum. If anisotropy is not an issue, the transformation mapping is actually more straightforward [18, 19]. Here, we illustrate the operation of the carpet cloak with the set up shown in Fig. 5.5b. The cloak is made of three parts: two triangular parts with $\varepsilon'_z = \mu'_{xx} = 2$, $\mu'_{yy} = 5$, and $\mu'_{xy} = \pm 3$, formed by the coordinate transformation $y' \pm 6x = 1/2 \cdot (y \pm 6x)$ and $x' = x$, and one rectangular part with $\varepsilon'_z = \mu'_{xx} = 2$ and $\mu'_{yy} = 0.5$, formed by the coordinate transformation $y' - 0.6 = 1/2 \cdot (y - 0.6)$ and $x' = x$. Obviously, there are no singular parameters in the case of carpet cloaks. Therefore, carpet cloaks are much easier to realize in experiment. In fact, most recent experiments on cloaking have been performed in such reflection geometries.

Since light does not enter into the hidden space of the cloak obtained by "blow up" transforms, anything inside it is cloaked. However, this isolation also prevents objects hidden inside the cloak from "seeing" light from the outside world. In the following section, we will show that there is actually a way to see the outside world while maintaining invisibility by using the notion of complementary media and transformation optics.

5.5 Cloaking at a Distance

In the previous scheme of invisibility cloaks, a transformation optics device that has the same function as a region of free space is created. The key principle behind this scheme is bending light around a domain using anisotropic materials, similar to the mirage effect. There are other cloaking schemes using transformation optics, as will be discussed here. In the following, we introduce the concept of "*cloaking*

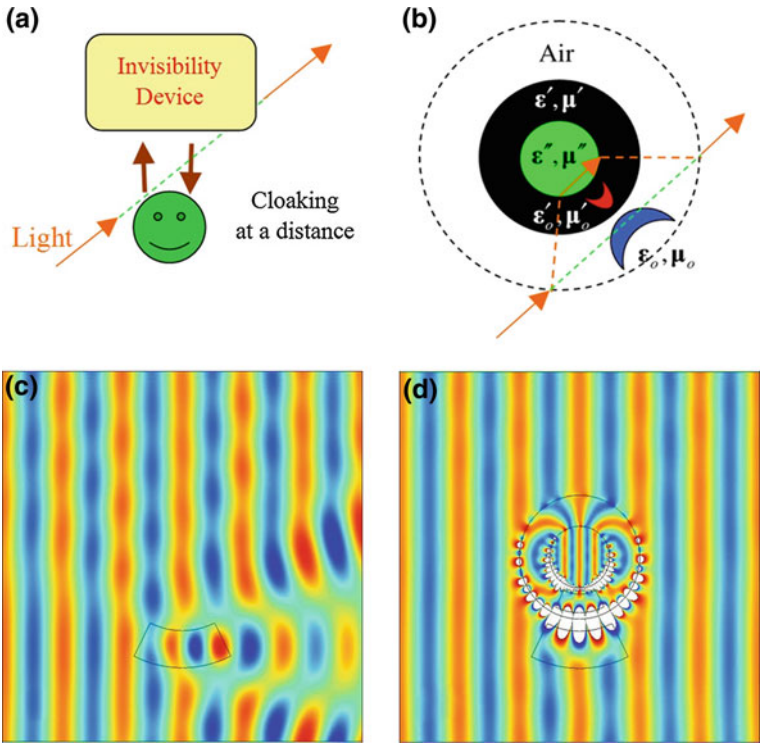

Fig. 5.6 **a** Schematic illustrating the idea of cloaking at a distance. **b** A picture illustrating the mechanism of cloaking at a distance. We want to make the object (*blue moon*) invisible without enclosing it. We cancel the space containing the object (*blue moon*) by a shell of complementary media (shown pictorially as *black* shell with *red* moon. We restore the canceled space with an illusionary free space by restoring media (*green core*). For ordinary objects with positive refractive indices, the complementary media shell is required to have negative refractive indices. The restoring media (*green core*) typically has high refractive index. **c** Numerical demonstration of the scattering of an object in free space. **d** Numerical demonstration of cloaking the object at a distance with an invisibility device. We note that the plane wave front is now restored and the object is not detectable at the designed frequency. However, the wave enters the object and the object is not "blind"

at a distance" [20], which makes objects invisible not by covering them with a metamaterial coating, but by placing a passive invisibility device at a distance to the objects, as shown pictorially in Fig. 5.6a. Such a cloaking scheme uses the notion of complementary media to optically cancel some real space containing the object to be hidden and thereby remove its identity, and an illusionary free space is created using a restoring medium.

The mechanism of cloaking at a distance is shown pictorially in Fig. 5.6b, in which a crescent-shaped object with material parameters $(\boldsymbol{\varepsilon}_o, \boldsymbol{\mu}_o)$ (blue colored) is made invisible by putting an invisibility device beside it. The invisibility device is circular and composed of two parts. The first part is a complementary media layer

(black colored) formed by folding a layer of space (within the dashed circle) containing the object inward. This folding operation results in a layer of parameters $(\boldsymbol{\varepsilon}', \boldsymbol{\mu}')$, but embedded within is a mirror object (an "anti-object") with parameters $\left(\boldsymbol{\varepsilon}'_o, \boldsymbol{\mu}'_o\right)$ (red). As discussed before, the function of this complementary media layer may be regarded as cancelling the original space and mapping the field on the dashed circle to the inner surface of the complementary media layer, as indicated by the orange dashed lines. In such a way, the propagating light is transferred to propagate inside the core media (green). When the light ray touches the complementary media layer the second time, it will be transferred again to the dashed circle and propagate in free space again. Now, the key step to making the system identical to a circle of free space is choosing the core media as one of high refractive index formed conceptually by compressing the circle of free space into the core. In this way, the optical path experienced by a light ray inside the core media will be exactly the same as that by a light ray propagating across the dashed circle in free space, as shown by the green dashed line in Fig. 5.6b. Therefore, any observers outside the dashed circle cannot see any scattered light from the object and the invisibility device, i.e., the system is invisible. In short, the real space containing the object is cancelled optically by the complementary media, and the core media restores an illusionary free space to achieve the invisibility effect. Thus, the core media is called a *restoring media*.

We now numerically demonstrate the phenomenon of cloaking at a distance in two dimensions. First, in Fig. 5.6c, we show the scattering effect of a dielectric object of $\varepsilon_o = 2$ under an incident plane wave of TE polarization from the left side. In Fig. 5.6d, we place a corresponding invisibility device beside the object. By using the linear mapping $r' = (b-a)\frac{c-r}{c-b} + a$ and $\theta' = \theta$ in Eq. (5.5), in which a, b, and c are the inner radius, outer radius, and the radius of the dashed circle, respectively, the complementary media layer material parameters can be written as $\varepsilon'_r = \mu'_r = -\frac{b-a}{c-b}\frac{r}{r'}$, $\varepsilon'_\theta = \mu'_\theta = -\frac{c-b}{b-a}\frac{r'}{r}$, and $\varepsilon'_z = \mu'_z = -\frac{c-b}{b-a}\frac{r}{r'}$ for the region outside the mirror object. Inside the region of the "anti-object", the permeability is the same as the region outside, while the permittivity is changed correspondingly into $\varepsilon'_r = -\frac{b-a}{c-b}\frac{r}{r'}\varepsilon_o$, $\varepsilon'_\theta = -\frac{c-b}{b-a}\frac{r'}{r}\varepsilon_o$, and $\varepsilon'_z = -\frac{c-b}{b-a}\frac{r}{r'}\varepsilon_o$. In Fig. 5.6d, we have chosen $a = 0.5\lambda_0$, $b = \lambda_0$, and $c = 2\lambda_0$. The plane wave pattern indicates that the whole system has no scattering, showing the effectiveness of cloaking at a distance.

In this scheme of cloaking at a distance, we note that the incident waves interact with the object directly, thus the object can still "see" the outside world, while at the same time being "cloaked" at a distance by the invisibility device. This is different from the original invisibility cloak scheme in which the cloaked object has no contact with the incident wave.

Like the original invisibility cloaks proposed in 2006, the mechanism of cloaking at a distance is also a result of space manipulations, and, hence, the cloak should work irrespective of the property of the incident light as well as the observation angle. This is illustrated in Fig. 5.7. In Fig. 5.7a–c, we demonstrate the effect of cloaking under various incident waves, including a plane wave incident from another direction (Fig. 5.7a), a point source (Fig. 5.7b), and a

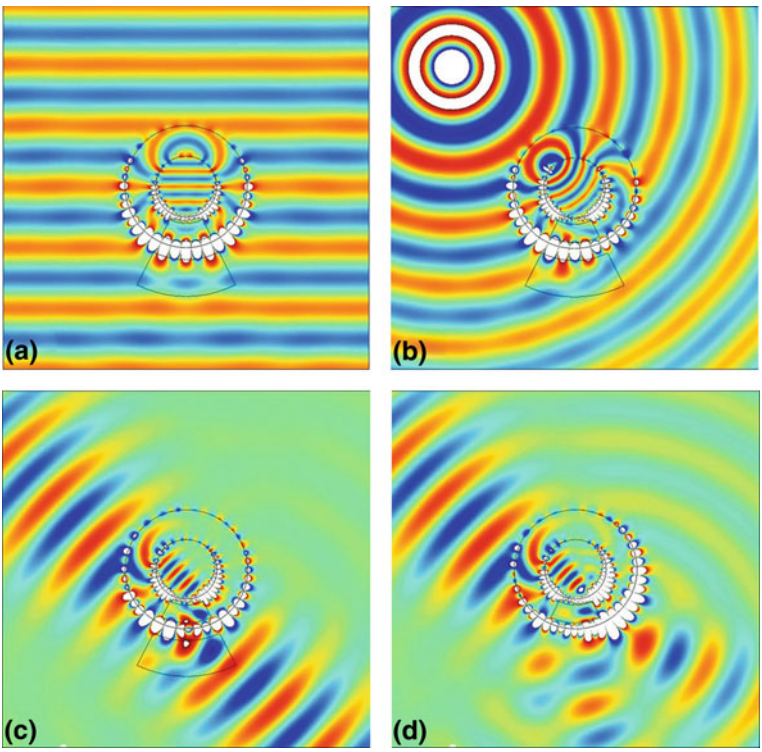

Fig. 5.7 Numerical demonstrations of cloaking at a distance. Panels (a)–(c) shows the performance of the cloak under different forms of illumination: **a** under a plane wave incident from top; **b** a point source at the *top left* corner; **c** a Gaussian beam incident from *top left*. These demonstrations show that remote cloak works irrespective of the direction and the nature of the incident wave. **d** The scattering of the invisibility device itself under the Gaussian beam

Gaussian beam (Fig. 5.7c). The cloak works as expected for different incident waves. However, unlike invisibility cloaks, cloaking at a distance works only when the invisibility device and the object are placed at a designed distance. In Fig. 5.7d, we show the scattered wave pattern of the invisibility device by itself when the same Gaussian beam as used in Fig. 5.7c impinges on the cloaking device. Obviously, scattering occurs. The remote invisibility device itself is not invisible as a standalone object, but it is invisible when it is placed at the pre-designed position next to the object to be cloaked.

From the viewpoint of wave interference, cloaking at a distance has demonstrated an example of achieving far-field destructive interference of all scattered waves by employing passive devices with strong multiple scattering interactions with the object to be "cloaked". This is an effect more subtle than the original invisibility cloak. However, the price to pay is the complexity of the metamaterial. We need to employ a negative index metamaterial with low-loss in the complementary media layer. The metamaterial should be able to produce strong surface

waves in the boundaries, as seen in Figs. 5.6d, 5.7a–c. As low loss double negative metamaterials are always difficult to make, particularly at high frequencies, the material issue here is at least as challenging as that in invisibility cloaks that operate by light bending. The requirement may be somewhat less stringent in the sense that there are no extreme parameters (zero or infinity) in the complementary media. Nevertheless, transmission line samples have been fabricated with negative parameters at microwave frequencies and the effect of cloaking at a distance has been demonstrated experimentally. We note in passing that the cloaking effect here is not the same the cloaking effect discovered by Milton et al. [21, 22], who demonstrated that a small dipolar object can be made undetectable as a result of an "anomalous resonance" when it is placed close enough to a perfect lens with a negative refractive index. The anomalous resonance effect can cloak an object only if certain conditions are satisfied. The object must be very small and must be placed close to the negative index slab. There is no "anti-object" or "restoring medium". In our approach, the underlying mechanism is the space cancellation effect of complementary media. There is no limit to the size of the object to be cloaked and there is in principle no limit to the distance between the device and the cloak if absorption is small.

5.6 Making Part of an Object Invisible

A significant advantage of applying folding action in space manipulation is the ability to make part of an object invisible [23]. In Fig. 5.8, we show the numerical demonstration of such an operation. In Fig. 5.8a, we show the scattering pattern when a plane wave impinges on a thin dielectric layer of $\varepsilon_o = 2$. In Fig. 5.8b, we use an invisibility device that is purposely designed to cloak just the upper part of a

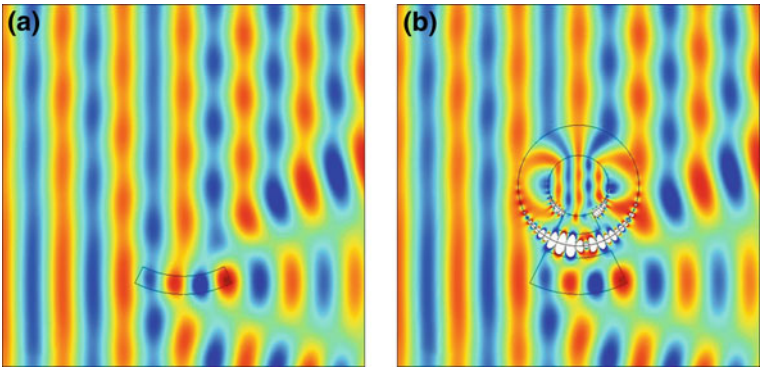

Fig. 5.8 **a** Scattering of plane wave by a dielectric object. **b** The anti-object is designed purposely to make the *upper part* of a thick dielectric layer invisible, while leaving the *lower part* unaffected. As a consequence of this partial cloaking effect, the scattering of the object in b becomes the same as the scattering due to the object in (**a**) although the object in (**b**) is bigger in size. A far field observer will believe that they are seeing the object shown in panel (**a**)

thick dielectric layer, leaving the lower part untouched. The "anti-object" is designed so that it only cancels part of the object. It is seen that the scattering pattern is the same as that of a lower thin dielectric layer, i.e., the upper part is made invisible while leaving the lower part unaffected. As the scattering patterns of configurations in Fig. 5.8a, b are the same to an outside observer; the observer will "see" an thin object instead of a thicker object.

Such a special effect is a derivative of cloaking at a distance and may lead to many interesting applications. For example, a wall of negative permittivity would certainly block electromagnetic waves, as most metals do. Information is thus blocked by the wall and we cannot see through the wall. In order to see information on the other side, one can of course drill a hole into the wall. However, we can obtain information non-invasively using the concept of remote cloaking [24]. Using transformation optics, we can make part of the wall invisible, which means that a virtual hole is opened in the wall through which light can tunnel into the outside as if there is a real hole.

In Fig. 5.9a, we show that electromagnetic waves radiated from a point source are blocked by a wall of $\varepsilon_o = -1$. In Fig. 5.9b, we show a transformation scheme that serves to open a virtual hole on such a wall. The invisibility device is also made of a complementary media part (black) and a restoring media part (green). Their combining function is to first optically cancel one part of the wall (bounded by black dashed lines), and then restore the canceled space with illusion of free space. When a beam of light (orange arrow) hits on left side of the wall, it tunnels to the other side. This is the property of complementary media. Then, it is guided to emit with the original momentum and proper position by the restoring media. The numerical demonstration of attaching an invisibility device on the outside of the wall is shown in Fig. 5.9c. We see that electromagnetic waves can now propagate to the right side of the wall. In Fig. 5.9d, we show the simulation of electromagnetic waves propagating through a real hole drilled through the wall. It is seen that the radiation pattern in the far field is almost the same as that in Fig. 5.9c. We note that the restoring medium (green colored part) is not needed if we just need light to leak out from the wall, but it is needed if we want the outgoing field to be the same as if a real hole was drilled into the wall.

In Fig. 5.9c, the geometry of the invisibility device is not cylindrical. The complementary media part is obtained by folding the canceled trapezoidal part of wall to the left black part, i.e., $x' = -x/2$, which results in an homogeneous medium of $\varepsilon'_z = 2$, $\mu'_x = -0.5$, and $\mu'_y = -2$. The restoring media part is formed by compressing an illusionary free space bounded by the black dashed lines into the region of the restoring media (green). Here, we take the simplest way of compressing two triangular parts and one rectangular part in the x direction, as shown in Fig. 5.9c. The upper and lower triangular parts are of $\varepsilon'_z = 4$, $\mu'_{xx} = 9.25$, $\mu'_{yy} = 4$, and $\mu'_{xy} = \mp 6$, formed by the coordinate transformation of $x' \pm 2(y \mp 0.5) = 1/4 \cdot (x \pm 2(y \mp 0.5))$ and $y' = y$, respectively. The middle rectangular part is of $\varepsilon'_z = 4$, $\mu'_x = 0.25$, and $\mu'_y = 4$, formed by the coordinate transformation of $x' - 0.2 = 1/4 \cdot (x - 0.2)$.

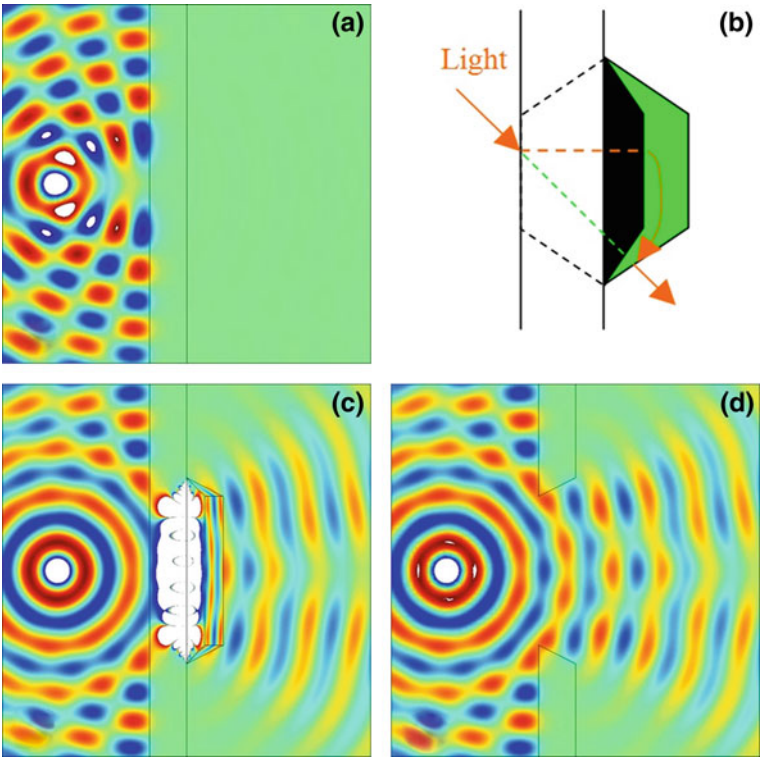

Fig. 5.9 **a** Numerical simulation of a point source placed on one side of a wall blocking electromagnetic waves. **b** Schematic design of a device that can make a virtual hole on the wall so that light can tunnel through the wall via the complementary (*black*) and restoring (*green*) media. **c** Numerical demonstration of waves propagating through the virtual hole to the other side. The source is the same as that in panel (**a**). **d** Numerical demonstration of waves propagating through a real hole

By using similar designs, such invisibility devices can also enable interesting applications such as turning a box into free space, so that we can see what is hidden inside the box. In addition to numerical demonstrations, a mathematical proof for the remote cloaking and illusion optics effect has also been shown. The interested reader may refer to the supplementary material of Ref. [24].

5.7 Other Cloaking Schemes

In addition to the invisibility cloak and cloaking at a distance, there are some other approaches to achieve invisibility. The brief description below is not intended to be comprehensive, but rather to show that transformation optics can provide many solutions to similar problems.

In one approach, an object is coated with metamaterial layers, such that the combined system can be regarded as illusionary free space. This method requires interaction between the object and the metamaterial layer. The simplest example is a homogeneous dielectric material of arbitrary shapes in two dimensions for TE polarization. As shown in Fig. 5.10a, by covering the dielectric object (purple) with certain transformation media, it is possible to perfectly guide light into the dielectric object and then out into free space at the other side. As a result, all the light travels as if passing through an illusionary free space (dashed lines). In Fig. 5.10b, we show the example of cloaking a dielectric object by covering it with a transformation medium that guides light into the object. Such a transformation medium is called a "concentrator" [25]. Recently, a variant of this cloaking scheme has been proposed using only single negative materials [26]. However, such an approach works only for making certain types of objects (that can be transformed into illusionary free space by transformation optics) invisible.

A schematic graph of the coordinate mapping in cylindrical radial coordinate is shown in Fig. 5.11 to demonstrate the different cases of invisibility cloaks, cloaking at a distance and the wave concentrator. In Fig. 5.11a, we show the coordinate mapping of invisibility cloaks, in which a cloak between R_1 and R_2 are formed by this mapping, which can be used to cloak any objects with R_1 (shown as an apple in Fig. 5.11a). In Fig. 5.11b, we show the coordinate mapping of cloaking at a distance, in which any objects between R_2 and R_3 (shown as an apple) can be made invisible by the "anti-object" (a red mirror image of the apple) embedded within the complementary media layer (between R_1 and R_2) as well as the restoring medium (within R_1). In Fig. 5.11c, we show the mapping of concentrator, which is invisible too. However, both the core and shell are formed by transformation optics and cannot be arbitrary objects.

There are other types of cloaking that also employs cancellation. For example, A. Alu et al. have proposed the use of a plasmonic coating to "cloak" a small

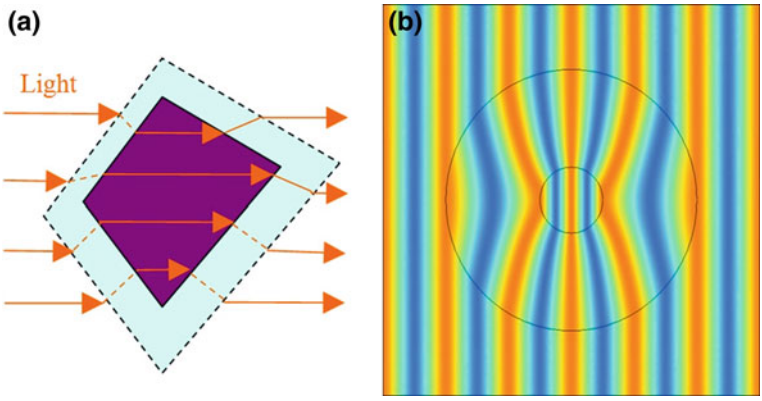

Fig. 5.10 **a** Demonstration of guiding light into an object by covering it with a transformation medium. **b** Numerical demonstration of a concentrator, which is an invisible device with a high refractive index core

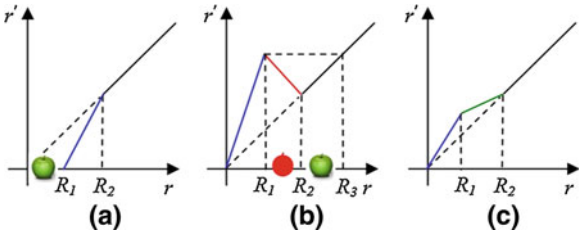

Fig. 5.11 Coordinate mappings in radial cylindrical coordinates: **a** Radial "blow up" mapping that achieves invisibility cloaks. **b** The mapping that can achieve of cloaking at a distance. The *red* color part gives materials with negative refractive index. **c** The mapping corresponding to a wave concentrator

object. In this case the negative permittivity layer serves to cancel the first order scattering of the dielectric core [27]. However, as the mechanisms are not based on transformation optics and space manipulation, we will not discuss it in detail here.

5.8 From Invisibility to Illusion Optics

We have previously shown that invisibility can be achieved by manipulation of optical spaces, i.e., turning the real space with objects into an illusionary free space without any objects. Indeed, both the light-bending invisibility cloak approach and the cloaking at a distance approach can be considered as creating an illusionary free space using transformation optics. With this knowledge, one simple question is: what if the illusionary space is not free space, but contains some illusion objects?

It turns out that it is feasible to create arbitrary stereoscopic passive illusions. For example, we can in principle make an apple look like a banana. Here, by passive illusions, we mean that the illusion of a banana is not generated by active devices such as TVs or projectors, but that the far field optical properties of the apple are indeed turned into that of the banana. Whatever light is incident upon the system, the scattered light will be exactly the same as that from a banana instead of an apple, therefore making an observer believe that a banana is there instead of an apple. This amazing effect is achieved by replacing the real space with an apple into an illusion space with a banana, as shown in Fig. 5.12, and is therefore denoted as *Illusion optics* [24].

As an example, we consider making a spoon look exactly like a cup outside a certain boundary. In Fig. 5.13a, we show the computed scattering pattern of a spoon of $\varepsilon_o = 2$ when a plane wave is incident from the left. In Fig. 5.13b, we demonstrate the schematic graph of using a passive illusion device to transform the optical response of the dielectric spoon into that of a cup of $\varepsilon_o = -1$. The illusion device is similar in composition to the invisibility device in Fig. 5.9b. It is composed of two parts, a complementary media part that cancels the optical space containing the spoon, and a restoring media part that refills in the illusionary

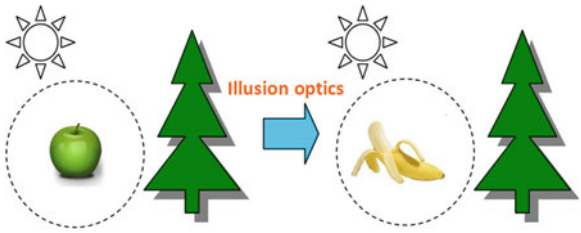

Fig. 5.12 Schematic graph of optically replacing a region of real space containing one object (an apple) into that of an illusion space containing an illusionary object (a banana), such that any observer will see a banana instead of an apple. Everything outside the region remains optically unchanged

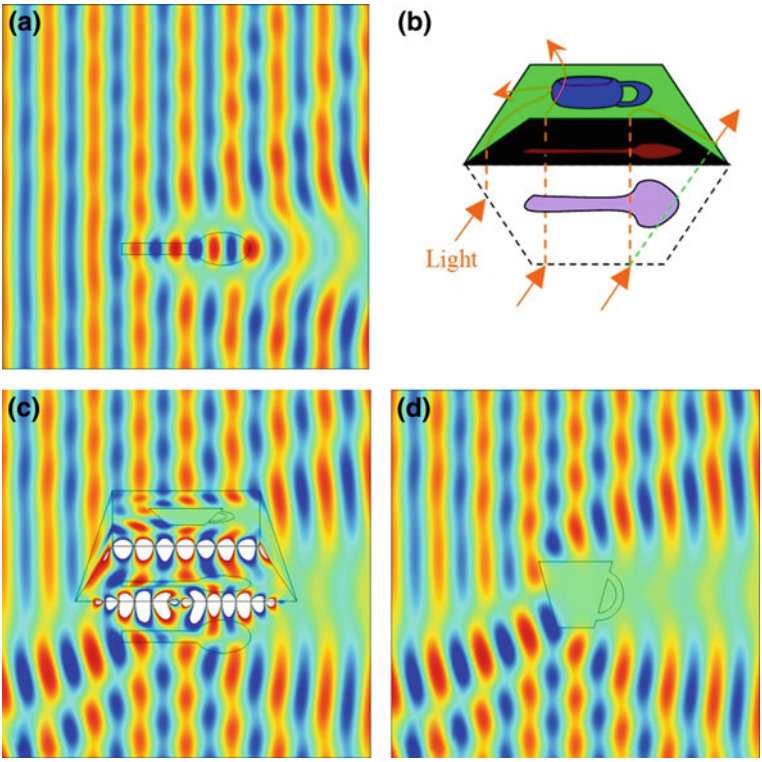

Fig. 5.13 **a** The scattering of *plane waves* by a spoon-like object. **b** Schematic graph of using an illusion device to transform the optical response of a spoon into that of a cup, an example of illusion optics. **c** Numerical demonstration of optically transforming the spoon into the cup. **d** Comparing with the numerical simulation in panel, which shows the scattering pattern of a cup, we see that the total scattering of the device and the spoon becomes the same as that of a standalone cup. The outside observer will see a cup instead of a spoon

optical space with the illusion cup. As a result, any light incident upon this region would propagate as if there is only a cup inside. The difference between an illusion device and an invisibility device is that there are illusionary objects in the illusionary space instead of pure free space. We note that the negative refractive index component in this device serves two purposes. As a component of the complementary media, it "cancels" the object. It also serves as a lens that forms the image of the cup.

The material parameters of the illusion device that we used in Fig. 5.13c are similar to those of the invisibility device in Fig. 5.9b, with the exchange between x and y directions and the additional insertion of an "anti-object" in the complementary media part as well as an illusion object in the restoring media part. As shown in Fig. 5.13c, the scattering pattern of whole system is changed by the illusion device. By comparing it with the scattering pattern of a single cup in free space, which is shown in Fig. 5.13d, it can be seen that the two patterns are almost exactly the same in the far field region. This indicates that the optical scattering of a spoon is indeed changed into that of a cup by the passive illusion device. Any observer will see a cup instead of a spoon at a distance. The illusion effect is thus demonstrated numerically.

Similar to invisibility devices, there are also more than one approaches to achieving illusions. We have demonstrated creating an illusion using the cancelling and restoring approach, similar to cloaking at a distance. In fact, the invisibility cloak can be modified to create illusions as well [28]. As shown in Fig. 5.14, by expanding a point (red dot) in a space with a crescent-shaped object, it is possible to obtain an illusion cloak that has exactly the same function as the original crescent-shaped object in free space. In the illusion cloak, any object can be hidden without being seen. Therefore, it is also capable of achieving stereoscopic illusions. Since the extension is straightforward, we will not give numerical examples for this case.

By using illusion optics, it is possible to change the optical response of a region of space almost at will, and there are many plausible applications. In the following, we will introduce two examples: the super-scatterer which has a scattering cross section that is much larger than the geometric cross section, and the super-absorber that can absorb light beyond its physical boundaries. There are many other applications that we cannot cover here such as a rotator that creates an illusionary rotating effect, a shifter that creates illusionary shifting effects, the remote control of light in cavities, shrinked optical devices, and ground illusion devices that create illusions in the reflection geometry, etc. The interested readers may refer to the references.

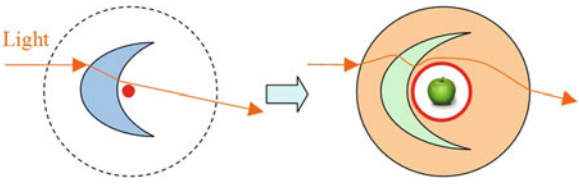

Fig. 5.14 Schematic graph of an illusion cloak that creates illusions. Any object placed inside the *red* circle will look like the crescent colored in *blue*

5.9 Super-Scatterers

One interesting example of illusion is the super-scattering effect [29]. The mechanism of a super-scatterer is shown pictorially in Fig. 5.15a. It is composed of a complementary media layer surrounding a PEC core (which repels waves), where any light incident on the virtual boundary of the device would tunnel to the surface of the PEC core and tunnel back, as if reflected at the virtual boundary. In other words, a super-scatterer creates an illusion of a larger PEC region. In Fig. 5.15b, we demonstrate the scattering pattern of the PEC core in free space under an incident plane wave from the left. In Fig. 5.15c, we show the scattering pattern of the super-scatterer, and Fig. in 5.15d, the scattering pattern of an illusionary larger PEC. It is immediately seen that the scattering patterns in the far field are almost the same in Fig. 5.15c, d. Thus, the illusionary PEC effect is proved. The parameters of the complementary media layer are the same as that in Fig. 5.6d except that there is no "anti-object" embedded inside.

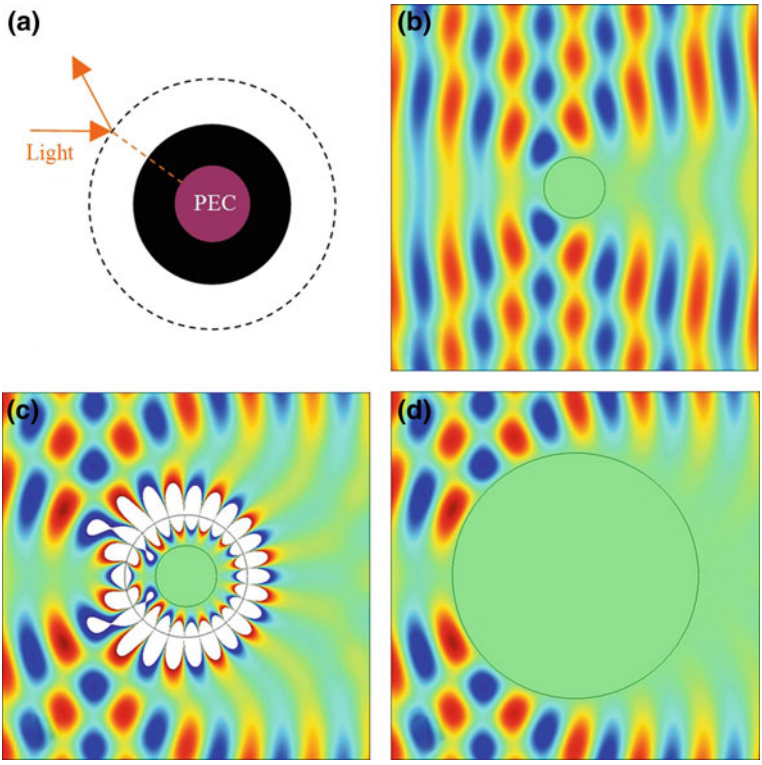

Fig. 5.15 **a** Schematic picture of a super-scatterer composed of a perfect electric conductor (*PEC*) and a complementary media layer. **b** The scattering pattern of the PEC. **c** The scattering pattern of the super-scatterer. **d** The scattering pattern of a illusionary larger PEC

A super-scatterer can also be achieved in Cartesian geometry. In Fig. 5.12c, if we remove the original spoon object, as well as the mirror spoon in the complementary media part and the illusionary cup in the restoring media part, and then we change the whole restoring media part into some materials that reflect light, then the illusion device turns into a super-scatterer, i.e. a scatterer with a much larger scattering cross section than its physical size. A schematic graph of the mechanism of such a super-scatterer is shown in Fig. 5.16a. Here we consider TE waves and we use the perfect electric reflectors (PECs) as the reflecting material. According to the function of complementary media, a beam of light incident on the virtual boundary (dashed lines) will be tunneled to the other side and get reflected by PEC boundary, and then tunneled back to propagate in another direction, as if it is reflected at the virtual boundary. In the view of space manipulations, such an illusion device creates an illusionary PEC which is much larger than the true one.

A numerical demonstration of such a super-scatterer is shown in Fig. 5.16b, in which the scattering pattern is very similar to the scattering pattern of a single larger PEC, as shown in Fig. 5.16c. This proves the effect of the super-scatterer.

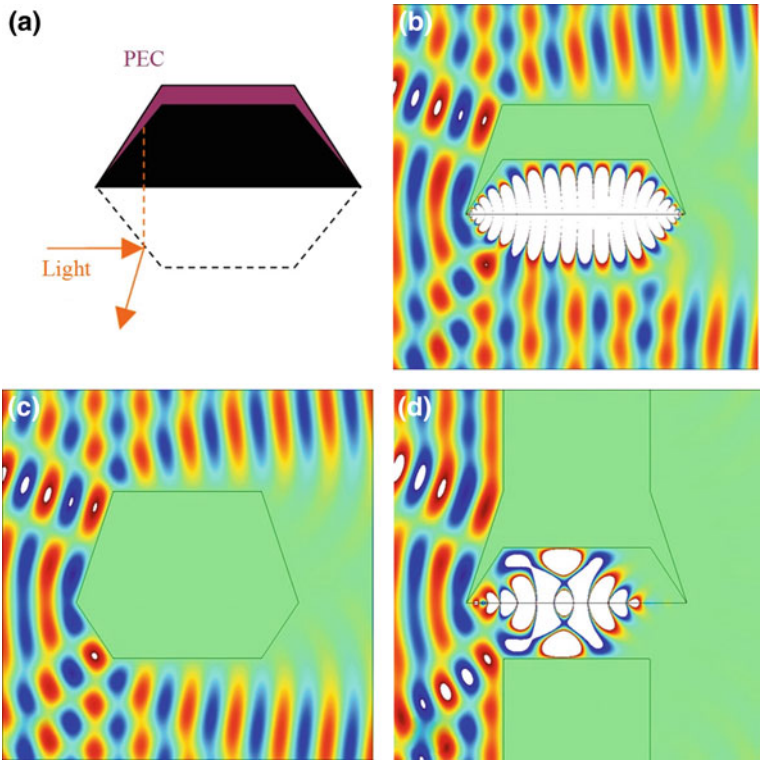

Fig. 5.16 **a** Schematic picture of a super-scatterer in the Cartesian geometry. **b** Scattering pattern of the super-scatterer. **c** Scattering pattern of an illusionary larger PEC. **d** Realization of a hidden portal with the super-scatterer

The super-scatterer has an interesting application. It can be used to create a hidden portal. As shown in Fig. 5.16d, a super-scatterer is embedded in a PEC wall. The electromagnetic waves will be reflected by an illusion of a continuous PEC wall, and therefore cannot transfer to the other side. However, there is a real gap in the wall in which physical objects or waves of other frequencies can go through [30].

5.10 Super-Absorbers

Another illusion effect is the super-absorber effect, where one enlarges an absorptive core by using illusion optics [31]. In most known situations, the absorption cross-section can only be slightly bigger than the geometric cross section except when we have small particles at resonance. While small particles can absorb more light than a blackbody of the same size, the absorption cross-section cannot increase without bound for fixed particle volume. Here we shall show that using illusion optics, it is possible to build a super absorber whose absorption cross-section can increase significantly beyond the physical cross-section at the working frequency, and the effect is not limited to small particles.

For simplicity, we consider the problem in two dimensions, but the problem can be generalized to three dimensions in a straightforward manner. The geometry of the super absorber, which consists of a core and a shell, is illustrated in Fig. 5.17a. In this case, instead of using a linear mapping, we have used the mapping of $r = b^2/r'$ for $a < r < b$, in which a and b are the core radius and the outer radius of the complementary media layer. The resulting complementary media parameters are $\varepsilon_s = -1$ and $\mu_s = -b^4/r^4$. Such a system would effectively behave as an illusionary cylinder of radius $r' = b^2/a$ with a "diluted" version of the absorbing core parameters, i.e., $\varepsilon_c = (1+i)$ and $\mu_c = (1+i)$. Figure 5.17b shows the extinction and absorption efficiencies for a super absorber considering illumination by transverse electric waves at normal incidence. It is seen that one can maintain

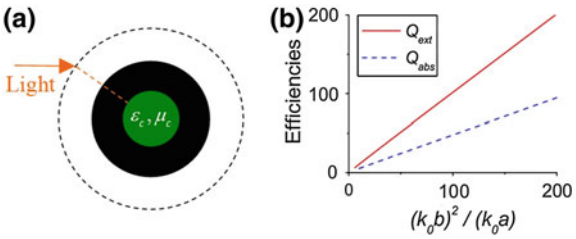

Fig. 5.17 **a** The geometry of the super absorber, which consists of a core of radius a and a shell of radius b. The core has constitutive parameters of ε_c and μ_c, and the shell has constitutive parameters of $\varepsilon_s = -1$ and $\mu_s = -b^4/r^4$ at the working frequency. **b** Extinction and absorption efficiencies for the super absorber with $\varepsilon_c = (1+i)b^4/a^4$, $\mu_c = (1+i)$, and $kb = 2$, and a is varying

the super absorber at the same physical size (fixed b), while increasing its efficiencies by decreasing a. When a tends to zero, the absorbing power of the system would increase without bound. Of course, for a too small, the constitutive parameters will become extreme.

5.11 Other Illusion Ideas and Experiments

There are many other interesting ideas in illusion optics. For example, it has been proposed to embed an "anti-object" in a ground of negative parameters, so as to cloak an object on the ground without using a carpet cloak [32]. The same approach is also capable of casting illusions in the reflection geometry. Other illusion effects that have been proposed include rotating [33], shifting and reshaping [34, 35], changing materials [36], anti-cloaking [37], and optically remote controlling [38], etc. They can all be understood via the concept of *illusion optics*, i.e., the replacement of optical spaces.

It is challenging to realize various kinds of illusion effects at optical frequencies due to the difficulty in realizing nano-scale metamaterials with suitable parameters. However, it is much easier to do experiments at microwave frequencies because the metamaterial fabrication is much easier at that length scale. Most of the experimental works are focusing on realizing carpet cloaks [18, 19, 39–43], but a few experiments are also emerging on invisibility cloaks [16], illusion optics [44, 45] and cloaking at a distance [46]. As the experimental techniques improve with time, experimental demonstrations will be easier to carry out.

5.12 Conclusions

We have demonstrated that optical spaces can be manipulated by using transformation optics and metamaterials (see Refs. [47–50] for reviews). We can optically isolate or cancel a piece of space with objects inside and restore into a piece of illusionary space with arbitrary illusion objects. In such a way, the optical properties of the original object are changed into that of the illusion object outside of a prespecified boundary, creating a perfect illusion that cannot be distinguished from reality by any observers in the far field. This is called *illusion optics*, first proposed in Ref. [24] and highlighted in Ref. [51]. In a nutshell, real optical space can be replaced with an arbitrary illusion optical space, therefore enabling the creation of arbitrary stereoscopic optical illusions, including invisibility.

Potential applications of illusion optics include various kinds of cloaking effects and illusion ideas such as invisibility cloaks, cloaking at a distance, super-scatterers, super absorbers, and many others. The idea of optical space replacement may be extended to more intriguing concepts such as cloaking with non-Euclidean spaces [52], optical black holes [53], and wormholes [54].

We have demonstrated some cases in two dimensions, but the principles work also for cases in three dimensions. Besides electromagnetic waves, it is also possible to create illusions for acoustic waves and other classical waves that are form-invariant under coordinate transformation (see e.g. [55–60]).

Acknowledgments This work is supported by Hong Kong CRF grant HKUST2/CRF/11G. LY is supported by the State Key Program for Basic Research of China (No. 2012CB921501), National Natural Science Foundation of China (No. 11104196), Natural Science Foundation of Jiangsu Province (Grant No. BK2011277), Program for New Century Excellent Talents in University (NCET), and a Project Funded by the Priority Academic Program Development of Jiangsu Higher Education Institutions (PAPD).

References:

1. Veselago VG (1968) The electrodynamics of substances with simultaneously negative values of ε and μ. Sov Phys Usp 10:509
2. Pendry JB, Holden AJ, Robbins DJ, Stewart WJ (1999) Magnetism from conductors and enhanced nonlinear phenomena. IEEE Trans Microwave Theory Tech 47:2075
3. Shelby RA, Smith DR, Schultz S (2001) Experimental verification of a negative index of refraction. Science 292:77
4. Smith DR, Padilla WJ, Vier DC, Nemat-Nasser SC, Schultz S (2000) Composite medium with simultaneously negative permeability and permittivity. Phys Rev Lett 84:4184
5. Yao J, Liu ZW, Liu YM, Wang Y, Sun G, Bartal G, Stacy AM, Zhang X (2008) Optical negative refraction in bulk metamaterials of nanowires. Science 321:930
6. Valentine J, Zhang S, Zentgraf T, Ulin-Avila E, Genov DA, Bartal G, Zhang X (2008) Three-dimensional optical metamaterial with a negative refractive index. Nature 455:376
7. Xiao SM, Drachev VP, Kildishev AV, Ni XJ, Chettiar UK, Yuan HK, Shalaev VM (2010) Loss-free and active optical negative-index metamaterials. Nature 466:735
8. Leonhardt U (2006) Optical conformal mapping. Science 312:1777
9. Pendry JB, Shurig D, Smith DR (2006) Controlling electromagnetic fields. Science 312:1780
10. Leonhardt U, Philbin TG (2006) General relativity in electrical engineering. New J Phys 8:247
11. Milton GW, Nicorovici NAP, McPhedran RC, Cherednichenko K, Jacob Z (2008) Solutions in folded geometries, and associated cloaking due to anomalous resonance. New J Phys 10:115021
12. Pendry JB (2000) Negative refraction makes a perfect lens. Phys Rev Lett 85:3966
13. Pendry JB, Ramakrishna SA (2002) Near field lenses in two dimensions. J Phys: Condens Matter 14:8463
14. Pendry JB, Ramakrishna SA (2002) Focusing light using negative refraction. J Phys: Condens Matter 15:6345
15. Greenleaf A, Lassas M, Uhlmann G (2003) Anisotropic conductivities that cannot be detected by EIT. Physiol Meas 24:413–419
16. Schurig D, Mock JJ, Justice BJ, Cummer SA, Pendry JB, Starr AF, Smith DR (2006) Metamaterial electromagnetic cloak at microwave frequencies. Science 314:977
17. Li J, Pendry JB (2008) Hiding under the carpet: a new strategy for cloaking. Phys Rev Lett 101:203901
18. Zhang BL, Luo Y, Liu XG, Barbastathis G (2011) Macroscopic invisibility cloak for visible light. Phys Rev Lett 106:033901
19. Chen XZ, Luo Y, Zhang JJ, Jiang K, Pendry JB, Zhang S (2011) Macroscopic invisibility cloaking of visible light. Nat Comm 2:176

20. Lai Y, Chen HY, Zhang ZQ, Chan CT (2009) Complementary media invisibility cloak that cloaks objects at a distance outside the cloaking shell. Phys Rev Lett 102:093901
21. Milton GW, Nicorovici NAP (2006) On the cloaking effects associated with anomalous localized resonance. Proc R Soc A 462:3027–3059
22. Dong JW, Zheng HH, Lai Y, Wang HZ, Chan CT (2011) Metamaterial slab as a lens, a cloak, or an intermediate. Phys Rev B 83:115124
23. Lai Y, Ng J, Chen HY, Zhang ZQ, Chan CT (2010) Illusion optics. Front Phys China 5:308–318
24. Lai Y, Ng J, Chen HY, Han DZ, Xiao JJ, Zhang ZQ, Chan CT (2009) Illusion optics: the optical transformation of an object into another object. Phys Rev Lett 102:253902
25. Rahm M, Schurig D, Roberts DA, Cummer SA, Smith DR, Pendry JB (2008) Design of electromagnetic cloaks and concentrators using form-invariant coordinate transformations of Maxwell's equations. Photo Nano Funda Appl 6:87–95
26. Zhu XF, Liang B, Kan WW, Zhou XY, Cheng JC (2011) Acoustic cloaking by a superlens with single-negative materials. Phys Rev Lett 106:014301
27. Alu A, Engheta N (2005) Achieving transparency with plasmonic and metamaterial coatings. Phys Rev E 72:016623
28. Jiang WX, Ma HF, Cheng Q, Cui TJ (2010) Illusion media: generating virtual objects using realizable metamaterials. Appl Phys Lett 96:121910
29. Yang T, Chen HY, Luo XD, Ma HR (2008) Superscatterer: enhancement of scattering with complementary media. Opt Express 16:18545
30. Chen HY, Chan CT, Liu SY, Lin ZF (2009) A simple route to a tunable electromagnetic gateway. New J Phys 11:083102
31. Ng J, Chen HY, Chan CT (2009) Metamaterial frequency-selective superabsorber. Opt Lett 34:644
32. Wu KD, Wang GP (2010) Hiding objects and creating illusions above a carpet filter using a Fourier optics approach. Opt Express 18:19894
33. Chen HY, Chan CT (2007) Transformation media that rotate electromagnetic fields. App Phys Lett 90:241105
34. Chen HY, Zhang XH, Luo XD, Ma HR, Chan CT (2008) Reshaping the perfect electrical conductor cylinder arbitrarily. New J Phys 10:113016
35. Jiang WX, Cui TJ (2010) Moving targets virtually via composite optical transformation. Opt Express 18:5161
36. Jiang WX, Ma HF, Cheng Q, Cui TJ (2010) Virtual conversion from metal object to dielectric object using metamaterials. Opt Express 18:11276
37. Chen HY, Luo XD, Ma HR, Chan CT (2008) The anti-cloak. Opt Express 16:14603
38. Liang ZX, Lin XL, Jiang XY (2010) Remote control of light behavior by transformation optical devices. Opt Express 18:2049
39. Liu R, Ji C, Mock JJ, Chin JY, Cui TJ, Smith DR (2009) Broadband ground-plane cloak. Science 323:366
40. Valentine J, Li J, Zentgraf T, Bartal G, Zhang X (2009) An optical cloak made of dielectrics. Nat Mater 8:568
41. Gabrielli LH, Cardenas J, Poitras CB, Lipson M (2009) Silicon nanostructure cloak operating at optical frequencies. Nat Photon 3:461
42. Ergin T, Stenger N, Brenner P, Pendry JB, Wegener M (2010) Three-dimensional invisibility cloak at optical wavelengths. Science 328:337
43. Ma HF, Cui TJ (2010) Three-dimensional broadband ground-plane cloak made of metamaterials. Nat Comm 1:21
44. Li C, Meng XK, Liu X, Li F, Fang GY, Chen HY, Chan CT (2010) Experimental realization of a circuit-based broadband illusion-optics analogue. Phys Rev Lett 105:233906
45. Jiang WX, Cui TJ (2011) Radar illusion via metamaterials. Phys Rev E 83:026601
46. Li C, Liu X, Liu GG, Li F, Fang GY (2011) Experimental demonstration of illusion optics with "external cloaking" effects. Appl Phys Lett 84:084104

47. Chen HY, Chan CT, Sheng P (2010) Transformation optics and metamaterials. Nat Mater 9:387
48. Kundtz NB, Smith DR, Pendry JB (2011) Electromagnetic design with transformation optics. Proc IEEE 99:1622
49. Wegener M, Linden S (2010) Shaping optical space with metamaterials. Phys Today 63:32
50. Liu YM, Zhang X (2011) Metamaterials: a Frontier of science and technology. Chem Soc Rev 40:2494
51. Pendry JB (2009) All smoke and metamaterials. Nature 460:579
52. Leonhardt U, Tyc T (2009) Broadband invisibility by non-euclidean cloaking. Science 323:110
53. Genov DA, Zhang S, Zhang X (2009) Mimicking celestial mechanics in metamaterials. Nat Phys 5:687–692
54. Greenleaf A, Kurylev Y, Lassas M, Uhlmann G (2007) Electromagnetic wormholes and virtual magnetic monopoles from metamaterials. Phys Rev Lett 99:183901
55. Milton GW, Briane M, Willis JR (2006) On cloaking for elasticity and physical equations with a transformation invariant form. New J Phys 8:248
56. Chen HY, Chan CT (2010) Acoustic cloaking and transformation acoustics. J Phys Conden Phys 43:113001
57. Zhang S, Xia CG, Fang N (2011) Broadband acoustic cloak for ultrasound waves. Phys Rev Lett 106:024301
58. Popa BI, Zigoneanu L, Cummer SA (2011) Experimental acoustic ground cloak in air. Phys Rev Lett 106:253901
59. Farhat M, Guenneau S, Enoch S (2009) Ultrabroadband elastic cloaking in thin plates. Phys Rev Lett 103:024301
60. Stenger N, Wilhelm M, Wegener M (2012) Experiments on elastic cloaking in thin plates. Phys Rev Lett 108:014301

Chapter 6
Transformation-Based Cloak/Anti-Cloak Interactions: A Review

Giuseppe Castaldi, Vincenzo Galdi, Andrea Alù and Nader Engheta

Abstract The intriguing concept of "anti-cloaking" was originally introduced within the framework of transformation optics (TO) as a "countermeasure" to invisibility-cloaking, i.e., to restore the scattering response of a cloaked target. More recently, its relevance was also suggested in applications to "sensor invisibility," i.e., to strongly reduce the scattering response while maintaining the field-sensing capabilities. In this chapter, we review our recent studies on two-dimensional (cylindrical) and three-dimensional (spherical) canonical scenarios. More specifically, via generalized (coordinate-mapped) Bessel-Fourier and Mie-series approaches, we address the analytical study of plane-wave-excited configurations featuring a cylindrical or spherical object surrounded by a TO-based invisibility cloak coupled to an anti-cloak via a vacuum layer, and explore the various interactions of interest. Via a number of selected examples, we illustrate the cloaking and field-restoring capabilities of various configurations, with special emphasis on the scattering versus absorption tradeoff, as well as possible ideas for approximate implementations that do not require the use of *double-negative* media.

G. Castaldi · V. Galdi
Waves Group, Department of Engineering, University of Sannio,
Corso Garibaldi 107 82100 Benevento, Italy
e-mail: castaldi@unisannio.it

V. Galdi
e-mail: vgaldi@unisannio.it

A. Alù (✉)
Department of Electrical and Computer Engineering, The University of Texas at Austin,
1 University Station, C0803, Austin, TX 78712, USA
e-mail: alu@mail.utexas.edu

N. Engheta
Department of Electrical and Systems Engineering, University of Pennsylvania,
200 South 33rd Street, Moore Building, Philadelphia, PA 19104, USA
e-mail: engheta@ee.upenn.edu

D. H. Werner and D.-H. Kwon (eds.), *Transformation Electromagnetics and Metamaterials*, DOI: 10.1007/978-1-4471-4996-5_6,

6.1 Introduction and Background

The past few years have witnessed a renewed interest in the development of approaches to achieve invisibility ("cloaking") of penetrable or impenetrable objects to an electromagnetic (EM) illumination. Thanks to the rapid advances in the engineering of special materials and "metamaterials," it is possible, in principle, to design a material "shell" capable of suppressing the overall (near- and far-field) scattering response of an inner object to be concealed, though with more or less severe restrictions in the frequency and polarization of the illumination.

In what follows, we will be mainly concerned in the *transformation-optics* (TO) approach [1, 2], which has emerged as a powerful and systematic framework for designing metameterials with desired field-manipulation capabilities (see, e.g., [3] for a recent review). TO-based cloaking strategies, successfully demonstrated experimentally at various (e.g., microwave [4] and optical [5]) frequencies, rely on the intuitive geometric idea of suitably bending the ray trajectories so as to re-route the energy around the object to be concealed. In this approach, the desired field distribution is designed in a fictitious curved coordinate space characterized by a "hole." Thanks to the formal invariance of Maxwell's equations under coordinate transformations, such field distribution may be equivalently obtained in a conventionally flat, Cartesian space, filled by a suitably anisotropic and spatially inhomogeneous "transformation medium" whose constitutive tensors may be systematically derived [1, 2]. The reader is referred to [6–13] for alternative approaches to invisibility cloaking and to [14, 15] for comparative studies.

In spite of the above-mentioned ray-optical intuitive interpretation, the applicability of TO-based cloaking is not necessarily limited to the asymptotic high-frequency regime. Actually, a series of analytical studies on canonical (cylindrical, spherical) geometries [16–19] have rigorously proved that, in the ideal limit (implying lossless, nondispersive, extreme-parameter transformation media) *complete isolation* (i.e., no power exchange) would be achieved between the inside and outside regions, at *any* frequency.

However, for the two-dimensional (2-D) cylindrical scenario, Chen et al. [20] showed that the cloaking effect on a *double positive* (DPS, with positive permittivity and permeability components) object may, in principle, be totally or partially compensated by inserting in the cloaked region a complementary-designed *double-negative* (DNG, i.e., with negative permittivity and permeability components) transformation medium. Such effect was accordingly termed "anti-cloaking."

Expanding upon this concept, in a series of recent studies [21–23], we have studied more general 2-D (cylindrical) and 3-D (spherical) scenarios, with cloak and anti-cloak not necessarily contiguous, and the anti-cloak not necessarily DNG. From these studies, it emerged that the anti-cloak concept could find other interesting applications (besides the originally proposed cloaking "countermeasure"), especially within the emerging framework of "sensor invisibility" [24–27], where one is interested in reducing the visibility (i.e., scattering) of a sensor without compromising its sensing (i.e., absorption) capabilities. Moreover, we have also

explored possible ideas for approximate anti-cloak implementations entirely based on DPS media, which would remove some of the most significant fabrication challenges.

This chapter contains a review of the above results, and is structured accordingly around two main Sects. 6.2 and 6.3, which summarize the essential analytical derivations and representative results for the cylindrical and spherical scenarios. Finally, Sect. 6.4 contains some brief concluding remarks and hints for future research.

6.2 Two-Dimensional Cloak/Anti-Cloak Interactions

6.2.1 Cylindrical Problem Geometry and Formulation

We begin considering a 2-D scenario in the auxiliary space (x', y', z') in Fig. 6.1a, consisting of an isotropic, homogeneous circular cylinder of radius R_2, with dielectric permittivity ε_1 and magnetic permeability μ_1, immersed in vacuum, which may be conveniently parameterized in the associated cylindrical (r', ϕ', z') reference system in terms of the permittivity and permeability distributions

$$\begin{aligned} \varepsilon'(r') &= \begin{cases} \varepsilon_1, & 0 < r' < R_2 \\ \varepsilon_0, & r' > R_2 \end{cases}, \\ \mu'(r') &= \begin{cases} \mu_1, & 0 < r' < R_2 \\ \mu_0, & r' > R_2 \end{cases}, \end{aligned} \tag{6.1}$$

with ε_0 and μ_0 denoting the vacuum dielectric permittivity and magnetic permeability, respectively. We then consider a *piecewise-linear* radial coordinate transformation (see Fig. 6.1b) to the actual physical space (x, y, z) (and associated (r, ϕ, z) reference system)

$$r' = f(r) = \begin{cases} r, & r < R_1, \quad r > R_4, \\ R_1 \left(\frac{R_2 + \Delta_2 - r}{R_2 + \Delta_2 - R_1} \right), & R_1 < r < R_2, \\ R_4 \left(\frac{r - R_3 + \Delta_3}{R_4 - R_3 + \Delta_3} \right), & R_2 < r < R_4, \end{cases} \tag{6.2}$$

which can assume arbitrary (but negative) values within the region $R_2 < r < R_3$.

Apart from the parameters Δ_2 and Δ_3 (assumed as *negligibly small* hereafter), the mappings pertaining to the layers $R_3 < r < R_4$ and $R_1 < r < R_2$ are readily recognized to generate an invisibility cloak [4] and anti-cloak [20], respectively. More specifically, while the cloak transformation compresses the cylindrical region $r < R_4$ into the concentric annular layer $R_3 < r < R_4$, thereby creating a "hole" of radius R_3, the somehow *reverse* anti-cloak transformation creates an "anti-hole" of radius $R_2 > R_1$ around the cylinder of radius R_1. This results in a four-layer cylindrical configuration of radii R_ν, $\nu = 1, \ldots, 4$ (see Fig. 6.1c),

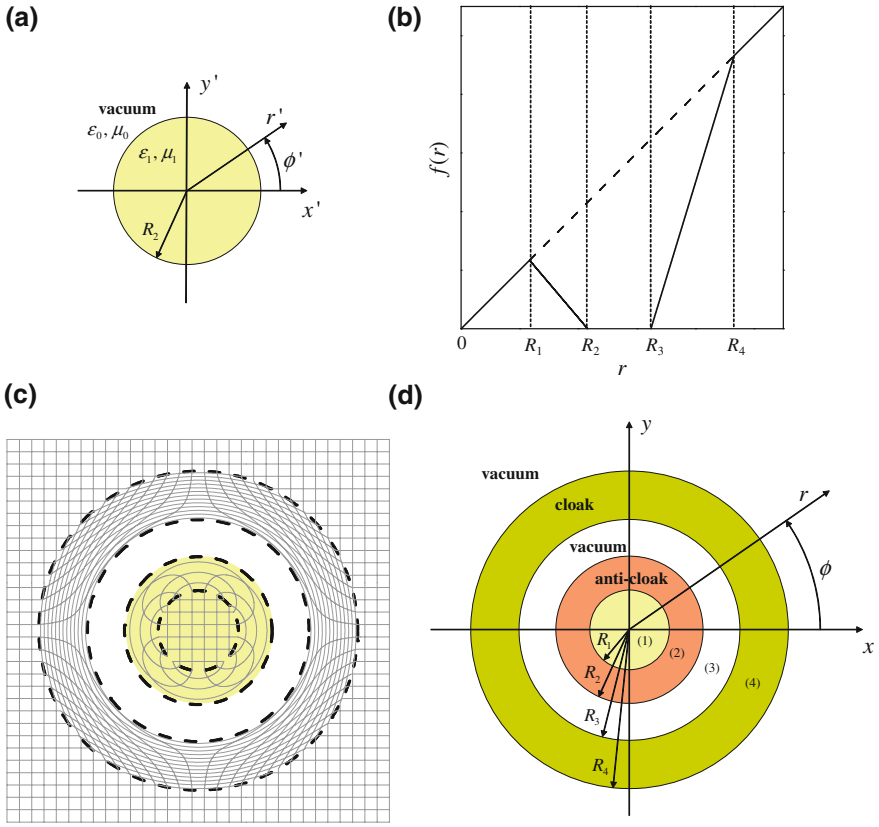

Fig. 6.1 Geometry of the problem. **a** Homogeneous *circular cylinder* in the auxiliary space. **b** Radial coordinate transformation, as in (6.2). Note that, in view of the vanishingly small character of the Δ_2 and Δ_3 parameters, the plotted case is hardly distinguishable from the ideal case. **c** Topological interpretation of the mapping, with curved coordinates in the transformed regions. **d** Alternative interpretation of the mapping in a globally flat, Cartesian space, with cloak—and anti-cloak-type transformation media. Reprinted from Castaldi et al. [21], with permission from the Optical Society of America

characterized by *curved coordinates* within the transformed regions $R_3 < r < R_4$ (cloak) and $R_1 < r < R_2$ (anti-cloak), and regular flat, Cartesian metrics within the regions $r < R_1$ and $r > R_4$. Interestingly, the layer $R_2 < r < R_3$ does not admit any physical image (i.e., $r' > 0$) in the auxiliary (x', y', z') space, thereby constituting a "cloaked" region *inaccessible* to the EM fields.

Within the TO framework, the above behavior may be equivalently obtained in a *globally flat* space with the transformed regions filled up by anisotropic, spatially inhomogeneous transformation media, whose relevant constitutive tensor components (in cylindrical coordinates) are given by Pendry et al. [2]

$$\begin{cases} \varepsilon_r(r) = \dfrac{\varepsilon'(r')}{\dot{f}(r)}\left(\dfrac{r'}{r}\right), \quad \varepsilon_\phi(r) = \varepsilon'(r')\dot{f}(r)\left(\dfrac{r}{r'}\right), \\ \mu_z(r) = \mu'(r')\dot{f}(r)\left(\dfrac{r'}{r}\right), \end{cases} \tag{6.3}$$

where the overdot denotes differentiation with respect to the argument, and a transverse-magnetic (TM) polarization (i.e., magnetic field parallel to the coaxial cylinders) is assumed.

To sum up, the scenario of interest in Fig. 6.1d comprises of a homogeneous, isotropic cylinder of radius R_1 and constitutive parameters $\varepsilon_1,\ \mu_1$, surrounded by the anti-cloak ($R_1 < r < R_2$) and cloak ($R_3 < r < R_4$) transformation-medium layers (6.3), separated by a vacuum gap $R_2 < r < R_3$. In the limit $\Delta_2, \Delta_3 \to 0$, this vacuum gap is cloaked and, in view of the matching conditions at the interfaces $r = R_4$ and $r = R_1$, no field is scattered in the region $r > R_4$. Moreover, the *non-monotonic* transformation (6.2) maps the interfaces bounding the cloaked layer ($r = R_2$ and $r = R_3$) in the same point $r' = 0$ in the auxiliary space (see Fig. 6.1b), thereby implying a counterintuitive mechanism of field transfer between these interfaces, via the "tunneling" through the cloaked layer.

In view of the negative slope of the transformation (6.2) in the anti-cloak layer $R_1 < r < R_2$, the corresponding constitutive parameters (6.3) are *opposite in sign* to those of the inner cylinder $(\varepsilon_1,\ \mu_1)$. This suggests *four* possible configurations of interest, involving the possible combinations of DPS and DNG, or alternatively *epsilon-negative* (ENG) and *mu-negative* (MNG) media.

In what follows, we review the EM (scattering and absorption) response of the above cloak/anti-cloak configuration under plane-wave illumination.

6.2.2 Review of Main Analytical Derivations

6.2.2.1 General Solution

Assuming a time-harmonic $(\exp(-i\omega t))$, TM-polarized plane-wave impinging from the positive x-direction, it is expedient to represent the incident magnetic field in the associated (r, ϕ, z) cylindrical coordinate system in terms of a Fourier-Bessel series:

$$\boldsymbol{H}^i(r,\phi) = \exp(ik_0 x)\hat{\boldsymbol{u}}_z = \sum_{n=-\infty}^{\infty} i^n J_n(k_0 r)\exp(in\phi)\hat{\boldsymbol{u}}_z, \tag{6.4}$$

where $k_0 = \omega\sqrt{\varepsilon_0\mu_0} = 2\pi/\lambda_0$ denotes the vacuum wavenumber (with λ_0 being the corresponding wavelength), and J_n denotes the nth-order Bessel function of the first kind [28]. In (6.4), and henceforth, boldface symbols identify vector quantities, and $\hat{\boldsymbol{u}}_\alpha$ denotes an α-directed unit vector. In [21], we worked out an analytical

calculation of the EM field in the four-layer configuration of Fig. 6.1d, based on the approaches originally proposed in [16–18, 29], whose main results are summarized below. The magnetic field in the various regions of Fig. 6.1d can be expressed in terms of a Bessel-Fourier series

$$H(r,\phi)=\sum_{n=-\infty}^{\infty}\left\{\left(a_n^{(v)}+\delta_{v5}i^n\right)J_n[g(r)]+b_n^{(v)}Y_n[g(r)]\right\}\exp(in\phi)\hat{\boldsymbol{u}}_z, \quad R_{v-1}<r<R_v,\quad v=1,\ldots 5, \tag{6.5}$$

where $a_n^{(v)}$ and $b_n^{(v)}$ are the expansion coefficients, $R_0=0$ and $R_5=\infty$ represent "dummy" parameters introduced for notational convenience, Y_n denotes the nth-order Bessel function of the second kind [28], δ_{pq} is the Kronecker delta [accounting for the plane-wave illumination, (6.4)], and

$$g(r)=\begin{cases} k_0 r, R_2<r<R_3, \\ \omega\sqrt{\varepsilon'[f(r)]\mu'[f(r)]}f(r), \quad r<R_2,\ r>R_3. \end{cases} \tag{6.6}$$

Referring the reader to Castaldi et al. [21] for details on the calculation of the expansion coefficients (via enforcement of the proper boundary and field-finiteness/continuity conditions, in the limit $\Delta_{2,3}\to 0$), the final relevant results can be summarized as follows:

$$b_n^{(4,5)}=ia_n^{(4,5)},\quad a_n^{(4)}=i^n+ia_n^{(5)},\quad b_n^{(1,2)}=0,\quad a_n^{(2)}=a_n^{(1)}, \tag{6.7}$$

$$a_0^{(1,3,5)}\sim b_0^{(3)}\sim O\left(\frac{1}{\log\Delta_3}\right), \tag{6.8}$$

$$a_n^{(1)}\sim O\left(\frac{\Delta_3^{|n|}}{\Delta_2^{|n|}}\right),\quad a_n^{(3)}\sim b_n^{(3)}\sim O\left(\Delta_3^{|n|}\right),\quad a_n^{(5)}\sim O\left(\Delta_3^{2|n|}\right),\quad n\neq 0, \tag{6.9}$$

where the Landau asymptotic notation $O(\cdot)$ is used in order to focus on the *scaling laws* (for $\Delta_{2,3}\to 0$), neglecting irrelevant constants and higher order terms. From (6.7) to (6.9), it is evident that, letting the parameters Δ_2 and Δ_3 go to zero while keeping their ratio *finite*, the expansion coefficients pertaining to the gap layer and to the exterior region can be made *vanishingly small*, while maintaining the ($n\neq 0$) coefficient pertaining to the inner region *nonzero*. In other words, as intuitively anticipated, the incident field can couple to the inner region $r<R_1$, tunneling through the cloaked layer $R_2<r<R_3$, and without exterior scattering.

Overall, the above results indicate the possibility of judiciously tailoring the competing cloaking and anti-cloaking effects so as to effectively cloak a region of space while maintaining the capability of somehow "sensing" the outside field from the inside. Similar ideas were recently explored in [24–27] within the suggestive framework of "sensor invisibility."

6.2.2.2 Effects of Permittivity Mismatch

In a sensor-cloaking scenario, the inner region $r<R_1$ is filled by an absorbing target (mimicking a sensor or a detector) and, thus, different from the above scenario, is not matched with the surrounding anti-cloak. Therefore, it makes sense to study the effects of a slightly mismatched electrical permittivity,

$$\bar{\varepsilon}_1 = (1+\Delta_\varepsilon)^2 \varepsilon_1, \tag{6.10}$$

of the target, with the small term Δ_ε parameterizing such mismatch. Referring the reader to Castaldi et al. [22] for details, below we summarize the results from a perturbative study:

$$\begin{gathered} \bar{b}_n^{(1)} = 0, \quad \bar{b}_n^{(4,5)} = i\bar{a}_n^{(4,5)}, \quad \bar{a}_n^{(4)} = i^n + i\bar{a}_n^{(5)}, \quad \bar{b}_n^{(2)} \sim \bar{a}_n^{(1)} O(\Delta_\varepsilon), \\ \bar{a}_n^{(2)} \sim \bar{a}_n^{(1)}[1+O(\Delta_\varepsilon)], \end{gathered} \tag{6.11}$$

$$\bar{a}_n^{(1)} \sim \frac{a_n^{(1)}}{1+O_n}, \quad \left\{ \begin{array}{c} \bar{a}_n^{(3,5)} \\ \bar{b}_n^{(3)} \end{array} \right\} \sim \left\{ \begin{array}{c} a_n^{(3,5)} \\ b_n^{(3)} \end{array} \right\} \left(\frac{1+O_n}{1+O_n} \right), \tag{6.12}$$

where the "overbar" denotes the expansion coefficients pertaining to the mismatched configuration, and

$$O_n = \begin{cases} O(\Delta_\varepsilon \log \Delta_3), & n=0, \\ O\left(\Delta_\varepsilon \Delta_3^{-2|n|}\right), & n \neq 0. \end{cases} \tag{6.13}$$

From (6.11) to (6.13), it is observed that the mismatch does not affect the cloaking function, but it deteriorates the anti-cloaking capability of restoring the field inside the target region. This implies that, for increasing mismatch levels, the cloaking effect eventually prevails, and the sensing capability is lost.

6.2.2.3 Effects of the Vacuum Gap

It is also insightful to study the effects of the vacuum gap $R_2<r<R_3$ in the EM response. While a general parameterization is not easy to achieve, it is interesting to focus on the limiting case

$$R_3 = (1+\Delta_G) R_2, \tag{6.14}$$

with the term Δ_G parameterizing a vanishingly small gap. Referring once again the reader to our work [22] for details, we obtained the relevant expansion coefficients in the target and exterior regions

$$a_n^{(1)} \sim \begin{cases} \dfrac{1}{1 + O(\Delta_G \log \Delta_3)}, & n = 0, \\ \dfrac{2i^n \gamma^{|n|} \varepsilon_1}{(\varepsilon_1 + \varepsilon_0)} \left(\dfrac{\Delta_3}{\Delta_2}\right)^{|n|} + O\left(\Delta_3^{2|n|}\right) + O(\Delta_G), & n \neq 0, \end{cases} \tag{6.15}$$

$$a_n^{(5)} \sim \begin{cases} \dfrac{O\left(\Delta_G \log^{-1} \Delta_3\right)}{O(\Delta_G) + O\left(\log^{-1} \Delta_3\right)}, & n = 0, \\ O\left(\Delta_3^{2|n|}\right)[1 + O(\Delta_G)], & n \neq 0, \end{cases} \tag{6.16}$$

where

$$\gamma = \frac{\sqrt{\varepsilon_0 \mu_0} R_4 (R_2 - R_1)}{\sqrt{\varepsilon_1 \mu_1} R_1 (R_4 - R_3)}. \tag{6.17}$$

From (6.15) to (6.17), we observe that, in the vanishing-gap limit, the scattered field maintains its vanishingly small character, whereas, in connection with the field coupled to the target region, the zeroth-order coefficient may be now recovered by letting $\Delta_G \to 0$ faster that $\log^{-1} \Delta_3$. In fact, assuming $\Delta_G = 0$ (i.e., $R_3 = R_2$) and enforcing the continuity of the transformation in (6.2), i.e., $f\left(R_2^+\right) = f\left(R_2^-\right)$, we obtain

$$\frac{R_1 \Delta_2}{R_2 + \Delta_2 - R_1} = \frac{R_4 \Delta_3}{R_4 + \Delta_3 - R_3}, \tag{6.18}$$

which, in the limit $\Delta_{2,3} \to 0$ reduces to

$$\gamma = \frac{\sqrt{\varepsilon_0 \mu_0}}{\sqrt{\varepsilon_1 \mu_1}} \left(\frac{\Delta_2}{\Delta_3}\right). \tag{6.19}$$

For a vacuum inner region ($\varepsilon_1 = \varepsilon_0, \quad \mu_1 = \mu_0$), this yields

$$a_n^{(1)} = i^n, \tag{6.20}$$

which, by comparison with (6.4), indicates that the impinging plane wave is completely restored in the inner region, i.e., the anti-cloak *perfectly compensates* the cloak, consistently with the results in [20]. However, for media different from vacuum, the field coupled to the inner region is a distorted version of the impinging one.

6.2.3 Review of Representative Numerical Results

6.2.3.1 Cloaking of Multiply Connected Regions

We start considering a configuration with a DPS (vacuum) inner cylinder ($\varepsilon_1 = \varepsilon_0, \ \mu_1 = \mu_0$) of radius $R_1 = 0.4\lambda_0$, surrounded by a DPS cloak and a DNG

anti-cloak with $R_2 = 0.75\lambda_0$, $R_3 = 1.7\lambda_0$, $R_4 = 2.5\lambda_0$, $\Delta_2 = R_2/200$, $\Delta_3 = R_3/200$, and very slight losses ($\tan\delta = 10^{-4}$). Figure 6.2a shows the real part of the magnetic field-map computed, while Fig. 6.2b shows a magnified detail with the normalized Poynting vector map superimposed. Basically, in the exterior region $r > R_4$, the picture resembles that of the conventional cloak, with quite low scattering and mild distortion of the original planar wavefronts. Inside the cloak, the anti-cloak and the inner cylinder form a "resonating cavity" which, via the vanishingly small coupling through the cloaked layer, is able to restore a modal field.

Similar results may be observed for the other three possible combinations (DPS-DNG, ENG-MNG, MNG-ENG) of cloak and anti-cloak parameters (see Castaldi et al. [21] for details).

In order to better illustrate the phenomenon, it is insightful to consider the possible presence of penetrable objects inside the cloaked layer. Referring to the scenario and parameters of Figs. 6.2, 6.3 shows the field maps in the presence of a dielectric coaxial annular layer of radii $R_a = \lambda_0$ and $R_b = 1.5\lambda_0$ (shown dashed), and permittivity $\varepsilon_{\text{obj}} = 2\varepsilon_0$ ($\tan\delta = 10^{-4}$). This configuration is also amenable to analytical treatment, via straightforward generalization of (6.5). It can be observed, also by comparison with Fig. 6.2, that the dielectric annular layer is effectively cloaked. This indicates the possibility of achieving *selective* cloaking of a *multiply connected* penetrable object.

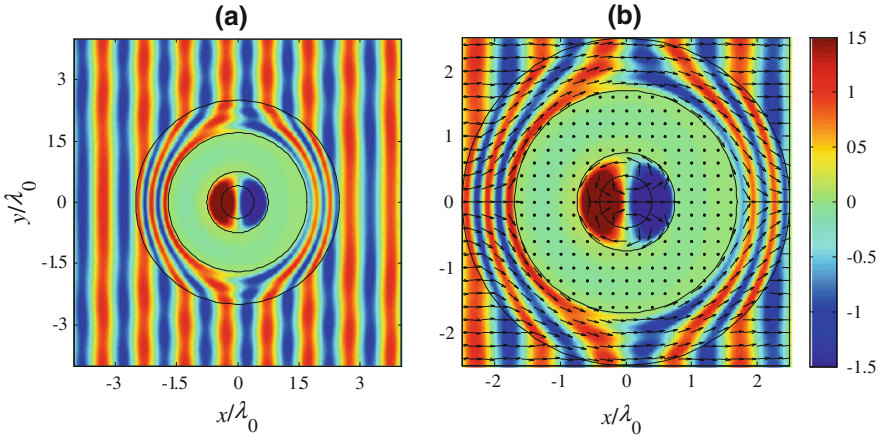

Fig. 6.2 **a** Magnetic field (real part) map for a configuration featuring a vacuum ($\varepsilon_1 = \varepsilon_0$, $\mu_1 = \mu_0$) *inner* cylinder and a DNG anti-cloak, with $R_1 = 0.4\lambda_0$, $R_2 = 0.75\lambda_0$, $R_3 = 1.7\lambda_0$, $R_4 = 2.5\lambda_0$, $\Delta_2 = R_2/200$, $\Delta_3 = R_3/200$, and $\tan\delta = 10^{-4}$. **b** Magnified view with a superimposed map of the real part of the Poynting vector (normalized in the uncloaked regions, so that it is only indicative of the power flow direction) Reprinted from Castaldi et al. [21] with permission from the Optical Society of America

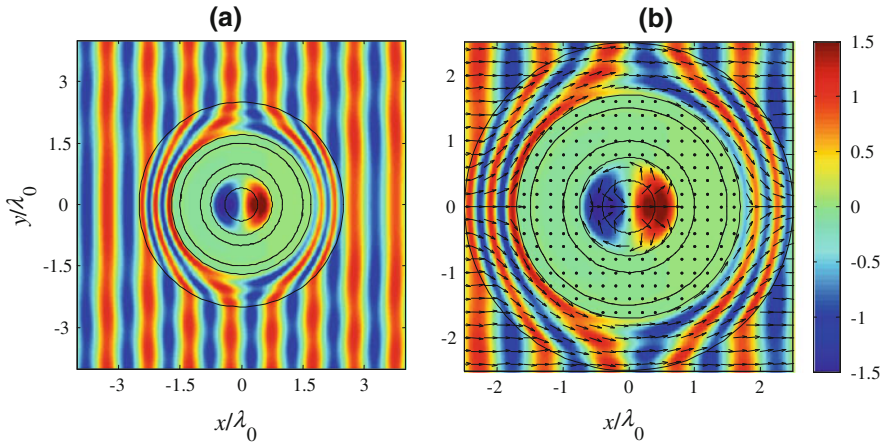

Fig. 6.3 As in Fig. 6.2, but with a dielectric coaxial annular layer of radii $R_a = \lambda_0$ and $R_b = 1.5\lambda_0$ (shown *dashed*) and permittivity $\varepsilon_{obj} = 2\varepsilon_0$ $(\tan\delta = 10^{-4})$ inside the cloaked layer. Reprinted from Castaldi et al. [21], with permission from the Optical Society of America

6.2.3.2 Scattering Versus Absorption Tradeoff: Sensor Cloaking

In order to explore to what extent a cloak/anti-cloak configuration may be exploited for sensing purposes, it is insightful to study the power absorption versus scattering tradeoff in the presence of a *slightly lossy* dielectric target in the region $r < R_1$. Recalling the results in Sect. 6.2.2.3, the vanishing-gap configuration would appear particularly well suited to this scenario, since it allows the recovery of the (otherwise logarithmically vanishing) zeroth-order terms in the Fourier-Bessel expansion of the transmitted field (and thus, in principle, a higher power absorption), while keeping the scattered field vanishingly small. In [22], we carried out a comprehensive parametric study (within and beyond the asymptotic limits $\Delta_{2,3,G,\varepsilon} \to 0$) in order to identify the "optimal" parameter configurations and possible tradeoffs, also in the more realistic case of slightly lossy cloak and anti-cloak. The overall scattering and absorption responses may be conveniently parameterized in terms of the total scattering cross-sectional width Q_s [25] and the time-averaged power P_a (per unit length along the z-axis) in the target region,

$$Q_s = \frac{2\lambda_0}{\pi} \sum_{n=-\infty}^{\infty} \left|\bar{a}_n^{(5)}\right|^2, \quad P_a = \frac{\omega \mathrm{Im}(\bar{\varepsilon}_1)}{2} \int_0^{R_1} r\mathrm{d}r \int_0^{2\pi} \mathrm{d}\phi |E(r,\phi)|^2, \tag{6.21}$$

with E denoting the local electric field (which may be obtained from (6.5) via the relevant Maxwell's curl equation).

With reference to a small dielectric (lossy) target with $R_1 = \lambda_0/8$ and $\varepsilon_1 = (4 + i0.25)\varepsilon_0$, Fig. 6.4 shows the two observables in (6.21) (in decibel scale, normalized to the values pertaining to the free-standing target in vacuum) as a function of the parameters Δ_2 and Δ_3, for $R_2 = \lambda_0/2$, $R_3 = (1 + \Delta_G)R_2$, $R_4 = \lambda_0$,

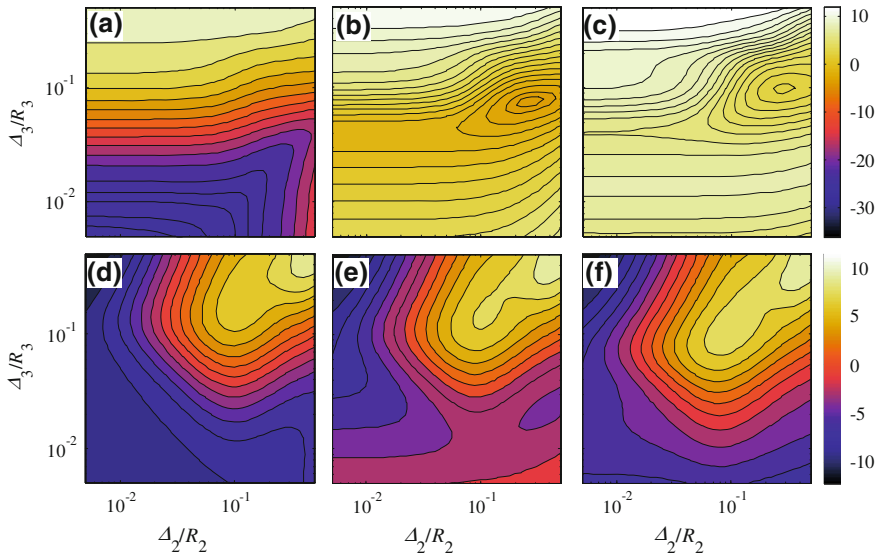

Fig. 6.4 Geometry as in Fig. 6.1a, with $\bar{\varepsilon}_1 = (4 + i0.25)\varepsilon_0$, $\mu_1 = \mu_0$, $R_1 = \lambda_0/8$, $R_2 = \lambda_0/2$, $R_3 = (1 + \Delta_G)R_2$, $R_4 = \lambda_0$, assuming a loss-tangent of 0.001 for the cloak and 0.01 for the anti-cloak. **a–c** Total scattering cross-sectional width in (6.21) normalized by the reference value in vacuum, in decibel scale, as a function of Δ_2/R_2 and Δ_3/R_3, for values of the gap-thickness parameter $\Delta_G = 0,\ 1/50,\ 1/25$, respectively. **d–f** Corresponding time-averaged dissipative power normalized by the reference value in vacuum. Reprinted from Castaldi et al. [22] with permission from the Optical Society of America

and three representative values of the vacuum gap thickness Δ_G, assuming a loss tangent of 0.001 for the (DPS) cloak shell, and 0.01 for the (DNG) anti-cloak shell. In agreement with our prediction from the analytical study in Sect. 6.2.2.3, the case in the absence of the gap turns out to be the most effective in terms of scattering reduction. However, it can be observed that the maximum scattering reduction generally does not coincide with the maximum absorption, and different parameter choices are possible (including *super-scattering* [30] and *super-absorption* [31] configurations, which are not of direct interest for this investigation). This is better explained and quantified in the tradeoff curves shown in Fig. 6.5, which, for a given value of the (normalized) scattering response $\bar{Q}_s$ yield the largest (normalized) absorption response $\bar{P}_a$ attainable for various values of the target loss levels. In particular, they illustrate how, in the absence of the gap and varying Δ_2 and Δ_3, it is possible to span the entire range of cloak/anti-cloak interactions, going from a regime featuring weak scattering and weak absorption (i.e., cloak-prevailing) to one featuring scattering and absorption levels comparable with those in vacuum (i.e., anti-cloak compensating the cloak). In between, there is a regime where it is possible to attain weak (though not weakest) scattering accompanied by sensible (though weaker than in vacuum) absorption. Thus, for instance, assuming $\mathrm{Im}(\bar{\varepsilon}_1) = 0.25\varepsilon_0$ (full square markers), and accepting a scattering reduction of

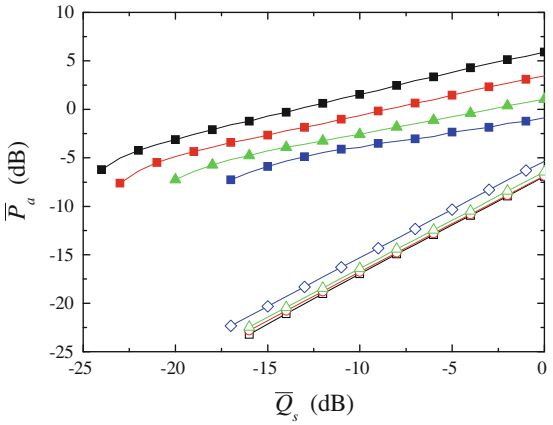

Fig. 6.5 Tradeoff curves (*full markers*) pertaining to the cloak/anti-cloak configuration in Fig. 6.4, for various values of the target loss levels (*squares*, *circles*, *triangles*, *diamonds*: $\mathrm{Im}(\bar{\varepsilon}_1) = 0.25\varepsilon_0,\quad 0.5\varepsilon_0,\quad \varepsilon_0,\quad 2\varepsilon_0$, respectively). Also shown (*empty markers*), as references, are the corresponding curves pertaining to an imperfect (lossless) cloak configuration (6.23). Reprinted from Castaldi et al. [22] with permission from the Optical Society of America

about 20 dB, one may achieve an absorption response nearly 3 dB below the reference case in vacuum.

For a deeper understanding of this somehow counterintuitive behavior, it is instructive to look at the analytical structure of the *total absorption cross-sectional width* [25]

$$Q_a = -\frac{2\lambda_0}{\pi}\sum_{n=-\infty}^{\infty}\left\{\left|\bar{a}_n^{(5)}\right|^2 + \mathrm{Re}\left[i^n \bar{a}_n^{(5)}\right]\right\}, \tag{6.22}$$

which is representative of the target absorption only in the ideal case of a lossless cloak and anti-cloak. By comparison with the total scattering cross-sectional width Q_s in (6.21), we note that, although Q_a must *asymptotically* vanish in the limit of zero scattering (i.e., $\bar{a}_n^{(5)} \to 0$), such vanishing trend may be *moderately slower* than that of Q_s, in view of the presence of the *linear* terms in (6.22). This explains the possibility of achieving, outside the asymptotic regime, significant scattering reductions while maintaining sensible absorption levels.

In order to better elucidate the role of the anti-cloak, also shown in Fig. 6.5 (empty markers) are the tradeoff curves pertaining to a TO-based imperfect cloak, characterized by the usual transformation

$$r' = f(r) = \begin{cases} r, & r < R_1, \quad r > R_4, \\ R_4\left(\frac{r - R_1 + \Delta_1}{R_4 - R_1 + \Delta_1}\right), & R_1 < r < R_4, \end{cases} \tag{6.23}$$

and same total thickness of the above cloak/anti-cloak configuration. As can be observed, in spite of the qualitatively similar trend, the imperfect-cloak tradeoff

curves (obtained by scanning the parameter Δ_1) are *much steeper*, thereby implying that significant reductions of the scattering can only be obtained at the expenses of comparable reductions in the absorption.

6.3 Three-Dimensional Cloak/Anti-Cloak Interactions

6.3.1 Spherical Problem Geometry and Formulation

Similar to the cylindrical case in Sect. 6.2, we begin considering an auxiliary vacuum space (x', y', z') (and associated spherical (r', θ', ϕ') reference system, Fig. 6.6a) containing a two-layer piecewise-homogeneous, isotropic *spherical* configuration:

$$\begin{aligned} \varepsilon'(r') &= \begin{cases} \varepsilon_1, & 0 < r' < R_1 \\ \varepsilon_2, & R_1 < r' < R_2, \\ \varepsilon_0, & r' > R_2 \end{cases} \\ \mu'(r') &= \begin{cases} \mu_1, & 0 < r' < R_1 \\ \mu_2, & R_1 < r' < R_2, \\ \mu_0, & r' > R_2 \end{cases} \end{aligned} \tag{6.24}$$

to which we apply the piecewise-linear radial mapping (in the associated (r, θ, ϕ) spherical reference system, Fig. 6.6b)

$$r' = f(r) = \begin{cases} r, & r < R_1, \quad r > R_4, \\ R_1' & \left(\frac{R_2 + \Delta_2 - r}{R_2 + \Delta_2 - R_1}\right), \quad R_1 < r < R_2, \\ R_4 & \left(\frac{r - R_3 + \Delta_3}{R_4 - R_3 + \Delta_3}\right), \quad R_3 < r < R_4. \end{cases} \tag{6.25}$$

This yields a four-layer spherical configuration in the actual physical space (x, y, z) (see Fig. 6.6c), which constitutes the 3-D spherical generalization of the cylindrical scenario in Sect. 6.2, and comprises a homogeneous, isotropic sphere (of radius R_1 and constitutive parameters $\varepsilon_1,\ \mu_1$) surrounded by an anti-cloak shell $(R_1 < r < R_2)$ and cloak shell $(R_3 < r < R_4)$ which are separated by a vacuum gap $(R_2 < r < R_3)$. The cloak and anti-cloak constitutive-tensor-components (in spherical coordinates) are given by [2, 18, 29]

$$\begin{cases} \varepsilon_r(r) = \dfrac{\varepsilon'(r')}{\dot{f}(r)} \left(\dfrac{r'}{r}\right)^2, \quad \varepsilon_\theta(r) = \varepsilon_\phi(r) = \varepsilon'(r')\dot{f}(r), \\ \mu_r(r) = \dfrac{\mu'(r')}{\dot{f}(r)} \left(\dfrac{r'}{r}\right)^2, \quad \mu_\theta(r) = \mu_\phi(r) = \mu'(r')\dot{f}(r). \end{cases} \tag{6.26}$$

Also in this scenario, the idea is to suitably tailor (via the small parameters Δ_2 and Δ_3) the competing cloak/anti-cloak effects so as to create an *effectively cloaked* region in the vacuum gap $R_2 < r < R_3$, while still being able to couple a

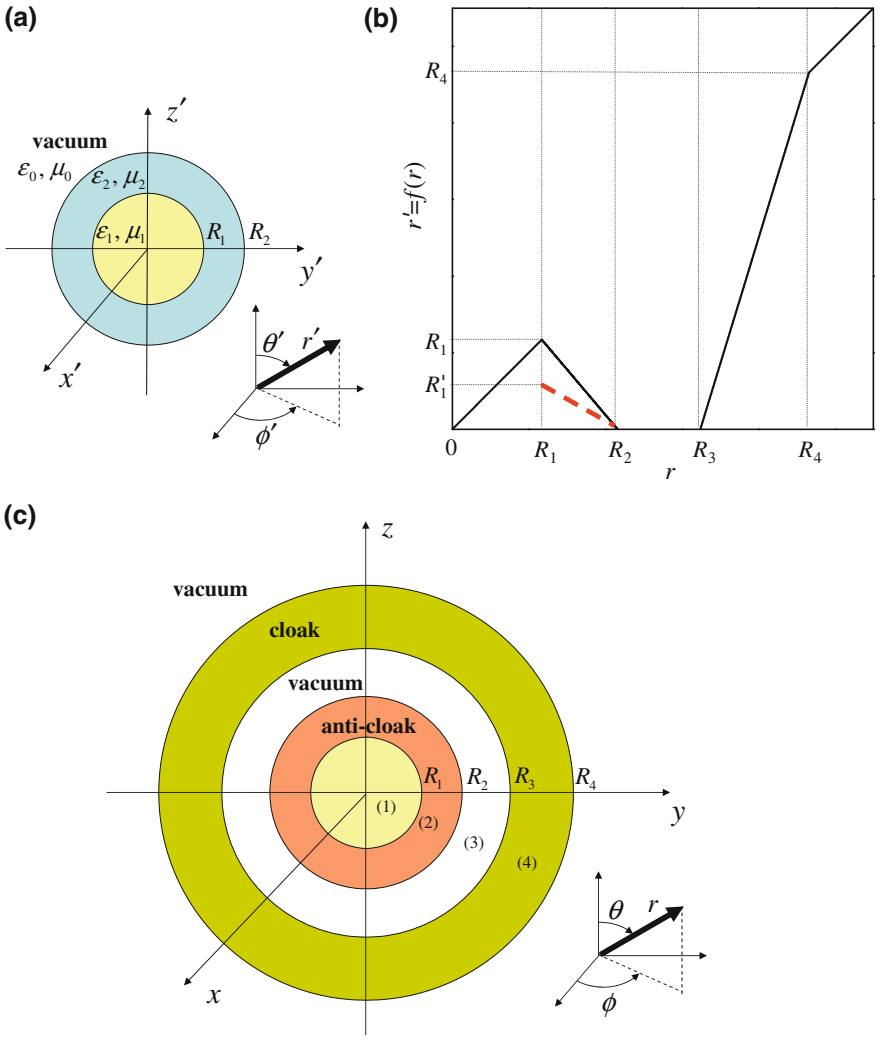

Fig. 6.6 Spherical problem geometry. **a** Two-layer piecewise-homogeneous, isotropic spherical configuration in the fictitious auxiliary space (x', y', z') (and associated (r', θ', ϕ') spherical coordinate system). **b** Piecewise-linear radial coordinate transformation in (6.25) (in the limit $\Delta_{2,3} \to 0$), with the *dashed part* illustrating the discontinuous case considered in Sect. 6.3.3. **c** General cloak/anti-cloak (with vacuum gap) configuration in the actual physical space (x, y, z) (and associated (r, θ, ϕ) spherical coordinate system). Reprinted from Castaldi et al. [23], with permission from Elsevier

non-negligible field in the inner region $r < R_1$. However, different from the cylindrical scenario in Sect. 6.2, we consider here the additional parameters ε_2, μ_2, R_1'. In particular, we note that a choice $R_1' \neq R_1$ renders the mapping in (6.25) *discontinuous* (see Fig. 6.6b). These extra degrees of freedom will be

exploited in one configuration only (see Sect. 6.3.2.3 below), while in all other examples the formal structure in Sect. 6.2 will be preserved by assuming $\varepsilon_2 = \varepsilon_1,\ \mu_2 = \mu_1,\ R_1' = R_1$.

6.3.2 Review of Main Analytical Derivations

6.3.2.1 General Solution

Also in this case, we are interested in characterizing the EM response to a time-harmonic plane-wave illumination. In particular, we assume an x-directed electric field, with incidence from the positive z-direction,

$$\boldsymbol{E}^i(z) = \exp(ik_0 z)\hat{\boldsymbol{u}}_x = \boldsymbol{E}^i_{TE}(r,\theta,\phi) + \boldsymbol{E}^i_{TM}(r,\theta,\phi), \tag{6.27}$$

which is conveniently split in the sum of transverse electric (TE) and magnetic (TM) components. In [23], we calculated an analytical solution, based on the generalized (coordinate-mapped) Mie-series approach proposed in [18, 29], which is compactly summarized below. First, the TE and TM components in (6.27) are represented in terms of scalar Debye potentials [32]:

$$\begin{cases} \boldsymbol{E}^i_{TE} = -\varepsilon_0^{-1}\nabla\times\left(\hat{\boldsymbol{u}}_r\Phi^i_{TE}\right), & \boldsymbol{H}^i_{TE} = -i\omega^{-1}\mu_0^{-1}\nabla\times\boldsymbol{E}^i_{TE}, \\ \boldsymbol{H}^i_{TM} = \mu_0^{-1}\nabla\times\left(\hat{\boldsymbol{u}}_r\Phi^i_{TM}\right), & \boldsymbol{E}^i_{TM} = i\omega^{-1}\varepsilon_0^{-1}\nabla\times\boldsymbol{H}^i_{TM}, \end{cases} \tag{6.28}$$

which admit the following spherical harmonic expansion [32]:

$$\begin{aligned} \Phi^i_{TE}(r,\theta,\phi) &= \sum_{n=1}^{\infty} i^n \frac{2n+1}{n(n+1)}\sin\phi P_n^1(\cos\theta)S_n(k_0 r), \\ \Phi^i_{TM}(r,\theta,\phi) &= \sum_{n=1}^{\infty} i^n \frac{2n+1}{n(n+1)}\cos\phi P_n^1(\cos\theta)S_n(k_0 r), \end{aligned} \tag{6.29}$$

with P_n^m denoting the associated Legendre functions of the first kind, $S_n(x) = xj_n(x)$ the nth-order Riccati-Bessel functions of the first kind, and j_n the nth-order spherical Bessel function of the first kind [28].

The fields in the various regions of Fig. 6.6c are likewise represented in terms of *coordinate-mapped* scalar Debye potentials:

$$\begin{cases} \boldsymbol{E}^{(v)}_{TE} = -\underline{\underline{\varepsilon}}^{-1}\cdot\nabla\times\left(\dot{f}\,\hat{\boldsymbol{u}}_r\Phi^{(v)}_{TE}\right), & \boldsymbol{H}^{(v)}_{TE} = -i\omega^{-1}\underline{\underline{\mu}}^{-1}\cdot\nabla\times\boldsymbol{E}^{(v)}_{TE}, \\ \boldsymbol{H}^{(v)}_{TM} = \underline{\underline{\mu}}^{-1}\cdot\nabla\times\left(\dot{f}\,\hat{\boldsymbol{u}}_r\Phi^{(v)}_{TM}\right), & \boldsymbol{E}^{(v)}_{TM} = i\omega^{-1}\underline{\underline{\varepsilon}}^{-1}\cdot\nabla\times\boldsymbol{H}^{(v)}_{TM}, \\ & R_{v-1} < r < R_v,\ v = 1,..,5, \end{cases} \tag{6.30}$$

$$\begin{cases} \Phi_{TE}^{(v)}(r,\theta,\phi) = & \sum_{n=1}^{\infty} i^n \frac{2n+1}{n(n+1)} \left\{ \left(a_{n,TE}^{(v)} + \delta_{v5} \right) S_n[g(r)] + b_{n,TE}^{(v)} C_n[g(r)] \right\} \sin\phi P_n^1(\cos\theta), \\ \Phi_{TM}^{(v)}(r,\theta,\phi) = & \sum_{n=1}^{\infty} i^n \frac{2n+1}{n(n+1)} \left\{ \left(a_{n,TM}^{(v)} + \delta_{v5} \right) S_n[g(r)] + b_{n,TM}^{(v)} C_n[g(r)] \right\} \cos\phi P_n^1(\cos\theta), \\ & R_{v-1} < r < R_v, \quad v = 1,..,5. \end{cases} \tag{6.31}$$

In (6.30) and (6.31), $a_{n,TE}^{(v)}$, $a_{n,TM}^{(v)}$, $b_{n,TE}^{(v)}$, $b_{n,TM}^{(v)}$ are unknown expansion coefficients, the constitutive tensors $\underline{\underline{\varepsilon}}$ and $\underline{\underline{\mu}}$ are given by (6.26) for the cloak and anticloak layers (and reduce to the appropriate scalar quantities in the regions $R_2 < r < R_3$, $r > R_4$ and $r < R_1$), $C_n(x) = -xy_n(x)$ denote the nth-order Riccati-Bessel functions of the second kind, y_n the nth-order spherical Bessel functions of the second kind [28], and all other quantities are formally defined as in Sect. 6.2.2.1 (but now implying *spherical* coordinates). As for the cylindrical scenario, the expansion coefficients are computed by enforcing the proper boundary and field-finiteness/continuity conditions, in the limit $\Delta_{2,3} \to 0$. In what follows, as in Sect. 6.2, we generally focus on the *scaling laws*, via the use of the asymptotic Landau notation $O(\cdot)$, and, for notational convenience, we omit the TE/TM subfixes since the results not depend on the polarization state.

6.3.2.2 Conventional Configuration

6.3.2.2.1 *With Vacuum Gap*

We start with the *direct* generalization of the cylindrical scenario in Sect. 6.2, by assuming

$$\varepsilon_2 = \varepsilon_1, \ \mu_2 = \mu_1, \ R_1' = R_1, \tag{6.32}$$

Referring the reader to Castaldi et al. [23] for details, we obtain:

$$a_n^{(1)} = a_n^{(2)}, \quad b_n^{(2)} = 0, \quad a_n^{(5)} = ib_n^{(4)}, \ a_n^{(4)} = 1 + ib_n^{(4)}, \tag{6.33}$$

$$a_n^{(1,2)} \sim O\left(\frac{\Delta_3^{n+1}}{\Delta_2^n} \right), \quad a_n^{(3)} \sim b_n^{(3)} \sim O\left(\Delta_3^{n+1} \right), \quad a_n^{(5)} = ib_n^{(4,5)} \sim O\left(\Delta_3^{2n+1} \right). \tag{6.34}$$

From (6.33) and (6.34), we observe that, in the limit $\Delta_3 \to 0$, the coefficients pertaining to the vacuum gap $R_2 < r < R_3$ and to the exterior region $r > R_4$ decay algebraically, thereby implying a *strong field suppression* in those regions. Conversely, the coefficients pertaining to the inner region $r < R_1$ depend on the ratio Δ_3/Δ_2, and thus they may be in principle partially recovered by letting $\Delta_2 \to 0$ *faster* than Δ_3. Therefore, similar to the cylindrical case in Sect. 6.2 (but via a different scaling law of Δ_2 and Δ_3), it is still possible to *effectively cloak* the vacuum gap $R_2 < r < R_3$, with very weak exterior scattering, while coupling to the inner region $r < R_1$ a *distorted* version of the illuminating field.

6.3.2.2.2 *Without Vacuum Gap*

Also in the spherical scenario, it is interesting to consider the case in the absence of the vacuum gap (i.e., $R_3 = R_2$). We found (see [23] for details)

$$a_n^{(1,2)} \sim \frac{O\left(\frac{\Delta_3^n}{\Delta_2^n}\right)}{1 + O\left(\frac{\Delta_2}{\Delta_3}\right)}, \quad a_n^{(5)} = ib_n^{(4,5)} \sim O\left(\Delta_3^{2n+1}\right)\left[\frac{1 + O\left(\frac{\Delta_3}{\Delta_2}\right)}{1 + O\left(\frac{\Delta_3}{\Delta_2}\right)}\right], \tag{6.35}$$

which indicates that, by letting $\Delta_2, \Delta_3 \to 0$ while keeping their ratio *finite*, it is possible to recover, in principle, *all* the coefficients pertaining to the inner region $r < R_1$. Interestingly, the particular choice

$$\frac{\Delta_3}{\Delta_2} = \frac{\sqrt{\varepsilon_1\mu_1}R_1(R_4 - R_3)}{\sqrt{\varepsilon_0\mu_0}R_4(R_2 - R_1)}, \quad \varepsilon_0\mu_1 = \varepsilon_1\mu_0 \tag{6.36}$$

yields

$$a_n^{(1,2)} \sim \sqrt{\frac{\varepsilon_1\mu_1}{\varepsilon_0\mu_0}} = \frac{\varepsilon_1}{\varepsilon_0}, \tag{6.37}$$

which implies that the impinging plane wave can be *perfectly* restored in the inner region $r < R_1$ with controllable amplitude (via the ratio $\varepsilon_1/\varepsilon_0$).

Also in this case, a particularly interesting application of the above configuration is in the framework of "sensor cloaking" [24–27]. In Sect. 6.2, in connection with the cylindrical scenario, we showed analytically (and verified numerically) that the best performance was indeed obtained in the absence of the vacuum gap. Although for the spherical scenario this conclusion cannot be taken for granted and would be rather involved to address, we will show in Sect. 6.3.3 below that a configuration featuring a slightly lossy spherical dielectric particle (mimicking the sensor loading effects) surrounded by a cloak/anti-cloak configuration with no vacuum gap may yield reasonably good performance.

6.3.2.3 Approximate DPS Implementation

As noted previously, the constitutive parameters characterizing the anti-cloak are opposite in sign to those possessed by the medium filling the auxiliary-space region to be transformed. This implies that, for a DPS inner region, a DNG anti-cloak is required, which represents a severe technological challenge. In [33], we proposed an *approximate* anti-cloak implementation based entirely on DPS materials, in connection with a particular class of 2-D transformations similar to those originally introduced in [34] in connection with square-shaped invisibility cloaks. In [23], we explored a different approach, applicable to the spherical scenario of interest, and based on the judicious exploitation of the additional parameters ε_2, μ_2, R_1' purposely introduced in the model (6.24). Within this

framework, the DPS character of the anti-cloak is enforced upfront, by starting with a DNG material in the auxiliary-space region $R_1 < r' < R_2$ (Fig. 6.6a), i.e., choosing $\varepsilon_2 < 0, \mu_2 < 0$, and recalling the *decreasing* character (i.e., $\dot{f} < 0$) of the coordinate-transformation in the anti-cloak layer (see. Fig. 6.6b). The DPS character of the inner spherical region $r < R_1$ is also ensured by keeping $\varepsilon_1 > 0, \mu_1 > 0$. This, however, implies a deleterious (for the anti-cloak function) parameter *mismatch* at the interface $r = R_1$, which can be (at least partially) compensated by purposely introducing a discontinuity of the coordinate transformation at that interface, by choosing $R_1' \neq R_1$ (see Fig. 6.6b). In particular, letting $k_1 = \omega\sqrt{\varepsilon_1\mu_1}$ and $k_2 = \omega\sqrt{\varepsilon_2\mu_2}$, it can be shown (see [23] for details) that instrumental to the anti-cloaking effects are the conditions

$$\frac{\dot{S}_n\left(k_2 R_1'\right)}{S_n\left(k_2 R_1'\right)} = \frac{-|\varepsilon_2|\sqrt{\varepsilon_1\mu_1}\dot{S}_n(k_1 R_1)}{\varepsilon_1\sqrt{\varepsilon_2\mu_2}S_n(k_1 R_1)}, \tag{6.38}$$

which are valid for both TE and TM polarizations provided that $\varepsilon_2/\varepsilon_1 = \mu_2/\mu_1$. For $\varepsilon_2 \neq \varepsilon_1$ and $\mu_2 \neq \mu_1$, the above numerable infinity of transcendental equations cannot be exactly satisfied. Nevertheless, by exploiting the available free (though sign-constrained) parameters $R_1' > 0$, $\varepsilon_1 > 0$, $\mu_1 > 0$, $\varepsilon_2 < 0$, $\mu_2 < 0$, we can still enforce a limited number of them (e.g., those pertaining to the lowest n orders), which results in *approximate* anti-cloaking effects.

The above results indicate that the proposed DPS anti-cloak implementation inherently implies an *imperfect* restoration of the field in the inner spherical region $r < R_1$, also in the absence of the gap. In Sect. 6.3.3 below, we review some representative results, also in connection with sensor cloaking, and compare them with those pertaining to standard implementations.

6.3.3 Review of Representative Numerical Results

We begin considering the conventional cloak/anti-cloak implementation with the vacuum gap (Sect. 6.3.2.2.1), i.e., the direct generalization of the cylindrical results in Sect. 6.2. In all examples presented below, we consider a slight level of losses (loss-tangent = 0.001) in the DPS media, and a higher level (loss-tangent = 0.01) in the DNG media. Figure 6.7a shows the field-map (real part of the electric field x-component) in the y–z plane, for a plane-wave-excited configuration featuring $\varepsilon_2 = \varepsilon_1 = \varepsilon_0$, $\mu_2 = \mu_1 = \mu_0$, i.e., a DNG anti-cloak. Similar effects as for the cylindrical case are also observed in this scenario, with strong field suppression in the vacuum gap (which is thus *effectively cloaked*) and very weak exterior scattering. Yet the anti-cloak allows coupling to a cavity-type mode in the inner vacuum region $r < R_1$. As for the cylindrical case in Sect. 6.2, qualitatively similar results (not shown for brevity) were observed for the alternative configuration featuring a DPS anti-cloak with a DNG inner sphere, as well as for an ENG anti-cloak with a MNG inner sphere (and vice versa).

For the same geometrical configuration, Fig. 6.7b shows the response obtained via an approximate DPS implementation of the anti-cloak (Sect. 6.3.2.3), obtained by fixing the constitutive parameters $\varepsilon_2 = -\varepsilon_0$, $\mu_2 = -\mu_0$, and enforcing the condition (6.38) for $n = 1$ only, by exploiting the remaining parameter R_1'. It can be observed that, in spite of the simplifications, the results are qualitatively comparable with those pertaining to the conventional (i.e., DNG anti-cloak) implementation.

Figure 6.8 shows instead the response of a configuration without the vacuum gap (Sect. 6.3.2.2.2), i.e., $R_3 = R_2$, satisfying the conditions in (6.36), from which it is evident the rather faithful restoration of the impinging planar wavefronts inside the inner region $r < R_1$, with amplitude twice as strong as the impinging one, owing to the choice $\varepsilon_2 = 2\varepsilon_0$ (6.37).

For illustration of the sensor-cloaking capabilities, we consider a small, lossy inner spherical target of radius $R_1 = \lambda_0/8$ and permittivity $\varepsilon_1 = (4 + 0.4i)\varepsilon_0$, in order to mimic the sensor-loading effects. As in Sect. 6.2, the overall target "visibility" (to a far-field observer) is parameterized in terms of total scattering cross section [35]

$$Q_s = \frac{\lambda_0^2}{2\pi} \sum_{n=1}^{\infty} (2n+1) \left(\left| a_{n,TE}^{(5)} \right|^2 + \left| a_{n,TM}^{(5)} \right|^2 \right), \tag{6.39}$$

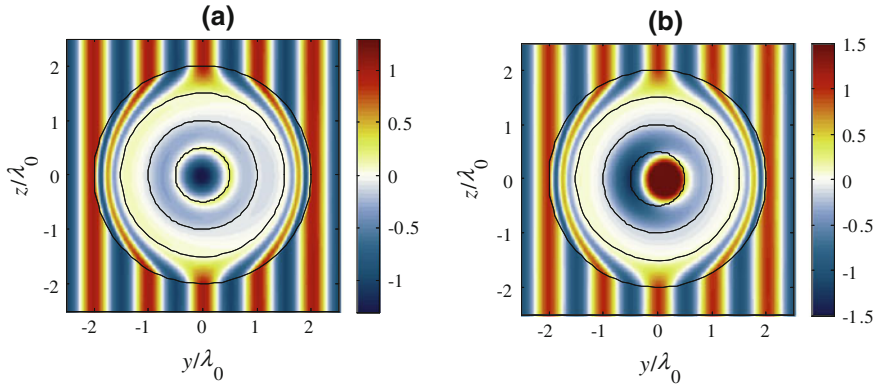

Fig. 6.7 Representative field-map (real part of electric field x-component in the y-z plane) for the plane-wave-excited configuration in Fig. 6.6c. **a** Conventional (DNG) anti-cloak implementation with $\varepsilon_2 = \varepsilon_1 = \varepsilon_0$, $\mu_2 = \mu_1 = \mu_0$, $R_1' = R_1 = \lambda_0/2$, $R_2 = \lambda_0$, $R_3 = 3\lambda_0/2$, $R_4 = 2\lambda_0$,$\Delta_2 = R_2/20$, and $\Delta_3 = R_3/100$. **b** Approximate DPS implementation of the anti-cloak, with $\varepsilon_2 = -\varepsilon_0$, $\mu_2 = -\mu_0$, and $R_1' = 0.732R_1$. Here, and henceforth, loss-tangent values of 0.001 and 0.01 are consistently assumed for DPS and DNG media, respectively. Reprinted from Castaldi et al. [23], with permission from Elsevier

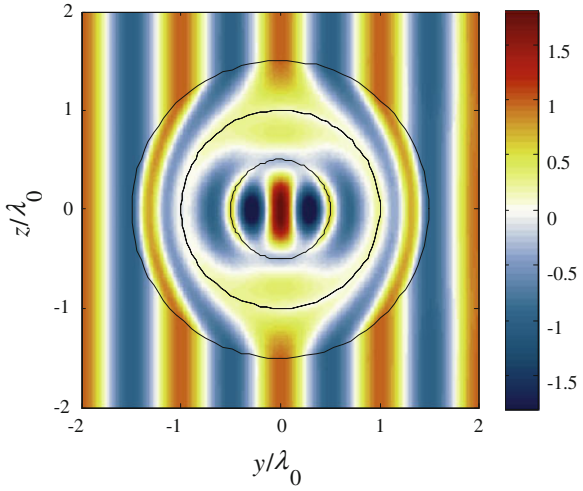

Fig. 6.8 As in Fig. 6.7a (i.e., DNG anti-cloak), but in the absence of the vacuum gap, and with $\varepsilon_2 = \varepsilon_1 = 2\varepsilon_0$, $\mu_2 = \mu_1 = 2\mu_0$, $R_3 = R_2 = \lambda_0$, $R_4 = 3\lambda_0/2$, $\Delta_2 = R_2/10$, $\Delta_3 = R_3/20$. Reprinted from Castaldi et al. [23], with permission from Elsevier

and the "sensing" (absorption) capabilities via the time-averaged dissipated power

$$P_a = \frac{\omega \mathrm{Im}(\varepsilon_1)}{2} \int_0^{R_1} dr \int_0^{\pi} d\theta \int_0^{2\pi} d\phi \; r^2 \sin\theta |\boldsymbol{E}(\boldsymbol{r}, \theta, \phi)|^2. \tag{6.40}$$

With reference to a conventional DNG anti-cloak implementation, Fig. 6.9 illustrates the response attainable, in terms of the above observables (normalized with respect to the corresponding reference values exhibited by the free-standing target in vacuum), as a function of the parameters Δ_2 and Δ_3. The results resemble those obtained for the cylindrical case in Sect. 6.2, with broad dynamic ranges spanning from strong scattering/absorption reductions to *super-scattering/absorption* behaviors. Qualitatively similar results, though with narrower dynamic ranges, are obtained in the case of DPS (approximate) anti-cloak implementation, shown in Fig. 6.10. As discussed in Sect. 6.2, it makes sense to quantify and compare the performance by means of tradeoff curves, as shown in Fig. 6.11. Also for the spherical scenario, a broad range of cloak/anti-cloak interactions can be span by varying Δ_2 and Δ_3, going from a *cloak-prevailing* regime (with weak scattering/absorption) to an *anti-cloak-prevailing* one (with scattering and absorption comparable with or even higher than those in vacuum), and passing through an intermediate regime featuring significant scattering reductions accompanied by acceptable absorption levels.

As expected, consistently better outcomes are attained by the DNG anti-cloak implementation, by comparison with the approximate DPS one. For instance, for a targeted scattering reduction of -15 dB, the DNG anti-cloak implementation yields a *super-absorption* of 7.7 dB. However, for the same targeted scattering reduction, the approximate DPS configuration yields an absorption only 1 dB below that of the free-standing target. Such moderate deterioration is, however, fairly counterbalanced by a significantly simpler implementation.

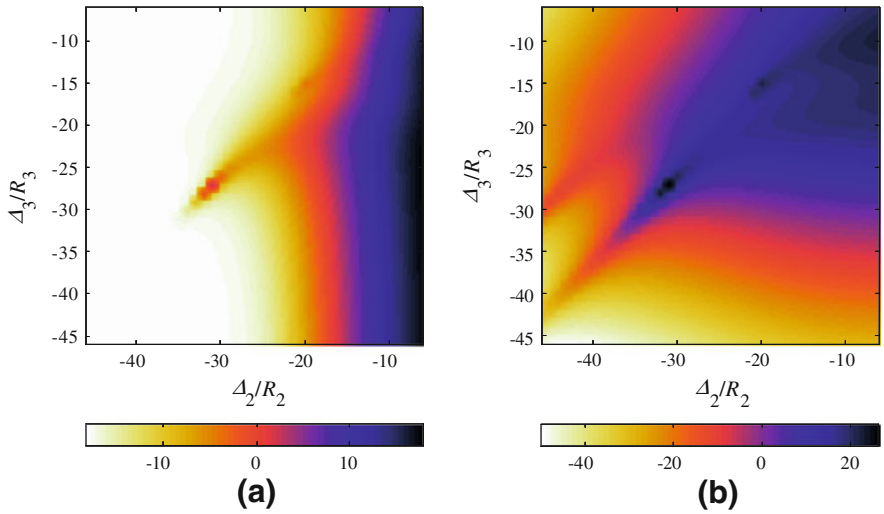

Fig. 6.9 Geometry as in Fig. 6.6c, but in the absence of the vacuum gap, with $\varepsilon_1 = (4 + 0.4i)\varepsilon_0$, $\varepsilon_2 = 4\varepsilon_0$, $\mu_2 = \mu_1 = \mu_0$ (i.e., DNG anti-cloak), $R_1' = R_1 = \lambda_0/8$, $R_2 = R_3 = \lambda_0/2$, and $R_4 = \lambda_0$. **a** Normalized total scattering cross section in dB scale, as a function of Δ_2/R_2 and Δ_3/R_3. **b** Corresponding normalized time-averaged dissipated power. Reprinted from Castaldi et al. [23], with permission from Elsevier

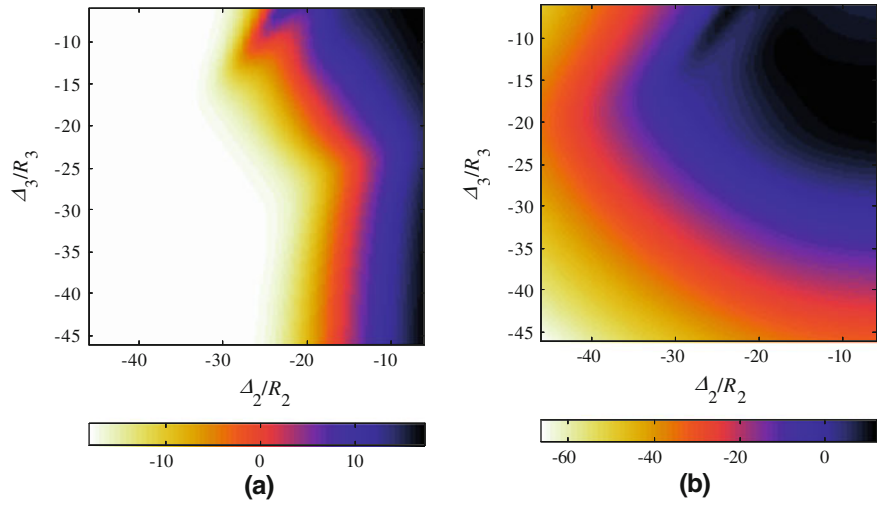

Fig. 6.10 As in Fig. 6.9, but for an approximate DPS implementation of the anti-cloak, with $\varepsilon_2 = -4\varepsilon_0$, $\mu_2 = -\mu_0$, and $R_1' = 0.56R_1$. Reprinted from Castaldi et al. [23], with permission from Elsevier

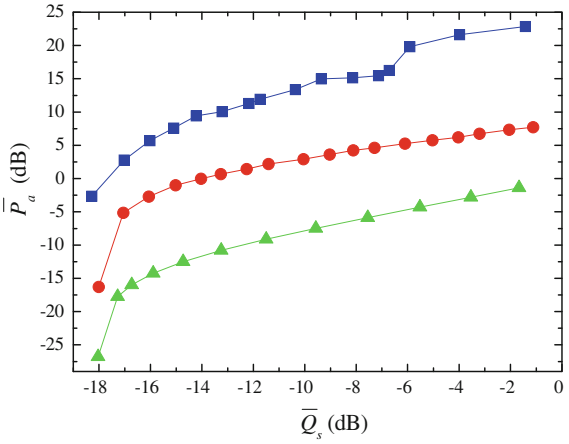

Fig. 6.11 Sensor-cloaking tradeoff curves pertaining to the DNG (*squares*) and approximate DPS anti-cloak (*circles*) configurations (Figs. 6.9 and 6.10, respectively). Also shown (*triangles*), as a reference, is the corresponding curve pertaining to an imperfect cloak configuration. Reprinted from Castaldi et al. [23], with permission from Elsevier

As in Sect. 6.2, in order to illustrate the important role played by the anti-cloak, also shown in Fig. 6.11 is the tradeoff curve pertaining to an imperfect cloak *alone* (i.e., without the anti-cloak), characterized by a conventional (linear) transformation and same total thickness as the above cloak/anti-cloak configurations (6.23), but assuming *spherical* coordinates). Also in this case, although the general trend looks similar to the above cases, the performance is considerably poorer, allowing significant scattering reductions (e.g., −15 dB) only at the expenses of severe curtails (−12 dB reduction in the absorption) of the sensing capabilities.

6.4 Conclusions and Perspectives

In this chapter, we have reviewed a body of results from our recent analytical studies of cloak/anti-cloak interactions in 2-D (cylindrical) and 3-D (spherical) scenarios [21–23]. Our studies have shown the possibility of effectively cloaking an annular (cylindrical or spherical) region separating the cloak and the anti-cloak, while still being able to restore in an inner region a (generally distorted) version of the impinging field. Moreover, with the cloak and anti-cloak *directly contiguous*, we have shown the possibility of "perfectly" restoring the impinging field, while maintaining a very weak exterior scattering, and have investigated the scattering versus absorption tradeoff of interest in sensor-cloaking scenarios. Finally, we have focused on the possibility of implementing *approximate* anti-cloaking effects via the use of DPS media only, which looks very promising from the practical implementation viewpoint.

Current and future studies are aimed at exploring further parameter simplifications/reductions, based, e.g., on *spatially-invariant* [36] or *non-magnetic* [37, 38] material parameters. Also of interest are comparative studies of the sensor-cloaking performance, against the alternative approaches [24–27]. In this

framework, we highlight that in our prototype studies [21–23] no particular effort was made to *exhaustively* optimize the parametric configurations pertaining to the application examples illustrated, and thus there should be significant room for further performance improvement.

References

1. Leonhardt U (2006) Optical conformal mapping. Science 312:1777–1780. doi:10.1126/science.1126493
2. Pendry JB, Schurig D, Smith DR (2006) Controlling electromagnetic fields. Science 312:1780–1782. doi:10.1126/science.1125907
3. Chen HY, Chan CT, Sheng P (2010) Transformation optics and metamaterials. Nature Mater 9:387–396. doi:10.1038/nmat2743
4. Schurig D, Mock JJ, Justice BJ, Cummer SA, Pendry JB, Starr AF, Smith DR (2006) Metamaterial electromagnetic cloak at microwave frequencies. Science 314:977–980. doi:10.1126/science.1133628
5. Cai WS, Chettiar UK, Kildishev AV, Shalaev VM (2007) Optical cloaking with metamaterials. Nature Photon 1:224–227. doi:10.1038/nphoton.2007.28
6. Alù A, Engheta N (2005) Achieving transparency with plasmonic and metamaterial coatings. Phys Rev E 72:016623. doi:10.1103/PhysRevE.72.016623
7. Milton GW, Nicorovici NAP (2006) On the cloaking effects associated with anomalous localized resonance. Proc Roy Soc A 462:3027–3059. doi:10.1098/rspa.2006.1715
8. Hakansson A (2007) Cloaking of objects from electromagnetic fields by inverse design of scattering optical elements. Opt Express 15:4328–4334. doi:10.1364/OE.15.004328
9. Alitalo P, Luukkonen O, Jylha L, Venermo J, Tretyakov SA (2008) Transmission-line networks cloaking objects from electromagnetic fields. IEEE Trans Antennas Propagat 56:416–424. doi:10.1109/TAP.2007.915469
10. Silveirinha MG, Alù A, Engheta N (2008) Cloaking mechanism with antiphase plasmonic satellites. Phys Rev B 78:205109. doi:10.1103/PhysRevB.78.205109
11. Alù A (2009) Mantle cloak: invisibility induced by a surface. Phys Rev B 80:245115. doi:10.1103/PhysRevB.80.245115
12. Edwards B, Alù A, Silveirinha MG, Engheta N (2009) Experimental verification of plasmonic cloaking at microwave frequencies with metamaterials. Phys Rev Lett 103:153901. doi:10.1103/PhysRevLett.103.153901
13. Alitalo P, Bongard F, Zuercher J-F, Mosig J, Tretyakov S (2009) Experimental verification of broadband cloaking using a volumetric cloak composed of periodically stacked cylindrical transmission-line networks. Appl Phys Lett 94:014103. doi:10.1063/1.3068749
14. Alù A, Engheta N (2008) Plasmonic and metamaterial cloaking: physical mechanisms and potentials. J Opt A: Pure Appl Opt 10:093002. doi:10.1088/1464-4258/10/9/093002
15. Alitalo P, Kettunen H, Tretyakov S (2010) Cloaking a metal object from an electromagnetic pulse: a comparison between various cloaking techniques. J Appl Phys 107:034905. doi:10.1063/1.3305322
16. Ruan Z, Yan M, Neff CW, Qiu M (2007) Ideal cylindrical cloak: perfect but sensitive to tiny perturbations. Phys Rev Lett 99:113903. doi:10.1103/PhysRevLett.99.113903
17. Zhang B, Chen H, Wu B-I, Luo Y, Ran L, Kong JA (2007) Response of a cylindrical invisibility cloak to electromagnetic waves. Phys Rev B 76:121101. doi:10.1103/PhysRevB.76.121101
18. Chen H, Wu B-I, Zhang B, Kong JA (2007) Electromagnetic wave interactions with a metamaterial cloak. Phys Rev Lett 99:063903. doi:10.1103/PhysRevLett.99.063903

19. Zhang B, Chen H, Wu B-I, Kong JA (2008) Extraordinary surface voltage effect in the invisibility cloak with an active device inside. Phys Rev Lett 100:063904. doi:10.1103/PhysRevLett.100.063904
20. Chen H, Luo X, Ma H, Chan CT (2008) The anti-cloak. Opt Express 16:14603–14608. doi:10.1364/OE.16.014603
21. Castaldi G, Gallina I, Galdi V, Alù A, Engheta N (2009) Cloak/anti-cloak interactions. Opt Express 17:3101–3114. doi:10.1364/OE.17.003101
22. Castaldi G, Gallina I, Galdi V, Alù A, Engheta N (2010) Power scattering and absorption mediated by cloak/anti-cloak interactions: a transformation-optics route towards invisible sensors. J Opt Soc Am B 27:2132–2140. doi:10.1364/JOSAB.27.002132
23. Castaldi G, Gallina I, Galdi V, Alù A, Engheta N (2011) Analytical study of spherical cloak/anti-cloak interactions. Wave Motion 48:455–467. doi:10.1016/j.wavemoti.2011.03.003
24. Alù A, Engheta N (2009) Cloaking a sensor. Phys Rev Lett 102:233901. doi:10.1103/PhysRevLett.102.233901
25. Ruan Z, Fan S (2010) Temporal coupled-mode theory for Fano resonance in light scattering by a single obstacle. J Phys Chem C 114:7324–7329. doi:10.1021/jp9089722
26. Greenleaf A, Kurylev Y, Lassas M, Uhlmann G (2011) Cloaking a sensor via transformation optics. Phys Rev E 83:016603. doi:10.1103/PhysRevE.83.016603
27. Chen XD, Uhlmann G (2011) Cloaking a sensor for three-dimensional Maxwell's equations: transformation optics approach. Opt Express 19:20518–20530. doi:10.1364/OE.19.020518
28. Abramowitz M, Stegun IA (1970) Handbook of mathematical functions, Ninth printing. Dover, New York
29. Luo Y, Chen H, Zhang J, Ran L, Kong JA (2008) Design and analytical full-wave validation of the invisibility cloaks, concentrators, and field rotators created with a general class of transformations. Phys Rev B 77:125127. doi:10.1103/PhysRevB.77.125127
30. Yang T, Chen H, Luo X, Ma H (2008) Superscatterer: enhancement of scattering with complementary media. Opt Express 16:18545–18550. doi:10.1364/OE.16.018545
31. Ng J, Chen H, Chan CT (2009) Metamaterial frequency-selective superabsorber. Opt Lett 34:644–646. doi:10.1364/OL.34.000644
32. Harrington RF (2001) Time-harmonic electromagnetic fields. IEEE Press-Wiley Interscience, Piscataway, NJ
33. Gallina I, Castaldi G, Galdi V, Alù A, Engheta N (2010) General class of metamaterial transformation slabs. Phys Rev B 8:125124. doi:10.1103/PhysRevB.81.125124
34. Rahm M, Schurig D, Roberts DA, Cummer SA, Smith DR, Pendry JB (2008) Design of electromagnetic cloaks and concentrators using form-invariant coordinate transformations of Maxwell's equations. Photon Nanostruct 6:87–95. doi:10.1016/j.photonics.2007.07.013
35. Stratton JA (1941) Electromagnetic theory. McGraw-Hill, New York
36. Luo Y, Zhang J, Chen H, Xi S, Wu B-I (2008) Cylindrical cloak with axial permittivity/permeability spatially invariant. Appl Phys Lett 93:033504. doi:10.1063/1.2953433
37. Cai W, Chettiar UK, Kildishev AV, Shalaev VM, Milton GW (2007) Nonmagnetic cloak with minimized scattering. Appl Phys Lett 91:111105. doi:10.1063/1.2783266
38. Castaldi G, Gallina I, Galdi V (2009) Nearly perfect nonmagnetic invisibility cloaking: Analytic solutions and parametric studies. Phys Rev B 80:125116. doi:10.1103/PhysRevB.80.125116

Chapter 7
Transformation Electromagnetics Design of All-Dielectric Antennas

Wenxuan Tang and Yang Hao

Abstract The discrete coordinate transformation is a practical implementation of transformation electromagnetics. It solves the transformation between coordinate systems in a discretized form. This method significantly relaxes the strict requirement for transformation media, and consequently leads to easily-realizable applications in antenna engineering. In this chapter, the discrete coordinate transformation is demonstrated and analyzed from the theory and is proved to provide an all-dielectric approach of device design under certain conditions. As examples, several antennas are presented, including a flat reflector, a flat lens, and a zone plate Fresnel lens. The Finite-Difference Time-Domain (FDTD) method is employed for numerical demonstration. Realization methods are also discussed, and a prototype of the carpet cloak composed of only a few dielectric blocks is fabricated and measured.

7.1 Introduction

The concept of transformation electromagnetics was first proposed in 2006 in pioneering theoretical works by Leonhardt and Pendry et al. independently [1, 2]. It provides us with a flexible method to manipulate the propagation of electromagnetic waves by using custom-engineered media. Novel functional devices have been successfully proposed and designed through transformation electromagnetics, such as the exotic 'cloak of invisibility' [3–6], EM rotators [7, 8], EM concentrators [9–11], sensor cloaks [12], optical black holes [13, 14], antenna devices

W. Tang · Y. Hao (✉)
School of Electronic Engineering and Computer Science, Queen Mary, University of London, London E1 4NS, United Kingdom
e-mail: yang.hao@eecs.qmul.ac.uk

W. Tang
State Key Laboratory of Millimeter Waves, Southeast University, Nanjing 210096, People's Republic of China

D. H. Werner and D.-H. Kwon (eds.), *Transformation Electromagnetics and Metamaterials*, DOI: 10.1007/978-1-4471-4996-5_7,

[15, 16], etc. However, there exist considerable problems when transformation-based devices are put into practice. One such problem is that those designs often include extreme values of constitutive parameters (e.g., near zero or extremely high permittivity or permeability). Even though metamaterials have been proved to be capable of providing a wide range of permittivity and permeability and even to achieve extreme values, they often require resonant unit cells which severely limit the operating bandwidth. In addition, many transformation-based devices require anisotropic permittivity and permeability simultaneously, which makes their practical realization even more difficult.

The discrete coordinate transformation (DCT) is therefore proposed to circumvent these problems [17]. Instead of global coordinates, the physical space and the virtual space are described with quasi-orthogonal local coordinates, and the transformation electromagnetics equations are applied between a pair of corresponding local coordinate systems in the two spaces. A well-known application of the DCT technique is the 'carpet cloak'. As demonstrated in [17], the carpet cloak can be constructed with conventional isotropic dielectrics instead of resonant metamaterials, and consequently overcomes the disadvantage of its narrow-band performance. Experimental validations of the carpet cloak have been done using low-loss and non-resonant artificial materials at microwave frequencies [18, 19] and at optical frequencies [20, 21].

Due to its easy realization and the broadband performance of the DCT based design, there are many possible applications other than the carpet cloak. For example, in antenna systems, many widely used devices have curved surfaces, such as parabolic reflectors and convex lenses. Using the discrete coordinate transformation, one can design equivalent devices that operate in the same manner but have flexible profiles. In the virtual space perceived by the electromagnetic waves, those devices have curved surfaces, contain homogeneous and isotropic materials, and can be described with distorted coordinate systems. By using appropriate transformations, these distorted coordinate systems are mapped to a physical space where the devices possess flat surfaces, contain spatially dispersive but isotropic materials, and are represented in new coordinate systems, for example, the Cartesian coordinate system.

The organization of this chapter is as follows: in Sect. 7.2, we begin with the theory of the discrete coordinate transformation, and give analyses towards its conditions of application. In Sect. 7.3, some examples of antenna devices are presented and numerically demonstrated. In Sect. 7.4, realization methods are discussed and a prototype of an all-dielectric device is fabricated and measured. A Summary of the above is in Sect. 7.5.

7.2 The Discrete Coordinate Transformation

To implement the discrete coordinate transformation, both the virtual space and the physical space are discretized into small cells using quasi-orthogonal local coordinate systems. For illustrative purpose we show in Fig. 7.1 an example of

transforming a parabolic reflector in the virtual space into a flat one in the physical space.

Suppose that the coordinate transformation between the virtual space (Fig. 7.1a) and the physical space (Fig. 7.1b) is $x' = x'(x, y, z)$, $y' = y'(x, y, z)$, $z' = z'(x, y, z)$, where (x, y, z) are local coordinates in the virtual space and (x', y', z') are local coordinates in the physical space. Based on the theory in [2], the permittivity and the permeability tensors in the physical space can be calculated as:

$$\bar{\bar{\varepsilon}}' = \frac{J\bar{\bar{\varepsilon}}J^T}{\det(J)}, \quad \bar{\bar{\mu}}' = \frac{J\bar{\bar{\mu}}J^T}{\det(J)}, \tag{7.1}$$

where the Jacobian matrix between each pair of local coordinate systems is

$$J = \begin{pmatrix} \frac{\partial x'}{\partial x} & \frac{\partial x'}{\partial y} & \frac{\partial x'}{\partial z} \\ \frac{\partial y'}{\partial x} & \frac{\partial y'}{\partial y} & \frac{\partial y'}{\partial z} \\ \frac{\partial z'}{\partial x} & \frac{\partial z'}{\partial y} & \frac{\partial z'}{\partial z} \end{pmatrix}. \tag{7.2}$$

Because the parabolic reflector (shown as the curved PEC in Fig. 7.1a) is placed in the free space, the original permittivity and permeability tensors are

$$\begin{aligned} \bar{\bar{\varepsilon}} &= \varepsilon_0 \mathbf{I}, \\ \bar{\bar{\mu}} &= \mu_0 \mathbf{I}, \end{aligned} \tag{7.3}$$

where $\mathbf{I}$ is the unitary matrix.

To simplify the problem, we assume that the transformation is two-dimensional (2D), and thus the device is infinite in the z direction normal to the $x - y$ plane defined in Fig. 7.1. The bold reduction from three dimensions to two dimensions makes the design process much simpler. In practice, because many devices are symmetric, or work at a specified polarization, three-dimensional (3D) transformation devices can be obtained by rotating or extending 2D models about an axis.

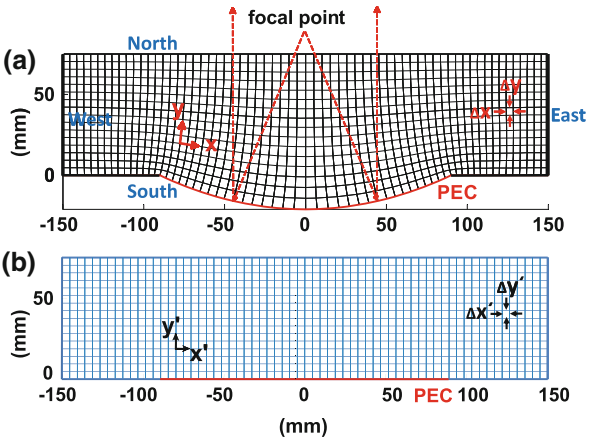

Fig. 7.1 (Section view) **a** The virtual space with distorted coordinates. A parabolic reflector is located in the free space, as illustrated by the curved PEC. **b** The physical space with Cartesian coordinates. The parabolic reflector is transformed into a flat PEC

Examples will be presented in Sect. 7.3. For a 2D E-polarized incident wave with electric field along the z direction, only the components of μ_{xx}, μ_{xy}, μ_{yy}, μ_{yx} and ε_{zz} contribute, and hence, the permittivity and the permeability become

$$\varepsilon_z' \equiv \varepsilon_{zz}' = \varepsilon_0 \det(J)^{-1}, \tag{7.4}$$

$$\bar{\bar{\mu}}' = \frac{\mu_0}{\det(J)} \begin{pmatrix} (\frac{\partial x'}{\partial x})^2 + (\frac{\partial x'}{\partial y})^2 & \frac{\partial x'}{\partial x}\frac{\partial y'}{\partial x} + \frac{\partial x'}{\partial y}\frac{\partial y'}{\partial y} \\ \frac{\partial y'}{\partial x}\frac{\partial x'}{\partial x} + \frac{\partial x'}{\partial y}\frac{\partial y'}{\partial y} & (\frac{\partial y'}{\partial x})^2 + (\frac{\partial y'}{\partial y})^2 \end{pmatrix}. \tag{7.5}$$

Based on the theoretical study presented in [17], for anisotropic materials an effective average refractive index n' can be defined as

$$n'^2 = n_{xx}' n_{yy}' / (\varepsilon_0 \mu_0) = \sqrt{\mu_{yy}' \varepsilon_z'} \sqrt{\mu_{xx}' \varepsilon_z'} / (\varepsilon_0 \mu_0) = \sqrt{\mu_{yy}' \mu_{xx}'} \varepsilon_z' / (\varepsilon_0 \mu_0), \tag{7.6}$$

where μ_{xx}' and μ_{yy}' are the principal values of the permeability tensor in Eq. (7.5) and n_{xx}' and n_{yy}' are the corresponding principal values of the refractive index tensor.

Equation (7.6) indicates that if $\mu_{xx}' \mu_{yy}' = \mu_0^2$, i.e. if there is no magnetic dependence, then the refractive index n', which determines the trace of the wave, can be realized by the permittivity alone, leading to an all-dielectric device. Next, we shall show that this condition is approximately satisfied if certain grids are properly chosen in the coordinate transformation.

The explicit value of $\mu_{xx}' \mu_{yy}'$ from Eq. (7.5) is

$$\mu_{xx}' \mu_{yy}' = \mu_0^2 \frac{[(\frac{\partial x'}{\partial x})^2 (\frac{\partial y'}{\partial x})^2 + (\frac{\partial x'}{\partial x})^2 (\frac{\partial y'}{\partial y})^2 + (\frac{\partial x'}{\partial y})^2 (\frac{\partial y'}{\partial x})^2 + (\frac{\partial x'}{\partial y})^2 (\frac{\partial y'}{\partial y})^2]}{[(\frac{\partial x'}{\partial x})^2 (\frac{\partial y'}{\partial y})^2 - 2\frac{\partial x'}{\partial x}\frac{\partial y'}{\partial y}\frac{\partial x'}{\partial y}\frac{\partial y'}{\partial x} + (\frac{\partial x'}{\partial y})^2 (\frac{\partial y'}{\partial x})^2]}. \tag{7.7}$$

According to Eq. (7.7), the approximate condition $\mu_{xx}' \mu_{yy}' \simeq \mu_0^2$ is satisfied when at the same time

$$\frac{\partial x'}{\partial y} \simeq 0, \tag{7.8}$$

and

$$\frac{\partial y'}{\partial x} \simeq 0. \tag{7.9}$$

Since x' and y' are functions of both x and y, Eqs. (7.8) and (7.9) can be also written using the chain rule as

$$\frac{\partial x'}{\partial y} = \frac{\partial x'}{\partial x}\frac{\partial x}{\partial y} \simeq 0, \tag{7.10}$$

$$\frac{\partial y'}{\partial x} = \frac{\partial y'}{\partial y}\frac{\partial y}{\partial x} \simeq 0. \tag{7.11}$$

The above condition can indeed be satisfied because we can generate a grid in the virtual space with quasi-orthogonal cells such that

$$\frac{\partial x}{\partial y} \simeq 0, \tag{7.12}$$

$$\frac{\partial y}{\partial x} \simeq 0. \tag{7.13}$$

To illustrate how this orthogonality restriction can be approximately satisfied, see for example the virtual space shown in Fig. 7.1a. A sample distorted cell is drawn in Fig. 7.2, and the 2×2 covariant metric g is re-defined to characterize the distortion as [22–24]:

$$g = \begin{pmatrix} g_{11} & g_{12} \\ g_{21} & g_{22} \end{pmatrix}, \tag{7.14}$$

$$g_{i,j} = \vec{a}_i \cdot \vec{a}_j \quad (i,j = 1,2). \tag{7.15}$$

$\vec{a}_1$ and $\vec{a}_2$ are the covariant base vectors defined in Fig. 7.2, and θ is the angle between them. We quantify the orthogonality of the grid using the parameter θ for each cell, defined through

$$\cos\theta = \sqrt{\frac{g_{12}g_{21}}{g_{11}g_{22}}}. \tag{7.16}$$

The distribution of the angle parameter θ is plotted in Fig. 7.3 for the grid shown in Fig. 7.1a. We observe that in most cells, θ is distributed around the 90° point, with a much smaller exception further away from 90°. The full width at half maximum (FWHM) index of the distribution is also measured from this plot, which is only 1°, indicating that most of the local coordinates are quasi-orthogonal. Thus, for a perfectly orthogonal grid, g is a unit matrix, $\cos\theta = 0$, FWHM $= 0$, and ultimately $\mu'_{xx}\mu'_{yy} = \mu_0^2$. And even for a quasi-orthogonal grid such as the one in Fig. 7.1a, these conditions can be approximately satisfied, yielding an all-dielectric device with very minor sacrifices in performance.

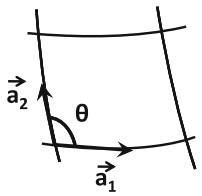

Fig. 7.2 The covariant base vectors in a 2D distorted cell

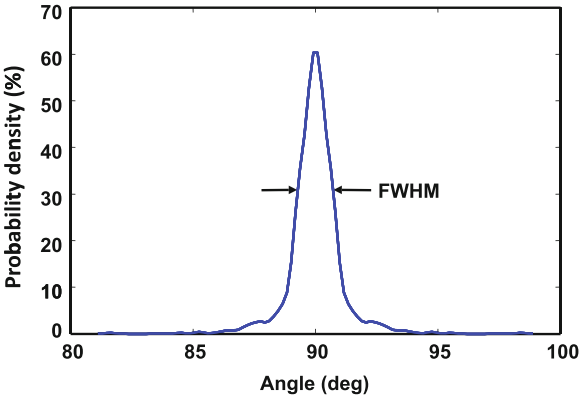

Fig. 7.3 Distribution of the angle between two local coordinates in every cell of the virtual space. The orthogonal property is quantified by the full width at half maximum (*FWHM*) index. When the FWHM index approaches zero, the local coordinates are quasi-orthogonal. In this case the index is only 1°

Furthermore, the near-orthogonal property ensures an approximation of Eq. (7.5) that

$$\bar{\bar{\mu}}' = \frac{\mu_0}{\det(J)} \begin{pmatrix} (\frac{\partial x'}{\partial x})^2 & 0 \\ 0 & (\frac{\partial y'}{\partial y})^2 \end{pmatrix}. \tag{7.17}$$

Because all cells are generated to be approximately square-shaped, μ'_{xx} and μ'_{yy} have very similar values which are close to unity. Accordingly, the relative permeability of the device can be assumed to be isotropic and unity, and the effective relative refractive index in Eq. (7.6) is only dependent on ε'_z as

$$n'^2 \simeq \varepsilon'_z/\varepsilon_0 = \frac{1}{\det(J)}. \tag{7.18}$$

Note that under the orthogonal condition of Eqs. (7.8) and (7.9), the refractive index profile of the device can be directly retrieved from each cell within the grid, using Eq. (7.2):

$$n'^2 \simeq \frac{1}{\frac{\partial x'}{\partial x}\frac{\partial y'}{\partial y}} \simeq \frac{\Delta x \Delta y}{\Delta x' \Delta y'}, \tag{7.19}$$

where $\Delta x, \Delta y, \Delta x', \Delta y'$ are the dimensions of cells in the two spaces, as marked in Fig. 7.1.

For the case of H polarization, similar results are obtained. Now the contributing components of the permittivity and the permeability are ε_{xx}, ε_{xy}, ε_{yy}, ε_{yx} and μ_{zz}. Under the orthogonality criteria of Eqs. (7.8) and (7.9), the permittivity and the permeability tensors become

$$\bar{\bar{\varepsilon}}' = \frac{\varepsilon_0}{\det(J)} \begin{pmatrix} (\frac{\partial x'}{\partial x})^2 & 0 \\ 0 & (\frac{\partial y'}{\partial y})^2 \end{pmatrix}, \mu'_z = \mu_0 \det(J)^{-1}, \tag{7.20}$$

while $\det(J) = \frac{\partial x'}{\partial x} \cdot \frac{\partial y'}{\partial y}$. The effective average refractive index is now

$$n'^2 = n'_{xx} n'_{yy} / (\varepsilon_0 \mu_0) = \sqrt{\varepsilon'_{yy} \varepsilon'_{xx}} \mu'_z / (\varepsilon_0 \mu_0). \tag{7.21}$$

It can be easily checked that in this case $\varepsilon'_{xx} \varepsilon'_{yy} \simeq \varepsilon_0^2$, and thus the effective average refractive index in this case is dependent on μ'_z only, similar to Eq. (7.18) as:

$$n'^2 \simeq \mu'_z / \mu_0 = \frac{1}{\det(J)}. \tag{7.22}$$

The above analysis indicates that a properly selected magnetic material can control the H-polarized wave, similar to how a dielectric material can control the E-polarized wave. Thus the designer can generate a grid under the assumptions specified in this section, calculate the refractive index distribution from Eq. (7.19), and choose to tune either ε or μ to operate using E-polarization or H-polarization respectively.

7.3 All-Dielectric Antennas Based on the Discrete Coordinate Transformation

7.3.1 A Flat Reflector

The parabolic reflector antenna is one of the most commonly used antennas from radio to optical frequencies [25]. This antenna serves to transform a spherical wave originated from its focal point into a plane wave, and consequently generates highly directive beams. Such an antenna device can be considerably large when operated at low frequencies, and difficult to construct due to the parabolic shape. In [26], the technique of discrete coordinate transformation was implemented to create an alternative to the parabolic reflector: an all-dielectric reflector that possesses a compact flat volume while maintaining the performance of the parabolic dish.

Figure 7.4a shows the geometry of a prototype of conventional parabolic reflector, whose shape follows the equation of

$$R = \frac{2F}{1 + \cos\theta}. \tag{7.23}$$

This parabolic reflector is designed to operate at the C-band (4–8 GHz) and the X-band (8–12 GHz). The focal length F is set to be 108.6 mm and the angle θ ranges from $-45°$ to $45°$. Accordingly, the aperture of the parabolic surface is 180 mm. This parabolic reflector is exactly the same as the one located in Fig. 7.1a. It is noted that in Fig. 7.1a the transformation region is chosen to be 300 mm $\times$ 75 mm, so as to ensure that in the physical space in Fig. 7.1b a source placed at the focal

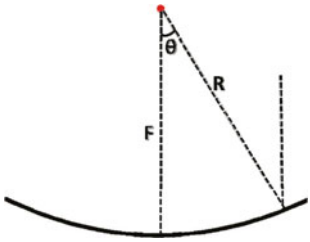

Fig. 7.4 Geometry of the parabolic reflector located in Fig. 7.1a

point is not embedded in the transformation media. Quasi-orthogonal grids are generated in both the virtual space and the physical space as illustrated in Fig. 7.1, using a commercial software called 'PointWise' [27]. Based on the analysis in previous section, these grids are indeed quasi-orthogonal, leading to an all-dielectric flat reflector in the physical space. The permittivity distribution of the transformation based flat reflector is calculated according to Eqs. (7.18) and (7.19). The complete permittivity map is shown in Fig. 7.5a, consisting of 64×16 square blocks.

To reduce the complexity of the flat reflector and to make it more realizable, some simplifications are adopted. First, materials with relative permittivity of less-than-unity value are neglected and replaced with those of $\varepsilon_r = 1$ as air or free space. In this design, materials with less-than-unity permittivities are found close to the bottom around $x = 80$ mm and $x = -80$ mm (see Fig. 7.5a). Since these areas are electrically small at operating frequencies, and those permittivity values are often very close to one, the simplification is considered to be safe. This fact has been demonstrated in Refs. [19, 26, 28], and will be shown later by simulation results in this section. The permittivity map without less-than-unity values is shown in Fig. 7.5b. It should be pointed out that materials with less-than-unity parameters are termed as 'dispersive materials' here, as they are strongly dispersive over operating frequencies. Strictly speaking, all materials are essentially dispersive in frequency. However, conventional dielectrics can be nearly non-dispersive at the X-band and the C-band [19].

The second step to approximate and simplify the transformation device is to reduce the resolution of permittivity map. This concept has been developed in the design of a simplified carpet cloak made of only a few blocks of isotropic all-dielectric materials [19, 29]. The fundamental limitation of resolution is based on the Nyquist-Shannon sampling theorem [30]. Sampling is the process of converting a signal (for example, a function of continuous time or space) into a numeric sequence (a function of discrete time or space). Shannon's version of the theorem states: *If a function f(t) contains no frequencies higher than W cps, it is completely determined by giving its ordinates at a series of points spaced 1/2W seconds apart.* Fig. 7.6 interprets this theorem in the spatial domain. When propagating in the physical space, at a fixed time, the electromagnetic wave is a function of continuous space. Transformation media with a high resolution discretize the space using a high sampling rate while low-resolution ones discretize the space using a low sampling rate. If the electromagnetic wave operates in a

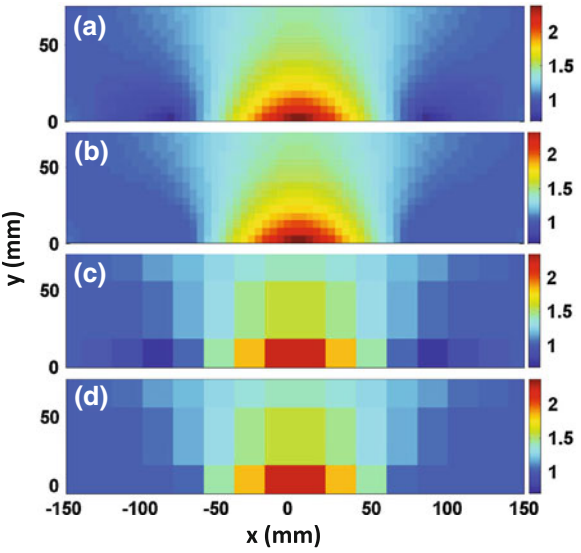

Fig. 7.5 **a** Relative permittivity map consisting of 64 × 16 blocks. **b** Relative permittivity map consisting of 64 × 16 blocks, without less-than-unity values. **c** Relative permittivity map consisting of 16 × 3 blocks. **d** Relative permittivity map consisting of 16 × 3 blocks, without less-than-unity values

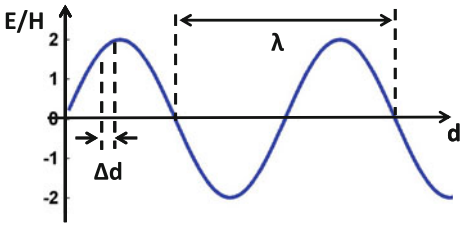

Fig. 7.6 An electromagnetic wave propagates in the spatial domain at a fixed time

frequency band from f_L to f_H, to accurately reconstruct information of the wave, the sampling rate f_s should satisfy

$$f_s > 2f_H. \tag{7.24}$$

Because

$$f_s = \frac{1}{\triangle d}, f = \frac{1}{\lambda}, \tag{7.25}$$

the resolution of the discrete space should satisfy

$$\triangle d < \frac{1}{2}\lambda_H. \tag{7.26}$$

$\triangle d$ is presented as the dimension of blocks in the permittivity map, and λ_H is the minimum wavelength within the frequency band. According to Eq. (7.26), as long as dielectric blocks are smaller than half a wavelength at operating frequencies, the simplified device can maintain the property of a high-resolution one. When the

operating frequency goes higher, the resolution of the permittivity map should increase accordingly.

The above simplifications have made significant advances for the transformation device to be able to be realized in practice. When applied to the present work, the high resolution permittivity map shown in Fig. 7.5a thus can be approximated using a relatively low resolution map of 16 × 3 blocks as shown in Fig. 7.5c. The size of each block is 18.75 mm, which is half a wavelength in free space at 8 GHz. To execute the simplification, the position of a block in Fig. 7.5a–d is defined as the position of its center point. Each low-resolution block in figure c/d can find a high-resolution one in figure a/b which has the closest position to it. Once the two blocks are decided, the permittivity in the high-resolution block is filled into the low-resolution one uniformly. Figure 7.5d shows the simplified map without values less than unity (we call it a 'non-dispersive map' in the following text).

The FDTD method based simulations are employed to compare the performance of the parabolic reflector and the flat reflector [31, 32]. For simplicity, we use 2D modelling with H_x, H_y and E_z components (E polarization). A 3D reflector is easily realizable by rotating the permittivity map in Fig. 7.5 to the y axis. For the reflector in this design, the simulation domain is relatively small and a conventional Cartesian grid is fine enough to accurately model the device. A spatial resolution of $\lambda/30$ is chosen for the FDTD grid. The total-field/scattered-field technique is applied to implement an incident plane wave. Perfectly matched layer (PML) absorbing boundary conditions are added surrounding the antennas in order to terminate the simulation domain. Dispersive modelling [33, 34] is also employed to simulate the full-mapped flat reflector with less-than-unity values.

First, a plane wave with E polarization comes along $+y$ direction at 8 GHz, in order to compare the low-resolution non-dispersive flat reflector shown in Fig. 7.5d with the parabolic reflector in term of the focal length. Figure 7.7a and b illustrate the real part of the E_z field from the transformed flat reflector and the conventional parabolic reflector, respectively, after the steady-state is reached. Their focal lengths are measured as the distances from the center of the PEC surface to the narrowest envelope marked with the dashed red line in Fig. 7.7a and b. The focal lengths in Fig. 7.7a and b are 102.6 and 102.7 mm respectively, very close to each other. In addition, slightly different reflections are observed on two sides of the reflectors. This difference is due to the neglecting of less-than-unity permittivities, and the discontinuity between the flat reflector and the air. In Fig. 7.7c and d we also compare the performance of these two reflectors when fed by a small horn with its phase center located at the focal point. The field distributions illustrated are indeed similar, which indicates that the flat reflector maintains the function of transforming an incident cylindrical wave to a plane wave and consequently obtains highly directive beams.

To investigate the directive property of the antennas, in Fig. 7.8 radiation patterns of the conventional reflector, flat reflectors with different resolutions, and the radiation pattern of a flat PEC surface alone, are compared. The near-to-far-field (NTFF) transformation is applied to observe the far-field characteristics [31].

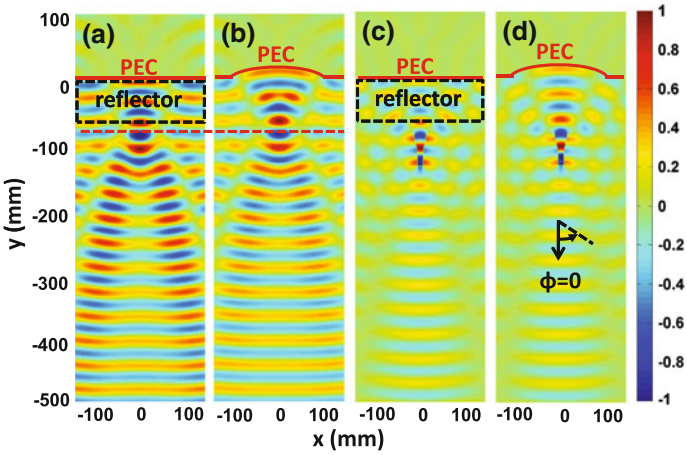

Fig. 7.7 Real part of the Ez field at 8 GHz. **a** A plane wave along the y direction illuminates a low-resolution flat reflector shown in Fig. 7.5d. The focal length (measured from the *dashed red line* to the *center* of the PEC) is 102.6 mm. **b** The same plane wave illuminates the conventional parabolic reflector. The focal length is 102.7 mm. **c** A small horn antenna is applied at the focal point to feed the flat reflector. **d** A small horn antenna is applied at the focal point to feed the conventional reflector

Using the data obtained from the near-field simulation, the NTFF transformation calculates the forward radiation patterns of the reflectors. The energy is calculated as $|E_z|^2$, and normalized to the peak energy when the conventional reflector is applied. It is shown in Fig. 7.8 that the conventional reflector and all the three flat reflectors produce highly directive beams around $\phi = 0$ (ϕ defined in Fig. 7.7d), which verifies the excellent cylindrical-to-plane wave transformation. The 64 × 16-block flat reflectors, dispersive (with less-than-unity permittivities) or non-dispersive (without less-than-unity permittivities), seem to have insignificant energy loss around the radiating direction when compared to the conventional parabolic one. In addition, when the less-than-unity values are removed from the full 64 × 16 map, the performance deteriorates only slightly, in term of the energy reduction around $\phi = 0$. Once the 16 × 3-block map is applied, the flat reflector suffers more energy loss in the radiating direction. However, its directive property is still comparable to that of the conventional reflector. When all reflectors are removed, obviously, the PEC surface alone cannot hold the directive property.

Furthermore, the bandwidths of the dispersive and non-dispersive flat reflectors are tested at different frequencies. Both the flat reflectors are composed of 16 × 3 large blocks, and the testing frequencies are 4, 6, 10 and 12 GHz respectively. Figure 7.9 shows that at frequencies higher than 8 GHz, the two reflectors have extremely similar radiation patterns. When the operating frequency goes lower, the dispersive reflector has higher radiation around the angle of $\phi = 0$, but slightly larger side-lobes than the non-dispersive one. This effect occurs since as the

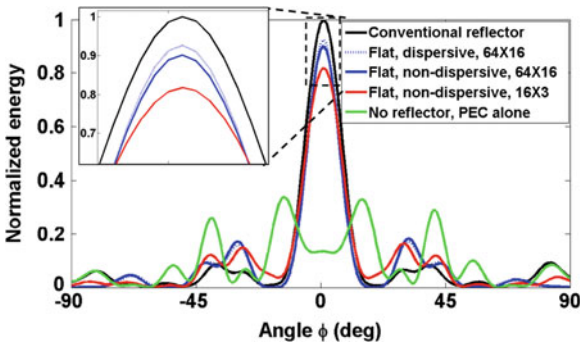

Fig. 7.8 The comparison of the radiation patterns at 8 GHz. The definition of Φ is shown in Fig. 7.7d

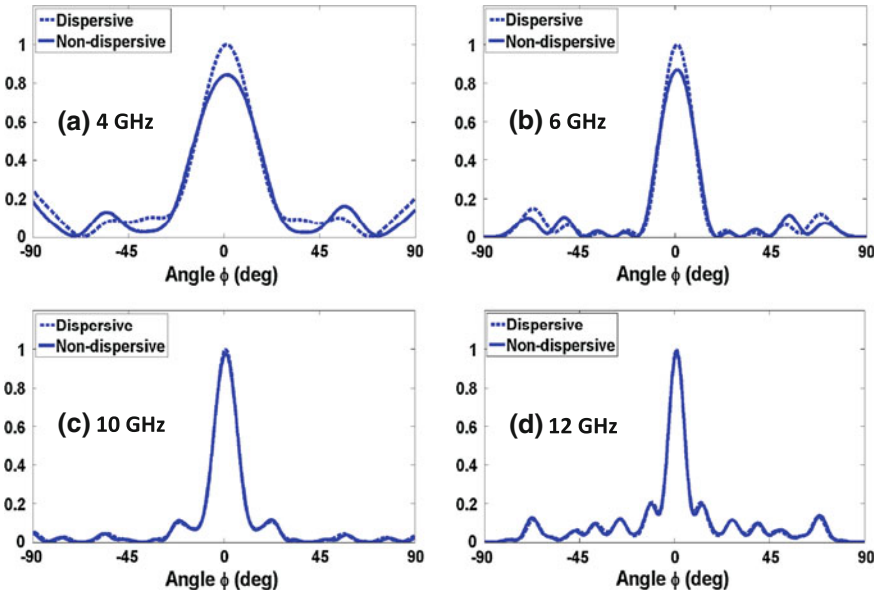

Fig. 7.9 Comparison of the radiation patterns between dispersive and non-dispersive flat reflectors at 4, 6, 10 and 12 GHz. Both the flat reflectors are composed of 16 × 3 blocks

operating frequency decreases, the less-than-unity values change more and more rapidly according to the Drude model. In conclusion, a non-dispersive reflector has a comparable radiating performance and a wider bandwidth than the dispersive one, and is much easier to realize.

7.3.2 A Flat Lens

A convex lens is another common device in antenna systems. It functions to transform a spherical wave from a point source (or a cylindrical wave from a line source in a 2D problem) located at its focal point to a plane wave at the other side. This device has been widely used at different frequencies and at various polarizations. In [26], an all-dielectric lens at the C-band and the X-band was created from a conventional convex lens by using the discrete coordinate transformation. The created lens obtained very similar performance as the convex one, whilst possessing a planar profile with half the thickness of the other one.

Figure 7.10a shows the section view of the virtual space where the original convex lens is located. It is supposed to be made of isotropic homogeneous dielectric with $\varepsilon_r = 3$. The aperture of the lens is 160 mm (4.3 λ_0 at 8 GHz), and the two surfaces are arcs on a circle with radius equal to 300 mm. The thickness varies from 45.6 to 23.8 mm, from the center ($x = 0$) to the two ends ($x = \pm$ 80 mm). Applying the discrete coordinate transformation, the conventional convex lens in the virtual space is completely compressed into the flat physical space with half the thickness, as shown in Fig. 7.10b. Contrary to the boundary condition in the flat reflector design, here the top and bottom boundaries in the virtual space are curves. Since the boundaries are different before and after the transformation, if we want to grant the transformation lens exactly the same property as the conventional one, we should add transformation media surrounding the flat profile (filling region II in Fig. 7.10b) in order to maintain the space and to palliate the impedance mismatching [35]. Unfortunately, such filling materials commonly have some permittivity values less than the unity, which results in narrow-band performance. In addition, if we fix the boundaries before and after transformation, the flat lens will lose the benefit of small volume. It is obvious that both of the above two factors are important to a broadband antenna. Therefore, we can assume that firstly a complete virtual space with air surrounding the convex lens (within the dashed red box in Fig. 7.10a) is transformed to a physical space (within the dashed red box

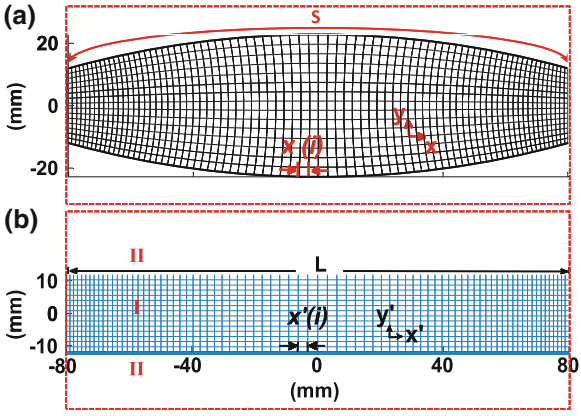

Fig. 7.10 **a** The virtual space with distorted coordinates. A convex lens made of dielectric with $\varepsilon_r = 3$ is imbedded in the air. **b** The physical space with Cartesian coordinates. The transformation lens is inside region I

in Fig. 7.10b), and then materials with less-than-unity parameters in the physical space are replaced with the air. Therefore, the flat lens in the physical space can have a compact size and potentially broadband performance. As long as the performance is properly maintained, as will be proved, this approximation is valid in practice.

Quasi-orthogonal grids are again generated to discretize both the virtual space and the physical space. In the virtual space, to achieve a good orthogonality, points on the top and bottom boundaries are no longer evenly distributed. More points assemble at the four corners, resulting in smaller cells at the two ends and larger cells in the central area. In the physical space, the points on the top and bottom boundaries are determined in the same proportion as that in the virtual space because x' is the projection of x. Note that since some cells in the physical space are not squares, the components of μ_{xx} and μ_{yy} have different values, implying that the transformation media in the physical space have become more anisotropic. Strictly speaking, the effective average refractive index has approximate values of $n'^2 \simeq \frac{1}{\det(J)}$ in the central area and at the two ends. Nevertheless, for a near-axis incidence, the isotropic approximation is acceptable, and the flat lens holds its performance, as will be demonstrated later. The covariant metric g is calculated for each cell, and the FWHM index is 3.6°, indicating that local coordinate systems are fairly orthogonal and the discrete coordinate transformation can be applied.

In Fig. 7.11 the permittivity maps with different resolutions are presented, calculated by Eqs. (7.18) and (7.19). The high-resolution map in Fig. 7.11a is composed of 80 × 15 blocks, with each block sized about 2 mm × 1.7 mm. Proper simplification is implemented to reduce the resolution using the same technique described in the previous sub-section, and a low resolution permittivity map is exhibited in Fig. 7.11b, consisting of 14 × 2 blocks sized 12.3 mm × 11.9 mm. It is noted that the two rows of blocks have the same permittivity values, therefore the low-resolution map is in fact composed of 14 × 1 blocks.

The FDTD method based simulations are employed again to predict the performance of the designed flat lens in a 2D E-polarized circumstance. In Fig. 7.12 the real part of the electric field under different excitations are depicted. To test the focusing property of the 14×1-block low-resolution lens, we compare the field

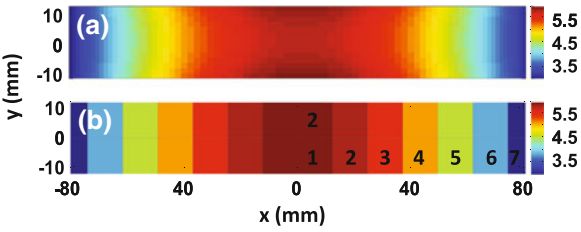

Fig. 7.11 Permittivity maps of the flat lens. **a** The map consisting of 80 × 15 blocks, with each block sized 2 × 1.7 mm. **b** The map consisting of 14 × 2 blocks. The first and last columns have a width of 6.2 mm and the rest have a width of 12.3 mm

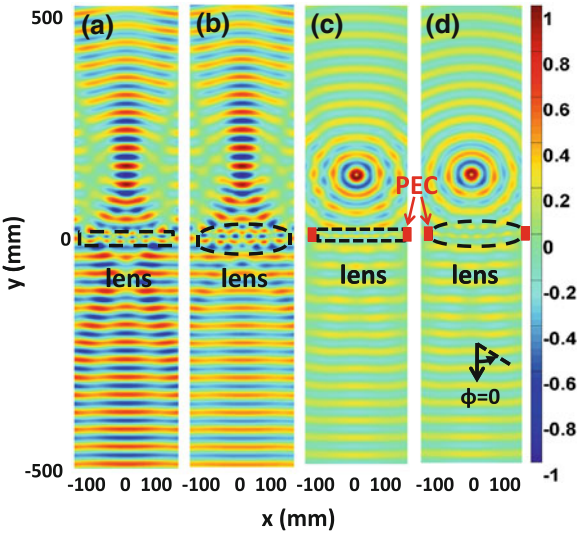

Fig. 7.12 The real part of the E_z field at 8 GHz. **a** A plane wave illuminates the low-resolution flat lens from the bottom. The focal length is 130 mm. **b** The same plane wave illuminates the conventional lens from the bottom. The focal length is 131 mm. **c** A line source is located at the focal point to feed the low resolution flat lens. **d** A line source is located at the focal point to feed the conventional lens

distribution when a plane wave is applied to illustrate the flat lens and the convex lens in Fig. 7.12a and b respectively. The focal length is measured from the center of the lens to the point with the maximum amplitude. The flat lens has a focal length of 130 mm, whilst the conventional convex lens has a focal length of 131 mm. Apparently, the two lenses focus energy to almost the same position, even though their profiles are quite different. Next, line sources are placed on the focal points of the two lenses in order to generate plane waves on the other side. Two blocks of PEC are added to the left and right sides of the lens to prevent interference from leaky waves. Figure 7.12c and d depict the real parts of the E_Z field when the low-resolution flat lens and the conventional lens are used, respectively. Indeed, plane waves are seen to emerge on the other side, which verifies the excellent performance of the simplified all-dielectric flat lens. Note also that the reflected waves are stronger on the side of $y > 0$ when the flat lens is applied. This is because blocks with large permittivity values are located in the central area of the flat lens, causing a stronger impedance mismatch to the air.

To test the relationship between the resolution and the antenna performance, in terms of the radiation pattern and the bandwidth, two additional permittivity maps with 40×8 blocks and 20×4 blocks are also generated (but are not given in Fig. 7.11). Since all these flat lenses are expected to operate from 4 to 12 GHz, the minimum wavelength is calculated at 12 GHz. In the transformation media, the average relative permittivity is about 5, therefore half the minimum wavelength is about 5.6 mm. It is apparently that blocks in the 80×15-block map and in the 40×8-block map are smaller than half the wavelength, which means that both resolutions are fine enough according to the sampling theorem. Blocks in the 20×4 map are slightly bigger than half the wavelength. This reduced resolution may harm the performance, but not significantly. The 14×1-block map has an

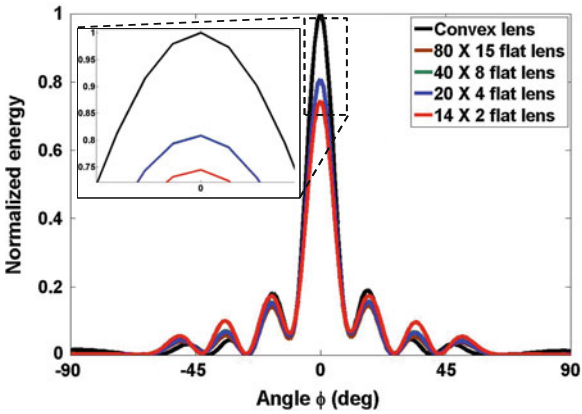

Fig. 7.13 Comparison of the radiation patterns at 8 GHz. The definition of Φ is shown in Fig. 7.12d

unqualified resolution, which will result in obvious degradation to the performance.

To prove the above assumption, the radiation patterns of the conventional lens and the four flat lenses with different resolutions are depicted in Fig. 7.13. When the permittivity map decreases from 80 × 15 blocks to 40 × 8 blocks and then to 20 × 4 blocks, the performance remains almost unchanged at 8 GHz. In the radiating direction of $\phi = 0°$, the three curves are exactly the same. The 20 × 4-block map has slightly increased side lobes compared with the other two. However, it can be considered as the threshold resolution. A visible degradation is observed when the map reduces to 14 × 1 blocks. The energy validated in the direction of $\phi = 0°$ drops to about 75 % (−1.25 dB) of that from a convex lens, accompanied with an obvious increase of side lobes. Although its performance is acceptable for many applications in practice, theoretically speaking, the properties of a propagating wave are not accurately re-constructed under this resolution. In Fig. 7.14, the radiation patterns are also tested at 4, 6, 10 and 12 GHz, respectively. Again, the 20 × 4-block map is proved to have almost the same performance as the 80 × 15-block map, indicating the resolution is adequate. As the operating frequency increases, the 14 × 1-block map brings in lower radiation around $\phi = 0°$ and different side lobes. However, from an engineering point of view, the 14 × 1-block flat lens operates effectively in a broad frequency band from 4 to 12 GHz.

Since the created flat lenses are made of isotropic dielectrics, a 3D model is straightforwardly accomplished by rotating a 2D model about its optical axis, as illustrated in Fig. 7.15. It has been demonstrated in 2D simulations that the 20 × 4-block map is a considerable threshold with a qualified resolution, whilst the 14 × 1-block map has an unqualified resolution. Accordingly, their 3D models are tested to further prove the relationship between performance and resolution. The commercial software, Ansoft HFSS [36], is applied as another tool for numerical simulation. An electric dipole is located at the focal point to generate an

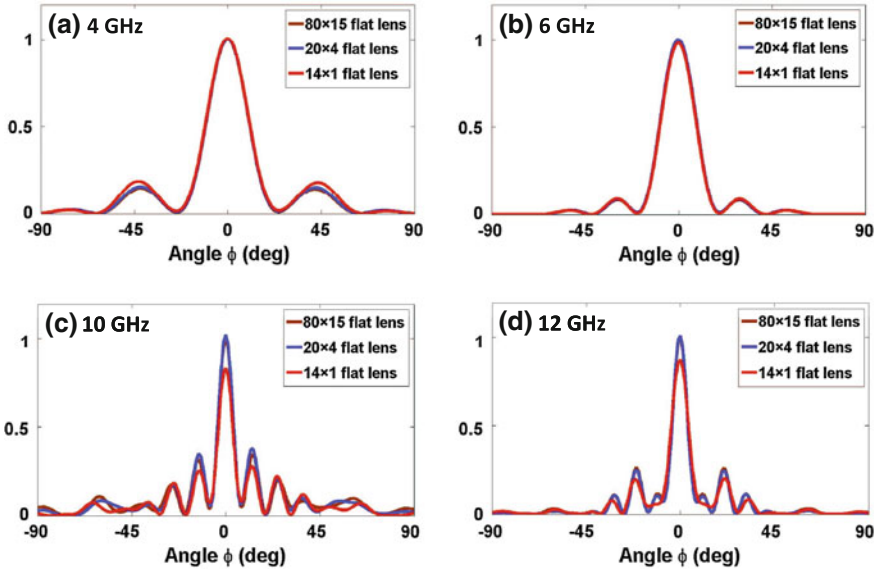

Fig. 7.14 Comparison of the radiation patterns when the flat lenses are fed by a line source at focal points. Three lenses with different resolutions (80 × 15 blocks, 20 × 4 blocks and 14 × 1 blocks) are tested at 4, 6, 10 and 12 GHz respectively

incident Hertzian-Dipole wave, and the directive property of both two flat lenses and the convex lens are compared.

Figure 7.16a–c present the directivity patterns of the three lenses in both the E-plane and the H-plane at 4, 8 and 12 GHz, respectively. At 4 GHz, when the resolution of the 14 × 1-block lens is similar to half the wavelength, the 14 × 1-block lens has almost the same directivity as the 20 × 4-block one. When the frequency increases to 8 GHz, the two lenses still have very similar directivity patterns. The lower-resolution one has slightly lower peak directivity (the maximum directivity over all the directions, as defined by HFSS), and slightly increased side lobes. As the operating frequency further increases to 12 GHz, the difference between the two lenses enlarges. The peak directivity of the low-resolution lens decreases further and the side lobes increase as well. However, the low-resolution lens still holds a good directivity pattern, which agrees well with the results from 2D simulations. Besides, the convex lens always has the best directivity in terms of the highest peak directivity and the lowest side lobes.

Figure 7.16d plots the peak directivity of the three lenses from 2 to 16 GHz, so as to compare their operating bandwidth. The convex lens has a −3 dB bandwidth from about 8.5 GHz to about 16.7 GHz (8.2 GHz span), the 20 × 4-block lens has a bandwidth from about 7.7 GHz to about 16 GHz (8.3 GHz span), and the 14 × 1-block lens has a bandwidth from about 6.6 GHz to about 15.5 GHz (8.9 GHz span). Overall, in the entire frequency band, the peak directivity decreases as the convex lens, the 20 × 4-block lens and the 14 × 1-block lens are applied respectively.

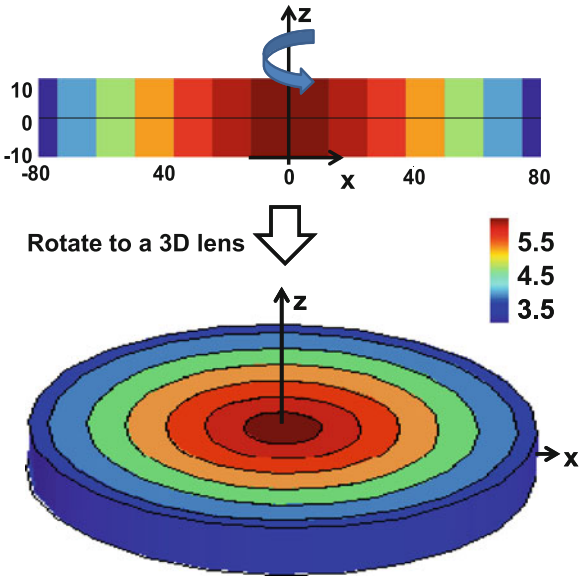

Fig. 7.15 A 3D flat lens is created by rotating the 2D permittivity map about its optical axis. The 3D lens is made of annular dielectric blocks. Colour bar shows the relative permittivity values

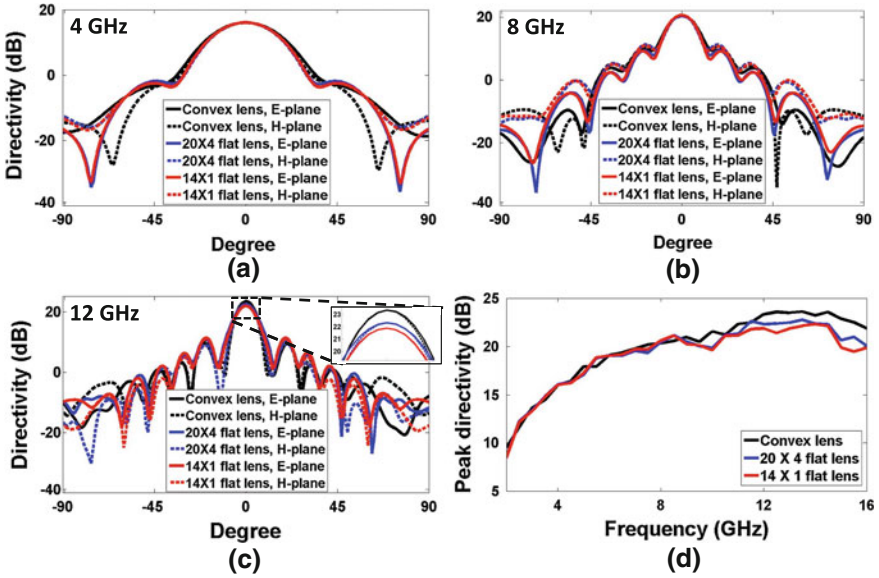

Fig. 7.16 Comparison of the directivity of the convex lens, the 20 × 4-block lens and the 14 × 1-block lens. The directivity patterns are drawn in the E-plane and the H-plane at **a** 4 GHz, **b** 8 GHz and **c** 12 GHz. In **d**, peak directivities of the three lenses are plotted from 2 to 16 GHz

The differences between the three lenses become larger as the operating frequency goes higher. It is also noted that at low frequencies, all three lenses have low directivity. The underlying physics is that when the aperture size of a lens is comparable to the wavelength, it cannot efficiently focus energy to the focal point, or reform the phase front of the wave.

7.3.3 A Broadband Zone Plate Lens

The diffractive lens, as an alternative to the traditional plano-convex lens for many optical applications, offers significantly reduced thickness with its flat profile, and thus possessing the merits of easy fabrication and small volume [37]. However, the tradeoff for such a low profile lens, based on the principle of wave diffraction instead of refraction, is narrow-band operation. For example, a Fresnel zone plate lens can obtain a very compact profile with its focal point being very close to the

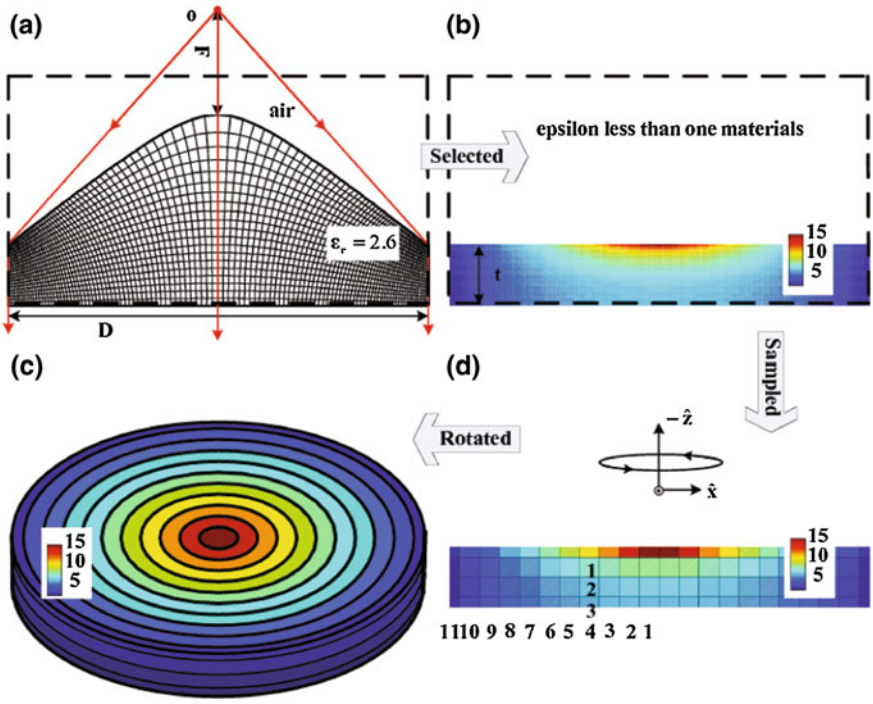

Fig. 7.17 Schematic showing of the zone plate lens design from the discrete coordinate transformation. **a** 2D hyperbolic lens in quasi-orthogonal coordinates. The parameters are $D = 63.5$ mm, $F = D/4$, $t = 9$ mm. **b** 2D flat lens with the permittivity map consisting of 110×20 blocks. **c** 2D flat lens with the permittivity map consisting of 22×4 blocks. The four layers have heights of 1.4, 3, 3 and 1.6 mm respectively in the z direction. The 1st to 10th annular thickness is 3 mm and the 11th annular thickness is 1.75 mm. **d** The 3D zone plate lens

plate [38–40], but becomes incapable of performing phase correction when the operating frequency varies. In [41], a zone plate lens utilizing a refractive instead of diffractive approach was presented for broadband operation. Using the discrete coordinate transformation, a conventional hyperbolic lens was compressed into a flat one with a few zone plates made of all-dielectric materials. Such a transformed lens maintained the broadband performance of the original lens and achieved an effectively reduced volume, thus providing a superior alternative to the diffractive Fresnel element which is inherently narrow band.

Figure 7.17 is the schematic showing of the design procedure. A quasi-orthogonal grid is generated in the virtual space where the hyperbolic lens is located, as shown in Fig. 7.17a. Figure 7.17b illustrates the permittivity map in the physical space consisting of 110 × 20 blocks. So far, a conventional hyperbolic lens in the virtual space has been completely compressed into the flat profile in the physical space, and hence the thickness of the lens is significantly reduced. After that, simplifications are again carried out, with the additional transformation layer in Fig. 7.17b neglected, and a low-resolution permittivity map (22 × 4 blocks) in Fig. 7.17d created. Finally, the 2D lens model is rotated to its optical axis and a 3D zone plate lens is therefore achieved in Fig. 7.17c.

A full-wave finite-element simulation using Ansoft HFSS is then performed to verify the proposed design. Three devices are simulated for comparison: the conventional hyperbolic lens, the transformed zone plate lens, and a quarter-wave phase-correcting Fresnel lens with the same aperture size D and the same thickness t as the zone plate lens. When a point source is placed on the focal point of each lens, all three lenses have high directivity and well-matched radiation patterns as expected at the designed central operating frequency of 30 GHz. The corresponding pattern for this scenario is shown in Fig. 7.18b. Compared with the original hyperbolic lens, the side lobes of the transformed lens become slightly higher, due to the simplification and approximation in the design. However, the transformed zone plate lens retains acceptable performance over a broad bandwidth from 20 to 40 GHz. In contrast, the phase-correcting Fresnel lens has a severely degraded directivity at both 20 and 40 GHz due to the phase error, as shown in Fig. 7.18a and c. Figure 7.18d further explores the bandwidth property of the phase-correcting Fresnel lens and the zone plate lens in term of directivity. The zone plate lens is proved to possess a steady performance over 20 to 40 GHz, while the phase correcting Fresnel lens only has 5 GHz bandwidth from 30 to 35 GHz.

7.4 Realization Methods

As pointed out in Sect. 7.2, constraints from less-than-unity permittivity or permeability have been completely removed in a device based on the discrete coordinate transformation. This fact significantly reduces the complexity of realizing a proposed design in practice, meanwhile grants the design with broadband performance because its composing material is no longer strongly dispersive in

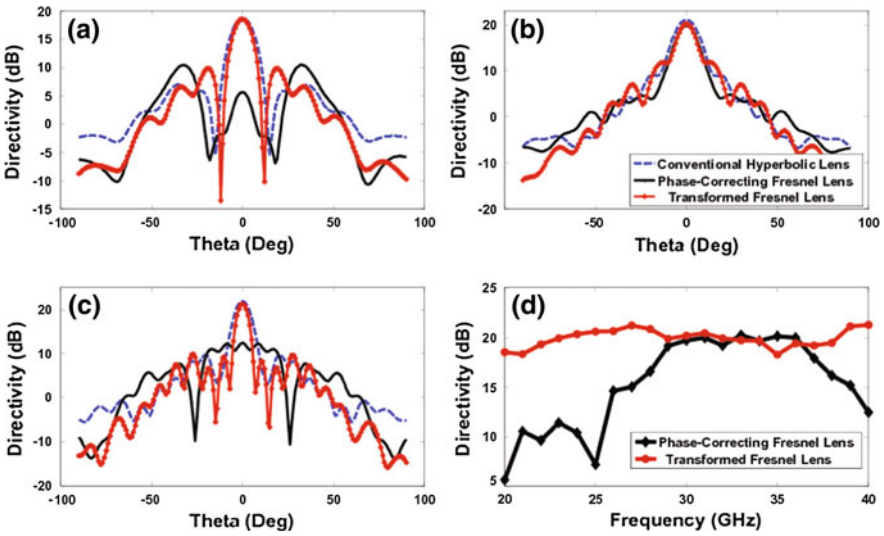

Fig. 7.18 Radiation patterns of the conventional hyperbolic lens, the transformed zone plate lens and the phase-correcting Fresnel lens at **a** 20 GHz, **b** 30 GHz, and **c** 40 GHz. **d** Comparison of broadband performance of the three lenses from 20 to 40GHz

frequency. In this section, a number of methods that can be adopted for realizing DCT based antennas are discussed.

The first option is to use sub-wavelength structure arrays, which have been well known as metamaterials [42–44]. This method is able to provide permittivity and/or permeability from negative values to almost infinitely high values, and therefore has been successfully used in many transformation optics-based devices such as the cloak reported in [3] and the carpet cloak reported in Refs. [18, 28]. Generally speaking, a metamaterial unit cell can be either an electric resonator or a magnetic one. For a DCT based antenna device that only requires higher-than-unity permittivities, a large array of electric resonators, for example, the I-shaped resonators, is an efficient option. Figure 7.19a shows a sample of the I-shaped resonator, and Fig. 7.19b illustrates the typical distribution of its effective permittivity. The real part of permittivity (blue curve) follows the Lorentz model, becomes extremely large around the resonance frequency (f_r), and changes rapidly. This property indicates an essential disadvantage of resonant metamaterials: narrow-band performance. However, as long as the required relative permittivities are not much higher or much lower than unity, such as in a DCT based antenna design, the resonant metamaterials can operate very well away from the resonance. For example, in Fig. 7.19b the I-shaped resonator has a relatively constant distribution of permittivity value over frequencies much lower than f_r. Figure 7.19c illustrates how to arrange an array of resonators to mimic a homogeneous block in a permittivity map. Full-wave simulations, the S-parameter retrieval technique [45, 46] and the effective medium theory [47] have been applied to decide the dimensions

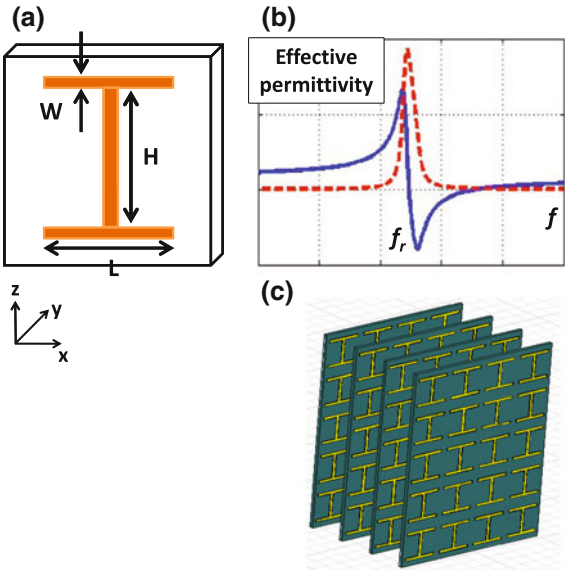

Fig. 7.19 The I-shaped electric resonator. **a** Dimensions of a unit cell. **b** The effective permittivity distribution of I-shaped resonator arrays. *Blue curve*: the real part. *Dashed red curve*: the imaginary part. **c** A group of I-shaped resonators to mimic a homogeneous block in a permittivity map

and arrangement of resonators, as described in Refs. [18, 28]. An advantage of using metamaterials based on printed circuit board (PCB) approaches as shown in Fig. 7.19c is its low cost and readiness for mass-production. The main drawback is that strong spatial and spectral dispersions may occur and therefore limit the bandwidth of the devices.

An alternative method is to drill sub-wavelength holes of different sizes in dielectric host medium. This is the same technology used in the developments of the conventional Fresnel lenses [39, 40] and the recent 3D carpet cloak [48]. These schemes can be regarded as a homogeneous medium replacing the air and the dielectric region. Generally, perforations in the host medium (ε_{r1}) lead to a lower relative permittivity value ε_{eff} ranging from $\varepsilon_{r2}^{\text{air}}$ to ε_{r1}. Apparently, several different host media may be needed to fulfill a transformation design corresponding to a required permittivity range. An efficient solution to this problem is to insert high-index dielectric cylinders ($\varepsilon_{r2}^{\text{high}}$) into the drilled holes to take place of the air. Therefore, the effective permittivity is expanded to $\varepsilon_{r2}^{\text{air}} < \varepsilon_{\text{eff}} < \varepsilon_{r2}^{\text{high}}$. Here we use this method to design the zone plate lens shown in Fig. 7.17 as an example. Figure 7.20 gives the graphical representation of the relationship between the effective permittivity and the perforation. The host material we employ here has a relative permittivity value of $\varepsilon_{r1} = 5.8$ and the filling high index dielectric has a value of $\varepsilon_{r2}^{\text{high}} = 36.7$. These specific permittivity values are chosen because they are from available dielectrics, and have been successfully applied in the conventional Fresnel lens fabrications [39, 40] and an unidirectional free space cloak design [49]. The effective permittivity can be estimated from the area ratio between the holes ($\pi d^2/4$) and the unit cell (l^2) [39, 40]. A more accurate way is to

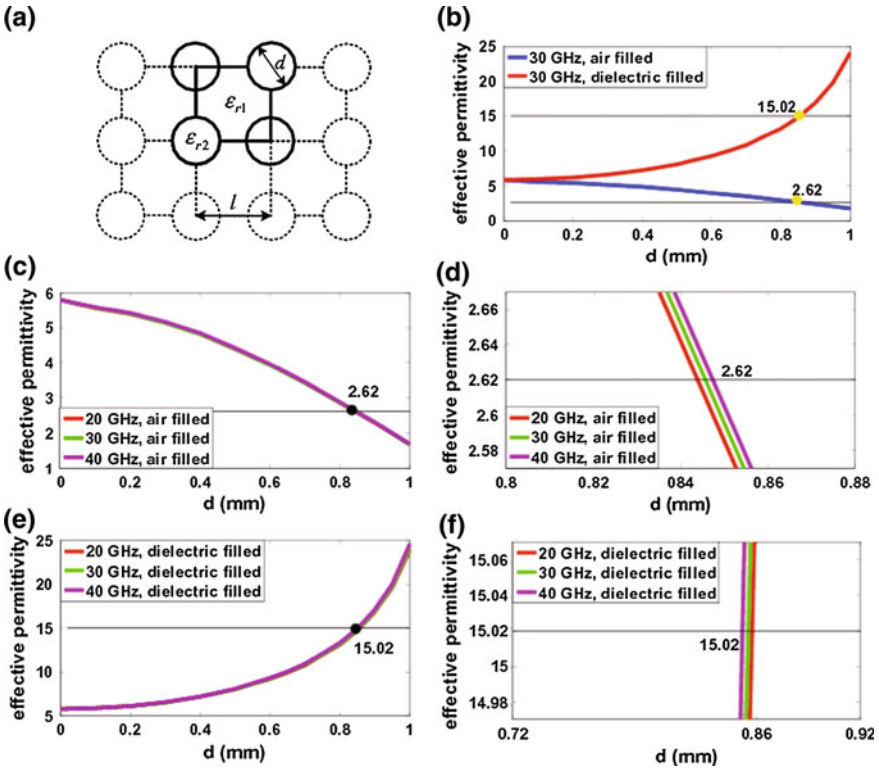

Fig. 7.20 Graphical representation of the relationship between the effective permittivity and the perforation. The host medium chosen here is $\varepsilon_{r1} = 5.8$, and the filling material is air $\varepsilon_{r2}^{\text{air}} = 1$ or $\varepsilon_{r2}^{\text{high}} = 36.7$. d refers to the hole diameter, and l refers to the length of side of the unit cell. $l = 1$ mm is sub-wavelength scaled in order to make the effective media more homogeneous. **a** Perforated host medium with square unit cell topology. **b** The effective permittivity achieved from the square unit topology at 30 GHz as d is varied. The maximum value is 24.11, and the minimum value is 1.68. **c** Frequency response of the effective perforated medium from 20 to 40 GHz. **d** Magnified picture of the frequency response in (**c**) around the effective permittivity equal to 2.62. **e** Frequency response of the perforated medium filled with high dielectric material from 20 to 40 GHz. **f** Magnified picture of the frequency response in (**e**) around the effective permittivity equal to 15.02. (The curves at different frequencies are very similar, and in (**c**), (**d**), (**e**), (**f**) clearly overlapped. This represents, for our purposes, dispersionless effective media. The parameter retrieval in (**b**), (**c**), (**d**), (**e**), and (**f**) assumes the unit cell to be periodically infinite. In practice, the finiteness of the structure will result in slight changes in effective permittivity)

retrieve the permittivity value from S parameters [46]. Given $l = 1$ mm, different d will lead to different effective permittivity, as shown in Fig. 7.20b. As d varies, the effective permittivity ranges from 1.68 to 24.11. In addition, we can see that the effective permittivity is for our purposes dispersionless, and does not vary much with the frequency as long as the unit cell is sub-wavelength, as shown in Fig. 7.20c–f. Table 7.1 gives the detailed value of d as a solution to realize the

Table 7.1 The perforation size (d) in every unit cell shown in Fig. 7.20. The unit size is $l = 1$ mm

d (mm)	1	2	3	4	5	6	7	8	9	10	11
1	0.85	0.83	0.74	0.68	0.59	0.50	0.36	0.19	0.31	0.57	0.76
2	0.52	0.51	0.49	0.46	0.40	0.34	0.15	0.21	0.46	0.66	0.82
3	0.34	0.33	0.31	0.29	0.24	0.14	0.13	0.34	0.52	0.69	0.84
4	0.28	0.28	0.25	0.23	0.16	0.00	0.26	0.36	0.52	0.69	0.85

required permittivity distribution shown in Fig. 7.17c. To be noted, for relative permittivities larger than 5.8, we drill holes and then fill in the high-index dielectric cylinders. In this way, the proposed zone plate lens in Sect. 7.3.3, whose relative permittivity ranges from 2.62 to 15.02, can be completely realized in practice.

Furthermore, the DCT based devices can be realized using non-magnetic and isotropic dielectrics which exhibit only slight dispersion and low loss. These materials are commonly available in nature and are easily controlled and produced. For demonstrating purpose, here we present an all-dielectric design of a carpet cloak that reported in [19].

To begin with, a carpet cloak is designed in [50], and the permittivity map is down-sampled to six dielectric blocks as shown in Fig. 7.21, with refractive indexes of 1.08, 1.14 and 1.21, corresponding to relative permittivities of 1.17, 1.30 and 1.46. These dielectrics are located around a metallic perturbation that is

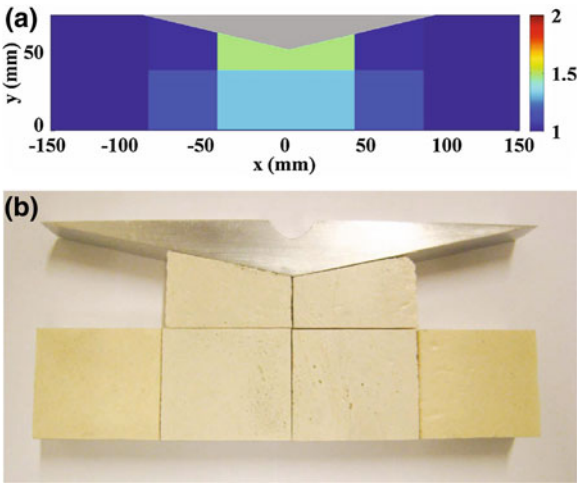

Fig. 7.21 The perturbation bounded by the composite dielectrics. The perturbation is an aluminium triangle of height 16 mm and base 144 mm. At the base of the triangle is a metal boundary. In **a**, the dielectric 2D map of the 4×2 blocks is shown. The dielectric blocks are rectangles of dimension 34. 25×30 mm^2. The fabricated cloak is shown in (**b**). In practice, a metallic ground plane is located at the base of the triangular perturbation, while the entire structure is enclosed within parallel metallic plates

to be 'hidden' from the incident electromagnetic waves. The dielectric blocks have a size of 34.25 × 30 mm^2 ($1.14\lambda \times \lambda$ at 10 GHz), with the dielectric blocks in contact with the perturbation cut appropriately as shown in Fig. 7.21. The perturbation is an electrically large aluminium triangle with a base of 144 mm and a height of 16 mm ($b = 4.8\lambda$ and $h = 0.53\lambda$ at 10 GHz). At the base of the triangle is a metallic ground plane. The fabricated cloak is shown in Fig. 7.21b.

The first stage in the realization of the cloak is the development and full characterization of the dielectric mixtures. The requirements for the composing materials of each block are that they exhibit low loss and low dispersion at microwave frequencies. Homogeneous composites of polyurethane and ceramic particles are required, with strong bonding between ceramic particles and the polymer matrix, and reasonably good mechanical properties. Additionally, composites with the requisite range of dielectric properties must be easily fabricated on demand. Accordingly, a dielectric mixture of polyurethane with high-κ barium titanate ($BaTiO_3$) is found to be suitable for this purpose. Polyurethane is used to create a low-κ foam matrix, and $BaTiO_3$ is used to load the foam in order to increase the effective permittivity while not greatly altering the mechanical properties of the structure. The density of $BaTiO_3$ powder is low, and the small particle size is advantageous when used in a dispersion system and is less likely to affect the polymer matrix structure. This results in less damage to the mechanical properties of the composite material. Both substances exhibit low loss and low dispersion at microwave frequencies, and are thus suitable for our requirements.

A range of $BaTiO_3$ / polyurethane composites were fabricated to realize the required permittivity values by changing the $BaTiO_3$ particle loading. The relative permittivity of the composite at 1 MHz and 10 GHz are measured and plotted in Fig. 7.22. The measured permittivities show very good agreement with the specified values, with errors of up to about 2 %. Furthermore, as the measured permittivities at both frequencies agree relatively well, it would imply that there is

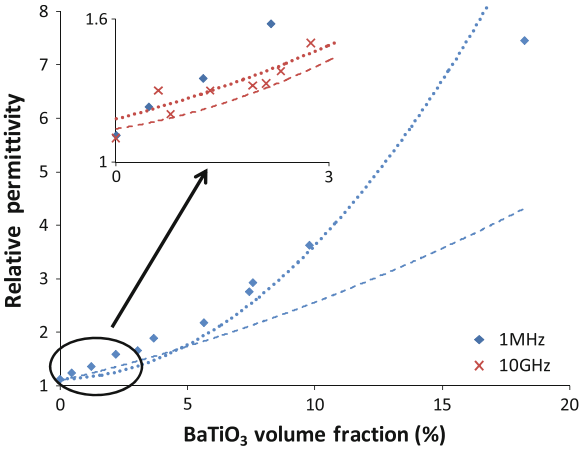

Fig. 7.22 Measured relative permittivity versus $BaTiO_3$ volume fraction of the $BaTiO_3$/polyurethane composite, at 1 MHz and 10 GHz. Measured points are plotted and compared with the Maxwell-Garnett (· · ·) and Bruggeman (——) effective medium relationships for three-phase mixtures

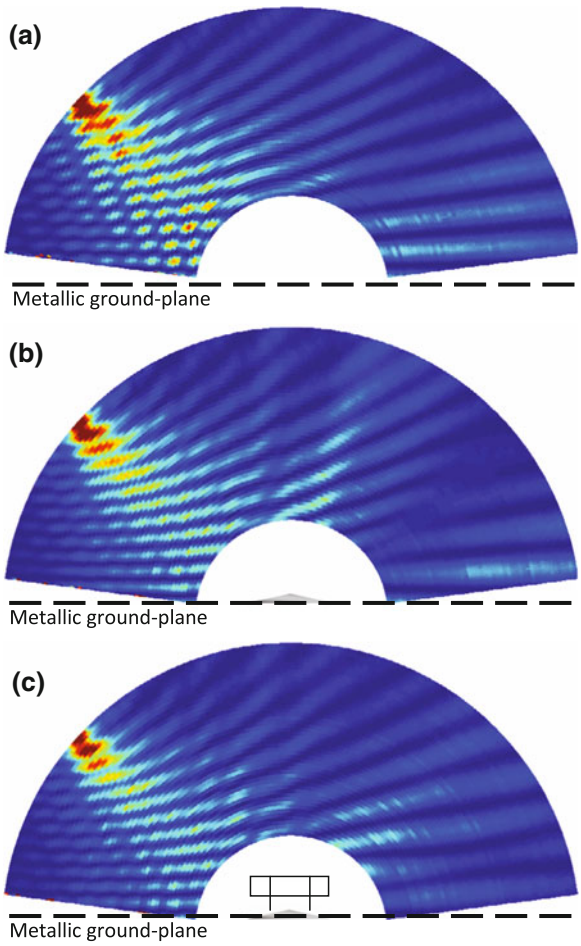

Fig. 7.23 Measured electric fields. The electric fields measured in the near-field scanning system are shown. Due to the setup of the scanning system, the semicircular region in which the perturbation and cloak are placed cannot be scanned and is left blank. **a** The empty system (no perturbation or cloak), showing only the incident wave reflecting off of the metallic ground plane. **b** The perturbation resting on the ground plane. **c** The cloaked perturbation. Strong scattering is evident with the perturbation. The cloak significantly reduces the scattering due to the perturbation, with the resulting field distribution similar to that of the perturbation-free system

little dispersion between the bands. It is clear that a large range of permittivity values can be attained by controlling the volume percentage of $BaTiO_3$.

A prototype of the all-dielectric carpet cloak is measured in a near-field scanner system which operates at frequencies between 6 and 12 GHz. It is composed of two parallel conducting plates, each with a diameter of 1 m and spaced 15 mm apart. Holes have been drilled in the top plate, which rotates at intervals that give a resolution of 5 mm. A monopole measures the fields between the two plates at each interval, while a wave is incident from a fixed X-band waveguide (single-mode operational frequency range: 8.2 to 12.4 GHz; cutoff frequency: 6.557 GHz). Details of the measurement setup is described in [19]. Figure 7.23 shows the measured electric fields inside the near-field scanner system. Firstly, the near-field scanner is tested with an empty setup. The measured 2D field amplitude plot is shown in Fig. 7.23a, with the well-formed wavefronts visible. Figure 7.23b represents the measured fields when the perturbation has been introduced. In this case,

the effect on the incoming wave is clearly evident, with scattering and diffraction leading to at least two visibly separate paths of the reflected waves. The goal of the carpet cloak is to 'hide' the electrically large metallic perturbation; reconstructing the scattered waves so that they appear identical to those of the empty scanner. To accomplish this, the dielectric materials are ordered around the object, as illustrated in Fig. 7.21b. In the measurement shown in Fig. 7.23c, it is clear that, in contrast to the perturbed case, the scattered fields appear less affected by the block; the two separate scattered beams are no longer visible, and the wavefront profile appears very similar to that of the empty scanner. In conclusion, the carpet cloak composed of only six dielectric blocks does function to 'hide' the perturbation.

7.5 Summary

In this chapter, the discrete coordinate transformation (DCT) was introduced as a practical implementation of the transformation electromagnetics to create all-dielectric antennas. It was demonstrated in theory that under certain orthogonal conditions, this method can lead to transformation devices composed of isotropic and non-magnetic dielectrics. Due to this property, the discrete coordinate transformation is extremely suitable for the design of broadband antennas with compact volumes, flexible profiles and even custom-projected electromagnetic performances, as well as specifying designs that are easy to fabricate. Several broadband antenna devices, including a flat reflector, a flat lens, and a zone plate Fresnel lens were designed and numerically validated as examples. In addition, three different realization methods for DCT based designs were discussed and demonstrated.

References

1. Leonhardt U (2006) Optical conformal mapping. Science 312:1777–1780
2. Pendry JB, Schurig D, Smith DR (2006) Controlling electromagnetic fields. Science 312:1780–1782
3. Schurig D, Mock JJ, Justice BJ, Cummer SA, Pendry JB, Starr AF, Smith DR (2006) Metamaterial electromagnetic cloak at microwave frequencies. Science 314:977–980
4. Cai W, Chettiar UK, Kildishev AV, Shalaev VM (2007) Optical cloaking with metamaterials. Nature Photon 1:224–227
5. Jiang WX, Chin JY, Li Z, Cheng Q, Liu R, Cui TJ (2008) Analytical design of conformally invisible cloaks for arbitrarily shaped objects. Phys Rev E 77:066607
6. Alù A, Engheta N (2008) Multifrequency optical invisibility cloak with layered plasmonic shells. Phys Rev Lett 100:113901
7. Luo Y, Chen H, Zhang J, Ran L, Kong JA (2008) Design and analytical full-wave validation of the invisibility cloaks, concentrators, and field rotators created with a general class of transformations. Phys Rev B 77:125127
8. Chen H, Hou B, Chen S, Ao X, Wen W, Chan CT (2009) Design and experimental realization of a broadband transformation media field rotator at microwave frequencies. Phys Rev Lett 102:183903

9. Rahm M, Schurig D, Roberts DA, Cummer SA, Smith DR, Pendry JB (2008) Design of electromagnetic cloaks and concentrators using form-invariant coordinate transformations of Maxwell's equations. Photon Nanostruct Fundam Appl 6:87–95
10. Yaghjian AD, Maci S (2008) Alternative derivation of electromagnetic cloaks and concentrators. New J Phys 10:115022
11. Jiang WX, Cui TJ, Cheng Q, Chin JY, Yang XM, Liu R, Smith DR (2008) Design of arbitrarily shaped concentrators based on conformally optical transformation of nonuniform rational B-spline surfaces. Appl Phys Lett 92:264101
12. Alù A, Engheta N (2009) Cloaking a sensor. Phys Rev Lett 102:233901
13. Narimanov EE, Kildishev AV (2009) Optical black hole: Broadband omnidirectional light absorber. Appl Phys Lett 95:041106
14. Cheng Q, Cui TJ, Jiang WX, Cai BG (2010) An omnidirectional electromagnetic absorber made of metamaterials. New J Phys 12:063006
15. Kong F, Wu B, Kong JA, Huangfu J, Xi S, Chen H (2007) Planar focusing antenna design by using coordinate transformation technology. Appl Phys Lett 91:253509
16. Kundtz N, Smith DR (2009) Extreme-angle broadband metamaterial lens. Nat Mater 9:129–132
17. Li J, Pendry JB (2008) Hiding under the carpet: A new strategy for cloaking. Phys Rev Lett 101:203901
18. Liu R, Ji C, Mock JJ, Chin JY, Cui TJ, Smith DR (2009) Broadband ground-plane cloak. Science 323:366–369
19. Bao D, Rajab KZ, Hao Y, Kallos E, Tang W, Argyropoulos C, Piao Y, Yang S (2011) All-dielectric invisibility cloaks made of BaTiO3-loaded polyurethane foam. New J Phys 13:103023
20. Valentine J, Li J, Zentgraf T, Bartal G, Zhang X (2009) An optical cloak made of dielectrics. Nat Mater 8:568–571
21. Gabrielli LH, Cardenas J, Poitras CB, Lipson M (2009) Silicon nanostructure cloak operating at optical frequencies. Nature Photon 3:461–463
22. Thompson JF, Soni BK, Weatherill NP (1999) Handbook of grid generation. CRC Press, Boca Raton
23. Holland R (1983) Finite-difference solution of maxwell's equations in generalized nonorthogonal coordinates. IEEE Trans Nucl Sci 30:4589–4591
24. Hao Y, Railton CJ (1998) Analyzing electromagnetic structures with curved boundaries on Cartesian FDTD meshes. IEEE Trans Microwave Theory Tech 46:82–88
25. Pozar DM (2005) Microwave engineering, 3rd edn. Wiley, London
26. Tang W, Argyropoulos C, Kallos E, Song W, Hao Y (2010) Discrete coordinate transformation for designing all-dielectric flat antennas. IEEE Trans Ant Propag 58:3795–3804
27. Mesh and grid generation software for CFD - Pointwise. http://www.pointwise.com/
28. Ma HF, Jiang WX, Yang XM, Zhou XY, Cui TJ (2009) Compact-sized and broadband carpet cloak and free-space cloak. Opt Express 17:19947–19959
29. Kallos E, Argyropoulos C, Hao Y (2009) Ground-plane quasicloaking for free space. Phys Rev A 79:63825
30. Shannon CE (1949) Communication in the presence of noise. Proc IRE 37:10–21
31. Taflove A, Hagness SC (2005) Computational electrodynamics : the finite-difference time-domain method, 3rd edn. Artech House, London
32. Hao Y, Mittra R (2009) FDTD modeling of metamaterials: theory and applications. Artech House, London
33. Zhao Y, Argyropoulos C, Hao Y (2008) Full-wave finite-difference time-domain simulation of electromagnetic cloaking structures. Opt Express 16:6717–6730
34. Argyropoulos C, Zhao Y, Hao Y (2009) A radially-dependent dispersive finite-difference time-domain method for the evaluation of electromagnetic cloaks. IEEE Trans Ant Propag 57:1432–1441

35. Yan M, Ruan Z, Qiu M (2007) Scattering characteristics of simplified cylindrical invisibility cloaks. Opt Express 15:17772–17782
36. HFSS: 3D full-wave electromagnetic field simulation. http://www.ansoft.com/products/hf/hfss
37. Loewen EG, Popov E (1997) Diffraction gratings and application. Marcel Dekker, New York
38. Hristov HD (2000) Fresnel zones in wireless lines, zone plate lenses and antennas. Wrtech House, London
39. Petosa A, Ittipiboon A (2003) Design and performance of a perforated dielectric Fresnel lens. IEE Proc Microw Antennas Propag 150:309–314
40. Petosa A, Ittipiboon A, Thirakoune S (2006) Investigation on arrays of perforated dielectric Fresnel lenses. IEE Proc Microw Antennas Propag 153:270–276
41. Yang R, Tang W, Hao Y (2011) A broadband zone plate lens from transformation optics. Opt Express 19:12348–12355
42. Pendry JB, Holden AJ, Stewart WJ, Youngs I (1996) Extremely low frequency plasmons in metallic mesostructures. Phys Rev Lett 76:4773–4776
43. Pendry JB, Holden AJ, Robbins DJ, Stewart WJ (1999) Magnetism from conductors and enhanced nonlinear phenomena. IEEE Trans Micr Theory Techn 47:2075–2084
44. Schurig D, Mock JJ, Smith DR (2006) Electric-field-coupled resonators for negative permittivity metamaterials. Appl Phys Lett 88:041109
45. Smith DR, Schultz S, Markoš P, Soukoulis CM (2002) Determination of effective permittivity and permeability of metamaterials from reflection and transmission coefficients. Phys Rev B 65:195104
46. Smith DR, Vier DC, Koschny Th, Soukoulis CM (2005) Electromagnetic parameter retrieval from inhomogeneous metamaterials. Phys Rev E 71:036617
47. Smith DR, Pendry JB (2006) Homogenization of metamaterials by field averaging. J Opt Soc 23:391
48. Ma HF, Cui TJ (2010) Three-dimensional broadband ground-plane cloak made of metamaterials. Nat Commun 1:21
49. Bao D, Kallos E, Tang W, Argyropoulos C, Hao Y, Cui TJ (2010) A broadband simplified free space cloak realized by nonmagnetic dielectric cylinders. Front Phys China 5:319–323
50. Kallos E, Argyropoulos C, Hao Y (2009) Ground-plane quasicloaking for free space. Phys Rev A 79:63825

Chapter 8
Transformation Electromagnetics Inspired Lens Designs and Associated Metamaterial Implementations for Highly Directive Radiation

Douglas H. Werner, Zhi Hao Jiang, Jeremiah P. Turpin, Qi Wu and Micah D. Gregory

Abstract In this chapter, the transformation electromagnetics (TE) approach for achieving highly directive radiation is introduced and demonstrated by both numerical simulations and experimental results obtained from laboratory prototypes. In addition to conventional approaches for designing directive antennas, the recently developed metamaterial-related techniques, such as the electromagnetic bandgap (EBG) structures, zero-index metamaterials, and transformation optics (TO), are reviewed. In particular, several coordinate transformations which can provide simplified material parameters are proposed, including the conformal mapping, quasi-conformal (QC) mapping, geometry-similar transformation, and the uniaxial media simplification method. All of these techniques are capable of achieving a certain degree of simplification in the transformed material parameters without sacrificing the device performance. The design and demonstration of various beam collimating devices illustrate their unique properties and suitability for different applications such as in compact wireless systems. In all, these TE-enabled lenses with simple material parameters are expected to find widespread applications in the fields of microwave antennas as well as optical nanoantennas.

D. H. Werner (✉) · Z. H. Jiang · J. P. Turpin · Q. Wu · M. D. Gregory
Department of Electrical Engineering, The Pennsylvania State University, University Park, PA 16802, USA
e-mail: dhw@psu.edu

Z. H. Jiang
e-mail: zuj101@psu.edu

J. P. Turpin
e-mail: jpt189@psu.edu

Q. Wu
e-mail: quw12@psu.edu

M. D. Gregory
e-mail: mdg243@psu.edu

D. H. Werner and D.-H. Kwon (eds.), *Transformation Electromagnetics and Metamaterials*, DOI: 10.1007/978-1-4471-4996-5_8,

8.1 Introduction

The field of worldwide wireless communication has been experiencing a revolutionary growth over the past two decades. As demand continues to increase for more agile wireless systems with superior performance, the creation of highly directive antennas that are light weight, low cost, and possess a small footprint are of great importance for a variety of applications such as automotive radars, multiple-input multiple-output (MIMO) systems, base station antennas, microwave positioning devices, and so on. In the past, several conventional techniques have been employed to achieve high directivity, including horn antennas, arrays, and lenses. However, these relatively large conventional antennas become less desirable as the size of the wireless system shrinks due to the use of advanced materials and improved electronics technology. Other recently developed methodologies including Fabry-Parot cavity and EBG structures have been shown to be effective in creating highly directive radiating beams with a lower profile and lighter weight. These exhibit certain advantages over their conventional counterparts at the expense of sacrificing some of the design flexibility such as bandwidth and the number and direction of the highly collimated beams. The nascent field of Transformation Optics (TO), sometimes also referred to as Transformation Electromagnetics (TE), was first introduced to the community through a demonstration of the invisibility cloak. Soon after its introduction, however, the potential of TO as a useful tool in antenna engineering began to be realized. One of the most compelling applications of TO has been in the development of highly directive antennas, where it offers additional degrees of freedom and design flexibility compared to conventional approaches. This TO design methodology holds great promise for future functionality-rich high-performance antenna systems. In this chapter, we first review some of the various techniques of generating highly directive antennas that have been commonly employed during the past as well as those that have been proposed very recently. We then introduce several TO-related design and synthesis methodologies for creating either single or multiple highly directive beams in both two and three dimensions. Several examples will be presented for each method which include simulations and experimental results.

8.2 Review of Directive Radiation Techniques

As early as the 1930s, engineers have been exploiting various approaches to increase the directivity of antennas for various applications ranging from radar, space, and military communications to public and private wireless networks and cell systems. In this section, a review is provided on some of the more conventional techniques that have been employed in antenna engineering to achieve highly directive radiation. New methods that have been proposed more recently are also examined.

8.2.1 Horn Antennas, Reflectors, Arrays, and Lenses

One of the most common devices used for realizing highly directive radiation in the microwave regime is the horn antenna [1–3]. The horn is formed simply by gradual expansion of the metallic profile of one or both axes of a waveguide, which provides an impedance matching transition from the guide to free space. When properly designed, the area at the opening of the horn determines the amount of gain. Horn antennas are very popular due to their relative ease of design and construction, moderate amount of bandwidth (typically that of the feeding waveguide), and high gain. The primary drawback to horn antennas is the large physical size and associated weight of the long phase-matching tapered section between the waveguide and the aperture. In addition, diffraction at the edges of the aperture leads to somewhat high sidelobe and backlobe levels, which can be mitigated with modification to the aperture edges [4] or by adding special linings to the walls of the horn [5].

Reflector antennas are another very popular option for achieving high directivity, sometimes utilized in combination with the aforementioned horn antenna which serves as a feed [3, 6]. This type of antenna is designed mainly using geometrical optics theory and ray tracing since the size of the reflector is on the order of many wavelengths. The reflector surface, most commonly parabolic, is configured such that incident radiation collects at the focal point, where another antenna is positioned to receive the energy. The reflector is a relatively simple method for allowing the antenna to collect or transmit energy over a much larger aperture area than the antenna in isolation. Commonly called dish antennas, these are used to create systems with extremely high directivity; however, the surface tolerances must be properly met to ensure beam focusing without aberrations. Beam steering is possible through mechanical rotation of the dish, or in the case of a spherical dish, by moving the feed. The radiation pattern of the dish depends on the feed antenna, which may be a horn, simple dipole or patch, or sometimes an array of antennas. Spillover and diffraction can occur at the edges of the dish, which must be considered for certain applications.

Antenna arrays have long been used as a method for increased directivity and gain in radio frequency systems. The two most common types are broadside and end-fire arrays [3]. Broadside arrays attempt to approximate a large aperture antenna, with the added benefit of being able to electronically steer the main beam through controlling the phase of individual elements. In addition, adjusting the amplitude and phase of the elements allows for very flexible radiation pattern customization [3, 7, 8]. These types of arrays most commonly come in a periodic linear or planar configuration to allow for high directivity (as well as beam steering) in one or two dimensions. When elements are placed in a regular lattice to create these large effective apertures and high directivity, care must be taken with respect to the element–element spacings so that grating lobes are avoided. Grating lobes appear when the electrical distance between elements in a broadside unsteered periodic array becomes greater than one wavelength, causing radiation

in undesired directions. Methods have been developed for the design of aperiodic arrays which are devoid of these gratings at the cost of increased design complexity compared to their periodic counterparts [9]. The main drawback of the antenna array is the complexity and expense of the feeding network, which typically contains either a beam forming network or phase shifters and feeding structure for each individual element.

End-fire arrays have seen a great deal of use since their inception [8, 10, 11]. This form of linear array has the greatest radiation along its axis, generating greater directivity than the cross-sectional aperture area would ordinarily suggest. Elements in this type of array must have phase tapers to ensure that the beam has greatest directivity at endfire, operating similarly to a standard linear array steered 90° from broadside. Certain refinements on the design of these types of arrays have been made which allow for higher directivity [10] as well as parasitic operation with a single driven element [12]. Broadcast television has greatly popularized the use of the Yagi-Uda antenna as a means for high directivity reception with a relatively simple mechanical structure. However, these linear arrays are usually narrowband due to the sensitive interference among the driven and parasitic directing elements. In addition, they are more suitable for applications that require unidirectional radiation due to the difficulty and complexity in producing a multibeam pattern using such configurations.

Dielectric lenses are most commonly used in the optical regime, however, they can have applications in the microwave spectrum as well. Like the reflector antennas, these are designed primarily by using optical techniques. Microwave lenses typically comprise metal [13, 14] or dielectric [15, 16], and operate similarly to their optical counterparts. The microwave lens aims to create a uniform phase front over a large aperture and is fed by another antenna, much like a reflector. Some special types of lenses such as the Luneberg [17] and Rotman [18] lenses have unique application in the radio frequency regime and can be used for simple beam scanning [19]. Microwave lenses can be used to achieve high directivity, however, they are often physically bulky and heavy. Simple lenses suffer from poor matching from free space to the dielectric unless some consideration to impedance matching is implemented [20] or a material with very low refractive index is used. For dielectric lenses, low-loss materials must be employed to avoid reduced gain through absorption.

8.2.2 Fabry–Perot Cavity and Electromagnetic Bandgap-Based Antennas

The Fabry–Perot interferometer was primarily an optical device when it originated in the late nineteenth century. It has since been adapted to the microwave and mm-wave spectrum for various purposes [21–23]. As in the optical domain, a source placed inside the cavity will lead to directive radiation from one or two partially

transmissive mirrors. These mirrors can take the form of dielectrics [22] or of a frequency-selective surface (FSS) screen [23]. Such antennas are capable of demonstrating very high directivity over only an extremely narrow bandwidth due to the structural resonance that creates the collimating effect, which is narrowband unless some manner of tuning is included [24]. Although it is possible for this type of antenna to be very light weight, especially with the metallic screen-based mirror implementation, the structure must be relatively thick to permit resonance at the radiating frequency, at least $\lambda/4$.

The recently introduced EBG structure was derived from the atomic bandgap systems found in solid-state physics [25, 26]. This type of periodic structure with a forbidden frequency band has found many applications in electromagnetic design including antenna synthesis. One very useful application is for high-impedance surfaces or artificial magnetic conductors (AMCs), which permit placing antennas very close to a ground plane [26–28]. These allow for directivity improvement when an antenna is placed in close proximity to the AMC reflecting panel without the reduction in input efficiency that would be experienced in the presence of an ordinary electrically conducting plate. Another application is to reduce or prevent mutual coupling from nearby antennas since the EBG material blocks the propagation of surface waves along a conductor [29]. EBGs are usually implemented with subwavelength periodic metallo-dielectric structures similar to frequency selective surfaces, such as the common mushroom structure [26, 29]. Several high-directivity antenna designs were published that utilize EBG structures as the partially transmissive mirror in Fabry–Perot resonators, which have been shown to exhibit directivity very close to that of an ideally illuminated aperture [30, 31].

8.2.3 Zero-Index Metamaterial Lenses

As a rapidly evolving field, metamaterials with exotic electromagnetic properties such as negative or zero/low index of refraction give rise to new phenomena that are unable to be achieved with conventional positive index materials [32–36]. Compared with negative index metamaterials, which have garnered intense research interest, zero/low index metamaterials (ZIMs/LIMs) [37–41] have received less attention but possess a growing repertoire of possible practical applications. A zero refractive index condition can be achieved by three different cases of the permittivity and permeability [42]. The first case, where the permittivity approaches zero, results in a large value for the effective impedance and a corresponding reflection coefficient approaching +1, meaning that the reflected wave is in-phase with the incident wave. In the second case, when the permeability approaches zero, the material acts like a perfect electric conductor, with the reflection coefficient approaching -1. Hence, in the first two cases the ZIM acts as either a perfect magnetic mirror (in-phase reflection) or a perfect electric mirror (180° out-of-phase reflection). The final and perhaps the most interesting case is when the permittivity and permeability simultaneously approach zero at the same

rate, resulting in a ZIM that is impedance-matched to free space [41]. This type of "matched" ZIM is an essential component in many TO devices such as an electromagnetic cloak. An important property of ZIMs, as revealed recently, is their ability to act as an effective collimator [37], i.e., to convert cylindrical or spherical waves emanating from a source embedded in the metamaterial to plane waves at the interface between the metamaterial and free space. Thus, ZIMs/LIMs have a great potential in applications involving the control of radiation directivity of microwave, terahertz, and even optical antennas.

The basic operation of the ZIM/LIM lenses can be explained by Snell's law [43]. As shown in Fig. 8.1, a line source is located inside a slab of material with a zero index of refraction. Without the ZIM, the line source radiates isotropically, creating a cylindrical wave front. However, with the slab of ZIM present, the radiated wave undergoes refraction when passing through the interface between the ZIM and the outside free space. Snell's law states that

$$\sin\theta_1/n_2 = \sin\theta_2/n_1 \tag{8.1}$$

where θ_1 and θ_2 are the refracted and incident angles, while n_1 and n_2 are the indices of refraction of free space and the ZIM. Since $n_1 = 1$, when the magnitude of n_2 approaches zero, θ_1 will be limited to a near-zero value regardless of the value of θ_2 (note that $0^\circ \le \theta_2 \le 90^\circ$.) That is to say, the radiated waves from the source are refracted in such a way that all the waves exiting the ZIM are propagating in a direction perpendicular to the interface. As a result, the ZIM is capable of producing highly directive radiated beams from a source embedded inside.

Several publications have reported work on the design and experimental demonstration of highly directive radiation using ZIMs. In 2002, Enoch et al. [37] first experimentally demonstrated highly directive emission using a wire-mesh type ZIM. The wire-mesh type ZIM structure can also be considered to have anisotropic properties with near-zero permittivity tensor components along the direction of the wire array. Inspired by this work, continuous-wire and cut-wire mesh type ZIMs in various configurations have been applied to enhance the directivity of a variety of antennas, including monopole antennas embedded in wire mesh covered by a metallic parallel plate waveguide [44, 45], embedding line sources inside a wire substrate [46, 47], and the addition of superstrates to patch

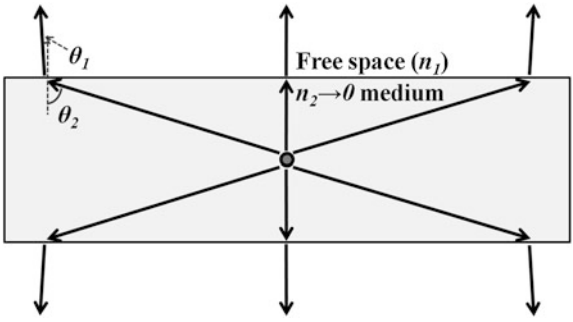

Fig. 8.1 Ray tracing of an isotropic line source embedded in a ZIM lens

antennas [48–52] and horn antennas [53, 54]. Apart from wire type ZIMs, other kinds of planar ZIMs comprising multilayer metallic patterns printed on dielectric substrates have been employed for gain enhancement of wire antennas [55, 56]. More complicated anisotropic ZIM substrates with specifications for both permittivity and/or permeability tensor parameters having near-zero values were also theoretically proposed and numerically validated to enhance the gain of embedded line sources [57–59] and planar Vivaldi antennas [60, 61]. Conventional wire and split ring resonator (SRR) composite metamaterials on printed circuit boards (PCB) have been proposed to construct such ZIM substrates [56, 62].

8.2.4 Transformation Optics/Electromagnetics Lenses

As a more recently introduced technique, the TO/TE [63–65] approach provides more comprehensive control over the propagation of electromagnetic waves in a predefined anisotropic and inhomogeneous medium. The anisotropic and spatially dependent material parameters can be calculated from the coordinate transformations that are constructed to describe the desired wave trajectories in the design. In particular, the TO/TE technique can be applied to tailor the radiation patterns of a source via the so-called source transformation, which involves redistributing the radiated power into specific directions for high directivity applications. This provides engineers and scientists with new ways of obtaining a variety of radiation patterns from a single source, such as a simple dipole, loop, or patch antenna.

To date, several TO/TE designs have been reported for achieving highly directive beams from an isotropic source embedded inside the transformed medium [66–80]. The earliest designs for TO wave collimators were based on mapping a circle in the original space into a square or rectangle in the transformed space in order to achieve highly directive radiated beams [66, 67], as shown in Fig. 8.2. The isotropically radiated waves from a line source are gradually transformed into plane-wave-like beams focusing in the far-field. Following this work, a more extensive search for transformations capable of achieving highly directive emissions was performed, resulting in designs that can produce both a single [77, 80] and multiple [68, 69] collimated beams. However, since the equi-amplitude, equiphase lines in the transformed space are not linear functions of those in the original space, the transformed media are in general strongly inhomogeneous and anisotropic and often require infinite or near-zero permittivity and/or permeability tensor parameters. This makes the realization of these transformation designs quite difficult, especially at optical wavelengths. Several other approaches have considered, instead of positive permittivity and permeability tensor parameters, negative index materials to achieve highly directive emission [70, 71]. In these methods, a non-monotonic function was employed in the coordinate transformation, thereby yielding negative values in the material parameters and compressing a large aperture into a small region, as shown in Fig. 8.3. This technique can be used to achieve highly directive emission from a relatively small aperture size.

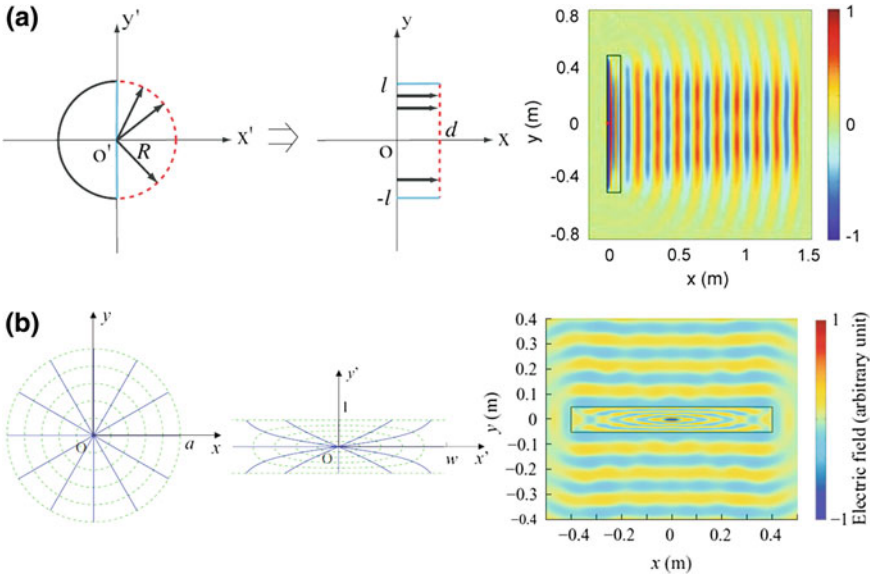

Fig. 8.2 **a** Transformation design for single highly directive radiated beam. Reproduced with permission from Zhang et al. [111], courtesy of The Electromagnetics Academy. **b** Transformation design for double highly directive radiated beams. Reproduced with permission from Kwon and Werner [67]

However, the negative values of material parameters make the implementation of a practical device difficult due to the inherently limited bandwidth and high absorption loss associated with negative index metamaterials.

More recently, highly directive emission with TO lenses that use only inhomogeneous but isotropic material parameters [73–75, 79] or homogeneous and anisotropic material parameters [72, 76, 78] have been proposed. These designs hold more promise for practical applications since the required transformed medium can be readily realized using commercially available dielectrics perforated with holes or feasible metamaterial building blocks. The class of highly directive emission transformations involving inhomogeneous isotropic material parameters can be designed using quasi-conformal (QC) mappings [81]. By eliminating the anisotropy, this TO approach only requires materials with spatially varying permittivity. Such permittivity distributions, though inhomogeneous, enable a broad operational bandwidth at the expense of slightly increased impedance mismatch at the interface between free space and the transformed medium. Broadband planar Luneburg lens antennas [73, 75], flattened reflectors [74], and multibeam antenna lenses [79] have been designed using this method. The type of transformation using only homogeneous and anisotropic materials can either be derived from conformal mappings [76] or be obtained by simplifying the geometrical shapes of both the original and transformed spaces [72, 78]. These designs can be readily implemented using anisotropic metamaterial elements, such

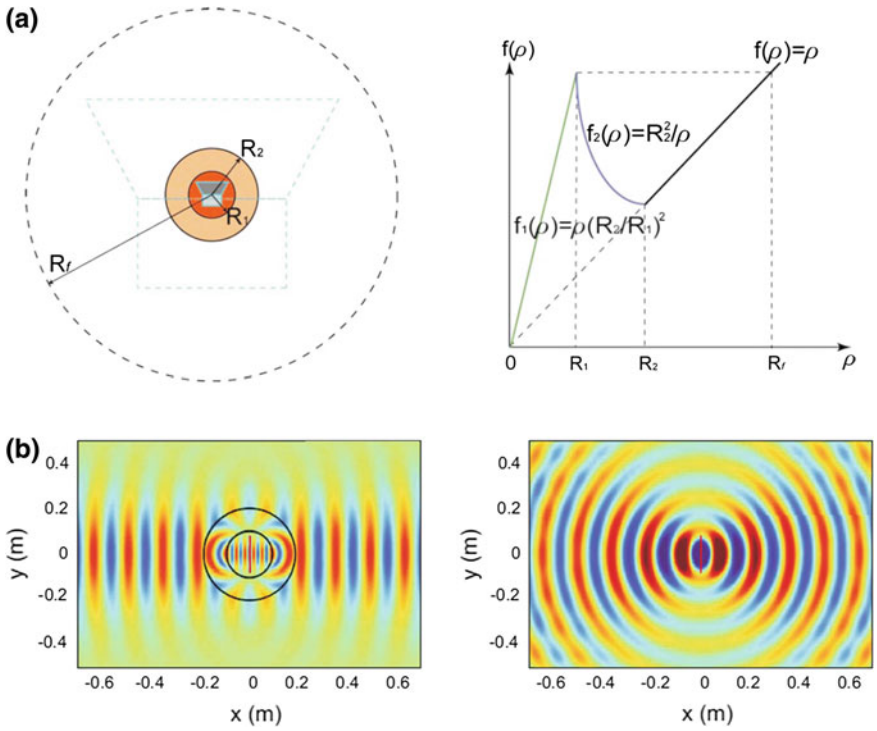

Fig. 8.3 Transformation design for highly directive emission with small antenna aperture using negative index material. Reproduced with permission from Luo et al. [70]

as cut wires and split-ring resonators, as the building blocks. By exploiting the low-index region of the metamaterials, which has lower loss and reduced dispersion compared to the negative-index region, these designs give rise to a broad bandwidth within which the highly directive emission effect can be achieved.

8.3 Design of Transformation Optics Lenses with Simple Material Parameters

In this section, several recently developed TO approaches for achieving highly directive radiation are presented, including the theory and design, full-wave simulations, as well as experimental results. The conformal mapping, geometry-similar transformation, and simplified uniaxial lens rely on the anisotropic properties of homogeneous materials, which are straightforward to implement by using identical metamaterial building blocks. The QC mapping technique, however, provides broader operational bandwidth by eliminating the anisotropy but maintaining the inhomogeneity so that devices can be realized using pure dielectrics (e.g., graded-index materials).

8.3.1 Conformal Mapping

When applying the TO design equations to an arbitrary transformation, the resulting material parameters required for implementation will be, in general, highly anisotropic and inhomogeneous. However, conformal mappings and their associated QC mappings produce TO devices with much simpler material parameters, containing only uniaxial anisotropy and inhomogeneity in the plane of the transformation [76, 82–84]. Uniaxial metamaterials are simpler to construct than those that require a general anisotropic tensor. Isotropic materials may even be substituted for the uniaxial structures in some cases where the polarization of the incident electromagnetic waves can be constrained.

8.3.1.1 Theory

Conformal mappings are functions in the complex plane (8.2) that satisfy the Cauchy-Riemann equations (8.3, 8.4).

$$g(z) = g(x + jy) = u(x, y) + jv(x, y) \tag{8.2}$$

$$\frac{\partial u}{\partial x} = \frac{\partial v}{\partial y} \tag{8.3}$$

$$\frac{\partial v}{\partial x} = -\frac{\partial u}{\partial y}. \tag{8.4}$$

Also known as analytic functions, conformal mappings are angle-preserving, meaning that the angles of intersection in the source and transformed domains will be maintained. By simplifying the mathematical expressions that represent a TO design using the differential identities defined by the Cauchy-Riemann equations, the following reduced form of the material parameters are obtained [76]:

$$\overline{\overline{\varepsilon}} = \overline{\overline{\mu}} = \begin{bmatrix} 1 & 0 & 0 \\ 0 & 1 & 0 \\ 0 & 0 & f(z) \end{bmatrix} \tag{8.5}$$

where

$$f(z) = \left(\frac{\partial u}{\partial x}\right)^2 + \left(\frac{\partial v}{\partial x}\right)^2 \tag{8.6}$$

When using a conformal mapping for the design of a TO device, the resulting material parameter tensors are uniaxial, with only one term that includes spatial variation. Since the u and v functions are both real-valued, $f(z)$ is also real-valued. If a TO device is intended for single-mode operation, *TE* or *TM* only, then further simplifications to the material parameters may be made. Since only one of either

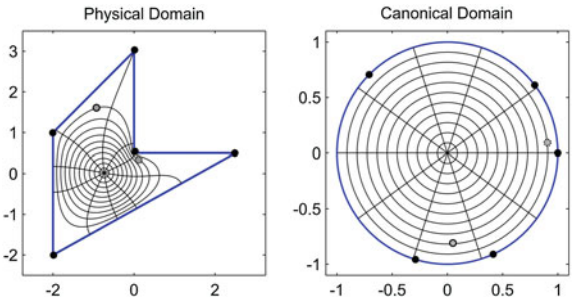

Fig. 8.4 An example of Schwartz-Christoffel mapping between a unit *disk* and a *polygon* in the complex plane

the electric or magnetic fields will interact with the inhomogeneous z-oriented optical axis of the material in such a device, then either the permeability or permittivity requirement on the material parameters may be eliminated. Similarly, the anisotropy may also be eliminated in some applications, leaving isotropic, spatially inhomogeneous material parameters that are much easier to implement. Limiting transformations to those that are conformal does reduce some design flexibility, but the ability to easily construct the conformal TO device justifies the reduced design flexibility.

Given a conformal mapping for application as a TO device, a relatively simple material implementation may be found. However, conformal mappings possessing desired properties for a TO device are difficult to generate in a straightforward fashion. Very simple conformal mappings may be easily constructed, but these will not, in general, be useful from a TO perspective. Alternatively, the Schwartz-Christoffel (SC) family of conformal mappings offer an algorithmic method of constructing useful transformations. SC transformations allow mappings to be constructed from the interior of arbitrary polygons in the complex plane to one of several canonical domains, including disks, finite and unbounded rectangles, and half-planes. A transformation is defined by a boundary polygon z_i with vertex angles α_i which are applied in Eq. (8.7) to determine the mapping function. For all except the most simple polygons, the SC equations are solved numerically, with the TO design equations also evaluated numerically [85]. Figure 8.4 shows an example of an SC mapping from the unit disk to a polygon in the complex plane.

$$f(z) = f(z_0) + c \int_{z_0}^{z} \prod_{j=1}^{n-1} (\zeta - z_j)^{\alpha_j - 1} \mathrm{d}\zeta \tag{8.7}$$

8.3.1.2 Multibeam Lenses

As an example of the conformal TO design technique, we consider the reciprocal transformation

$$g(z) = \frac{1}{z} = \frac{x - jy}{x^2 + y^2}. \tag{8.8}$$

This function is analytic according to the Cauchy-Riemann conditions, and the material parameters meet the assumptions in (8.5). Computing the material parameter tensor values as described above yields

$$\overline{\overline{\varepsilon}}_{zz} = \overline{\overline{\mu}}_{zz} = \left(\alpha x^2 + \alpha y^2\right)^2. \tag{8.9}$$

Since no boundaries are specified in the transformation, the TO device boundaries are chosen arbitrarily to be a rectangle surrounding the origin. In the vicinity of the origin, the z-oriented permittivity and permeability are very small, allowing for the approximation $\overline{\overline{\varepsilon}}_{zz} = \overline{\overline{\mu}}_{zz} \cong 0$ to be made for easier simulation and implementation. Simulation results in Fig. 8.5 show that the square lens with a normally oriented line source at the origin will create four equal-magnitude plane waves, one from each face of the square. This principle can be extended easily by noting that an arbitrary number of beams may be formed in any direction by changing the shape of the lens. Changing the length of a face will determine the directivity of the beam from the corresponding face; longer faces, acting as a larger aperture, will produce beams with higher directivity. Thus, for example, rectangular lenses will create two primary beams and equilateral triangular lenses will produce three beams.

The behavior of the lens can be explained by examining the material parameters and their implications. Approximating the inhomogeneous TO device as a homogeneous slab of vertically oriented uniaxial zero-index material (ZIM) with zero permittivity and free-space permeability does not change the device behavior when the lens is excited with a vertically polarized line source. The vertically polarized E-field interacts only with the z-oriented component of the permittivity tensor, allowing the uniaxial material to be replaced with an isotropic ZIM structure for analysis purposes. The effective phase velocity of electromagnetic waves is very large in a near-ZIM, approaching infinity as the index approaches zero. Thus, when the index of a slab is small enough relative to the size of the slab, the phase of the waves inside the material may be considered uniform throughout

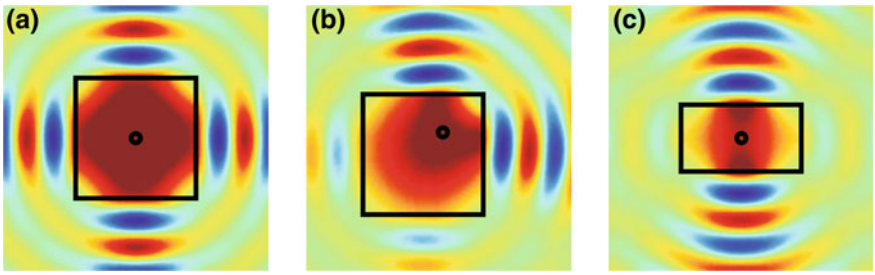

Fig. 8.5 Three examples of multibeam lenses derived using the inverse transformation. Examples of **a** quad-beam, **b** perpendicular-beam, and **c** dual-beam lenses

the device, including the boundaries. The uniform phase demonstrated at each long face of such a lens results in highly collimated radiation, thus creating the beams demonstrated by the simulations.

A near-zero-index metamaterial is required for the implementation of this TO lens. The simplest approach is to use a wire mesh metamaterial, which is composed of a large number of short vertical wire segments aligned in a grid [76]. Adjusting the gaps between wires and the wire density changes the plasma frequency of the effective medium. Near the plasma frequency, the effective permittivity in the vertical direction is near-zero, while the effective permeability and horizontal permittivity is not greatly affected by the presence of the thin wires. Thus, such a metamaterial satisfies the design requirements. Full-wave simulations of such lenses have successfully demonstrated their operation. However, the wire mesh metamaterial is bulky, offers a relatively narrow ZIM bandwidth, and requires very large unit cells. Other electric metamaterials such as the electric LC (ELC) resonator [86] and end-loaded dipole (ELD) structures [87] would be better choices for a practical implementation.

In summary, a multibeam uniaxial ZIM lens was suggested by a TO design, and the specified material parameters were approximated by a homogeneous, uniaxial ZIM metamaterial slab. The lens creates multiple high-directivity beams when fed with a vertically polarized antenna. Shortfalls include poor impedance matching to the antenna feed and to the surrounding air. However, the design flexibility provided by simple geometry adjustments is quite advantageous, making this and other similar designs worth further consideration despite their remaining implementation complexities.

8.3.1.3 Reconfigurable Lenses

The multibeam lenses discussed previously may be designed to have an arbitrary beam pattern, but those beam patterns are fixed at the design stage. This makes such lenses less attractive for some applications in which conventional phased array antennas are typically employed. However, constructing the lenses with a tunable or switchable metamaterial capable of changing from a near-ZIM 'ON' state to a near-free-space 'OFF' state allows for beam reconfigurability [88]. The shape of the ZIM slab determines the number and relative magnitude of the beams. By changing different regions of the tunable metamaterial slab to the 'OFF' state as illustrated in Fig. 8.6, the effective shape of the lens can be adjusted dynamically, thus enabling the construction of a reconfigurable single- or multibeam lens.

The reconfigurable lens is an extension of the conformal TO design, enhanced in performance through the addition of tunable metamaterials. The selection of the lens shape so as to determine the metamaterial state throughout the lens uses the same strategy as the static multibeam ZIM lens [76], but the configuration is now determined electrically rather than by the physical shape of the slab. To maximize flexibility, the tunable metamaterial may be constructed in the shape of a large cylinder, and sections of the cylinder selectively turned OFF to focus the beams.

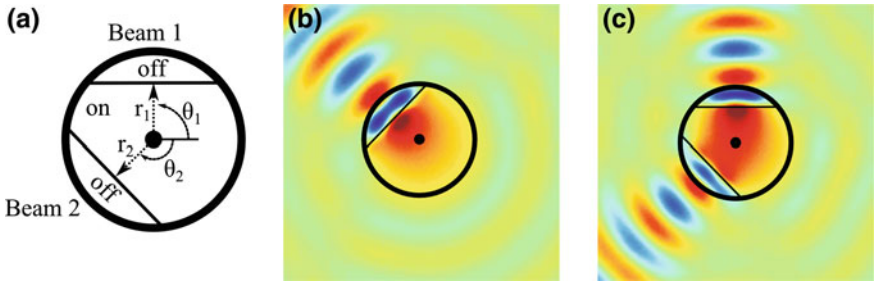

Fig. 8.6 **a** Reconfigurable TO lens antenna for which the shape of the lens determines the radiation pattern. **b** Lens configured for a single beam. **c** Lens configured for multiple beams

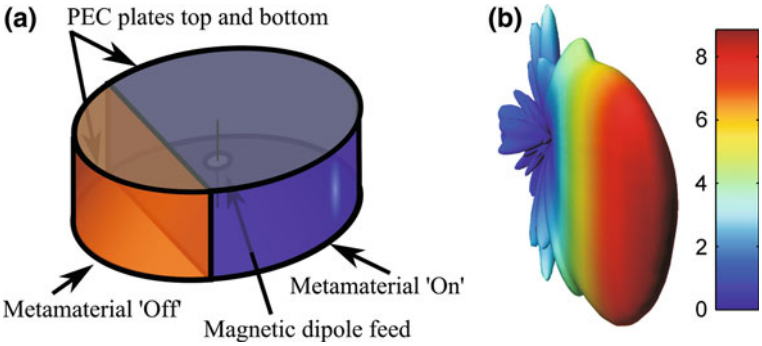

Fig. 8.7 **a** Cylindrical ZIM lens with magnetic feed. **b** Representative radiation pattern of the cylindrical lens. The antenna forms a *fan-shaped* radiation pattern due to a height that is smaller than the cylinder radius, forming a short and wide rectangular effective aperture

The cylindrical lens and a representative radiation pattern are illustrated in Fig. 8.7.

The tunable lens may be implemented using a switchable split-ring-resonator-based metamaterial that employs varactor diodes to switch between a resonant and non-resonant state [89]. The control circuitry for the SRRs should be chosen to ensure manufacturability. As seen in Fig. 8.8a, groups of six SRRs may share control and bias circuitry and be arranged into a hexagon. Tiling the hexagonal 'unit cells' in a spiral as illustrated in Fig. 8.8b allows an approximate cylinder to be constructed and enables control signals to individually address each SRR while maintaining the approximately periodic tiling of the metamaterial. The simulated material parameters in Fig. 8.8c show the low-permeability condition just above 2.5 GHz.

Many tunable metamaterials have been proposed previously, but constructing reconfigurable metamaterials that maintain individual addressing and tuning over a large spatial region remains a challenging problem. The techniques presented here, magnetic SRRs controlled by a distributed shift register, may be useful for other

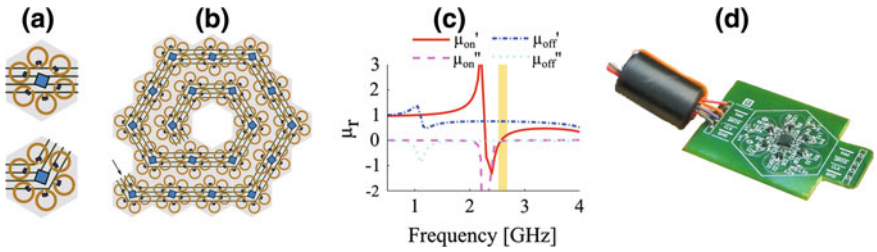

Fig. 8.8 **a** SRRs are collected into groups of six to share common control and varactor biasing circuitry. Two fundamental unit cells, with *straight* and 60-degree interconnections are illustrated. **b** The two unit cells may be combined to form a large panel of individually addressable unit cells. **c** The metamaterial changes from low-permeability to near-free-space values at the switching frequency around 2.5 GHz. **d** Photograph of the prototype unit cell

applications of spatially reconfigurable metamaterials. Minimizing the effects of the planar control circuitry by working to affect the normally oriented magnetic field is also an important consideration.

8.3.2 Quasi-Conformal Embedded Transformation

As discussed in the introduction, materials designed using the TO technique are generally complex, exhibiting anisotropy and spatial inhomogeneity. Besides conformal mapping, another way to reduce material complexities is to employ (QC) transformations, which can minimize the anisotropy of the constitutive materials and allow the use of all-dielectric implementations [81]. As a result, nearly isotropic gradient index (GRIN) materials with broad bandwidth and low losses may be employed, leading to practical QCTO devices such as carpet cloaks, beam benders, and various flat lenses [73, 75, 82, 90–95].

8.3.2.1 Theory

QC mappings are those that approximately satisfy the Cauchy-Riemann equations discussed previously, and can then be treated as containing all of the properties of a conformal mapping for the purposes of TO. QC mappings may be implemented by the same uniaxial material parameters as specified previously. Generally, QC maps are numerically generated orthonormal grids, for which various algorithms and techniques may be used for construction [96, 97]. Similar to the SC conformal mappings, the commonly defined QC mapping algorithms generate a transformation between an arbitrary polygon and a rectangle defined in the complex plane. Other transformed domains besides the rectangle are possible, such as the unit circle, but the rectangle is the most common. Unlike arbitrary TO, QCTO devices are specified completely by the polygonal source and rectangular destination

boundaries. More complicated internal structure of the transformation cannot be explicitly specified, but may be implemented through the use of several adjacent QCTO devices with matching boundary curves.

8.3.2.2 QCTO Collimating Lens Designs

Various transformations have been employed for wave collimators that can convert spherical or cylindrical waves into plane waves as mentioned in Sect. 8.2.4 [66, 68, 98]. In addition, modified TO lenses with reduced reflection losses and simplified material requirements have been investigated, demonstrating highly directive emission in both the near- and far-field regions [76, 99]. Recently, a TO lens composed of homogeneous and anisotropic LIMs was developed to emit directive beams at microwave frequencies [78]. However, these TO lenses mostly rely on metamaterials with either complex material tensors or refractive index values that are less than one, for which the intrinsic loss and dispersion-associated bandwidth limitations typically encountered by metamaterials are difficult to avoid. Alternatively, the QCTO-based designs presented here only contain GRIN materials with permittivity larger than unity, providing a promising path for synthesizing TO devices with low loss and broad bandwidth. They also offer dramatic simplification of the TO device implementation with reduced size, weight, and cost.

We consider here a coordinate transformation, as shown in Fig. 8.9a, which maps a region containing a circle into a rectangle. The additional flat protrusions in the original virtual space are chosen in order to facilitate orthogonal grid generation through QC mappings. When a line source is placed in free space at the center of the virtual space, the diverging cylindrical waves have equi-amplitude, equi-phase lines in concentric circles, including the curved boundaries. Since the circular arcs are mapped into straight lines in the transformed physical space, planar wavefronts will emerge from the top and bottom surfaces of the TO lens.

The permittivity and permeability tensors of the transformation media can be found using the general TO recipe [65]. We assume a transverse electric (*TE*) polarized wave and characterize the TO devices by the spatial distribution of their refractive index. Figure 8.9b shows the resulting material parameters for this transformation. It is found that the off-diagonal terms are nearly zero, and all the in-plane diagonal elements are near-unity except for n_{zz}, which has a maximum value of 2.5. Therefore, we can neglect the anisotropy of the transformation media and realize TO devices using isotropic GRIN materials.

In order to characterize the performance of the GRIN collimating lens, numerical simulations are performed using the finite-difference time-domain (FDTD) method. The index profile in Fig. 8.9b is truncated by keeping the central region where n_{zz} is greater than one. The resulting device measures 11 λ_0 by 9 λ_0 in terms of the free space wavelength λ_0, as shown in Fig. 8.10a. Figure 8.10b illustrates snapshots of the electric field (E_z) distributions excited by a line source placed at the center of the device. Waves that emerge from the collimating faces of

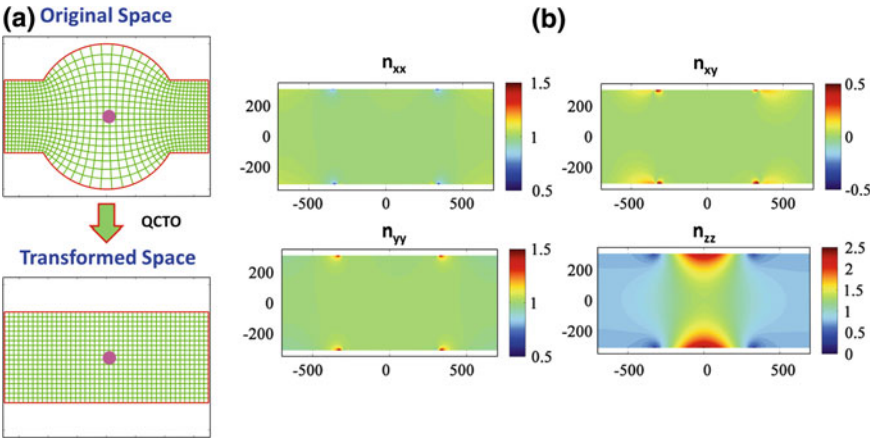

Fig. 8.9 **a** The quasi-conformal mapping transforms a *circular* region with protrusions in the virtual space into a *rectangular* region in the physical space. A *line* source is embedded at the *center* of both domains. **b** The components of the refractive index tensor for the QCTO collimating lens

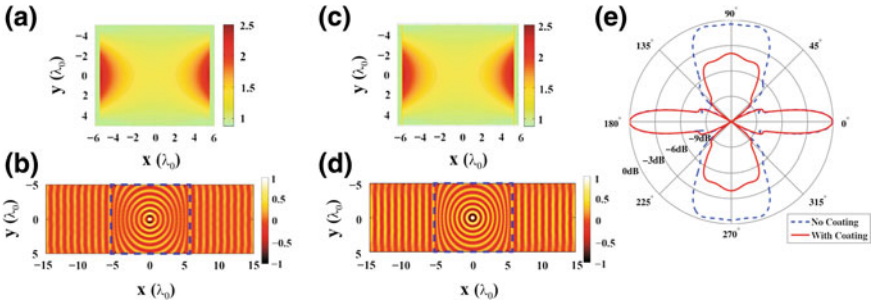

Fig. 8.10 QCTO collimator designs **a** without **b** with anti-reflection coatings along the collimating surfaces. **a**, **c** The refractive index profiles of the QCTO collimators and **b**, **d** snapshots of the electric field (E_z) distributions with a current line source located at the *center* of the device. The *dashed lines* indicate the boundaries of the QCTO collimating lens. **e** The normalized far-field radiation patterns of the QCTO collimating lenses with and without the anti-reflection coatings

the device parallel to the y-axis possess planar equi-amplitude equi-phase fronts while cylindrical waves emerge from the other faces. As a result, the QCTO focusing lenses can be designed to produce highly collimated radiation in any desired directions.

It is apparent that the emerging wave fronts in Fig. 8.10b are not perfectly planar and contain small ripples. These are primarily attributed to the impedance mismatch at the boundary between the collimator and free space. As the QCTO collimator is only composed of dielectric materials, different anti-reflection

coatings can be conveniently incorporated to improve the impedance matching. For instance, two quarter-wave layers of dielectric with an index of 1.58 are attached to the collimating surfaces of the device in Fig. 8.10c. Illustrated by the electric field distributions in the bottom part of Fig. 8.10d, these simple coatings can effectively reduce the reflection at the interfaces, providing enhanced field intensity and improved beam collimation. According to FDTD simulations, the collimated beam intensity from the coated device increases by 53 % compared to that of the original lens without the coatings.

To evaluate the performance of the QCTO GRIN collimator as an antenna, the normalized far-field radiation patterns are also computed and shown in Fig. 8.10e. Two collimated radiation beams directed toward $\phi = 0°$ and 180° are clearly seen for both lenses in Fig. 8.10a and c. When anti-reflection coatings are employed to reduce the reflection, more energy from the line source is emitted from the collimating surfaces of the lens, resulting in much lower radiation lobes in the $\phi = 90°$ and 270° directions.

Recognizing the square shape and the two-fold symmetrical index distribution of the QCTO GRIN lens shown in Fig. 8.10a, we can also develop a quad-beam collimating lens by forcing the refractive index to be symmetrical about the diagonal planes as well. As shown in Fig. 8.11a, the resulting index profile exhibits four-fold symmetry and possesses high values toward each face of the

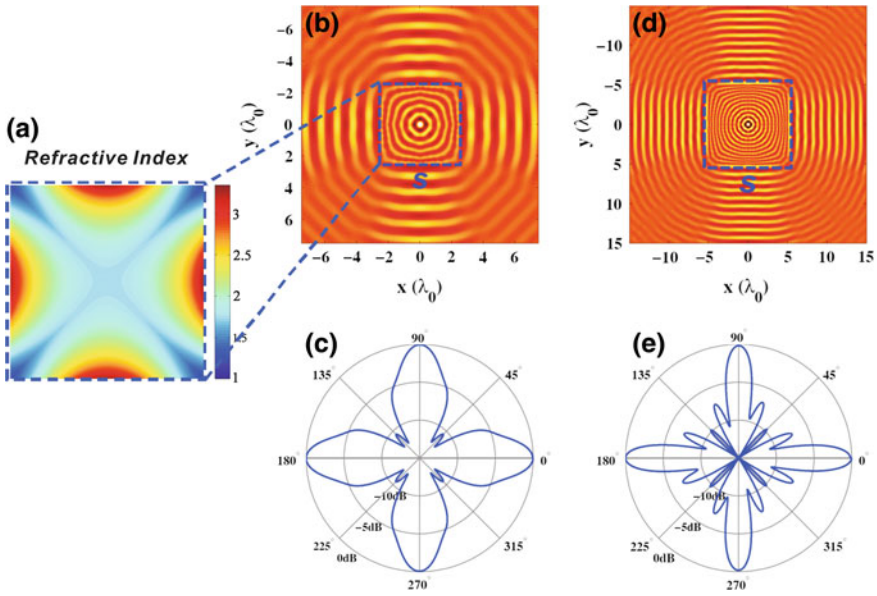

Fig. 8.11 **a** Refractive index profile of a QCTO lens which produces quad-beam radiation. **b**, **d** Snapshots of the electric field distribution demonstrate four collimated beams uniformly distributed. The *dashed purple lines* indicate the boundaries of the TO lens. **c**, **e** The normalized far-field radiation patterns of the quad-beam collimators. The operating wavelength for **b** and **d** are 0.4 and 0.2 S, respectively

lens. Figure 8.11b–e demonstrates the performance of the quad-beam collimating lens via FDTD simulations, in which an electric line source is embedded at the center of the lens. To reduce undesired reflection at each surface of the collimating lens due to impedance mismatch, thin anti-reflection coatings comprised of dielectrics are utilized. Figure 8.11b and d illustrate snapshots of the electric field (E_z) distributions of the collimator excited by line sources operating at different frequencies. The corresponding wavelength is 0.4 and 0.2 S, respectively, where S is the length of the square collimator. Four collimated beams are produced pointing in directions normal to each of the device surfaces.

The normalized far-field patterns of the quad-beam collimating lens are also calculated at two different frequencies. Figure 8.11c and e present the corresponding normalized radiation patterns of the lens antenna. As expected, narrower beams are realized at the higher frequency due to the larger antenna aperture size with respect to the operating wavelength. As a result, the collimating lens antenna will exhibit larger directivity at higher frequencies.

These collimating lenses were designed using the QCTO technique to radiate multiple directive beams when fed by a simple embedded line source. With the FDTD method, well-collimated beams can be visualized in the near-field region of the TO devices with a corresponding directive radiation pattern demonstrated in the far-field. Such designs only require spatially varying dielectric materials with no magnetic properties, facilitating low-loss, broadband operation in both the microwave and optical regimes.

In order to fully exploit the broadband impedance and radiation characteristics of the QCTO lens antenna, an open sleeve monopole was used to feed the TO lens. As shown in Fig. 8.12a, the open sleeve monopole feed is located in the middle of the QCTO collimating lens. Such simple open sleeves can effectively broaden the impedance bandwidth of a monopole, making the combined structure a suitable feed for the broadband QCTO lens. The length of the outer edge of the QCTO lens is 102 mm, while the height of the lens is 30 mm. A 14 by 14 cm PEC plate is

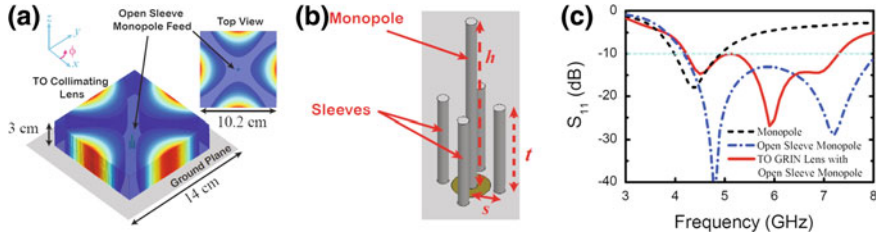

Fig. 8.12 **a** The schematic of a TO GRIN collimating lens antenna fed by an *open sleeve monopole* at the *center* of the device. The lens has a width of 10.2 cm and a thickness of 3 cm. The PEC ground plane measures 14 cm on a side. The color scale represents the refractive index distribution of the TO lens. **b** An *open sleeve monopole* antenna is used to feed the QCTO collimating lens. **c** Reflection coefficients of a simple monopole antenna, an *open* sleeve monopole, and a QCTO collimating lens antenna fed by the *open sleeve monopole*. The height of the monopole and the sleeves is 16 and 7.5 mm, respectively. The distance between the monopole and sleeves is 3 mm

used as the ground plane. The color scale represents the refractive index profile of the TO lens, which has a minimal value of 1.0 in the middle and a maximal value of 1.9 at the four collimating faces of the lens.

The configuration of the open sleeve monopole is shown in Fig. 8.12b. The feed is composed of a quarter-wave monopole of length $h = 16$ mm at the center and four equally distributed open sleeves with a height of $t = 7.5$ mm surrounding the monopole. Both the monopole and the open sleeves are made of metallic wires with a diameter of 1 mm and are placed on a ground plane. A coaxial cable with an impedance of 50 Ω was connected to the center monopole underneath the ground plane. The center-to-center distance between the monopole and each open sleeve is $s = 3$ mm.

The simulated S_{11} of the open sleeve monopole with and without the TO lens is demonstrated in Fig. 8.12c. In comparison, the reflection coefficient of a single 16 mm tall monopole is also presented, which exhibits a −10 dB bandwidth of 18 % centered at 4.45 GHz. Compared to the single monopole, the open sleeve monopole possesses a much broader impedance bandwidth through the creation of an additional resonance at higher frequencies. With the TO lens present, the open sleeve monopole exhibits a −10 dB bandwidth of 53 % (4.25–7.30 GHz), giving rise to an increase of about 194 % compared to the single monopole. As the TO lens has a refractive index around 1.0 near the center where the feed is located, the impedance characteristics of the feed are not significantly affected. As shown in Fig. 8.12c, the bandwidth of the open sleeve monopole only reduces slightly at the high frequency end of the band when the QCTO lens was employed. Therefore, such a GRIN collimating lens provides a broader bandwidth than its anisotropic counterpart (see Sec 8.3.3.3).

In addition to the broad impedance bandwidth, the GRIN collimating lens can produce directive radiation across the band. Figure 8.13a and b (left column) demonstrate the simulated radiation patterns of the feed with and without the QCTO lens at 4.5 and 7.5 GHz, respectively. Without the lens, the open sleeve monopole exhibits an omnidirectional pattern in the *H*-plane as illustrated by the black dashed curves. With the lens, however, four highly directive beams are produced at 0°, 90°, 180°, and 270°, as shown by the solid red curves. At 7.5 GHz, for instance, the collimating lens provides an enhancement in directivity by more than 6 dB in the desired directions. The radiation patterns with and without the lens in the *E*-plane are also presented in Fig. 8.13a and b (right column). Since the refractive indices of the QCTO lens are invariant along the z-axis, the radiated beams were not significantly affected in the *E*-plane. The increase in the directivity is mainly attributed to the redistribution of radiated power in the *H*-plane.

Figure 8.13c illustrates the peak directivities of the QCTO lens antenna (solid) and the open sleeve monopole feed (dashed) in the *H*-plane as a function of frequency. The monopole feed radiates a stable omnidirectional pattern within the band of interest, where a small variation of about 0.9 dB in directivity is caused by the finite ground plane size. The QCTO collimating lens increases the *H*-plane directivity by 2.8–6.5 dB within the frequency band of 4.5–8.0 GHz. It is noticed that the directivity of the lens antenna does not grow monotonically as the

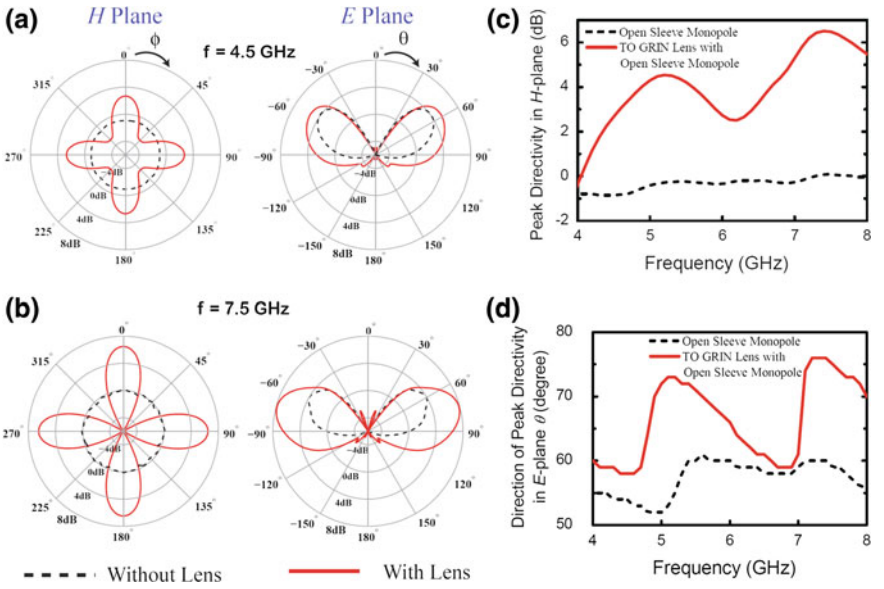

Fig. 8.13 Radiation patterns of the QCTO collimating lens antenna (*solid*) and that of the feed alone (*dashed*) evaluated at frequencies of **a** 4.5 GHz and **b** 7.5 GHz, respectively. **c** Peak directivities of the QCTO collimating lens antenna (*solid*) and the open sleeve monopole (*dashed*) in the *H*-plane as a function of frequency. **d** Direction (represented by the elevation angle θ) of maximum radiation of the QCTO collimating lens antenna (*solid*) and the open sleeve monopole (*dashed*) in the $\phi = 0$ plane as a function of frequency

frequency increases, which is mainly due to the variation of its radiation pattern in the elevation plane. The maximum radiation direction of the QCTO lens and the open sleeve monopole in the *E*-plane are compared in Fig. 8.13d. Without the lens, the feed has maximum radiation in the direction between 50° and 60° from broadside ($\theta = 0°$) due to the finite ground plane. With the QCTO lens, on the other hand, the beam maxima bends toward the horizon and points to directions with θ between 59° and 76° across a broad bandwidth due to the normal directions of the lens apertures. It is noticed that the maximum radiation direction of the QCTO lens antenna exhibits a wobbling as a function of frequency, which is mainly due to the finite size of the lens and the ground plane.

8.3.3 Geometry-Similar Coordinate Transformation

Apart from the conformal and QC mapping techniques discussed in the previous sections, simple embedded coordinate transformations [100, 101] which require only anisotropic and homogeneous material can also be employed for the design of highly directive multibeam antenna lenses. Such simple transformations are made

possible by finding the geometrical similarities between the physical and transformed spaces. Notably, the technique presented here is capable of converting the radiation from an embedded omnidirectional source into any number of highly directive beams, each radiating in an arbitrary direction within a broad bandwidth. First, the mathematical equations of polarization-independent two- and three-dimensional embedded coordinate transformations are derived that result in simple material parameters for directive radiation. Several full-wave simulation examples are then presented to numerically validate the theory. Finally, as an experimental demonstration, a broadband TO metamaterial lens is designed, fabricated and characterized. This lens generates a quad-beam radiation pattern from a simple embedded monopole with efficient operation over a broad bandwidth.

8.3.3.1 Theory

In this subsection, the analytical expressions of the embedded coordinate transformations for directive emission in both two- and three-dimensions are derived. We first consider a two-dimensional directive emission transformation, where the fields are restricted to be invariant along the z-direction. The schematic of the embedded coordinate transformation is shown in Fig. 8.14 where an air-filled, fan-shaped virtual space with a central angle of Θ_1 (see Fig. 8.14a) is mapped to an isosceles triangle with a vertex angle of Θ_2 in the physical space (see Fig. 8.14c) which has material parameters denoted by $\overline{\overline{\varepsilon_r}}'(x', y')$ and $\overline{\overline{\mu_r}}'(x', y')$. An isotropic line source is located at the center (point O), with either the electric field or magnetic field along the z-direction, representing the *TE* or transverse magnetic (*TM*) polarization, respectively. Note that the value of Θ_1 should be much smaller than the value of Θ_2 to correspond to high directivity in the virtual space. Since the equi-amplitude, equi-phase lines of the virtual space form a set of parallel arcs while those of the physical space form a set of parallel straight lines, a direct

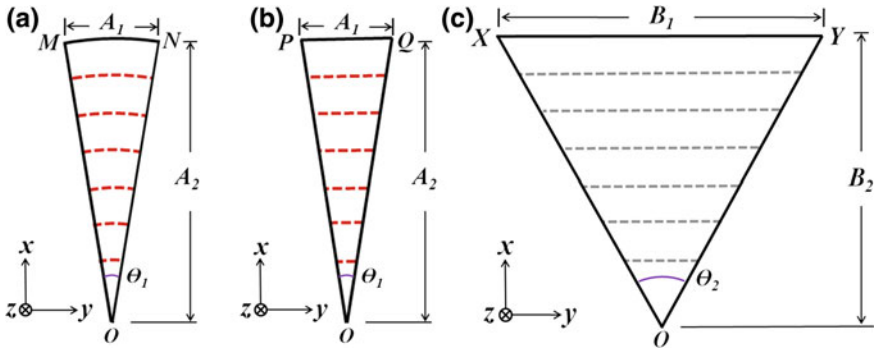

Fig. 8.14 Two dimensional directive emission coordinate transformation. **a** Geometry of the *fan-shaped* virtual space. **b** Geometry of the simplified *triangular virtual space*. **c** Geometry of the *triangular physical space*

mapping from the fan region to the triangular region will inevitably result in spatially-dependent anisotropic transformed material parameters. This is caused by the nonlinearity of the point-to-point mapping relation between the virtual and physical spaces as encountered in several previously reported cylindrical-to-plane wave source transformation designs [66–68].

To reduce the unwanted spatial dependency of the transformed material parameters in the physical space, a geometrical simplification can be applied to the virtual space geometry. Since the value of Θ_1 is small, the fan region can be approximated by an isosceles triangle with the same central angle as shown in Fig. 8.14b. Thus, an intermediate space which possesses a linear geometrical similarity with the physical space can be inserted into the transformation process to simplify the transformed material parameters. Now, the transformation can be written as

$$\begin{cases} x' = B_2 x / A_2 \\ y' = B_1 y / A_1 \\ z' = z \end{cases} \tag{8.10}$$

where (x, y, z) and (x', y', z') denote the coordinates of the virtual and physical space, respectively. By virtue of the metric invariance of Maxwell's equations, the relative permittivity and permeability tensors of the transformed medium in the physical space can be expressed as

$$\bar{\bar{\varepsilon}}_r{}' = \bar{\bar{\mu}}_r{}' = \begin{bmatrix} B_2 A_1 / A_2 B_1 & 0 & 0 \\ 0 & A_2 B_1 / B_2 A_1 & 0 \\ 0 & 0 & A_2 A_1 / B_2 B_1 \end{bmatrix}. \tag{8.11}$$

These tensor parameters can be divided into two groups (μ'_{rx}, μ'_{ry}, ε'_{rz} and ε'_{rx}, ε'_{ry}, μ'_{rz}) which are active under the *TE* and *TM* polarization, respectively. As prescribed by Maxwell's equations, the dispersion relations and the wave trajectory in the physical space remain the same provided that $\mu'_{rx}\varepsilon'_{rz}$, $\mu'_{ry}\varepsilon'_{rz}$, $\mu'_{rz}\varepsilon'_{rx}$, and $\mu'_{rz}\varepsilon'_{ry}$ are held constant [43]. Thus, the material tensor expressions can be scaled to

$$\bar{\bar{\varepsilon}}_r{}' = \bar{\bar{\mu}}_r{}' = \mathrm{diag}\left[(A_1/B_1)^2, (A_2/B_2)^2, 1\right]. \tag{8.12}$$

Since the radiated beam is highly focused in the x-direction which is perpendicular to the interface between the transformed medium and free space, we further let $A_2 = B_2$ so that the impedance is matched on the interface. The relative permittivity and permeability tensors can then be written as

$$\bar{\bar{\varepsilon}}_r{}' = \bar{\bar{\mu}}_r{}' = \mathrm{diag}\left[(A_1/B_1)^2, 1, 1\right], \tag{8.13}$$

where each requires only one parameter possessing a low value. It should be noted that the conformal mapping enabled collimating lens [76] presented in Sect. 8.3.1

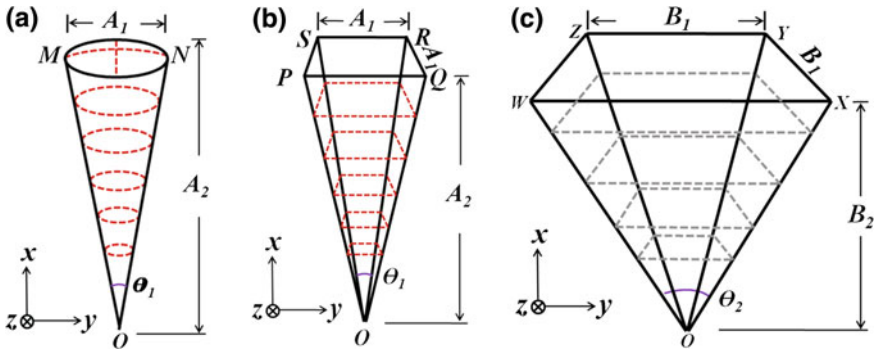

Fig. 8.15 Three-dimensional directive emission coordinate transformation. **a** Geometry of the *spherical cone shaped virtual space*. **b** Geometry of the simplified *square pyramid shaped virtual space*. **c** Geometry of the *square pyramid shaped physical space*

is actually a special case of the coordinate transformation proposed here when we set $A_1B_2 = B_1A_2$ in (8.11). In this sense, (8.11) is a general expression for achieving directive emission with homogenous anisotropic media and can be simplified to design transformed media with different anisotropy.

In certain applications, however, multibeam radiation is desired with beams pointing at specific directions in three dimensions. To fulfill this potential design requirement, a three-dimensional coordinate transformation and associated numerical validations are provided. As shown in Fig. 8.15a, the virtual space is an air-filled, spherical cone with a cone angle of Θ_1. It is mapped to a square pyramid with an apex angle of Θ_2 in the physical space (see Fig. 8.15c) which has material parameters denoted by $\overline{\overline{\varepsilon}}_r{}'(x', y', z')$ and $\overline{\overline{\mu}}_r{}'(x', y', z')$. Similar to the two-dimensional case, the direct mapping between the virtual and physical spaces is not a linear transformation, thus leading to inhomogeneous anisotropic material parameters with extreme values. Here, we can also make a geometrical approximation by using a square pyramid with an apex angle Θ_1 the same as in the virtual space (see Fig. 8.15b). The coordinate transformation can thus be expressed as

$$\begin{cases} x' = B_2 x / A_2 \\ y' = B_1 y / A_1 \\ z' = B_1 z / A_1 \end{cases} \tag{8.14}$$

where (x, y, z) and (x', y', z') are the coordinates of the virtual and physical space, respectively. Like the two-dimensional case, simplification can also be made to match the impedance of the transformed medium to free space for the directive radiating beam. The resulting relative permittivity and permeability tensors of the transformed medium are again

$$\overline{\overline{\varepsilon}}' = \overline{\overline{\mu}}' = \mathrm{diag}\left[(A_1/B_1)^2,\ 1,\ 1\right]. \tag{8.15}$$

8.3.3.2 Full-Wave Numerical Simulations

In addition, by applying the coordinate rotation transformation [102] to the above directive emission transformation, more advanced highly directive multibeam lenses can be synthesized by surrounding the embedded isotropic source with several triangular segments. Importantly, this type of lens can provide an arbitrary number of collimated beams, each radiating in a prescribed direction. As shown in Fig. 8.16a, the material tensors of each lens segment can be expressed as

$$\bar{\bar{\varepsilon}}_r{}' = \bar{\bar{\mu}}_r{}' = \begin{bmatrix} \frac{A_1^2}{B_1^2}\cos^2\phi_n + \sin^2\phi_n & \left(\frac{A_1^2}{B_1^2} - 1\right)\cos\phi_n \sin\phi_n & 0 \\ \left(\frac{A_1^2}{B_1^2} - 1\right)\cos\phi_n \sin\phi_n & \frac{A_1^2}{B_1^2}\sin^2\phi_n + \cos^2\phi_n & 0 \\ 0 & 0 & 1 \end{bmatrix}. \tag{8.16}$$

It should be noted that although the mathematical expression contains non-zero off-diagonal tensor parameters, the medium can be implemented by rotating the directions of the subwavelength metamaterial building block resonators.

To validate the concept, two-dimensional full-wave simulations were carried out using the COMSOL finite element solver [103]. For simplicity, only *TE* polarization with a *z*-directed *E*-field was used in the simulations. Considering that the outer radiation boundary is 5λ away from the source, these simulations exhibit both the near- and far-field behavior of the lenses. The first lens has four collimated beams uniformly distributed in the $x - y$ plane pointing at $\phi = \{0^\circ, 90^\circ, 180^\circ, 270^\circ\}$ as shown in Fig. 8.16b. To demonstrate the flexibility of controlling the radiated beams, a second lens is displayed in Fig. 8.16c having five customized collimated beams, each radiating at the desired angles of $\phi = \{30^\circ, 90^\circ, 165^\circ, 247.5^\circ, 322.5^\circ\}$. Both lenses have a low-value of the $\bar{\bar{\mu}}_r{}'$ parameter with a magnitude of 0.01 for each of the segments. From the electric field distribution, it is observed that the waves radiated from the central

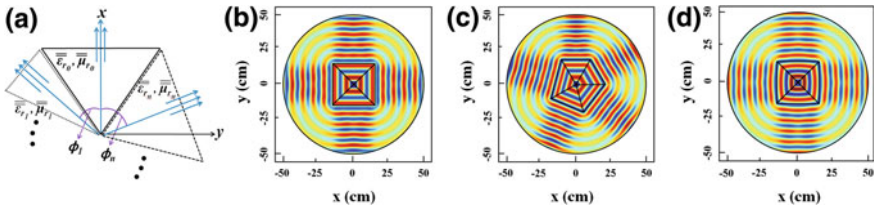

Fig. 8.16 **a** Configuration of multiple rotated lens segments to produce multibeam radiation. Snapshots of the *z*-directed near- and far-zone electric field determined via a 2D COMSOL simulation of the TO lens at 3 GHz **b** with four radiated beams uniformly distributed and **c** five radiated beams non-uniformly distributed in the *x*–*y* plane. Note that in both cases the corresponding $\bar{\bar{\mu}}_r{}'$ parameter in the direction of the radiated beam has a magnitude of 0.01 for each segment of the lens. 2D COMSOL simulations of a similar lens to **b** but when the corresponding $\bar{\bar{\mu}}_r{}'$ parameter in the direction of the radiated beam has a magnitude of **d** 0.2 for each segment of the lens

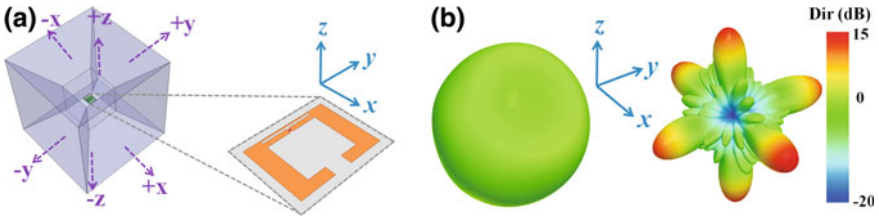

Fig. 8.17 Three dimensional coordinate transformation lens applied to a quasi-isotropic antenna proposed in [105]. **a** The three dimensional directive emission lens and the embedded quasi-isotropic antenna. The lens is designed to produce six highly directive beams; one normal to each face of the lens as indicated by the labels. **b** The HFSS simulated radiation pattern of the quasi-isotropic antenna without (*left*) and with (*right*) the lens

omni-directional source are well-collimated, even in close proximity to the source. To study the impact of the variations in the material parameter values on the lens performance, one additional quad-beam lens similar to the one shown in Fig. 8.16b was simulated with the magnitude of the $\overline{\overline{\mu}}_r{}'$ parameter in the direction of the radiated beams set to be 0.2 for each lens segment. As presented in Fig. 8.16d, the beam width of the lenses broadens as the magnitude of the corresponding $\overline{\overline{\mu}}_r{}'$ parameter increases. However, the lenses are still able to maintain highly directive beams in the four desired directions. Since most metamaterial realizations of effective media are less dispersive in the low-index band [104], this type of TO lens comprised of LIMs is suitable for broadband applications.

Similarly, a highly directive multibeam TO lens can be formed by applying the 3-D coordinate rotation mapping [102] to the material tensors of each lens segment. This type of lens can convert the radiation from an embedded omni-directional source to a customized radiation pattern in three dimensions. As an example, we surrounded a previously reported quasi-isotropic radiator [105] shown in Fig. 8.17a with six lens segments, each having low-value $\overline{\overline{\varepsilon}}_r$ and $\overline{\overline{\mu}}_r$ parameters with a magnitude of 0.01 in the direction of the radiated beam. Figure 8.17b shows the 3D radiation patterns with and without the presence of the TO lens simulated by Ansoft HFSS^{TM} finite element solver [106]. We can observe that the antenna alone has a near-omni-directional radiation pattern, whereas with the lens present, the radiation pattern exhibits six highly directive beams. It should be noted that not all of the six directive beams have the same linear polarization, which is due to the quasi-omni-directional source antenna employed here and not the TO lens since its response is polarization independent.

8.3.3.3 Design, Fabrication, and Measurement

To experimentally verify the proposed multibeam directive emission coordinate transformation, a quad-beam metamaterial lens was designed that tailors the radiation of a G-band quarter-wavelength monopole which nominally radiates

omnidirectionally in the *H*-plane around 4–5 GHz. Because the radiated electric fields are nearly perpendicular to the ground plane in the *H*-plane, the lens needs only to work for the *TE* polarization. Following the configuration of the two-dimensional quad-beam lens example in Fig. 8.16b, the monopole is surrounded with four triangular anisotropic metamaterial lens segments as depicted in Fig. 8.18a. Segments 1 and 3 have a low value of effective μ_{rx}, and segments 2 and 4 have a low value of effective μ_{ry}.

The effective medium properties of the SRRs were obtained according to the diagram shown in Fig. 8.18b, where periodic boundary conditions were assigned to the walls in the *x*- and *y*-directions. A *TE* polarized plane wave (contained in the $y - z$ plane), with the *E*-field oriented along the *x*-direction, is incident from the upper half-space at an angle of θ ($0° \leq \theta \leq 90°$) with respect to the z-axis. The three active effective material tensor quantities (μ_{ry}, μ_{rz} and ε_{rx}) were retrieved from the *S*-parameters calculated at different angles of incidence using HFSS$^{\mathrm{TM}}$. In

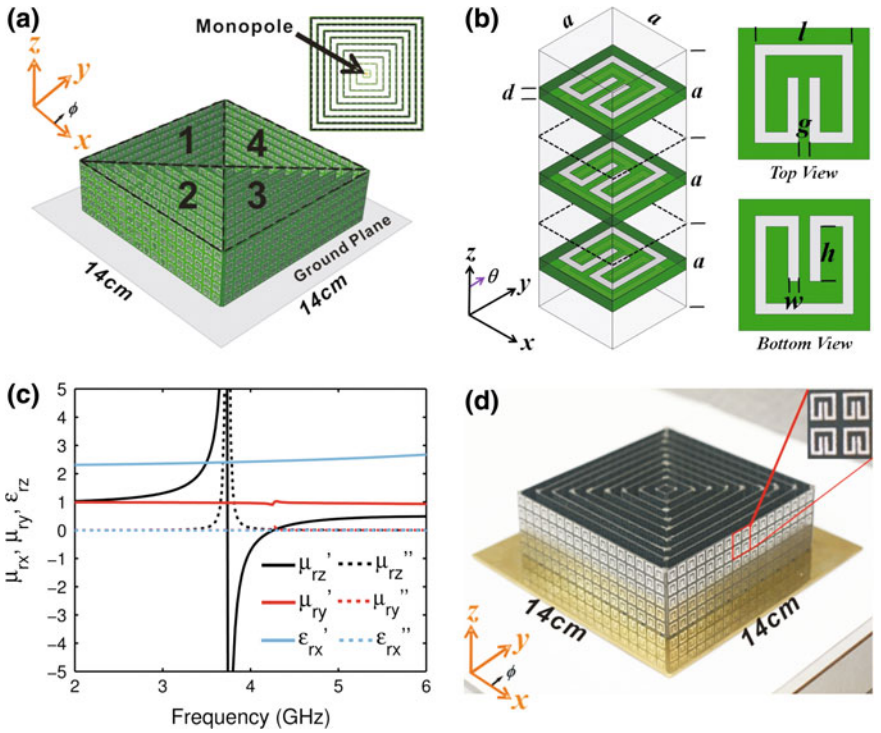

Fig. 8.18 **a** Configuration of the metamaterial TO lens HFSS model. **b** Schematic of metamaterial unit cell simulation. The dimensions are $a = 6$ mm, $d = 4.5$ mm, and $g = 0.5$ mm. The lens substrate is 0.031 inch thick Rogers RT/Duroid 5880. **c** The retrieved effective material parameters $(\mu_{rx}, \mu_{ry}, \varepsilon_{rz})$. **d** Photograph of the fabricated quad-beam TO lens. The length of the outer edge of the lens is 102 mm ($\sim 1.6\ \lambda$ at 4.8 GHz) and the height is 30 mm ($\sim 0.5\ \lambda$ at 4.8 GHz)

order to account for the near-field coupling between the SRRs and the monopole and to fully exploit the dispersive property of the SRRs, their dimensions were tuned in the presence of the monopole. As has been previously demonstrated [104, 107], the inherent dispersive nature of metamaterials, which is often considered as a drawback, can actually improve the device performance when properly utilized. As seen from the effective material parameters of the optimized SRRs shown in Fig. 8.18c, ε_{rx} and μ_{ry} are weakly dispersive across the entire frequency range, with an effective impedance for normal incidence nearly matched to free space ($\sqrt{\mu_{\mathrm{ry}}/\varepsilon_{\mathrm{rz}}} \approx 0.7$), thus ensuring low reflection loss at the lens-air interface. Additionally, μ_{rz} has a Lorentz-shaped resonance at 3.8 GHz and maintains a low value throughout the resonance tail (i.e. $0 \leq \mu_{\mathrm{rz}} \leq 0.4$) over a broad bandwidth (4.25–5.2 GHz). It should be noted that the μ_{rz} in the unit cell simulation is the same as μ_{rx} for lens segments 1 and 3 and μ_{ry} for lens segments 2 and 4. A prototype of the lens was fabricated and assembled (see Fig. 8.18d).

The simulated and measured reflection coefficients (S_{11}) of the monopole with and without the lens are shown in Fig. 8.19a, exhibiting strong agreement in terms of both resonant frequencies and bandwidth. In addition to the resonance of the monopole at 4.75 GHz, the lens introduces two other resonances at 4.4 and 5.4 GHz due to the near-field coupling between the monopole and the nearby SRRs. Compared to the original monopole, the −10 dB bandwidth is significantly improved from 0.78 to 1.35 GHz by adding the TO lens. The 70 % bandwidth broadening is attributed to the slowly growing ε_{rz} and μ_{rx} components which compensate the monopole length-to-wavelength ratio at both lower and higher frequencies.

As shown in Fig. 8.19b–i, the measured *H*-plane and *E*-plane far-field realized gain patterns at 4.25, 4.5, 4.85, and 5.2 GHz are found to have good agreement with those simulated using HFSS$^{\mathrm{TM}}$. The small discrepancies are primarily due to measurement imperfections and fabrication tolerances. Without the lens, the monopole exhibits an omni-directional gain pattern in the $x - y$ plane with a variation of about 0.7 dB due to the finite ground plane size. However, with the lens present, four highly-directive beams can be observed at $\phi = \{0°, 90°, 180°, 270°\}$. Within the frequency range of 4.25–5.2 GHz, the peak realized gain of the four beams varies between 4.3 and 5.8 dB, about 6 dB higher than that of the monopole alone. The average half-power beamwidths of the four beams are approximately 35°, 34°, 32°, and 30° over the four frequencies, indicating that the TO lens is effectively functioning as a collimator, even with its relatively compact size. A larger lens can be used to further increase the gain and yield even narrower beams. It is observed that there is a double-dip characteristic in the null regions of the measured radiation pattern as shown in Fig. 8.19b. This is primarily caused by the imperfect assembly at the glued corners of the fabricated lens, leading to a small amount of wave leakage at certain frequencies. However, considering that the minor beams are 10 dB or more below the main beams, they will not affect the desired performance of the entire TO lens. Moreover, it is expected that the double-dip features in the radiation patterns could be eliminated by using tighter

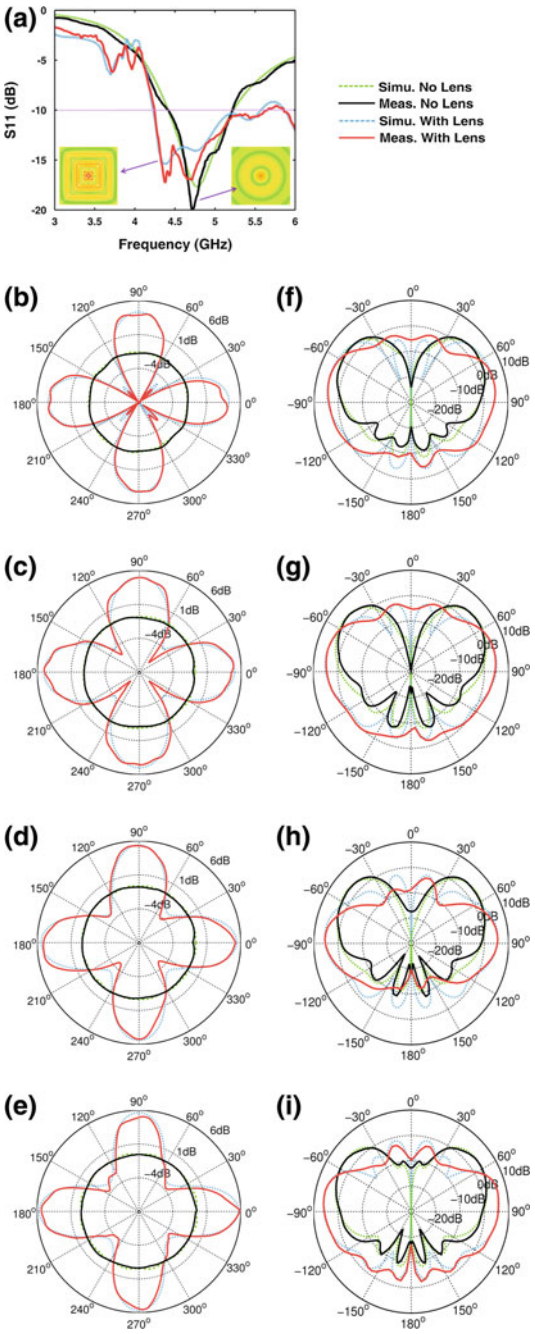

Fig. 8.19 **a** Simulated and measured S_{11} of the monopole with and without the TO lens. Simulated and measured *H*-plane realized gain patterns of the monopole with and without the TO lens at **b** 4.25 GHz, **c** 4.5 GHz, **d** 4.8 GHz, and **e** 5.2 GHz. Simulated and measured *E*-plane realized gain patterns of the monopole with and without the TO lens at **f** 4.25 GHz, **g** 4.5 GHz, **h** 4.8 GHz, and **i** 5.2 GHz

manufacturing tolerances for the lens. The inset plots of Fig. 8.19a compare the simulated *E*-field distributions on the ground plane with and without the lens. The monopole alone gives a circular pattern, whereas the lens transforms the field pattern to a square shape, indicating that the fields are well-collimated even inside the actual metamaterial lens. The measured *E*-plane patterns confirm the beam bending effect in the θ-direction. Without the lens, the monopole alone has a measured beam maxima moving from 45° to 40° off-horizon as the frequency increases. With the lens present, the beam maxima is maintained at approximately 8°–12° from the horizon. This property shows that, in addition to reshaping the radiated beams in the *H*-plane, the proposed TO metamaterial lens can also overcome the commonly observed edge diffraction in the *E*-plane caused by the finite sized ground plane [108].

8.3.4 Simplified Uniaxial Anisotropic Lens

Although helpful, it is not always necessary to design a transformation specifically for reduced complexity material parameters, as is done with the conformal and QC mapping approaches, and was performed with the multibeam TO lens. In some cases, the required parameters of TO designs with reasonable performance may be reexamined and reduced to enable more practical fabrication.

8.3.4.1 Theory

The far-field collimating lens developed by Kwon and Werner [65, 67, 99] is a good example of material parameter complexity reduction. This transformation was created by mapping a section of a circle into a rectangle above a source placed at the origin, flattening the cylindrical equal-phase fronts into approximate plane waves and creating a highly collimated beam in the far-field. Figures 8.20 and 8.21 illustrate the transformation geometry and the behavior of the waves in the transformed space.

Examining the material parameters of the transformation in Fig. 8.22, it is seen that the index in the direction of propagation (y in the figure) is low over most of the lens, and the transverse indices are high. All three terms are nearly uniform in the center of the lens, with all of the variation along the tangential axis. Since it is difficult at present to meet the constraints of the anisotropic, inhomogeneous material parameters exactly, it is reasonable to search for approximations. An appropriate simplification for this TO device would be to remove the inhomogeneity, and substitute a homogeneous, uniaxial metamaterial slab with low index in the direction of propagation. The cross-terms of the tensors would be eliminated, and the permittivity in the transverse direction assigned to a homogeneous value between 6 and 8. The parameters of the simplified structure are illustrated for comparison purposes in Fig. 8.23.

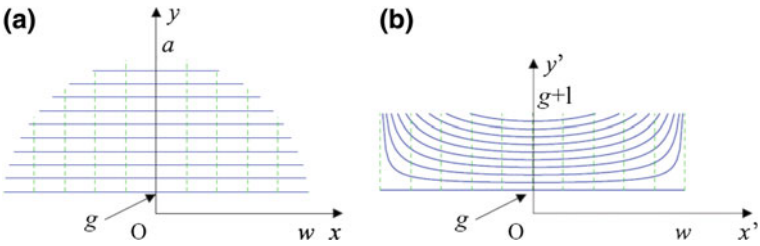

Fig. 8.20 Coordinate transformation. **a** Source domain and **b** destination domain for TO collimating lens, designed by Kwon and Werner [67]. Reproduced with permission from Kwon and Werner [67]

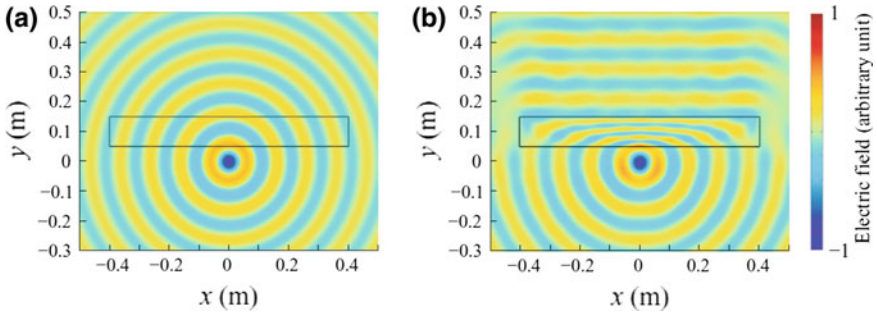

Fig. 8.21 **a** EM wave radiating from a point source. **b** The same source, radiating in the presence of the collimating TO lens [67]. Reproduced with permission from Kwon and Werner [67]

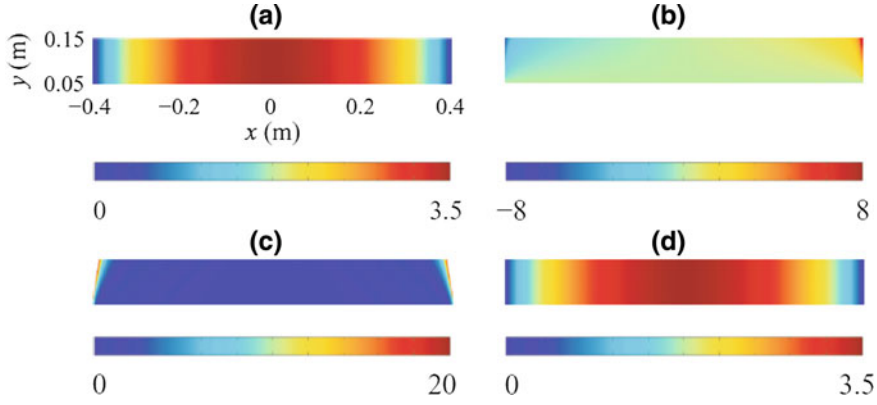

Fig. 8.22 Anisotropic, inhomogeneous material parameters required by the original TO lens **a** ε_{xx}, **b** ε_{xy}, **c** ε_{yy}, and **d** ε_{zz}. Reproduced with permission from Kwon and Werner [67]

The simplified uniaxial zero-index lens may be compared to the zero-index TO lenses discussed previously to gain insight into its operation. It was demonstrated that uniaxial zero-index metamaterials can be used to create collimated beams

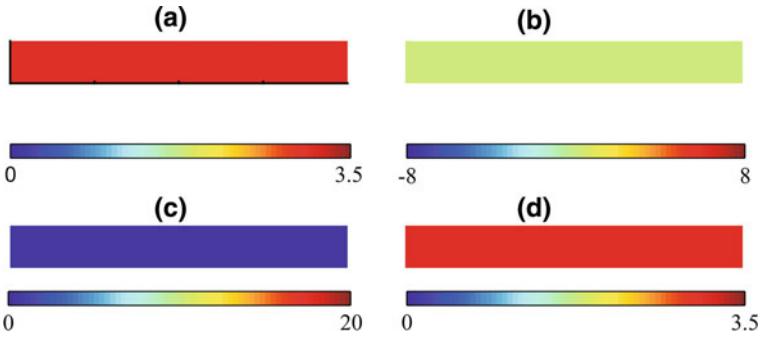

Fig. 8.23 Simplified uniaxial, homogeneous material parameters for the ZIM lens **a** ε_{xx}, **b** ε_{xy}, **c** ε_{yy}, and **d** ε_{zz}

under two conditions: with the electric field parallel to the optical axis as in the multibeam conformal mapping lens, and with the wave propagation parallel to the optical axis as in the quad-beam lens. This collimating lens uses the second configuration and places the feed antenna outside the lens. The uniaxial ZIM has better energy coupling compared to isotropic ZIMs due to the higher index in the tangential direction, which interacts with the normally propagating waves from the feed. Slightly off-normal waves are both refracted closer to the lens normal and reflected, making the ZIM lens behave as an angular spatial filter and yielding one explanation for why the material functions as a collimator.

8.3.4.2 Design, Fabrication, and Measurement

A metamaterial implementation for a dual-polarization version of this lens was designed, constructed, and tested. Allowing operation in both polarizations requires that the full material parameter tensor be implemented for both permittivity and permeability. Thus, a combined magneto-dielectric metamaterial was designed so as to give a low index in the direction of propagation for both ε and μ, and a high index in the tangential direction. Strips of PEC material around the exterior of the lens prevent power from leaking out the side of the lens. The PEC also forms an approximation of the index gradient along the periphery of the lens as required by the original TO material parameters. A dual-polarization crossed-dipole feed antenna backed by an electric ground plane completes the system, which is illustrated in Fig. 8.24. The lens and feed were tuned to operate around 7 GHz.

Near-ZIM materials are required to be dispersive by the principle of causality, since the low-index conditions exist at the tail of a resonance. The bandwidth of ZIMs will be limited by the dispersion, but the achievable bandwidth can be much wider than that of devices utilizing negative-index metamaterials. The metamaterial structure can be tailored to create a very wide, slowly recovering resonance that supports a relatively wide low-index band with negligible absorption loss.

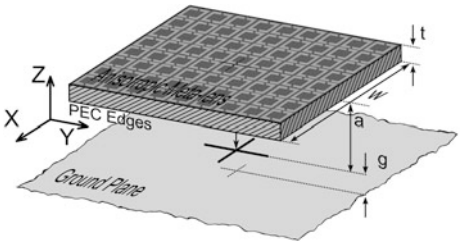

Fig. 8.24 Illustration of the zero-index dual-polarization TO-inspired metalens, placed over a ground plane and the crossed-dipole feed antenna

The metamaterial slab was constructed as a combined cubic array of horizontal modified SRRs to create the normal near-zero permeability and vertical ELD elements to create the normal near-zero permittivity. The unit cells were constructed using printed circuit board technology to transfer thin metallic traces onto a Rogers RF substrate. Strips of ELDs were interleaved to create a grid, whereas large panels of split-ring resonators were placed on the top and bottom. Moderate size unit cells were employed ($\sim \lambda/8.5$ at 7 GHz) to create strong resonances with wide resonance tails. Illustrations of the unit cells and of the equivalent material parameters are provided in Figs. 8.25 and 8.26. The material parameters are low, near-zero, for a range of frequencies surrounding 7 GHz. Although resonant metamaterials in general are only useful over very narrow bandwidths, operating in the tail of the resonance at the near-zero index band where the slope of the permittivity curve versus frequency is small can yield operational bandwidths of greater than 10 %.

The lens and feed structure were simulated using full-wave computational tools to verify their performance. The lens changes the gain pattern of the crossed dipole antenna from a nearly omnidirectional pattern with 9 dB peak gain to a directive beam with 15 dB peak gain, demonstrating a 6 dB improvement, over $\sim$10 % bandwidth, with symmetric patterns for both feed polarizations. Measurements of the fabricated lens confirmed the simulations, with measured pattern, polarization, gain, and return loss data illustrated in Figs. 8.27 and 8.28.

The vertical profile of the metalens antenna may be reduced with the addition of an AMC ground plane. Related to EBG surfaces, an AMC will have unity reflection magnitude and a reflection phase close to zero degrees. A simple implementation of these properties uses a series of square mushroom-type

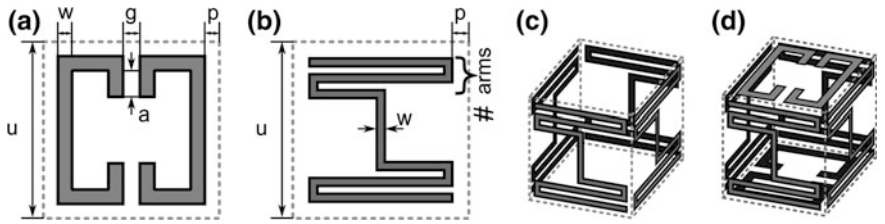

Fig. 8.25 **a** Split-ring resonator and **b** end-loaded dipole metamaterial elements are combined to form the **c** volumetric ELD and the (**d**) combined magneto-electric zero-index metamaterial

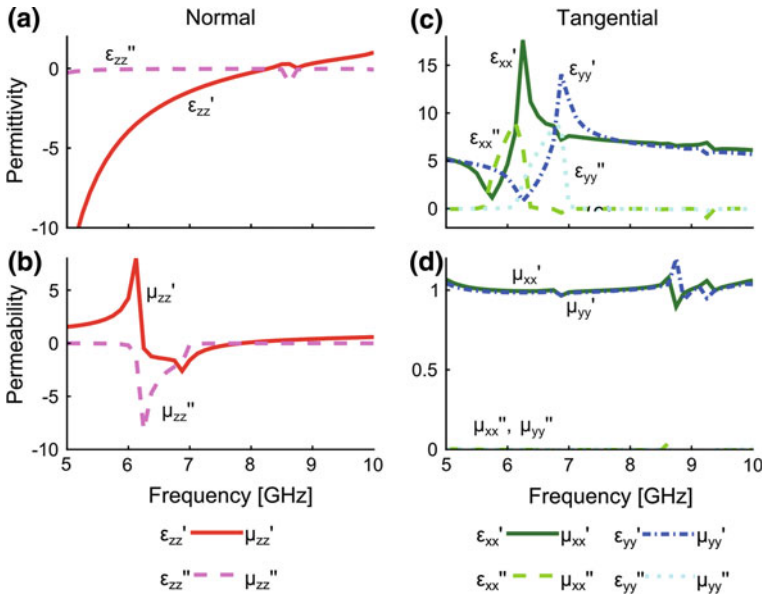

Fig. 8.26 Dispersive effective material parameters of the combined magneto-electric metamaterial. Note the simultaneous low-index condition near 8 GHz

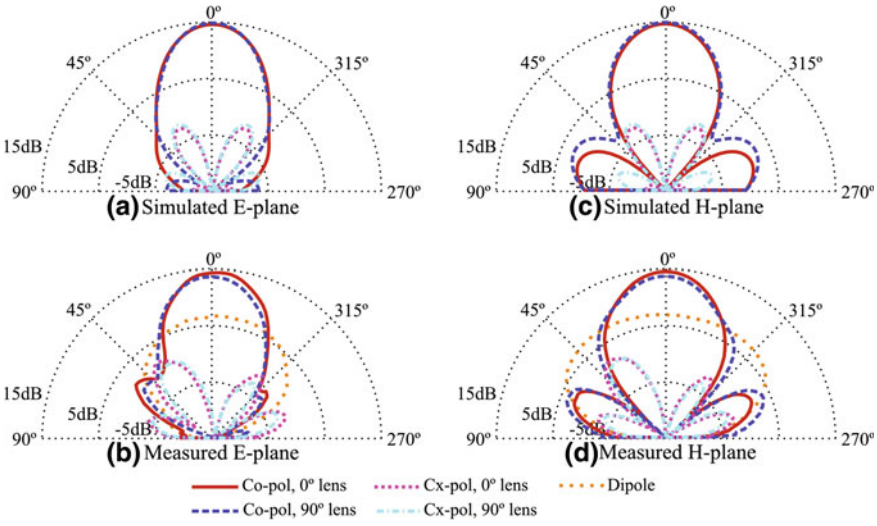

Fig. 8.27 Simulated and measured *E*-plane and *H*-plane gain patterns of the metalens at 6.875 GHz

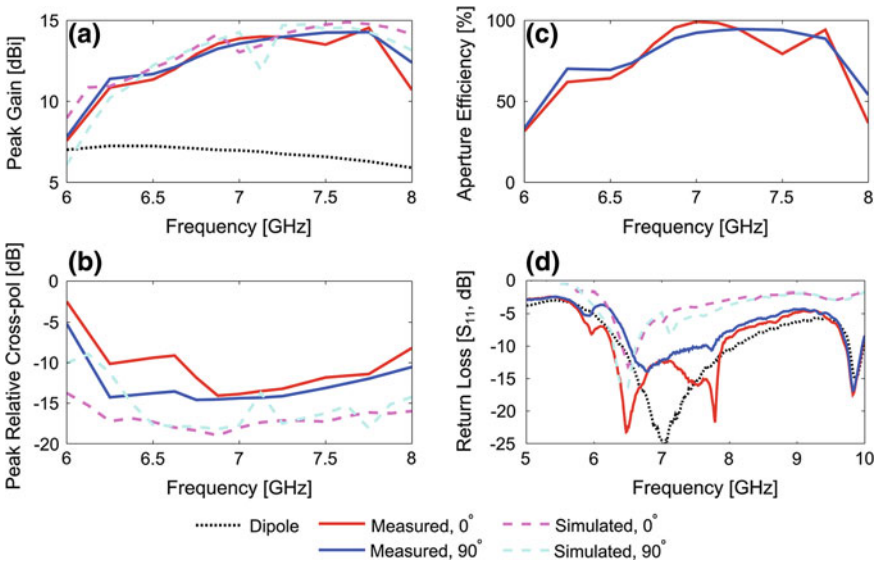

Fig. 8.28 **a** Simulated and measured peak gain versus frequency of the metalens antenna, **b** simulated and measured peak cross-pol versus frequency, **c** measured aperture efficiency versus frequency, and **d** measured and simulated return loss. The measured return loss is much better than the simulations due to the presence of an impedance-matching balun, which was not included in simulations

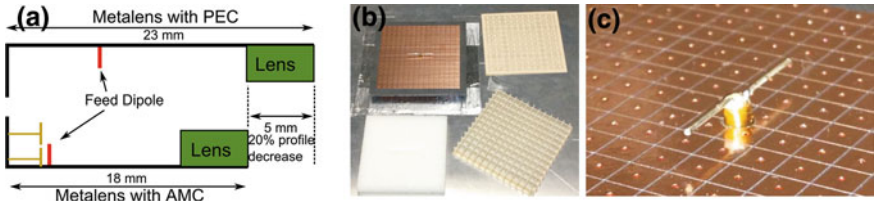

Fig. 8.29 **a** Diagram showing profile reduction of ZIM metalens with AMC ground plane. **b** Photo of (clockwise from *upper left*) AMC ground plane and dipole, *top cover*, metalens without *top cover*, and foam spacer. **c** Close-up of dipole feed antenna over the AMC ground plane

structures supported by vias to the ground plane to form a high-impedance surface (also known as a Sievenpiper surface) [26]. The frequency and bandwidth of the zero-phase crossing may be tuned by adjusting the thickness, dielectric constant, patch size, and gap size of the structure. An AMC is a dispersive approximation of an ideal perfect magnetic conducting (PMC) boundary that allows horizontal antennas to be placed adjacent to the surface without suffering efficiency losses. By using a magnetic ground plane in the metalens antenna system such that the antenna may be placed arbitrarily close to the ground, the total thickness of the

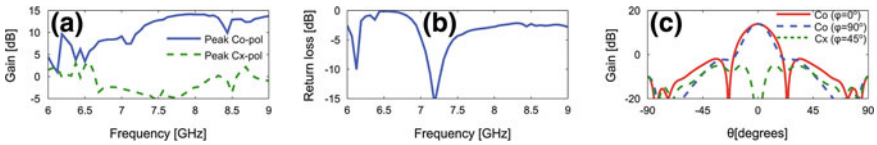

Fig. 8.30 Simulations of the AMC/metalens showing good performance, albeit over a narrowband due to the narrow AMC bandwidth, compared to the original metalens design

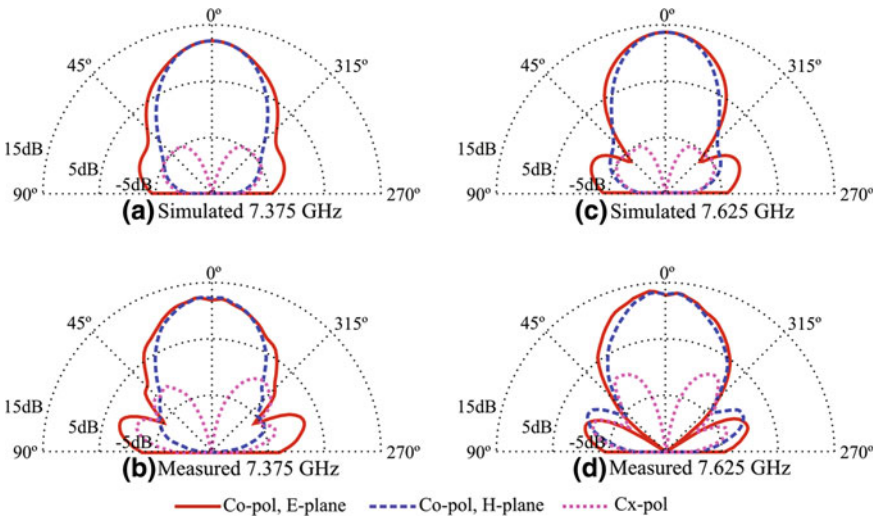

Fig. 8.31 Measurements and simulations of the AMC/metalens radiation patterns at **a–b** 7.375 GHz and **c–d** 7.625 GHz. The results confirm directive, symmetric patterns with very good agreement between simulations and measurements

lens may be decreased. A prototype AMC surface functioning between 7 and 7.5 GHz was designed and fabricated to test with the existing lens. As seen in Fig. 8.29 a, use of the AMC ground reduced the antenna profile by 20 %. Figure 8.29 b–c shows photographs of the manufactured lens. Simulated performance characteristics for the reduced-profile AMC/metalens antenna are presented in Fig. 8.30 and measured directivity patterns in Fig. 8.31.

The simplified TO lens possesses very similar wave collimation properties to the full TO design and allowed for prototype construction and testing. Even if the original anisotropic inhomogeneous TO material specification could have been constructed using metamaterials, the wide range of resonant materials that would have been required to implement the gradients would not have supported such a wide bandwidth as was achieved with the homogeneous materials. The approximation method for complex designs may be applied to other TO devices as well [109], and is a viable route to implementation when simplifications at the design stage that are possible with QC mappings, for example, do not yield acceptable results.

8.4 Conclusions

TO has been found to provide a powerful tool with great flexibility in manipulating the radiation of antennas, especially in creating highly directive beam(s) from simple antenna elements such as dipoles and/or monopoles. Several TO design methodologies have been introduced based on different coordinate transformations, including the conformal mapping, QC mapping, geometry-similar transformation, and material parameter simplification method. All of these techniques are capable of achieving a certain degree of simplification to the transformed material parameters in some way without sacrificing the device performance. Numerical and experimental examples associated with each method demonstrate the concepts and also show their unique properties and suitability for different applications. We expect that these simplified TO concepts will be applied to other types of microwave antennas and potentially even extended for use with nano-antennas [110].

Acknowledgments The authors wish to thank Erik Lier, Bonnie Martin, and Matt Bray of Lockheed Martin for their assistance with fabrication and measurements of the metalens designs. Portions of this work were supported by the Lockheed Martin University Research Initiative (LM URI) program. The QCTO and the geometrical similar coordinate transformation work were partially supported by the National Science Foundation's Material Research Science and Engineering Center (MRSEC) Grant No. DMR-0820404.

References

1. Barrow WL, Greene FM (1938) Rectangular hollow-pipe radiators. Proc IEEE 26:1498–1519
2. Barrow WL, Chu LJ (1939) Theory of the electromagnetic horn. Proc IEEE 27:51–64
3. Balanis CA (2005) Antenna theory: analysis and design, 3rd edn. Wiley, Hoboken
4. Burnside W, Chuang C (1982) An aperture-matched horn design. IEEE Trans Antennas Propag 30:790–796
5. Lawrie RE, Peters L (1965) Modification of horn antennas for low sidelobe levels. In: Proceedings of International Symposium Antennas Propagation, pp 289–293
6. Love AW (1978) Reflector antennas. IEEE Press, New York
7. Dolph CL (1946) A current distribution for broadside arrays which optimizes the relationship between beam-width and side-lobe level. Proc IRE 34:335–348
8. Foster RM (1926) Directive diagrams of antenna arrays. Bell Syst Tech J 5:292–307
9. Gregory MD, Petko JS, Spence TG, Werner DH (2010) Nature-inspired design techniques for ultra-wideband aperiodic antenna arrays. IEEE Antennas Propag Mag 52:28–45
10. Hansen WW, Woodyard JR (1938) A new principle in directional antenna design. Proc IRE 26:333–345
11. King RWP, Sandler SS (1964) The theory of endfire arrays. IEEE Trans Antennas Propag 12:276–280
12. Yagi H, Uda S (1926) Projector of the sharpest beam of electric waves. In: Proceedings of the imperial academy of Japan, vol 2, pp 49–52
13. Kock WE (1946) Metal-lens antennas. Proc IRE 34:828–836
14. Ruze J (1950) Wide-angle metal-plate optics. Proc IRE 38:53–59

15. Martindale JPA (1953) Lens aerials at centimetric wavelengths: a critical survey of the present position. J British IRE 13:243–259
16. Holt FS, Mayer A (1957) A design procedure for dielectric microwave lenses of large aperture ratio and large scanning angle. IRE Trans Antennas Propag 5:25–30
17. Luneberg RK (1944) Mathematical theory of optics. Brown University Press, Providence
18. Rotman W, Turner R (1963) Wide-angle microwave lens for line source applications. IEEE Trans Antennas Propag 11:623–632
19. Rinehart RF (1948) A solution of the problem of rapid scanning for radar antennae. J Appl Phys 19:860–862
20. Alitalo P, Luukkonen O, Vehmas J, Tretyakov SA (2008) Impedance-matched microwave lens. IEEE Antennas Wireless Propag Lett 7:187–191
21. Chang K (2005) Encyclopedia of RF and microwave engineering. Wiley, Hoboken
22. Akalin T, Danglot J, Vanbésien O, Lippens D (2002) A highly directive dipole antenna embedded in a Fabry-Pérot cavity. IEEE Microwave Wirel Compon Lett 12:48–50
23. Guérin N, Enoch S, Tayeb G, Sabouroux P, Vincent P, Legay H (2006) A metallic Fabry-Pérot directive antenna. IEEE Trans Antennas Propag 54:220–224
24. Costa F, Carrubba E, Monorchio A, Manara G (2008) Multi-frequency highly directive Fabry-Pérot based antenna. In: Proceedings of IEEE International Symposium Antennas Propagation
25. Yablonovitch E (1993) Photonic band-gap structures. J Opt Soc Am 10:283–295
26. Sievenpiper D, Zhang L, Jimenez Broas RF, Alexópolous NG, Yablonovitch E (1999) High-impedance electromagnetic surfaces with a forbidden frequency band. IEEE Trans Microw Theory Tech 47:2059–2074
27. Yang F, Rahmat-Samii Y (2003) Reflection phase characterizations of the EBG ground plane for low profile wire antenna applications. IEEE Trans Antennas Propag 51:2691–2703
28. Kern DJ, Werner DH, Monorchio A, Lanuzza L, Wilhelm MJ (2005) The design synthesis of multi-band artificial magnetic conductors using high impedance frequency selective surfaces. IEEE Trans Antennas Propag 53:8–17
29. Yang F, Rahmat-Samii Y (2003) Microstrip antennas integrated with electromagnetic band-gap (EBG) structures: a low mutual coupling design for array applications. IEEE Trans Antennas Propag 51:2936–2946
30. Thèvenot M, Cheype C, Reineix A, Jecko B (1999) Directive photonic-bandgap antennas. IEEE Trans Microw Theory Tech 47:2115–2122
31. Cheype C, Serier C, Thèvenot M, Monédière T, Reineix A, Jecko B (2002) An electromagnetic bandgap resonator antenna. IEEE Trans Antennas Propag 50:1285–1290
32. Shelby RA, Smith DR, Schultz S (2001) Experimental verification of a negative index of refraction. Science 292:77–79
33. Smith DR, Pendry JB, Wiltshire MCK (2004) Metamaterials and negative refractive index. Science 305:788–792
34. Soukoulis CM, Linden S, Wegener M (2007) Negative refractive index at optical wavelengths. Science 315:47–49
35. Valentine J, Zhang S, Zentgraf T, Ulin-Avila E, Genov DA, Bartal G, Zhang X (2008) Three-dimensional optical metamaterial with a negative refractive index. Nature 455:376–379
36. Scarborough CP, Jiang ZH, Werner DH, Rivero-Baleine C, Drake C (2012) Experimental demonstration of an isotropic metamaterial super lens with negative unity permeability at 8.5 MHz. Appl Phys Lett 101:014101/1–3
37. Enoch S, Tayeb G, Sabouroux P, Guérin N, Vincent P (2002) A metamaterial for directive emission. Phys Rev Lett 89:213902/1–4
38. Ziolkowski RW (2004) Propagation in the scattering from a matched metamaterial having a zero index of refraction. Phys Rev E 70:046608/1–12
39. Kwon DH, Werner DH (2008) Low-index metamaterial designs in the visible spectrum. Opt Express 15:9267–9272

40. Kocaman S, Aras MS, Hsieh P, McMillan JF, Biris CG, Panoiu NC, Yu MB, Kwong DL, Stein A, Wong CW (2011) Zero phase delay in negative-refractive-index photonic crystal superlattices. Nat Photon 5:499–505
41. Yun S, Jiang ZH, Xu Q, Liu Z, Werner DH, Mayer TS (2012) Low-loss impedance-matched optical metamaterials with zero-phase delay. ACS Nano 6:4475–4482
42. Jiang ZH, Bossard JA, Wang X, Werner DH (2011) Synthesizing metamaterials with angularly independent effective medium properties based on an anisotropic parameter retrieval technique coupled with a genetic algorithm. J Appl Phys 109:013515/1–11
43. Kong JA (2000) Electromagnetic wave theory. EMW Cambridge, Boston
44. Bonefačić D, Hrabar S, Kvakan D (2006) Experimental investigation of radiation properties of an antenna embedded in low permittivity thin-wire-based metamaterial. Microw Opt Technol Lett 48:2581–2586
45. Zhou R, Zhang H, Xin H (2010) Metallic wire array as low-effective index of refraction medium for directive antenna application. IEEE Trans Antennas Propag 58:79–87
46. Lovat G, Burghignoli P, Capolino F, Jackson DR (2006) High directivity in low-permittivity metamaterial slabs: ray-optic vs. leaky-wave models. Microw Opt Technol Lett 48:2542–2548
47. Lovat G, Burghignoli G, Capolino F, Jackson DR, Wilton DR (2006) Analysis of directive radiation from a line source in a metamaterial slab with low permittivity. IEEE Trans Antennas Propag 54:1017–1030
48. Weng Z, Song Y, Jiao Y, Zhang F (2008) A directive dual-band and dual-polarized antenna with zero index metamaterial. Microw Opt Technol Lett 50:2902–2904
49. Xu H, Zhao Z, Lv Y, Du C, Luo X (2008) Metamaterial superstrate and electromagnetic band-gap substrate for high directive antenna. J Infrared Mill Terahz Waves 29:493–498
50. Ju J, Kim D, Lee WJ, Choi JI (2009) Wideband high-gain antenna using metamaterial superstrate with the zero refractive index. Microw Opt Technol Lett 51:1973–1976
51. Zhou H, Qu S, Pei Z, Yang Y, Zhang J, Wang J, Ma H, Gu C, Wang X, Xu Z, Peng W, Bai P (2010) A high-directive patch antenna based on all-dielectric near-zero-index metamaterial superstrates. JEMWA 24:1387–1396
52. Zhao G, Jiao YC, Zhang F, Zhang FS (2010) Design of high-gain low-profile resonant cavity antenna using metamaterial superstrate. Microw Opt Technol Lett 52:1855–1858
53. Xiao Z, Xu H (2008) Low refractive metamaterials for gain enhancement of horn antenna. J Infrared Mill Terahz Waves 30:225–232
54. Kim D, Choi J (2010) Analysis of antenna gain enhancement with a new planar metamaterial superstrate: an effective medium and a Fabry-Pérot resonance approach. J Infrared Mill Terahz Waves 31:1289–1303
55. Zhou H, Pei Z, Qu S, Zhang S, Wang J, Li Q, Xu Z (2009) A planar zero-index metamaterial for directive emission. JEMWA 23:953–962
56. Zhu LX, Wang FM, Jiang ZY, Shen T, Ran LF (2009) Directive emission based on a new type of metamaterial. Microw Opt Technol Lett 51:2178–2180
57. Wu BI, Wang W, Pacheco J, Chen X, Lu J, Grzegorczyk TM, Kong JA, Kao P, Theophelakes PA, Hogan MJ (2008) Anisotropic metamaterials as antenna substrate to enhance directivity. Microw Opt Technol Lett 48:680–683
58. Yuan Y, Shen L, Ran L, Jiang T, Huangfu J, Kong JA (2008) Directive emission based on anisotropic metamaterials. Phys Rev A 77:053821/1–4
59. Ma YG, Wang P, Chen X, Ong CK (2009) Near-field plane-wave-like beam emitting antenna fabricated by anisotropic metamaterial. Appl Phys Lett 94:044107/1–3
60. Zhou B, Cui TJ (2011) Directivity enhancement to Vivaldi antennas using compactly anisotropic zero-index metamaterials. IEEE Antennas Wirel Propag Lett 10:326–329
61. Zhou B, Li H, Zou XY, Cui TJ (2011) Broadband and high-gain planar Vivaldi antennas based on inhomogeneous anisotropic zero-index metamaterials. PIER 120:235–247
62. Wu BI, Wang W, Pacheco J, Chen X, Grzegorczyk TM, Kong JA (2005) A study of using metamaterials as antenna substrate to enhance gain. PIER 51:295–328

63. Pendry JB, Schurig D, Smith DR (2006) Controlling electromagnetic fields. Science 312:1780–1782
64. Leonhardt U (2006) Optical conformal mapping. Science 312:1777–1780
65. Kwon DH, Werner DH (2010) Transformation electromagnetics: an overview of the theory and applications. IEEE Antennas Propag Mag 52:24–46
66. Zhang JJ, Luo Y, Xi S, Chen HS, Ran LX, Wu BI, Kong JA (2008) Directive emission obtained by coordinate transformation. PIER 81:437–446
67. Kwon DH, Werner DH (2008) Transformation optical designs for wave collimators flat lenses and right-angle bends. N J Phys 10:115023/1–13
68. Jiang WX, Cui TJ, Ma HF, Zhou XY, Cheng Q (2008) Cylindrical-to-plane-wave conversion via embedded transformation. Appl Phys Lett 92:261903/1–3
69. Jiang WX, Cui TJ, Ma HF, Yang XM, Cheng Q (2008) Layered high-gain lens antennas via discrete optical transformation. Appl Phys Lett 93:221906/1–3
70. Luo Y, Zhang J, Chen H, Huangfu J, Ran L (2009) High-directivity antenna with small antenna aperture. Appl Phys Lett 95:193506/1–3
71. Lu W, Lin Z, Chen H, Chan CT (2009) Transformation media based super focusing antenna. J Phys D: Appl Phys 42:212002/1–4
72. Cheng Q, Cui TJ (2010) Radiation of planar electromagnetic waves by a line source in anisotropic metamaterials. J Phys D: Appl Phys 43:335406/1–6
73. Kundtz N, Smith DR (2009) Extreme-angle broadband metamaterial lens. Nat Mater 9:129–132
74. Tang W, Argyropoulos C, Kallos E, Song W, Hao Y (2010) Discrete coordinate transformation for designing all-dielectric flat antennas. IEEE Trans Antennas Propag 58:3795–3804
75. Ma HF, Cui TJ (2010) Three-dimensional broadband and broad-angle transformation-optics lens. Nat Commun 1:124/1–7
76. Turpin JP, Massoud AT, Jiang ZH, Werner PL, Werner DH (2010) Conformal mappings to achieve simple material parameters for transformation optics devices. Opt Express 18:244–252
77. Tichit PH, Burokur SN, Germain D, Lustrac A (2011) Design and experimental demonstration of a high-directive emission with transformation optics. Phys Rev B 83:155108/1–7
78. Jiang ZH, Gregory MD, Werner DH (2011) Experimental demonstration of a broadband transformation optics lens for highly directive multibeam emission. Phys Rev B 84:165111/1–6
79. Garcia-Meca C, Martinez A, Leonhardt U (2011) Engineering antenna radiation patterns via quasi-conformal mappings. Opt Express 19:23743–23750
80. Yao K, Jiang X, Chen H (2012) Collimating lenses from non-Euclidean transformation optics. N J Phys 14:023011/1–9
81. Li J, Pendry JB (2008) Hiding under the carpet: a new strategy for cloaking. Phys Rev Lett 101:203901/1–4
82. Landy NI, Padilla WJ (2009) Guiding light with conformal transformations. Opt Express 17:14872–14879
83. Zeng Y, Liu J, Werner DH (2011) General properties of two-dimensional conformal transformations in electrostatics. Opt Express 19:20035–20047
84. Zeng Y, Werner DH (2012) Two-dimensional inside-out Eaton lens: wave properties and design technique. Opt Express 20:2335–2345
85. Driscoll TA (1996) A MATLAB toolbox for Schwarz-Christoffel mapping. ACM Trans Math Soft 22:168–186
86. Schurig D, Mock JJ, Smith DR (2006) Electric-field-coupled resonators for negative permittivity metamaterials. Appl Phys Lett 88:041109/1–3
87. Turpin JP, Wu Q, Werner DH, Martin B, Bray M, Lier E (2012) Low cost and broadband dual-polarization metamaterial lens for directivity enhancement. IEEE Trans Antennas Propag 60:5717−5726

88. Turpin JP, Werner DH (2012) Cylindrical metamaterial lens for single-feed adaptive beamforming. In: Proceedings of IEEE International Symposium Antennas Propagation
89. Turpin JP, Werner DH (2012) Switchable near-zero-index magnetic metamaterial for dynamic beam-scanning lens. In: Proceedings of IEEE International Symposium Antennas Propagation
90. Ma HF, Cui TJ (2010) Three-dimensional broadband ground-plane cloak made of metamaterials. Nat Commun 1:21/1–6
91. Valentine J, Li J, Zentgraf T, Bartal G, Zhang X (2009) An optical cloak made of dielectrics. Nat Mater 8:568–571
92. Semouchkina E, Werner DH, Semouchkin GB, Pantano C (2010) An infrared invisibility cloak composed of glass. Appl Phys Lett 96:233503/1–3
93. Ergin T, Stenger N, Brenner P, Pendry JB, Wegener M (2010) Three-dimensional invisibility cloak at optical wavelengths. Science 328:337–339
94. Gabrielli LH, Cardenas J, Poitras CB, Lipson M (2009) Silicon nanostructure cloak operating at optical frequencies. Nat Photon 3:461–463
95. Lee J, Blair J, Tamma V, Wu Q, Rhee S, Summers C, Park W (2009) Direct visualization of optical frequency invisibility cloak based on silicon nanorod array. Opt Express 17:12922–12928
96. Thompson NP, Soni JF, Weatherill BK (1999) Handbook of grid generation. CRC Press, Boca Raton
97. Mastin CW, Thompson JF (1984) Quasiconformal mappings and grid generation. SIAM J Sci Stat Comput 5:305–310
98. Tichit PH, Burokur S, Lustrac A (2009) Ultradirective antenna via transformation optics. J Appl Phys 105:104912/1–3
99. Kwon DH, Werner DH (2009) Flat focusing lens designs having minimized reflection based on coordinate transformation techniques. Opt Express 17:7807–7817
100. Zhang B, Luo Y, Liu X, Barbastathis G (2011) Macroscopic invisibility cloak for visible light. Phys Rev Lett 106:033901/1–4
101. Chen X, Luo Y, Zhang J, Jiang K, Pendry JB, Zhang S (2011) Macroscopic invisibility cloaking of visible light. Nat Commun 2:176/1–6
102. David H (1999) New foundations for classical mechanics. Kluwer Academic Publishers, Dordrecht
103. http://www.comsol.com/
104. Lier E, Werner DH, Scarborough CP, Wu Q, Bossard JA (2011) An octave-bandwidth negligible-loss radiofrequency metamaterial. Nat Mater 10:216–222
105. Cho C, Choo H, Park I (2008) Printed symmetric inverted-F antenna with a quasi-isotropic radiation pattern. Microw Opt Technol Lett 50:927–930
106. http://www.ansoft.com/products/hf/hfss/
107. Caloz C, Itoh T (2005) Electromagnetic metamaterials: transmission line theory and microwave applications. Wiley, Hoboken
108. Jiang ZH, Gregory MD, Werner DH (2012) Broadband high directivity multi-beam emission through transformation optics enabled metamaterial lenses. IEEE Trans Antennas Propag 60:5063−5074
109. Schurig D, Mock JJ, Justice BJ, Cummer SA, Pendry JB, Starr AF, Smith DR (2006) Metamaterial electromagnetic cloak at microwave frequencies. Science 314:977–980
110. Novotny L, Hulst N (2007) Antennas for light. Nat Photon 5:83–90
111. Zhang JJ, Luo Y, Xi S, Chen H, Ran L-X, Wu B-I, Kong JA (2008) Directive emission obtained by coordinate transformation. Prog Electromagnet Res 81:437–446

Chapter 9
Transformation Electromagnetics for Antenna Applications

Bae-Ian Wu

Abstract In recent years, transformation electromagnetics has found potential applications in propagation, waveguiding, scattering, and radiation. For antenna applications, using transformation techniques, one can transform bulky antennas to low profile ones. In general, the resulting medium will be both inhomogeneous and anisotropic. In this chapter, we proposed a spherical core-shell structure which can achieve arbitrarily large directivity. We investigated the problem by finding the transformed constitutive tensors and solving the equivalent problem in the core-shell configuration. Using the Ricatti-Bessel functions, we can represent the field components with Debye potentials and subsequently solve for the fields in all regions. We applied the formulation to several cases of dipole arrays within the shell, corresponding to both free-space and half-space problems in the virtual space. Overall, the calculation demonstrated that the formation of virtual aperture is indeed theoretically possible and the effects of loss on the number of available spherical harmonics and directivity are investigated.

9.1 Introduction

Transformation electromagnetics has received a lot of interests in recent years. It has found potential applications in several major areas of electromagnetics: propagation, waveguiding, scattering, and radiation. Using transformation electromagnetics, it is possible to manipulate the electromagnetic waves to achieve novel effects. For propagation and waveguiding, transformed structures allow waves to propagate and bend without suffering from reflections. Regarding scattering, both monostatic and bistatic scattering can be reduced. In this chapter, we

B.-I. Wu (✉)
Sensors Directorate, Air Force Research Laboratory, Wright Patterson AFB, Dayton, OH 45433, USA
e-mail: bae-ian.wu@wpafb.af.mil

D. H. Werner and D.-H. Kwon (eds.), *Transformation Electromagnetics and Metamaterials*, DOI: 10.1007/978-1-4471-4996-5_9,

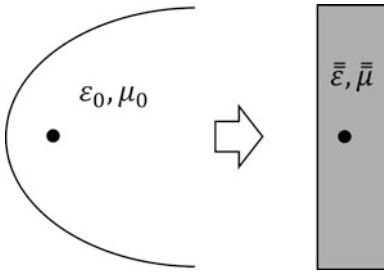

Fig. 9.1 Transformation of a parabolic antenna into a low profile antenna. *Left* Original space. *Right* Transformed space

are primarily interested in antenna applications. For antenna applications, transformation techniques, including compression and conformal mapping, allow the transformation of bulky antennas to low profile ones. For example, consider the parabolic antenna in Fig. 9.1. The parabolic antenna on the left with isotropic medium can be transformed into a low profile antenna on the right [1]. The resulting medium will be both inhomogeneous and anisotropic.

For the horn antenna shown in Fig. 9.2, the structure on the left with isotropic medium can be transformed into a smaller package with compression. The resulting medium in this case is anisotropic but can be homogeneous. This has also found potential applications for decreasing the spacing between antennas and ground planes to reduce the typically quarter-wavelength distance. The resulting medium, compressed in the normal direction, will have constitutive parameters: $\bar{\bar{\varepsilon}} = \hat{x}\hat{x}a\varepsilon_1 + \hat{y}\hat{y}a\varepsilon_1 + \hat{z}\hat{z}(1/a)\varepsilon_1$ and $\bar{\bar{\mu}} = \hat{x}\hat{x}a\mu_1 + \hat{y}\hat{y}a\mu_1 + \hat{z}\hat{z}(1/a)\mu_1$, where the original medium has isotropic permittivity ε_1 and permeability μ_1. The thickness is reduced by a factor of a. Notably, the idea of using materials with high permittivity or high permeability can be thought of as an approximation of the ideal transformed case. Such an approximation will naturally have good performance for radiation in the broadside direction, but for other directions equivalence of the complex fields in the entire region of interest with respect to the uncompressed case can only be obtained via the inclusion of effective anisotropy, even though this specific transformation is not unique.

Whether we are transforming a parabolic reflector or achieving low profile via simple compression, the effective aperture does not increase without space projection. This can be understood from the previous idea of "perfect lens" [2], which has been reinterpreted using coordinate transformations [3]. Effectively, space projection can create or cancel out space and maintain the perfect matching between the media.

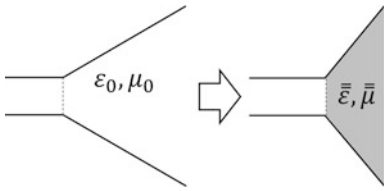

Fig. 9.2 Transformation of a horn antenna. *Left* Original space. *Right* Transformed space

In this chapter, we present a layered spherical structure that is able to form a virtual aperture in empty space by applying the appropriate space projection. Subsequently, the radiated fields will be emitted as if they are from the virtual aperture. Reducing the dimensions of radiators is always of great interest in the antenna engineering community. It is well known that there is no mathematical upper limit to the directive gain of an antenna of a given size [4]. However, there still lacks a general design capable of producing arbitrarily large directivity. With our proposed model, any arbitrarily large directivity can be theoretically achieved. The underlying concept has been demonstrated in [5]. Here we formulate the problem with a difference in terms of the potentials used to represent the fields. In addition, we also analyze the limit of the achievable farfield resolution.

In Sect. 9.2, the formulation for the transformed constitutive parameters and the solution to the radiation problem will be given. In Sect. 9.3, we will look at the fields and farfield radiation patterns for different cases and explore the resolution limit. Whereas many problems in transformation electromagnetics can be solved numerically via electromagnetics software packages, it is hoped that the analysis here will provide basis for future comparisons, allow us to analyze the effect of loss, and provide some insights to the resolution limit.

9.2 Formulation

In this section, we will set up the problem in such a way that instead of using coordinate transformations to calculate the fields, we will be solving a transformed version of the original problem in the physical space. The transformation will result in a shell whose medium will be radially inhomogeneous and anisotropic. We will be using the time-harmonic convention $e^{-i\omega t}$ throughout this chapter. The time-harmonic Maxwell's equations are:

$$\nabla \times \overline{E} = i\omega \overline{B} \,, \tag{9.1}$$

$$\nabla \times \overline{H} = -i\omega \overline{D} + \overline{J} \,, \tag{9.2}$$

$$\nabla \cdot \overline{D} = \rho \,, \tag{9.3}$$

$$\nabla \cdot \overline{B} = 0, \tag{9.4}$$

where for non bianisotropic media, the constitutive relations [6] can be written as:

$$\overline{D} = \overline{\overline{\varepsilon}} \cdot \overline{E} \quad \text{and} \quad \overline{B} = \overline{\overline{\mu}} \cdot \overline{H} \,. \tag{9.5}$$

The permittivity and permeability tensors, in general, will be functions of space. Figure 9.3 shows the general configuration that we will be using for this chapter. Using the transformation in [5], the empty sphere of radius c is compressed into a smaller sphere of radius a (region 1), and the empty shell between

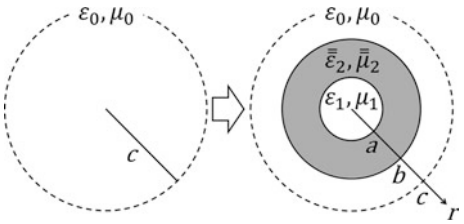

Fig. 9.3 Transformation of free space into a layered configuration. *Left* Original space. *Right* Transformed space

$r = b$ and $r = c$ is mapped into another shell between $r = a$ and $r = b$ (region 2). Region 3 corresponds to the space where $r > b$. The line at $r = c$ corresponds to the boundary outside which is the region of equivalence. To solve the radiation problem, we need to find the transformed constitutive tensors and solve the transformed problem.

9.2.1 Transformation of the Constitutive Parameters

Since we will eventually be working on the transformed space rather than the original virtual space, in this subsection we will use the unprimed notation to signify the transformed physical space and the primed notation for the virtual space. For other parts of this chapter, the primed notation is used to represent the source coordinates. Figure 9.4 shows the relationship between the radius in the physical space r and the radius in the virtual space r'. The region between $r = a$ and $r = b$ has a negative slope, corresponding to space projection. The resulting constitutive parameters are thus expected to have negative real parts. For the r direction,

$$\begin{array}{ll} r' = \frac{c}{a} r & \text{for } r < a\ , \\ r' = -Ar + B & \text{for } a < r < b, \text{ and} \\ r' = r & \text{for } r > b\ . \end{array} \tag{9.6}$$

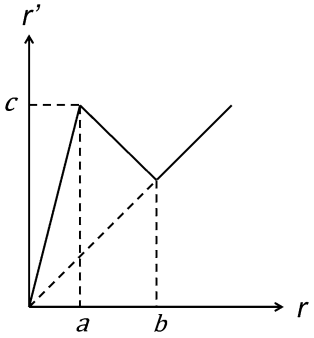

Fig. 9.4 The relationship between the radius in the physical space r and the radius in the virtual space r'. a, b, and c correspond to the dimensions in Fig. 9.3

In region 2,

$$A = \frac{c-b}{b-a} \quad \text{and} \quad B = \frac{b(c-a)}{b-a} \ . \tag{9.7}$$

Under this transformation, θ and ϕ are unchanged, thus $\theta = \theta'$ and $\phi = \phi'$.

Using the Jacobian [7], the transformed $\overline{\overline{\varepsilon}}$ and $\overline{\overline{\mu}}$ can be expressed in terms of the original constitutive tensors:

$$\overline{\overline{\varepsilon}} = \frac{\overline{\overline{J}}_{rr'} \cdot \overline{\overline{\varepsilon}}' \cdot \overline{\overline{J}}_{rr'}^{T}}{|\overline{\overline{J}}_{rr'}|} \quad \text{and} \quad \overline{\overline{\mu}} = \frac{\overline{\overline{J}}_{rr'} \cdot \overline{\overline{\mu}}' \cdot \overline{\overline{J}}_{rr'}^{T}}{|\overline{\overline{J}}_{rr'}|} \ . \tag{9.8}$$

In spherical coordinates, the Jacobian takes the form:

$$\overline{\overline{J}}_{rr'} = \begin{bmatrix} \frac{\partial A_r}{\partial r'} & \frac{1}{r'}\frac{\partial A_r}{\partial \theta'} & \frac{1}{r'\sin\theta'}\frac{\partial A_r}{\partial \phi'} \\ \frac{r\partial A_\theta}{\partial r'} & \frac{r}{r'}\frac{\partial A_\theta}{\partial \theta'} & \frac{r}{r'\sin\theta'}\frac{\partial A_\theta}{\partial \phi'} \\ \frac{r\sin\theta\partial A_\phi}{\partial r'} & \frac{r\sin\theta}{r'}\frac{\partial A_\phi}{\partial \theta'} & \frac{r}{r'}\frac{\partial A_\phi}{\partial \phi'} \end{bmatrix} . \tag{9.9}$$

The resulting Jacobian is a constant in region 1 and region 3, and it is diagonal in region 2:

$$\begin{aligned} \overline{\overline{J}}_{rr'} &= \overline{\overline{I}}\frac{a}{c} && \text{for } r<a \ , \\ \overline{\overline{J}}_{rr'} &= \text{diag}[-\tfrac{1}{A},\ \tfrac{r}{r'},\ \tfrac{r}{r'}] && \text{for } a<r<b, \text{ and} \\ \overline{\overline{J}}_{rr'} &= \overline{\overline{I}} && \text{for } r>b. \end{aligned} \tag{9.10}$$

Using these results in Eqs. 9.8, we have:

$$\begin{aligned} \tfrac{\varepsilon_1}{\varepsilon_0} = \tfrac{\mu_1}{\mu_0} &= \tfrac{c}{a} && \text{for} < a \ , \\ \tfrac{\overline{\overline{\varepsilon}}_2}{\varepsilon_0} = \tfrac{\overline{\overline{\mu}}_2}{\mu_0} &= \text{diag}[-\tfrac{(-Ar+B)^2}{Ar^2},\ -A,\ -A] && \text{for} < r < b, \text{ and} \\ \tfrac{\varepsilon_3}{\varepsilon_0} = \tfrac{\mu_3}{\mu_0} &= 1 && \text{for } r>b \ . \end{aligned} \tag{9.11}$$

Note that in the above expression for region 2, A and B are positive numbers and consequently the constitutive parameters in the physical space for the shell region have negative real parts. This is consistent with the planar case in which space projection results in negative permittivity and permeability. Because we will be analyzing the effects of loss, we introduce a factor of $(1 - i\delta)$ to both $\overline{\overline{\varepsilon}}_2$ and $\overline{\overline{\mu}}_2$ in region 2, where δ is the loss tangent. Note that in region 1 both ε_1 and μ_1 are scalar constants, and in region 2 the transverse components are constant. Only the radial components in region 2 are functions of the radius r.

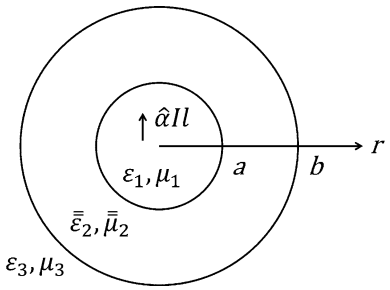

Fig. 9.5 Configuration of the problem. The dipole with magnitude $I\ell$ is oriented arbitrarily in the $\hat{\alpha}$ direction in region 1

9.2.2 Solution to the Wave Equation

In this subsection we consider a radiator inside a radially inhomogeneous and anisotropic shell as a result of the coordinate transformation presented in the previous section. This problem can be solved analytically by matching the boundary conditions. To facilitate this effort, we will use the formulation based on Mie scattering [6, 8, 9]. Consider the Hertzian dipole shown in Fig. 9.5 with magnitude $I\ell$, oriented in the $\hat{\alpha}$ direction, and positioned at (r', θ', ϕ') in region 1. Decomposing the waves in all three regions into TM and TE components with respect to $\hat{r}$, we can express the electric and magnetic fields in terms of the Debye potentials π_e and π_m. For TM modes,

$$\overline{H}_{\mathrm{TM}} = \nabla \times \hat{r}\Phi_{\mathrm{TM}} = \nabla \times \overline{r}\pi_e \ , \tag{9.12}$$

$$\overline{E}_{\mathrm{TM}} = \frac{1}{-i\omega}(\bar{\bar{\varepsilon}}^{-1} \cdot \nabla \times \nabla \times \overline{r}\pi_e) \ . \tag{9.13}$$

For TE modes,

$$\overline{E}_{\mathrm{TE}} = \nabla \times \hat{r}\Phi_{\mathrm{TE}} = \nabla \times \overline{r}\pi_m \ , \tag{9.14}$$

$$\overline{H}_{\mathrm{TE}} = \frac{1}{i\omega}(\bar{\bar{\mu}}^{-1} \cdot \nabla \times \nabla \times \overline{r}\pi_m) \ . \tag{9.15}$$

We can also use the potentials to represent $\overline{D}$ and $\overline{B}$ instead of $\overline{E}$ and $\overline{H}$ [10, 11].

Using the Maxwell equations, we can now form the wave equations for π_e and π_m. Here, we will show the procedure for TM modes, noting that the corresponding results for TE modes can be obtained by invoking duality. For TM modes, the wave equation can be written as:

$$\nabla \times \frac{1}{-i\omega}(\bar{\bar{\varepsilon}}^{-1} \cdot \nabla \times \nabla \times \overline{r}\pi_e) = i\omega\bar{\bar{\mu}} \cdot \nabla \times \overline{r}\pi_e \ . \tag{9.16}$$

Note that only the transverse components of the permeability tensor will be used, and $\bar{\bar{\mu}}$ can effectively be treated as μ_t. Also, since ε_t and μ_t are not functions of r and are constant, we can expand both sides and equate the arguments of the curl operators with the addition of the gradient of a scalar potential Φ_e to obtain:

$$\frac{1}{\omega^2}\begin{bmatrix} \frac{1}{\mu_t\varepsilon_r}\frac{1}{r}\frac{1}{r\sin\theta}\left[\frac{\partial}{\partial\theta}(-\sin\theta\frac{\partial r\pi_e}{\partial\theta})-\frac{1}{\sin\theta}\frac{\partial^2 r\pi_e}{\partial\phi^2}\right] \\ \frac{1}{\mu_t\varepsilon_t}\frac{1}{r}\frac{\partial}{\partial r}(\frac{\partial r\pi_e}{\partial\theta}) \\ \frac{1}{\mu_t\varepsilon_t}\frac{1}{r}\frac{1}{\sin\theta}\frac{\partial}{\partial r}(\frac{\partial r\pi_e}{\partial\phi}) \end{bmatrix} = \begin{bmatrix} r\pi_e+\frac{\partial\Phi_e}{\partial r} \\ \frac{1}{r}\frac{\partial\Phi_e}{\partial\theta} \\ \frac{1}{r\sin\theta}\frac{\partial\Phi_e}{\partial\phi} \end{bmatrix} . \tag{9.17}$$

For $\hat{\theta}$ and $\hat{\phi}$ components,

$$\frac{1}{\omega^2}\frac{1}{\mu_t\varepsilon_t}\frac{\partial}{\partial\theta}\frac{\partial r\pi_e}{\partial r}=\frac{\partial\Phi_e}{\partial\theta} \quad \text{and} \quad \frac{1}{\omega^2}\frac{1}{\mu_t\varepsilon_t}\frac{\partial}{\partial\phi}\frac{\partial r\pi_e}{\partial r}=\frac{\partial\Phi_e}{\partial\phi} . \tag{9.18}$$

We can thus obtain Φ_e as:

$$\Phi_e=\frac{1}{\omega^2}\frac{1}{\mu_t\varepsilon_t}\frac{\partial r\pi_e}{\partial r} . \tag{9.19}$$

Using this result, we have the following for the $\hat{r}$ component:

$$\frac{\varepsilon_r}{\varepsilon_t}\frac{1}{r}\frac{\partial^2 r\pi_e}{\partial r^2}+\frac{1}{r^2\sin\theta}\frac{\partial}{\partial\theta}(\sin\theta\frac{\partial\pi_e}{\partial\theta})+\frac{1}{r^2\sin^2\theta}\frac{\partial^2\pi_e}{\partial\phi^2}+k_t^2\frac{\varepsilon_r}{\varepsilon_t}\pi_e=0 , \tag{9.20}$$

where $k_t=\omega\sqrt{\mu_t\varepsilon_t}$ is the wavenumber corresponding to the transverse constitutive parameters with respect to $\hat{r}$. This is the wave equation for π_e. If we define:

$$\begin{aligned}\nabla_t^2\pi_e &= \nabla^2-\frac{1}{r^2}\frac{\partial}{\partial r}(r^2\frac{\partial\pi_e}{\partial r}) \\ &= \frac{1}{r^2\sin\theta}\left[\frac{\partial}{\partial\theta}(\sin\theta\frac{\partial\pi_e}{\partial\theta})\right]+\frac{1}{r^2\sin^2\theta}\frac{\partial^2\pi_e}{\partial\phi^2} ,\end{aligned} \tag{9.21}$$

we can simplify the wave equation to:

$$\frac{\varepsilon_r}{\varepsilon_t}\frac{1}{r}\frac{\partial^2 r\pi_e}{\partial r^2}+\nabla_t^2\pi_e+k_t^2\frac{\varepsilon_r}{\varepsilon_t}\pi_e=0 . \tag{9.22}$$

In particular, when ε_r=ε_t and μ_r=μ_t,

$$(\nabla^2+k^2)\pi_e=0 , \tag{9.23}$$

and the Helmholtz equation is recovered. This is the case for region 1 and 3.

We can now use the separation of variables to solve for π_e. We do so by letting $\pi_e=f_r(r)f_\theta(\theta)f_\phi(\phi)$. Regarding f_ϕ, we have:

$$\frac{d^2 f_\phi}{d\phi^2}+q^2 f_\phi=0 \text{ and } f_\phi=e^{\pm im\phi} , \tag{9.24}$$

where m is an integer from 0 to n. For f_θ, we have:

$$\frac{1}{\sin\theta}\frac{d}{d\theta}(\sin\theta\frac{df_\theta}{d\theta})+(p^2-\frac{q^2}{\sin^2\theta})f_\theta=0 . \tag{9.25}$$

In terms of $\cos\theta$, with $p = n(n+1)$, we have:

$$(1-\cos^2\theta)\frac{d^2 f_\theta}{d(\cos\theta)^2} - 2\cos\theta\frac{df_\theta}{d\cos\theta} + \left[n(n+1) - \frac{m^2}{1-\cos^2\theta}\right]f_\theta = 0 \ , \tag{9.26}$$

for which the associated Legendre polynomials are solutions to. Thus $f_\theta = P_n^m(\cos\theta)$, where n is an integer from 0 to ∞. Using the results for f_ϕ and f_θ, regarding f_r we have:

$$\frac{\varepsilon_r}{\varepsilon_t} r\frac{d^2 r f_r}{dr^2} + \left[\frac{\varepsilon_r}{\varepsilon_t}k_t^2 r^2 - n(n+1)\right]f_r = 0 \ . \tag{9.27}$$

At this point we can put in the explicit r dependence of $\frac{\varepsilon_r}{\varepsilon_t}$:

$$\frac{\varepsilon_t}{\varepsilon_r} = \left(\frac{r}{r-R}\right)^2 \ , \quad \text{in which} \quad R = \frac{b(c-a)}{(c-b)} \ . \tag{9.28}$$

Rewriting, we have:

$$r\frac{d^2 r f_r}{dr^2} + \left[k_t^2 r^2 - \frac{r^2}{(r-R)^2}n(n+1)\right]f_r = 0 \ . \tag{9.29}$$

If for f_r we write $f_r(r) = r^{-1}F(k_t\tilde{r})$, where $\tilde{r} = (r-R)$, it is readily shown that F satisfies the Riccati-Bessel equation [12, 13]:

$$(k_t\tilde{r})^2 F'' + [(k_t\tilde{r})^2 - n(n+1)]F = 0 \ , \tag{9.30}$$

where $F = \hat{b}_n$ denotes the Riccati-Bessel function, defined as:

$$\hat{b}_n(k_t\tilde{r}) = (k_t\tilde{r})b_n(k_t\tilde{r}) \ , \tag{9.31}$$

in which b_n is the spherical Bessel function. In our case, we only use the spherical Bessel function of the first kind (j_n) and the spherical Hankel function of the first kind ($h_n^{(1)}$). Because we will only use the spherical Hankel function of the first kind, we suppress the superscript and use h_n from here onwards. The general solution for $\pi_{e/m}$ will thus be a double summation over both m and n, where for each m, n:

$$\pi_{e/m} = \frac{1}{r}\hat{b}_n(k_t\tilde{r})P_n^m(\cos\theta)e^{\pm im\phi} \ , \tag{9.32}$$

in which $\hat{b}_n(k_t\tilde{r})$ is either $\hat{j}_n(k_t\tilde{r}) = (k_t\tilde{r})j_n(k_t\tilde{r})$ or $\hat{h}_n(k_t\tilde{r}) = (k_t\tilde{r})h_n(k_t\tilde{r})$. When the medium is homogeneous and isotropic, we can simply set $k_t = k$ and $R = 0$. Throughout this chapter, it is useful to note that:

$$j_n(z) = \sqrt{\frac{\pi}{2z}} J_{n+\frac{1}{2}}(z) , \tag{9.33}$$

$$h_n(z) = \sqrt{\frac{\pi}{2z}} \left[J_{n+\frac{1}{2}}(z) + iY_{n+\frac{1}{2}}(z) \right] , \tag{9.34}$$

in which $J_{n+\frac{1}{2}}(z)$ and $Y_{n+\frac{1}{2}}(z)$ are the cylindrical Bessel functions of the first and second kind with fractional order $n + \frac{1}{2}$. Also, for the derivatives, we have:

$$\hat{b}_n'(z) = (z) b_{n-1}(z) - n b_n(z) , \tag{9.35}$$

$$\frac{d}{d\theta} P_n^m(\cos\theta) = \frac{1}{\sin\theta} \left[(n\cos\theta) P_n^m(\cos\theta) - (m+n) P_{n-1}^m(\cos\theta) \right] . \tag{9.36}$$

These expressions are useful for implementing $\hat{b}_n$ and evaluating the fields numerically.

9.2.3 Fields and Boundary Conditions

In general, the fields will contain both TM and TE components. We can express the electric and magnetic fields in terms of π_e and π_m. For the radial components:

$$E_r = -\frac{1}{i\omega\varepsilon_t} \left(\frac{\partial^2 r\pi_e}{\partial r^2} + k_t^2 r\pi_e \right) \tag{9.37}$$

and

$$H_r = \frac{1}{i\omega\mu_t} \left(\frac{\partial^2 r\pi_m}{\partial r^2} + k_t^2 r\pi_m \right) . \tag{9.38}$$

For the transverse components, using the notation in [8], we have:

$$\begin{bmatrix} E_\theta \\ E_\phi \end{bmatrix} = \begin{bmatrix} \frac{i}{\omega\varepsilon_t} \frac{1}{r} \frac{\partial^2}{\partial r \partial\theta} r & \frac{1}{\sin\theta} \frac{\partial}{\partial\phi} \\ \frac{i}{\omega\varepsilon_t} \frac{1}{r\sin\theta} \frac{\partial^2}{\partial r \partial\phi} r & -\frac{\partial}{\partial\theta} \end{bmatrix} \cdot \begin{bmatrix} \pi_e \\ \pi_m \end{bmatrix} \tag{9.39}$$

and

$$\begin{bmatrix} H_\theta \\ H_\phi \end{bmatrix} = \begin{bmatrix} \frac{1}{\sin\theta} \frac{\partial}{\partial\phi} & -\frac{i}{\omega\mu_t} \frac{1}{r} \frac{\partial^2}{\partial r \partial\theta} r \\ -\frac{\partial}{\partial\theta} & -\frac{i}{\omega\mu_t} \frac{1}{r\sin\theta} \frac{\partial^2}{\partial r \partial\phi} r \end{bmatrix} \cdot \begin{bmatrix} \pi_e \\ \pi_m \end{bmatrix} . \tag{9.40}$$

These expressions can be used for all three regions to find the fields and match the boundary conditions.

The boundary conditions consist of matching the fields at the source and the interfaces. For the source, which in our case exists only in region 1, we use the

expansion of a Hertzian dipole. Consider a dipole moment $\hat{\alpha} I\ell$. For the TM components, we have:

$$\pi_e^i = \frac{i}{4\pi}\frac{I\ell}{k_1}\hat{\alpha}\cdot\nabla'\times\nabla'\times\hat{r}'\sum_{n=0}^{\infty}\sum_{m=-n}^{n}\frac{(2n+1)(n-|m|)!}{n(n+1)(n+|m|)!} \\ \frac{1}{r}\hat{j}_n(kr_<)\hat{h}_n(kr_>)P_n^{|m|}(\cos\theta')P_n^{|m|}(\cos\theta)e^{im(\phi-\phi')} \ . \tag{9.41}$$

For the TE components, we have:

$$\pi_m^i = i\omega\mu_1\frac{i}{4\pi}\frac{I\ell}{k_1}\hat{\alpha}\cdot\nabla'\times\hat{r}'\sum_{n=0}^{\infty}\sum_{m=-n}^{n}\frac{(2n+1)(n-|m|)!}{n(n+1)(n+|m|)!} \\ \frac{1}{r}\hat{j}_n(kr_<)\hat{h}_n(kr_>)P_n^{|m|}(\cos\theta')P_n^{|m|}(\cos\theta)e^{im(\phi-\phi')} \ . \tag{9.42}$$

In these two expressions r', θ', and ϕ' correspond to the coordinates of the source and the operators $\nabla'\times\nabla'\times$ and $\nabla'\times$ operate only on the source coordinates. Also, $r_< = \min\{r', r\}$ and $r_> = \max\{r', r\}$, depending on the radius r of the observation point. We note that the factor $\frac{1}{r}P_n^{|m|}(\cos\theta)e^{im\phi}$ is common for each m and n. Upon suppressing, we can simplify the notation for the potentials corresponding to the incident spectrum of waves in region 1 as:

$$\pi_{1<}^i = b_1\hat{j}_n(k_1 r) \quad \text{for } r<r' \ , \text{ and} \tag{9.43}$$

$$\pi_{1>}^i = a_1\hat{h}_n(k_1 r) \quad \text{for } r>r' \ . \tag{9.44}$$

Furthermore, the forms for π^{TM} and π^{TE} are identical, therefore we can simply use $\pi_{1,2,3}$ for each region, keeping in mind that each $\pi_{1,2,3}$ represents two cases. Thus for region 1, taking into account the reflections at the boundaries [8], we write:

$$\pi_{1<} = a_1\tilde{R}_{12}\hat{j}_n(k_1 r) + b_1\hat{j}_n(k_1 r) \quad \text{for } r<r' \ , \tag{9.45}$$

$$\pi_{1>} = a_1[\hat{h}_n(k_1 r) + \tilde{R}_{12}\hat{j}_n(k_1 r)] \quad \text{for } r>r' \ . \tag{9.46}$$

In region 2, we have:

$$\pi_2 = a_2[\hat{h}_n(k_{2t}\tilde{r}) + R_{23}\hat{j}_n(k_{2t}\tilde{r})] \ , \tag{9.47}$$

and in region 3,

$$\pi_3 = \tilde{T}_{13}a_1\hat{h}_n(k_3 r) \ . \tag{9.48}$$

In the above expressions involving $\pi_{1,2,3}$,

$$a_2 = \frac{T_{12}}{1-R_{21}R_{23}}a_1 \ , \tag{9.49}$$

$$\tilde{R}_{12} = R_{12} + \frac{T_{21}R_{23}T_{12}}{1 - R_{21}R_{23}} \ , \tag{9.50}$$

and

$$\tilde{T}_{13} = \frac{T_{12}T_{23}}{1 - R_{21}R_{23}} \ . \tag{9.51}$$

$\tilde{R}_{12}$ and $\tilde{T}_{13}$ are the total reflection and transmission coefficients, which account for the multiple reflections. The reflection and transmission coefficients for each interface can be found by matching the boundary conditions. For example:

$$R_{12}^{\mathrm{TM}} = \frac{\sqrt{\varepsilon_{2t}\mu_{1t}}\hat{h}_n(k_{2t}\tilde{a})\hat{h}'_n(k_{1t}a) - \sqrt{\varepsilon_{1t}\mu_{2t}}\hat{h}'_n(k_{2t}\tilde{a})\hat{h}_n(k_{1t}a)}{\sqrt{\varepsilon_{1t}\mu_{2t}}\hat{j}_n(k_{1t}a)\hat{h}'_n(k_{2t}\tilde{a}) - \sqrt{\varepsilon_{2t}\mu_{1t}}\hat{h}_n(k_{2t}\tilde{a})\hat{j}'_n(k_{1t}a)} \ , \tag{9.52}$$

$$R_{21}^{\mathrm{TM}} = \frac{\sqrt{\varepsilon_{2t}\mu_{1t}}\hat{j}_n(k_{2t}\tilde{a})\hat{j}'_n(k_{1t}a) - \sqrt{\varepsilon_{1t}\mu_{2t}}\hat{j}_n(k_{1t}a)\hat{j}'_n(k_{2t}\tilde{a})}{\sqrt{\varepsilon_{1t}\mu_{2t}}\hat{j}_n(k_{1t}a)\hat{h}'_n(k_{2t}\tilde{a}) - \sqrt{\varepsilon_{2t}\mu_{1t}}\hat{h}_n(k_{2t}\tilde{a})\hat{j}'_n(k_{1t}a)} \ , \tag{9.53}$$

$$T_{12}^{\mathrm{TM}} = \frac{i\varepsilon_{2t}\sqrt{\mu_{2t}/\varepsilon_{1t}}}{\sqrt{\varepsilon_{1t}\mu_{2t}}\hat{j}_n(k_{1t}a)\hat{h}'_n(k_{2t}\tilde{a}) - \sqrt{\varepsilon_{2t}\mu_{1t}}\hat{h}_n(k_{2t}\tilde{a})\hat{j}'_n(k_{1t}a)} \ , \tag{9.54}$$

and

$$T_{21}^{\mathrm{TM}} = \frac{i\varepsilon_{1t}\sqrt{\mu_{1t}/\varepsilon_{2t}}}{\sqrt{\varepsilon_{1t}\mu_{2t}}\hat{j}_n(k_{1t}a)\hat{h}'_n(k_{2t}\tilde{a}) - \sqrt{\varepsilon_{2t}\mu_{1}}\hat{h}_n(k_{2t}\tilde{a})\hat{j}'_n(k_{1t}a)} \ . \tag{9.55}$$

We will also need the coefficients R_{23} and T_{23}, which we can obtain by simply changing subscripts 1 and 2 of R_{12} and T_{12} to 2 and 3, respectively. To obtain the coefficients for TE modes, we can invoke duality by swapping ε and μ.

We now derive the dipole expansion coefficients for a dipole with moment $\hat{z}I\ell$ corresponding to each m, n. Evaluating the coefficients for TM and TE modes that precede each $\frac{1}{r}\hat{b}_n(k_1 r)P_n^{|m|}(\cos\theta)e^{im\phi}$ yields:

$$\begin{aligned} a_1^{\mathrm{TM}} = b_1^{\mathrm{TM}} &= A_{mn}(-\hat{\theta})\cdot\nabla'\times\nabla'\times\hat{r}'\hat{b}_n(k_1 r')P_n^{|m|}(\cos\theta')e^{-im\phi'} \\ &= -A_{mn}\frac{k_1}{r'}\frac{n\cos\theta'}{\sin\theta'}\hat{b}'_n(k_1 r')P_n^{|m|}(\cos\theta')e^{-im\phi'} \\ &\quad + A_{mn}\frac{k_1}{r'}\frac{(m+n)}{\sin\theta'}\hat{b}'_n(k_1 r')P_{n-1}^{|m|}(\cos\theta')e^{-im\phi'} \end{aligned} \tag{9.56}$$

and

$$\begin{aligned} a_1^{\mathrm{TE}} = b_1^{\mathrm{TE}} &= i\omega\mu_1 A_{mn}(-\hat{\theta})\cdot\nabla'\times\hat{r}'\hat{b}_n(k_1 r')P_n^{|m|}(\cos\theta')e^{-im\phi'} \\ &= i\omega\mu_1 A_{mn}\frac{im}{r'\sin\theta'}\hat{b}_n(k_1 r')P_n^{|m|}(\cos\theta')e^{-im\phi'}, \end{aligned} \tag{9.57}$$

where

$$A_{mn} = \frac{i}{4\pi}\frac{I\ell}{k_1}\frac{(2n+1)(n-|m|)!}{n(n+1)(n+|m|)!} \ . \tag{9.58}$$

We have now completely formulated the problem for the potentials and fields. In the next section, we will apply this formulation to several different cases.

9.3 Results and Discussions

In this section, we will show the computed results based on the formulation described in the previous section. Subsequently, these computations are used to illustrate various aspects regarding the effects of enhanced virtual apertures. In particular, we are interested in the effects of loss on resolution in the farfield. We will primarily be studying the $\hat{\theta}$-directed electric field in the xy plane. The other field components at other observation points can be obtained in a similar fashion. In the xy plane, $\theta = \pi/2$. For each m and n, the electric field in the $\hat{\theta}$ direction is:

$$\begin{aligned} E_\theta = {} & a^{\mathrm{TM}}\frac{i}{\omega\varepsilon_t}\frac{k_t}{r}[-(m+n)]\hat{b}_n'(k_t\tilde{r})P_{n-1}^{|m|}(\cos\theta)e^{im\phi} \\ & + a^{\mathrm{TE}}\frac{im}{r}\hat{b}_n'(k_t\tilde{r})P_n^{|m|}(\cos\theta)e^{im\phi} \ . \end{aligned} \tag{9.59}$$

In comparison, the corresponding exact expression for the $\hat{\theta}$-directed electric field in the xy plane due to a $\hat{z}$-oriented dipole at the origin in free space is [6]:

$$E_\theta = -i\omega\mu_0 I\ell\frac{e^{ikr}}{4\pi r}\left[1+\frac{i}{kr}+(\frac{i}{kr})^2\right] \ . \tag{9.60}$$

Then, based on Eq. 9.60, we can calculate the reference value of the expected electric field corresponding to the lossless case.

9.3.1 4-Dipole Array in Free Space

We first consider the configuration as shown in Fig. 9.6. In the corresponding virtual space, there is a 4-dipole array in free space. The dipoles are oriented in the $\hat{z}$ direction, and each has an in-phase dipole moment with magnitude $I\ell = 1$. The dipoles are separated from each other by $\lambda/2$ and are arranged along the x axis. In the transformed space, with $a = 0.25\lambda$, $b = 0.5\lambda$, and $c = 1\lambda$, the effective physical aperture is reduced from c to b, or by a factor of 2. The compression ratio a/c is 0.25. In the ideal case with no loss, we expect the two cases to produce identical fields for $r > c$.

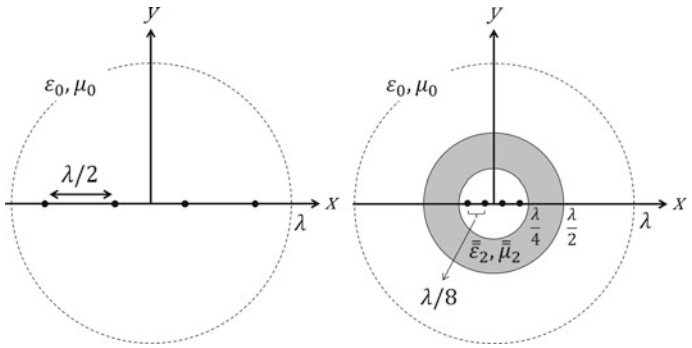

Fig. 9.6 A 4-dipole array in free space with $\lambda/2$ spacing. In the transformed space, $a = 0.25\lambda$, $b = 0.5\lambda$, and $c = 1\lambda$. In the lossless case, the regions for $r > c$ are equivalent

For numerical stability, we use the value of $\delta = 10^{-15}$ to represent the lossless case. In Fig. 9.7, we show the field value $|Re\{E_z\}|$ in the xy plane using Eq. 9.60. The range is between $\pm 6\lambda$ for both axes. The main beams at $\phi = \pm\pi/2$ as well as the sidelobes are clearly observed. In Fig. 9.8, we show the field value $|Re\{E_z\}|$ in the xy plane using Eq. 9.59 for $r > b$. Visually, they look similar in both cases, but, as shown in Fig. 9.9, the fields are in fact different for $b < r < c$. Because of the extremely low-loss and the well-matched condition created by the transformation, high field values not unlike that of surface resonances are observed at points near $r = b$. The field value for $r > c$ converges to the reference value rapidly, as shown in Fig. 9.10.

In Fig. 9.11, we plot the magnitude of the electric field component E_θ at $r = 100\lambda$, corresponding to the farfield value. The pattern is effectively identical to

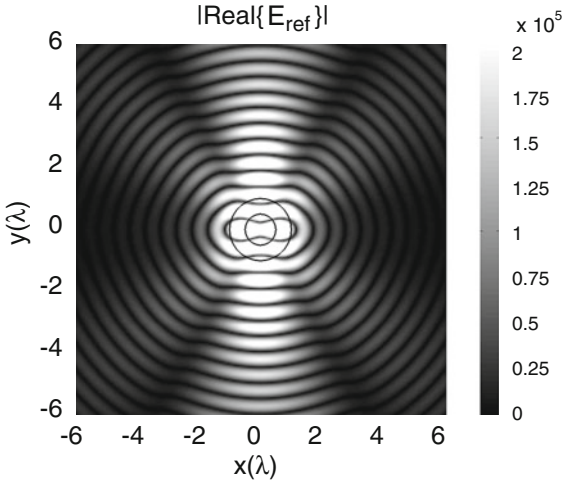

Fig. 9.7 2D scan of $|Re\{E_z\}|$ in the xy plane using Eq. 9.60. The *inner circle* corresponds to $r = 0.5\lambda$ and the *outer circle* corresponds to $r = 1\lambda$

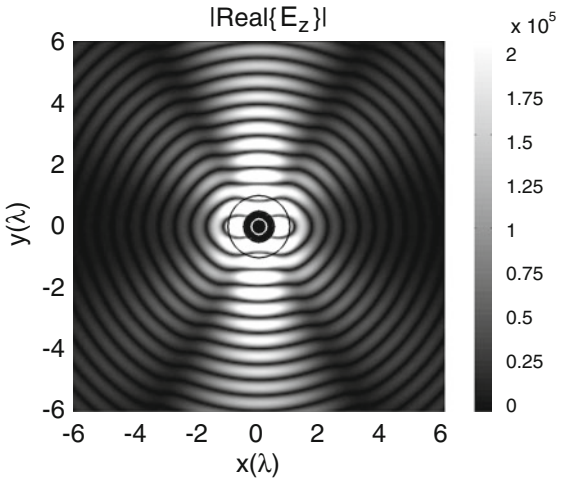

Fig. 9.8 2D scan of $|Re\{E_z\}|$ in the xy plane in region 3 ($r > b$) using Eq. 9.59. The circles correspond to $r = 0.25\lambda,\ 0.5\lambda,$ and 1λ

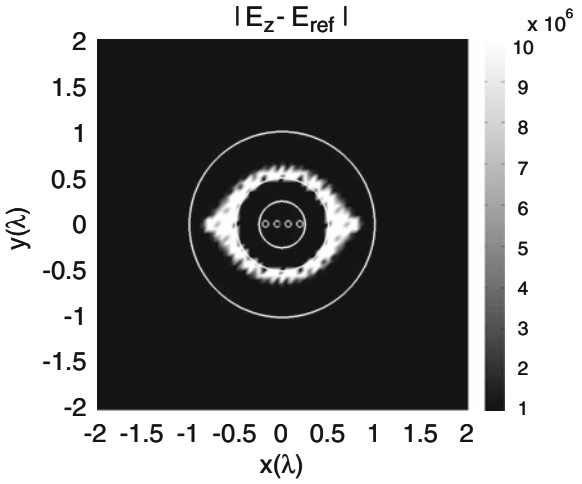

Fig. 9.9 Zoomed 2D scan of the magnitude of the difference between the two methods. The field values for $r > c$ are practically identical while the field values for $b < r < c$ are different. This is expected because the regions of equivalence are for $r > c$ only

the reference one. This can also be seen from Fig. 9.12, where we plot the magnitude of the coefficient T_n^{TM} as a function of n. This is the value of $\tilde{T}_{13}$ shown in Sect. 9.2 for TM modes given n. The coefficients T_n^{TE} have the same values as T_n^{TM} due to the symmetry between $\overline{\overline{\varepsilon}}_2$ and $\overline{\overline{\mu}}_2$. In the lossless case, $T_n^{\mathrm{TM}} = 0.25$, and it remains the same for all n, suggesting that there is no loss of angular resolution, and the original radiation pattern is preserved. Thus, a physical aperture with diameter λ has formed a virtual aperture with diameter 2λ.

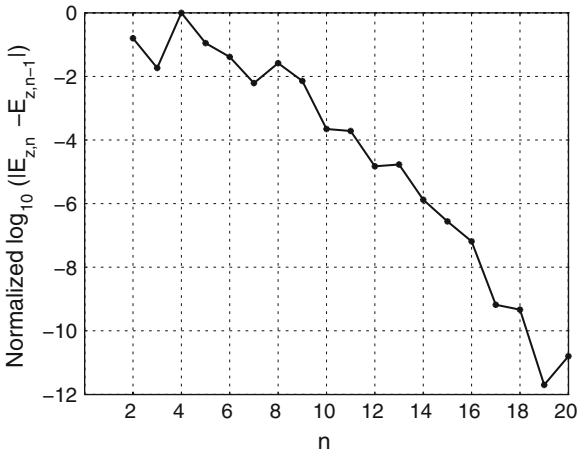

Fig. 9.10 Convergence of the electric field value as n increases. The point chosen corresponds to the corner in Fig. 9.8

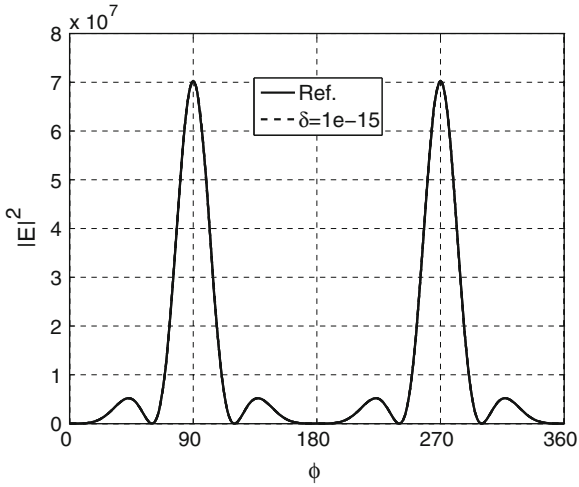

Fig. 9.11 Farfield radiation pattern of E_θ for the physical and virtual 4-dipole array. The patterns are essentially identical due to the low loss tangent of $\delta = 10^{-15}$

9.3.2 4-Dipole Array with Ground Plane

Consider the configuration as shown in Fig. 9.13. It is similar to the one in Fig. 9.6, except that here the dipole elements are placed $\lambda/4$ above a PEC ground plane. In the transformed space, $a = 0.25\lambda$, $b = 0.5\lambda$, and $c = 1\lambda$. The compression ratio is maintained to be 0.25. Image theory is used here to calculate the fields where we put four dipoles with amplitudes $I\ell = -1$ at $y = -0.0625\lambda$ so that they form mirror images of the physical dipoles. The region of interest ranges only from $\phi = 0$ *to* $\pi/2$, and the maximum electric field strength is expected to be double that of the free-space case. In Fig. 9.14 we plot the farfield radiation pattern of E_θ in the xy plane. The radiation pattern from the virtual antenna formed by a smaller core-shell structure is

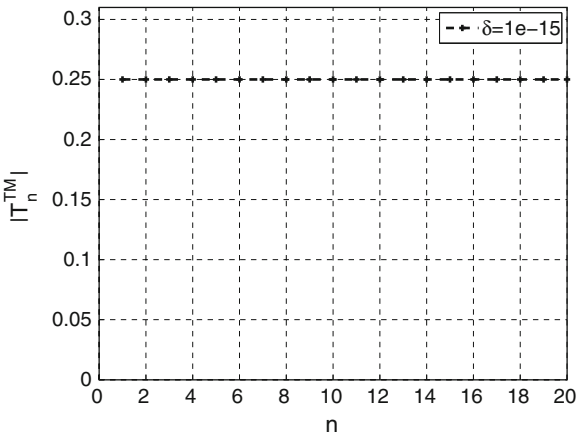

Fig. 9.12 Magnitude of the coefficient T_n^{TM} as a function of n. The magnitude is the same as the compression ratio $a/c = 0.25$ for n from 1 to 20

equivalent to that from a physical antenna with a larger dimension. The mainlobe amplitude and the sidelobe positions agree with the reference case.

Since c can be arbitrarily large, it would seem that we can theoretically use this method to build a structure with a smaller dimension and achieve an aperture with arbitrarily large directivity. However, there are several effects we need to consider, including coupling and loss. By virtue of the equivalence due to the transformation, dipole coupling is no worse than the situation in the virtual space, despite the spacing between the elements being physically much closer. However, loss will introduce substantial modifications to the radiated power and beamwidth. This effect is shown in the same figure, in which increasing the loss causes a reduction in directivity and an expanded beamwidth. The magnitude of the beam also decreases significantly as the loss tangent goes up. The loss also introduces both mismatches as well as ohmic loss into the system.

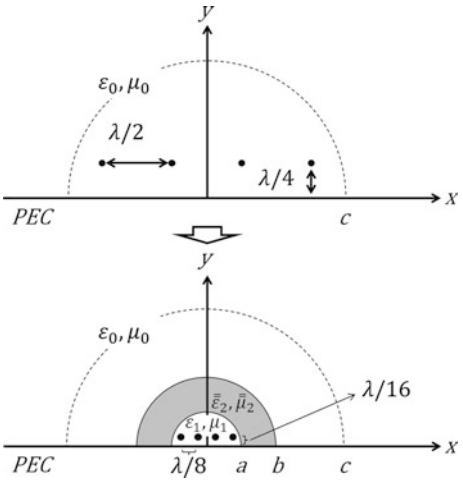

Fig. 9.13 A 4-dipole array with $\lambda/2$ element spacing positioned $\lambda/4$ above a PEC ground plane. In the transformed space, $a = 0.25\lambda, b = 0.5\lambda$, and $c = 1\lambda$. Image theory is used to calculate the fields

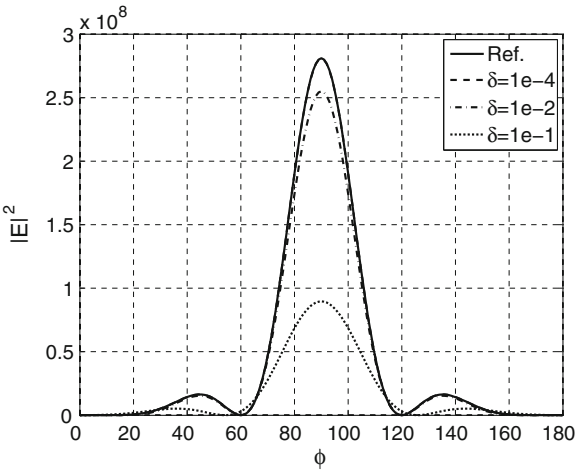

Fig. 9.14 Farfield radiation pattern of E_θ corresponding to various δ for the physical and virtual 4-dipole array positioned over a ground plane. The compression ratio is 0.25 in this case

In Fig. 9.15, we plot the magnitude of the coefficient T_n^{TM} as a function of n for different loss values. It is observed that for a low loss tangent of $\delta = 10^{-4}$, the transmission coefficients remain the same as before up to $n = 12$. As the loss increases, $|T_n^{\mathrm{TM}}|$ decreases more rapidly. For example, when $\delta = 10^{-2}$, the rolloff occurs at $n = 6$, contributing to the decrease of farfield resolution.

In Fig. 9.16, we plot the farfield radiation pattern of E_θ in the xy plane for $c = 2\lambda$ instead of 1λ. Hence, the compression ratio changes from 0.25 to 0.125. The decay of performance is now even more rapid than in the previous case. For the same δ as before, we now have degraded beamwidth and magnitude. This is also evident from the plot of the transmission coefficients in Fig. 9.17, where the rolloff occurs for smaller n.

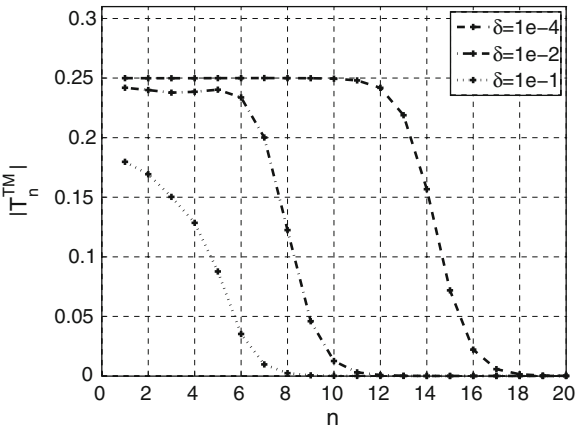

Fig. 9.15 Magnitude of the coefficient T_n^{TM} as a function of n. The magnitude decreases as n increases. The decay is faster for a higher loss value

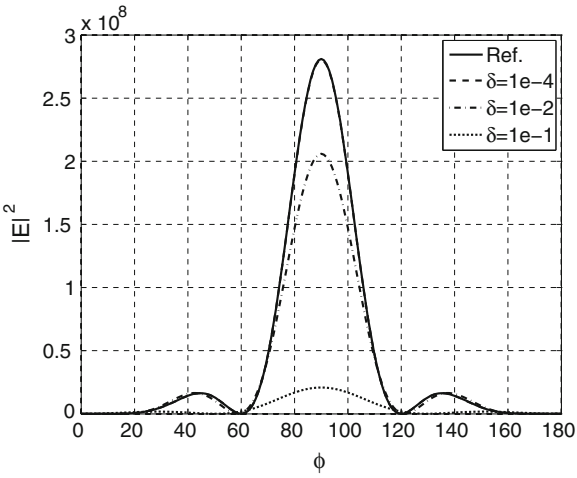

Fig. 9.16 Farfield radiation pattern of E_θ corresponding to various δ for the physical and virtual 4-dipole array positioned over a ground plane. The compression ratio is 0.125 in this case

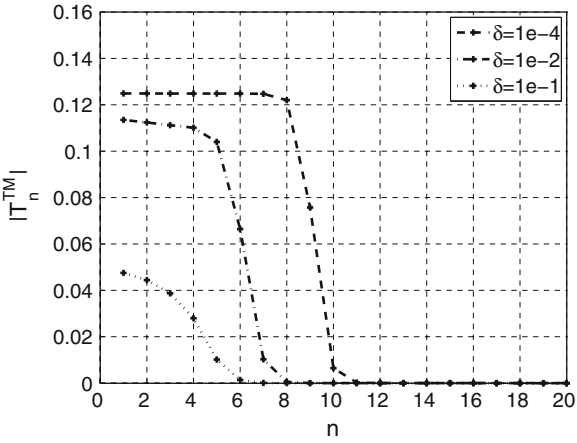

Fig. 9.17 Magnitude of the coefficient T_n^{TM} as a function of n. The magnitude decreases as n increases. The decay is further increased due to the higher compression

9.3.3 8-Dipole Array with Ground Plane

Maintaining the same compression ratio of $a/c = 0.125$ and element spacing in the virtual space as in the 4-dipole configuration, we now change the number of dipoles to 8, keeping the same spacing in the virtual space. In Fig. 9.18, the gray dots indicate the dipole positions in the virtual space and the black dots correspond to the transformed ones. When we had 4 dipoles for the same compression ratio, we were not taking advantage of the gain in virtual aperture size. Here, we are now taking advantage of the virtual aperture size with a gain factor of 4, from a physical aperture of 1λ to a virtual aperture of 4λ. In Fig. 9.19, it is seen that when we have $\delta = 10^{-4}$, the performance is discernibly different from the reference case. We observe a more dramatic change in the radiation patterns for each corresponding increase in δ. The same trend for $|T_n^{\mathrm{TM}}|$ is illustrated in Fig. 9.20.

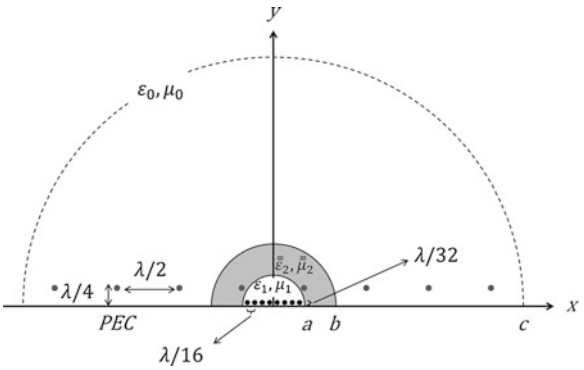

Fig. 9.18 An 8-dipole array positioned $\lambda/4$ above a PEC ground plane with $\lambda/2$ element spacing. In the transformed space, $a = 0.25\lambda$, $b = 0.5\lambda$, and $c = 2\lambda$. Image theory is used to calculate the fields

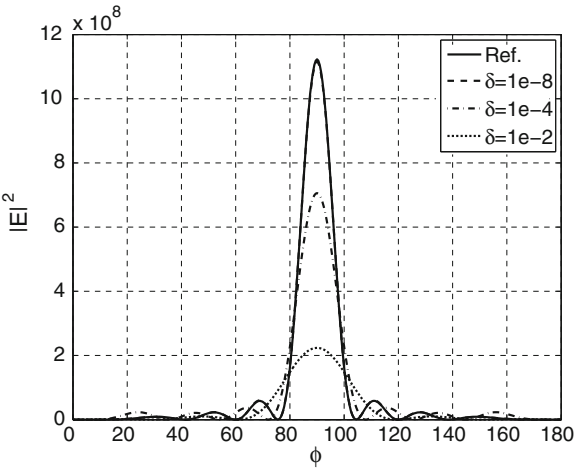

Fig. 9.19 Farfield radiation pattern of E_θ corresponding to various δ for the physical and virtual 8-dipole array positioned over a ground plane. The compression ratio is 0.125 in this case

9.3.4 Virtual Aperture and Farfield Resolution

Clearly, there is a relationship between the transmission coefficients $T_n^{\mathrm{TM/TE}}$, the beamwidth, and the loss tangent δ. In this subsection, we will investigate this issue. For each previous case where the compression ratio is 0.125, we can numerically solve for the null-to-null beamwidth of E_θ by starting from the normal direction $\hat{y}$ and scanning for a ϕ that corresponds to the first minimum field value. The results are shown in Figs. 9.21 and 9.22. The horizontal axes correspond to the loss tangent in a $\log_{10}$ scale and the vertical axis is the null-to-null beamwidth in degrees. In Fig. 9.21, for the 4-dipole case subject to a loss tangent smaller than 10^{-3}, the beamwidth converges to 60°, corresponding to the lossless case. It gradually diverges to approximately 80° as the loss tangent reaches 10^{-1}. In Fig. 9.22, for the 8-dipole case, even when the loss tangent is 10^{-5}, the beamwidth does not converge to the value of the lossless case. It also gradually diverges to

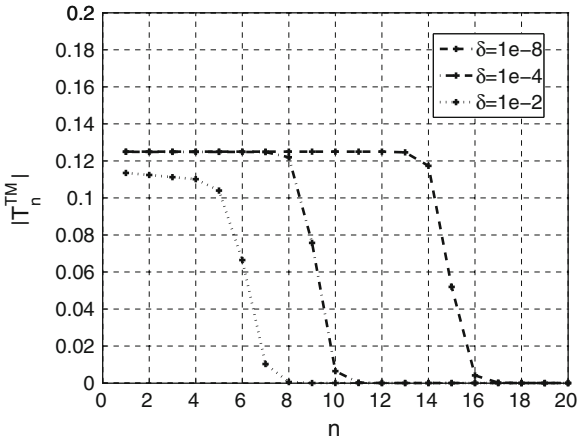

Fig. 9.20 Magnitude of the coefficient T_n^{TM} as a function of n. The magnitude decreases as n increases. The decay follows the same trend as in Fig. 9.17

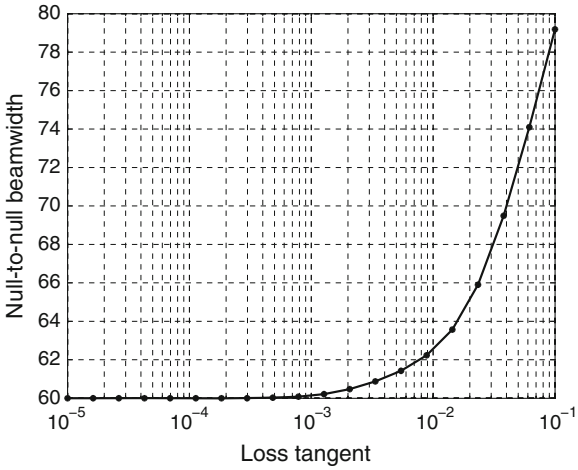

Fig. 9.21 Null-to-null beamwidth for a 4-dipole array with $a = 0.25\lambda$, $b = 0.5\lambda$, and $c = 2\lambda$. A smooth transition is observed as δ varies

approximately 80° as the loss tangent approaches 10^{-1}. However, here the overall angle deviation is larger. For the same range in δ, the angle now changes by 50° rather than 20°. Even though the traces of the plots are not linear with respect to $\log_{10}\delta$, the expansion of the beam clearly relates more closely to the log of δ rather than just δ itself.

In addition to observing the changes in beamwidth, we can also look at how the coefficients $T_n^{\mathrm{TM/TE}}$ change with n. $T_n^{\mathrm{TM/TE}}$ are the TM/TE transmission coefficients from region 1 to region 3 for each n. Their complex values are different for each n in the presence of loss. In Figs. 9.23 and 9.24, we show the 3D plots of $|T_n^{\mathrm{TM}}|$ as a function of n and δ, where $a = 0.25\lambda$, $b = 0.5\lambda$, and $c = 1\lambda$ or 2λ. The three axes correspond to n, $\log_{10}\delta$, and $|T_n^{\mathrm{TM}}|$. When the compression ratio is 0.25, $T_n^{\mathrm{TM}} = a/c = 0.25$ for the lossless case, and it is 0.125 for $a/c = 0.125$.

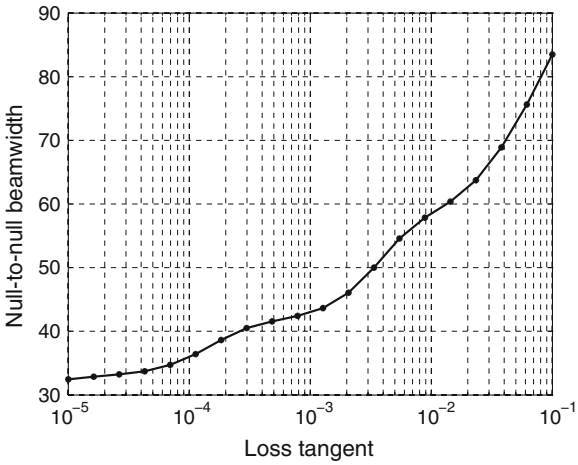

Fig. 9.22 Null-to-null beamwidth for a 8-dipole array with $a = 0.25\lambda$, $b = 0.5\lambda$, and $c = 2\lambda$. The beamwidth broadens faster than the 4-dipole case

In the first plot (Fig. 9.23), with a compression ratio of 0.25, the flat region of $|T_n^{\mathrm{TM}}|$ is rather large and a cliff-like structure is observed. The edge starts approximately from $n = 8$ on the n axis to $\log_{10}\delta = -5$ on the δ axis. In the second plot (Fig. 9.24), with a compression ratio of 0.125, the flat region of $|T_n^{\mathrm{TM}}|$ is smaller and a cliff-like structure is observed again. The edge starts approximately from $n = 8$ on the n axis to $\log_{10}\delta = -10$ on the δ axis. These two plots show quantitatively how the transmission coefficients vary with n and δ.

For comparison, consider a sphere with characteristic dimension kr, where k is the wavenumber and r is the radius of the sphere. The maximum number of modes supported is related to kr. Take Fig. 9.25 for example, where we are plotting the same parameters as in Fig. 9.23, except that we use an isotropic medium for region 2, with $\varepsilon_2 = \varepsilon_0(1 + i\delta)$, and $\mu_2 = \mu_0(1 + i\delta)$. Effectively, the sphere has a radius of $a = 0.25\lambda$ despite the shell. We keep the medium in region 1 to be the same as the previous case with $a/c = 0.25$; thus, $k_1 a = 2\pi$. It is seen that $|T_n^{\mathrm{TM}}|$ drops extremely fast with respect to n. When the loss tangent δ is high, say at around 10^{-1}, we still see a significant drop in amplitude, but we no longer see a diagonal cliff-like shape. This is one reason why by simply putting a radiating source inside a sphere with high dielectric medium alone will not support high angular resolution beyond a certain level regulated by the cutoffs of the transmission coefficients.

Besides studying the effects of the transmission coefficients numerically, we can also look at it analytically. Recall that for each n, the transmission coefficient $\tilde{T}_{13}$ can be written as:

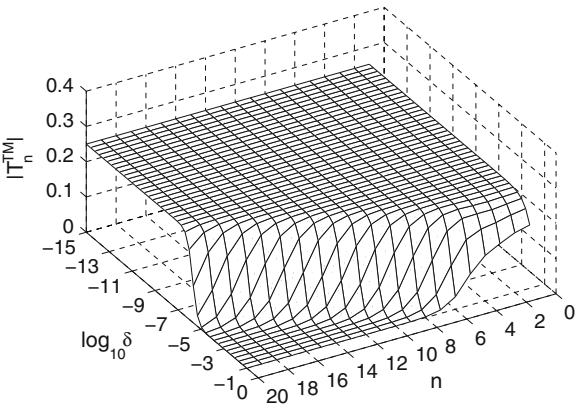

Fig. 9.23 3D plot of $|T_n^{\mathrm{TM}}|$ as a function of n and δ. $a = 0.25\lambda, b = 0.5\lambda$, and $c = 1\lambda$. $|T_n^{\mathrm{TM}}| = 0.25$ for the lossless shell

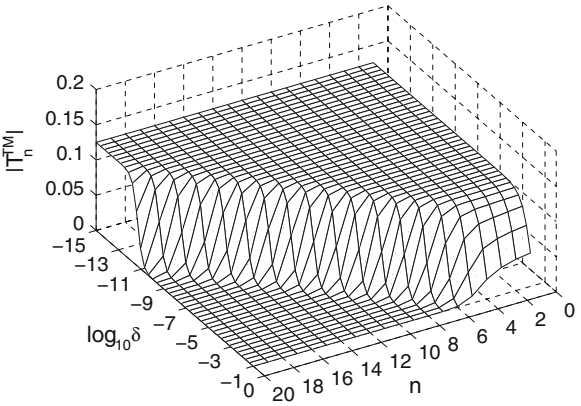

Fig. 9.24 3D plot of $|T_n^{\mathrm{TM}}|$ as a function of n and δ. $a = 0.25\lambda$, $b = 0.5\lambda$, and $c = 2\lambda$. $|T_n^{\mathrm{TM}}| = 0.125$ for the lossless shell

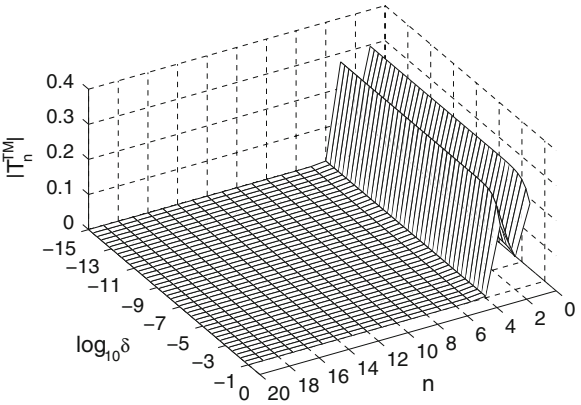

Fig. 9.25 3D plot of $|T_n^{\mathrm{TM}}|$ as a function of n and δ. $a = 0.25\lambda$, $b = 0.5\lambda$. Instead of a transformed shell, a regular shell from $r = a$ to b is used with $\varepsilon_2 = \varepsilon_0(1 + i\delta)$ and $\mu_2 = \mu_0(1 + i\delta)$

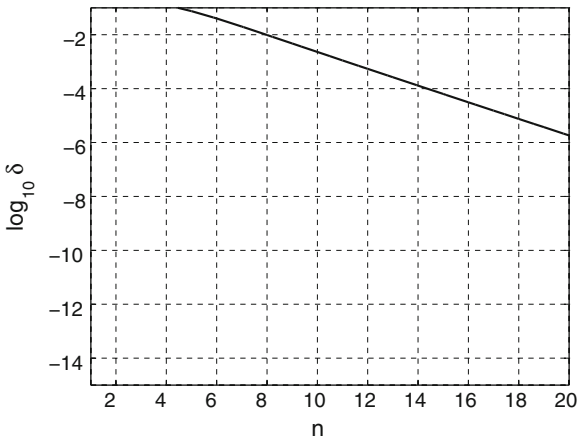

Fig. 9.26 Interpolated contour plot of Eq. 9.62 as a function of n and δ. $c = 1\lambda$. *The upper right region* corresponds to the cutoffs of the transmission coefficients and loss of resolution

$$\tilde{T}_{13} = \frac{T_{12}T_{23}}{1 - R_{21}R_{23}} \ . \tag{9.61}$$

In the above equation, T_{12}, T_{23}, R_{21}, and R_{23} themselves are functions of the constitutive and geometrical parameters. Note each one contains the Riccati-Bessel functions and their derivatives. We can look at the arguments of the Riccati-Bessel functions involved, which are $k_1 a, k_3 b, k_{2t}\tilde{a}$, and $k_{2t}\tilde{b}$. It is straightforward to show that $k_1 a = k_0 c$ and $k_{2t}\tilde{a} = k_0 c(1 - i\delta)$. Also, $k_3 b = k_0 b$ and $k_{2t}\tilde{b} = k_0 b(1 - i\delta)$. Other than the arguments of the Riccati-Bessel functions, the factors $\sqrt{\varepsilon_{2t}\mu_1}$ and $\sqrt{\varepsilon_3\mu_2}$ are the same as $\sqrt{\varepsilon_1\mu_{2t}}$ and $\sqrt{\varepsilon_{2t}\mu_3}$, respectively. Therefore, $R_{21} = R_{23} = 0$ and $T_{12}T_{23} = a/c$ for the lossless case.

Because the arguments within each denominator of the single layer coefficients are the same for the lossless case, when loss is present the denominators of R_{21}, R_{23}, T_{12}, T_{23} all perturb around their lossless Wronskian value of "i". Whereas the nominators of T_{12} and T_{23} remain close to a/c under perturbation, the nominators of R_{21} and R_{23} are extremely sensitive to δ. Based on this, it can be shown that within the scope of this chapter, the contour of the following equation yields a rough estimate on the cutoffs of the transmission coefficients:

$$\left|\left(\hat{j}_n(R_1')\hat{j}_n'(R_1) - \hat{j}_n(R_1)\hat{j}_n'(R_1')\right)\left(\hat{h}_n(R_2')\hat{h}_n'(R_2) - \hat{h}_n(R_2)\hat{h}_n'(R_2')\right)\right| = 1 \ , \tag{9.62}$$

where $R_1 = k_1 a, R_1' = k_1 a(1 - i\delta), R_2 = k_3 b$, and $R_2' = k_3 b(1 - i\delta)$. It should be noted that for planar slabs with the real parts of the constitutive parameters as $(-\varepsilon_0, -\mu_0)$ and similar loss tangent relationships as in the cases shown here, the spatial resolution in terms of the maximum tangential wavenumber before transmission cutoff is governed by a simple expression: $(1/d)\ln(2/\delta)$, where δ is the loss tangent and d is the thickness of the slab [14, 15]. In both the planar and spherical cases, the rapid deterioration of the spatial and angular resolution is related to the log of δ. The difference is that in the virtual aperture case considered here, the geometry is spherical and the angular harmonics are discrete rather than

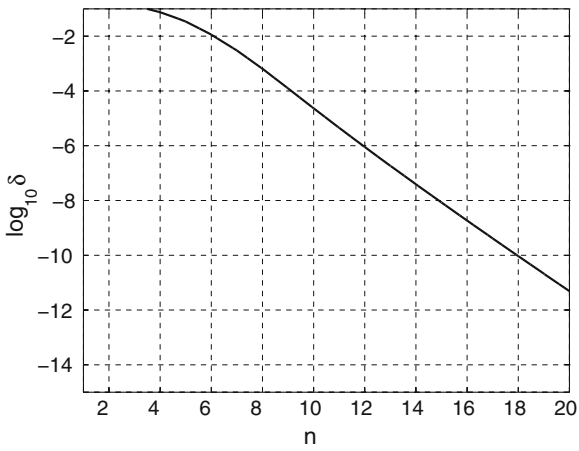

Fig. 9.27 Interpolated contour plot of Eq. 9.62 as a function of n and δ. $c = 2\lambda$. The *upper right region* corresponds to the cutoffs of the transmission coefficients and loss of resolution

continuous like the tangential wavenumber of a slab. Consequently, one cannot directly solve Eq. 9.62. However, one can plot the corresponding contour via interpolation. The contour plots for the two virtual aperture cases discussed in this subsection are shown in Figs. 9.26 and 9.27. The contours correspond to the edges of the cliff-like shapes in the previous 3D plots. It is seen that the contours provide reasonable estimates for the cutoffs of the transmission coefficients and hence the farfield resolution.

9.4 Conclusion

In this chapter, we proposed a spherical core-shell structure which can achieve arbitrarily large directivity. The structure was predicted and obtained from the proper coordinate transformations. A large virtual aperture can be projected to free space with a small physical dimension, subsequently leading to a large directivity. We investigated the problem by finding the transformed constitutive tensors and solving the equivalent problem in the core-shell configuration. Using the Ricatti-Bessel functions, we can represent the field components with Debye potentials and subsequently solve for the fields in all regions. We applied the formulation to several cases of dipole arrays within the shell, corresponding to both free-space and half-space problems in the virtual space. Both the near field and farfield phenomena were investigated. The relationship between the beamwidths and transmission coefficients for different loss values has been studied and an estimation for the cutoffs of the transmission coefficients was provided. Overall, the loss is linked directly to the farfield resolution in terms of the available angular harmonics. It is found that the deterioration of beamwidth changes rapidly with the increase of loss tangent in the shell medium. Even though one can theoretically construct an antenna aperture with arbitrarily high directivity in a small package,

based on the specific transformation used here, there is a practical limit as to how strongly a large aperture can be compressed into a small one. It can be reasoned that if a moderate loss tangent value can be reached, a virtual aperture gain factor of at least two should be achievable.

Acknowledgments This work is in part supported by the Air Force Office of Scientific Research.

References

1. Zhang JJ, Luo Y, Chen HS, Wu BI (2008) Manipulating the directivity of antennas with metamaterial. Optics Express 16:10962–10967
2. Pendry JB, Schurig D, Smith DR (2006) Controlling electromagnetic fields. Science 312:1780–1782
3. Leonhardt U, Philbin TG (2006) General relativity in electrical engineering. New J Phys 8:247
4. Chu LJ (1948) Physical limitations of omni-directional antennas. J Appl Phys 19:1163–1175
5. Zhang BL, Wu BI, Chen HS (2009) High directive antenna with virtual aperture. In: Proceedings 2009 IEEE APS International, Symposium, pp 3506–3509
6. Kong JA (2008) Electromagnetic wave theory. EMW, Cambridge
7. Kildishev AV, Cai W, Chettiar UK, Shalaev VM (2008) Transformation optics: approaching broadband electromagnetic cloaking. New J Phys 10:115209
8. Chew WC (1995) Waves and fields in inhomogeneous media. IEEE Press, Piscataway
9. Stratton JA (2007) Electromagnetic theory. IEEE Press, Piscataway
10. Chen HS, Wu BI, Zhang BL, Kong JA (2007) Electromagnetic wave interactions with a metamaterial cloak. Phys Rev Lett 99:063903
11. Zhang BL, Chen HS, Wu BI, Kong JA (2008) Extraordinary surface voltage effect in the invisibility cloak with an active device inside. Phys Rev Lett 100:063904
12. Abramowitz M, Stegun I (1965) Handbook of mathematical functions. Dover, New York
13. Zhang BL (2009) Electromagnetics of transformation media. Dissertation, MIT
14. Wu BI, Grzegorczyk TM, Zhang Y, Kong JA (2003) Guided modes with imaginary transverse wavenumber in a slab waveguide with negative permittivity and permeability. J Appl Phys 93:9386–9389
15. Lu J, Grzegorczyk TM, Wu BI, Pacheco J, Chen M, Kong JA (2005) Effect of poles on subwavelength focusing by an LHM slab. Microwave Opt Technol Lett 45:49–53

Chapter 10
Invisibility Cloak at Optical Frequencies

Shuang Zhang

Abstract The invisibility cloak is an intensively studied topic in the fields of electromagnetism and optics. Since the first theoretical formulation of invisibility, growing attention has been paid to this rapidly growing field, both in theory and experiments. In this chapter, we review the recent progress in the invisibility cloak and transformation optics at optical frequencies.

10.1 Introduction

It is well known that a transparent object becomes invisible when it is placed in a liquid with the same refractive index. This is because the index matching condition ensures that light does not undergo reflection or refraction at the interface between the transparent object and the surrounding medium. With no changes to the rays of light, the object is not visible in the medium. On the other hand, rendering objects with arbitrary optical properties (transparent, opaque) invisible, has been quite a challenge. This involves tricking light to bend around the objects without interacting with them. Bending of light at the interface between two materials with different optical densities, or refractive indices, is the most common optical phenomenon in nature. This principle has been utilized to design various optical elements to control light, including lenses and prisms. Traditionally, the trajectory of light is calculated for a given geometry and configuration of the optical elements. Transformation optics [1–3], a newly emerging branch of optics, deals with the reverse problem, where the desired trajectory of light is prescribed and then the distribution of the optical materials is formulated. Transformation optics is an

S. Zhang (✉)
School of Physics and Astronomy, University of Birmingham, Birmingham, UK
e-mail: zhangs75@gmail.com; s.zhang@bham.ac.uk

D. H. Werner and D.-H. Kwon (eds.), *Transformation Electromagnetics and Metamaterials*, DOI: 10.1007/978-1-4471-4996-5_10,

extremely powerful tool to design optical elements, and in most cases, materials with spatially varying optical properties are required.

Invisibility cloaks have been realized recently with the help of transformation optics [4–19], which enables one to control light at will, given that the prescribed optical properties can be found in nature or engineered using micro- and nanofabrication techniques. It is important that the cloaks work for all incident angles, at least in a two-dimensional (2D) setting. Although an invisibility cloak based on retro-reflective projection technology was claimed in 2003, involving capturing images from one side using a camera and projecting to the other side by a beam splitter, it only works for light incident from a specific direction [20]. With simpler configurations, such as a combination of lenses and/or prisms, it is possible to squeeze light to avoid going through a certain spatial region. However, it does not work for all incident angles. Transformation optics allows for the design of invisibility cloaks operating at all angles because it is based on a one-to-one spatial mapping from a virtual space to the real optical space. Indeed, the significance of transformation optics goes beyond that of the invisibility cloak, as it points to a new venue of designing various functional optical devices, ranging from optical beam benders and beam expanders [21] to multi-functional devices such as optical Janus devices [22].

Several years in the past have witnessed rapid progress in the field of transformation optics and invisibility. In particular, much effort has been spent on scaling down the invisibility cloaks to operate at optical frequencies. Two theoretical innovations played important roles in the realization of invisibility cloaks at visible frequencies: nonmagnetic invisibility cloaks [23] and the carpet invisibility cloak [3]. These two theoretical frameworks have allowed great simplification of the design of invisibility cloaks. In addition, advanced nanofabrication technologies, such as electron beam lithography and focused ion beam lithography, have been instrumental to the experimental implementation of these theoretical concepts.

10.2 Nonmagnetic Optical Invisibility Cloak

As simple and elegant as the theory of transformation optics seems to be, the realization of an invisibility cloak is not straightforward, as invisibility cloaks, in their ideal forms, need to be made from anisotropic materials with both permittivity and permeability expressed as tensors. Moreover, at least six tensor elements along the local principal directions need to be carefully designed at each spatial point. This is a formidable task, even with metamaterials, as the operation of most metamaterials reported to-date is limited to a certain polarization for light propagating in a 2D plane. An ideal invisibility cloak, based on a rigorous optical transformation, requires optical materials with suitable electric permittivity and magnetic permeability tensors. This poses a great challenge to the metamaterial design for achieving the required material properties. Fortunately, in practice, this

requirement can be relaxed if one wants to design an invisibility cloak for a reduced dimensionality and for a specific polarization state of the incident electromagnetic waves.

10.2.1 Invisibility Cloak Without Magnetic Materials

Shortly after the first theoretical formulation of the principle of invisibility cloaks [1, 2], Schurig et al. [4] showed the first demonstration of an invisibility cloak in the microwave regime . This experimentally realized cloak was a compromise between the simplification of the electromagnetic parameters and the cloaking performance. The reduced scheme only focuses on controlling two of the six tensor elements of the electromagnetic parameters for the cloaking material. The tradeoff is that the cloak only works for a single polarization, and there was scattering at the interface of cloaks as there was an impedance mismatch between the cloaking shell and the surrounding free space. Nonetheless, the electromagnetic wave follows exactly the same trajectories as if it were a perfect cloak.

The first invisibility cloak demonstrated at microwave frequencies requires magnetic responses in the constituent metamaterials. While strong artificial magnetism with low loss can be achieved at low frequencies such as radio, microwave, and terahertz frequencies where the metals are close to perfect electric conductors [24–27], strong artificial magnetism is difficult to attain at optical frequencies due to the electron inertia and higher ohmic losses in metals [28–32]. Fortunately, it has been shown that magnetism is not a necessary condition for realizing an invisibility cloak.

In a 2D configuration, the relevant optical parameters for wave propagation are ε_z, μ_θ, μ_r for the transverse electric (TE) polarization, and ε_r, ε_θ, μ_z for the transverse magnetic (TM) polarization. For the TM polarization, the nonzero fields are E_x, E_y, and H_z, and Maxwell's equations can be written as,

$$\frac{\partial E_y}{\partial x} - \frac{\partial E_x}{\partial y} = -\mu_0 \mu_z \frac{\partial H_z}{\partial t} \tag{10.1}$$

$$\boldsymbol{e}_x \frac{\partial H_z}{\partial y} - \boldsymbol{e}_y \frac{\partial H_z}{\partial x} = \varepsilon_0 \varepsilon_{x-y} \frac{\partial \boldsymbol{E}}{\partial t} \tag{10.2}$$

where ε_{x-y} is the subdomain tensor of permittivity in the x–y plane, i.e., $\varepsilon_{x-y} = \begin{pmatrix} \varepsilon_{xx} & \varepsilon_{xy} \\ \varepsilon_{xy} & \varepsilon_{yy} \end{pmatrix}$. Taking the derivative of Eq. (10.2) with respect to time, and plugging the result into Eq. (10.1), we have,

$$\boldsymbol{e}_x \frac{\partial}{\partial y}\left(\frac{\partial E_y}{\partial x} - \frac{\partial E_x}{\partial y}\right) - \boldsymbol{e}_y \frac{\partial}{\partial x}\left(\frac{\partial E_y}{\partial x} - \frac{\partial E_x}{\partial y}\right) = -\frac{1}{c^2}\mu_z \varepsilon_{x-y} \frac{\partial^2 \boldsymbol{E}}{\partial t^2} \tag{10.3}$$

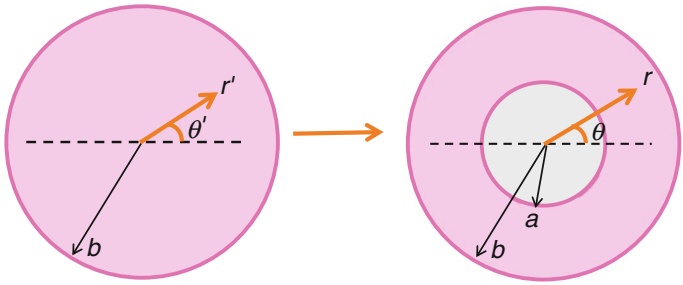

Fig. 10.1 Illustration of optical transformation for a cylindrical invisibility cloak

Equation (10.3) shows that the only optical parameter that controls the flow of light for the TM polarization in the medium is $\mu_z \varepsilon_{x-y}$, representing the anisotropic refractive index tensor in the x–y plane.

In 2007, Cai et al. [23] proposed a nonmagnetic cylindrical invisibility cloak. The schematic diagram of the invisibility cloak is shown in Fig. 10.1. The design of the cloak is based on a linear transformation from a virtual space consisting of a cylinder of radius b filled with $\varepsilon = 1$ and $\mu = 1$ (Fig. 10.1, left), to a physical space consisting of a coaxial shell with inner radius a and outer radius b (Fig. 10.1, right). Mathematically, the transformation from the virtual space (r', θ', z') to the physical space (r, θ, z) is expressed as,

$$r = a + \frac{b-a}{b} r', \ \theta = \theta', \ z = z' \tag{10.4}$$

The transformation leads to the following spatially varying electromagnetic properties in the cloak shell region in the physical space [4],

$$\begin{aligned} \varepsilon_r = \mu_r = \frac{r-a}{r}, \ \varepsilon_\theta = \mu_\theta = \frac{r}{r-a}, \\ \varepsilon_z = \mu_z = \left(\frac{b}{b-a}\right)^2 \frac{r-a}{r} \end{aligned} \tag{10.5}$$

Equation 10.5 shows that both permittivity and permeability in the cloaking region have to be designed carefully to achieve perfect invisibility. Furthermore, at $r = a$, all tensor elements of the permittivity and permeability approach either zero or infinity, which present great challenges for experimental implementation at optical frequencies. Cai et al. showed that the invisibility cloak could be reduced to a nonmagnetic cloak that maintains the same light trajectory as the ideal one, with the optical parameters given by,

$$\varepsilon_r = \left(\frac{b}{b-a}\right)^2 \left(\frac{r-a}{r}\right)^2, \ \varepsilon_\theta = \left(\frac{b}{b-a}\right)^2, \ \mu_z = 1 \tag{10.6}$$

The reduced nonmagnetic invisibility cloak, described by Eq. 10.6, poses fewer requirements on the electromagnetic parameters than the ideal one. First, magnetic

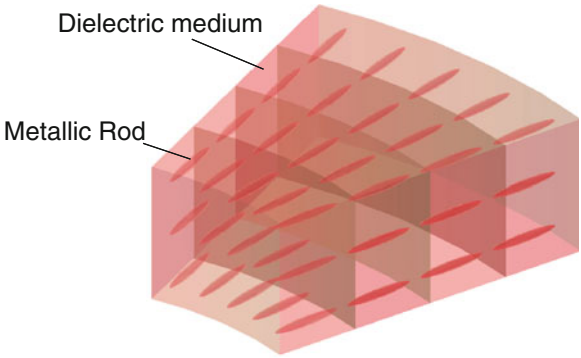

Fig. 10.2 Schematic diagram of the metamaterial design for realizing a cylindrical nonmagnetic invisibility cloak at optical frequencies. The metamaterial consists of plasmonic nanorods oriented along the radial direction. The geometries of the particles are inhomogeneous along the radial direction to satisfy the cloaking condition set by Eq. 10.5. Courtesy of W. Cai and adapted from Cai et al. [23]

responses are not required in the design of the cloak. Although magnetic responses have been demonstrated at optical frequencies, the optical loss introduced by the magnetic resonance is very large, and therefore hinders the applications of optical magnetism to an invisibility cloak. Second, as shown by Eq. 10.6, among the three relevant parameters for the TM polarization, two parameters (ε_θ, μ_z) are constant (i.e., spatially homogeneous), which dramatically simplifies the implementation of the metamaterials in the cloaking shell. However, it should be noted that the simplification of the invisibility cloak brought by the reduced design comes at two costs: (1) the nonmagnetic invisibility cloak works for only a single polarization and (2) the impedance is mismatched at the outer boundary of the cloak, leading to significant scattering at the interface between the cloak and the surrounding medium.

The nonmagnetic invisibility cloak can be implemented by using anisotropic metamaterials that consist of elliptical metallic particles [23], as shown by Fig. 10.2. By carefully designing the geometry of the metallic particles at each layer, the condition of invisibility given by Eq. (10.5) can be satisfied. The performance of the invisibility cloak has been numerically demonstrated. As shown by Fig 10.3a, the nonmagnetic invisibility cloak is capable of bending light around the object (the metallic cylinder in the center). For comparison, a cylinder without the cloak strongly scatters light (Fig. 10.3b). This serves as numerical evidence of the efficacy of the nonmagnetic invisibility cloak in controlling the trajectory of light. Note that in the simulation of the invisibility cloak, the ohmic loss of the metamaterials has been ignored. In reality, the metal loss will significantly affect the performance of the invisibility cloak, as light will be strongly attenuated after propagating through the shell of the cloak. In addition, the impedance mismatch at the interface between the cloak shell and surrounding medium (air) leads to scattering, as evidenced by the strong modulation of the field intensity outside the invisibility cloak.

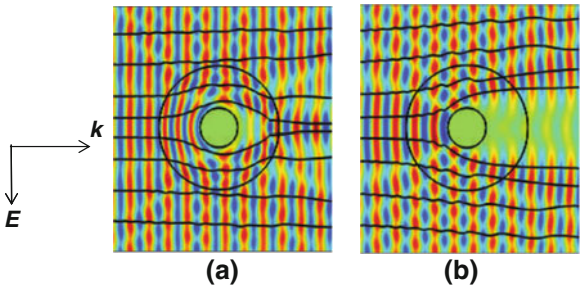

Fig. 10.3 Numerical simulation of the nonmagnetic invisibility cloak operating at optical frequencies. **a** Scattering of light by a PEC cylinder surrounded by the cylindrical invisibility cloak. **b** Scattering by the PEC cylinder without the cloak, as a control study. Courtesy of W. Cai and adapted from Cai et al. [23]

10.2.2 Nonlinear Transformation to Minimize Scattering

In order to minimize the reflection at the outer interface, Cai et al. further proposed a nonlinear optical transformation that leads to impedance matching at the interface between the cloak and the surrounding medium [33]. In a cylindrical invisibility cloaking system as shown in Fig. 10.1, the transformation from the virtual space to the physical space can be written in a more general form,

$$r = g(r'),\ \theta = \theta',\ z = z' \tag{10.7}$$

where the function $g(\bullet)$ is monotonically increasing with $g(0) = a$ and $g(b) = b$. The corresponding electromagnetic parameters inside an ideal invisibility cloak shell region are given as,

$$\varepsilon_r = \mu_r = \frac{r'}{r} g'(r'),\ \varepsilon_\theta = \mu_\theta = \frac{r}{r' g'(r')},\quad \varepsilon_z = \mu_z = \frac{r'}{r g'(r')} \tag{10.8}$$

It is straightforward to prove from Eq. (10.8) that the impedance for TM and TE polarized waves at the outer shell, given by $Z_{\mathrm{TM}} = \sqrt{\mu_z/\varepsilon_\theta}$ and $Z_{\mathrm{TE}} = \sqrt{\mu_\theta/\varepsilon_z}$ respectively, are both equal to unity at the outer shell ($r = b$), confirming that the impedance is perfectly matched to the surrounding medium. The nonmagnetic cloaking design for the TM polarization is introduced by setting μ_z to 1 and meanwhile keeping the products $\varepsilon_r\mu_z$ and $\varepsilon_\theta\mu_z$ unchanged. The electromagnetic parameters of the nonmagnetic invisibility cloak are described by,

$$\varepsilon_r = \left(\frac{r'}{r}\right)^2,\ \varepsilon_\theta = \left(\frac{1}{g'(r')}\right)^2,\ \mu_z = 1. \tag{10.9}$$

By imposing the impedance matching condition at the outer boundary of the cloaking shell, that is, by setting the impedance $Z_{\mathrm{TM}} = \sqrt{\mu_z/\varepsilon_\theta} = g'(r') = 1$ at $r = b$, the electromagnetic parameters (ε_r, ε_θ, μ_z) at the outer boundary are all unity, ensuring that the electromagnetic properties are continuous across the outer interface between air and the cloak. This will lead to a significant reduction of scattering in comparison to the nonmagnetic invisibility cloak with a linear transformation.

Numerical simulations were performed to compare the effect of an ideal cloak, a nonmagnetic cloak with linear transformation, and a nonmagnetic cloak with a nonlinear transformation for achieving impedance matching at the outer boundary, with the results shown in Fig. 10.4. An ideal invisibility cloak is capable of completely eliminating the scattering, as shown by Fig. 10.4b. On the other hand, despite that a nonmagnetic invisibility cloak with a linear transformation preserves the light trajectory, it causes significant scattering due to the impedance mismatch (Fig. 10.4c). The nonmagnetic invisibility cloak with a nonlinear transformation to

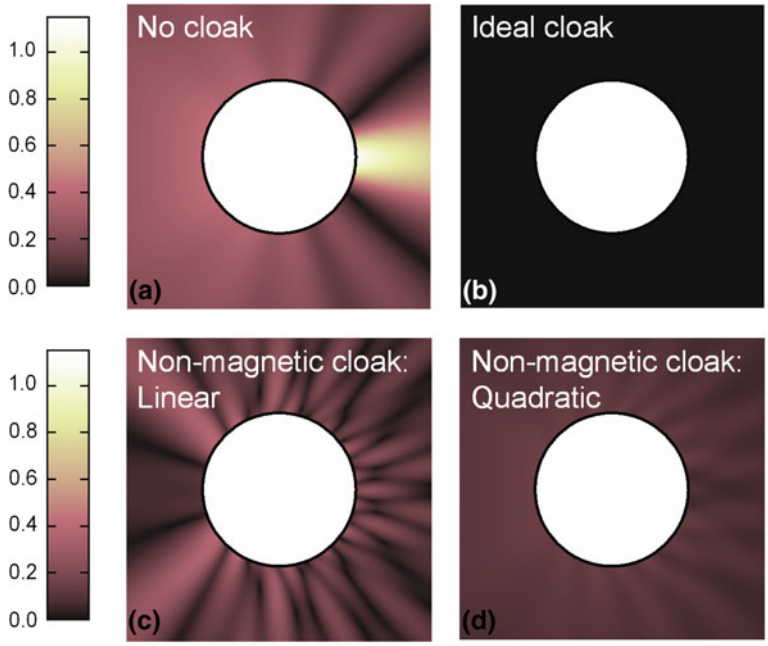

Fig. 10.4 The field distribution of light scattered by a metallic cylinder with and without an invisibility cloak. **a** Light scattered by a bare cylinder. **b** An ideal cloak that totally eliminates scattering. **c** A nonmagnetic invisibility cloak with a linear transformation, which exhibits significant scattering because of the impedance mismatch at the outer boundary of cloak. **d** A nonmagnetic invisibility cloak that has a nonlinear transformation such that the impedance match is satisfied at the interface between the cloak and the surrounding medium. As a result, the scattering is dramatically reduced compared to **c**. Reprinted with permission from Cai et al. [33]

match the impedance reduces the scattering dramatically (Fig. 10.4d). Thus, the numerical results confirm the efficacy of this nonlinear transform scheme to improve the performance of an invisibility cloak with reduced parameters.

10.3 Carpet Invisibility Cloak

10.3.1 Concept of the Carpet Invisibility Cloak

Although the nonmagnetic cylindrical invisibility cloak eliminates the requirement of magnetism, the dielectric parameters in the cloak still require extreme optical parameters, which can only be obtained by using resonant metallic-dielectric nanostructures. Consequently, high loss and narrow bandwidth seem to be inevitable, which limit the usefulness of the invisibility cloak for practical applications. In 2008, Li and Pendry proposed a new cloaking scheme, dubbed 'carpet invisibility', which simultaneously solves the problem of narrow band operation and the loss issue, and paves the way toward proof-of-concept demonstrations of invisibility cloaks at optical frequencies. The carpet invisibility cloak is capable of rendering an object invisible on a reflective surface. An illustrative schematic of the carpet invisibility cloak is shown in Fig. 10.5. When an object is placed on a reflective surface, such as a flat mirror, it is clearly visible as it scatters light into the observers' eyes. A reflective curved cover can be placed over the object to hide it, however, the cover itself is visible as it distorts the reflection of the light. On top of the cover, a carefully designed optical material can transform the curved reflective cover into a flat mirror with infinitesimal thickness. As a result, the curved cover does not scatter light anymore, as it is simply part of the flat reflective surface to outside observers. Anything hidden underneath the curved cover is thus made invisible.

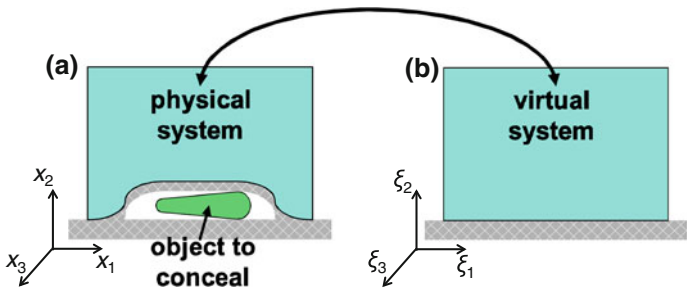

Fig. 10.5 Schematic showing the principle of the carpet invisibility cloak. Physical space **a** where an object on a ground surface is covered by an invisibility cloak which optically transforms the curved inner surface into a flat one in the virtual space **b**. Reprinted with permission from Li and Pendry [3]

In cylindrical or spherical invisibility cloaks, the extreme optical parameters are introduced by the singularity involved in transforming a single point, or a single line to a surface of finite area. In contrast, the carpet invisibility cloak works by optically transforming a flat surface of finite size into a curved one, therefore the transformation does not introduce a singularity in the optical parameters of the cloak. Consequently, only moderate material parameters are required to construct the invisibility cloak. Intuitively, this can be viewed as a spatial domain of finite volume being flattened into an infinitely thin mirror, which cannot be seen if placed on top of another mirror surface.

10.3.2 Quasi-Conformal Mapping

Ideally, the optical properties of the materials in carpet invisibility cloaks need to be anisotropic, i.e., at each local point inside the carpet cloak, the refractive indices are different along the principle directions. This, in general, complicates the metamaterial design for realizing the carpet invisibility cloak. Li and Pendry proposed a quasi-conformal mapping method to eliminate the requirement of anisotropy. Consider the mapping in a 2D configuration from a virtual space (ξ_1, ξ_2, ξ_3) shown in Fig. 10.5b to a physical space (x_1, x_2, x_3) in Fig. 10.5a,

$$x_1 = x_1(\xi_1, \xi_2),\ x_2 = x_2(\xi_1, \xi_2),\ x_3 = \xi_3.$$

The electromagnetic parameters in the cloak region in the physical space are given by,

$$\varepsilon = \varepsilon_{\text{ref}} \frac{\Lambda\Lambda^T}{\sqrt{\det(\Lambda\Lambda^T)}},\ \mu = \frac{\Lambda\Lambda^T}{\sqrt{\det(\Lambda\Lambda^T)}} \tag{10.10}$$

where ε_{ref} is the permittivity in the virtual space, ε and μ are the permittivity tensor and permeability tensor in the physical system, respectively, $\Lambda = \partial(x_1,x_2,x_3) / \partial(\xi_1, \xi_2, \xi_3)$ is the Jacobian matrix, and $\Lambda\Lambda^{\text{T}}$ can be explicitly written as,

$$\Lambda\Lambda^T = \begin{pmatrix} \left(\frac{\partial x_1}{\partial \xi_1}\right)^2 + \left(\frac{\partial x_2}{\partial \xi_1}\right)^2 & \frac{\partial x_1}{\partial \xi_1}\frac{\partial x_1}{\partial \xi_2} + \frac{\partial x_2}{\partial \xi_1}\frac{\partial x_2}{\partial \xi_2} & 0 \\ \frac{\partial x_1}{\partial \xi_1}\frac{\partial x_1}{\partial \xi_2} + \frac{\partial x_2}{\partial \xi_1}\frac{\partial x_2}{\partial \xi_2} & \left(\frac{\partial x_1}{\partial \xi_2}\right)^2 + \left(\frac{\partial x_2}{\partial \xi_2}\right)^2 & 0 \\ 0 & 0 & 1 \end{pmatrix}. \tag{10.11}$$

Let g be the 2×2 subspace tensor of $\Lambda\Lambda^{\text{T}}$ in the (x_1, x_2) plane, from Eq. (10.11) it is obvious that $\det(g) = \det(\Lambda\Lambda^{\text{T}})$. The permittivity and permeability tensors can be diagonalized to obtain their principle values (ε_{T}, ε_{L}, $\varepsilon_{\text{ref}}/\sqrt{\det(g)}$) and ($\mu_{\text{T}}$, μ_{L},$1/\sqrt{\det(g)}$). Taking the permeability tensor as an example, the eigenvalue equation is given as,

$$\lambda^2 - \frac{\mathrm{Tr}(g)}{\sqrt{\det(g)}}\lambda + 1 = 0.$$

The two roots of the eigenvalue equation satisfy:

$$\begin{aligned} \mu_T \mu_L &= 1 \\ \mu_T + \mu_L &= \frac{\mathrm{Tr}(g)}{\sqrt{\det(g)}}. \end{aligned} \tag{10.12}$$

For TE polarization, the anisotropy of the invisibility cloak arises from the difference between μ_{T} and μ_{L}. The main idea of a quasi-conformal mapping is to find a suitable design that minimizes the differences between them, and then both of them are replaced by the average permeability $\mu = 1$. In this way, the refractive index is isotropic for light propagating in the plane, and the cloak does not require magnetism. The target function to minimize, as proposed by Li et al., is the Modified-Liao functional given by Knupp and Steinberg [34],

$$\phi = \frac{1}{A}\iint \mathrm{d}\xi_1 d\xi_2 \frac{Tr(g)^2}{\det(g)}. \tag{10.13}$$

A carpet invisibility cloak designed using a conformal mapping was numerically demonstrated by Li et al. [3], with performance shown in Fig. 10.6. By carefully designing the index profile inside the cloaking region (the dashed box), the light incident onto a bump at the bottom surface is reflected without distortion

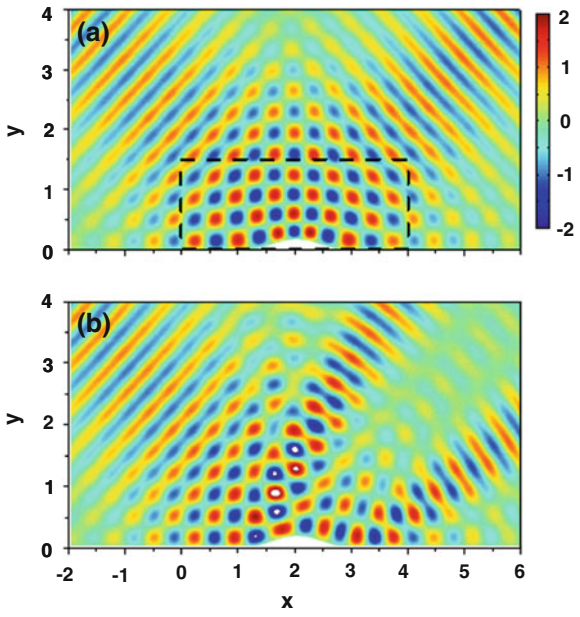

Fig. 10.6 **a** A numerical simulation shows that the invisibility cloak effectively transforms the curved surface into a flat one, and as such an input Gaussian beam is not scattered. **b** A control simulation shows that without the cloak, the beam is strongly disturbed by the presence of the curved surface. Reprinted with permission from Li and Pendry [3]

or scattering, as evidenced by the Gaussian output beam profile (Fig. 10.6a), whereas without the carpet cloak, a Gaussian beam is strongly scattered upon incidence onto the bump (Fig. 10.6b).

10.3.3 Nanofabricated Optical Invisibility Cloaks in 2D Configurations

As discussed in Sect. 10.3.2, the carpet invisibility cloak enables broadband operation, as the electromagnetic parameters of the constituent materials of the cloak only show a mild spatial variation, and therefore resonances are not required. Thus, it is possible to use dielectric materials to construct an invisibility cloak with both broadband operation and low optical loss. This mitigation of the stringent requirements on the material parameters of an invisibility cloak has led to the proof-of-concept demonstrations of invisibility cloaks at optical frequencies by several groups recently [8, 9, 11, 13–17] .

The first demonstrations of optical invisibility cloaks were independently accomplished by Valentine et al. and Gabrielli et al. [8, 9]. In both works, the invisibility cloaks were demonstrated in a 2D waveguide configuration, as shown in Fig. 10.7. The carpet cloaks were fabricated on silicon-on-insulator (SOI) wafers using either focused ion beam lithography [8], or electron beam lithography [9], two of the most common top–down lithography techniques capable of producing arbitrary patterns with spatial resolutions in the nanometer scale. The SEM images of the invisibility cloaks are shown in Fig. 10.7a and b. In the experiment, light was confined along the vertical direction in the high dielectric layer of silicon, sandwiched between air and silicon dioxide. In Fig. 10.7a, the background region, which consists of a 2D array of holes with uniform density and diameter, serves as the uniform background medium. According to the requirement of the quasi-conformal mapping in the initially proposed carpet cloak [3], the refractive index profile is spatially inhomogeneous and therefore needs to be carefully engineered at each spatial point. This is enabled by an all-dielectric metamaterial design, where the density of the nanostructured holes controls the local effective index of the waveguide. As the design is based on a quasi-conformal mapping, no anisotropy is required. The cloaks have lateral dimensions on the order of tens of micrometers. The cloaked regions, which are marked by the curved bumps, have dimensions of a few micrometers. To minimize scattering of light by the holes, the spacing of the holes needed to be much less than the operating wavelength.

In the demonstration of an invisibility cloak by Valentine et al. light was coupled from free space to the waveguide mode by a grating coupler. Figure 10.8 shows the performance of the invisibility cloak at infrared wavelengths. Without the invisibility cloak (Fig. 10.8a), the incident beam was scattered by the bump into several spots when it reached the out-coupling gratings. This served as a

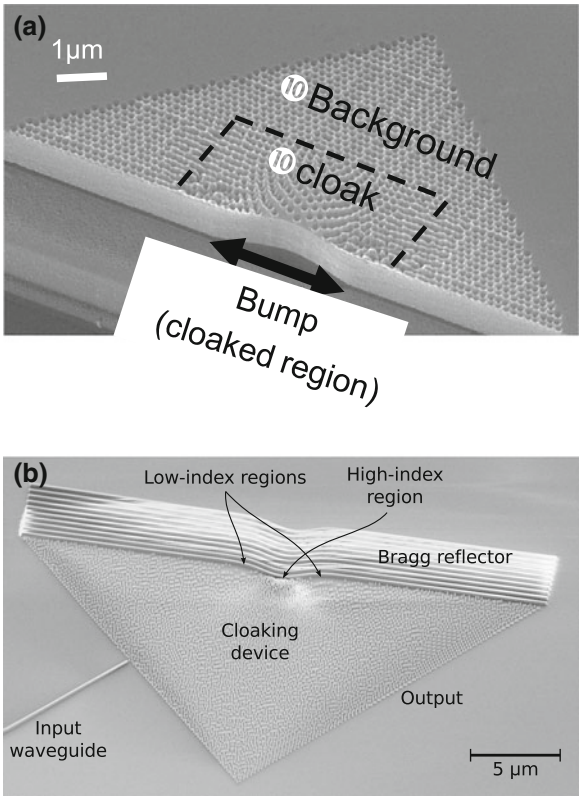

Fig. 10.7 Experimental demonstrations of carpet invisibility cloaks that operate at near-infrared frequencies. **a** A carpet invisibility cloak fabricated on a silicon-on-insulator wafer consisting of deep subwavelength sized holes with controlled densities. The cloak is fabricated using focused ion beam lithography. Courtesy from J. Valentine and adapted from [8]. **b** A carpet invisibility cloak nanofabricated by electron beam lithography. Courtesy from L. Gabrielli and adapted from [9]

control experiment to show that, despite the small size of the bump (comparable to the wavelength), the reflected beam was strongly disturbed. Remarkably, with the carpet cloak covering the bump, the reflected beam showed a single Gaussian beam profile, which verified that the bump was optically transformed into a flat ground plane by the nanofabricated carpet invisibility cloak.

As the cloaking material is made from nonresonant dielectric structures, the dispersion is significantly less than for metamaterials made from metallo-dielectric composites. Consequently, broadband operation of the dielectric invisibility cloak is observed for wavelengths in the range between 1,400 and 1,800 nm, where the beam profile at the location of the out-coupling grating exhibited patterns similar to a Gaussian profile. However, at shorter wavelengths, the effective medium theory breaks down as the wavelength of light inside the waveguide approaches the lattice size of the holes, and the refractive index of the structured surface is not well defined as nonlocal effects become significant.

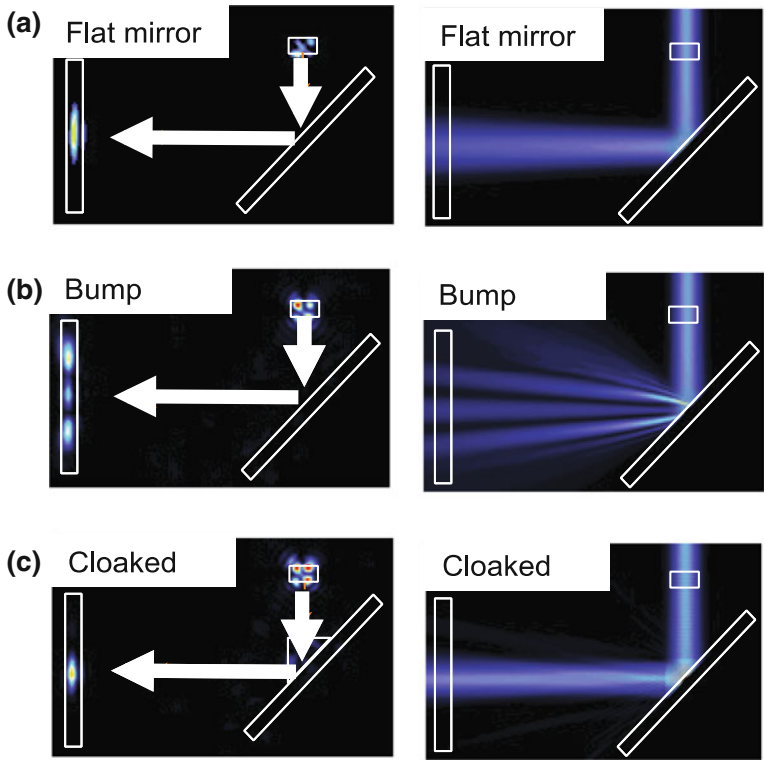

Fig. 10.8 Experimental demonstration of optical invisibility on a nanofabricated carpet invisibility cloak. The experimental results and simulations are shown in the *left* and *right columns*, respectively. **a** A control experimental configuration, where light was reflected by a flat mirror without scattering. **b** In the presence of a curved bump on the mirror surface, the incident light was strongly scattered. **c** With a nanostructured carpet invisibility cloak covering the bump, the scattering was eliminated, serving as evidence that the carpet cloak optically transformed the bump into a flat surface. Courtesy from J. Valentine and adapted from Valentine et al. [8]

10.3.4 Nanofabricated 3D Invisibility Cloaks

Extending the invisibility cloak from 2D waveguide configurations to three dimensions has practical significance as we live in a three dimensional world. At optical frequencies, this has been enabled by a three-dimensional (3D) nanofabrication technique—direct laser writing [35, 36]. The direct laser writing technique works by tightly focusing a laser beam into a space filled with photoresist. At the focused spot, the resin of the photoresist turns from liquid to solid. By continuously scanning the focused spot in the photoresist, 3D structures with a resolution in the scale of a few hundred nanometers can be formed. Direct laser writing has been employed recently to fabricate 3D metamaterials such as bianisotropic and chiral metamaterials operating at infrared frequencies [37, 38]. The

first 3D invisibility cloak was demonstrated in 2010 by Wegener et al. [11]. The structure consists of woodpile structure, a well-studied structure for 3D photonic crystals over the past decade [39, 40]. In the invisibility cloak demonstration, the wavelength of light is much larger than the lattice constant, therefore the effective medium theory can be applied. By controlling the filling ratio of polymer at each spatial location, the refractive index can be continuously tuned to match the desired spatial profile required for the carpet invisibility cloak. The cloaking effect was directly observed in reflection under a microscope by comparing the profiles of the beams reflected by a bump, with and without the invisibility cloak, under the microscope. Without the cloak, highly nonuniform intensity profiles are observed, due to the strong scattering of the gold bump. On the other hand, with the 3D cloak covering the bump, the scattering largely disappear, leaving an almost uniform intensity profile for the reflected beam.

10.4 Macroscopic Invisibility Cloaks for Visible Light

As most invisibility cloaks require inhomogeneous material properties, top–down nanofabrication techniques, such as electron beam lithography, focused ion beam lithography, and direct laser beam writing, have been primarily employed for the nanofabrication of invisibility cloaks at optical frequencies [8, 9, 11]. However, these techniques are time-consuming and have limited invisibility cloaks to hide objects in the scale of a few micrometers to tens of micrometers (comparable to the wavelengths of light). For practical applications, it is desirable to realize macroscopic invisibility cloaks that are capable of concealing objects with size much larger than the wavelength of light. A number of theoretical works have shown the possibility of realizing invisibility cloaks by using homogeneous, anisotropic materials [41, 42]. Inspired by these theoretical predictions, two groups have independently demonstrated macroscopic invisibility cloaks using a naturally birefringent crystal, calcite [13, 14]. These demonstrations mark a significant advancement in the field of optics, as it was the first time that objects that can be seen with naked eyes were made invisible. As the crystals are highly transparent, the invisibility effect is not obscured by the loss that is normally present in metamaterials.

10.4.1 Cloak Design and Characterization

The key to the homogeneous invisibility cloaks is a linear transformation between two polygonal spatial domains. A triangular invisibility cloak is the simplest implementation of this idea. A schematic showing the design of a triangular invisibility cloak is shown in Fig. 10.9. In the transformation, we mathematically map a virtual spatial domain with a triangular cross section of height H_2 filled with

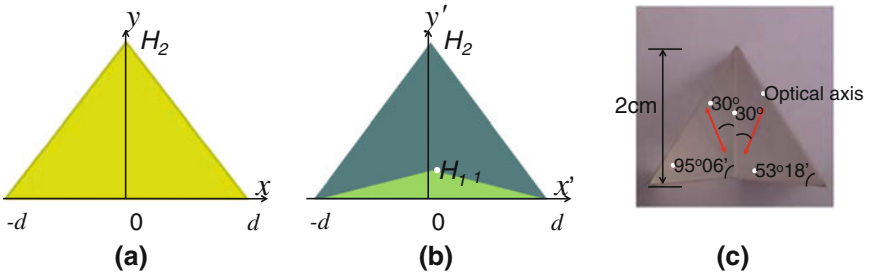

Fig. 10.9 Illustration of the optical transformation and cloaking design. In the transformation, a triangular cross section in a virtual space **a** filled with isotropic materials is mapped to a quadrilateral (*blue region* in **b**) with uniform and anisotropic optical properties. The cloaked region is defined by the *small green triangle*. **c** A photograph of the triangular cloak, which consists of two calcite prisms glued together, with the geometrical parameters indicated in the figure. Reprinted with permission from Chen et al.[13]

an isotropic material of permittivity ε and μ ($\mu = 1$) (Fig. 10.9a) to a quadrilateral region in the physical space with anisotropic electromagnetic properties ε' and μ' (blue region in Fig. 10.9b). The small green triangle of height H_1 and half-width d in Fig. 10.9b is excluded in the mapping, and consequently it represents the cloaked region where light cannot get access and objects can be made invisible. The transformation is mathematically expressed as:

$$x' = x,\ y' = \frac{H_2 - H_1}{H_2} y + \frac{d - x\mathrm{sgn}(x)}{d} H_1,\ z' = z \tag{10.14}$$

where (x', y', z') and (x, y, z) are the coordinates of the physical space and virtual space, respectively. The electromagnetic parameters of the invisibility cloak, derived through transformation optics, are given as:

$$\varepsilon' = \varepsilon \hat{M},\ \mu' = \hat{M} \tag{10.15}$$

with

$$\hat{M} = \begin{pmatrix} \frac{H_2}{H_2 - H_1} & -\frac{H_1 H_2}{(H_2 - H_1)d}\mathrm{sgn}(x) & 0 \\ -\frac{H_1 H_2}{(H_2 - H_1)d}\mathrm{sgn}(x) & \frac{H_2 - H_1}{H_2} + \frac{H_2}{H_2 - H_1}\left(\frac{H_1}{d}\right)^2 & 0 \\ 0 & 0 & \frac{H_2}{H_2 - H_1} \end{pmatrix}. \tag{10.16}$$

The electromagnetic parameters given by Eqs. 10.15 and 10.16 are homogeneous and anisotropic. This greatly simplifies the design of the carpet invisibility cloak. In order to further eliminate the requirement for magnetism, a nonmagnetic design for TM polarization that maintains the same light trajectory as the ideal invisibility cloak is given as

$$\varepsilon'_{x-y} = \varepsilon \begin{pmatrix} \left(\frac{H_2}{H_2-H_1}\right)^2 & -\frac{H_1 H_2^2}{(H_2-H_1)^2 d}\mathrm{sgn}(x) \\ -\frac{H_1 H_2^2}{(H_2-H_1)^2 d}\mathrm{sgn}(x) & 1+\left(\frac{H_2}{H_2-H_1}\right)^2\left(\frac{H_1}{d}\right)^2 \end{pmatrix} \tag{10.17}$$

$$\mu'_z = 1 \tag{10.18}$$

With the electromagnetic parameters described by Eqs. (10.17) and (10.18), it is obvious that homogeneous naturally birefringent crystals can be used for realizing the triangular carpet invisibility cloak. The geometrical parameters of the cloak, the optical axis orientation γ, and the permittivity of the virtual space, ε are related to each other by:

$$\frac{H_1}{d} = -\frac{(n_e^2 - n_0^2)\sin\gamma\cos\gamma}{n_0^2\cos^2\gamma + n_e^2\sin^2\gamma} \tag{10.19}$$

$$\frac{H_1}{H_2} = 1 - \frac{n_0 n_e}{n_0^2\cos^2\gamma + n_e^2\sin^2\gamma} \tag{10.20}$$

$$\varepsilon = \frac{n_0^2 n_e^2}{n_0^2\cos^2\gamma + n_e^2\sin^2\gamma} \tag{10.21}$$

In nature, there exist many crystals that exhibit birefringence at optical frequencies. Among them, calcite is a uniaxial crystal with significant birefringence, with refractive indices of ordinary (n_o) and extraordinary light (n_e) of approximately 1.66 and 1.49 at visible wavelengths.

The triangular invisibility cloak can be constructed by two pieces of calcite crystal prisms glued together with the protruding bottom surface serving as a deformed mirror, underneath which objects can be made invisible, as shown in Fig. 10.9c. The geometrical parameters of the calcite cloak are calculated using Eqs. 10.19–10.21. The cloaked triangular region is approximately 1.2 mm high, which is several orders of magnitude larger than the optical wavelengths. The refractive index of the virtual space is 1.532 according to Eq. 10.21, which is the refractive index of the background medium wherein the invisibility cloak can operate.

A ray tracing calculation is performed to check the performance of the calcite invisibility cloak, with results shown in Fig. 10.10. With the invisibility cloak, a beam of light with TM polarization incident onto the triangular cloak is reflected without distortion at two different incident angles (Fig. 10.10 a, b). On the other hand, for a beam with TE polarization, there is no cloaking effect, and therefore it serves as a control case to study the scattering of light by the bump in the absence of an invisibility cloak. As shown by Fig. 10.10c and d, a beam of TE polarization is split into two directions by the triangular protruding facets.

The performance of the calcite cloak is first characterized in air using a green laser at a 532 nm wavelength, as shown by Fig. 10.11a, left. In the experiment, a mask is placed in front of the laser head, such that the emitted laser beam exhibits

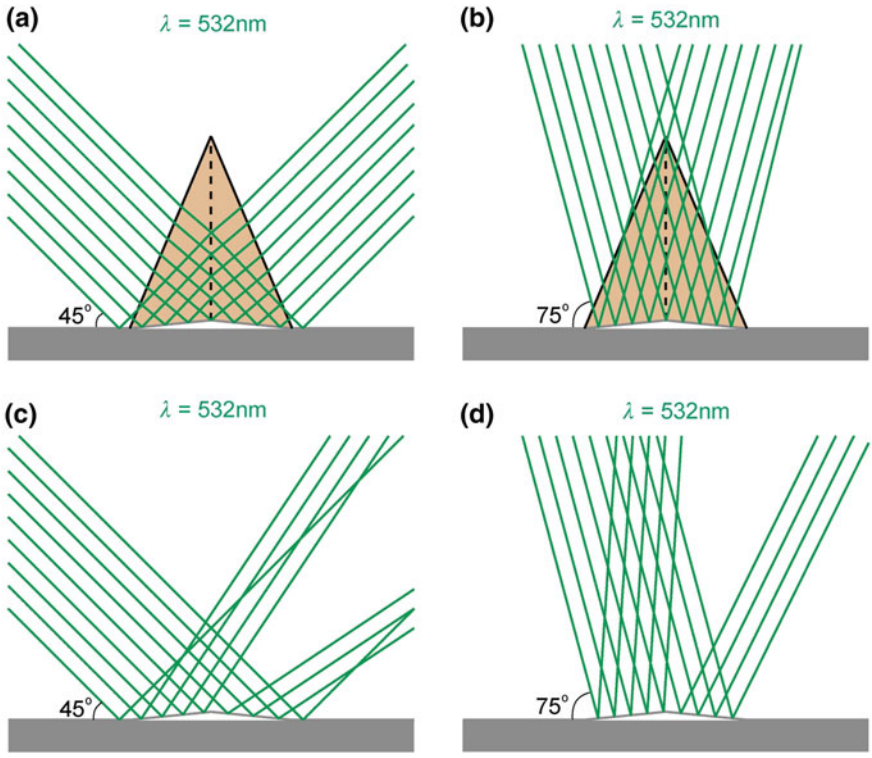

Fig. 10.10 Ray tracing calculation of light reflected by the triangular calcite cloak at 532 nm. **a**, **b** Light incident upon a cloaked bump at incident angles of **a** 45° and **b** 15°. **c**, **d** Without cloaking, the bump strongly scatters the light into different directions. Reprinted with permission from Chen et al. [13]

the pattern of an arrow (Fig. 10.11a, right). A linear polarizer is used to switch the polarization of the incident beam between TE and TM. The reflected beam is subsequently captured by a CCD camera. As a reference, the image of the laser beam reflected by the flat mirror is shown in Fig. 10.11b.

For the TE polarization, as there is no cloaking effect, the bottom surface of the cloak splits the incident laser beam into two beams. The beam splitting is experimentally observed as shown in Fig. 10.11c. The angle between the two reflected beams is over 30°, which is consistent with the ray tracing calculation. For the TM polarization, the reflected beam shows no distortion at all (Fig. 10.11d), in contrast to the case with TE polarization. The invisibility cloaking effect is observed at different incident angles, as shown in Fig. 10.11e–g. In the figures, the central image corresponds to the TM polarization and the two projected arrow segments away from the center of the image correspond to the TE polarization. The calcite cloak is also characterized for red light with wavelengths ranging from 630 to 680 nm with a spectral peak at $\lambda = 650$ nm. The invisibility

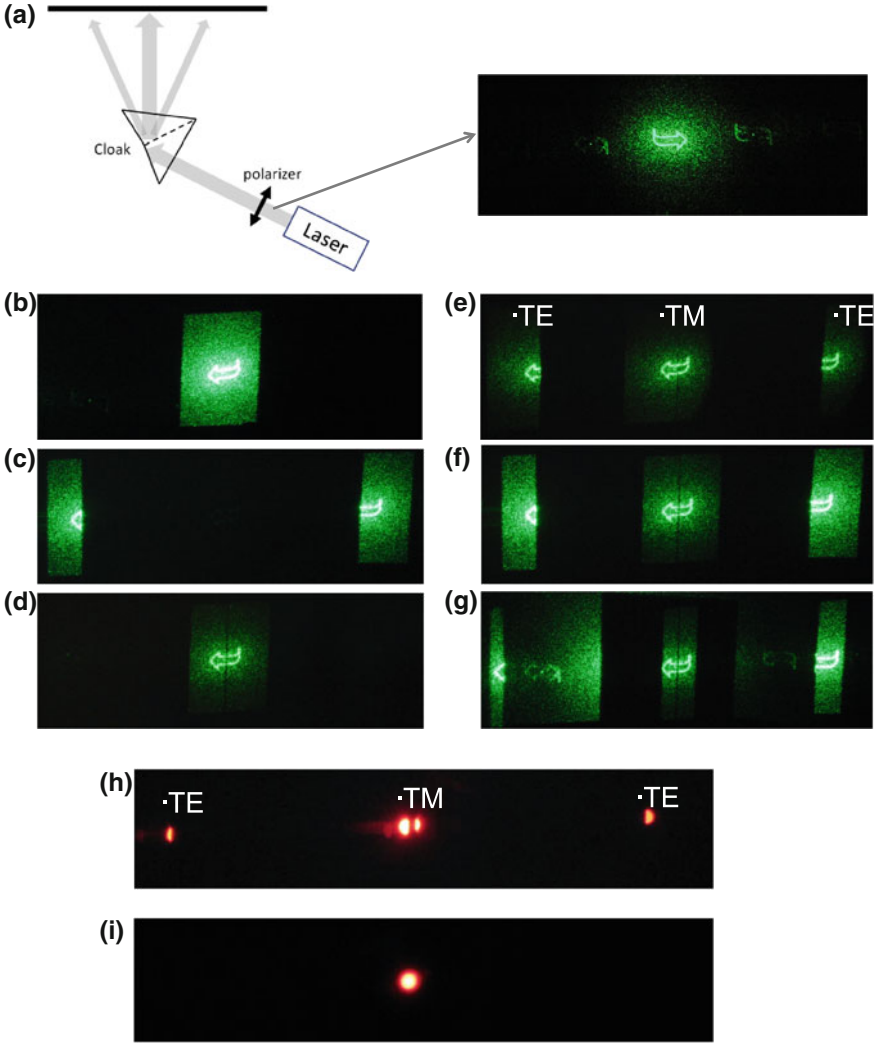

Fig. 10.11 Optical characterization of the cloak using *green* and *red* laser beams. **a** (*left*) Schematic of the experimental setup. (*right*) The original pattern of the laser beam. **b** The pattern of the laser beam as reflected by a flat surface. **c**, **d**. The projected image of the laser beam reflected by the calcite cloak for the TE and TM polarizations, respectively **e**, **f**, **g** the projected images for mixed TE and TM polarizations at incidence angles of 39.5°, 64.5°, and 88°, respectively. **h**, **i**. The photographs of a *red* laser beam with mixed TE and TM polarizations projected on the screen after being reflected by **h** calcite cloak and **i** a flat surface, respectively, at an incident angle of 64.5°. Reprinted with permission from Chen et al. [13]

cloak performs reasonably well at these wavelengths, as shown in Fig. 10.11h. It should be noted that a small gap appears in the central image (TM polarization) due to the optical dispersion of the calcite crystal.

To show broadband operation, the calcite cloak is further characterized by imaging the reflection of white-color alphabet letters by the cloak system, with results shown in Fig. 10.12. A schematic of the measurement is shown in Fig. 10.12a. Light with the TE polarization (Fig. 10.12b) undergoes a large splitting caused by the mirror deformation, as a result, the reflected image consists of letters from two largely separated locations ('C', 'D', 'R' to 'U'). In contrast, light with the TM polarization exhibits almost perfect reflection as evidenced by the imaging of five consecutive letters (from 'H' to 'L') from the same location (Fig. 10.12c). Only a slight rainbow effect can be observed at the edge of the letters arising from the dispersion of the calcite crystal. The experiment with white color objects unambiguously demonstrates the broadband operation of the calcite invisibility cloak.

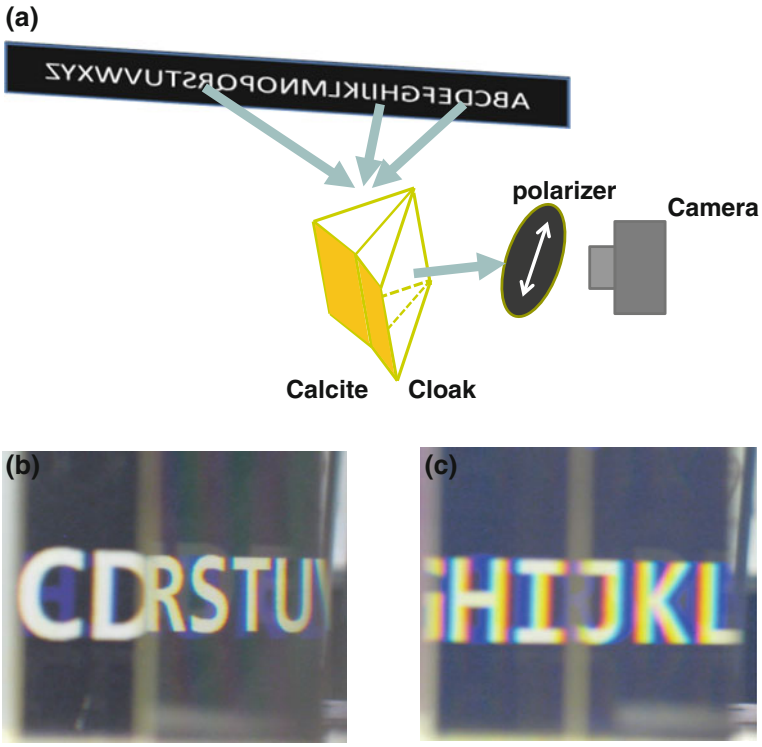

Fig. 10.12 Reflection of white alphabet letters by the cloak. **a** Schematic of the optical setup. **b**, **c** The reflected images captured by the camera for the TE and TM polarizations, respectively. Note that a rainbow appears at the edge of each letter for the TM polarization due to the optical dispersion of the calcite crystal. Reprinted with permission from [13]

10.4.2 Operation of a Macroscopic Invisibility Cloak in Liquid

The triangular invisibility cloak made from calcite crystals can optically transform a protruding reflective surface into a flat one and thus render any object underneath the protruding surface invisible. However, in air, the cloak itself is clearly visible as the cloak is designed for a specific background refractive index given by Eq. 10.21, which is greater than 1. Thus, in order to make the calcite cloak invisible, it needs to be immersed in a liquid with the same refractive index as that of the virtual space in the optical transformation.

The experimental setup for the demonstration of an invisibility cloak immersed in liquid is shown in Fig. 10.13a. The liquid is an index matching fluid, whose refractive index can be adjusted by controlling the temperature to match the invisibility cloaking condition. The calcite cloak is placed on top of a flat mirror. A black sheet of paper with white colored printed text of horizontally flipped "University of Birmingham" and "Imperial College of London" was held above the liquid surface. A camera was used to capture the reflected image of the text. As

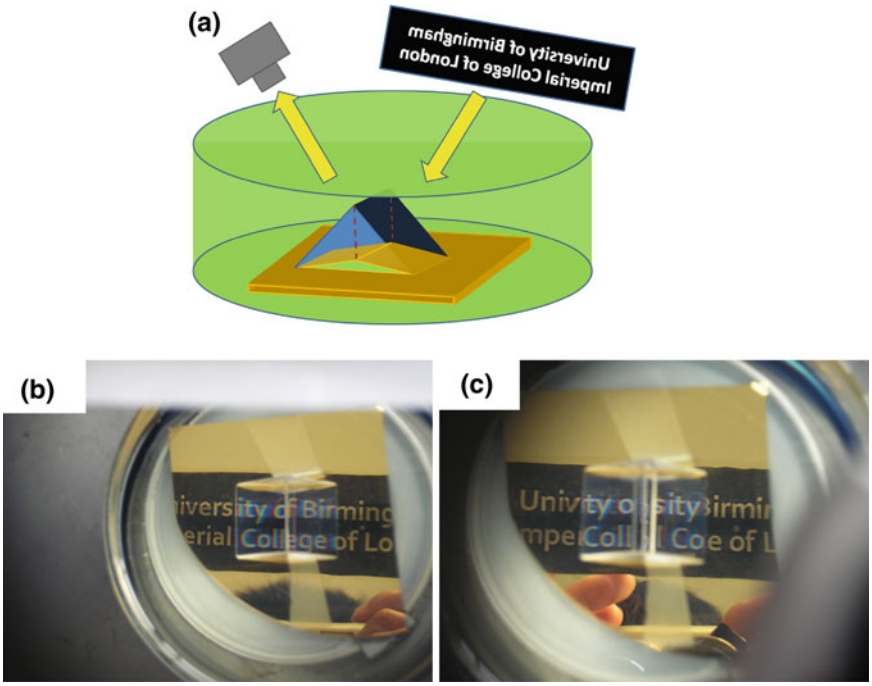

Fig. 10.13 **a** The experimental setup for the invisibility cloak demonstration immersed in an index matching liquid. The cloaking effect is observed by looking at the reflection of a printed paper through the carpet cloak. **b** For the TM polarization, the reflection shows an undistorted image. **c** For the TE polarization, as there is no cloaking effect, the image is distorted

shown by Fig. 10.13b and c, part of the image is reflected through the calcite crystals and the rest is directly reflected by the flat mirror. For the TM polarization, the reflection through the calcite cloak fits nicely with the rest of the image that is directly reflected by the mirror. This indicates that the calcite cloak not only transforms the bottom protruding surface into a flat one, but also preserves the position of the reflected beam relative to that reflected by the flat mirror. On the other hand, with the TE polarization which does not experience the cloaking effect, the bottom bulging surface scatters light and scrambles the sequence of the letters.

In the calcite invisibility cloak, the light transmits through three interfaces, the surrounding medium/calcite, the interface between the two calcite crystals with different crystal orientations, and the calcite/surrounding medium. Interestingly, no reflection exists at the interface between the two constituent calcite crystals despite their crystal orientations being different. This is consistent with a previous study that shows that, for two contacting anisotropic crystals with their optical axes symmetric about the interface, there is no reflection at the interface regardless of the direction of light [43]. On the other hand, because we have adopted a simplified form of cloaking design which eliminates the requirement of magnetism, a small impedance mismatch is introduced between the surrounding optical medium and the cloak, which results in a small amount of reflection at their interface. Nonetheless, this reflection can be eliminated if the interface is nanostructured in such a way that the permittivity undergoes an adiabatic transition from the calcite crystal and the surrounding medium, and the cloak itself would become completely invisible.

10.4.3 Compact Homogeneous Invisibility Cloak

One main issue that hinders practical applications of invisibility cloaks is the large size of the cloak relative to the object to be hidden. In most of the demonstrations of carpet invisibility cloaks [8, 9, 11, 13, 14], the ratio between the size of the cloak and the size of the cloaked region is above 20. Let us take the triangular invisibility cloak as an example. Starting from Eq. (10.20), it can be shown that the ratio between the cloaked region and the overall size of the cloak in a triangular invisibility cloak has an upper limit of,

$$\left(\frac{H_1}{H_2}\right)_{\max} = 1 - \frac{\min(n_e, n_o)}{\max(n_e, n_o)} \equiv \frac{\Delta n}{\max(n_e, n_o)} \tag{10.22}$$

The ratio is limited by the small birefringence of natural crystals—the relative difference between n_e and n_o is in the order of 10 %, indicating that the cloaked region has to be at least 10 times smaller than the invisibility cloak. With metamaterials, it is possible to achieve a significantly stronger birefringence. One example is a 1D dielectric grating, as shown in Fig. 10.14. For a grating period

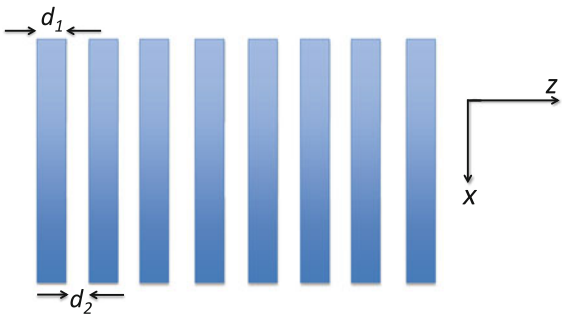

Fig. 10.14 Schematic of a composite material consisting of a periodic arrangement of two different materials with widths of d1 and d2, respectively

much less than the wavelength of light, the grating is effectively an anisotropic material with the permittivity tensor given as,

$$\begin{aligned} \varepsilon_x = \varepsilon_y &= p\varepsilon_1 + (1-p)\varepsilon_2 \\ \frac{1}{\varepsilon_z} &= \frac{p}{\varepsilon_1} + \frac{(1-p)}{\varepsilon_2} \end{aligned} \tag{10.23}$$

where ε_1 and ε_2 are the permittivities of medium 1 and 2, respectively, and $p = d_1/(d_1 + d_2)$ is the filling ratio of medium 1 in the grating. It is straightforward to show that the anisotropy, defined as the ratio between the dielectric tensor elements along the z and the $x(y)$ direction, is given by

$$A = p^2 + (1-p)^2 + p(1-p)\left(\frac{\varepsilon_1}{\varepsilon_2} + \frac{\varepsilon_2}{\varepsilon_1}\right) \equiv p(1-p)\left(\frac{\varepsilon_1}{\varepsilon_2} + \frac{\varepsilon_2}{\varepsilon_1} - 2\right) \tag{10.24}$$

The maximum anisotropy, which occurs at $p = 0.5$, is given as,

$$A_{\max} = \frac{\frac{\varepsilon_1}{\varepsilon_2} + \frac{\varepsilon_2}{\varepsilon_1} - 2}{4} \tag{10.25}$$

The corresponding ordinary and extraordinary refractive indices are given by,

$$n_o = \sqrt{\frac{\varepsilon_1 + \varepsilon_2}{2}}, \quad n_e = \sqrt{\frac{2\varepsilon_1\varepsilon_2}{\varepsilon_1 + \varepsilon_2}} \tag{10.25}$$

Equation (10.25) shows that a large anisotropy can be obtained by forming a grating using two materials with a large contrast in their permittivities. At infrared frequencies, semiconductors, such as silicon and GaAs, have very large dielectric constants over 10. Take silicon as an example, the dielectric constant at near-infrared frequencies is around 11.9. The maximum anisotropy of a grating made from silicon and air is around 2.5, and the ordinary and extraordinary indices are 2.54 and 1.36 respectively, corresponding to a maximum ratio of 0.46 (or roughly 1:2) between the cloaked region and the cloak.

A carpet invisibility cloak made from uniform silicon gratings was experimentally demonstrated by Zhang et al. [17]. Similar to several previous works [8, 9], the experiment was carried out in a 2D configuration on a SOI wafer. The

silicon carpet cloak was fabricated by electron-beam lithography and reactive ion etching processes on an SOI wafer. Light is confined in the vertical direction due to the low indices of air and silicon dioxide on the two sides of the 250 nm silicon layer. Figure 10.15b shows an SEM image of the cloaking device. The bottom width and height of the triangular silicon cloak are 10 and 8 μm, respectively. The triangular region where objects can be concealed has a bottom width of 10 μm and a height of 1.84 μm. The incident beam is guided by a tapered input waveguide towards the cloak. The output beam is coupled to free space propagation by a grating coupler, and its image is captured by an infrared camera. The schematic and SEM images of the silicon invisibility cloak are given in Fig. 10.15. The pitch of the silicon gratings is 140 nm, and the filling factor of silicon is 0.5. Importantly, the ratio between the cloaked region and the cloak is about 1:4, significantly larger than all the previous experimental demonstrations of invisibility cloaks.

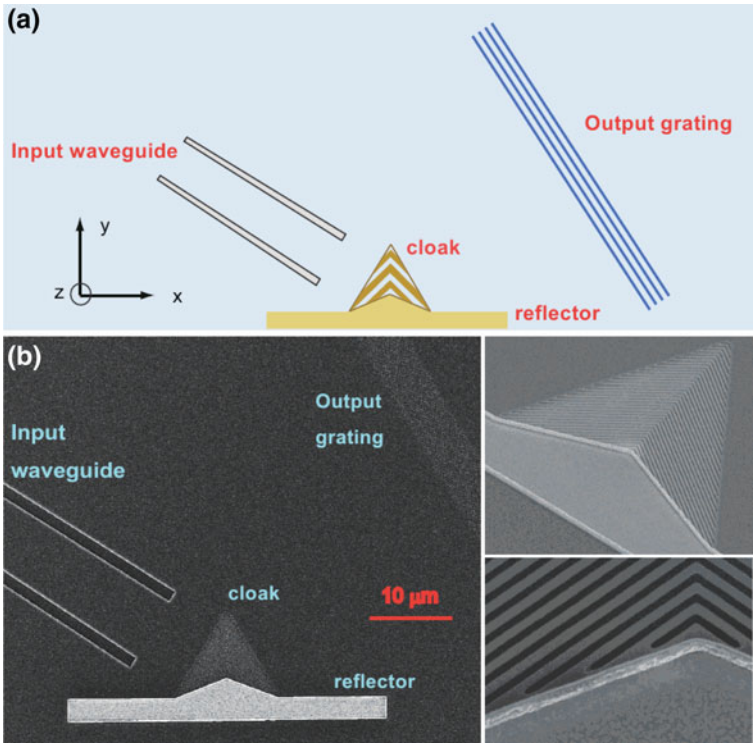

Fig. 10.15 Experimental realization of a compact invisibility cloak made from uniform silicon gratings. **a** Schematic of the carpet cloak made of a silicon grating and the experimental configuration. Light is incident onto the cloak through the input waveguide and reflected by the gold mirror at the *bottom* of the silicon cloak. The reflected beam is converted to free space propagation by the out-coupling grating. **b**. SEM image of a nanofabricated carpet cloak. The *insets* show the zoomed view of the silicon carpet cloak. Reprinted with permission from Zhang et al.[17]

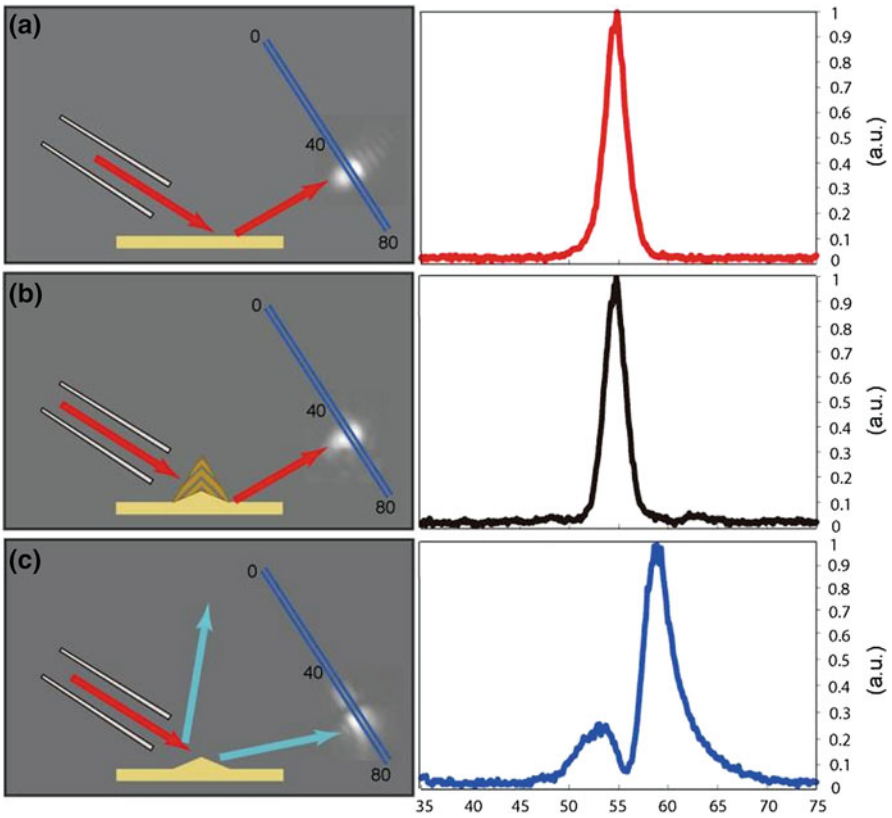

Fig. 10.16 Experimental characterization of the silicon invisibility cloak. Experimental results for a Gaussian beam reflected from a flat surface (**a**), a triangular surface (**b**), and the same triangular surface covered by a silicon carpet cloak. The *left column* shows the intensity of the beam at the output grating coupler. The *right column* shows the plot of intensity along the output grating at 1,500 nm. Reprinted with permission from Zhang et al. [17]

In the measurement, light with the TM polarization from a tunable laser (1,480–1,580 nm) was used to characterize the performance of the silicon invisibility cloak. Figure 10.16 shows the measured scattering of light by a triangular bump, with and without the silicon carpet cloak. With the cloak, the triangular bump scatters light into a single Gaussian spot at the output grating, which is almost identical to that reflected by a flat mirror in Fig. 10.16a. While without the silicon cloak, the triangular bump split the light into two peaks at the output grating. The measurement shows the superior performance of the compact carpet invisibility cloak.

References

1. Pendry JB, Schurig D, Smith DR (2006) Controlling electromagnetic fields. Science 312:1780–1782
2. Leonhardt U (2006) Optical conformal mapping. Science 312:1777–1780
3. Li J, Pendry JB (2008) Hiding under the carpet: a new strategy for cloaking. Phys Rev Lett 101:203901
4. Schurig D et al (2006) Metamaterial electromagnetic cloak at microwave frequencies. Science 314:977–980
5. Liu R et al (2009) Broadband ground-plane cloak. Science 323:366–369
6. Tretyakov S, Alitalo P, Luukkonen O, Simovski C (2009) Broadband electromagnetic cloaking of long cylindrical objects. Phys Rev Lett 103:103905
7. Edwards B, Alu A, Silveirinha MG, Engheta N (2009) Experimental verification of plasmonic cloaking at microwave frequencies with metamaterials. Phys Rev Lett 103:153901
8. Valentine J, Li J, Zentgraf T, Bartal G, Zhang X (2009) An optical cloak made of dielectrics. Nat Mater 8:568–571
9. Gabrielli LH, Cardenas J, Poitras CB, Lipson M (2009) Silicon nanostructure cloak operating at optical frequencies. Nat Photon 3:461–463
10. Smolyaninov II, Smolyaninova VN, Kildishev AV, Shalaev VM (2009) Anisotropic metamaterials emulated by tapered waveguides: application to optical cloaking. Phys Rev Lett 102:213901
11. Ergin T, Stenger N, Brenner P, Pendry JB, Wegener M (2010) Three dimensional invisibility cloak at optical wavelengths. Science 328:337–339
12. Ma HF, Cui TJ (2010) Three-dimensional broadband ground-plane cloak made of metamaterials. Nat Comm 1:21
13. Chen XZ, Luo Y, Zhang JJ, Jiang K, Pendry JB, Zhang S (2011) Macroscopic invisibility cloaking of visible light. Nat Comm 2:176
14. Zhang B, Luo Y, Liu X, Barbastathis G (2001) Macroscopic invisibility cloak for visible light. Phys Rev Lett 106:033901
15. Ergin T, Fischer J, Wegener M (2011) Optical phase cloaking of 700 nm light waves in the far field by a three-dimensional carpet cloak. Phys Rev Lett 107:173901
16. Gharghi M et al (2011) A carpet cloak for visible light. Nano Lett 11:2825–2828
17. Zhang J, Liu L, Luo Y, Zhang S, Mortensen NA (2011) Homogeneous optical cloak constructed with uniform layered structures. Opt Exp 19:8625–8631
18. Zhou F, Bao Y, Cao W, Stuart CT, Gu J, Zhang W, Sun C (2011) Hiding a realistic object using a broadband terahertz invisibility cloak. Sci Rep 1:78
19. Chen H, Zheng B (2011) Broadband polygonal invisibility cloak for visible light. Sci Rep 2:255
20. Tachi S (2003) Telexistence and retro-reflective projection technology (RPT). Proceedings of the 5th Virtual reality international conference, 69/1–69/9, Lava Virtual 2003, France
21. Rahm M, Roberts DA, Pendry JB, Smith DR (2008) Transformation-optical design of adaptive beam bends and beam expanders. Opt Exp 16:11555–11567
22. Zentgraf T, Valentine J, Tapia N, Li J, Zhang X (2010) An Optical "Janus" device for integrated photonics. Adv Mat 22:2561
23. Cai W, Chettiar UK, Kildishev AV, Shalaev VM (2007) Optical cloaking with metamaterials. Nat Photon 1:224–227
24. Pendry JB et al (1999) Magnetism from conductors and enhanced nonlinear phenomena. IEEE Trans Microwave Theory Tech 47:2075–2084
25. Smith DR et al (2000) Composite medium with simultaneously negative permeability and permittivity. Phys Rev Lett 84:4184–4187
26. Shelby RA, Smith DR, Schultz S (2001) Experimental verification of a negative index of refraction. Science 292:77–79

27. Yen TJ et al (2004) Terahertz magnetic response from artificial materials. Science 303:1494–1496
28. Zhang S et al (2005) Midinfrared resonant magnetic nanostructures exhibiting a negative permeability. Phys Rev Lett 94:037402
29. Linden S et al (2004) Magnetic response of metamaterials at 100 terahertz. Science 306:1351–1353
30. Enkrich C et al (2005) Magnetic metamaterials at telecommunication and visible frequencies. Phys Rev Lett 95:203901
31. Ishikawa A, Tanaka T, Kawata S (2005) Negative magnetic permeability in the visible light region. Phys Rev Lett 95:237401
32. Zhou J, Koschny T, Kafesaki M, Economou EN, Pendry JB, Soukoulis CM (2005) Saturation of the magnetic response of split-ring resonators at optical frequencies. Phys Rev Lett 95:223902
33. Cai W, Chettiar UK, Kildishev AV, Milton GW, Shalaev VM (2007) Nonmagnetic cloak with minimized scattering. Appl Phys Lett 91:111105
34. Knupp P, Steinberg S (1994) Fundamentals of grid generation. CRC Press, Boca Raton
35. Kawata S, Sun HB, Tanaka T, Takada K (2001) Finer features for functional microdevices. Nature 412:697–698
36. Deubel M et al (2004) Direct laser writing of three-dimensional photonic-crystal templates for telecommunications. Nat Mater 3:444–447
37. Rill MS, Plet C, Thiel M, Staude I, Freymann GV, Linden S, Wegener M (2008) Photonic metamaterials by direct laser writing and silver chemical vapour deposition. Nat Mat 7:543–546
38. Gansel JK et al (2009) Gold helix photonic metamaterial as broadband circular polarizer. Science 325:1513–1515
39. Ogawa SP et al (2004) Control of light emission by 3D photonic crystals. Science 305:227–229
40. Takahashi S et al (2009) Direct creation of three-dimensional photonic crystals by a top–down approach. Nat Mater 8:721–725
41. Luo Y, Zhang JJ, Chen HS, Ran LX, Wu BI, Kong JA (2009) A rigorous analysis of plane-transformed invisibility cloaks. IEE Trans Antenn Propag 57:3926–3933
42. Xi S, Chen H, Wu BI, Kong JA (2009) One directional perfect cloak created with homogeneous material. IEEE Microw. Wirel Compon Lett 19:131–133
43. Zhang Y, Fluegel B, Mascarenhas A (2005) Total negative refraction in real crystals for ballistic electrons and light. Phys Rev Lett 91:157404

Chapter 11
Experimental Characterization of Electromagnetic Cloaking Devices at Microwaves

Pekka Alitalo and Sergei A. Tretyakov

Abstract Electromagnetic cloaking has attracted much interest in recent years. In this chapter, we will describe experimental methods that can be applied to the analysis of electromagnetic cloaks in the microwave regime. Each method is explained and accompanied with real-life examples. At the end of the chapter, we also discuss experimental techniques for characterization of individual small particles ("artificial molecules") which are useful in the design of various cloaks or low-scattering objects.

11.1 Introduction

In this chapter, we will give an overview of experimental demonstrations and characterization methods that can be readily applied to most of the known realizable electromagnetic cloaking devices in the microwave frequency range. We begin by introducing the concept of "electromagnetic cloaking", defining it by a general physical criterion in terms of the scattered electric and/or magnetic fields in the far-zone of the scatterer. In the rest of this chapter, we will describe experimental methods that can be used to either *demonstrate* the cloaking phenomenon or *characterize* the cloaking efficiency. By *demonstration* we mean an experimental illustration of the cloaking effect. This does not necessarily yield a well-defined numerical value that would measure the cloaking quality. By *characterization* we mean a direct or indirect measurement of the total scattering cross

P. Alitalo · S. A. Tretyakov (✉)
Department of Radio Science and Engineering/SMARAD Centre of Excellence,
Aalto University, P.O. Box 13000 00076 Aalto, Finland
e-mail: sergei.tretyakov@aalto.fi

P. Alitalo
e-mail: pekka.alitalo@aalto.fi

D. H. Werner and D.-H. Kwon (eds.), *Transformation Electromagnetics and Metamaterials*, DOI: 10.1007/978-1-4471-4996-5_11,

section or width. A typical example of the former case is the measurement of the near-field distribution inside and/or outside the cloaked object. This allows illustration of the cloaking effect without giving an exact value to characterize the quality of the scattering reduction.

The rest of this chapter is organized as follows: In Sect. 11.2 we discuss at a very general level what is meant by electromagnetic cloaking and briefly review some of the important practical techniques to achieve it. Section 11.3 gives mathematical descriptions of various definitions that can be used to characterize the cloaking effect, such as the total scattering cross section and width. The rest of the sections present experimental and numerical results for various microwave cloaking devices, so that each section considers one type of measurement setup. Section 11.4 deals with the parallel-plate waveguide and Sect. 11.5 with rectangular waveguide measurements. Sections 11.6 and 11.7 consider free-space measurements: Section 11.6 concentrates on bistatic scattering measurements in free space and Sect. 11.7 focuses on the demonstration of the cloaking effect by antenna radiation pattern measurements. Section 11.8 discusses measurements of polarizabilities of small particles. Such measurements may be essential in the design and fabrication of individual resonating particles (artificial "molecules") that make up a cloaking device or in the design of stand-alone low-scattering ("invisible") particles.

11.2 Electromagnetic Cloaking

The concepts of "electromagnetic cloaking" and "invisibility" of objects have recently attracted much interest from the scientific community. In this context, cloaking refers to a *significant reduction of the total power scattered by this object*. In other words, a cloaking device can reduce the effective scattering cross section of an arbitrary or a specific object not only in one direction but in all directions where scattering occurs. For example, cloaking can be achieved by placing an object inside a "cloaking" device. The "cloak" prevents the incident field from interacting with the object inside. The possibility of making scattering objects undetectable to probing electromagnetic fields may have countless applications in the areas of radar, measurement, and telecommunication technologies. With the emergence of the metamaterial concept, practical realizations of cloaking devices have appeared and the interest in cloaking technologies is on the rise.

The majority of the work related to electromagnetic cloaking and invisibility are based on different types of field transformations [1, 2]. Although transformation designs and their realizations may vary quite significantly, we will refer to all these designs simply as "transformation-electromagnetic cloaks". The basic idea in these works is to make the impinging electromagnetic wave go around a scattering object, so that in the ideal case the total scattering cross section of the cloaked object approaches zero. To achieve this, the space around the scattering object is transformed. Thus, the rays of electromagnetic waves travel through the

cloak on a straight line in electromagnetic space, but on a curved line (around the object that is hidden) in physical space. Several transformations along with approximations and simplifications have been studied during recent years, e.g., [3–15]. Simplifications of these transformations have allowed for practical realization. In most suggested practical realizations of this type of cloaking, the material comprising the cloak is anisotropic and the material parameters depend on the radial position within the cloak. Such material parameters are extremely difficult to realize in practice, especially within wide frequency bands.

Another approach to scattering reduction of arbitrary or specific objects is the so-called scattering cancellation or plasmonic cloaking [16–18]. This technique employs a material cover in which the induced dipole moments have the sign opposite to the dipole moments induced in the object to be cloaked. As a whole this system can be designed so that the total induced dipole moment is close to zero. The benefit of the technique is that cloaking of dielectric objects can be achieved with relatively simple materials, and these materials can be isotropic. This approach has been widely studied with most efforts concentrated on device operation in the optical regime and efforts focused on various sensor applications [19–25]. The main drawbacks of this technique are that the suppression of only the dipolar scattering makes the cloaking of electrically large scatterers difficult (higher-order modes become significant and their scattering should be compensated as well) and that cloaking of impenetrable objects (such as conducting ones) requires materials that are difficult to realize.

In 2008, the so-called "transmission-line cloaking" was introduced as an alternative to the previous two cloaking techniques to allow cloaking without the need to realize any exotic material parameters [26–28]. As the electromagnetic wave is allowed to travel through the cloaked object, an efficient and broadband cloaking effect is easier to realize, as compared to, e.g., the two previous methods. However, the range of objects/geometries that can be cloaked is very limited, since the transmission-line network must be placed inside the object that is being cloaked [28]. Essentially, what can be cloaked are arrays of separate particles or three-dimensional mesh-like structures [28].

Since the transmission-line cloak cannot be used to hide a bulky object such as a metal sphere or cylinder of moderate electrical size, another waveguiding cloak was introduced in 2009. This "metal-plate cloak" uses conical conducting surfaces to guide the electromagnetic wave around a cloaked region [29]. Although in this case the wave must go around the cloaked object, this technique should not be confused with the transformation-electromagnetics cloak: The metal-plate cloak does not employ anisotropic materials which are generally required in the transformation-electromagnetics concept; instead, the conical plates form a waveguide which allows the wave to travel through the cloak with very small reflections. Due to the waveguiding nature of the structure, it is not expected to work well when hiding electrically large objects: In [30] it was shown that increasing the diameter of the cloaked conducting cylinder to about one wavelength is possible, but the cloaking efficiency drops as the object is made electrically larger. Of course, in theory, the transformation-electromagnetics cloak can be designed to

hide an object of any electrical size. It is important to note that there are cloaks of similar shape like the metal-plate cloak, but their design is based on the transformation-electromagnetics approach and they operate for the orthogonal polarization [31].

Even in addition to all the previous techniques, there exist several other approaches or techniques that can be called or at least related to the concept of "electromagnetic cloaking" [32–35]. Here we do not go into specifics of all these cloaking techniques. Instead the reader is encouraged to revert to recent review papers on the topic [17, 27, 28, 36, 37].

11.3 Characterization of Scattering

The intensity of waves scattered by an object determines the "visibility" of this object when it is being detected by the use of electromagnetic waves. The most commonly used measure to characterize the scattering intensity in a specific direction is the scattering cross section of the object. The scattering cross section σ tells us how strongly the object scatters electromagnetic waves into a certain direction in the far-zone if it is excited by a given incident field. The definition of σ in the frequency domain for a finite-size scatterer reads

$$\sigma = \lim_{R\to\infty} 4\pi R^2 \frac{|\overline{E}_{\rm sca}|^2}{|\overline{E}_{\rm inc}|^2} = \lim_{R\to\infty} 4\pi R^2 \frac{|\overline{H}_{\rm sca}|^2}{|\overline{H}_{\rm inc}|^2}, \tag{11.1}$$

where R is the distance from the object to the observation point. The scattered electric and magnetic fields $\overline{E}_{sca}$ and $\overline{H}_{sca}$ are calculated or measured at distance R from the object, and $\overline{E}_{inc}$ and $\overline{H}_{inc}$ are the incident fields at the position of the object. The scattering cross section is determined by the electromagnetic properties of the object at the test frequency, the direction from which the object is illuminated, the scattering direction, and by the properties of the incident wave (e.g., polarization). The *radar cross section* (or *RCS*, or *back-scattering cross section*, or *monostatic cross section*) is a special case of this parameter for the situation when the scattered fields are calculated or measured in the direction from where the incident wave comes.

From (11.1) we can see that if the scattering cross section is zero, the scattered fields in the far zone are zero, and the presence of the object cannot be detected if the observer is located in that specific direction. In stealth applications, minimization of the radar cross section is usually the goal, but in order to hide an object *shape completely*, the scattering in all directions should be minimized. Thus, a more appropriate scattering parameter in case of cloaking is the *total scattering cross section*, defined as

$$\sigma_{\rm tot} = \frac{1}{4\pi}\int \sigma \, d\Omega = \frac{P_{\rm sca}}{w_{\rm inc}}, \tag{11.2}$$

where the integration of σ is performed over the whole solid angle around the scatterer. P_{sca} is the total scattered power and w_{inc} is the intensity of the incident wave (the magnitude of the Poynting vector of the incident wave) at the position of the object.

In the case of infinite cylindrical objects, instead of using the scattering cross section, we can use the scattering width σ_W, which refers to the scattering cross section per unit length of the cylinder. This parameter is defined as

$$\sigma_W = \lim_{\rho \to \infty} 2\pi\rho \frac{|\overline{E}_{\text{sca}}|^2}{|\overline{E}_{\text{inc}}|^2}, \tag{11.3}$$

where ρ and ϕ are the polar coordinates with the origin inside the scattering cylinder (cylinder cross section does not have to be circular). The corresponding parameter describing the total scattering is the total scattering width, defined as

$$\sigma_{W tot} = \frac{1}{2\pi} \int_0^{2\pi} \sigma_W \, d\phi. \tag{11.4}$$

Electromagnetic cloaking is defined in general as *significant reduction of the total scattering cross section* of an object, or in the case of an electrically tall object excited by a normally incident plane wave, it is defined as *significant reduction of the total scattering width* of an object. If the total scattering cross section or width is zero, this means that the total power scattered by the object in the far zone is zero, and in this sense, the object is truly "invisible". If the total scattering cross section is equal to zero, this implies that the scattered field amplitude is zero *in any direction*. In particular, cloaked objects create no shadows because the scattered field is zero behind the objects. Thus, the total field there is equal to the incident field. From the forward-scattering theorem (see, e.g., [50]), we can conclude that perfectly cloaked objects (together with their respective cloaks) do not absorb any power—they are lossless structures. However, in the adopted definition, cloaked objects (or cloaks themselves) can be in principle detected in the near-field zone of the object because the definition in terms of the scattering cross section contains measure of only far-zone fields.

From the characterization point of view, estimation of cloak performance requires effective computation or accurate measurement of the total scattering cross section (or width) of the structure. A practical figure of merit for the cloak operation is the normalized total scattering cross section or width, where the reference object is the "bare" object without the cloak. In addition, one can analyze the distribution of the total fields in the presence and absence of the cloak which helps in visualizing the cloak performance.

In general, cloaking devices are designed in such a way that they aim to make an illusion that the cloak itself, as well as the volume inside the cloak, is simply free space (or whatever is the background medium). If this is achieved, the cloak and the object it tries to hide will have a very small total scattering cross section

(or width). If this value is then normalized to the total scattering cross section of the bare, uncloaked object, the normalized total scattering cross section will approach zero. However, from (11.1) to (11.4) we see that the total scattering cross section or width is always defined only for a certain incident field. This means that for a specific incident wave type (plane wave, cylindrical wave, etc.) and for a specific polarization (horizontal or vertical linear polarization, circular polarization, etc.) the cloak produces a very small normalized total scattering cross section or width. It may behave very differently in the case of another incident wave. Usually, the type of wave is not so important, but the polarization is important. In fact, all of the experimental cloaks considered in this chapter essentially work for only a single linear polarization. Therefore, the limitations of specific designs should always be kept in mind when considering possible real-life applications of cloaks.

It is very important to have a consistent way of expressing the polarization of the wave incident on the studied scatterer. In literature the definitions vary: Some authors prefer to express the polarization with respect to the surface of the scatterer (transverse electric—TE and transverse magnetic—TM, these are convenient in the study of cylindrical objects illuminated normally, as the scattering problem is two-dimensional). Some authors use the more general expression which is suitable also in three-dimensional scattering problems and arbitrary illumination angles (for example: TE_z, TM_z). An example of the use of these definitions would be an incident wave illuminating a cylindrical object with normal incidence, so that the electric field is parallel to the cylinder's axis. According to the first definition, this would be called the TE incidence. This is because the electric field in this case is always transverse to the normal of the object's surface. With the latter definition, this same example would be called the TM_z incidence if the cylinder's axis is the z-axis, since the magnetic field is always transverse to the z-axis. In the rest of this chapter, we define the polarization of the incident wave with respect to the surface of the scatterer, since in all the considered example cases, the cloaks and cloaked objects are long cylindrical objects illuminated normally. The two main incidence cases are also illustrated in Fig. 11.1.

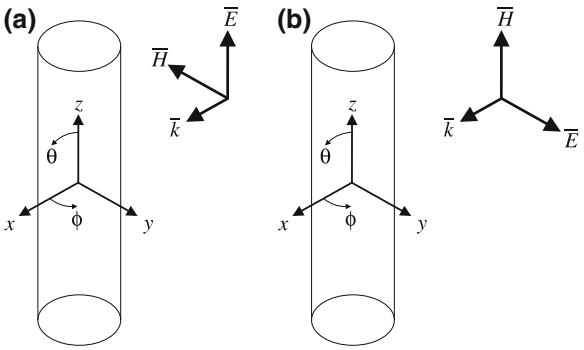

Fig. 11.1 Definitions of TE and TM incidences adopted in this Chapter, for the case of an incident wave illuminating a cylindrical scattering object. **a** TE incidence. **b** TM incidence

11.4 Parallel-Plate Waveguide Measurements

11.4.1 Demonstration of Cloaking with Parallel-Plate Waveguides

The first experimental demonstrations of electromagnetic cloaking using the transformation-electromagnetics approach were conducted with a parallel-plate waveguide setup [3]. This setup is convenient due to its limited size and low complexity as compared to a free space measurement setup (see Sect. 11.6). Essentially, the setup volume is limited by two parallel conducting surfaces, but it is intended to model infinite free space utilizing reflections from these two surfaces. Indeed, for an excitation wave with a vertically directed electric field and therefore, orthogonal to the conducting planes, the setup emulates a section of space which is infinitely periodical in the vertical direction. Thus, this is a very convenient way to study a device/structure which is homogeneous or periodical in the vertical direction like the cloak in [3].

The cloak design, whose operation was first demonstrated in [3] and later accurately characterized in [11], is based on utilizing small resonant particles (split ring resonators or SRRs) to create an artificial magnetic response. Namely, the inclusion dimensions vary with the radial distance inside the cloak as illustrated in Fig. 11.2. It is important to note that close to the inner part of the cloak the radial component of the relative permeability is smaller than unity and actually approaches zero at the inner boundary of the cloak. By properly designing the resonators and placing them radially around the cloaked region, one can create an anisotropic permeability that satisfies a simplified (approximate) cloaking condition [3]. In the first experiment [3] the cloaked metal cylinder has the diameter

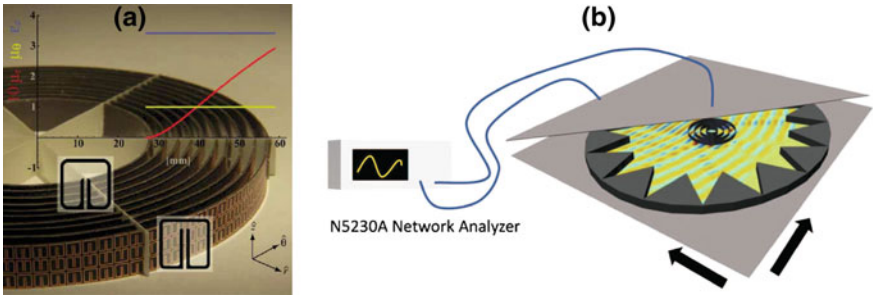

Fig. 11.2 **a** A transformation-electromagnetics cloak for TE incidence [3]. The object that is cloaked is a metal cylinder with diameter $1.42\lambda_0$ at 8.5 GHz. (This figure was reproduced with permission from the Amerian Association for the Advancement of Science.) **b** Illustration of the parallel-plate waveguide setup used in [3, 11]. The bottom plate's position is swept mechanically to map the field inside the waveguide (this figure was reproduced with permission from the Institute of Physics Publishing)

50 mm, while the outer diameter of the cloak is 117 mm. The design frequency is 8.5 GHz.

Excitation of the parallel-plate waveguide, i.e., creation of the incident wave, can be made in several ways by placing a source of electromagnetic radiation inside the waveguide. For example, open ends of rectangular waveguides, antennas, or small probes can be used for this purpose. To analyze the fields traveling inside the parallel-plate waveguide, one has to somehow measure these fields without influencing these very fields that are being measured. Another issue is that usually one needs to make a mapping of the field profile, i.e., the fields need to be measured in many positions inside the waveguide. One solution is to place a small probe (which should very weakly interact with the fields) inside the parallel-plate waveguide, and then mechanically sweep the position of this probe in order to fully map the fields. In practice this can be done, e.g., by fixing the probe at a certain position on the top or the bottom of the waveguide and then sweeping the position of one of the planar conductors [3] (see Fig. 11.2). To prevent scattering from the edges of the parallel-plate waveguide, absorbing materials can be used, preferably in the arrangement shown in Fig. 11.2. This arrangement minimizes reflections from the air/absorber boundary and maximizes absorption. The measurement itself can be carried out, for example, with a vector network analyzer (VNA) that measures the complex transmission between the source and the probe.

Figure 11.3 shows the results of three measurements conducted with the setup of Fig. 11.2: the incident field (in the empty waveguide) and the total field at two different frequencies with the cloaked object placed inside the waveguide [11]. Here the cloak design is similar to the one shown in Fig. 11.2. The metal cylinder that will be cloaked has the same size, but in this case, the optimal cloaking frequency is 10 GHz. As can be seen from Fig. 11.3, the incident wave is not a plane wave. A perfect plane wave would be difficult to produce in such a limited space inside the parallel-plate waveguide. However, for the illustration of the

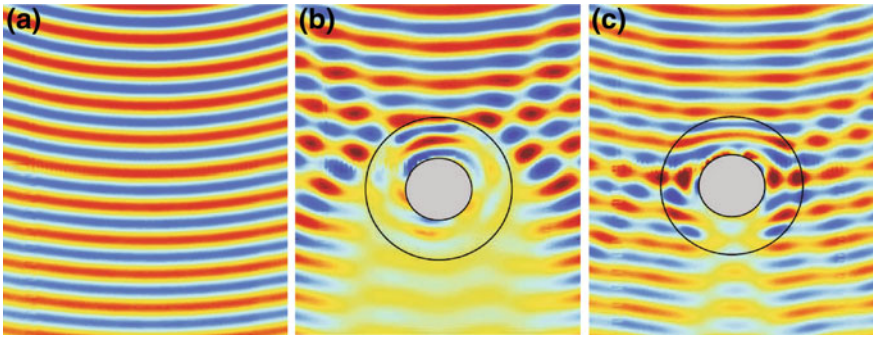

Fig. 11.3 Snapshots of measured field distributions inside the parallel-plate waveguide [11]. **a** Empty waveguide, $f = 10$ GHz. **b** Cloaked object inside the waveguide, $f = 9$ GHz. **c** Cloaked object inside the waveguide, $f = 10$ GHz. The diameter of the metal cylinder which is cloaked is $1.67\lambda_0$ at 10 GHz (this figure was reproduced with permission from the Institute of Physics Publishing)

cloaking effect and for the calculation of the total scattering widthσ_W, one can use any type of exciting wave. One should of course take into account that the cloak's operation may be different for different incident wave types (plane wave, cylindrical wave, etc.). At the optimal cloaking frequency of 10 GHz, the cloaking device is shown to reproduce (to a certain extent) the field profile which would be expected based on the transformation-electromagnetics design [3]. However, still a clear shadow is seen behind the cloaked object, demonstrating that the cloaking effect is rather limited. These results cannot give a well-defined value for characterization of the cloaking effect. They can only be used to illustrate the field and wave propagation profiles. On the other hand, the wavefronts inside the cloak nicely follow the calculated and simulated cases of the ideal and approximate transformation-electromagnetics cloak designs [3]. Thus, the measurements in [3, 11] give a convincing demonstration of the power and practical realizability of the transformation-electromagnetics concept.

Another solution to realize the parallel-plate waveguide measurement is to make one of the conducting plates weakly penetrable to the fields: This way the setup still behaves effectively like a parallel-plate waveguide with conducting walls, but a very small portion of the field extends out from the waveguide, and this field can then be measured with a probe placed outside the waveguide. The latter solution is somewhat simpler to realize since only the probe antenna needs to be moved, instead of the whole plate of the waveguide. Examples of experiments with such waveguides can be found, e.g., in [38, 39]. In [38] it was demonstrated that an incident electromagnetic wave can be effectively coupled to a transmission-line network. Inside the transmission-line network, the wave travels like in a homogeneous medium which allows for the cloaking of objects that are placed inside the network where fields, for the most part, do not penetrate. This was actually the first experimental demonstration of the transmission-line cloak idea that was originally proposed in [26]. On the other hand in [39], a transformation-electromagnetics cloak comprised of resonant canonical spiral inclusions was experimentally tested and field mappings similar to Fig. 11.3 were obtained. The same measurement technique with a weakly penetrable waveguide wall was earlier used in experimental investigations of microwave superlenses [40, 41].

11.4.2 Characterization of Cloaks with Parallel-Plate Waveguides

In order to characterize the cloaking phenomenon with a parallel-plate waveguide setup, one should first find the relation between the incident fields and the far-field scattered fields [either electric fields or magnetic fields, see (11.1)–(11.4)]. Since a parallel-plate waveguide setup is rarely large enough to allow direct measurements of the fields in the far-zone of the scattering object, one has to rely on measurements in the near-field zone and then make a transformation of the near-field to the far-field analytically.

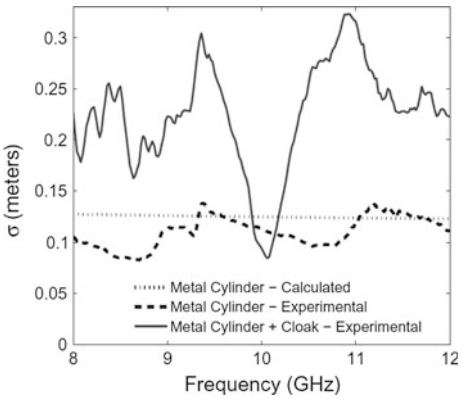

Fig. 11.4 Total scattering widths of uncloaked and cloaked objects [11]. The object that is cloaked is a *metal cylinder* with diameter $1.67\lambda_0$ at 10 GHz (this figure was reproduced with permission from the Institute of Physics Publishing)

In practice, one can conduct the measurements at discrete points around a circle that encompasses the cloak, and then expand the measured fields to their corresponding far-field quantities [11]. It should be noted that in order to find the far-field scattering width corresponding to each measurement point, one needs to measure the total field (field with the scattering object in the waveguide) as well as the incident field (field in the empty waveguide). Such measurements were conducted for the same transformation-electromagnetics cloak discussed in Sect. 11.4.1 [11], and the resulting total scattering widths of uncloaked and cloaked objects are given in Fig. 11.4 as functions of the frequency. The maximum reduction of the total scattering width obtained with the cloak is reported to be about 24 % near the design frequency of 10 GHz.

Yet another example of a parallel-plate waveguide measurement is the plasmonic cloak characterized in Ref [18]. In that case, the cloak's operation was based on the scattering cancelation idea, i.e., the cloak was effectively a material cover with the relative permittivity smaller than unity, and it was placed around a dielectric cylinder (the object to be cloaked). This artificial material cover is realized by radially positioned metal fins embedded in acetone (see Fig. 11.5). The dimensions of the fins and the permittivity of the embedding medium are designed to produce an effective relative permittivity of the whole cover which is smaller than unity and has the desired value at the design frequency. The diameter of the cloaked cylinder, which has a relative permittivity of 6, is 38 mm, while the outer diameter of the cloak is 62.6 mm. The design frequency of operation is around 2 GHz.

In this case the authors used a somewhat different approach to retrieve the scattering cross sections from the measurements. The upper plate of the waveguide was made of a perforated metal sheet to allow for placement of the measurement probe inside the waveguide at specific points (see Fig. 11.5). The vertical component of the electric field was then measured at 52 points (in fact, four measurements were carried out around each of these points [18]) where the points were distributed on the edges of a square enclosing the cloak. From the spatial derivatives of the measured electric field (E_z), one can find the corresponding

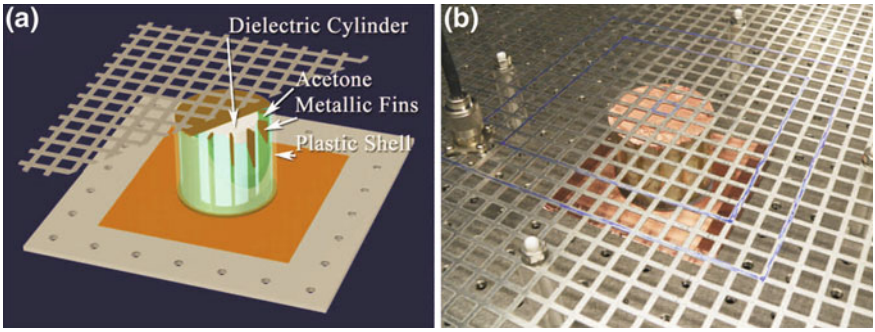

Fig. 11.5 **a** Illustration of the plasmonic cloak (enclosing the cloaked object) for TE incidence, placed inside the parallel-plate waveguide setup [18]. The object to be cloaked is a *dielectric cylinder* with diameter approximately $\lambda_0/4$ at 2 GHz. **b** Photograph of the same (this figure was reproduced with permission from the American Physical Society)

magnetic fields (H_x, H_y) and from these three components, the x- and y-components of the real part of the Poynting vector. By integrating the outward component of the Poynting vector around the square and dividing this by the result of the incident field (empty waveguide), one obtains the total scattering width of the measured object.

A practical way of illustrating the cloaking effect is to plot the normalized total scattering width as a function of frequency. This is just the total scattering width of the cloaked object divided by the total scattering width of the uncloaked object. This is also how the authors of [18] presented the results of their measurements (see Fig. 11.6). Although there is some difference in the locations of the minima corresponding to analytical, numerical, and experimental results, all the results indicate a strong reduction of scattering (about 75 %) close to the design frequency of 2 GHz.

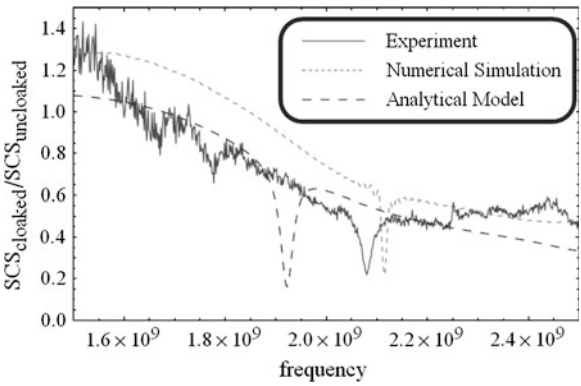

Fig. 11.6 Analytical, numerical, and measured normalized total scattering widths corresponding to the plasmonic cloak [18] (this figure was reproduced with permission from the American Physical Society)

11.5 Rectangular Waveguide Measurements

The parallel-plate waveguide is a very convenient way to measure the total scattering widths of infinitely high or periodic objects. However, the use of this approach requires electrically large setups, since the transversal size of the waveguide must be large enough to avoid unwanted reflections from the edges of the waveguide or from the edges of the absorbers. Especially at low microwave frequencies, the size of a parallel-plate waveguide may become too large and the weight too heavy for the measurements to be practical in a standard laboratory environment. Moreover, speedy measurements with the parallel-plate waveguide require an automated measurement setup including computer-controlled motors, since the probe needs to measure the fields in hundreds or even thousands of points.

A more practical way of measuring a cloaking device is to place the device inside a rectangular waveguide. This method requires only a vector network analyzer and a metallic rectangular waveguide with appropriate transitions to, e.g., coaxial cables, which are all standard laboratory equipment. Again, as in the case of the parallel-plate waveguide, the measurement can be done for the polarization with a vertical, linearly polarized electric field, and the measurement is emulating an infinitely periodic structure due to the boundary conditions on the top and bottom waveguide walls. However, unlike in the parallel-plate waveguide, here the modes of the waves inside the waveguide are more restricted due to the metallic side walls, and this in fact causes the measurement to emulate a case where the object placed inside the waveguide is also periodical in the horizontal direction. In the following examples, we have used only the fundamental mode (TE_{10} mode) of the rectangular waveguide. The idea behind the actual measurement is very simple: We compare the transmission through an empty waveguide to the cases of uncloaked and cloaked objects inside the same waveguide. This offers a nice and fast demonstration of cloaking, since the magnitudes and phases of the transmission coefficient are easy to compare.

In [42] a rectangular waveguide is used to demonstrate experimentally the cloaking capability of a transmission-line cloak. See Fig. 11.7 for the geometry of the cloak. The cloaked object in this case is a two-dimensional array of electrically thin metal rods, through which the electromagnetic wave is allowed to flow by the use of the cloak [27, 28]. The outer diameter of this cloaked object is approximately 25 mm, which is equal to one quarter of the wavelength at the design frequency of 3 GHz. The outer diameter of the cloak is about 70 mm. The cloak was designed for TE plane waves (electric field parallel to the z-axis in Fig. 11.7) incident from free space, and its operation in this case was verified with numerical simulations of the normalized total scattering width [42].

The waveguide used is a modified WR-340 waveguide with a width of 86.36 mm and the height equal to a multiple of the height of a single cloak layer (the cloak is periodic along the vertical direction). The height of the waveguide was chosen to be equal to four times the height of a single cloak layer which

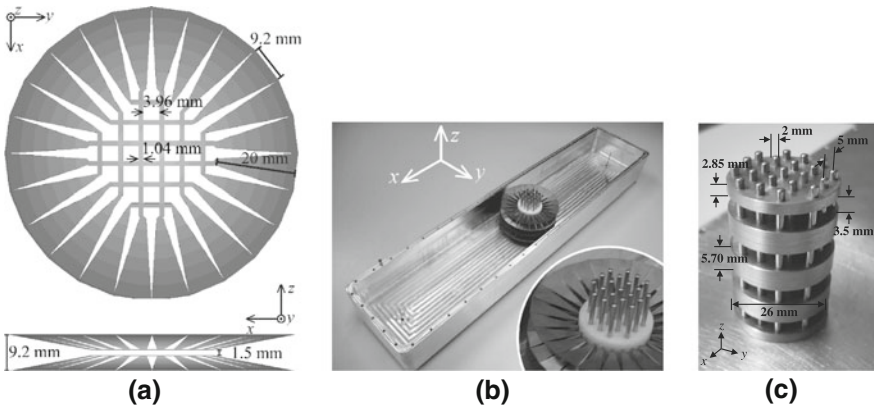

Fig. 11.7 **a** Geometry and dimensions of the transmission-line cloak for TE incidence [42]. (This figure was reproduced with permission from the American Institute of Physics.) **b** Photograph of the rectangular waveguide (with its top removed) [42]. The inset shows a magnification of the cloak, enclosing the object that is cloaked (a two-dimensional array of long metal rods, with the outer diameter of the array being approximately $\lambda_0/4$ at 3 GHz.) (this figure was reproduced with permission from the American Institute of Physics.) **c** A more complicated, fully three-dimensional object which is also possible to cloak with the same structure

resulted in a total height of 36.8 mm. The waveguide has a passband centered at around 3 GHz. A photograph of the waveguide with the cloaked object inside it is shown in Fig. 11.7.

It is very important to note that although the cloak was designed for a plane wave incidence in free space, the cloaking effect is achieved also in the waveguide, where the wave is essentially a superposition of two obliquely incident plane waves (the incidence angle varies with the frequency, as one can notice by studying the relation between the free space wavenumber and the wavenumber of the TE_{10} mode of the waveguide). Also, as explained above, the measurement emulates a case of an infinitely long array of cloaks placed along the transversal (y-) direction. The reason for the cloaking effect in these two different scenarios (free space and waveguide) is due to the fact that the cloak is operating well for all incidence angles in the horizontal (xy-) plane and its operation is not strongly affected by other similar cloaks placed in its near field. This may not be the case for all cloaks, so one should be careful when making conclusions about a free-standing cloak in free space based on rectangular waveguide measurements.

By using a VNA to measure the scattering parameters (S-parameters) of the waveguide section with an empty waveguide, uncloaked object inside the waveguide, and cloaked object inside the waveguide, we can determine how well the cloak can "hide" the object from the TE_{10} mode travelling in the waveguide. This is of course only a demonstration of the cloaking effect, as we only compare the different cases to each other to illustrate the cloaking effect.

In [42] the waveguide measurement was conducted for the transmission-line cloak of Fig. 11.7, and the results were extended and further analyzed in [27, 43].

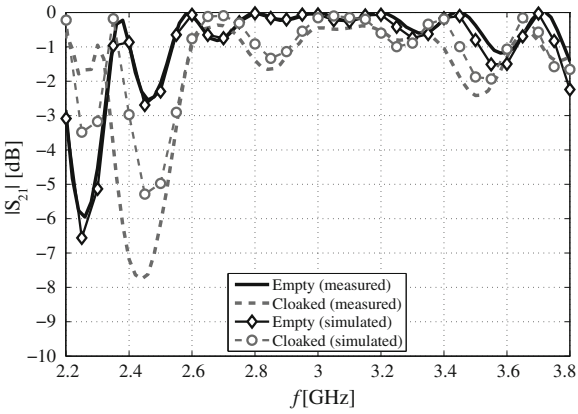

Fig. 11.8 Transmission-line cloak: measured and simulated magnitude of S_{21} for the empty waveguide and with cloaked object inside the waveguide. For the shown frequency band, the uncloaked object has $|S_{21}| < -10$ dB [42]

A more complicated, fully three-dimensional cloaked object, namely, the one shown on the right in Fig. 11.7, was also measured with the same waveguide in [27]. Here we compare the measured magnitude of the transmission coefficient ($|S_{21}|$) of the empty waveguide to the cases of cloaked and uncloaked objects placed in the center of the waveguide to the numerical results of each. In the simulations, we take into account the Rohacell insulating material, which is used to separate the transmission-line strips from each other, the losses of copper in the cloak, and the object to be cloaked [44]. The numerical results are obtained with Ansys HFSS [45]. These comparisons were previously presented in [44], where the simulation setups are described in detail. The results for the S_{21} magnitude are presented in Fig. 11.8 and demonstrate a good agreement between measured and simulated results. Refer to [28, 43] for the measured phase of S_{21}, as well as a comparison between the two different cloaked objects.

Another broadband and simple cloak design, the metal-plate cloak, was later introduced and also measured with the same rectangular waveguide as in [29]. Although it has an even simpler structure than the transmission-line cloak, this one is able to hide a solid cylindrical volume just like the previously shown transformation-electromagnetics cloak. However, as the cloaking phenomenon is not based on transformation-electromagnetics but on a waveguiding phenomenon enabled by periodically stacked conical waveguides, this cloaking technique is limited in the (electrical) diameter of the cloaked cylindrical volume. The metal cylinder cloaked in [29] has the diameter of 30 mm, while the design frequency is around 3 GHz. The outer diameter of the cloak is 70 mm. Later it was numerically [30] and experimentally [46] shown that the diameter can be extended to about one wavelength by slightly compromising the cloaking efficiency. The basic geometry of the metal-plate cloak is shown in Fig. 11.9. Again, in this case, the cloak is designed to operate for a linearly polarized wave with the electric field oriented vertically (along the z-axis in Fig. 11.9).

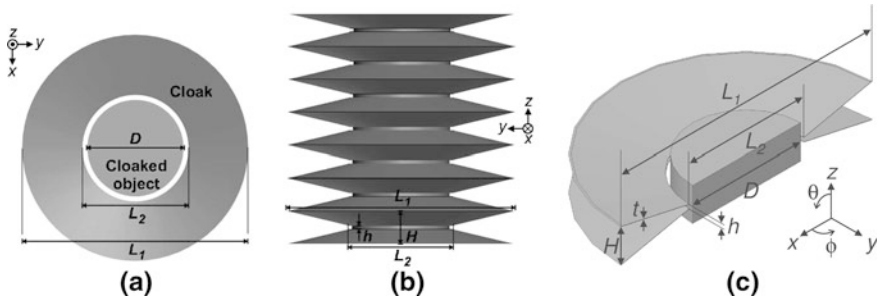

Fig. 11.9 Geometry of the metal-plate cloak for TE incidence [29, 30]. **a** Top view. **b** Side view. **c** Perspective view (only one half, cut along the xz symmetry plane, of a single cloak period is shown). The object that is cloaked is a metal cylinder with diameter $0.3\lambda_0$ at 3 GHz (this figure was reproduced with permission from the American Physical Society)

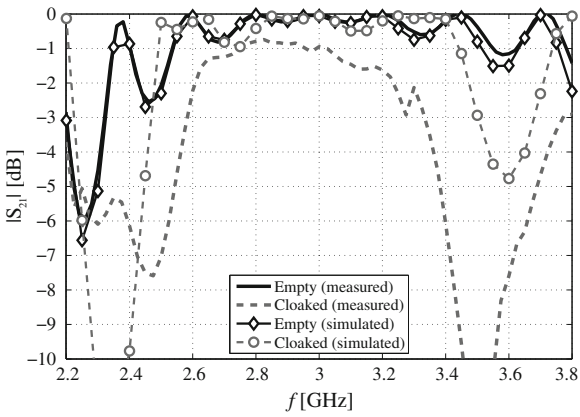

Fig. 11.10 Metal-plate cloak: measured and simulated magnitude of S_{21} for the empty waveguide and with cloaked object inside the waveguide. For the shown frequency band, the uncloaked object has $|S_{21}| < -10$ dB [29]

In [29] the height of a single cloak layer was chosen to be 9.2 mm, so that we could place four layers of the metal-plate cloak inside the waveguide and around a solid metal cylinder with diameter 30 mm. To compare the measured results with numerical ones, we simulate the WR-340 waveguide with four layers of the cloak inside it, taking into account the Rohacell insulating material and losses of copper in the cloak and cylinder [44]. The results for the S_{21} magnitude for the empty waveguide and for the cloaked object are presented in Fig. 11.10. The transmission-line cloak and metal plate cloak are similar in that we can observe a significant increase in transmission when comparing the uncloaked and cloaked cases. See [29] for the measured phase of S_{21}.

11.6 Free-Space Measurements

11.6.1 Demonstration of Cloaking in Free Space

A transformation-electromagnetics cloak based on a different realization than the one discussed in Sect. 11.4 was experimentally studied in [47]. Here the illuminating wave is TM polarized, i.e., the magnetic field is parallel to the metal cylinder's (object to be cloaked) axis. Due to the different polarization, it should be the radial component of the relative permittivity that is varying with the radial position [47]. Again split ring resonators (SRRs) are used as the resonant particles to comprise the metamaterial, but in this case, only their electric response is utilized, i.e., the magnetic field does not penetrate the loops of the SRRs and therefore does not excite the magnetic dipole. The geometry of the unit cell and a photograph of the cloak structure are shown in Fig. 11.11. The inner and outer radii of the cloak are 60 mm and 150 mm; respectively, while at the operating frequency of 11 GHz the wavelength is 27.3 mm.

The device was measured in a free-space setup comprising of an illuminating horn antenna, the cloaked/uncloaked object, and a measurement probe (a loop which measures the magnetic field strength). A VNA is connected to both the horn antenna and the probe, and it is used to measure the complex transmission between the two. The setup is surrounded by absorbers to avoid reflections from the surroundings. See Fig. 11.12 for an illustration of the setup. With this setup, one can obtain essentially similar field mappings as shown in Fig. 11.3. Refer to [47] for numerical and experimental results of such field mappings concerning the cloak of Fig. 11.11. With such measurement data, it would also be possible to characterize the cloaking effect (that is, to obtain the normalized total scattering cross section or width) in the same manner as discussed in Sect. 11.4.2 and in [11, 18].

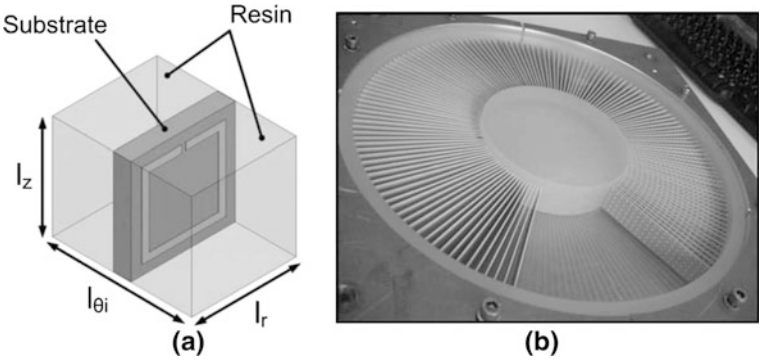

Fig. 11.11 **a** Unit cell of the metamaterial [47]. **b** Photograph of the partly assembled cloak for TM incidence [47]. The cloaked metal cylinder has the diameter of $4.4\lambda_0$ at 11 GHz (this figure was reproduced with permission from the American Physical Society)

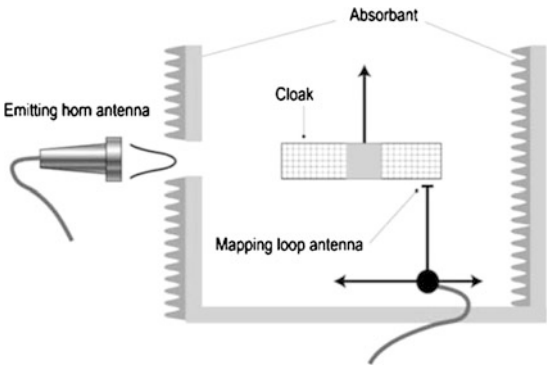

Fig. 11.12 Illustration of the free space measurement setup used in [47] (this figure was reproduced with permission from the American Physical Society)

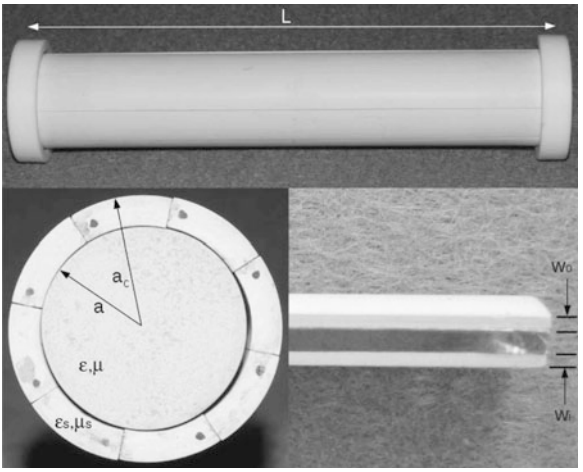

Fig. 11.13 Photographs of the plasmonic cloak studied in [48]. The object that is cloaked is a dielectric cylinder with diameter 25 mm, which equals to $\lambda_0/4$ at the frequency of 3 GHz (this figure was reproduced with permission from the Institute of Physics Publishing)

11.6.2 Characterization of Scattering Cross Sections with Bistatic Measurements in Free Space

Characterization of cloaking in practice means that the total scattering cross sections or widths of uncloaked and cloaked objects are obtained from experimental data. In Sect. 11.4.2 this was achieved by calculating the far-field quantities from the measured near-fields around the scatterer. An alternative, more straightforward way is of course simply to measure the scattered electric or magnetic fields of (11.1), (11.3) directly in the far-field, and then integrate the results over the solid angle as in (11.2) to obtain the total scattering cross section, or one could integrate over the angle in the horizontal plane (11.4) to obtain the total scattering width. Measuring the scattered electric or magnetic fields in the far-field of the scatterer requires a bistatic measurement setup with one antenna

creating the incident wave and another antenna measuring the fields at various angles around the scatterer. As in all the previous examples, a VNA can be used to measure the complex transmission coefficient between the two antennas.

In order to find, for example, the scattered electric field in a certain direction, two measurements are required: One with the incident field alone (without any scattering object), and another one with the scattering object. The latter measurement gives the *total* field with the scatterer from which one can then subtract the previous result, i.e., the *incident* field, in order to determine the *scattered* field.

In [48] such measurements were conducted for the plasmonic cloak shown in Fig. 11.13. In this case the cloaked object is a dielectric cylinder with a relative permittivity of 3 and a diameter of 25 mm, while the design frequency is 3 GHz (the free-space wavelength equals 100 mm). In this case the optimal cloak, i.e., the required dielectric material cover placed over the cylinder, is found to be a material with a relative permittivity of -13.6 [48]. As in [18] this negative-permittivity metamaterial is also realized with radially positioned metal plates embedded in a usual dielectric. The outer diameter of the cloak is 32.5 mm.

Paper [48] presents experimental results for the scattering cross sections (see (11.1)) of uncloaked and cloaked objects for various scattering angles and for various angles of incidence. All these results are not discussed here; instead, we concentrate on the TE incidence (normally incident wave with electric field parallel to the axis of the cloak) and the measured scattering cross sections in backward and forward directions. With the notations of Fig. 11.1, backscattering occurs in the direction $\phi = 180^\circ$ while forward scattering occurs in the direction $\phi = 0^\circ$. See Fig. 11.14 for the measured results. As the scattering measurements were conducted in [48] using a rather large angular step (30°), it is not possible to accurately integrate the measured scattering cross sections over the angle in order to find the total scattering cross section (nor width). However, in [48] numerical results for the total scattering cross section (for TE incidence) are given, resulting

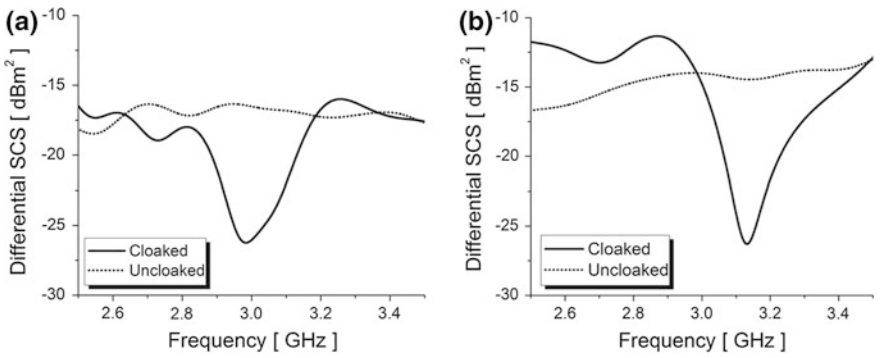

Fig. 11.14 Scattering cross sections for uncloaked and cloaked objects (plasmonic cloak), measured in free space [48]. **a** Backscattering cross section. **b** Forward scattering cross section (this figure was reproduced with permission from the Institute of Physics Publishing)

in good agreement with the data shown in Fig. 11.14. In addition to far-field scattering cross section measurements, the operation of the cloak was verified also using near-field measurements [48].

11.6.3 Characterization of Total Scattering Widths with Bistatic Measurements in Free Space

As discussed in Sect. 11.6.2, in order to experimentally characterize the total scattering cross sections or width, it is required that the scattered fields are measured in a large enough range of angles with a small enough step in the angle to make sure that the results are integrable over the angle with enough accuracy. Of course, in reality the measured scattered fields are only summed up together, so this is only an approximation of the integration of (11.2), (11.4). In practice the measurement setup must therefore include an automated sweep of the position of at least one of the antennas in order to make such a measurement feasible.

Such bistatic measurements have been carried out at the Microwaves and Radar Institute of the German Aerospace Center (DLR) in Germany. The setup used comprises of two X-band horn antennas equipped with dielectric focusing lenses. One of the antennas (transmitter, Tx) is stationary, while the other (receiver, Rx) can be swept around the measured object in the horizontal (*xy*-) plane by a rotating arm. The distances of the antennas from the measured object are kept constant, so that the focal point of the lenses is at the position of the object. A VNA is used to measure the reflection coefficients as well as the transmission coefficients between the antennas. See Fig. 11.15 for a photograph of the setup.

Because the cloaked and uncloaked objects are symmetrical with respect to the *xz*-plane, it is enough to measure the scattered fields in an angular range of 180°, i.e., between 0° and 180° for the determination of the total scattering widths.

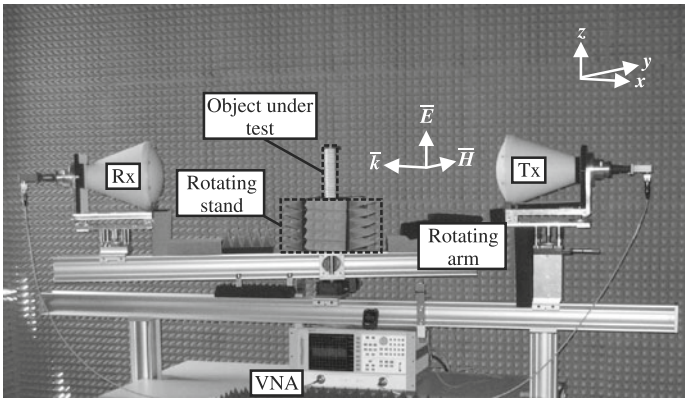

Fig. 11.15 Photograph of the bistatic X-band measurement setup at DLR

However, due to the finite sizes of the antennas and especially the bulky lenses, a full 180° measurement is not possible: The measurement can in practice be done only in the angular range of $\phi = 22-180°$ (note that here, in contrast to the notations in the previous sections, $\phi = 0°$ is the backscattering direction and $\phi = 180°$ is the forward scattering direction [46, 49], see the coordinate axes in Fig. 11.15). Therefore, we compare the experimental results to two sets of numerical results obtained with Ansys HFSS in which the integration is done over the full angular range as well as the limited range. For more details of the setup see [46, 49]. As will be shown later in this section, the limited angular range is not a problem, since it has a very small effect on the normalized total scattering widths in the case of the tested cloaked and uncloaked objects, for which most of the scattering occurs in the forward direction. See also the bistatic measured and simulated field intensities as functions of the angle ϕ, which also verify this conclusion [46, 49].

Two microwave cloaks have been measured with this setup in the X-band (8.2–12.4 GHz): A transmission-line cloak [49] and a metal-plate cloak [46]. The transmission-line cloak geometry is similar to the one shown in Fig. 11.7, except that the transition layer that enables the coupling between the surrounding free space and the volumetric transmission-line network is now made of solid conical layers. See Fig. 11.16 for the geometry and Fig. 11.17 for photographs of the uncloaked and cloaked objects. In this case, the cloaked object is similar to the one shown on the right in Fig. 11.7, but the dimensions are of course scaled down due to the higher operational frequency. Now the diameter of the cloaked metal object is 12.6 mm while the outer diameter of the cloak is 60 mm. Both the uncloaked and cloaked objects are periodical along the vertical direction, with the actual device comprising of 20 layers, resulting in a total height of 132 mm. The design frequency is 10 GHz.

The measured normalized total scattering width of this cloak is shown on the right in Fig. 11.17, where the experimental results are also compared to numerical ones. It is clearly shown that even with the slightly limited angular range one can accurately

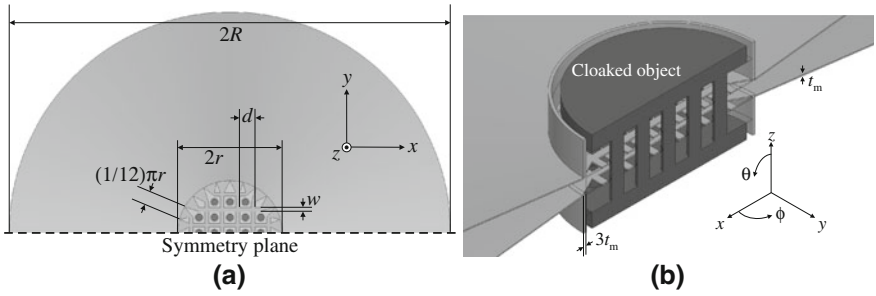

Fig. 11.16 Geometry of the transmission-line cloak for TE incidence in [49]. **a** Top view (cut along the *xz* symmetry plane). **b** Perspective view (cut along the *xz* symmetry plane), the insulating sheets between the transmission-line strips as well as the cloak and cloaked object are not shown for clarity

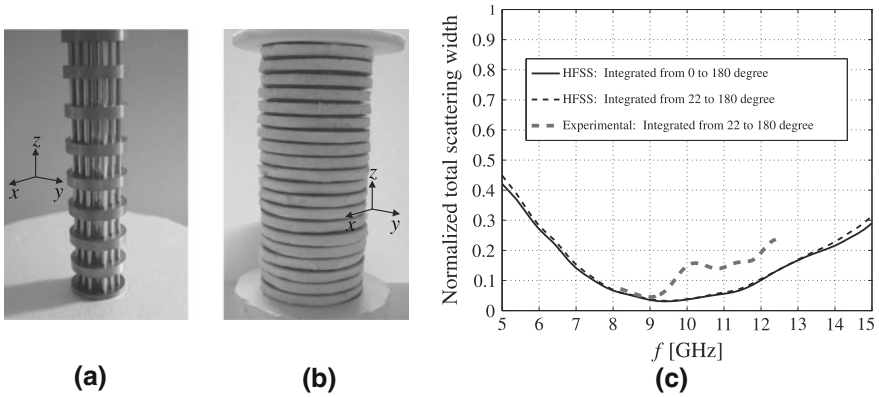

Fig. 11.17 **a** Photograph of a part of the uncloaked object [49]. The uncloaked object has diameter $0.42\lambda_0$ at 10 GHz. **b** Photograph of the cloaked object [49]. The white layers are dielectric material (relative permittivity of which is close to (1) that is used for support to make the structure more rigid. **c** Measured and simulated normalized total scattering width

describe the normalized total scattering width, since the scattering in the forward direction dominates the total scattering [46, 49]. There is some deviation between the numerical and experimental values, which is explained in part by the problems of accuracy in measuring very small scattered fields (such as that of a cloak) and in part by the problems in accurate positioning of the adjacent transmission-line layers in manual assembly, which is explained in more detail in [49]. However, close to the frequency of 9 GHz, the experimental results are in good agreement with the numerical ones, in which both show about a 95 % reduction in the total scattering width. At higher frequencies the experimental results show a slightly smaller reduction in scattering than the numerical results predict.

The metal-plate cloak studied in [46] has the geometry of Fig. 11.9, but compared to Sect. 11.5, some of the dimensions are changed due to the increased frequency. Also, to allow for cloaking of an electrically larger cylinder, the inclination of the cones is very different. The design used in [46] was numerically studied first in [30]. In this case the cloaked cylinder is indeed larger: The diameter of the metal cylinder is 30 mm, while the outer diameter of the cloak is 61 mm. The cloak is periodical along the vertical axis, with the actual device comprising of 20 layers, resulting in the total height of 184 mm (this also equals to the height of the uncloaked metal cylinder). For this cloak the design frequency is 10 GHz. See Fig. 11.18 for a photograph of the cloak.

In this case the bistatic measurement is much more accurate compared to the transmission-line cloak above, since both the uncloaked and cloaked objects scatter more. This is partly due to the larger electrical size of the uncloaked object and partly due to the less impressive cloaking effect. As shown on the right in Fig. 11.18, the experimental results are in good agreement with the numerical ones, demonstrating the reduction in total scattering width of about 70 % at 10 GHz.

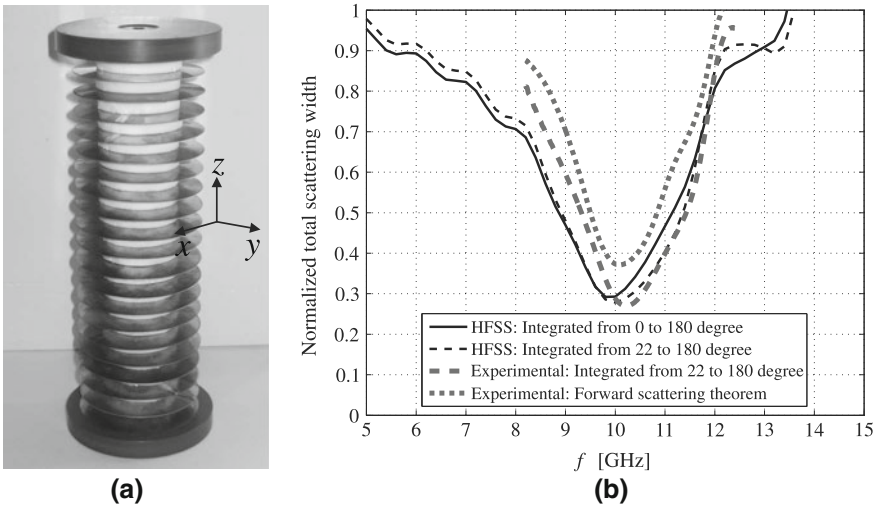

Fig. 11.18 **a** Photograph of the metal-plate cloak for TE incidence, enclosing the object that is cloaked [46]. This object is a metal cylinder with diameter λ_0 at 10 GHz. **b** Measured and simulated normalized total scattering width [46]

In addition to the integration of the scattered fields as in (11.2), (11.4), it is also possible to use the so-called forward scattering theorem (or, "optical theorem", see, e.g., [50]), to find the total scattering cross section or width. In this case it is only required to measure the complex scattered field in the forward direction. This of course makes the measurement procedure much simpler, as the scattering in only one direction needs to be measured. This theorem was used in the case of the metal-plate cloak in [46], where the method itself as well as the used equations are presented in detail. The resulting normalized total scattering width is plotted for comparison in the same figure as the result of the integration of the bistatic field measurements (see Fig. 11.18). As was discussed in detail in [46], the result based on the forward scattering theorem is much less accurate than the one based on the integration of the scattered field intensity. This is due to the fact that if the cloak is a weak scatterer, the error in the measured field value is the highest in the forward direction.

The forward scattering theorem has also been used much earlier in the experimental characterization of scattering reduction devices. For example, the reduction of scattering from antenna struts by the use of hard surfaces was experimentally studied already in 1996 [32].

11.7 Antenna Radiation Pattern Measurements

Measurement of an antenna radiation pattern is a well-known and a fairly simple measurement. It can be done with a much simpler setup than, e.g., the bistatic measurements discussed in the previous section. A common way to measure an

antenna's radiation pattern (in one plane) is to rotate the antenna under test (AUT) around its own axis, while measuring the transmission between the AUT and a stationary antenna with a VNA. Of course the two antennas need to be in each other's far-field. Such antenna measurement facilities can be found in most well-equipped microwave laboratories.

Using this simple method and readily available measurement setups together with well-established measurement procedures, the antenna blockage caused by a transmission-line cloak was numerically and experimentally studied in [51]. This is again only a demonstration of the cloaking effect, and the main idea is to compare an antenna's radiation patterns in free space with the cases of an uncloaked and a cloaked object placed in front of the antenna. If the cloak is operating as it should, the blockage (change in the antenna's radiation pattern as compared to the free space case) caused by the cloaked object should be strongly mitigated as compared to the uncloaked case.

The geometry of the cloak itself is similar to Fig. 11.16 with the exception that the transition from free space to the cloak is made with cones of solid metal instead of thin metal sheets [51]. Also, the dimensions are scaled in order to achieve the optimal cloaking effect at the frequency of 3 GHz. In the final design, the diameter of the cloaked metal object (similar to that of Fig. 11.17) is 39 mm while the outer diameter of the cloak is 180 mm. The realized cloak is made up from 20 layers, resulting in the total height of 240 mm (see Fig. 11.19 for a photograph of the cloak, enclosing the cloaked object). For details of other dimensions, refer to [51].

To demonstrate the cloaking effect, the H-plane radiation pattern of a commercially available Schwarzbeck BBHA 9120A horn antenna was measured in an anechoic chamber in three cases: (1) the antenna alone, (2) the antenna with the uncloaked object in front of it, and (3) the antenna with the cloaked object in front

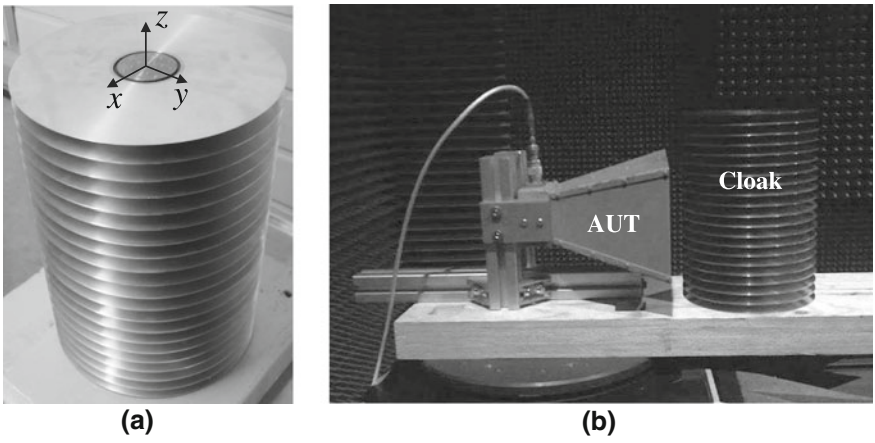

Fig. 11.19 **a** Photograph of the transmission-line cloak (enclosing the object to be cloaked) for TE incidence [51]. The diameter of the object that is cloaked is $0.39\lambda_0$ at 3 GHz. **b** Photograph of the AUT placed inside an anechoic chamber, with the cloaked object in front of it [51]

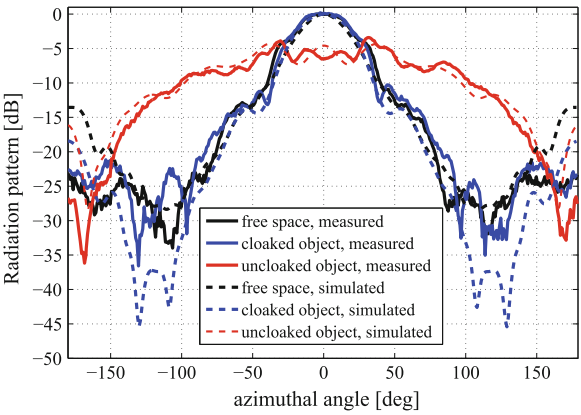

Fig. 11.20 Measured and simulated radiation patterns of the AUT in different scenarios at the frequency 3 GHz [51]. All the patterns are normalized to the free space case in the main radiation direction

of it. See Fig. 11.19 for a photograph of the last case. As shown in the photograph, the cloak is placed very close to the AUT in its near-field region. The distance from the center of the cloak to the aperture of the AUT is 100 mm.

The AUT is placed in a large anechoic chamber on a computer-controlled rotating stand. Then, a stationary antenna is placed in the far-field of the AUT. By rotating the AUT (and of course the cloaked/uncloaked objects with the AUT) and simultaneously measuring the transmission between the two antennas, we can obtain the radiation patterns in all three cases. These are presented in Fig. 11.20 for the frequency 3 GHz along with the corresponding numerical results. See [51] for results at other frequencies (demonstrating the bandwidth of cloaking). As shown in Fig. 11.20, the uncloaked object causes severe blockage to the antenna, practically destroying the radiation pattern. This is expected since we placed a tall metallic object just in front of the antenna aperture. The pattern with the cloaked object in front of the antenna on the other hand corresponds very well to the case of the antenna alone in free space, thus providing a nice demonstration of the cloaking phenomenon.

11.8 Polarizability Measurements

Many approaches to cloaking rely on the design and realization of artificial electromagnetic materials built from engineered particles, which are also known as electrically small “artificial molecules”. Also, there is interest in possibilities to reduce scattering from electrically small particles (making particles “invisible”). Such particles should not be confused with “cloaks”, as they obviously cannot hide any other object from the electromagnetic waves. Instead, such invisible objects could be found useful, for example, as low-scattering sensors or in the design of weakly scattering structures.

Experimental electromagnetic characterization of small particles means measuring their response to certain electromagnetic excitation and extracting the values of the particle polarizabilities from the measured results. In this section, we will review methods for electromagnetic characterization of small particles.

11.8.1 Particle Characterization with Free-Space Measurements

Let us first discuss how the particle polarizability can be estimated from free-space measurements of fields scattered from a small particle. Since the particle is assumed to be electrically small, in most cases it is enough to model the scattering processes with the use of only the lowest-order current moments: the electric dipole moment $\overline{p}$ and the magnetic dipole moment $\overline{m}$. In the most general case of linear response, the relations between the induced moments and the exciting fields take the following form:

$$\overline{p} = \overline{\overline{\alpha}}_{ee} \cdot \overline{E}_{\text{inc}} + \overline{\overline{\alpha}}_{em} \cdot \overline{H}_{\text{inc}} \tag{11.5}$$

$$\overline{m} = \overline{\overline{\alpha}}_{mm} \cdot \overline{H}_{\text{inc}} + \overline{\overline{\alpha}}_{me} \cdot \overline{E}_{\text{inc}} \,. \tag{11.6}$$

These relations are called *bianisotropic relations*. They assume that the particle response can be anisotropic (the induced moment is not necessarily parallel to the incident field), and they include magnetoelectric coupling due to spatial dispersion (electrically finite size of the particle) and possibly non-reciprocity of the particle [52]. Probably the most natural way to estimate the polarizabilities experimentally is to measure the scattering cross section for various excitations and find a connection between the measured values and the polarizabilities. In the case of a simple particle, for instance, an electric-dipole particle which has only one non-trivial polarizability component, scalar α_{ee}, it is enough to measure the usual radar or scattering cross section (11.1), because for a dipole particle the amplitude of the scattered field in the far zone is given by

$$|E_{\text{sca}}| = \frac{\omega\eta k}{R}|p| = \frac{\omega\eta k}{R}|\alpha_{ee}||E_{\text{inc}}|, \tag{11.7}$$

where η is the wave impedance and k the wave number. Substitution into 11.1 immediately gives

$$|\alpha_{ee}| = \frac{2\sqrt{\pi}}{\omega\eta k}\sqrt{\sigma}. \tag{11.8}$$

In order to find the phase of the polarizability, we need to know not only the scattered power (which defines the scattering cross section) but also the phase of the scattered field and rewrite this relation in terms of the complex scattering amplitude.

For more complex particles characterized by dyadic polarizabilities several test excitations are necessary. Following [53] we will consider an example of a canonical chiral particle with reciprocal magnetoelectric coupling. In the design of cloaks, these particles allow to realize artificial materials with nearly equal permittivity and permeability [39], which is one of the essential requirements for transformation-electromagnetics cloaks [2]. As an illustrative example let us consider a uniaxial chiral particle which is characterized by the relations

$$\begin{aligned} \overline{p} &= [\alpha_{ee}^{(zz)} \overline{z}_0 \overline{z}_0 + \alpha_{ee}^{(t)} \overline{\overline{I}}_t] \cdot \overline{E}_{\text{inc}} + \alpha_{em} \overline{z}_0 \overline{z}_0 \cdot \overline{H}_{\text{inc}} \\ \overline{m} &= \alpha_{mm}^{(zz)} \overline{z}_0 \overline{z}_0 \cdot \overline{H}_{\text{inc}} - \alpha_{em} \overline{z}_0 \overline{z}_0 \cdot \overline{E}_{\text{inc}}. \end{aligned} \tag{11.9}$$

Here $\overline{\overline{I}}_t$ is the transverse unit dyadic ($\overline{\overline{I}}_t = \overline{\overline{I}} - \overline{z}_0 \overline{z}_0$) and the corresponding term describes the electric polarization of the spiral by electric fields polarized orthogonally to the axis of the spiral (the unit vector $\overline{z}_0$).

Probing this particle with a plane wave with the electric field polarized along z, the co-polarized response is defined solely by the electric polarizability component $\alpha_{ee}^{(zz)}$:

$$\sigma_e^{\text{co}} = \frac{1}{4\pi} (\omega k \eta)^2 |\alpha_{ee}^{(zz)}|^2. \tag{11.10}$$

This is because the magnetic moment induced in the particle due to the magnetoelectric coupling is directed along the same axis z, and the field created by this moment in the far zone is orthogonally polarized with respect to the incident field. Measuring the cross-polarized field scattered by the same particle we can determine the chirality parameter α_{em}. To this end we define the cross-polarized scattering cross section by

$$\sigma_e^{cr} = \lim_{R \to \infty} 4\pi R^2 \frac{|E_{sca,t}|^2}{|E_{inc,z}|^2}. \tag{11.11}$$

Here the indices z and t mark the longitudinal (along z) and transverse components of the fields. Substituting the field scattered by the induced magnetic dipole we find that

$$\sigma_e^{cr} = \frac{1}{4\pi} (\omega k)^2 |\alpha_{em}|^2. \tag{11.12}$$

Probing the same particle with a plane wave whose magnetic field is polarized along the spiral axis, the scattering cross section will depend on the magnetic polarizability

$$\sigma_h^{co} = \frac{1}{4\pi}(\omega k)^2 \left| \frac{\alpha_{mm}^{(zz)}}{\eta} - \alpha_{ee}^{(t)} \eta \right|^2 . \tag{11.13}$$

but also contain a term proportional to $\alpha_{ee}^{(t)}$. Often these two polarizabilities resonate at different frequencies, which allows one to separate the responses due to the two polarization mechanisms. At low frequencies (well below the resonance of the magnetic polarizability $\alpha_{mm}^{(zz)}$), the contribution of $\alpha_{ee}^{(t)}$ dominates, because $\alpha_{mm}^{(zz)}$ decays as ω^2 with decreasing frequency while $\alpha_{ee}^{(t)}$ tends to approach a finite static limit [52, 53]. If both terms are significant, more complicated experimental arrangements are required in order to measure the two terms separately. For example, illumination of the particle by two plane waves coming from different directions.

11.8.2 Particle Characterization with Waveguide Measurements

Alternatively, polarizabilities of small particles can be measured in a waveguide set-up, where the measurable quantity is the reflection coefficient from the particle in the matched waveguide. Transmission coefficient measurements can be utilized as well. Here we will discuss how the electric and magnetic polarizabilities of a small particle can be extracted from the measured reflection coefficient. As an example, let us position a particle with the polarization response modeled by (11.9) in the center of the cross-section area of a rectangular waveguide supporting the fundamental TE_{10} mode. The particle axis is oriented along the wide wall of the waveguide, so that the modal magnetic field couples well to the particle. In this configuration the chirality parameter does not affect the reflection coefficient, because the horizontal electric moment induced by the horizontal magnetic field of the waveguide mode couples only to evanescent modes of the waveguide. Considering for simplicity the case when the electric polarization in the vertical direction (measured by $\alpha_{ee}^{(t)}$) is negligible, we can find the parameter $\alpha_{mm}^{(zz)}$ from the measured reflection coefficient.

The main difference with the free-space testing set-up is that the field exciting the particle cannot be assumed to be equal to the field of the incident plane wave. This is because the particle is inside the waveguide and experiences influence from the fields reflected from the walls. In other words, the exciting ("local") field is the sum of the incident field and the field created by the particle in the waveguide. In order to find the relation between particle polarizabilities and the measured reflection coefficient we will consider (for the start) a small isotropic magneto-dielectric particle (parameters ε and μ) and make use of the Lorentz lemma (e.g., [54]). The geometry of the problem is illustrated in Fig. 11.21. In the Lorentz lemma we choose the first set of fields to be the fields $\overline{E}$, $\overline{H}$ in the waveguide when

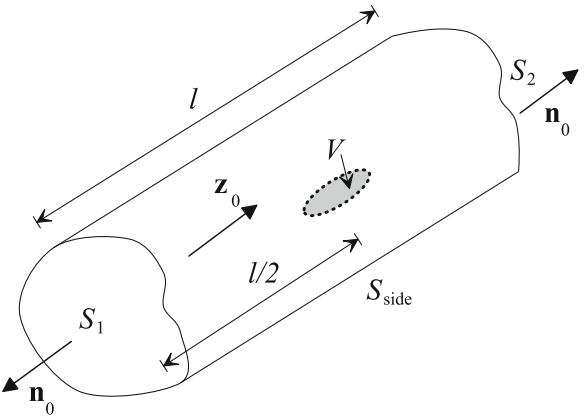

Fig. 11.21 Arbitrary cross-section closed waveguide with a small particle inside

the particle is present, and set 2 will be the fields in the empty waveguide $\overline{E}_0$, $\overline{H}_0$ (excited by the same source at the same frequency ω). Integrating the differential Lorentz lemma over the volume between cross-sections S_1 and S_2 we get

$$\begin{aligned} &-\int_{S_1}(\overline{E}\times\overline{H}_0-\overline{E}_0\times\overline{H})\cdot\overline{z}_0\,dS+\int_{S_2}(\overline{E}\times\overline{H}_0-\overline{E}_0\times\overline{H})\cdot\overline{z}_0\,dS \\ &=j\omega\int_V[(\mu-\mu_0)\overline{H}\cdot\overline{H}_0+(\varepsilon-\varepsilon_0)\overline{E}\cdot\overline{E}_0]\,dV. \end{aligned} \tag{11.14}$$

Let us assume that the waveguide supports only one propagating mode and that the cross-sections $S_{1,2}$ are far enough from the particle, so that the higher-order modes are negligible there. We denote by $\overline{E}_{t0}$ the transverse electric field of the empty waveguide at S_1 (t denotes the transverse component with respect to $\overline{z}_0$) and write them in terms of the reflection (R) and transmission (T) coefficients. At S_1 we have

$$\overline{E}_{t0}|_{S_1}=\overline{E}_{t0},\qquad \overline{E}_t|_{S_1}=\overline{E}_{t0}(1+R) \tag{11.15}$$

$$\overline{H}_{t0}|_{S_1}=\frac{1}{Z_0}(\overline{z}_0\times\overline{E}_{t0}),\qquad \overline{H}_t|_{S_1}=\overline{H}_{t0}(1-R) \tag{11.16}$$

and at S_2

$$\overline{E}_{t0}|_{S_2}=\overline{E}_{t0}e^{-j\beta_0 l},\qquad \overline{E}_t|_{S_2}=\overline{E}_{t0}T \tag{11.17}$$

$$\overline{H}_{t0}|_{S_2}=\frac{1}{Z_0}(\overline{z}_0\times\overline{E}_{t0})e^{-j\beta_0 l},\qquad \overline{H}_t|_{S_2}=\overline{H}_{t0}|_{S_1}T. \tag{11.18}$$

Here β_0 and Z_0 are the propagation constant and characteristic impedance of the fundamental mode, and R and T are the fundamental-mode reflection and transmission coefficients. Substitution into (11.14) determines the reflection coefficient:

$$R = -\frac{j\omega Z_0}{2N_0}\int_V [(\mu-\mu_0)\overline{H}\cdot\overline{H}_0 + (\varepsilon-\varepsilon_0)\overline{E}\cdot\overline{E}_0]\,dV, \tag{11.19}$$

where $N_0 = \int_{S_1} \overline{E}_{t0}\cdot\overline{E}_{t0}\,dS$.

Next we consider an example of a small dielectric sphere, in which case the internal field inside the sphere reads $\overline{E} = \frac{3\varepsilon_0}{\varepsilon+2\varepsilon_0}\overline{E}_{\text{loc}}$, where $\overline{E}_{\text{loc}}$ is the local field in the waveguide at the position of the sphere. The assumption of the sphere being "small" means that the local field can be assumed to be approximately uniform over the volume of the sphere. To understand the nature of the local field in this case we can use the image principle and model the effects of the waveguide walls on the field created by the sphere by its mirror images in the walls. The local field is the sum of the incident field and the fields of all the images of the sphere in the walls (in this infinite array of images the original sphere is not included). Thus, the local field can be written as the sum of the incident field and the interaction field, which is proportional to the dipole moment of the sphere: $\overline{E}_{\text{int}} = C\overline{p}$. The interaction constant C for this case has been calculated in [55, 56] (see also references therein). The interaction field contains three components: the fundamental-mode reflected field created by the sphere, reactive field due to higher-order modes existing near the inhomogeneity, and the field scattered by the inhomogeneity of the array of the mirror images of the spheres (recall that the sphere at the origin is missing in this infinite array). For applications in practical measurements the local field can be approximated as the sum of the incident field and the fundamental-mode component of the field scattered by the sphere: $\overline{E}_{\text{loc}} = \overline{E}_0(1+R)$ (R is the reflection coefficient), neglecting the reactive field near the sphere and the single-dipole scattering term. In terms of the theory of reflection from periodical arrays of particles this basically means approximating the local field by the averaged field in array plane. Reactive interaction fields can be usually neglected, because these fields lead only to a small shift in the measured resonance frequency as compared to that for the same object in free space. Neglecting the field scattered by the inhomogeneity of the array of the mirror images means that the polarizability extracted from the measurement does not contain the term which corresponds to scattering losses from the object under test.

Substituting the internal field into (11.19) and taking into account that the quasi-static polarizability of a small dielectric sphere equals $\alpha_{ee} = \frac{3\varepsilon_0(\varepsilon-\varepsilon_0)}{\varepsilon+2\varepsilon_0}V$ (V is the sphere volume), we can find the polarizability from the experimentally known reflection coefficient:

$$\alpha_{ee} = \frac{1}{E_{t0}^2}\frac{2jN_0Re^{j\beta_0 l}}{\omega Z_0(1+R)}. \tag{11.20}$$

The scattering losses term can be restored in the final result by adding the corresponding value to the inverse polarizability (see, e.g., [57]):

$$\frac{1}{\alpha_{ee}} \rightarrow \frac{1}{\alpha_{ee}} + j\frac{k_0^3}{6\pi\varepsilon_0}. \tag{11.21}$$

If the VNA (or any other device used to measure R) is calibrated so that the phase reference plane is at the position of the particle, the exponential factor disappears:

$$\alpha_{ee} = \frac{1}{E_{t0}^2}\frac{2jN_0}{\omega Z_0}\frac{R}{1+R} \tag{11.22}$$

and there is no need to know the electrical length from the measuring cell port to the sample. Finally, we note that in the expression of the particle polarizability, the result will not change if the particle is in fact not a dielectric sphere but any other particle with the polarizability α_{ee}. Thus, we can use it to extract the polarizability from the measured reflection coefficient for any small electrically polarizable particle. For magnetically polarizable particles, using duality we get

$$\alpha_{mm} = \frac{1}{E_{t0}^2}\frac{2jN_0Z_0}{\omega}\frac{R}{1-R}. \tag{11.23}$$

If both α_{ee} and α_{mm} are not zero, one measurement is not enough to determine both parameters.

The particle is usually positioned at the center of the cross section, and the eigenwave functions are usually normalized so that $E_{t0} = 1$ at this point. Then, for rectangular waveguides, denoting the waveguide sizes as a and b ($a > b$), we have

$$N_0 = b\int_0^a \sin^2\frac{\pi}{a}x\,dx = \frac{ab}{2} \tag{11.24}$$

and the mode impedance for the fundamental mode is

$$Z_0 = \frac{\sqrt{\mu_0/\varepsilon_0}}{\sqrt{1-(\omega_c/\omega)^2}}, \tag{11.25}$$

where $\omega_c = \pi c/a$ is the cut-off frequency of the fundamental mode. Refer to [58] as an example of the practical use of this technique for measuring the polarizability of an artificial resonant magnetic particle, metasolenoid.

Measurements of bianisotropic particles in a waveguide setup are based on the effect of mode coupling or coupling to another waveguide. If the coupling amplitude is proportional to the electromagnetic coupling coefficient, the coefficient can be found from measurement of the transmission coefficient from one mode to the other or from one waveguide to the other. An example of such experiment is described in [59], where coupling from a rectangular waveguide to a

coaxial cable probe was measured to find the non-reciprocal magneto-electric coupling coefficient.

References

1. Leonhardt U (2006) Optical conformal mapping. Science 312:1777–1780
2. Pendry JB, Schurig D, Smith DR (2006) Controlling electromagnetic fields. Science 312:1780–1782
3. Schurig D, Mock JJ, Justice BJ, Cummer SA, Pendry JB, Starr AF, Smith DR (2006) Metamaterial electromagnetic cloak at microwave frequencies. Science 314:977–980
4. Cummer S, Popa B-I, Schurig D, Smith DR, Pendry JB (2006) Full-wave simulations of electromagnetic cloaking structures. Phys Rev E 74:036621
5. Cai W, Chettiar UK, Kildishev AV, Shalaev VM (2007) Optical cloaking with metamaterials. Nature Photonics 1:224–227
6. Zhang B, Chen H, Wu B-I, Luo Y, Ran L, Kong JA (2007) Response of a cylindrical invisibility cloak to electromagnetic waves. Phys Rev B 76:121101(R)
7. Yan M, Ruan Z, Qiu M (2007) Cylindrical invisibility cloak with simplified material parameters is inherently visible. Phys Rev Lett 99:233901
8. Gaillot DP, Croenne C, Zhang F, Lippens D (2008) Transformation optics for the full dielectric electromagnetic cloak and metaldielectric planar hyperlens. New J Phys 10:115039
9. Liu R, Ji C, Mock JJ, Chin JY, Cui TJ, Smith DR (2009) Broadband ground-plane cloak. Science 323:366–369
10. Ergin T, Stenger N, Brenner P, Pendry JB, Wegener M (2010) Three-dimensional invisibility cloak at optical wavelengths. Science 328:337–339
11. Kundtz N, Gaultney D, Smith DR (2010) Scattering cross-section of a transformation optics-based metamaterial cloak. New J Phys 12:043039
12. Li C, Liu X, Li F (2010) Experimental observation of invisibility to a broadband electromagnetic pulse by a cloak using transformation media based on inductor-capacitor networks. Phys Rev B 81:115133
13. Yang C, Yang J, Huang M, Xiao Z, Peng J (2011) An external cloak with arbitrary cross section based on complementary medium and coordinate transformation. Opt Expr 19:1147–1157
14. Castaldi G, Gallina I, Galdi V, Alù A, Engheta N (2011) Analytical study of spherical cloak/anti-cloak interactions. Wave Motion 48:455–467
15. Zedler M, Eleftheriades GV (2011) Anisotropic transmission-line metamaterials for 2-D transformation optics applications. Proc IEEE 99:1634–1645
16. Alù A, Engheta N (2005) Achieving transparency with plasmonic and metamaterial coatings. Phys Rev E 72:016623
17. Alù A, Engheta N (2008) Plasmonic and metamaterial cloaking: physical mechanisms and potentials. J Opt A 10:093002
18. Edwards B, Alù A, Silveirinha MG, Engheta N (2009) Experimental verification of plasmonic cloaking at microwave frequencies with metamaterials. Phys Rev Lett 103:153901
19. Alù A, Engheta N (2008) Multifrequency optical invisibility cloak with layered plasmonic shells. Phys Rev Lett 100:113901
20. Bilotti F, Tricarico S, Vegni L (2008) Electromagnetic cloaking devices for TE and TM polarizations. New J Phys 10:115035
21. Alù A, Engheta N (2009) Cloaking a sensor. Phys Rev Lett 102:233901
22. Alù A, Engheta N (2010) Cloaked near-field scanning optical microscope tip for noninvasive near-field imaging. Phys Rev Lett 105:263906

23. Bilotti F, Tricarico S, Vegni L (2010) Plasmonic metamaterial cloaking at optical frequencies. IEEE Trans Nanotechnology 9:55–61
24. Tricarico S, Bilotti F, Alù A, Vegni L (2010) Plasmonic cloaking for irregular objects with anisotropic scattering properties. Phys Rev E 81:026602
25. Bilotti F, Pierini F, Vegni L (2011) Employment of metamaterial cloaks to enhance the resolution of near-field scanning optical microscopy systems based on aperture tips. Metamaterials 5:119–124
26. Alitalo P, Luukkonen O, Jylhä L, Venermo J, Tretyakov SA (2008) Transmission-line networks cloaking objects from electromagnetic fields. IEEE Trans Antennas Propagat 56:416–424
27. Alitalo P, Tretyakov S (2009) Electromagnetic cloaking with metamaterials. Materials Today 12:22–29
28. Alitalo P, Tretyakov SA (2011) Broadband electromagnetic cloaking realized with transmission-line and waveguiding structures. Proc IEEE 99:1646–1659
29. Tretyakov S, Alitalo P, Luukkonen O, Simovski C (2009) Broadband electromagnetic cloaking of long cylindrical objects. Phys Rev Lett 103:103905
30. Alitalo P, Tretyakov SA (2010) Electromagnetic cloaking of strongly scattering cylindrical objects by a volumetric structure composed of conical metal plates. Phys Rev B 82:245111
31. Smolyaninov II, Smolyaninova VN, Kildishev AV, Shalaev VM (2009) Anisotropic metamaterials emulated by tapered waveguides: application to optical cloaking. Phys Rev Lett 102:213901
32. Kildal P-S, Kishk AA, Tengs A (1996) Reduction of forward scattering from cylindrical objects using hard surfaces. IEEE Trans Antennas Propagat 44:1509–1520
33. Hakansson A (2007) Cloaking of objects from electromagnetic fields by inverse design of scattering optical elements. Opt Exp 15:4328–4334
34. Milton GW, Nicorovici N-AP (2006) On the cloaking effects associated with anomalous localized resonance. Proc R Soc A 462:3027–3059
35. Milton G, Nicorovici N-A, McPhedran R, Cherednichenko K, Jacob Z (2008) Solutions in folded geometries and associated cloaking due to anomalous resonance. New J Phys 10:115021
36. Chen H, Chan CT, Sheng P (2010) Transformation optics and metamaterials. Nature Materials 9:387–396
37. Guenneau S, McPhedran RC, Enoch S, Movchan AB, Farhat M, Nicorovici N-AP (2011) The colours of cloaks. J Opt 13:024014
38. Alitalo P, Ranvier S, Vehmas J, Tretyakov S (2008) A microwave transmission-line network guiding electromagnetic fields through a dense array of metallic objects. Metamaterials 2:206–212
39. Guven K, Saenz E, Gonzalo R, Ozbay E, Tretyakov S (2008) Electromagnetic cloaking with canonical spiral inclusions. New J Phys 10:115037
40. Maslovski S, Tretyakov SA, Alitalo P (2004) Near-field enhancement and imaging in double planar polariton-resonant structures. J Appl Phys 96:1293–1300
41. Alitalo P, Maslovski S, Tretyakov S (2006) Near-field enhancement and imaging in double cylindrical polariton-resonant structures: enlarging superlens. Phys Lett A 357:397–400
42. Alitalo P, Bongard F, Zürcher J-F, Mosig J, Tretyakov S (2009) Experimental verification of broadband cloaking using a volumetric cloak composed of periodically stacked cylindrical transmission-line networks. Appl Phys Lett 94:014103
43. Alitalo P, Kettunen H, Tretyakov S (2010) Cloaking a metal object from an electromagnetic pulse: a comparison between various cloaking techniques. J Appl Phys 107:034905
44. Alitalo P, Tretyakov SA (2012) Numerical modeling and characterization of selected electromagnetic cloaking structures. International Journal of RF and Microwave Computer-Aided Engineering 22:483–495
45. Homepage of Ansys HFSS: http://www.ansoft.com/products/hf/hfss/

46. Alitalo P, Culhaoglu AE, Osipov AV, Thurner S, Kemptner E, Tretyakov SA (2012) Bistatic scattering characterization of a three-dimensional broadband cloaking structure. J Appl Phys 111:034901
47. Kante B, Germain D, de Lustrac A (2009) Experimental demonstration of a nonmagnetic metamaterial cloak at microwave frequencies. Phys Rev B 80:201104(R)
48. Rainwater D, Kerkhoff A, Melin K, Soric JC, Moreno G, Alù A (2012) Experimental verification of three-dimensional plasmonic cloaking in free-space. New J Phys 14:013054
49. Alitalo P, Culhaoglu AE, Osipov AV, Thurner S, Kemptner E, Tretyakov SA (2012) Experimental characterization of a broadband transmission-line cloak in free space. IEEE Trans Antennas Propagat 60(10):4963–4968
50. Bowman JJ, Senior TBA, Uslenghi PLE (eds) (1969) Electromagnetic and acoustic scattering by simple shapes. North-Holland Publishing Company, Amsterdam
51. Vehmas J, Alitalo P, Tretyakov SA (2012) Experimental demonstration of antenna blockage reduction with a transmission-line cloak. IET Microw Antennas Propagat 6:830–834
52. Serdyukov AN, Semchenko IV, Tretyakov SA, Sihvola A (2001) Electromagnetics of bi-anisotropic materials: theory and applications. Gordon and Breach Science Publishers, Amsterdam
53. Tretyakov SA, Mariotte F, Simovski CR, Kharina TG, Heliot J-P (1996) Analytical antenna model for chiral scatterers: comparison with numerical and experimental data. IEEE Trans Antennas Propagat 44:1006–1014
54. Collin RE (2001) Foundations for Microwave Engineering, 2nd edn. IEEE Press, New York
55. Belov PA, Simovski CR (2005) Homogenization of electromagnetic crystals formed by uniaxial resonant scatterers. Phys Rev E 72:026615
56. Belov PA, Simovski CR (2005) Subwavelength metallic waveguides loaded by uniaxial resonant scatterers. Phys Rev E 72:036618
57. Tretyakov S (2003) Analytical Modeling in Applied Electromagnetics. Artech House, Norwood
58. Maslovski S, Ikonen P, Kolmakov I, Tretyakov S, Kaunisto M (2005) Artificial magnetic materials based on the new magnetic particle: metasolenoid. Progress in Electromagnetics Research 54:61–81
59. Tretyakov SA, Maslovski SI, Nefedov IS, Viitanen AJ, Belov PA, Sanmartin A (2003) Artificial tellegen particle. Electromagnetics 23:665–680

Chapter 12
Broadening of Cloaking Bandwidth by Passive and Active Techniques

Silvio Hrabar, Zvonimir Sipus and Iva Malcic

Abstract This chapter deals with the most serious drawback of transformation electromagnetic-based cloaking devices: narrow operating bandwidth (BW). It is shown that the maximal operating BW of every passive cloak is limited by the basic background physics (so-called energy-dispersion constraints). It is also shown possible to optimize the cloak parameters in order to achieve either the maximal BW or the maximal invisibility gain (IG). Finally, it is shown possible to go around the dispersion-energy constraints by inclusion of non-Foster active components, and to achieve a very broad operating BW that fairly exceeds the BW of passive cloaks.

12.1 Introduction

The realization of structures that do not scatter electromagnetic fields, i.e., structures that appear 'invisible' for EM waves, is not a new concept. The possibility of a plane wave passing without distortions through a structure with an anisotropic filling was first investigated theoretically in the 1960s [1]. The basis of the work was the invariance property of Maxwell's equations with respect to the transformation of space metric and permeability and permittivity tensors of the medium. In [2–3] it was shown that for certain combinations of permittivities in a two-layer

S. Hrabar (✉) · Z. Sipus · I. Malcic
Faculty of Electrical Engineering and Computing, University of Zagreb,
Unska 3 HR-10000 Zagreb, Croatia
e-mail: Silvio.Hrabar@fer.hr

Z. Sipus
e-mail: Zvonimir.Sipus@fer.hr

I. Malcic
e-mail: ivaelizabeta@gmail.com

D. H. Werner and D.-H. Kwon (eds.), *Transformation Electromagnetics and Metamaterials*, DOI: 10.1007/978-1-4471-4996-5_12,

dielectric ellipsoid, the scattered field is zero. The analysis revealed that at least one of the layers should have relative permittivity smaller than one (with $0 < \varepsilon_r < 1$). This property is a result of local negative polarizability, which is inherent to plasma, plasmonic materials, and plasma-like epsilon-near-zero (ENZ) metamaterials.

Plasmonic and plasma-like metamaterials (and their counterparts, mu-near-zero metamaterials (MNZ), in which $0 < \mu_r < 1$) are also used in plasmonic cloaking. Plasmonic cloaking is, in the simplest case, based on cancelation of scattering from a shell that encloses an object (target) and the scattering from the object itself [4].

Probably the most commonly reported cloaking approach is based on Transformation Electromagnetics (TO) [5]. This approach controls the propagation paths of electromagnetic waves within an anisotropic cylindrical (or spherical) shell, with an object placed in the center. More precisely, a special (meta)-material was used to render a volume effectively invisible to incident radiation, i.e., to squeeze space from a volume into a cylindrical (or spherical) shell surrounding the concealment volume. The coordinate transformations used do not influence the form of Maxwell's equations, but they affect permittivity and permeability tensors (ε and μ, respectively), making the needed (meta)-materials spatially varying and anisotropic. It is important to notice that some parts of the cloak must have local ENZ or MNZ properties. When viewed externally, the concealed volume and the cloak both appear to have propagation properties of free space, i.e., they appear invisible to electromagnetic waves.

The basic principles of both plasmonic and transformational electromagnetic cloaks have already been demonstrated theoretically and experimentally in numerous studies [4–6]. However, the achieved 'cloaking bandwidth (CBW)' (the bandwidth (BW) in which the scattering cross-section of the cloaked target is lower that the scattering cross-section of a bare target) is rather narrow. Some representative BWs vary from only 0.24 % in the case of anisotropic cloaking [7] up to 10 % for plasmonic cloaking [4]. Clearly, these BWs are too narrow for most practical applications. The inherent narrowband operation is probably the most serious problem for possible future applications of cloaking technology.

It should be noted that for some of the proposed cloak designs there is no need to use metamaterial structures. For example, hard surfaces have been used in the design of supporting struts of reflector antenna feeds [8], and parallel-plate waveguide structures have been used to reduce scattering from dielectric or metallic obstacles [9, 10]. Several other concepts for obtaining invisible scatterers were proposed, like minimum scattering antennas and active scatterers [11, 12].

The purpose of this chapter is to analyze the physical background of inherent narrowband cloaking of an anisotropic cloak and propose the methods of BW enhancement.

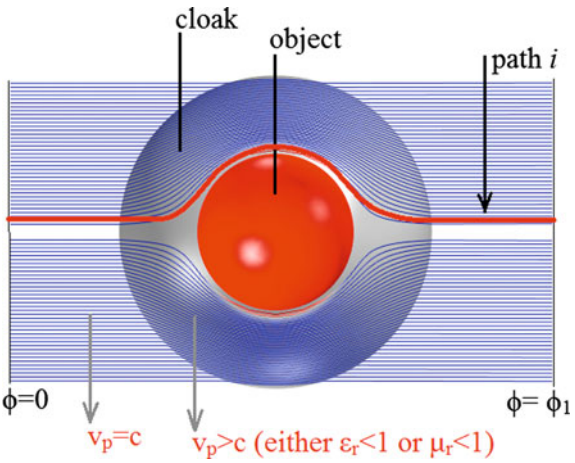

Fig. 12.1 EM wave propagation inside the cloak

12.2 Basics of Anisotropic Transformation Electromagnetics Cloak

The commonly used (simplified) explanation of a TO 2D cloak [5, 7] is sketched in Fig. 12.1.

It depicts a plane wave impinging on an object covered by an ideal cloak. The ideal cloak is a lossless cylindrical shell constructed in such a way that it does not allow the existence of a scattered field. Therefore, the distribution of the EM fields on an arbitrary plane behind the object (both amplitude and phase) must be equal to the distribution that would exist on the same plane if there were no object. The cloak should actually 'bend' the flow of EM energy around the object, maintaining the unchanged amplitude and phase distributions on the observation plane. Each 'ray' should travel along a path that is obviously longer than the path in free space, which means that the phase velocity (v_p) must be greater than the speed of light (c) (so-called 'superluminal propagation'). In other words, this type of cloak must employ anisotropic materials that, within some spatial regions, have either local relative effective permittivity (ε_r) or local relative effective permeability (μ_r) greater than zero, but smaller than one, i.e., an ENZ material with $0 < \varepsilon_r < 1$ or a MNZ material with $0 < \mu_r < 1$. The mathematical background of the transformation cloak is briefly explained in the next paragraph.

12.2.1 Fully Anisotropic Cloak

A circular-cylindrical cloak oriented with the axis in z-direction as shown in Fig. 12.2 is considered.

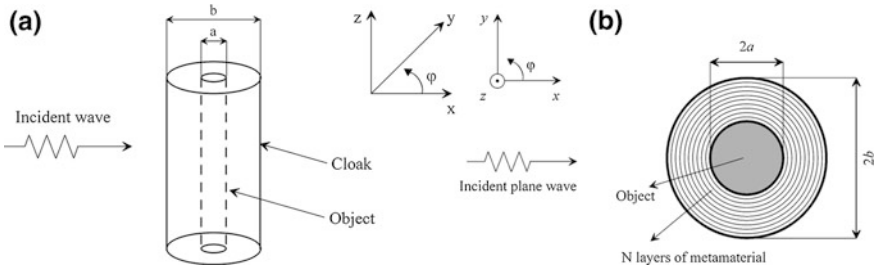

Fig. 12.2 A sketch of the anisotropic cloak. **a** A general case with hypothetical continuous material. **b** Multilayer realization

The inner and outer radii of the cloak are denoted with a and b, respectively. The permeability and permittivity tensors in the cylindrical coordinate system are given by:

$$\underline{\mu} = \mu_0 \begin{bmatrix} \mu_{\rho\rho} & 0 & 0 \\ 0 & \mu_{\phi\phi} & 0 \\ 0 & 0 & \mu_{zz} \end{bmatrix}, \tag{12.1}$$

$$\underline{\varepsilon} = \varepsilon_0 \begin{bmatrix} \varepsilon_{\rho\rho} & 0 & 0 \\ 0 & \varepsilon_{\phi\phi} & 0 \\ 0 & 0 & \varepsilon_{zz} \end{bmatrix}. \tag{12.2}$$

For the cloak design, a coordinate transformation which compresses free space from a cylindrical region $0 < \rho < b$ into a concentric cylindrical shell $a < \rho' < b$ is applied. Actually, the design of a cloaking structure is based on the transformation of space (or, loosely speaking, transformation of a Cartesian coordinate system into a new curvilinear system). Maxwell's equations are invariant under spatial transformations, i.e., they take the same form in the transformed coordinate system:

$$\nabla' \times \mathbf{E}' = -j\omega\boldsymbol{\mu}'\mathbf{H}', \quad \nabla' \times \mathbf{H}' = j\omega\boldsymbol{\varepsilon}'\mathbf{E}'. \tag{12.3}$$

Here $\mathbf{E}'$ and $\mathbf{H}'$ are electric and magnetic fields in transformed space. The permeability and permittivity tensors $\boldsymbol{\mu}'$ and $\boldsymbol{\varepsilon}'$ are related to the tensors $\boldsymbol{\mu}$ and $\boldsymbol{\varepsilon}$ in the original space via simple equations:

$$\boldsymbol{\mu}' = \frac{\mathbf{A}\boldsymbol{\mu}\,\mathbf{A}^T}{\det \mathbf{A}}, \quad \boldsymbol{\varepsilon}' = \frac{\mathbf{A}\boldsymbol{\varepsilon}\mathbf{A}^T}{\det \mathbf{A}}, \tag{12.4}$$

where $\mathbf{A}$ is the Jacobian matrix of the spatial transformation

$$\mathbf{A} = \begin{bmatrix} \partial x'/\partial x & \partial x'/\partial y & \partial x'/\partial z \\ \partial y'/\partial x & \partial y'/\partial y & \partial y'/\partial z \\ \partial z'/\partial x & \partial z'/\partial y & \partial z'/\partial z \end{bmatrix}. \tag{12.5}$$

In the considered case the circular annular cloak is obtained by using the following transformation:

$$\rho' = a + \frac{b-a}{b}\rho, \quad \phi' = \phi, \quad z' = z, \tag{12.6}$$

and the Jacobian matrix is given by

$$A = \begin{bmatrix} \frac{b-a}{b} & 0 & 0 \\ 0 & \frac{\rho'}{\rho} & 0 \\ 0 & 0 & 1 \end{bmatrix} \tag{12.7}$$

This transformation allows the design of a 2D cylindrical electromagnetic invisibility cloak by compressing all the fields from the region $\rho < b$ into the region $a < \rho < b$ so that the permittivity and permeability of the medium located within the cloaking shell are free to take any value without contributing to electromagnetic scattering. For $a < \rho < b$ the permittivity and permeability values are [13]:

$$\begin{aligned} \varepsilon_{\rho\rho} &= \mu_{\rho\rho} = \tfrac{\rho-a}{\rho} \\ \varepsilon_{\phi\phi} &= \mu_{\phi\phi} = \tfrac{\rho}{\rho-a} \\ \varepsilon_{zz} &= \mu_{zz} = \left(\tfrac{b}{b-a}\right)^2 \tfrac{\rho-a}{\rho} \end{aligned} \tag{12.8}$$

It should be noted that all the components of the tensors are functions of radius, which implies a very complicated metamaterial design. This is referred to as an ideal anisotropic cloak and it is insensitive to the polarization of an incoming wave. Realization of such a cloak has not yet been reported. The fabrication of a metamaterial with continuous spatial variation of effective parameters is not feasible at the present state of art. Hence, it is common practice to use a stepwise approximation of the continuous variation of constitutive parameters by use of n different metamaterial layers (each of them with some prescribed values of effective parameters; Fig. 12.2) Several cloak designs intended to work when illuminated with a normal incident plane wave of specific polarization [5, 14] are described in the next two paragraphs.

12.2.2 Simplified TM Cloak

The metamaterial cloak reported in [5], is intended for use with the TM_z polarization. It is clear that only ε_{zz}, $\mu_{\rho\rho}$ and $\mu_{\phi\phi}$ components are relevant in this case. Therefore, it is possible to vary the values of permeability and permittivity tensors as long as the products $\varepsilon_{zz} \cdot \mu_{\rho\rho}$ and $\varepsilon_{zz} \cdot \mu_{\phi\phi}$ are kept the same. In addition, a significantly simplified design can be achieved by fixing the values of ε_{zz} and $\mu_{\phi\phi}$

Table 12.1 The values of permittivity and permeability tensors of the considered cloaks (a and b represent the inner and outer radius of the cloak, and ρ is the radial coordinate)

Ideal anisotropic cloak [13]	TM cloak [5]	TE cloak [14]
$\varepsilon_{\rho\rho} = \mu_{\rho\rho} = \frac{\rho-a}{\rho}$	$\mu_{\rho\rho} = \left(\frac{\rho-a}{\rho}\right)^2$	$\varepsilon_{\rho\rho} = \left(\frac{b}{b-a}\right)^2\left(\frac{\rho-a}{\rho}\right)^2$
$\varepsilon_{\phi\phi} = \mu_{\phi\phi} = \frac{\rho}{\rho-a}$	$\mu_{\phi\phi} = 1$	$\varepsilon_{\phi\phi} = \left(\frac{b}{b-a}\right)^2$
$\varepsilon_{zz} = \mu_{zz} = \left(\frac{b}{b-a}\right)^2\frac{\rho-a}{\rho}$	$\varepsilon_{zz} = \left(\frac{b}{b-a}\right)^2$	$\mu_{zz} = 1$

(ε_{zz} is determined by the supporting dielectric material and $\mu_{\phi\phi}$ is simply equal to 1), and letting only $\mu_{\rho\rho}$ vary along the radial direction:

$$\mu_{\rho\rho} = \left(\frac{\rho-a}{\rho}\right)^2,\ \mu_{\phi\phi} = 1,\ \varepsilon_{zz} = \left(\frac{b}{b-a}\right)^2. \tag{12.9}$$

The first cloak based on this principle [5] was implemented using an inclusion-based metamaterial (Sect. 12.3.3) in a 10 GHz microwave band. The cloak was put into a scattering chamber and measurements of the distribution of the vertical component of the electric field around the cloak were performed. The obtained results showed a noticeable decrease of the scattered field. Although the level of the scattered field was not quantified, it was the first successful realization of the TO cloaking principle.

12.2.3 Simplified TE Cloak

Similarly to the realization of a so-called TM_z cloak, a TE_z version of the TO cloak was suggested theoretically for applications in the optical regime [14]. In the TE_z cloak only the components μ_{zz}, $\varepsilon_{\rho\rho}$ and $\varepsilon_{\phi\phi}$ are relevant, making it possible to simplify the metamaterial design by allowing only $\varepsilon_{\rho\rho}$ to vary in the radial direction:

$$\varepsilon_{\rho\rho} = \left(\frac{b}{b-a}\right)^2\left(\frac{\rho-a}{\rho}\right)^2,\ \varepsilon_{\phi\phi} = \left(\frac{b}{b-a}\right)^2,\ \mu_{zz} = 1. \tag{12.10}$$

Again, the products $\varepsilon_{\rho\rho}\cdot\mu_{zz}$ and $\varepsilon_{\phi\phi}\cdot\mu_{zz}$ are kept the same. The first practical realization in the microwave frequency range was presented in Kanté et al. [6, 15]. Table 12.1 gives the comparison of the permittivity and permeability values of fully anisotropic, TM_z and TE_z cloaks.

12.3 Cloaking Phenomenon Frequency Dependence

12.3.1 *Influence of Material Dispersion on Cloaking Bandwidth*

Ordinary materials (with $\varepsilon_r > 0$ and $\mu_r > 0$) are usually considered to be frequency independent (dispersionless) across the entire RF spectrum. It would be very convenient to have a similar behavior in the case of ENZ and MNZ metamaterials used in cloaking technology (Fig. 12.3a). Unfortunately, the values of the constitutive parameters of ENZ or MNZ metamaterials change significantly with frequency. This change is, in general, described by the Lorentz dispersion model (Fig. 12.3b).

It is intuitively clear that the Lorentz dispersion curve (Fig. 12.3b) should describe a resonant process that occurs in ENZ and MNZ metamaterials. Due to this resonant process, the losses and the operating BW are inevitably mutually dependent. This can also be seen from the mathematical description of the Lorentz model [16]:

$$\mu_{\text{eff}}(\varepsilon_{\text{eff}}) = 1 - \frac{\omega_{\text{ser}}^2 - \omega_{\text{par}}^2}{\omega^2 - \omega_{\text{par}}^2 + j\gamma\frac{\omega}{2\pi}}. \tag{12.11}$$

Here, ω is the angular frequency of the signal, ω_{ser} denotes the angular frequency of the 'series resonance', at which, in a lossless case $\mu_{\text{eff}} = 0$ (or $\varepsilon_{\text{eff}} = 0$) ('plasma frequency'). The symbol ω_{par} stands for the angular frequency of the

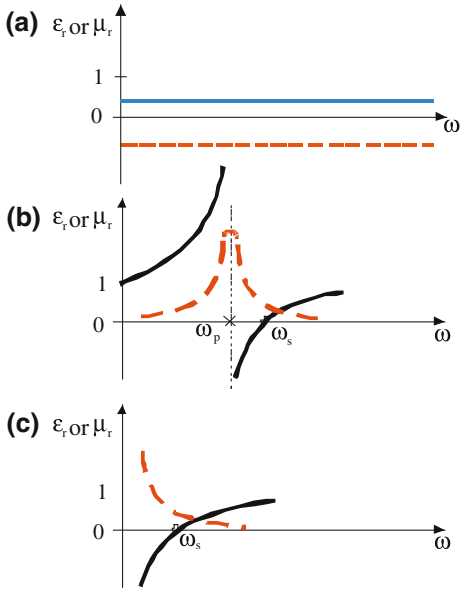

Fig. 12.3 Dispersion behavior of different metamaterials. **a** Behavior of fictitious lossless and dispersionless metamaterial, *solid*—ENZ or MNZ metamaterial, *dashed*—ENG or MNG metamaterial. **b** Behavior of realistic metamaterial with Lorentz dispersion. **c** Behavior of realistic metamaterial with Drude dispersion *solid*—real part, *dashed*—imaginary part

'parallel resonance', at which μ_{eff} (or ε_{eff}) diverges, and γ represents losses. This is a general dispersion model, while some metamaterials obey a simplified Lorentz model, in which $\omega_{\text{par}} = 0$ (the Drude dispersion model) [16]:

$$\mu_{\text{eff}}(\varepsilon_{\text{eff}}) = 1 - \frac{\omega_{\text{ser}}^2}{\omega^2 + j\gamma\frac{\omega}{2\pi}}. \tag{12.12}$$

Unfortunately, the direct comparison of the BWs of different metamaterials is not so straightforward. In the metamaterial community, the term (operating) BW is often used for the frequency band in which a particular constitutive parameter has the required sign (for instance the BW of negative permittivity or negative permeability). This (loosely constructed and certainly imprecise) definition led to the commonly accepted opinion that transmission-line-based metamaterials are inherently broadband. Indeed, the fractional BW, in which the constitutive parameters are negative (i.e., the backward-wave propagation band) can be as wide as 50 % in the case of the transmission-line-based metamaterials [17–19]. This is not the case for the split-ring-resonator (SRR) or complementary split-ring-resonator (CSRR) types of metamaterials (see Sect. 12.3.3) which have a fractional BW of only a few percent [17–19]. However, a wide band with required negative (or near-zero) parameters does not guarantee a wideband operation for every application.

The cloaking application requires fixed (predetermined) values of constitutive parameters, therefore the change of equivalent permittivity or permeability within the required band should be minimized (this means dealing with the 'flatness' of the dispersion curve). In this chapter, a term 'dispersion bandwidth' (DBW) is used for the above-mentioned purposes. Since all types of passive metamaterials are highly dispersive compared to conventional (positive) materials, they are all inherently narrowband (Fig. 12.3c). It is interesting that this important issue, although pretty obvious, is widely overlooked. For instance, the DBW can be defined (completely arbitrarily) by accepting the change of the constitutive parameters by 15 %. In such a case, the BW of a typical SRR-based MNG metamaterial would be less than 1 % [16, 20].

The influence of metamaterial dispersion can be estimated by introducing a very simple parameter- the phase shift $\Delta\phi_i$ along a differential segment of an arbitrary path i (Fig. 12.1):

$$\Delta\phi_i = -d_i\frac{\omega}{c}\sqrt{\varepsilon_r(i,\omega)\mu_r(i,\omega)}. \tag{12.13}$$

Here d_i is the differential path length and ω the angular frequency. The arguments of the material parameters (i, ω) emphasize that effective permittivity and permeability might both depend on spatial coordinates (anisotropy) and frequency (dispersion). If dispersion is present, a change in the material parameters (μ, ε) would cause a change in the phase shift for each path. This change in the phase shift affects the operation of the cloak. In order to get a rough estimation of the influence of dispersion on the cloaking, phase shift per unit width of a simple

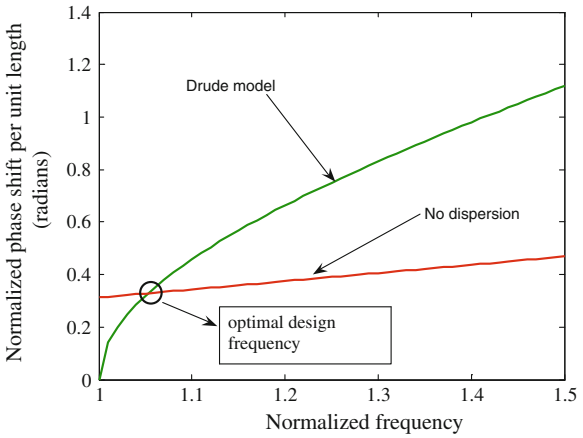

Fig. 12.4 Calculated phase shift of materials with different dispersion [53]

metamaterial slab was calculated using (12.13). The results are sketched in Fig. 12.4.

Two types of materials were used in this calculation. The first slab (green solid line) was assumed to be made out of ordinary material that obeys the Drude dispersion model (e.g., wire-based metamaterial [16, 20]). The second slab was presumably made of a hypothetical dispersionless 'plasma-like ENZ' ($0 < \varepsilon_r < 1$) material. It is clear that a dispersionless passive metamaterial does not exist in reality (in Sect. 12.7 the possibility of constructing it using active non-Foster elements will be shown). The optimal local permittivity of an anisotropic cloak is also marked. It can be seen that the change in frequency causes significant deviation of the permittivity from the optimal value. This (unwanted) effect is much more pronounced in the case of an ordinary plasmonic slab with the Drude dispersion. Hence, it appears that the material dispersion is indeed a major limiting factor on the operating BW of the proposed cloaking devices.

12.3.2 Energy-Dispersion Constraints

In order to understand the dispersion issue, some basic underlying physics of energy (W) stored within a passive loss-free material should be studied [21, 37, 53]:

$$W = \frac{1}{2}\frac{\partial[\omega \cdot \varepsilon(\omega)]}{\partial\omega}|E|^2 + \frac{1}{2}\frac{\partial[\omega \cdot \mu(\omega)]}{\partial\omega}|H|^2. \tag{12.14}$$

Here, E is the electric field and H is the magnetic field. The net energy is a strictly positive quantity, therefore $W > 0$. In addition, a certain amount of energy is necessary to polarize any material, thus the energy in (12.14) is always greater than the energy stored in vacuum (W_0):

$$W > W_0, \quad W_0 = \frac{1}{2}\varepsilon_0|E|^2 + \frac{1}{2}\mu_0|H|^2. \tag{12.15}$$

In (12.15) ε_0 and μ_0 stand for the free-space permittivity and permeability, respectively. Equations (12.14) and (12.15) lead to a strong form of well-known energy-dispersion constraints [21, 37, 53]:

$$\frac{\partial[\omega \cdot \varepsilon(\omega)]}{\partial\omega} > \varepsilon_0, \quad \frac{\partial[\omega \cdot \mu(\omega)]}{\partial\omega} > \mu_0. \tag{12.16}$$

From (12.16) it can be deduced that $(\partial\varepsilon/\partial\omega) > 0$ and $(\partial\mu/\partial\omega) > 0$ for any lossless passive material (or any metamaterial, irrespective of its internal structure). The circuit theory analog to (12.16) is Foster's reactance theorem [$(\partial X/\partial\omega) > 0$ and $(\partial B/\partial\omega) > 0$, X and B being reactance and susceptance, respectively] [22, 37, 55]. In the case of 'negative' and 'plasma-like' materials, the constraints in (12.16) actually show the existence of a resonant phenomenon.

For instance, the electric field energy stored in a material with $0 < \varepsilon_r < 1$ (ENZ) should always be lower than the energy stored in the electric field in vacuum. The only way to achieve this without violating (12.16) is to *redistribute* a fraction of the energy from the electric field into the magnetic field. Due to causality, the energy redistribution cannot occur instantaneously but it is a dynamic process that occurs within each period of applied EM field. The amount of redistributed energy is a function of frequency and it reaches its maximum at one specific frequency. Thus, the process of energy redistribution is actually *a resonant process* that occurs in *every passive* ENZ (*meta*)*-material* causing dispersion and narrowband operation.

In the case of natural plasma, this resonant process is related to mechanical oscillations of free electrons excited by the applied dynamic electric field. A very similar process takes place in a passive metamaterial, however, on the macroscopic level, within some kind of electromagnetic resonator.

12.3.3 Passive ENZ and MNZ Metamaterials Used in Cloak Realization

Roughly speaking, ENZ and MNZ passive metamaterials used in cloak realization fall into one of two main groups: transmission-line-based metamaterials and inclusion-based metamaterials. The background physics of both types of metamaterials deals with the resonant energy exchange that causes dispersion. A typical one-dimensional (1D) implementation of ENZ metamaterial uses a transmission line periodically loaded with lumped inductances (Fig. 12.5a).

Here, Z and Y stand for the distributed impedance and admittance of the line, respectively. Apart from the transmission line implementation, this equivalent circuit describes a well-known wire medium [17]. The resonator in Fig. 12.5a is actually a tank circuit formed by the line shunt capacitance $C\Delta x$ (C being the

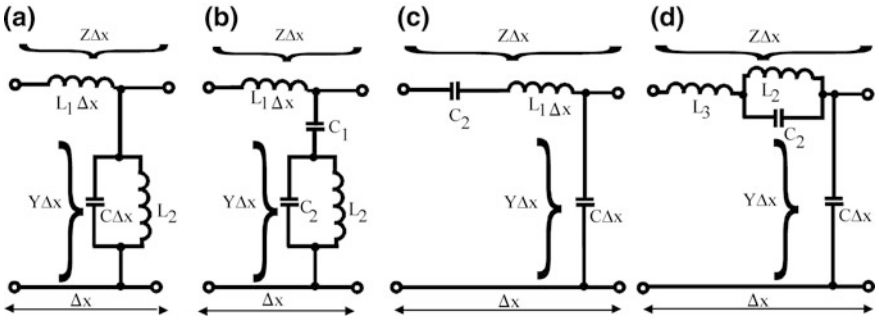

Fig. 12.5 Equivalent circuits of a differential section of different passive 1D ENZ metamaterials. **a** Passive ENZ metamaterial that obeys Drude dispersion model. **b** Passive ENZ metamaterial that obeys Lorentz dispersion model. **c** Passive MNZ metamaterial that obeys Drude dispersion model. **d** Passive MNZ metamaterial that obeys Lorentz dispersion model

distributed capacitance and Δx being the line segment length) and a lumped inductor L_2. This circuit obeys the Drude dispersion model (i.e., the Lorentz model with $\omega_p = 0$):

$$\varepsilon_r(\omega) = \frac{Y(\omega)}{j\omega\varepsilon_0} = \frac{j\omega\left(C - \frac{1}{\omega^2 L_2 \Delta x}\right)}{j\omega\varepsilon_0} = \left[\frac{1}{\varepsilon_0}\left(C - \frac{1}{\omega^2 L_2 \Delta x}\right)\right]. \tag{12.17}$$

Above the resonant frequency there is "a lack" of energy stored in the electric field (it is converted into the energy stored in the magnetic field). Within this narrow band, the expression in square brackets in (12.17) has a value smaller than one, which shows ENZ behavior ($0 < \varepsilon_r < 1$). In the above analysis, an ideal tight coupling between the inductance and the main transmission line (or with free space in the case of a wire medium) is assumed. In the case of an inclusion-based metamaterial (an array of inductively loaded short dipoles [17]), the coupling is not tight and it can be modeled as coupling via a distributed capacitance (Fig. 12.5b). Additional capacitance introduces an additional resonance turning the Drude dispersion model into the Lorentz dispersion model:

$$\varepsilon_r(\omega) = \frac{Y(\omega)}{j\omega\varepsilon_0} = \frac{j\omega C_1(1 - \omega^2 L_2 C_2)}{j\omega\varepsilon_0(1 - \omega^2 L_2(C_1 + C_2))}\frac{1}{\Delta x} = \left[\frac{1}{\varepsilon_0 \Delta x}\frac{C_1(1 - \omega^2 L_2 C_2)}{(1 - \omega^2 L_2(C_1 + C_2))}\right] \tag{12.18}$$

Similarly, in the case of a transmission-line-based MNZ metamaterial the distributed reactance will be a series LC tank circuit that modifies equivalent permeability. The equivalent relative permeability can be derived easily:

$$\mu_r(\omega) = \frac{Z(\omega)}{j\omega\mu_0} = \frac{j\omega\left(L_1 - \frac{1}{\omega^2 C_2 \Delta x}\right)}{j\omega\mu_0} = \left[\frac{1}{\mu_0}\left(L_1 - \frac{1}{\omega^2 C_2 \Delta x}\right)\right]. \tag{12.19}$$

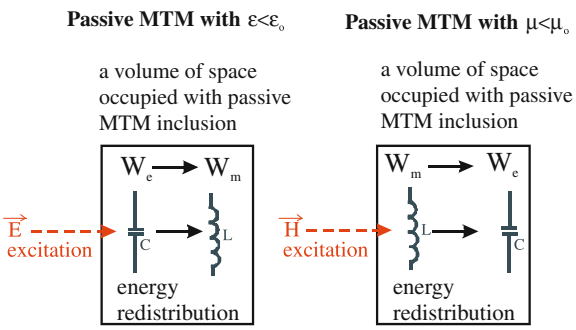

Fig. 12.6 The basic principle of passive ENZ and MNZ metamaterials

Here, there is again the Drude resonant behavior due to the decrease of the amount of energy stored in the magnetic field above the resonant frequency. In the case of non-ideal coupling [the case of an array of capacitively loaded small loops (SRR)] a parallel LC circuit will be coupled via additional coupling inductance (Fig. 12.5d). This additional inductance introduces the additional resonance turning the Drude dispersion model into the Lorentz dispersion model:

$$\mu_r(\omega) = \frac{Z(\omega)}{j\omega\mu_0} = \frac{\left(j\omega L_3 + \frac{j\omega L_2}{1-\omega^2 L_2 C_2}\right)\frac{1}{\Delta x}}{j\omega\mu_0} = \frac{1}{\mu_0 \Delta x}\left[L_3 + \frac{L_2}{1-\omega^2 L_2 C_2}\right]. \quad (12.20)$$

It is important to stress that all known passive metamaterials (SRR-based [17], wire-based [17], CSRR-based [17], transmission-line-based [18, 19], 'fishnet'-based [23], etc.) behave in a very similar way. Thus, all known passive metamaterials (within some frequency range) show a phenomenon of resonant energy exchange (Fig. 12.6) and, inevitably, exhibit dispersion. This dispersion will always limit the CBW.

Some ENZ and MNZ metamaterials commonly used in cloaking technology are compared in Table 12.2. Since every cloaking device contains at least several layers of different metamaterials, the CBW will always be smaller than the DBW of a particular metamaterial.

12.3.4 Quantification of Cloaking Bandwidth

Previous analysis led to the conclusion that cloaking is always frequency dependent due to inherent dispersion. Therefore, 2D radar cross-section (the scattering width) [24] was introduced as a parameter for the quantitative comparison of different cloaks. It is defined as a ratio of scattered power per unit length of an infinite cylindrical object (target):

Table 12.2 Comparison of passive metamaterials used in cloaking technology

Type of passive MTM		Dispersion model	Typical bandwidth		Typical loss	Mechanism of NG and NZ behavior
			BW (%)	DBW (%)		
Wire medium [17]		Drude	50	15	Not pronounced (FOM $\approx$ 10)	Resonant energy redistribution caused by energy-dispersion constraints (Foster's theorem)
Resonant inclusions [18]	Inductively loaded dipole (loop-wire, CSRR)	Lorentz	5	1	Pronounced (FOM $\approx$ 0.5–1)	
	Capacitively loaded loop (SRR)	Lorentz	5	1		
Transmission-line-based [18, 19]		Drude	50	15	Not pronounced (FOM $\approx$ 5–10)	

Here, FOM stands for figure of merit defined as a ratio of real and imaginary parts of equivalent permittivity (or permeability)

$$\sigma_{2D}(\phi) = \lim_{\rho\to\infty}\left[2\pi\rho\frac{P_s(\phi)}{P_i}\right] = \lim_{\rho\to\infty}\left[2\pi\rho\frac{|E_s(\phi)|^2}{|E_i|^2}\right]. \tag{12.21}$$

Here σ_{2D} is the scattering width and ρ is the radial distance defined in Fig. 12.2. The symbols P_s and P_i stand for scattered and incident power densities (modulus of associated Poynting vectors) while E_s and E_i stand for scattered and incident electric fields, respectively. Scattering width can be defined for any observation angle (ϕ), hence (12.21) defines a so-called bistatic scattering width. It is very convenient for identifying the direction of maximal scattering for a particular application.

However, in order to achieve ideal cloaking, the scattering width should be zero for all observation angles. Therefore, total scattering width is defined as:

$$\sigma_T = \int_{\phi=0}^{\phi=2\pi} \sigma_{2D}(\phi)\,\mathrm{d}\phi. \tag{12.22}$$

In addition, 'invisibility gain' (IG) can be defined as a ratio of the scattering width of a bare object and the scattering width of a cloaked object:

$$\mathrm{IG} = \frac{\sigma_{\mathrm{Tobject}}}{\sigma_{\mathrm{Tcloak}}}. \tag{12.23}$$

Finally, in order to compare different cloaks it is convenient to define the 'CBW', i.e., the BW in which the invisibility gain is higher than one (IG $>$ 1).

12.4 Analysis of Passive Cylindrical Cloaks

12.4.1 Mathematical Background

The circular-cylindrical cloak from Fig. 12.2 is considered, assuming that the object to be hidden is a simple PEC cylinder. The incident plane wave propagates in the positive x-direction (i.e., normal incidence), while the electric field is assumed to be parallel with the z-axis (TM_z polarization; the TE_z polarization can be treated in the same way). In cylindrical coordinates the E_z electric field component of the incident wave is given in the form:

$$E_z^{\text{inc}}(\rho,\phi) = E_0 \sum_{m=-\infty}^{\infty} j^m J_m(k_0\rho)e^{-jm\phi} \tag{12.24}$$

where J_m is the m-th order Bessel function of the first kind and k_0 is the wave number ($k_0 = 2\pi/\lambda_0$). The scattered field has the form:

$$E_z^{\text{scat}}(\rho,\phi) = E_0 \sum_{m=-\infty}^{\infty} R_m H_m^{(2)}(k_0\rho)e^{-jm\phi} \tag{12.25}$$

Here R_m represents the complex amplitudes of scattered outgoing cylindrical waves and $H_m^{(2)}$ is the Hankel function of the second kind of order m. Since the incident wave propagates perpendicularly to the cylinder axis, there is no variation of the field in the z-direction (i.e., $\frac{\partial}{\partial z} = 0$). Consequently, the curl Maxwell equations can be written as:

$$\begin{aligned} H_\rho &= -\tfrac{1}{j\omega\mu_\rho\rho}\tfrac{\partial E_z}{\partial\phi} \\ H_\phi &= -\tfrac{1}{j\omega\mu_\phi}\tfrac{\partial E_z}{\partial\rho} \\ \tfrac{1}{\rho}\left(\tfrac{\partial}{\partial\rho}(rH_\phi) - \tfrac{\partial H_\rho}{\partial\rho}\right) &= j\omega\varepsilon_z E_z \end{aligned} \tag{12.26}$$

By combining these equations and assuming a piecewise constant approximation of radial permeability variation, the following form of Bessel's differential equation for the E_z component of the electric field is obtained:

$$\rho^2\frac{\partial^2 E_z}{\partial\rho^2} + \rho\frac{\partial E_z}{\partial\rho} + (k^2\rho^2 - \overline{m}^2)E_z = 0 \tag{12.27}$$

where $k = \omega^2\mu_\phi\varepsilon_z$ and $\overline{m}^2 = m\sqrt{\mu_\phi/\mu_r}$. The general solution of (12.27) is:

$$C_1 J_{\overline{m}}(k\rho) + C_2 H_{\overline{m}}^{(2)}(k\rho), \tag{12.28}$$

where C_1 and C_2 represent constants (to be determined from the boundary conditions), while $J_{\overline{m}}$ and $H_{\overline{m}}^{(2)}$ are Bessel functions of the first kind and Hankel functions of the second kind of order $\overline{m}$, respectively. For the TE_z cloaking

Table 12.3 Dimensions of the cylindrical cloak

	Dimension (cm)	Dimension (wavelength)
Inner diameter $2a$	5.42	1.44
Outer diameter $2b$	11.78	3.34
Thickness of one layer (10-layer case)	0.318	0.09

cylinder the equivalent differential equation is obtained by applying the substitutions $E_z \rightarrow H_z,\ \varepsilon \rightarrow \mu$ and $\mu \rightarrow \varepsilon$. It should be noted that the resulting order of the Bessel functions ($\overline{m}$) for both cloaks is not an integer and it depends on both permeability and permittivity tensors (μ and ε).

The results given in this chapter are calculated using the G1DMULT algorithm [25], which calculates the spectral-domain Green's functions in the same way for planar, circular-cylindrical and spherical geometries. The algorithm is based on dividing the multilayer problem into equivalent subproblems, one for each dielectric layer. For normal incidence the fields inside each layer of the cylindrical structure are of the form (e.g., the E_z component):

$$E_z(\rho, m) = a_m^i J_{\overline{m}}(k^i \rho) + b_m^i H_{\overline{m}}^{(2)}(k^i \rho). \tag{12.29}$$

Here k^i is the wave number in i-th layer, and a_m^i and b_m^i are the unknown coefficients to be determined. The equivalent subproblems are interrelated (and the coefficients a_m^i and b_m^i are calculated) by enforcing the continuity of tangential components of electric and magnetic fields over the layer interfaces, in the spectral domain. More details about G1DMULT can be found in [25].

In order to quantify the level of "invisibility" achieved by metamaterials, total scattering width (σ_T) of the cloaked cylinder was calculated (Sect. 12.3.4). It can be calculated using the following expression [24]:

$$\sigma_T = \frac{4}{k_0} \sum_{n=-\infty}^{\infty} \left[|R_n|^2 + |C_n|^2 \right], \tag{12.30}$$

where R_n and C_n are the co-polarization and cross-polarization contributions, respectively. For normal incidence C_n coefficients are equal to zero, but for oblique incidence the presence of the cloak induces cross-polarization components (see [26] for details). The angular variation of bistatic scattering width $\sigma_T(\phi)$ was calculated so as to check for any direction with distinctively stronger scattered field.

The intention was to thoroughly investigate the cloak that was experimentally realized by Schurig et al. [5]. Therefore, the same dimensions and the working frequency as in the experimental model case were selected (see Table 12.3).

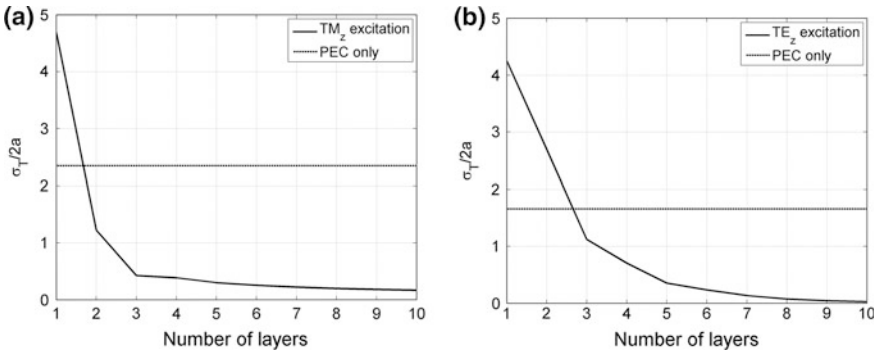

Fig. 12.7 Normalized total scattering width versus number of layers for ideal cloak. **a** TM_z polarization. **b** TE_z polarization [7]

12.4.2 Dependence of Scattering Width on Design Parameters

First the influence of the stepwise approximation of the continuous variation of constitutive parameters was investigated (Fig. 12.2b). In order to analyze how the subtlety of the approximation of radial anisotropy influences the total scattering width, i.e., "the invisibility", the required radial variation of constitutive parameters has been approximated by 1–10 step piecewise constant functions.

Due to full anisotropy, the ideal cloak is supposed to work for arbitrary polarization (material parameters are given in Table 12.1). Hence, complete analysis is provided for both the cloak excited by the TE_z and the cloak excited by TM_z polarized waves. The simulations were performed at the central frequency (8.5 GHz). The calculated total scattering width and the angular variation of bistatic scattering width are shown in Figs. 12.7 and 12.8, respectively. It can be

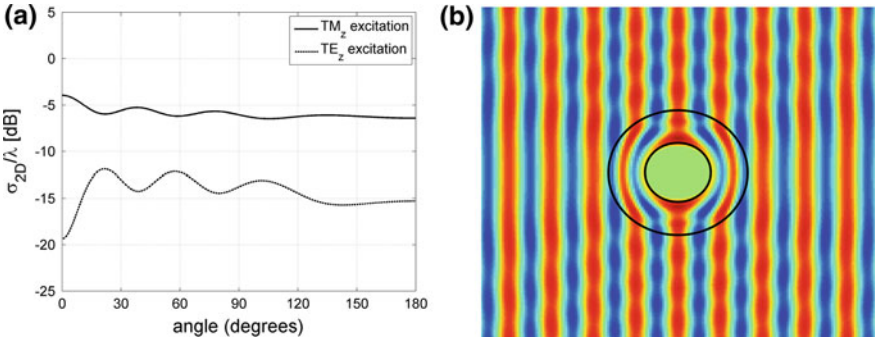

Fig. 12.8 **a** Normalized bistatic scattering width (TM_z and TE_z polarizations) [7]. **b** Electric field distribution in the vicinity of the cloaked object (TM_z polarization) of the 10-layer realization of an ideal cloak

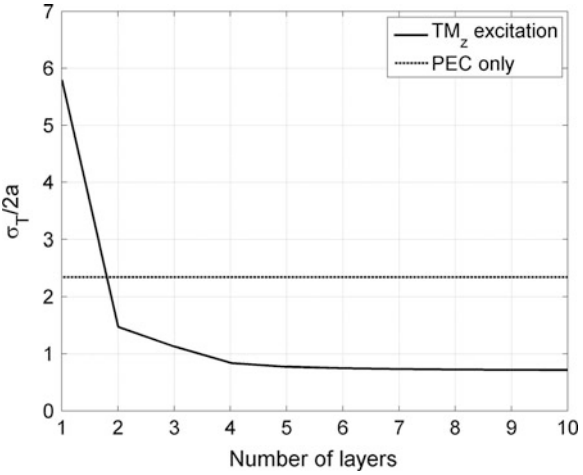

Fig. 12.9 Normalized total scattering width versus number of layers for the TM_z cloak (TM_z polarization) [7]

seen that by increasing the number of metamaterial layers, the achieved invisibility improves. Thus, it can be concluded that the 10-layer approximation of a continuous anisotropic structure is good enough for practical purposes (even the 5-layer realization has a very good performance). It can also be noted that the level of the scattered field is low for both polarizations and, as expected, invisibility was achieved for both excitations.

For the TM_z cloak, the coordinate transformations for metamaterial design have been simplified, so the metamaterial constitutive parameters were calculated by Eq. (12.9). Such a simplified cloak should work only for the TM_z polarization. The normalized total scattering width is given in Fig. 12.8, and it can be seen that for structures with more than 5 layers there is practically no improvement of the obtained invisibility—the obtained total scattering width reduction is around 3. The main reason for such a small gain was the reflection of the incident wave from the cloak surface due to the impedance mismatch. The level of scattered power can be approximated by

$$\frac{\left(\sigma_T^{\text{Cloak}}/2b\right)\big|_{\text{CLOAK}}}{\left(\sigma_T^{\text{PEC}}/2a\right)\big|_{\text{PEC}}} \approx \left|\frac{\eta-1}{\eta+1}\right|^2 = \left|\frac{\sqrt{\mu_{\phi\phi}/\varepsilon_{zz}}-1}{\sqrt{\mu_{\phi\phi}/\varepsilon_{zz}}+1}\right|^2 = \left(\frac{a}{2b-a}\right)^2. \qquad (12.31)$$

Here CLOAK and PEC denote the total scattering width of the cloaked and uncloaked cylinder, respectively. The comparison of the calculated (0.15) and the approximated value (0.09) suggests that the main reason the Schurig cloak scatters a large amount of power is the impedance mismatch. The angular variation of the scattered electric field and the field distribution in the vicinity of the cloaked object are given in Fig. 12.9 and show that the reflection from the cloak surface causes ripples in the electric field distribution.

For the cross-polarization excitation (TE_z) the radial anisotropy of μ_r does not affect the value of calculated total scattering width. This is because the magnetic field

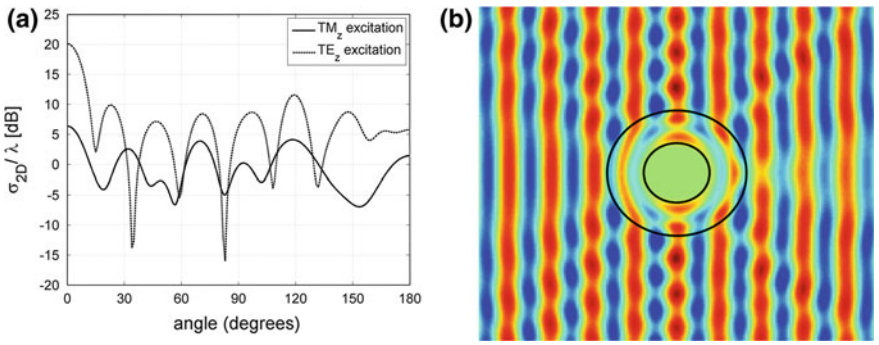

Fig. 12.10 **a** Normalized bistatic scattering width (TM_z and TE_z polarizations) [7]. **b** Electric field distribution in the vicinity of the cloaked object (TM_z polarization) of the 10-layer realization of a TM_z cloak

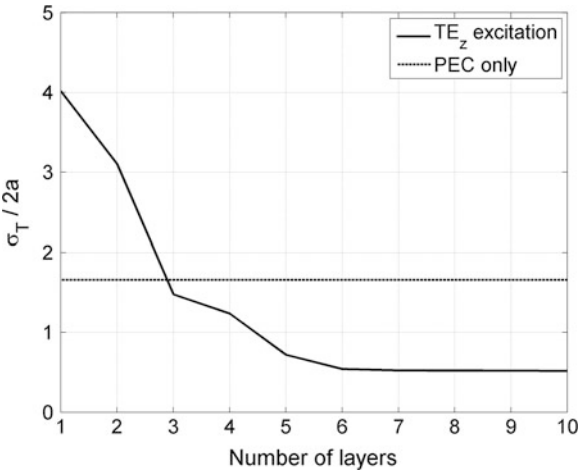

Fig. 12.11 Normalized total scattering width versus number of layers for a TE_z cloak (TE_z polarization) [7]

is parallel to the z-axis and thus it is zero in the radial direction. Figure 12.10 shows the angular variation of bistatic scattering width of the TM_z cloak for both polarizations. It should be noted that the level of scattered field for the TE_z polarization is much larger than the one calculated for the TM_z polarization. Therefore, the TM_z cloak is indeed unsuitable for cross-polarized excitation, as presumed.

The TE_z cloak was designed as a completely dual cloak to the TM_z cloak described in the previous section and the metamaterial constitutive parameters were calculated by Eq. (12.10). The results of the simulations performed for the TE_z cloak are shown in Figs. 12.11 and 12.12. As expected, the results are complementary to the ones provided for the TM_z cloak. The realized reduction of the total scattering width is again smaller than in the ideal case, i.e., it is around 3 for structures with more than 5 layers. As expected, the cloak is found to be suitable only for a TE_z excitation.

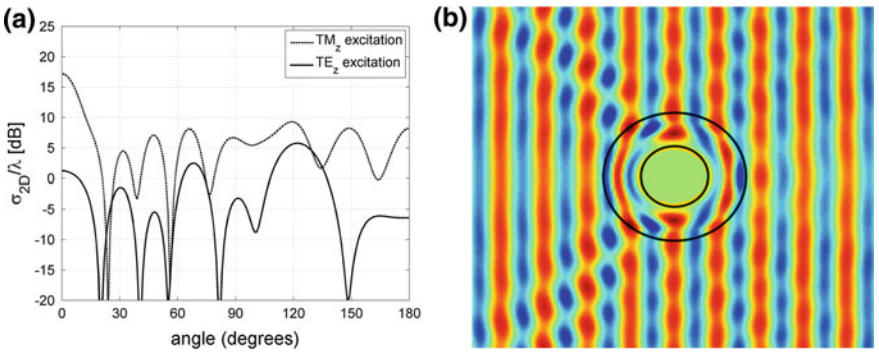

Fig. 12.12 **a** Normalized bistatic scattering width (TM_z and TE_z polarizations) [7]. **b** Electric field distribution in the vicinity of the cloaked object (TE_z polarization) of the 10-layer realization of a TE_z cloak

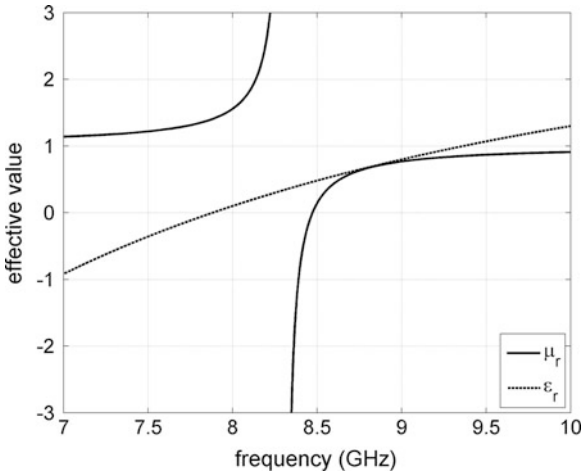

Fig. 12.13 Frequency dependence of $\mu_{\rho\rho}$ and $\varepsilon_{\rho\rho}$ used in bandwidth analysis (Lorentz and Drude model) [7]

12.4.3 Dependence of Scattering Width on Frequency

The performed simulations show that for the simplified cloak realizations (TM_z and TE_z cloaks) the achieved total scattering width reduction is around 3, though only for one excitation frequency. In reality, the magnetic permeability and the electric permittivity of passive metamaterials are always frequency dependent as explained in Sects. 12.3.1 and 12.3.2 and this dispersion has an effect on the level of achieved invisibility. The frequency dependence of the magnetic permeability (realized with split rings, Sect. 12.3.3) is given by the Lorentz dispersion model (12.11). Here, the measured values of practical SRR-based metamaterials published in [17, 27] were used in calculation (by $\omega_{ser} = 1.02 \cdot \omega_{par}$). On the other hand, the frequency dependence of the electric permittivity (realized with an array

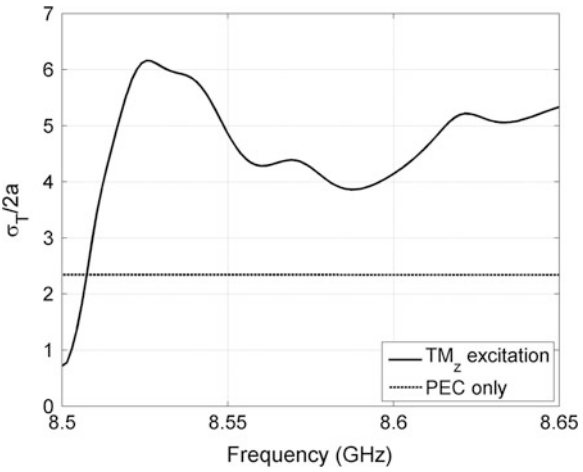

Fig. 12.14 Normalized total scattering width versus frequency for TM_z cloak with included dispersion (TM_z polarization) [7]

of thin wires, 12.3.3) is given by the Drude dispersion model. The wire-medium losses were neglected in the calculations because they are significantly lower than losses of SRRs. The frequency dependencies of the relative magnetic permeability and relative electric permittivity (in radial direction) used in the calculations are shown in Fig. 12.13. For the central frequency $f = 8.5$ GHz it is assumed that the radial components of the permittivity and permeability tensors are $\mu_{\rho\rho} = 0.14$ (for the TM_z cloak) and $\varepsilon_{\rho\rho} = 0.48$ (for the TE_z cloak). These are the values needed for the cloak realizations with only one layer. It is now obvious that if $\mu_{\rho\rho}$ or $\varepsilon_{\rho\rho}$ throughout the structure are designed according to (12.9) and (12.10), these values can be achieved only at a certain frequency. Due to inherent dispersion, the values of $\mu_{\rho\rho}$ or $\varepsilon_{\rho\rho}$ grow with increasing frequency. Therefore, the achieved level of invisibility changes too.

The cloaks were designed with 10 layers of metamaterial, which is a good approximation of a continuous radial change of permittivity or permeability values, as shown in Sect. 12.2.1. The analysis is provided in a narrow frequency range around the central frequency (8.5 GHz), for which the $\mu_{\rho\rho}$ or $\varepsilon_{\rho\rho}$ values had been designed. Figure 12.14 shows the frequency dependence of the invisibility parameters for the simplified cloaks.

The BW of the cloak is defined as a frequency range (normalized to the central frequency) in which the total scattering width of the cloaked object is smaller than of the hidden object (PEC cylinder in this case). In other words, the cloak BW represents the frequency range in which the invisibility gain is larger than one (see Eq. (12.23); definitions of the total scattering width and of the invisibility gain are given in Sect. 12.3.4). It can be seen that invisibility has been achieved only in a narrow frequency range around the central frequency (8.5 GHz). Therefore, it has also been found that the metamaterial cloak is not suitable for applications that require a larger frequency BW (e.g., invisibility to radar signal). Supposing that the cloak behaves similarly at frequencies lower than the central one, it is found that

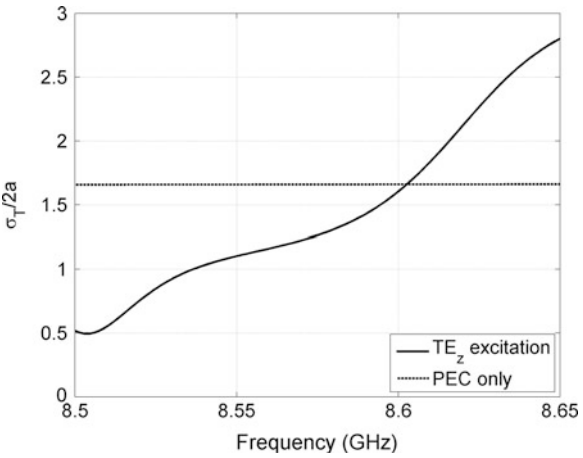

Fig. 12.15 Normalized total scattering width versus frequency for TE_z cloak with included dispersion (TE_z polarization) [7]

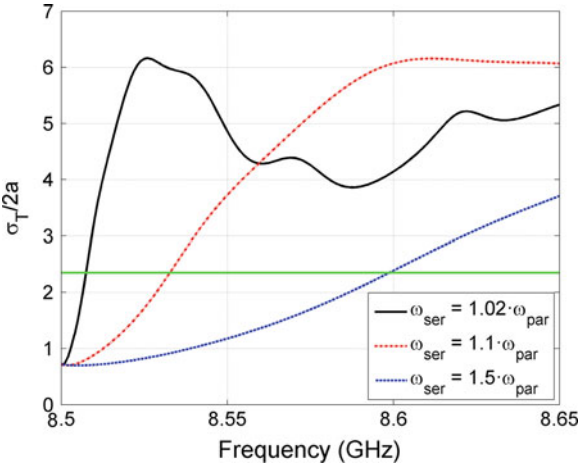

Fig. 12.16 Normalized total scattering width as a function of ratio $\omega_{ser}/\omega_{par}$ for TM_z cloak (TM_z polarization)

the approximate BWs of the TM_z and TE_z cloaks are 0.02 and 0.2 GHz, respectively (0.24 and 2.4 % of the central frequency as shown in Figs. 12.14 and 12.15). The TE_z cloak has a larger BW due to a weaker frequency dependence of constitutive parameters (see Fig. 12.13). The comparison to the reference case (PEC cylinder without any cloak) is also given.

The BW results of the TM_z cloak strongly depend on the ratio between the frequencies ω_{ser} (the frequency at which $\mu_{eff} = 0$ for the lossless case) and ω_{par} (the frequency at which μ_{eff} diverges for the lossless case). Since this ratio depends on the particular realization of the split-ring resonator, the dependence of the cloak BW on that ratio was investigated. Figure 12.16 illustrates this dependence. It can be seen that with the ratio $\omega_{ser} = 1.5\ \omega_{par}$ the obtained BW is 10 times larger, i.e., the BW of around 2.4 % for the TM_z polarized incident wave. Therefore, it can be

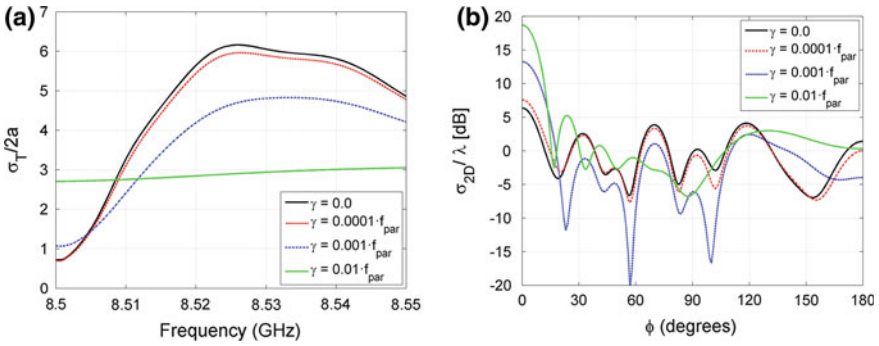

Fig. 12.17 Normalized total scattering width (**a**) and bistatic scattering width (**b**) as a function of losses (factor γ) for TM_z cloak (incident wave is TM_z polarized; bistatic scattering width is calculated at $f = 8.5$ GHz)

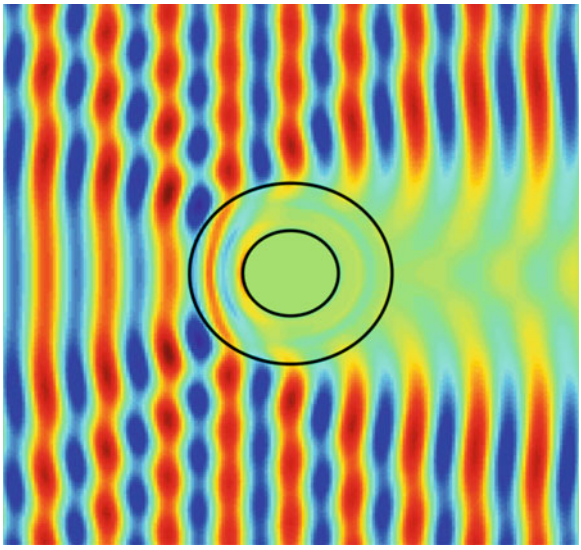

Fig. 12.18 Electric field distribution in the vicinity of the cloaked object (TM_z polarization) of the 10-layer realization of a TM_z cloak; losses are $\gamma = 0.01 \cdot f_{\text{par}}$

concluded that if the cloak is made from resonant elements the BW will be quite narrow, typically several percent.

It should be noted that due to dispersion there is a time delay in the cloaking effect (important for pulse excitation) and during this transition period a strong scattered field is observed [28]. Furthermore, the pulses themselves are deformed due to the presence of the dispersive cloak, and the shape of the pulse depends on the observation point (i.e., on the position relative to the cloaked object).

The influence of losses of the periodic structure is investigated in Fig. 12.17 where the total and bistatic scattering widths are calculated as functions of losses (described with the factor γ from Eqs. (12.24) and (12.25). It can be seen that if the value of γ is smaller than $0.001\, f_{\text{par}}$ then the difference between the lossy and

lossless case is negligible (f_{par} is defined as $f_{par} = \omega_{par}/2\pi$). However, for larger losses the cloak loses its cloaking behavior and starts to behave as an absorber (i.e., the forward scattered field is drastically enlarged and the backward scattered field is reduced). That can be clearly seen in Fig. 12.18 which illustrates the electric field distribution in the vicinity of the 10-layer realization of the TM_z cloaking cylinder with $\gamma = 0.01\, f_{par}$. The cloak starts to behave as an absorber resulting in a strong forward scattered field.

At this point, it is convenient to compare these simulation results to the published experimental results. To the best of our knowledge, there is only one experimentally realized metamaterial-based cloak for which the data about the obtained invisibility and BW are available [29]. This was a reduced parameter TM cloak (similar to the original proposal in [5] and it was based on SRR inclusions). The central frequency was 10 GHz, and the measurements showed the reduction of total scattering width (of the bare PEC cylinder) within the frequency range 9.91–10.14 GHz. In other words, the obtained invisibility BW was 230 MHz or 2.3 % (which corresponds well to theoretical predictions). The reduction of total scattering width was 24 % (i.e., the invisibility gain was only 1.32). Possible causes for such a small invisibility gain were not discussed in [29] (for instance, it could happen due to losses or imperfections in the experimental realization).

12.5 Enhancement of Bandwidth of Passive Cylindrical Cloak by Optimization of Design Parameters

Recently, several research groups investigated the optimization of cylindrical cloaks [30–33]. Primarily cloaks with simplified constitutive parameters were investigated, i.e., cloaks that can be obtained relatively easily in the microwave frequency region using periodic structures (in practice such cloaks change constitutive parameters only in one direction). All the presented results are for Schurig-type cloaks, i.e., cloaks that have only the radial component of permeability that varies along the radial direction. Similar results can be obtained for TE_z cloaks with only the radial component of permittivity being a function of the radial coordinate.

Using the particle swarm optimization (PSO) algorithm [34–35] the relevant constitutive parameters ($\mu_{\rho\rho}$ and ε_{zz}) of each layer of the circular-cylindrical cloak were optimized, in order to obtain a cloak that does not scatter the electromagnetic field at the central frequency, i.e., the "perfect" cloak for normal incidence. It should be noted that such a "perfect" cloak is designed with the assumption of a lossless metamaterial ($\gamma = 0$). The calculated relevant constitutive parameters of the Schurig cloak and the optimized cloak are given in Table 12.4. The considered number of layers is 10, i.e., both the Schurig cloak and the optimized cloak consist of the same number of layers. Layer number 1 represents the innermost layer while layer number 10 is the outermost one. The level of complexity of the construction of the optimized cloak is the same as in the construction of the Schurig cloak

Table 12.4 Relevant constitutive parameters of the Schurig cloak and the optimized cloaks

Layer no.	Schurig cloak $\varepsilon_z = 3.431;\ \mu_\phi = 1.0$ μ_r	Optimized cloak $\varepsilon_z = 3.858;\ \mu_\phi = 1.0$ μ_r	Optimized cloak ($\gamma = 0.0003$) $\varepsilon_z = 3.813;\ \mu_\phi = 1.0$ μ_r
1	0.003	0.056	0.020
2	0.022	0.025	0.016
3	0.051	0.010	0.020
4	0.085	0.092	0.078
5	0.119	0.587	0.192
6	0.154	0.046	0.068
7	0.187	0.216	0.193
8	0.219	0.999	0.500
9	0.249	0.076	0.093
10	0.278	0.616	0.503

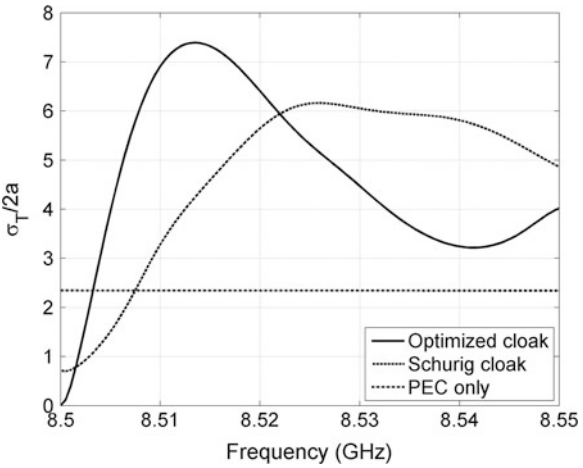

Fig. 12.19 Normalized total scattering width versus frequency for the Schurig cloak and the invisibility gain—optimized cloak [33]. The constitutive parameters of both cloaks are given in Table 12.4

(if necessary, the interval of obtainable permeability values can be easily adjusted in the optimization process if some of $\mu_{\rho\rho}$ values cannot be obtained in the practical cloak realization). However, the physical insight into wave propagation through the optimized cloak is lost.

The calculated total scattering width of the optimized cloak, together with the comparison to the original Schurig cloak, is given in Fig. 12.19. The results are given in a narrow frequency range above the central frequency (8.5 GHz), since the cloak behaves quite symmetrically for frequencies below the central frequency. The invisibility gain is simply obtained by dividing the total scattering widths of the referent case (PEC only) and the case with the cloak present. It is evident that by using the optimization process it is possible to design a virtually invisible cloak with the obtained invisibility gain of about 1,400 (although the physical insight of the cloak is lost). Note that the BW of the optimized cloak is reduced even more, compared to the Schurig cloak. While in the Schurig cloak the estimated

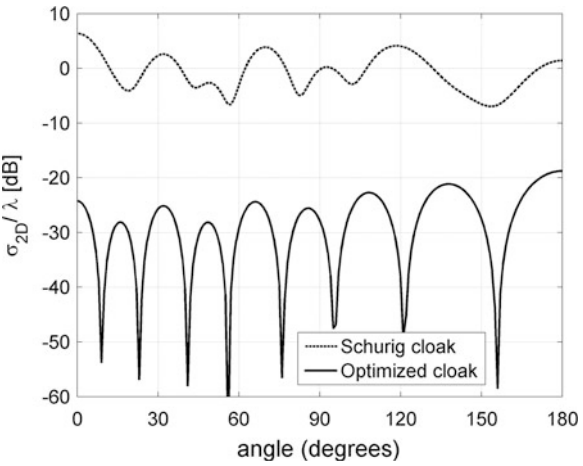

Fig. 12.20 Normalized bistatic scattering width of the considered cloak realizations at the central frequency (8.5 GHz) [33]. The constitutive parameters of both cloaks are given in Table 12.4

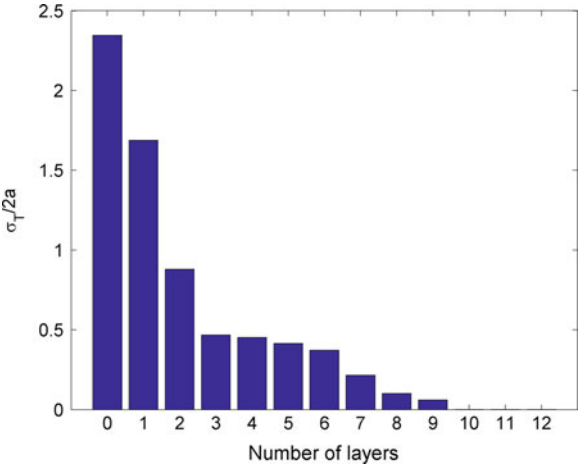

Fig. 12.21 Normalized total scattering width versus number of layers for a cloaked cylinder with 1.5 λ diameter [33]. The parameters of layers where optimized with PSO at a single frequency of 8.5 GHz

invisibility BW is approximately 0.2 %, for the optimized cloak the BW is only about 0.08 % (in both cases $\omega_{ser} = 1.02\,\omega_{par}$ was assumed). The angular variation of the bistatic scattering width (σ_{2D}) has been calculated at the central frequency just to check if there is any direction with distinctively stronger scattered field (Fig. 12.20). As can be seen, the scattered field of the optimized cloak is around 20 dB lower than that of the Schurig cloak.

12.5.1 Influence of Number of Layers

The Schurig cloak consists of 10 metamaterial layers, which is the starting point of this study on how the number of layers in the cloak, i.e., the subtlety of the

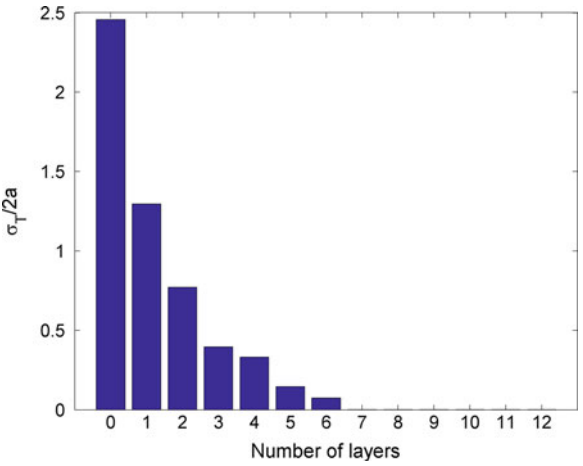

Fig. 12.22 Normalized total scattering width versus number of layers for a cloaked cylinder with 1.0 λ diameter. The parameters of layers were optimized with a PSO at the single frequency of 8.5 GHz

approximation of radial permeability, relates to the level of invisibility obtained by optimization. All the results have been obtained by PSO optimization, keeping the total dimensions of the cloak intact (i.e., the inner and outer radii). From Fig. 12.21 it can be seen that the normalized total scattering width decreases as the number of layers increases. It is interesting to note that better invisibility performance than with the Schurig cloak (that has $\sigma_T/2a = 0.717$) can be obtained with only three metamaterial layers. Also, it should be stressed that the level of achieved invisibility is significantly increased once the tenth layer is added. With 10 layers the cloak becomes practically invisible, although only at a single frequency.

The influence of the radius of the cylinder that is to be cloaked on the needed number of cloak layers was investigated. The cylinder considered in the Schurig case had approximately a 1.5 λ diameter. In Fig. 12.22 the cylinder with a 1.0 λ diameter was investigated (at a central frequency 8.5 GHz), while the ratio of the outer and inner cloak radius was kept the same (i.e., the considered radii are $a = 1.765$ cm and $b = 3.836$ cm). It is interesting to note that with the reduction of the cloaked cylinder radius the needed number of layers in order to obtain "the perfect cloak" is also reduced, and in this case only 7 layers are needed to obtain invisibility gain larger than 1,000.

12.5.2 Influence of Loss and Tolerances

To estimate the influence of losses in the material on the maximum achievable invisibility gain, the optimization procedure was performed for different γ values, starting from the lossless case and gradually increasing the losses (once more $\omega_{ser} = 1.02\ \omega_{par}$ was assumed). As expected, the total scattering width increases as the losses increase and therefore the obtained invisibility gain decreases (Fig. 12.23). It has also been found that losses of $\gamma = 1\,0^{-3} f_{par}$ are still acceptable,

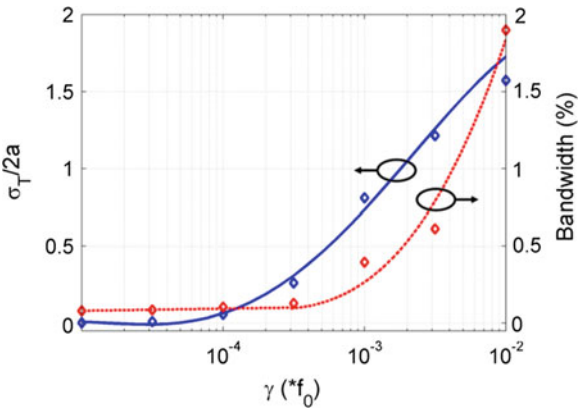

Fig. 12.23 Dependence of obtained total scattering width and bandwidth on losses for the invisibility gain—optimized cloak [33]

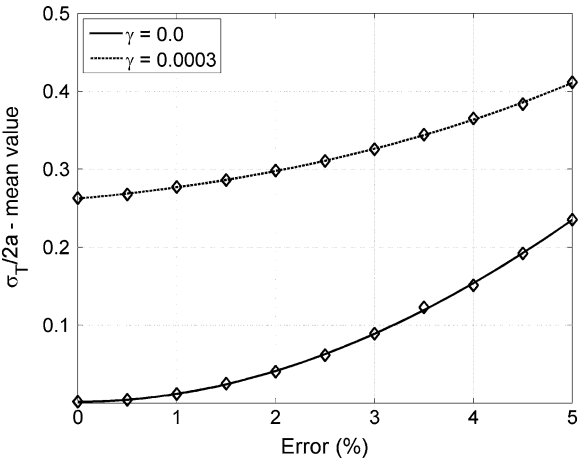

Fig. 12.24 Dependence of obtained total scattering width on construction tolerances for the invisibility gain—optimized cloak [33]. The mean value of total scattering width is shown

for the invisibility gain of the optimized lossy cloak has fallen to approximately the same value as the invisibility gain of the lossless Schurig cloak (around 3). In the same figure the influence of material losses on the BW of the cloak was plotted (i.e., the frequency range where invisibility gain is larger than 1). It can be seen that the BW increases with the introduction of losses, while the maximum invisibility gain is reduced.

Furthermore, sensitivity of the optimal solution to construction tolerances has been tested. To estimate how much the variation (as a result of construction tolerances) of the values of the radial component of permeability $\mu_{\rho\rho}$ and permittivity tensor ε_{zz} influences the obtained total scattering width, a statistical analysis was performed. Figure 12.24 shows the mean value of the total scattering width if $\mu_{\rho\rho}$ and ε_{zz} are varied randomly by 0–5 % of their initial (ideal) value with uniform distribution (worst case). Two cases are shown—with and without losses. It can be seen that the cloak is not too sensitive to parameter tolerances and lossy

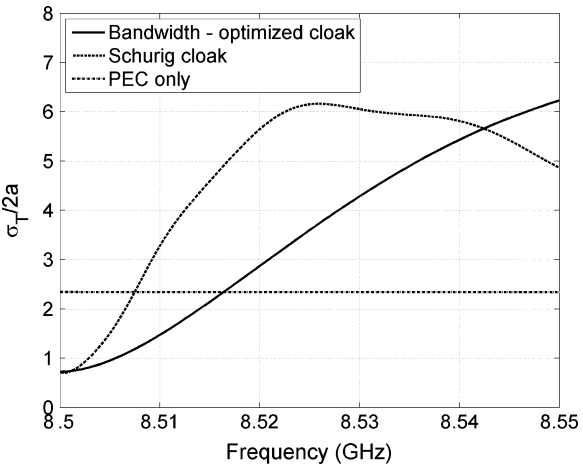

Fig. 12.25 Normalized total scattering width versus frequency for the Schurig cloak and the bandwidth optimized cloak [33]. Lossless cloaks are considered $(\gamma = 0)$

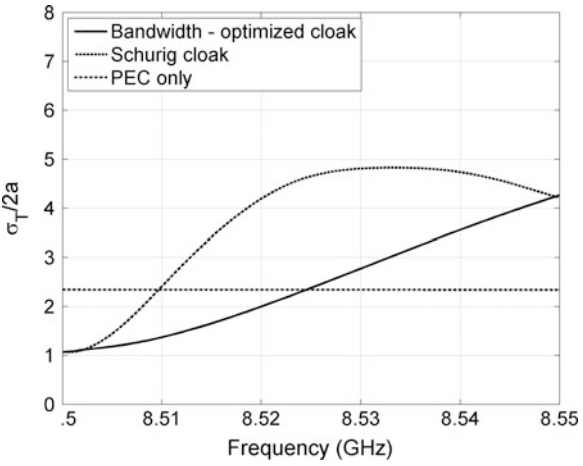

Fig. 12.26 Normalized total scattering width versus frequency for the Schurig cloak and the bandwidth optimized cloak [33]. Lossy cloaks are considered $(\gamma = 10^{-3} f_{\text{par}})$

cloaks are even less sensitive. It can be deduced that cloaks that are quite invisible can be realized even with reasonably large parameter variances.

12.5.3 Bandwidth: Optimized Cloak

The possibility of enlarging the BW of the cloak while keeping the same level of the invisibility gain (i.e., the minimum of the total scattering width) as that of the Schurig cloak was investigated. Two cases have been considered—the optimization of the lossless cloak ($\gamma = 0$) and the optimization of the lossy cloak with small losses of $\gamma = 10^{-3} f_{\text{par}}$, which have been shown to be still acceptable (the assumed ratio of ω_{ser} and ω_{per} was again $\omega_{\text{ser}} = 1.02\,\omega_{\text{par}}$). The calculated total scattering

widths are shown in Figs. 12.25 and 12.26. The comparison with the Schurig cloak (lossless and lossy, respectively) is also given. The optimized BW is around 0.4 % for the lossless case and about 0.58 % for the lossy case. Meanwhile, the Schurig cloak exhibits BWs of 0.2 % (lossless case) and 0.24 % (lossy case). In other words, the improvement in the BW compared to the Schurig cloak is between 2 and 2.5 in both considered cases.

In [36] an analytic approach was proposed for determining the parameters of a cloak with extended BW. It was found that causality requirements impose severe constraints on the system parameters of the transformation medium, and that a specific form of "reduction" can help to create a cloak that offers a reduced (non-zero) cross-section in a finite frequency range. In the described example the obtained extension of the BW (comparing to the Schurig cloak) was around 2.3.

12.6 Broadband Active Metamaterial Based on Non-Foster Elements

12.6.1 Basic Idea of Overcoming the Energy-Dispersion Constraints by Active Metamaterials

In Sect. 12.3 it was shown that every passive ENZ or MNZ metamaterial (thus, every metamaterial needed for realization of an anisotropic cloak) must be dispersive. Is it possible to go around the basic dispersion constraints (12.16) and construct broadband dispersionless ENZ and MNZ metamaterials? From the circuit-theory point of view, the dispersion essentially happens because of the different frequency behavior of the capacitive susceptance ($+j\omega C$) compared to the inductive susceptance ($-j/\omega L$). Because of this difference, the equivalent capacitance (or equivalent permittivity) of the LC tank circuit in Fig. 12.5 is a non-linear function of frequency (12.17).

In order to avoid this non-linear behavior, a negative capacitance $C_n < 0$ and a negative inductance $L_n < 0$, that violate Foster's theorem (thus $\partial X/\partial\omega > 0$) are introduced [37, 53]. The susceptances of these fictitious 'negative' elements read:

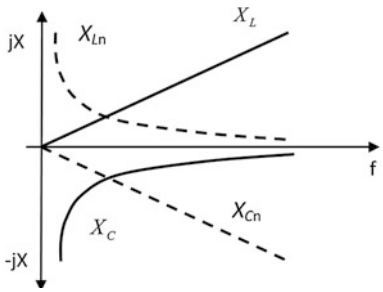

Fig. 12.27 Reactance of positive (*solid line*) and negative (*dashed line*) reactive elements

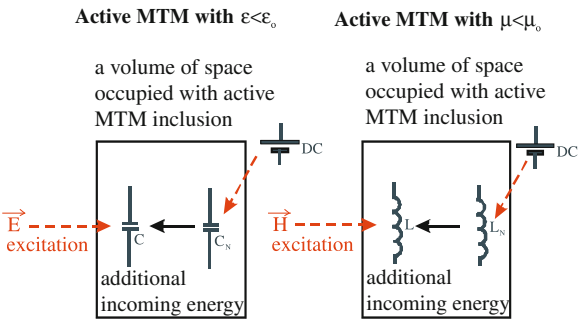

Fig. 12.28 The basic principle of an active non-foster metamaterial

$$B_{L_n} = -j\frac{1}{\omega L_n} = +j\frac{1}{\omega|L_n|}, \quad B_{\bar{C}} = j\omega C_n = -j\omega|C_n|. \tag{12.32}$$

The dispersion curves of negative elements are the inverse of their counterparts for the ordinary elements (Fig. 12.27). Hence, it is expected for the dispersion of ordinary passive metamaterials to be compensated with the 'inverse' dispersion of non-Foster elements, resulting in broadband ENZ or MNZ behavior. The key principle is to keep the energy stored in a passive reactive element constant across the whole operating band. It can be achieved by introducing an additional (frequency dependent) flow of energy from active 'negative' elements [37, 53] (Fig. 12.28). Here, the basic background theory is presented, while the problems of practical implementation and a short overview of the state of the art are given in the next section.

The dispersion of an ordinary capacitor can be compensated by the inverse dispersion of a negative capacitor. To this end, the lumped inductor L_2 in the equivalent circuit of a passive ENZ metamaterial from (Fig. 12.5b) is replaced with a lumped negative capacitor C_n. The equivalent permittivity of this active metamaterial (Fig. 12.29) reads [37, 53]:

$$\varepsilon_r(\omega) = \frac{Y(\omega)}{j\omega\varepsilon_0} = \frac{j\omega\left(C - \frac{|C_n|}{\Delta x}\right)}{j\omega\varepsilon_0} = \left[\frac{1}{\varepsilon_0}\left(C - \frac{|C_n|}{\Delta x}\right)\right]. \tag{12.33}$$

It can be seen that this new equivalent permittivity (12.33) is *not at all frequency dependent*. Thus, if $(|C_n|/\Delta x) < C$ is to be chosen, an entirely dispersionless ENZ metamaterial could be obtained [37, 53]. What is the background physics of this counter-intuitive behavior? Essentially, the negative capacitor behaves as a frequency-dependent active inductor (a source) that supplies additional current to the positive capacitor. This additional current causes faster charging and therefore decreases the effective capacitance. Since the dispersion curves of a positive capacitor and a 'frequency-dependent inductor' are exactly inverse, the resultant behavior is not frequency dependent. Clearly, the CC_n circuit is not a tank circuit at all (in a classical sense). This is just a capacitor with arbitrary low value of capacitance.

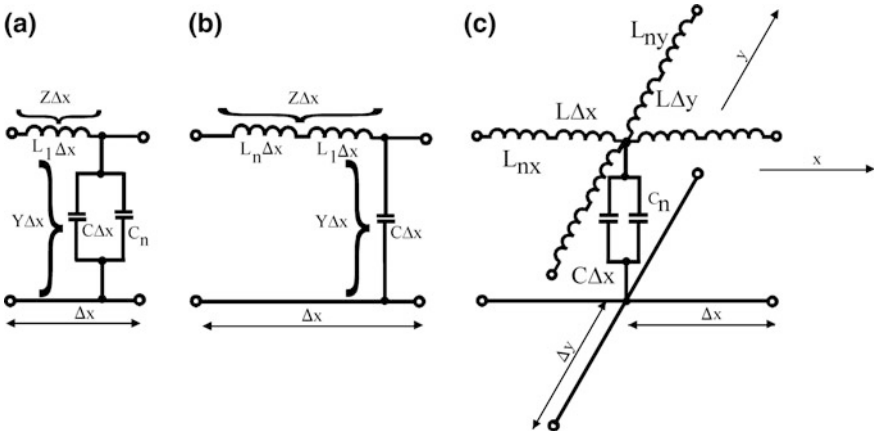

Fig. 12.29 **a** active 1D ENZ metamaterial. **b** Active 1D MNZ metamaterial. **c** Active 2D anisotropic MENZ metamaterial

Of course, the extension of the proposed principle to the design of an active MNZ metamaterial is straightforward. A classical passive MNZ transmission-line-based metamaterial (Fig. 12.5) employs periodical loading with series lumped capacitors. In the active version, series lumped capacitor is replaced with a non-Foster negative inductor L_n (Fig. 12.29b). Following the previous analysis, one directly derives the equivalent effective permeability:

$$\mu_r(\omega) = \frac{Z(\omega)}{j\omega\mu_0} = \frac{j\omega\left(\frac{L_1}{\Delta x} - |L_n|\right)}{j\omega\mu_0} = \left[\frac{1}{\mu_0}\left(\frac{L_1}{\Delta x} - |L_n|\right)\right]. \tag{12.34}$$

The physical explanation is very similar to the case with a negative capacitor. The negative inductor acts as an additional energy source-sink lowering the net 'magnetic' energy. In fact, the LL_n circuit behaves as an inductor with an arbitrary low value of inductance.

So far, the principles of 1D implementation of active ENZ and MNZ metamaterials have been shown. The extension of this idea to the 2D case using a well-known approach from passive transmission-line-based metamaterials is straightforward [18].

The most general 2D anisotropic case is sketched in Fig. 12.29c. The constitutive tensors of this metamaterial are:

$$\begin{aligned} \mu_{r\,\mathrm{eff}} &= \begin{bmatrix} \mu_{xx} & 1 \\ 1 & \mu_{yy} \end{bmatrix}, \; 0 \geq \mu_{xx} \geq 1, \quad 0 \geq \mu_{yy} \geq 1 \\ \varepsilon_{r\,\mathrm{eff}} &= \begin{bmatrix} \varepsilon_r & 1 \\ 1 & \varepsilon_r \end{bmatrix}, \; 0 \geq \varepsilon_r \geq 1. \end{aligned} \tag{12.35}$$

The isotropic version of the aforementioned active metamaterial can be achieved by a simple selection of identical values of the reactance in the x and y branches.

So far, it was presumed that the negative lumped capacitors and inductors are physically realizable devices (the practical realization issues of negative elements and the results achieved so far are tackled in the next section). On the other hand, even at this system level there are several important problems. The majority of transmission-line-based metamaterials are organized in a regular rectangular grid [18]. So, the 2D anisotropic unit cells from Fig. 12.29c will have uniaxial constitutive tensors in a rectangular co-ordinate system (12.35). The constitutive tensors of an anisotropic cylindrical cloak are uniaxial in the cylindrical system but in the rectangular system they contain non-zero off-diagonal entries. Thus, the transmission line implementation in a rectangular grid should contain some cross-coupling elements such as transformers. Undoubtedly, this would be impractical from a technological point of view. One of the solutions could be the diagonalization of constitutive tensors in the cylindrical system which results in simple networks without cross-coupling elements [38] (the right part of Fig. 12.30). Diagonalization is done by a discretization of Maxwell's curl equations in a cylindrical system and comparing them to the telegrapher's transmission line equations (mathematical details are given in [38]). The results of this procedure are the expressions that show the mapping between the values of lumped elements and the associated values of permittivity and permeability:

$$\frac{L_r'}{d} = \mu_{\phi\phi}\frac{\Delta\rho}{\rho\Delta\phi},\ \frac{L_\phi'}{d} = \mu_{rr}\frac{\rho\Delta\phi}{\Delta\rho},\ C_z'd = \varepsilon\rho\Delta\rho\Delta\phi. \tag{12.36}$$

Here, L_r' and L_θ' represent the equivalent inductance values in the radial and angular direction, respectively, C_z' is the equivalent capacitance value in the vertical direction. The symbol d stands for the thickness of the cloak in the vertical direction, Δr is the thickness of a single unit cell in the radial direction and $\Delta\theta$ is the differential angle between two adjacent cells. It should be taken into consideration that the values of the elements in (12.36) are sometimes not physically

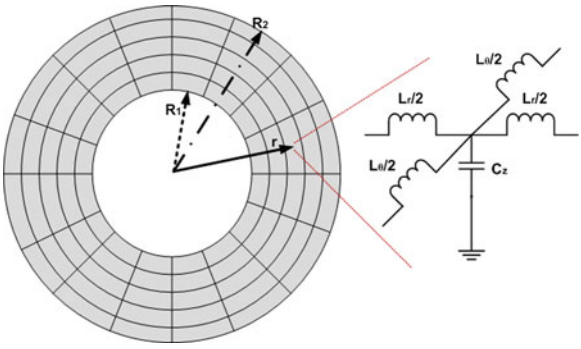

Fig. 12.30 A periodic cylindrical cloaking structure based on a TL approach; each unit cell is much smaller than the wavelength of the EM wave propagating through the metamaterial

feasible (if the values of the distributed capacitance and inductance are lower than ε_0 and μ_0, respectively, thus in the case of ENZ or MNZ behavior [38]). Hence, in an ordinary, passive cloak, resonant LC combinations that result in the needed values of capacitances and inductances must be used. Again, this is a consequence of the resonant energy exchange described by the dispersion-energy constraints (Foster's theorem) (12.16). Although this issue is indeed very basic and extremely important, it was not discussed in [38]. Using active non-Foster elements, it is possible to synthesize a network that would behave as dispersionless capacitors and inductors, values of which are given by (12.36) (these are actually the circuits in Fig. 12.29). The unit cells of the cloak can be organized into a web-like grid sketched in Fig. 12.30 [38].

Apart from the diagonalization of constitutive tensors in the cylindrical system, there are several novel approaches that enable synthesis of transmission line metamaterials with full tensors in the familiar rectangular system [39, 40]. It would be very interesting to combine these approaches with non-Foster elements but such efforts have not been published so far.

Both approaches (diagonalization of constitutive tensors in a cylindrical system and synthesis of anisotropic unit cells with full tensors) presume a planar realization, therefore a kind of matching layer should be used (in reality, it is actually an array of antennas) [41–43] for interfacing the cloak with free space.

Finally, there is a problem with realizing the volumetric cylindrical structure in Fig. 12.2 with planar metamaterials. A possible solution could be the stacking of many layers of the planar metamaterials from Fig. 12.30 embedded in parallel plate waveguides (similarly to the classical approach used in the first plasma-like artificial structures [44]).

All these problems are challenging, but they belong to the field of classical electromagnetics of passive structures and their solutions appear to be feasible. Certainly the most critical issue is the feasibility of a practical implementation of negative non-Foster elements.

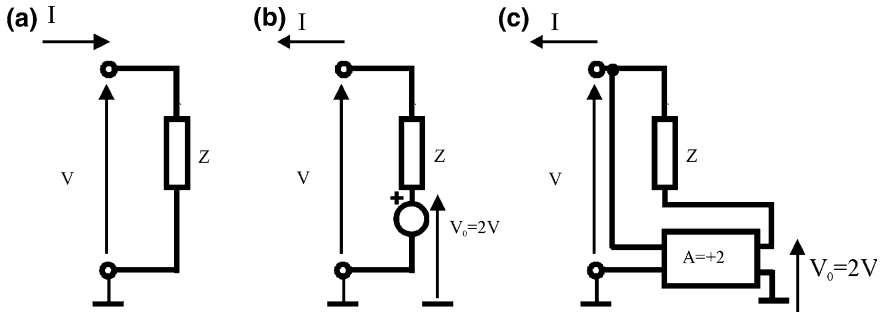

Fig. 12.31 An example of the operating principle of negative non-Foster impedance

12.6.2 Technological Constraints and State of the Art

Negative 'non-Foster' networks are based on the negative impedance converter (NIC), originally introduced back in the 1950s [45]. Although this idea is indeed old, there are only a few papers [46–52] in the open literature that report successful practical implementations of negative capacitors or negative inductors in the RF and microwave ranges. The main problem is the inherent instability caused by the fact that all NIC circuits employ amplifiers with positive feedback.

Both the basic idea of impedance inversion and the origin of the stability problem can be understood by analysis of the simple amplifier-based circuit in Fig. 12.31.

The impedance that should be inverted (Z) is shown in the Fig. 12.31a). In order to invert the impedance, one should swap the sign of either the voltage across the element (V) or the sign of the current flowing through it (I). This can be achieved by inserting an additional 'dependent' voltage source of amplitude $2V$ in series with impedance Z (Fig. 12.31b). Since the voltage drop across the impedance is negative, the current I now flows outward from the circuit causing the inversion of the impedance Z_{in}:

$$Z_{\text{in}} = \frac{V}{I} = \frac{V}{\frac{V-2V}{Z}} = -\frac{V}{I} = -Z. \tag{12.37}$$

A possible realization of a dependent source by an ideal amplifier with voltage gain A =+2 is shown in Fig. 12.31c). This circuit employs positive feedback so, under specific circumstances, it can turn into an oscillator, i.e., it can become unstable. Thorough investigation in [53, 54] revealed that the method chosen for assessing the stability issue is of crucial importance. Traditionally, RF and microwave engineers analyze the stability in the frequency domain with the help of 'stability factors' [55], based on the input reflection coefficient of a circuit. In addition, almost all standard RF and microwave circuit simulators use these stability factors. However, it is very often overlooked that all stability factors based on reflection coefficient presume that the Nyquist stability criterion is a priori satisfied, i.e., that the transfer function has no poles in the right half-plane. If this fact is neglected, it is possible that the analysis of the stability factor predicts stable operation even for a circuit that is inherently unstable. Actually, it was recently found [54] that the stability criteria depend not only on the negative elements but also on the topology of the remaining passive part of the network. An effective circuit theory method of predicting stability for any network topology was reported in [54]. Simply stated, in order to achieve stable operation, a net capacitance (or a net inductance) of the whole circuit (containing both 'negative' and 'positive' elements) must be positive. Obviously, this is fulfilled for ENZ and MNZ metamaterials needed in cloaking technology (overall permittivity/permeability i.e., capacitance/inductance are arbitrarily small but always positive numbers).

Practical issues regarding negative capacitors and negative inductors are analyzed in detail in [54]. There are two main issues, the choice of appropriate circuit topology and appropriate technology. There are many types of classical NICs with BJT-based circuits [56] and FET-based circuits. All these designs are sensitive to unwanted phase shifts and parasitic capacitances and inductances. Due to these problems, there are only a few circuits for which successful realizations have been reported so far: the Linvill-Yanagisawa design in BJT technology [56], the Meunier-Kolev design [57] and a very popular design with cross-coupled transistors in FET technology [58, 59]. There are many design details explained in the recent study [54], but the most important issue is the transit frequency of the active element (BJT or FET). It was shown that it should be significantly higher than the required highest operating frequency of the negative capacitor (negative inductor). As a rule of thumb, one could say that the transit frequency should be at least ten times higher than the maximal operating frequency. This comes from the very simple fact that the operation of all NIC circuits is based on either voltage or current inversion. The inversion requires a phase shift of exactly 180° between the input and the output of the active device. This phase shift can be achieved only at very low frequencies, for which the transit time across the active device can be neglected. This is not the case at higher frequencies, at which the finite transit time and additional phase shift cannot be neglected. This additional phase shift introduces a real part (usually negative) of the input impedance that deteriorates the properties of negative capacitance or negative inductance. The publicly available studies [54] reported a maximal operating frequency of BJT and FET NIC circuits of approximately 100 MHz in discrete technology and approximately 2 GHz in integrated technology. Recently, there have been several conference reports about NIC circuits with maximal achieved frequencies of 400 MHz using BJT technology and more than 10 GHz using integrated CMOS FET technology. However, design details of these efforts are not publicly available and they cannot be cross-checked.

Almost all of the above prototypes were designed for use in broadband matching of small antennas, which has been the most popular application of non-Foster elements for many years. The first non-Foster-based active dispersionless ENZ metamaterial was presented in [37] and further improved in [53]. The negative capacitors were constructed using FET-based circuits that employ Kolev's topology [57] (Fig. 12.32a). Two prototypes for operation in the RF band (50–100 MHz) and the lower microwave band (1–2 GHz) were manufactured and

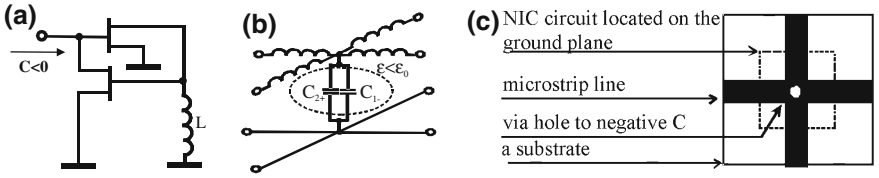

Fig. 12.32 First published 2D broadband non-Foster metamaterial [37]. **a** Basic negative capacitor circuit. **b** 2D active ENZ unit cell. **c** A sketch of realized unit cell

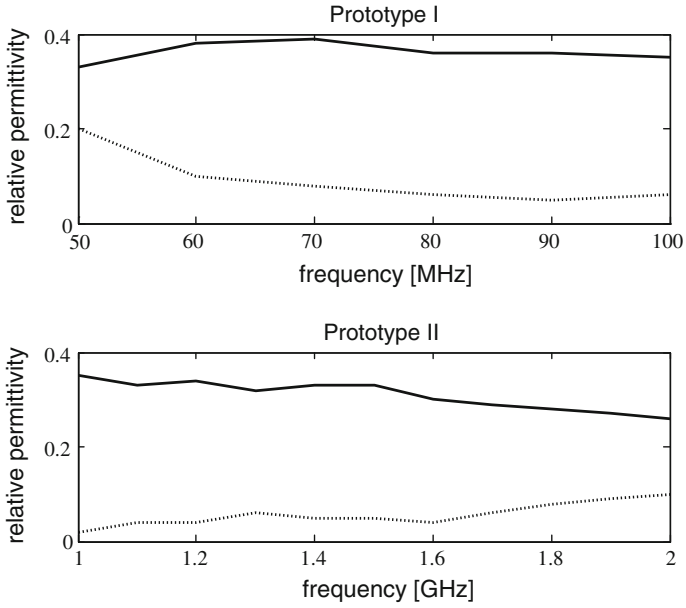

Fig. 12.33 Measured relative permittivity of unit cells of first published 2D broadband non-Foster metamaterial (*solid*—real part, *dashed*—imaginary part) [37]

measured. The RF circuit (prototype I) employs four BF999 Si MOS FETs while the microwave circuit (prototype II) is based on two MGF1412 GaAs FETs.

Two different 2D unit cells of active ENZ metamaterials were assembled. Each cell comprised two mutually perpendicular electrically short microstrip lines ($<\lambda/20$, λ being the guiding wavelength) (Fig. 12.32b) forming a cross on a 25 × 25 mm substrate. The prototyped active capacitance circuit was back-to-back mounted on the ground plane and connected to the junction of the microstrip lines through a hole. Following (12.33), the parameters of the microstrip lines were chosen in such a way that the generated negative capacitance partially cancelled the distributed line capacitance. Consequently, one expects to obtain an equivalent unit cell permittivity smaller than one. The equivalent permittivities of these unit cells, extracted from the measured results, are shown in Fig. 12.33.

It can be seen that in both cases, the permittivity is fairly constant within one octave (50–100 MHz for prototype I and 1–2 GHz for prototype II). These measured results were also used as input data for an ADS^{TM} simulation of a proposed active 2D plasmonic cloak [37] and the obtained relative operating BW was 100 % comparing to a relative BW of 20 % for the passive cloak (in [37], the CBW is defined by the 'blockage factor' that is different than the invisibility gain in (12.23), but they are roughly comparable). Although the study in [37] dealt only with a plasmonic cloak, it was the first demonstration of a possible application of non-Foster elements for broadening the CBW.

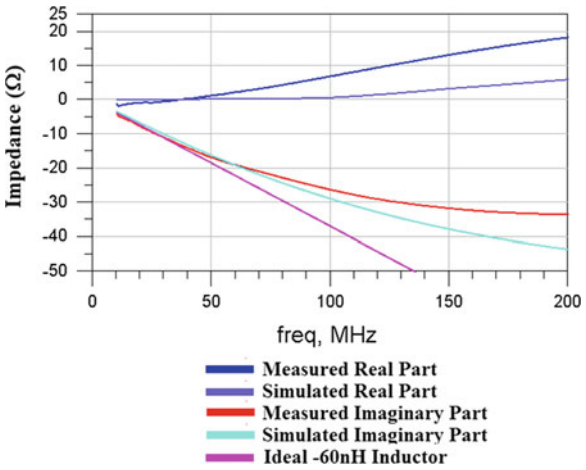

Fig. 12.34 Simulated and measured impedance of the active negative inductor [60]

Similar efforts toward a practical realization of 2D active MNZ metamaterials were reported in [60]. It used Kolev's topology from Fig. 12.32a), in which the loading capacitor was replaced with a loading inductor. The simulation and measurements results of the generated negative inductance are shown in Fig. 12.34. It can be seen that the negative inductance shows almost ideal dispersionless (and nearly lossless) behavior in the frequency band from 10 to 50 MHz (more than two octaves). This means that the effective permeability of the associated 2D unit cell of the MNZ metamaterial should have a very similar behavior, which was proven in a recent conference report [61].

Examples discussed so far have dealt only with a single active unit cell while in practical cloaking application there could be thousands of these cells. Thus, there is the obvious concern regarding possible interactions that could lead to stability problems. In order to clarify this issue, it was attempted to build a whole 1D active ENZ metamaterial (active ENZ transmission line). Unfortunately, it was found that the negative capacitors developed in [37] are sensitive to parasitic phase shifts caused by finite track lengths in the prototypes. Actually, both prototype I and prototype II in [37] were 'hand-crafted' and it is not surprising that the effective permittivity varied slightly among the different samples. This unwanted property is not an obstacle for verification of the basic idea, but it might be a problem in the design of an active line that comprises many identical unit cells.

In order to improve the repeatability, several negative capacitors were built using high-speed operational amplifiers operating in very low RF band (<100 MHz), in which the parasitic capacitances and unwanted phase shifts can be neglected [62]. This prototype was intended to be some kind of a 'demonstrator', which, if successful, would lead to further microelectronic realizations. The developed negative capacitor was based on the AD8099, an ultra-fast voltage feedback operational amplifier (Fig. 12.35a). The circuit generates a negative capacitance, the value of

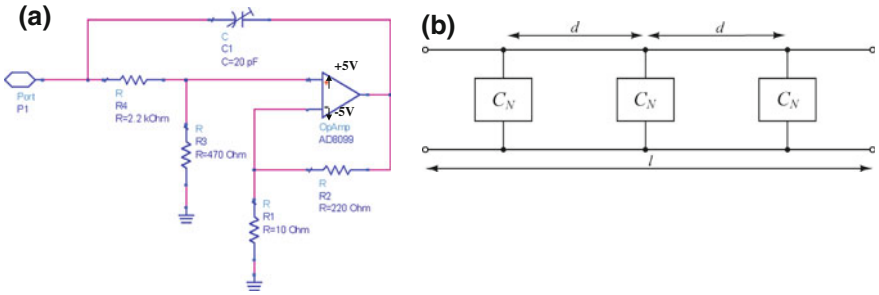

Fig. 12.35 **a** OpAmp-based RF negative capacitor, **b** 1D ENZ metamaterial based on transmission line loaded with three negative capacitors [62]

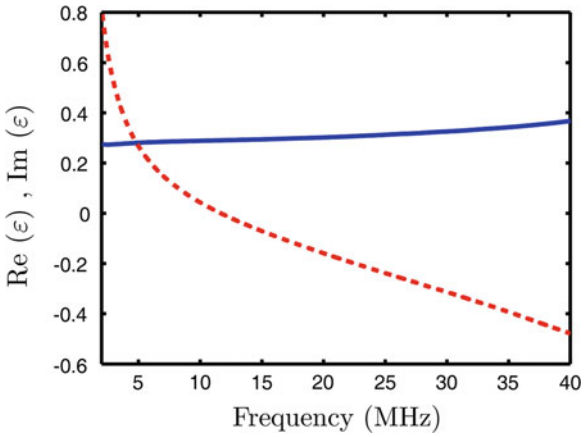

Fig. 12.36 Measurement results of active 1D ENZ metamaterial [62], *solid*—real part, *dashed*—imaginary part

which can be adjusted (by varying a capacitance of C_1) to an arbitrary value in the range −20 to −100 pF, in the frequency band from 2 to 40 MHz.

Three negative capacitors were built and the measurement of input reflection coefficient revealed stable operation with an input capacitance of −60 pF in the frequency range from 2 to 40 MHz. A simple, air transmission line was manufactured and periodically loaded with three negative capacitors [62] (Fig. 12.35b). The distance d between the elements was much smaller than the wavelength (approximately $\lambda/20$ at the highest frequency, λ being the free-space wavelength). Complex permittivity was extracted from the measurements of scattering matrix using the standard procedure and a sample of the obtained results is shown in Fig. 12.36.

It can be seen that the real part of the effective permittivity is rather constant (it varies from 0.27 to 0.37 in the frequency range of more than four octaves (2 – 40 MHz). The change of the imaginary part is more pronounced (it varies from +0.8 to −0.5), which would certainly limit possible applications in cloaking technology. However, it should be stressed that the frequency dependence of the imaginary part is due to technological limitations only (it is primarily caused by

Table 12.5 Comparison of some practically implemented non-Foster ENZ and MNZ metamaterials

Reference	Type of developed metamaterial	Technology	Absolute BW with negligible dispersion (15 % change of ε and μ)	Relative BW with negligible dispersion (15 % change of ε and μ)
Hrabar et al. [37]	2D ENZ (unit cell)	FET (discrete)	50–100 MHz	1:2
Hrabar et al. [37]	2D ENZ (unit cell)	FET (discrete)	1–2 GHz	1:2
Ugarte-Munoz et al. [60]	2D MNZ (unit cell)	FET (discrete)	10–50 MHz	1:5
Hrabar et al. [62]	1D ENZ (TL)	OpAmp-based (discrete)	2–40 MHz	1:20
Hrabar [61]	1D ENZ (TL)	Gain block (discrete)	2–200 MHz	1:100
Hrabar [61]	1D MNZ (TL)	Gain block (discrete)	2–200 MHz	1:100

the low transit frequency of the operational amplifier used) and not by underlying physical concepts. The latest prototype presented in [61] used a more advanced integrated amplifier (gain block) and obtained results showed almost dispersionless effective permittivity (within 15 % limit, as defined in Sect. 12.3.1) in the frequency range of 1:100 (2–200 MHz) with negligible imaginary part (less than 0.05). Obtained BW is considerably wider than the BW of all passive ENZ metamaterials available at present, and it clearly proves the correctness of the proposed concept. It is interesting that these non-Foster metamaterials support both superluminal phase and group velocity [62]. Although this fact looks counterintuitive, it is in a perfect agreement with causality since the group velocity of non-Foster metamaterial is not equal to the energy velocity [62].

Of course, it is clear that the technology of broadband non-Foster metamaterials is in its infant phase. Some of the representative experimental efforts that show the present state of the art are summarized in Table 12.5. At the moment, this technology is available only at very low RF frequencies (up to 2 GHz). However, it should not be overlooked that all the prototypes in Table 12.5 were 'hand-crafted'. It is certain that significant advances could be expected by the use of microelectronic technology. Some preliminary numerical studies showed that using standard CMOS integrated technology; it should be possible to increase the highest operating frequency to above 5 GHz [62].

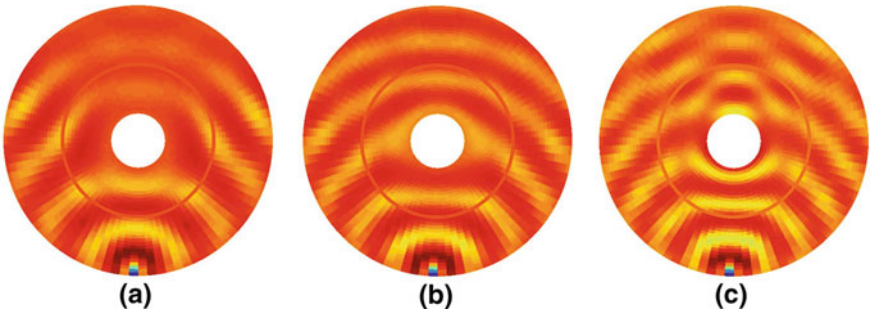

Fig. 12.37 ADS^{TM} simulation of a cloaked conducting cylinder- design based on LC circuits (the point source is located at the bottom of the computational domain; warmer colors correspond to higher node voltages). **a** $f/f_0 = 0.9$, **b** $f/f_0 = 1$, and **c** $f/f_0 = 1.1$

12.7 Analysis of Active Cylindrical Cloaks Based on Non-Foster Metamaterial

In the previous section, it was shown that dispersionless non-Foster ENZ and MNZ metamaterials are indeed feasible. However, maximal operating frequency reported so far does not exceed 2 GHz.

In this section, a numerical analysis of the BW of an anisotropic cloak based on-non Foster ENZ and MNZ metamaterials is presented. The calculations are based both on ideal non-Foster metamaterials without dispersions and on realistic non-Foster metamaterials. In the realistic case, the measurement data from the best currently available active metamaterial [61, 62] were used in the calculation. All the results are presented as a function of relative frequency f/f_0 (f_0 being the frequency for which the cloak was designed).

12.7.1 Cloak Based on Ideal Non-Foster Metamaterial

In the first step, a circuit-theory model of transmission-line-based cloak from Fig. 12.30 was constructed. Following an idea from [38], a commercial circuit theory simulator (ADS^{TM}) was used for analysis in the frequency domain [63, 64]. The model was designed as a simplified TM cloak (Sect. 12.2.2), intended for operation at the frequency of 1 GHz. The inner radius of the cloak shell was $a = 15$ cm (0.5λ) and the outer radius $b = 45$ cm (1.5λ), where λ corresponds to the free-space wavelength. The equivalent thickness of the cloak in the z direction was chosen to be $d = 3$ cm ($\lambda/10$). The model consisted of 40 concentric layers in the radial direction, of which the inner 7 layers represented the bare conducting cylinder, the consequent 15 layers represented the cloak and the outer 18 layers represented the free-space background. Thus, the whole model comprised 3,600

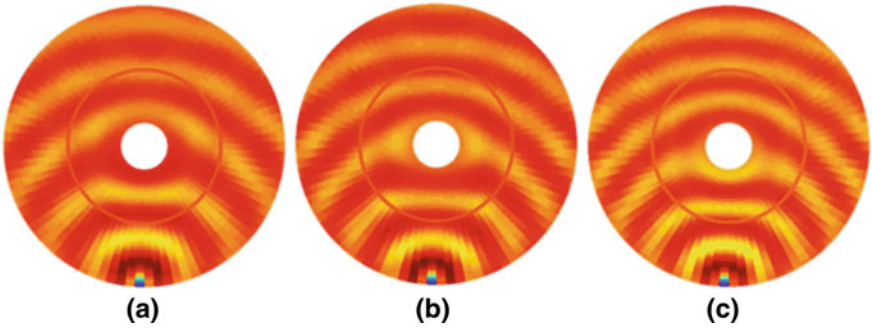

Fig. 12.38 ADS^{TM} simulation of a cloaked conducting cylinder-design based on lumped circuits that contain ideal negative non-Foster capacitors and inductors, (the point source is located at the bottom of the computational domain; warmer colors correspond to higher node voltages). **a** $f/f_0 = 0.9$, **b** $f/f_0 = 1$, and **c** $f/f_0 = 1.1$

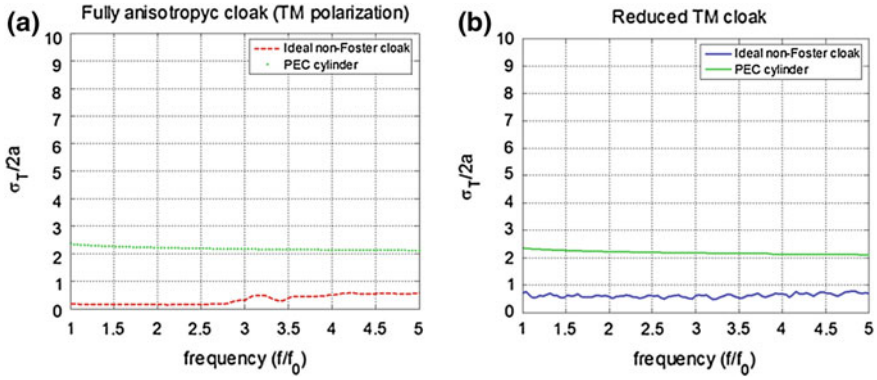

Fig. 12.39 **a** Calculated scattering width for fully anisotropic TM cloak with ideal non-Foster metamaterial. **b** Calculated scattering width for reduced TM cloak with ideal non-Foster metamaterial

unit cells [65]. The cylindrical grid-like structure was terminated with Bloch impedances that mimic the infinite background medium, i.e., free space. In the first group of simulations, ordinary passive unit cell with LC circuits was used, values of which were calculated using (12.9) and (12.36). The distribution of node voltages across the whole grid was post-processed and visualized in MATLAB^{TM}, and a sample of the obtained results is shown in Fig. 12.37.

As expected, it was found that the change of frequency of ± 10 % seriously deteriorates cloaking, due to inherent dispersion.

In the second group of simulations, ideal non-Foster negative capacitances and inductances were implemented in the model emulating ideal dispersionless ENZ and MNZ metamaterials and no deterioration of cloaking with change of frequency was observed (Fig. 12.38). This shows that use of non-Foster ENZ and MNZ metamaterials can indeed broaden the BW of an anisotropic cloak.

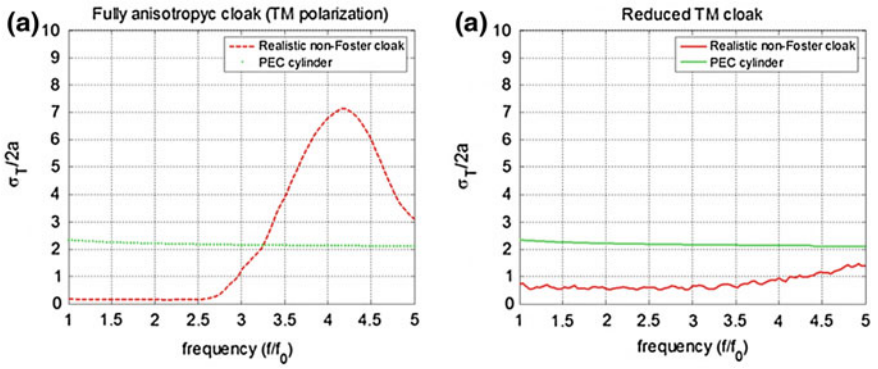

Fig. 12.40 **a** Calculated scattering width for fully anisotropic TM cloak with realistic non-Foster metamaterial. **b** Calculated scattering width for reduced TM cloak with realistic non-Foster metamaterial

After these phenomenological results that prove the basic idea, the detailed calculation of invisibility gain was performed using an analytical approach already used in the case of a passive cloak (Sect. 12.4). Ten layers of ideal dispersionless non-Foster metamaterials were assumed in the calculation and the results are shown in Fig. 12.39. It can be seen that the obtained BW is extremely large and it exceeds 1:5 (more than two octaves), both in the case of the fully anisotropic cloak and the reduced TM cloak.

12.7.2 Cloak Based on Realistic Non-Foster Metamaterial

Finally, the scattering width of an anisotropic cloak with realistic non-Foster metamaterials was calculated. As expected, the obtained results (Fig. 12.40) were worse than those in the ideal case but they are still excellent. The CBW of a fully anisotropic cloak is approximately 1:3 while the BW of the reduced TM cloak is larger than 1:5. At first sight, it is surprising that the BW of a fully anisotropic cloak is narrower, but the explanation is rather simple. As it was shown in Sect. 12.5 this cloak (due to its complex design) is more sensitive to variation of design parameters (and dispersion). These results clearly show that the use of non-Foster metamaterials may significantly increase the BW of an anisotropic cloak (Fig. 12.40).

12.8 Conclusions

The propagation with a phase velocity that is greater than the speed of light (i.e., superluminal propagation) is necessary for the operation of classical transformation electromagnetic anisotropic cloaks. In other words, it means that ENZ and MNZ metamaterials must be used in cloak design. Unfortunately, all passive ENZ and MNZ metamaterials suffer from inherent narrow operating BW, which is a consequence of the basic energy-dispersion constraints (Foster's reactance theorem). In addition, practical cloak realizations always include several layers made of ENZ (MNZ) metamaterials with different constitutive parameters. This is actually a multifrequency resonant system, which further decreases the CBW.

It has been demonstrated that it is possible to improve the operation of a passive anisotropic cloak by optimization of design parameters (number of layers and the values of constitutive parameters of used metamaterials). As expected, it was shown that it is possible to increase either the invisibility gain (up to a factor of 500) or the invisibility BW (up to a factor of 2.5), but not both simultaneously. Specifically, it was shown that it is possible to design a TM cloak with reduced parameters with ideal invisibility properties at one single frequency. It was also shown possible to obtain ideal invisibility for an optimized cloak with only three layers. Although the optimization significantly improves the cloaking performances, it, of course, cannot beat out the background physics. Therefore, the CBW is still rather narrow (less than 1 %) as a direct consequence of basic dispersion-energy constraints.

In addition, it was shown that it is possible to go around basic-energy dispersion constraints by using a novel approach based on non-Foster metamaterials. At the present state of the art, non-Foster metamaterials offer extremely broad almost dispersionless operation (operation BW up to 1:100). These metamaterials are in their infant phase and they are currently available only in the low RF regime (up to 2 GHz). However, it is expected that the use of microelectronic technology could increase the maximal frequency up to more than 5 GHz.

Finally, the measured effective parameters of available non-Foster metamaterials were used as input data for calculation of the CBW. The obtained results revealed the BW of up to 1:5 for a cloak based on realistic metamaterials, which fairly exceeds the performances of a passive cloak.

References

1. Dollin LS (1961) On the possibility of comparison of three-dimensional electromagnetic systems with nonuniform anisotropic filling. Izv VUZov Radiofizika 4(5):964–967
2. Kerker M (1975) Invisible bodies. J Opt Soc Am 65:376–379
3. Edwards B, Alu A, Silveirinha MG, Engheta N (2009) Experimental verification of plasmonic cloaking at microwave frequencies with metamaterials. Phys Rev Lett 103:153901

4. Alu A, Engheta N (2005) Achieving transparency with plasmonic and metamaterial coatings. Phys Rev E72:016623
5. Schurig D, Mock JJ, Cummer SA, Pendry JB, Starr AF, Smith DR (2006) Metamaterial electromagnetic cloak at microwave frequencies. Science 314:977–980. doi:10.1126/science.1133628
6. Kanté B, Germain D, de Lustrac A (2009) Experimental demonstration of a nonmagnetic metamaterial cloak at microwave frequencies. Phys Rev B 80:201104
7. Ivsic B, Sipus Z, Hrabar S (2009) Analysis of uniaxial multilayer cylinders used for invisible cloak realization. IEEE Trans Antennas Propag 57:1521–1526. doi:10.1109/TAP.2009.2016695
8. Kildal PS, Kishk AA, Tengs A (1996) Reduction of forward scattering from cylindrical objects using hard surfaces. IEEE Trans Antennas Propag 44:1509–1520
9. Silveirinha MG, Alu A, Engheta N (2007) Parallel-plate metamaterials for cloaking structures. Phys Rev E 75:036603
10. Tretyakov S, Alitalo P, Luukkonen O, Simovski C (2009) Broadband electromagnetic cloaking of long cylindrical objects. Phys Rev Lett 103:103905
11. Kahn WK, Kurss H (1965) Minimum-scattering antennas. IEEE Trans Antennas Propag 13:671–675
12. Alexopoulos NG, Uzunoglu NK (1978) Electromagnetic scattering from active objects: invisible scatterers. Appl Opt 17:235–239
13. Pendry JB, Schurig D, Smith DR (2006) Controlling electromagnetic fields. Science 312:1780–1782. doi:10.1126/science.1125907
14. Cai W, Chettiar UK, Kildishev AV, Shalaev VM (2007) Optical cloaking with non-magnetic metamaterials. Nat Photonics 1:224–227
15. Kanté B, de Lustrac A, Lourtioz JM, Burokur SN (2008) Infrared cloaking based on the electric response of split ring resonators. Opt Express 16:9191–9198
16. Hrabar S (2006) Waveguide experiments to characterize the properties of SNG and DNG metamaterials. In: Physics and engineering explorations, Wiley and IEEE
17. Engheta N, Ziolkowski RW (2008) Metamaterials: Physics and engineering explorations. Wiley, New Jersey
18. Eleftheriades GV, Balmain KG (2005) Negative-refraction metamaterials: fundamental principles and applications. Wiley, New Jersey
19. Caloz C, Itoh T (2006) Electromagnetic MTMs: transmission line theory and ticrowave applications. Wiley, New Jersey
20. Hrabar S, Bartolic J, Sipus Z (2007) Re to: comments on waveguide miniaturization using uniaxial negative permeability metamaterial. IEEE Trans Antennas Propag 55:1017–1018
21. Auzanneau F, Ziolkowski RW (1998) Theoretical study of synthetic bianisotropic materials. J Electromagn Waves Apps 12(3):353–370
22. Ziolkowski RW (1997) The design of Maxwellian absorbers for numerical boundary conditions and for practical applications using engineered artificial materials. IEEE Trans Antennas Propag 45:656–671
23. Zhang S, Fan W, Panoiu NC, Malloy KJ, Osgood M, Brueck DR (2006) Optical negative-index bulk metamaterials consisting of 2D perforated metal-dielectric stacks. Opt Exp 14:6778–6787
24. Knott EF, Shaeffer JF, Tuley MT (2004) Radar cross section. SciTech Publishing Inc, New York
25. Sipus Z, Kildal PS, Leijon R, Johansson M (1998) An algorithm for calculating green's functions for planar, circular cylindrical and spherical multilayer substrates. ACES J 13:243–254
26. Bojanjac D, Sipus Z (2012) Oblique incidence performance of anisotropic cylindrical structures used for invisibility cloak design. IEEE Trans Antennas Propag 60:4814–4821
27. Hrabar S, Benic L, Bartolic J (2006) Simple experimental determination of complex permittivity or complex permeability of SNG metamaterials. In: Proceedings on 36th European microwave conference 2006, pp 1395–1398

28. Liang Z, Yao P, Sun X, Jiang X (2008) The physical picture and the essential elements of the dynamical process for dispersive cloak structures. App Phys Lett 92:131118
29. Kundtz N, Gaultney D, Smith DR (2010) Scattering cross-section of a transformation optics-based metamaterial cloak. New J Phys 15:043039
30. Popa BI, Cummer SA (2009) Cloaking with optimized homogeneous anisotropic layers. Phys Rev A 79:023806
31. Yu Z, Feng Y, Xu X, Zhao J, Jiang T (2011) Optimized cylindrical invisibility cloak with minimum layers of non-magnetic isotropic materials. J Phys D Appl Phys 44:185102
32. Komljenovic T, Sipus Z (2011) Optimizing electromagnetic problems at University of Zagreb—an overview. In: Proceedings of ELMAR 2011, pp 353–356
33. Ivsic B, Komljenovic T, Sipus Z (2010) Optimization of uniaxial multilayer cylinders used for invisible cloak realization. IEEE Trans Antennas Propag 58:3397–3401. doi:10.1109/TAP.2010.2055789
34. Robinson J, Rahmat-Samii Y (2004) Particle swarm optimization in electromagnetics. IEEE Trans Antennas Propag 52(2):397–407
35. Kennedy J, Eberhart RC (1995) Particle swarm optimization. In: Proceedings of IEEE conference on neural networks IV, Piscataway
36. Chen H, Liang Z, Yao P, Jiang X, Ma H, Chan T (2007) Extending the bandwidth of electromagnetic cloaks. Phys Rev B76:241104
37. Hrabar S, Krois I, Matvijev M (2009) Is it possible to overcome basic dispersion constraints and achieve broadband cloaking? In: Proceedings on 3rd international congress on advanced electromagnetic—materials in microwaves and optics, pp 408–410
38. Liu X, Li C, Yao K, Meng X, Li F (2009) Invisibility cloaks modeled by anisotropic MTM based on inductor- capacitor networks. IEEE Trans Antennas Propag 8:1154–1157. doi:10.1109/LAWP.2009.2034675
39. Zedler Elefteriades GV (2011) Anisotropic transmission line metamaterials for 2-D transformation optics applications. Proc of the IEE 10:1634–1645
40. Gok G, Grbic A (2010) Tensor transmission line metamaterials. IEEE Trans Antennas Propag 58:5
41. Alitalo P, Ranvier S, Vehmas J, Tretyakov S (2008) A microwave transmission line network guiding electromagnetic fields through a dense array of metallic objects. Metamaterials 2(4):206–212. doi:10.1016/j.metmat.2008.09.001
42. Alitalo P, Bongard F, Zürcher JF, Mosig J, Tretyakov S (2009) Experimental verification of broadband cloaking using a volumetric cloak composed of periodically stacked cylindrical transmission line networks. Appl Phys Lett 94:014103
43. Hrabar S, Bonefacic D, Muha D (2008) ENZ-based shortened horn antenna—an experimental study. Antennas and propagation society international symposium. doi:10.1109/APS.2008.4619853
44. Rotman W (1962) Plasma simulation by artificial dielectrics and parallel plate media. IRE Tran Antennas Propag 10:82–95
45. Linvill JG (1953) Transistor negative impedance converters. Proc IRE 41:725–729
46. Skahill, G, Ruish RM et al (1998) Electrically small, efficient, wide-band, low-noise antenna elements. In: Proceedings on the 1998 antenna applications symposium, pp 213–214
47. Aberle J, Lomak R (2007) Antennas with non-Foster matching networks. Morgan & Claypool, San Rafael
48. Sussman-Fort SE (2006) Matching network design using non-Foster impedances. Int J RF Microw CAE 16(2):135–142
49. Sussman-Fort SE (2009) Non-Foster impedance matching of electrically-small antennas. IEEE Trans Antennas Propag 57(8):2230–2241
50. Perry AK (1973) Broadband antenna systems realized from active circuit conjugate impedance matching. Naval Postgraduate School, Monterey
51. Leifso CR (2000) Design and analysis of novel RF active impedance synthesizing circuits. Ph.D. thesis, Department of Electrical and Computer Engineering, University of Calgary
52. Leifso CR, Hasett, JW (2001) Active tunable inductor. US Patent, Patent No: US 6,211,753 B1

53. Hrabar S, Krois I, Kiricenko A (2010) Towards active dispersionless ENZ metamaterial for cloaking applications. Metamaterials 4(2–3):89–97
54. Hrabar S, Krois I, Bonic I, Kiricenko A, Ugante Munoz E (2010) Active broadband ENZ and MNZ metamaterials. AFRL and The European Office of Aerospace Research and Development (EOARD), contract FA8655-10-1-3030, final report
55. Pozar DM (2005) Microwave engineering, 3rd edn. Wiley, New Jersey
56. Sussman-Fort SE (1998) Gyrator-based biquad filters and negative impedance converters for microwaves. Int J RF Microw CAE 8:86–101
57. Kolev S, Delacressonniere B, Gautier J (2001) Using a negative capacitance to increase the tuning range of a varactor diode in MMIC technology. IEEE Trans Micro Theor Tech 49(12):2425–2430
58. Park H, Lee S, Lee J, Sangwoo N (2009) A 0.1–1 GHz CMOS variable gain amplifier using wideband negative capacitance. IECE Trans Electron 92(10):1311–1314
59. Kwisung Y, Mohammed M et al (2007) Negative impedance circuit and its application to inductorless resonant oscillators. In: Proceedings of international SOC conference in Seoul 2007, pp 13–16
60. Ugarte-Munoz E, Hrabar S, Segovia-Vargas D (2011), Investigation of stability of negative impedances in active metamaterials and antennas. In: Proceedings on Eucap 2011, pp 2059–2063
61. Hrabar S (2012) Active non-Foster metamaterials: from intriguing background physics to real-world applications. Metamaterials 2012, plenary talk, Sankt Petersburg
62. Hrabar S, Krois I, Bonic I, KiricenkoA (2011) Negative capacitor paves the way to ultra-broadband metamaterials. Appl Phys Lett 99 25:254103–254104. doi:10.1063/1.3671366
63. Hrabar S, Malcic I, Nanut S, Juricev-Sudac L (2010) Feasibility of use of lumped elements in anisotropic 2D cloak. In: IEEE ICECom, 2010 conference proceedings, pp 1–4. 978-9-5360-3758-2
64. Hrabar S, Malcic I (2011) Bandwidth analysis of lumped-element-based planar anisotropic cloak. In: IEEE proceedings of the 5th E conference on antennas and propagation (EUCAP), pp 840–841. 978-1-4577-0250-1
65. Malcic I, Hrabar S, Juricev-Sudac L (2011) Numerical analysis of a lumped-element-based planar anisotropic cloak. In: IEEE ELMAR, 2011 proceedings, pp 369–372. 978-953-7044-12-1

Chapter 13
Anisotropic Representation for Spatially Dispersive Periodic Metamaterial Arrays

Arthur D. Yaghjian, Andrea Alù and Mário G. Silveirinha

Abstract A rigorous anisotropic (as opposed to bianisotropic) representation for three-dimensional (3D) spatially dispersive periodic arrays of passive inclusions separated in free space is developed, beginning with the microscopic Maxwell equations, that yields causal, macroscopic permittivities and inverse permeabilities for the fundamental Floquet modes of the arrays. (Macroscopic magnetoelectric coefficients are not required.) Reality conditions, reciprocity relations, passivity conditions, and causality relations are derived for these spatially dispersive macroscopic permittivity and permeability constitutive parameters. A significant feature of the formulation is that the macroscopic permittivities and permeabilities reduce to their anisotropic-continuum definitions in terms of ordinary macroscopic averages at the low spatial and temporal frequencies. In addition, diamagnetic metamaterial arrays require no special considerations or modifications to accommodate their unusual characteristics. Analytic and numerical examples of 3D arrays with dielectric-sphere inclusions and two-dimensional (2D) arrays with circular-cylinder inclusions are given that confirm the theoretical results for the macroscopic permittivities and permeabilities of these arrays which exhibit electric and magnetic or diamagnetic macroscopic polarizations. The realization of the potential innovations provided by transformation electromagnetics depends strongly upon the development of metamaterials. This chapter aspires to enhance the understanding of metamaterials and thus to facilitate their development.

A. D. Yaghjian (✉)
Electromagnetics Research Consultant, 115 Wright Road, Concord, MA 01742, USA
e-mail: a.yaghjian@comcast.net

A. Alù
Department of Electrical & Computer Engineering, The University of Texas, Austin, TX 78712, USA
e-mail: alu@mail.utexas.edu

M. G. Silveirinha
Department of Electrical Engineering-Instituto de Telecomunicações, University of Coimbra, Coimbra, Portugal
e-mail: mario.silveirinha@co.it.pt

D. H. Werner and D.-H. Kwon (eds.), *Transformation Electromagnetics and Metamaterials*, DOI: 10.1007/978-1-4471-4996-5_13, © Springer-Verlag London 2014

13.1 Introduction

This work was originally motivated by the desire to determine a rigorous and therefore causal macroscopic permeability for diamagnetic metamaterials (materials with artificial inclusions rather than molecules). To understand the difficulties encountered in dealing with diamagnetism, consider a three-dimensional (3D) cubic periodic array of perfectly electrically conducting (PEC) spheres separated in free space. When this array is described by a spatially nondispersive dipolar continuum, it has a macroscopic permittivity $\epsilon(\omega)$ and a macroscopic permeability $\mu(\omega)$, which are functions of frequency ω, such that $\mathbf{D}_\omega(\mathbf{r}) = \epsilon(\omega)\mathbf{E}_\omega(\mathbf{r})$ and $\mathbf{H}_\omega(\mathbf{r}) = \mu^{-1}(\omega)\mathbf{B}_\omega(\mathbf{r})$, where $\mathbf{E}_\omega$ and $\mathbf{B}_\omega$ are the primary electric and magnetic vectors and $\mathbf{D}_\omega = \epsilon_0\mathbf{E}_\omega + \mathbf{P}_\omega$ and $\mathbf{H}_\omega = \mu_0^{-1}\mathbf{B}_\omega - \mathbf{M}_\omega$ are the secondary electric and magnetic vectors in Maxwell's macroscopic equations with electric and magnetic polarization densities, $\mathbf{P}_\omega(\mathbf{r})$ and $\mathbf{M}_\omega(\mathbf{r})$ (electric-charge-defined electric dipole moment per unit volume and electric-current-defined magnetic dipole moment per unit volume). For simplicity, we can consider transverse electromagnetic (TEM) propagation in one of the three principal directions.

Assume that a dipolar homogenization procedure exists for determining a causal $\epsilon(\omega)$ and $\mu^{-1}(\omega)$ for this PEC-sphere array. Since both the electric and magnetic dipole moments of PEC spheres in a source-free incident field approach zero as $\omega \to \infty$, we also have that $\epsilon(\omega) \to \epsilon_0$ and $\mu^{-1}(\omega) \to \mu_0^{-1}$ as $\omega \to \infty$ where ϵ_0 and μ_0 are the permittivity and permeability of free space. Consequently, the causal functions $[\epsilon(\omega) - \epsilon_0]$ and $[\mu^{-1}(\omega) - \mu_0^{-1}]$ should obey the Kramers–Kronig relations written in compact form as [1, p. 98][1]

$$\epsilon(\omega) - \epsilon_0 = \frac{i}{\pi}\int_{-\infty}^{+\infty} \frac{\epsilon(v) - \epsilon_0}{\omega - v}\,\mathrm{d}v \tag{13.1a}$$

$$\mu^{-1}(\omega) - \mu_0^{-1} = \frac{i}{\pi}\int_{-\infty}^{+\infty} \frac{\mu^{-1}(v) - \mu_0^{-1}}{\omega - v}\,\mathrm{d}v\,. \tag{13.1b}$$

[1] It can be proven using Lu's book [2, Eq. (2.16) on p. 23, Eq. (5.11) on p. 57, and the equation in exercise 4 on p. 28] that sufficient conditions for (13.1) to hold are that $\epsilon(\omega_c)$ and $\mu^{-1}(\omega_c)$ are analytic and single-valued (that is, holomorphic) functions in the upper half ($\omega_i > 0$) of the complex $\omega_c = \omega + i\omega_i$ plane having boundary values equal to $\epsilon(\omega)$ and $\mu^{-1}(\omega)$ [that is, $\lim_{\omega_i \to 0} \epsilon(\omega_c) = \epsilon(\omega)$ with ω_i in the upper half plane, and similarly for $\mu^{-1}(\omega_c)$] such that these boundary values are Hölder continuous, and $\epsilon(\omega_c) - \epsilon_0$ and $\mu^{-1}(\omega_c) - \mu_0^{-1}$ both $\sim 1/|\omega_c|^\alpha$, $\alpha > 0$, as $|\omega_c| \to \infty$ for $\omega_i \geq 0$. These sufficient conditions for the Kramers–Kronig relations also imply (with ordinary continuity replacing the stronger Hölder continuity) the corresponding time-domain causality relations by means of the Cauchy theorem for continuous functions [2, p. 64; 3, p. 347]. For example $\int_{-\infty}^{+\infty}[\epsilon(\omega) - \epsilon_0]e^{-i\omega t}\mathrm{d}\omega = 0$ for $t < 0$.

Passivity in a spatially nondispersive dipolar continuum also demands that [1, p. 96][2]

$$\omega \mathrm{Im}[\epsilon(\omega)] \geq 0 \tag{13.2a}$$

$$\omega \mathrm{Im}[\mu(\omega)] \geq 0\,. \tag{13.2b}$$

The expressions in (13.1a) and (13.2a), and in (13.1b) and (13.2b), can be combined to prove that

$$\epsilon(0) \geq \epsilon_0 \tag{13.3a}$$

$$\mu(0) \geq \mu_0 \tag{13.3b}$$

under the assumptions that the imaginary parts of $\epsilon(\omega)$ and $\mu(\omega)$ are negligible in the neighborhood of $\omega = 0$ and that $\omega \mathrm{d}\epsilon(\omega)/\mathrm{d}\omega$ and $\omega \mathrm{d}\mu^{-1}(\omega)/\mathrm{d}\omega$ both $\to 0$ as $\omega \to 0$ [5, Sect. 84; 6]—assumptions satisfied by the $\epsilon(\omega)$ and $\mu^{-1}(\omega)$ of the PEC-sphere array. The inequality for permittivity in (13.3a) is certainly obeyed by the 3D array of PEC spheres. However, the inequality for permeability in (13.3b) is clearly violated by the PEC sphere array, which is strongly diamagnetic [7, Sect. 9.5, 8, Fig. 8][3] at low frequencies and thus has $\mu(0) < \mu_0$.

This apparent paradox can be explained by noting that we are assuming that the array behaves as a spatially nondispersive dipolar continuum for all frequencies ω. In fact, as the frequency increases, the electromagnetic properties of the array can no longer be described by macroscopic Maxwellian equations for a spatially nondispersive continuum characterized by dipolar $\epsilon(\omega)$ and $\mu(\omega)$ that necessarily satisfy the causality relations in (13.1) or the passivity conditions in (13.2) [10]. In the case of the PEC spheres, this inadequacy of a spatially nondispersive continuum description of the array at higher frequencies is manifested in part by the paradoxical conclusion that $\mu(0) \geq \mu_0$. In particular, it is impossible for a function

---

[2] The theorem in the Appendix or in [4, Sect. 123] can be invoked to prove that $\epsilon^{-1}(\omega) - \epsilon_0^{-1}$ or $\mu^{-1}(\omega) - \mu_0^{-1}$ is causal if $\epsilon(\omega) - \epsilon_0$ or $\mu(\omega) - \mu_0$ is causal (and vice versa), provided $\epsilon(\omega)$ and $\mu(\omega)$ satisfy the passivity conditions in (13.2). Nonetheless, we show the Kramers–Kronig relations in (13.1b) for $\mu^{-1}(\omega) - \mu_0^{-1}$ rather than for $\mu(\omega) - \mu_0$ because when spatial dispersion is taken into account later by introducing an arbitrary real plane-wave propagation vector $\boldsymbol{\beta}$, we find that the passivity conditions in (13.2) are coupled and do not necessarily hold separately where the spatial or temporal dispersion is large. Thus, in general, for spatially dispersive macroscopic permittivity and permeability, only $\epsilon(\boldsymbol{\beta}, \omega) - \epsilon_0$ and $\mu^{-1}(\boldsymbol{\beta}, \omega) - \mu_0^{-1}$ satisfy causality at each fixed $\boldsymbol{\beta}$ for electric charge-current defined polarizations.

[3] The Bohr–van Leeuwen theorem, which states that a classical material composed of free charges in thermal equilibrium cannot be effected by a magnetic field because the magnetic field does no work on moving charges [9, Sects. 24–27], is often used to argue that classical electromagnetics cannot describe diamagnetism. This theorem assumes that all the energy at thermal equilibrium is in the kinetic and potential energy of the charge carriers. However, by using a conducting metamaterial inclusion as a model for a molecule, an additional inductive magnetic-field energy is introduced such that the Bohr–van Leeuwen theorem no longer applies and one is able to classically describe diamagnetic materials and metamaterials.

$\mu(\omega)$ or $\mu^{-1}(\omega)$ to satisfy the Kramers–Kronig causality relations [given in (13.1b) for $\mu^{-1}(\omega)$] and the passivity condition in (13.2b) if $\mu(\omega)$ or $\mu^{-1}(\omega)$ is real and continuously differentiable near $\omega = 0$ and $\mu(0) < \mu_0$.[4] Moreover, using a bianisotropic description of the PEC-sphere array and expanding the induced fields of the array with higher-order multipole moments, while maintaining a spatially nondispersive continuum description of the array, allow additional constitutive parameters but still require a diamagnetic $\mu(\omega)$ with $\mu(0) < \mu_0$ that violates the Kramers–Kronig causality relations for $\mu(\omega)$ or $\mu^{-1}(\omega)$.

Consequently, to adequately describe a 3D array in a way that reduces at lower spatial and temporal frequencies to a continuum description in terms of permittivity and permeability, we proceed to formulate an anisotropic representation for 3D periodic arrays that rigorously takes into account spatial ($\boldsymbol{\beta}$) as well as temporal (ω) dispersion. We show that such a formulation automatically produces a macroscopic permittivity and inverse permeability that satisfy causality and are free of inconsistencies even if the array exhibits diamagnetism.

Most homogenization theories in the past have been formulated for source-free arrays in which the propagation vectors $\boldsymbol{\beta}$ are functions of the frequency ω [12–15]. However, to fully characterize the effects of spatial dispersion in plasmas and crystals, Landau and Lifshitz [5, Chap. 12], Silin and Rukhadze [16], and Agranovich and Ginzburg [17] decompose the fields and sources of a spatially dispersive, homogeneous continuum into a spectrum of $e^{i(\boldsymbol{\beta}\cdot\mathbf{r}-\omega t)}$ plane waves, where $\boldsymbol{\beta}$ is a real propagation vector and ω is a real angular frequency. These authors combine all electric and magnetic polarization effects (including all multipoles) into a single electric-magnetic polarization density $\mathbf{P}_L(\boldsymbol{\beta}, \omega)$ (based on a single microscopic electric current density induced by an applied electric current density).[5] They then assign a single permittivity dyadic $\overline{\boldsymbol{\epsilon}}_L(\boldsymbol{\beta}, \omega)$ to the single polarization vector such that $\mathbf{P}_L(\boldsymbol{\beta}, \omega) = [\overline{\boldsymbol{\epsilon}}_L(\boldsymbol{\beta}, \omega) - \epsilon_0\overline{\mathbf{I}}] \cdot \mathbf{E}(\boldsymbol{\beta}, \omega)$, where $\mathbf{E}(\boldsymbol{\beta}, \omega)$ is

[4] In Refs. [6] and [11], inequalities for $\epsilon(\omega)$ and $\mu(\omega)$ in a spatially nondispersive dipolar continuum that were derived from an energy-conservation inequality also imply the inequalities in (13.3) under the same assumptions. Although not stated explicitly in Refs. [6] and [11], the energy-conservation inequality that was used does not hold, in general, for diamagnetic $\mu(\omega)$ produced by induced magnetic dipole moments on molecules (or inclusions) that have no permanent magnetic dipole moments; that is, the energy-conservation theorem in [6] and [11] assumes that the macroscopic $\mu(\omega)$ is produced entirely by the alignment of initially randomly oriented permanent magnetic dipoles.

[5] Landau and Lifshitz introduced the use of the single polarization vector for "natural optical activity" in Sect. 83 of the first edition (1957) of their book, *Electrodynamics of Continuous Media* [5]. Later, Silin and Rukhadze [16] and Agranovich and Ginzburg [17] continued to use this single-polarization approach in their general formulation of spatial dispersion. In the formulation of spatial dispersion for continua given in Sect. 103 of the second edition of the Landau and Lifshitz (and Pitaevskii) book [5], unlike in the formulations of [16] and [17], they do not show an applied electric current density explicitly in Maxwell's equations and yet they assume arbitrary real values of the propagation vector $\boldsymbol{\beta}$ and frequency ω. This is understandable because they show only the space-time $(\mathbf{r}, t)$ Maxwell equations in which the applied source densities can be localized. Nonetheless, one must assume in the Landau–Lifshitz–Pitaevskii formulation that applied electric current density is present in the $(\boldsymbol{\beta}, \omega)$ representation.

the electric field and $\overline{\mathbf{I}}$ is the unit dyadic. Agranovich and Ginzburg [17, Chap. 3] discuss the conditions under which this continuum formulation applies to the fundamental Floquet mode of a natural crystal lattice. More recently, Silveirinha [18–20] has extended and applied the single-polarization formulation to 2D and 3D periodic metamaterial arrays.

Although the single-polarization formulation for a continuum [5, 16, 17] and periodic metamaterials [18–20] is both accurate and elegant, and has the advantage of an appealing simplicity for many applications, it has some disadvantages as well. For instance, practical solutions to the Maxwellian microscopic equations for metamaterial arrays usually require the separate determination of electric and magnetic polarizations, whether or not the two polarizations are eventually combined. Moreover, the $\overline{\boldsymbol{\epsilon}}_L(\boldsymbol{\beta}, \omega)$ dyadic for the single polarization does not reduce to a scalar even if the medium is an isotropic continuum and, thus, in reality often requires no fewer unknowns than the conventional formulation that uses both electric and magnetic polarizations. The single-polarization formulation is especially awkward for dealing with inclusions that produce significant macroscopic magnetization effects in periodic arrays, and does not provide a definitive prescription for determining causal permittivity and permeability dyadics from the single-polarization dyadic $\overline{\boldsymbol{\epsilon}}_L(\boldsymbol{\beta}, \omega)$, although recipes for determining approximate permittivities and permeabilities from the single polarization have been given in [18].

To help alleviate the drawbacks of the single-polarization approach, Fietz and Shvets [21] introduce applied magnetic current density in addition to applied electric current density and approximate macroscopic averages in such a way that certain boundary integrals of the microscopic and macroscopic fields over the unit cells are equal in order to formulate a spatially dispersive macroscopic bianisotropic representation of metamaterials. In this bianisotropic formulation, they find that, even with nonbianisotropic, centro-symmetric inclusions, a lattice bianisotropy [22] can be induced for $\boldsymbol{\beta} \neq 0$.

Alù [23] has developed a straightforward spatially dispersive bianisotropic representation for periodic metamaterials with applied electric and magnetic current densities by expanding the induced electric and magnetic polarization densities with a multipole power series in the propagation vector $\boldsymbol{\beta}$. In Alù's formulation, weak spatial dispersion effects may be properly assigned to local bianisotropic parameters that allow a physically meaningful homogenized description of the array in the limit of low spatial and temporal frequencies.

General reciprocity relations, passivity conditions, and causality relations are not determined for the spatially dispersive bianisotropic constitutive parameters in either [21] or [23], and these relationships are not necessarily the same as those in a spatially nondispersive continuum.

In the present work, we excite 3D periodic arrays with applied plane-wave $e^{i(\boldsymbol{\beta}\cdot\mathbf{r}-\omega t)}$ electric current density only, and decompose the induced equivalent electric current density into generalized electric and magnetic polarization densities that maintain the Maxwellian representation for the fundamental Floquet

modes of the 3D periodic, spatially dispersive metamaterial arrays comprised of general lossy or lossless polarizable inclusions electrically separated in free space. We show that, with this decomposition, anisotropic permittivity and permeability [24, Chap. 1] are sufficient to characterize the electric and magnetic macroscopic properties of the fundamental Floquet modes of the arrays; that is, the macroscopic magnetoelectric dyadics of a bianisotropic formulation are not required. The constitutive parameters (permittivity, inverse permeability, and their associated susceptibilities) of this anisotropic representation have the further advantage of satisfying causality (at each fixed $\boldsymbol{\beta}$) and well-defined (though coupled) reciprocity relations and passivity conditions, while maintaining a convenient decomposition into separate electric and magnetic polarizations.

Interestingly, the generalized electric and magnetic polarization densities do not involve generalized multipole moments of higher order than generalized electric quadrupole moments. As both $\boldsymbol{\beta}$ and ω become sufficiently small, the enforced and free-space wavelengths become much larger than the separation distance d between the unit cells of the inclusions and the periodic-array formulation approaches that of an anisotropic continuum fully described by the permittivity and permeability of the fundamental Floquet mode of the array. Moreover, for array inclusions having nonzero electric and/or magnetic dipole moments as $|\boldsymbol{\beta}d|$ and $|k_0 d|$ both become sufficiently small (where $k_0 = \omega\sqrt{\mu_0\epsilon_0} = \omega/c$), the arrays can be represented by an anisotropic dipolar continuum with negligible higher-order multipole densities. In this anisotropic dipolar continuum, the electric and magnetic fields as well as the polarization densities are defined in terms of the same macroscopic averages used for conventional dipolar continua and thus, for example, in the absence of delta-function surface polarizations, the tangential components of the macroscopic E-electric and H-magnetic fields across interfaces (thin transition layers) between free space and the array or between two arrays become approximately continuous as $|\boldsymbol{\beta}d|$ and $|k_0 d|$ both become sufficiently small.

Within the framework of the macroscopic, spatially dispersive anisotropic formulation, it is significant that diamagnetism presents no unusual causality problems in that the resulting inverse of diamagnetic permeability exhibits a zero time-domain response for time $t < 0$ and satisfies the Kramers–Kronig dispersion relations at each fixed $\boldsymbol{\beta}$. That is, the theory requires no special considerations or modifications for arrays with inclusions that produce macroscopic diamagnetic permeability.

One of the unusual features of this anisotropic formulation is that the passivity conditions for the macroscopic permittivity and permeability dyadics are coupled at the higher values of $\boldsymbol{\beta}$ or ω such that the imaginary parts of the diagonal elements of either the permittivity or permeability dyadic can be negative as well as positive (or zero) while power dissipation within the inclusions remains greater than or equal to zero. This departure from spatially nondispersive dipolar continuum behavior of the imaginary parts of the constitutive parameters of the fundamental Floquet modes of the arrays is caused by the strong spatial or temporal dispersion at the higher values of $\boldsymbol{\beta}$ or ω.

Although the macroscopic, spatially dispersive anisotropic representation implies that a macroscopic, spatially dispersive bianisotropic representation of metamaterials is not required, a macroscopic bianisotropic formulation [21, 23] may for some applications be more suitable and useful, especially for arrays with magnetoelectric coupling in the material of the inclusions. For example, if magnetoelectric coupling at the inclusion level remains significant as the propagation vector $\boldsymbol{\beta}$ and the frequency ω approach zero, the macroscopic permittivity or permeability in the anisotropic formulation (unlike the macroscopic bianisotropic constitutive parameters) can retain a strong dispersion.[6]

The development of the anisotropic representation proceeds from this Introduction to Sect. 13.2 in which the basic macroscopic equations for the fundamental Floquet modes of 3D periodic arrays are derived from the microscopic equations for the general lossy or lossless polarizable material of the inclusions of the arrays. Sufficient conditions are given for the array to approximate an electromagnetic continuum, and boundary conditions are given for an electric quadrupolar continuum.

Section 13.3 develops the anisotropic constitutive relations for the fundamental Floquet modes of 3D arrays and determines expressions for the full permittivity and permeability dyadics in terms of their components transverse to the propagation vector $\boldsymbol{\beta}$.

In Sect. 13.4, the reality conditions, reciprocity relations, passivity conditions, and causality relations are determined for the spatially dispersive anisotropic macroscopic permittivity and permeability.

In Sect. 13.5, we use the derived expressions for the generalized electric and magnetic polarizations to find the electric and magnetic polarizabilities of lossy or

---

[6] Bianisotropic constitutive relations for both applied magnetic and electric plane-wave $e^{i(\boldsymbol{\beta}\cdot\mathbf{r}-\omega t)}$ dependent current exciting the inclusions of the array are expressible as $\mathbf{D}_b = \overline{\boldsymbol{\epsilon}}_b \cdot \mathbf{E}_b + \overline{\boldsymbol{\tau}}_b \cdot \mathbf{B}_b$ and $\mathbf{H}_b = \overline{\boldsymbol{\mu}}_b^{-1} \cdot \mathbf{B}_b + \overline{\boldsymbol{\nu}}_b \cdot \mathbf{E}_b$ with finite bianisotropic constitutive parameters $(\overline{\boldsymbol{\epsilon}}_b, \overline{\boldsymbol{\tau}}_b, \overline{\boldsymbol{\mu}}_b^{-1}, \overline{\boldsymbol{\nu}}_b)$, which, like the fields, are functions of $\boldsymbol{\beta}$ and ω. Then if the applied magnetic current is set equal to zero so that $\omega\mathbf{B} = \boldsymbol{\beta} \times \mathbf{E}$ (now omitting the subscripts "b" on the fields) as in (13.11a), the corresponding anisotropic permittivity dyadic and inverse transverse (to $\boldsymbol{\beta}$) permeability dyadic are given by $\overline{\boldsymbol{\epsilon}} = \overline{\boldsymbol{\epsilon}}_b + \overline{\boldsymbol{\tau}}_b \cdot \overline{\boldsymbol{\beta}}/\omega$ and $\overline{\boldsymbol{\mu}}_{\rm tt}^{-1} = \overline{\boldsymbol{\mu}}_{b\rm tt}^{-1} - \omega\overline{\boldsymbol{\nu}}_{b\rm tt} \cdot \overline{\boldsymbol{\beta}}/|\boldsymbol{\beta}|^2$ with $\overline{\boldsymbol{\beta}}\cdot$ denoting the antisymmetric dyadic equivalent to $\boldsymbol{\beta}\times$ and given explicitly in (13.75) below. From the results in [22] and [23], it can be shown that as $(\boldsymbol{\beta} \to 0,\ \omega \to 0)$ the magnetoelectric parameters, $\overline{\boldsymbol{\tau}}_b$ and $\overline{\boldsymbol{\nu}}_{b\rm tt}$, have a lattice contribution that is generally proportional to $\omega\boldsymbol{\beta}$ plus a bianisotropic-inclusion contribution that approaches a constant. (A third contribution to $\overline{\boldsymbol{\nu}}_b$ proportional to ω can be produced by the contribution from the electric dipole moment of an inclusion to its magnetic dipole moment [1, Eq. (2.9); 25]. However, the origin of the unit-cell integration can always be chosen with respect to the inclusion to make this contribution go to zero as $\boldsymbol{\beta} \to 0$ such that it becomes proportional to $\omega\boldsymbol{\beta}$ like the lattice contribution. It should be noted that although helical metal inclusions can produce bianisotropic effects, this geometrically produced bianisotropy vanishes at low enough frequencies ω for inclusions electrically isolated from one another—an assumption made throughout.) Therefore, only if the bianisotropy at the inclusion level does not become negligible at the low spatial and temporal frequencies $(\boldsymbol{\beta} \to 0,\ \omega \to 0)$, does the anisotropic constitutive parameters $\overline{\boldsymbol{\epsilon}}(\boldsymbol{\beta}, \omega)$ or $\overline{\boldsymbol{\mu}}_{\rm tt}^{-1}(\boldsymbol{\beta}, \omega)$ exhibit strong temporal or spatial dispersion as $\omega/|\boldsymbol{\beta}| \to 0$ or $|\boldsymbol{\beta}|/\omega \to 0$, respectively. Nevertheless, both $\overline{\boldsymbol{\epsilon}}(\boldsymbol{\beta}, \omega)$ and $\overline{\boldsymbol{\mu}}_{\rm tt}(\boldsymbol{\beta}, \omega)$ generally remain finite (nonsingular) as $|\boldsymbol{\beta}|/\omega \to 0$.

lossless dielectric spheres illuminated by an incident plane wave with propagation vector $\boldsymbol{\beta}$ approaching zero. Letting the dielectric constant approach infinity in these polarizabilities, we find the corresponding Clausius–Mossotti electric and magnetic susceptibilities for a 3D PEC sphere array and show that these Clausius–Mossotti approximate susceptibilities satisfy causality. Finally, we compute the exact fundamental Floquet-mode macroscopic permittivity and permeability as $\boldsymbol{\beta}$ approaches zero for a two-dimensional (2D) array of circular cylinders comprised of material that satisfies a Drude dielectric model. In accordance with the predictions of the theory, the exact fundamental Floquet-mode macroscopic permittivity and inverse permeability of the two-dimensional array satisfy causality and the coupled passivity conditions, whereas the exact fundamental Floquet-mode macroscopic permeability does not satisfy causality.

In an Appendix, sufficient conditions are given for the inverse of a causal constitutive parameter to also be causal.

In concluding this Introduction, it seems appropriate, in view of the subject of this book, to mention that the potential innovations brought about by transformation electromagnetics usually require material properties that cannot be found in natural materials. Thus, these transformation-electromagnetics innovations rely heavily upon the development of metamaterials for their realization. Hopefully, this chapter will not only enhance the understanding of metamaterials, but also aid in their design and development.

13.2 Derivation of Maxwellian Macroscopic Equations for the Fundamental Floquet Modes on 3D Periodic Arrays of Lossy or Lossless Polarizable Inclusions

We assume the inclusions (artificial molecules) of the 3D periodic array can support electric current density $\mathcal{J}_\omega(\mathbf{r})$ [with associated charge density $\rho_\omega(\mathbf{r})$], dipolar electric polarization density $\mathcal{P}_\omega(\mathbf{r})$, and dipolar magnetic polarization density (microscopic Amperian magnetization) $\mathcal{M}_\omega(\mathbf{r})$, where the subscripts "$\omega$" indicate that $e^{-i\omega t}$ time dependence has been suppressed, and the coordinate system in which $\mathbf{r}$ is measured is fixed with respect to the inclusions. The inclusions are assumed to be electrically separated in free space and comprised of lossy or lossless polarizable material. Thus, the array can be described electromagnetically by the following microscopic (inclusion-level) Maxwell differential equations in the space-frequency $(\mathbf{r}, \omega)$ domain [26, Chap. 1]

$$\nabla \times \mathcal{E}_\omega(\mathbf{r}) - i\omega \mathcal{B}_\omega(\mathbf{r}) = 0 \tag{13.4a}$$

$$\frac{1}{\mu_0} \nabla \times \mathcal{B}_\omega(\mathbf{r}) + i\omega\epsilon_0 \mathcal{E}_\omega(\mathbf{r}) - \mathcal{J}^p_\omega(\mathbf{r}) - \nabla \times \mathcal{M}_\omega(\mathbf{r}) = \mathcal{J}_{a\omega}(\mathbf{r}) \tag{13.4b}$$

$$\nabla \cdot \boldsymbol{\mathcal{B}}_\omega(\mathbf{r}) = 0 \tag{13.4c}$$

$$\epsilon_0 \nabla \cdot \boldsymbol{\mathcal{E}}_\omega(\mathbf{r}) = \rho^p_\omega(\mathbf{r}) + \rho_{a\omega}(\mathbf{r}) \tag{13.4d}$$

where the equivalent electric current and charge densities are

$$\boldsymbol{\mathcal{J}}^p_\omega = \boldsymbol{\mathcal{J}}_\omega - i\omega \boldsymbol{\mathcal{P}}_\omega \tag{13.5a}$$

$$\rho^p_\omega = \rho_\omega - \nabla \cdot \boldsymbol{\mathcal{P}}_\omega \,. \tag{13.5b}$$

The $\boldsymbol{\mathcal{E}}_\omega$ and $\boldsymbol{\mathcal{B}}_\omega$ vectors are taken as the primary electric and magnetic fields, $\boldsymbol{\mathcal{J}}_{a\omega}(\mathbf{r})$ is the applied electric current density, and μ_0 and ϵ_0 are the free-space permeability and permittivity, respectively. Hypothetical induced and applied magnetic current and charge densities[7] have been taken as zero in (13.4a) and (13.4c) to keep the equations as simple as possible while still allowing the applied electric current density to vary arbitrarily; in particular, to have the general plane-wave dependence given in (13.7) below. The induced and applied electric charge densities, ρ^p_ω and $\rho_{a\omega}$, are related to the induced and applied electric current densities, $\boldsymbol{\mathcal{J}}^p_\omega$ and $\boldsymbol{\mathcal{J}}_{a\omega}$, through the continuity equations

$$\nabla \cdot \boldsymbol{\mathcal{J}}^p_\omega(\mathbf{r}) - i\omega \rho^p_\omega(\mathbf{r}) = 0 \tag{13.6a}$$

$$\nabla \cdot \boldsymbol{\mathcal{J}}_{a\omega}(\mathbf{r}) - i\omega \rho_{a\omega}(\mathbf{r}) = 0 \,. \tag{13.6b}$$

Assume that the applied electric current density has the general plane-wave dependence

$$\boldsymbol{\mathcal{J}}_{a\omega}(\mathbf{r}) = \mathbf{J}_a(\boldsymbol{\beta}, \omega) e^{i\boldsymbol{\beta}\cdot\mathbf{r}} \tag{13.7}$$

with the rectangular components of the propagation vector $\boldsymbol{\beta}$ and the angular frequency ω having independent real values ranging from $-\infty$ to $+\infty$. Then, the periodicity of the array requires that the fields and induced source densities satisfy the Floquet modal equations; for example, the electric field can be expressed as

$$\boldsymbol{\mathcal{E}}_\omega(\mathbf{r}) = e^{i\boldsymbol{\beta}\cdot\mathbf{r}} \sum_{(l,m,n)=-(\infty,\infty,\infty)}^{+(\infty,\infty,\infty)} \mathbf{E}_{lmn}(\boldsymbol{\beta}, \omega) e^{i\mathbf{b}_{lmn}\cdot\mathbf{r}} \tag{13.8}$$

[7] Except where explicitly stated otherwise in the contexts of Footnote 6 and Eq. (13.52), we avoid introducing hypothetical applied magnetic currents in addition to the applied electric currents into the microscopic Maxwellian equations because this would require either a macroscopic bianisotropic representation [21, 23] or a much more complicated macroscopic anisotropic formulation for the fundamental modes of the arrays in terms of applied sources that would involve macroscopic bianisotropic constitutive parameters. Also, of course, magnetic currents or charges on the right-hand side of (13.4a) or (13.4c) have never been observed experimentally.

and similarly for the magnetic field and source densities. For simplicity, we shall assume a cubic array with lattice spacing d such that

$$\mathbf{b}_{lmn} = \frac{2\pi l}{d}\hat{\mathbf{x}} + \frac{2\pi m}{d}\hat{\mathbf{y}} + \frac{2\pi n}{d}\hat{\mathbf{z}} \tag{13.9}$$

where $(\hat{\mathbf{x}}, \hat{\mathbf{y}}, \hat{\mathbf{z}})$ are the unit vectors in the (x, y, z) principal directions of the 3D cubic array. Since $\mathbf{b}_{000} = 0$, the $(l, m, n) = (0, 0, 0)$ term in (13.8) with spatial propagation vector $\boldsymbol{\beta}$ is called the fundamental Floquet mode.

The applied plane-wave current spectrum $\mathbf{J}_a(\boldsymbol{\beta}, \omega)$ in (13.7) for all real $\boldsymbol{\beta}$ can be used to represent an arbitrary localized applied current density $\mathcal{J}^a_\omega(\mathbf{r})$ through the Fourier transform

$$\mathcal{J}^a_\omega(\mathbf{r}) = \int_{-\infty}^{+\infty}\int_{-\infty}^{+\infty}\int_{-\infty}^{+\infty} \mathbf{J}_a(\boldsymbol{\beta}, \omega) e^{i\boldsymbol{\beta}\cdot\mathbf{r}} d^3\beta \tag{13.10a}$$

with $\mathbf{J}_a(\boldsymbol{\beta}, \omega)$ given by the inverse Fourier transform

$$\mathbf{J}_a(\boldsymbol{\beta}, \omega) = \frac{1}{(2\pi)^3}\int_{-\infty}^{+\infty}\int_{-\infty}^{+\infty}\int_{-\infty}^{+\infty} \mathcal{J}^a_\omega(\mathbf{r}) e^{-i\boldsymbol{\beta}\cdot\mathbf{r}} d^3r \tag{13.10b}$$

and similarly for the accompanying spectra of the fields.

For any fixed value of real $\boldsymbol{\beta}$, arrays of lossless inclusions can have homogeneous (source-free: $\mathbf{J}_a = 0$) "eigenmode" (sometimes called "normal-mode") solutions to (13.4) and (13.11) at discrete real frequencies $\omega = \omega_{\text{eig}}(\boldsymbol{\beta})$. At these discrete frequencies, the inhomogeneous solution for the fields with applied current density in (13.7) generally diverges [whereas the macroscopic permittivity and permeability defined in Sect. 13.3 remain finite and continuous as $\omega \to \omega_{\text{eig}}(\boldsymbol{\beta})$]. For both theoretical analyses and numerical solvers, the solution to the lossless array can often be investigated more easily near the eigenmodes at real $(\boldsymbol{\beta}, \omega)$ by inserting a small loss into the material of the inclusions to eliminate the singularities from the solution at real $(\boldsymbol{\beta}, \omega)$. Also, the applied fields will diverge if $\omega = \pm|\boldsymbol{\beta}|/\sqrt{\mu_0\epsilon_0}$ and thus these two values of ω should be avoided. (As an aside, we mention that source-free eigenmodes with complex propagation constants can exist even on lossless arrays [27]. These complex waves can, nonetheless, be represented by an integration of the plane-wave spectra over real $\boldsymbol{\beta}$—as can be demonstrated by closing the contours of the real $\boldsymbol{\beta}$ integrations in the complex $\boldsymbol{\beta}$ planes.)

Inserting the electric field from (13.8), and the similar Floquet modal expressions for the magnetic field and source densities, into the Maxwell equations in (13.4), then multiplying the resulting equations by $e^{-i\boldsymbol{\beta}\cdot\mathbf{r}}$ and integrating over the volume of any one unit cell, we obtain the spectral domain Maxwellian equations for the fundamental Floquet mode of the array

$$i\boldsymbol{\beta} \times \mathbf{E}(\boldsymbol{\beta}, \omega) - i\omega \mathbf{B}(\boldsymbol{\beta}, \omega) = 0 \tag{13.11a}$$

$$\frac{1}{\mu_0} i\boldsymbol{\beta} \times \mathbf{B}(\boldsymbol{\beta}, \omega) + i\omega\epsilon_0 \mathbf{E}(\boldsymbol{\beta}, \omega) - \mathbf{J}^p(\boldsymbol{\beta}, \omega) - i\boldsymbol{\beta} \times \mathbf{M}(\boldsymbol{\beta}, \omega) = \mathbf{J}_a(\boldsymbol{\beta}, \omega) \tag{13.11b}$$

in which we have defined $\mathbf{E}(\boldsymbol{\beta}, \omega) \equiv \mathbf{E}_{000}(\boldsymbol{\beta}, \omega)$ and similarly omitted the "000" subscripts on the other fundamental Floquet modal spectra. Likewise, the continuity equations in (13.6) transform to

$$i\boldsymbol{\beta} \cdot \mathbf{J}^p(\boldsymbol{\beta}, \omega) - i\omega\rho^p(\boldsymbol{\beta}, \omega) = 0 \tag{13.12a}$$

$$i\boldsymbol{\beta} \cdot \mathbf{J}_a(\boldsymbol{\beta}, \omega) - i\omega\rho_a(\boldsymbol{\beta}, \omega) = 0 \tag{13.12b}$$

with $\rho^p = \rho - i\boldsymbol{\beta} \cdot \mathbf{P}$. The form of these spectral Maxwellian equations for the fundamental Floquet mode is identical to the corresponding continuum spectral equations for applied sources with $e^{i(\boldsymbol{\beta}\cdot\mathbf{r}-\omega t)}$ plane-wave dependence. The divergence equations corresponding to (13.4c) and (13.4d) need not be included separately in (13.11) because they can be obtained (for $\boldsymbol{\beta} \neq 0$ or $\omega \neq 0$) by taking the scalar product of $\boldsymbol{\beta}$ with (13.11a) and (13.11b) and using the continuity equations in (13.12).[8]

Multiplying (13.8) by $e^{-i\boldsymbol{\beta}\cdot\mathbf{r}}$ and integrating over the volume V_c of a unit cell, we find that

[8] The externally applied fields satisfy the Maxwell time-domain equations given by

$$\nabla \times \boldsymbol{\mathcal{E}}_{a\omega}(\mathbf{r}) - i\omega \boldsymbol{\mathcal{B}}_{a\omega}(\mathbf{r}) = 0 \tag{13.13a}$$

$$\frac{1}{\mu_0} \nabla \times \boldsymbol{\mathcal{B}}_{a\omega}(\mathbf{r}) + i\omega\epsilon_0 \boldsymbol{\mathcal{E}}_{a\omega}(\mathbf{r}) = \boldsymbol{\mathcal{J}}_{a\omega}(\mathbf{r}) \tag{13.13b}$$

$$\nabla \cdot \boldsymbol{\mathcal{B}}_{a\omega}(\mathbf{r}) = 0 \tag{13.13c}$$

$$\epsilon_0 \nabla \cdot \boldsymbol{\mathcal{E}}_{a\omega}(\mathbf{r}) = \rho_{a\omega}(\mathbf{r}) \tag{13.13d}$$

and the corresponding spectral-domain Maxwellian equations given by

$$i\boldsymbol{\beta} \times \mathbf{E}_a(\boldsymbol{\beta}, \omega) - i\omega \mathbf{B}_a(\boldsymbol{\beta}, \omega) = 0 \tag{13.14a}$$

$$\frac{1}{\mu_0} i\boldsymbol{\beta} \times \mathbf{B}_a(\boldsymbol{\beta}, \omega) + i\omega\epsilon_0 \mathbf{E}_a(\boldsymbol{\beta}, \omega) = \mathbf{J}_a(\boldsymbol{\beta}, \omega)\,. \tag{13.14b}$$

Since the externally applied fields hold in free space with no induced sources, only the fundamental Floquet mode is nonzero for the applied spectral-domain fields. Taking the dot product of $\boldsymbol{\beta}$ with (13.14b) shows that $\boldsymbol{\beta} \cdot \mathbf{E}_a = \boldsymbol{\beta} \cdot \mathbf{J}_a/(i\omega\epsilon_0)$ and thus the longitudinal (parallel to $\boldsymbol{\beta}$) component of $\mathbf{E}_a$ diverges as $1/\omega$ for $\mathbf{J}_a$ equal to a nonzero value as $\omega \to 0$. Therefore, for some numerical solutions, it may be beneficial to choose the longitudinal component of $\mathbf{J}_a$ proportional to ω.

$$\mathbf{E}(\boldsymbol{\beta},\omega)=\frac{1}{d^3}\int\limits_{V_c}\boldsymbol{\mathcal{E}}_\omega(\mathbf{r})e^{-i\boldsymbol{\beta}\cdot\mathbf{r}}d^3r \tag{13.15}$$

with similar integral expressions holding for the other fundamental Floquet modal spectra.[9] In particular, the fundamental Floquet-mode induced electric current spectrum can be expressed as

$$\mathbf{J}^p(\boldsymbol{\beta},\omega)=\frac{1}{d^3}\int\limits_{V_c}\boldsymbol{\mathcal{J}}^p_\omega(\mathbf{r})e^{-i\boldsymbol{\beta}\cdot\mathbf{r}}d^3r\,. \tag{13.17}$$

To decompose $\mathbf{J}^p(\boldsymbol{\beta},\omega)$ into generalized electric and magnetic polarization densities, begin with the microscopic equivalent electric current density $\boldsymbol{\mathcal{J}}^p_\omega(\mathbf{r})$ and the vector-dyadic identity

$$\boldsymbol{\mathcal{J}}^p_\omega=\nabla\cdot(\boldsymbol{\mathcal{J}}^p_\omega\mathbf{r})-(\nabla\cdot\boldsymbol{\mathcal{J}}^p_\omega)\mathbf{r}\,. \tag{13.18}$$

Re-expressing $\boldsymbol{\mathcal{J}}^p_\omega\mathbf{r}$ as

$$\boldsymbol{\mathcal{J}}^p_\omega\mathbf{r}=\frac{1}{2}(\boldsymbol{\mathcal{J}}^p_\omega\mathbf{r}-\mathbf{r}\boldsymbol{\mathcal{J}}^p_\omega)+\frac{1}{2}(\boldsymbol{\mathcal{J}}^p_\omega\mathbf{r}+\mathbf{r}\boldsymbol{\mathcal{J}}^p_\omega) \tag{13.19a}$$

and using the identity

$$\nabla\cdot(\boldsymbol{\mathcal{J}}^p_\omega\mathbf{r}-\mathbf{r}\boldsymbol{\mathcal{J}}^p_\omega)=\nabla\times(\mathbf{r}\times\boldsymbol{\mathcal{J}}^p_\omega) \tag{13.19b}$$

allows the space-domain electric current in (13.18) to be rewritten as [14]

$$\begin{aligned}\boldsymbol{\mathcal{J}}^p_\omega&=-(\nabla\cdot\boldsymbol{\mathcal{J}}^p_\omega)\mathbf{r}+\frac{1}{2}\nabla\cdot(\boldsymbol{\mathcal{J}}^p_\omega\mathbf{r}+\mathbf{r}\boldsymbol{\mathcal{J}}^p_\omega)+\frac{1}{2}\nabla\times(\mathbf{r}\times\boldsymbol{\mathcal{J}}^p_\omega)\\&=-i\omega\rho^p_\omega\mathbf{r}+\frac{1}{2}\nabla\cdot(\boldsymbol{\mathcal{J}}^p_\omega\mathbf{r}+\mathbf{r}\boldsymbol{\mathcal{J}}^p_\omega)+\frac{1}{2}\nabla\times(\mathbf{r}\times\boldsymbol{\mathcal{J}}^p_\omega)\end{aligned} \tag{13.20}$$

with the help of the continuity equation in (13.6a), where, as in (13.15) and (13.17)

$$\rho^p_\omega(\mathbf{r})=e^{i\boldsymbol{\beta}\cdot\mathbf{r}}\sum_{(l,m,n)=-(\infty,\infty,\infty)}^{+(\infty,\infty,\infty)}\rho^p_{lmn}(\boldsymbol{\beta},\omega)e^{i\mathbf{b}_{lmn}\cdot\mathbf{r}}\,. \tag{13.21}$$

Substitution of $\boldsymbol{\mathcal{J}}^p_\omega$ from (13.20) into (13.17) gives

[9] All the Floquet modal coefficients, in addition to the fundamental ones, are found from the space-frequency fields simply by replacing $\boldsymbol{\beta}$ in the integrand of (13.15) or (13.17) by $\boldsymbol{\beta}_{lmn}=\boldsymbol{\beta}+\mathbf{b}_{lmn}$ to give

$$\mathbf{E}_{lmn}(\boldsymbol{\beta},\omega)=\frac{1}{d^3}\int\limits_{V_c}\boldsymbol{\mathcal{E}}_\omega(\mathbf{r})e^{-i\boldsymbol{\beta}_{lmn}\cdot\mathbf{r}}d^3r\,,\quad \mathbf{J}^p_{lmn}(\boldsymbol{\beta},\omega)=\frac{1}{d^3}\int\limits_{V_c}\boldsymbol{\mathcal{J}}^p_\omega(\mathbf{r})e^{-i\boldsymbol{\beta}_{lmn}\cdot\mathbf{r}}d^3r \tag{13.16}$$

and similarly for the other fields and sources.

$$\mathbf{J}^p(\boldsymbol{\beta},\omega) = -i\omega\mathbf{P}^e_\rho(\boldsymbol{\beta},\omega) + \frac{\omega}{2}\boldsymbol{\beta}\cdot\overline{\mathbf{Q}}^e(\boldsymbol{\beta},\omega) + i\boldsymbol{\beta}\times\mathbf{M}^e(\boldsymbol{\beta},\omega) \tag{13.22}$$

with the generalized macroscopic electric charge polarization density $\mathbf{P}^e_\rho$, electric current magnetic polarization density $\mathbf{M}^e$, and dyadic electric quadrupolar polarization density $\overline{\mathbf{Q}}^e$ defined as

$$\mathbf{P}^e_\rho(\boldsymbol{\beta},\omega) = \frac{1}{d^3}\int_{V_c}\rho^p_\omega(\mathbf{r})\mathbf{r}_c e^{-i\boldsymbol{\beta}\cdot\mathbf{r}}d^3r \tag{13.23a}$$

$$\mathbf{M}^e(\boldsymbol{\beta},\omega) = \frac{1}{2d^3}\int_{V_c}\mathbf{r}_c\times\mathcal{J}^p_\omega(\mathbf{r})e^{-i\boldsymbol{\beta}\cdot\mathbf{r}}d^3r \tag{13.23b}$$

$$\overline{\mathbf{Q}}^e(\boldsymbol{\beta},\omega) = -\frac{1}{i\omega d^3}\int_{V_c}[\mathcal{J}^p_\omega(\mathbf{r})\mathbf{r}_c + \mathbf{r}_c\mathcal{J}^p_\omega(\mathbf{r})]e^{-i\boldsymbol{\beta}\cdot\mathbf{r}}d^3r \tag{13.23c}$$

where $\mathbf{r}_c$ is the position vector measured from a fixed point within the unit cell of integration (so that for the same fixed point with respect to each of the unit cells, the polarization densities in (13.23) are independent of which unit cell is chosen for the integration). It should be noted that this replacement of the factors $\mathbf{r}$ by $\mathbf{r}_c$ in (13.23) is valid because (13.20) holds with the factors $\mathbf{r}$ replaced by $\mathbf{r}_c$. *Moreover, it is assumed that the surface S_c of the volume V_c of the unit cell lies in free space, that is, S_c does not intersect the induced sources of the inclusions, so that the volume integral of the first divergence term on the right-hand side of* (13.18)*, for example, converts to a surface integral over S_c that is zero.* (Thus, the theory is not directly applicable to electrically connected inclusions such as those that form some wire media.) The superscripts "e" in (13.23) denote generalized polarization densities produced by the induced equivalent electric charge-current.[10] The

[10] One might object that the induced magnetization current $\nabla\times\boldsymbol{\mathcal{M}}_\omega(\mathbf{r})$ is not included in addition to the induced equivalent electric current $\mathcal{J}^p_\omega(\mathbf{r})$ in the decomposition (13.18–13.23) since this Amperian magnetization current is also an equivalent electric current in the microscopic Maxwell equations as given by (13.4). The reason it is not included is that if $\nabla\times\boldsymbol{\mathcal{M}}_\omega(\mathbf{r})$ were included with $\mathcal{J}^p_\omega(\mathbf{r})$ in (13.20), one finds that it would produce no additional electric polarization in (13.23a), an additional magnetization in (13.23b) equal to

$$\mathbf{M}(\boldsymbol{\beta},\omega) + \frac{1}{2d^3}\int_{V_c}\mathbf{r}\times[i\boldsymbol{\beta}\times\boldsymbol{\mathcal{M}}_\omega(\mathbf{r})]e^{-i\boldsymbol{\beta}\cdot\mathbf{r}}d^3r \tag{13.24}$$

and an additional electric quadrupole term in (13.23c) equal to

$$-\frac{1}{i\omega d^3}\int_{V_c}\{[i\boldsymbol{\beta}\times\boldsymbol{\mathcal{M}}_\omega(\mathbf{r})]\mathbf{r} + \mathbf{r}[i\boldsymbol{\beta}\times\boldsymbol{\mathcal{M}}_\omega(\mathbf{r})]\}e^{-i\boldsymbol{\beta}\cdot\mathbf{r}}d^3r\,. \tag{13.25}$$

That is, it would merely produce extra terms of order $\boldsymbol{\beta}$ higher than the $\mathbf{P}^e(\boldsymbol{\beta},\omega)$ and $\mathbf{M}^e(\boldsymbol{\beta},\omega) + \mathbf{M}(\boldsymbol{\beta},\omega)$ terms in (13.28) produced by keeping $\nabla\times\boldsymbol{\mathcal{M}}_\omega$ separate from $\mathcal{J}^p_\omega$ in (13.18–13.23), and these extra terms would become negligible as $\boldsymbol{\beta}\to 0$ and the generalized averages in

effective microscopic electric charge-current polarization densities are found from (13.23) as

$$\mathcal{P}^e_{\rho\omega}(\mathbf{r}) = \rho^p_\omega(\mathbf{r})\mathbf{r}_c \tag{13.26a}$$

$$\mathcal{M}^e_\omega(\mathbf{r}) = \frac{1}{2}\mathbf{r}_c \times \mathcal{J}^p_\omega(\mathbf{r}) \tag{13.26b}$$

$$\overline{\mathcal{Q}}^e_\omega(\mathbf{r}) = -\frac{1}{i\omega}[\mathcal{J}^p_\omega(\mathbf{r})\mathbf{r}_c + \mathbf{r}_c\mathcal{J}^p_\omega(\mathbf{r})]\,. \tag{13.26c}$$

These effective source densities have the same fundamental $e^{i\boldsymbol{\beta}\cdot\mathbf{r}}$ variation as $\rho^p_\omega(\mathbf{r})$ and $\mathcal{J}^p_\omega(\mathbf{r})$. Observe that $\overline{\mathcal{Q}}^e_\omega(\mathbf{r})$ and $\overline{\mathbf{Q}}^e(\boldsymbol{\beta},\omega)$ are symmetric dyadics. Equations (13.23) are generalizations of similar expressions in the "scaling homogenization theory" of [14].

With $\mathbf{J}^p$ in (13.22) inserted into (13.11b), we can define a total generalized electric polarization density as

$$\mathbf{P}^e(\boldsymbol{\beta},\omega) \equiv \mathbf{P}^e_\rho(\boldsymbol{\beta},\omega) + i\boldsymbol{\beta}\cdot\overline{\mathbf{Q}}^e(\boldsymbol{\beta},\omega)/2 \tag{13.27}$$

as well as a generalized electric displacement vector $\mathbf{D}$ and a magnetic field vector $\mathbf{H}$ as

$$\mathbf{D}(\boldsymbol{\beta},\omega) \equiv \epsilon_0\mathbf{E}(\boldsymbol{\beta},\omega) + \mathbf{P}^e(\boldsymbol{\beta},\omega) \tag{13.28a}$$

$$\mathbf{H}(\boldsymbol{\beta},\omega) \equiv \mathbf{B}(\boldsymbol{\beta},\omega)/\mu_0 - \mathbf{M}^e(\boldsymbol{\beta},\omega) - \mathbf{M}(\boldsymbol{\beta},\omega)\,. \tag{13.28b}$$

Then the spectral Maxwellian equations in (13.11) for the fundamental Floquet mode of the array can be written as

$$i\boldsymbol{\beta}\times\mathbf{E}(\boldsymbol{\beta},\omega) - i\omega\mathbf{B}(\boldsymbol{\beta},\omega) = 0 \tag{13.29a}$$

$$i\boldsymbol{\beta}\times\mathbf{H}(\boldsymbol{\beta},\omega) + i\omega\mathbf{D}(\boldsymbol{\beta},\omega) = \mathbf{J}_a(\boldsymbol{\beta},\omega). \tag{13.29b}$$

To obtain this traditional form of the macroscopic Maxwell's equations in (13.29) for these "electric current" polarizable inclusions satisfying the microscopic equations in (13.4) with $(\boldsymbol{\mathcal{E}}_\omega, \boldsymbol{\mathcal{B}}_\omega)$ as the primary fields, we have had to choose $(\mathbf{E},\mathbf{B})$ as the primary macroscopic fields (obtained from the generalized average, as in (13.15), of the corresponding microscopic fields) and $(\mathbf{D},\mathbf{H})$ as the secondary fields defined in (13.28) in terms of the macroscopic primary fields and the macroscopic polarization densities in (13.23).

The fundamental definitions of the generalized macroscopic polarization densities in (13.23) in terms of integrals over the microscopic sources at a fixed $\boldsymbol{\beta}$ is

(Footnote 10 continued)
(13.23) become ordinary averages. Moreover, the electric quadrupole term in (13.25) and the magnetic dipole integral term in (13.24) cancel when they are inserted into the electric quadrupole and magnetic dipole contributions in (13.22).

what ensures the causality of these polarizations and that of their associated constitutive parameters. These causal integral definitions distinguish themselves from the spherical multipole definitions of polarization in terms of external fields (as in the Mie series), which exhibit an inherent noncausality generated by the finite size of the inclusions [28]. Only as the size of the inclusions become infinitesimal do the integral and spherical multipole definitions yield the same macroscopic polarizations.

The total Floquet-mode equivalent electric current

$$\begin{aligned}\mathbf{J}^{\text{tot}}(\boldsymbol{\beta},\omega) &= \mathbf{J}^{p}(\boldsymbol{\beta},\omega) + i\boldsymbol{\beta}\times\mathbf{M}(\boldsymbol{\beta},\omega)\\ &= -i\omega\mathbf{P}_{\rho}^{e}(\boldsymbol{\beta},\omega) + \omega\boldsymbol{\beta}\cdot\overline{\mathbf{Q}}^{e}(\boldsymbol{\beta},\omega)/2 + i\boldsymbol{\beta}\times[\mathbf{M}^{e}(\boldsymbol{\beta},\omega)+\mathbf{M}(\boldsymbol{\beta},\omega)]\end{aligned} \tag{13.30}$$

is equal to the Landau–Lifshitz single-polarization vector $-i\omega\mathbf{P}_L(\boldsymbol{\beta},\omega)$ [5, Chap. 12; 18] mentioned in the Introduction; that is

$$\mathbf{J}^{\text{tot}}(\boldsymbol{\beta},\omega) = -i\omega\mathbf{P}_L(\boldsymbol{\beta},\omega)\,. \tag{13.31}$$

The Eqs. (13.28–13.29) are noteworthy, not only because they are Maxwellian equations for the fundamental Floquet modes of 3D arrays of lossy or lossless polarizable inclusions, but also because they involve no generalized multipole moments of higher order than the generalized electric quadrupole moment contained in (13.27) as part of the total generalized electric polarization density $\mathbf{P}^{e}(\boldsymbol{\beta},\omega)$. Moreover, the fields $\mathbf{E}$ and $\mathbf{D}$ involve only electric type quantities and the fields $\mathbf{B}$ and $\mathbf{H}$ involve only magnetic type quantities.

The generalized electric-quadrupole polarization in (13.27) is grouped with the generalized electric-dipole polarization rather than the generalized magnetic-dipole polarization because an expansion of the generalized electric-dipole polarization in (13.23a) as $\boldsymbol{\beta}\to 0$ produces a term equal to $-i\boldsymbol{\beta}\cdot\overline{\mathbf{Q}}^{e}$; see (13.34) below. Combining the electric dipole and quadrupole moments into a single electric polarization allows a single bulk permittivity dyadic $\overline{\boldsymbol{\epsilon}}$ in Sect. 13.3 to characterize the electric properties of the array. However, this bulk permittivity dyadic does not reveal how much of the macroscopic polarization is contributed individually by the generalized electric-dipole polarization $\mathbf{P}_{\rho}^{e}$ and the electric-quadrupole polarization $\overline{\mathbf{Q}}^{e}$. If desirable, it is a simple matter to separate the contributions from $\mathbf{P}_{\rho}^{e}$ and $i\boldsymbol{\beta}\cdot\overline{\mathbf{Q}}^{e}/2$ to the bulk permittivity dyadic $\overline{\boldsymbol{\epsilon}}$ and thus to determine separate generalized electric-dipole and electric-quadrupole dyadic susceptibilities.

The value of the generalized macroscopic polarizations in (13.23) and the constitutive parameters (defined in Sect. 13.3) depend on the position of the inclusion within the unit cell of integration, or, more precisely, on the position of the origin of the vector $\mathbf{r}_c$ with respect to the inclusion [25]. However, the value of the total macroscopic equivalent electric current $\mathbf{J}^{\text{tot}}(\boldsymbol{\beta},\omega)$ in (13.30), obtained by adding the macroscopic polarization currents, is independent of the position of the

inclusions within the unit cell, and thus the primary macroscopic fields $\mathbf{E}(\boldsymbol{\beta},\omega)$ and $\mathbf{B}(\boldsymbol{\beta},\omega)$ are uniquely defined.

13.2.1 Definition of an Electromagnetic Continuum[11]

The foregoing development of the macroscopic equations for the fundamental Floquet modes on 3D arrays provides a convenient set of equations for defining an electromagnetic "continuum." An array of electrically isolated inclusions can be treated as an electromagnetic "continuum" if two conditions are satisfied:

(1) $|\boldsymbol{\beta}d|$ is small enough (generally $|\boldsymbol{\beta}d| \ll 1$)[12] that the ordinary averages (that is, averages without the $e^{-i\boldsymbol{\beta}\cdot\mathbf{r}}$ weighting factor) of the microscopic fields and sources over the unit cell approximately equal the fields and sources of the fundamental Floquet mode; for example, for the electric field in (13.8)

$$\frac{1}{d^3}\int\limits_{V_c} \boldsymbol{\mathcal{E}}_\omega(\mathbf{r})d^3r = \frac{1}{d^3}\int\limits_{V_c}\left[e^{i\boldsymbol{\beta}\cdot\mathbf{r}}\sum_{(l,m,n)=-(\infty,\infty,\infty)}^{+(\infty,\infty,\infty)}\mathbf{E}_{lmn}(\boldsymbol{\beta},\omega)e^{i\mathbf{b}_{lmn}\cdot\mathbf{r}}\right]d^3r \approx \mathbf{E}(\boldsymbol{\beta},\omega)e^{i\boldsymbol{\beta}\cdot\mathbf{r}_0} \tag{13.32}$$

where $\mathbf{r}_0$ is the center of the unit cell, and similarly for the microscopic magnetic field, $\boldsymbol{\mathcal{B}}_\omega(\mathbf{r})$, and the microscopic sources, $\boldsymbol{\mathcal{P}}^e_{\rho\omega}(\mathbf{r})$, $\boldsymbol{\mathcal{M}}^e_\omega(\mathbf{r})$, $\boldsymbol{\mathcal{M}}_\omega(\mathbf{r})$, and $\overline{\boldsymbol{\mathcal{Q}}}^e_\omega(\mathbf{r})$.

(2) $|k_0 d| = |\omega d/c|$ is small enough (generally $|k_0 d| \ll 1$; see Footnote 12) that the wave numbers $\boldsymbol{\beta}_{\text{eig}}(\omega)$ of the "propagating" source-free eigenmodes of the array (that would be excited by discontinuities or terminations of the array) satisfy the requirement of condition (1) of small enough $|\boldsymbol{\beta}_{\text{eig}}d|$ that the fundamental Floquet modes dominate. This second continuum condition implies that the quasi-static fields of the electrically separated inclusions dominate over the length of several or more unit cells. On lossy arrays, the $\boldsymbol{\beta}_{\text{eig}}$ of the propagating eigenmodes can be complex with small imaginary parts for small values of $|k_0 d|$ without destroying the continuum nature of the array. In addition, even for small values of $|k_0 d|$, there may be "evanescent" complex eigenmodes on lossy and lossless arrays with $|\text{Im}(\boldsymbol{\beta}_{\text{eig}}d)| > 1$ (see, for example, [27, Part 2, Fig. 10c]). However, these evanescent waves are irrelevant for defining a continuum because they decay to a negligible value in "transition layers" a small fraction of a wavelength from discontinuities or termination surfaces of an array (see Sect. 13.2.1.1 on boundary conditions).

---

[11] Sections 13.2.1–13.2.1.1 are not essential to the development in the rest of the chapter.

[12] This criterion of "$\ll 1$" can sometimes be relaxed to "<1" [8], and in the special case of homogeneous inclusion material that occupies nearly the entire volume of the unit cell, the criterion can be relaxed to values greater than 1. Although such a nominally periodic array can be considered a continuum over spatial and frequency bandwidths, $|\boldsymbol{\beta}d|$ and $|k_0 d|$, greater than 1, it is a relatively uninteresting case that we shall ignore in the discussion of continua and their boundary conditions in this section and the following Sect. 13.2.1.1.

If the above conditions (1) and (2) are met, ordinary averages over electrically small (quasi-static) macroscopic volumes ΔV within the array, but outside any transition layers of discontinuities or terminations of the array, and containing many inclusions (such that the surfaces of the macroscopic volumes do not intersect the inclusions) will produce physically meaningful averages at each value of $\boldsymbol{\beta}$ and ω satisfying the small $|\boldsymbol{\beta}d|$ and small $|k_0 d|$ criteria of conditions (1) and (2). Specifically, we can write

$$\mathbf{E}_{\text{ave}}(\mathbf{r},t) \approx \mathbf{E}(\boldsymbol{\beta},\omega)e^{i(\boldsymbol{\beta}\cdot\mathbf{r}-\omega t)} \tag{13.33a}$$

$$\mathbf{B}_{\text{ave}}(\mathbf{r},t) \approx \mathbf{B}(\boldsymbol{\beta},\omega)e^{i(\boldsymbol{\beta}\cdot\mathbf{r}-\omega t)} \tag{13.33b}$$

$$\mathbf{P}^e_{\rho,\text{ave}}(\mathbf{r},t) \approx \mathbf{P}^e_{\rho}(\boldsymbol{\beta},\omega)e^{i(\boldsymbol{\beta}\cdot\mathbf{r}-\omega t)} \tag{13.33c}$$

$$\mathbf{M}^e_{\text{ave}}(\mathbf{r},t) + \mathbf{M}_{\text{ave}}(\mathbf{r},t) \approx [\mathbf{M}^e(\boldsymbol{\beta},\omega) + \mathbf{M}(\boldsymbol{\beta},\omega)]e^{i(\boldsymbol{\beta}\cdot\mathbf{r}-\omega t)} \tag{13.33d}$$

$$\overline{\mathbf{Q}}^e_{\text{ave}}(\mathbf{r},t) \approx \overline{\mathbf{Q}}^e(\boldsymbol{\beta},\omega)e^{i(\boldsymbol{\beta}\cdot\mathbf{r}-\omega t)} \tag{13.33e}$$

and from (13.27)

$$\mathbf{P}^e_{\text{ave}}(\mathbf{r},t) \approx \mathbf{P}^e(\boldsymbol{\beta},\omega)e^{i(\boldsymbol{\beta}\cdot\mathbf{r}-\omega t)} = [\mathbf{P}^e_{\rho}(\boldsymbol{\beta},\omega) + i\boldsymbol{\beta}\cdot\overline{\mathbf{Q}}^e(\boldsymbol{\beta},\omega)/2]e^{i(\boldsymbol{\beta}\cdot\mathbf{r}-\omega t)} \tag{13.33f}$$

that is, the ordinary macroscopic-volume averages at each $\boldsymbol{\beta}$ and ω within the small spatial and temporal bandwidths defining the continuum are given approximately by the fundamental Floquet mode. The constitutive parameters of a continuum, in particular the permittivity and permeability dyadics defined in Sect. 13.3, can be spatially dispersive (as well as temporally dispersive) and even strongly spatially dispersive near inclusion resonances [5, Sects. 103–106].

Next, with the help of the polarizations defined in (13.23), we will show that the continuum can be characterized by ordinary multipole moments with ordinary electric-dipole, magnetic-dipole, and electric-quadrupole moments dominating at sufficiently small values of $|\boldsymbol{\beta}d|$. Consider the integrations in (13.23) over the unit cell in which the coordinate-system origin of the position vector $\mathbf{r}$ is located, and then let $\mathbf{r}_c = \mathbf{r}$. With $|\boldsymbol{\beta}d|$ sufficiently <1, the approximation $e^{-i\boldsymbol{\beta}\cdot\mathbf{r}} \approx 1 - i\boldsymbol{\beta}\cdot\mathbf{r}$ holds for this unit cell and, thus, to first order in $|\boldsymbol{\beta}d|$ (13.23) yields

$$\mathbf{P}^e_{\rho}(\boldsymbol{\beta},\omega) = \mathbf{P}^e_0(\boldsymbol{\beta},\omega) - i\boldsymbol{\beta}\cdot\overline{\mathbf{Q}}^e_0(\boldsymbol{\beta},\omega) + O(|\boldsymbol{\beta}d|^2) \tag{13.34a}$$

so that

$$\mathbf{P}^e(\boldsymbol{\beta},\omega) = \mathbf{P}^e_{\rho}(\boldsymbol{\beta},\omega) + i\boldsymbol{\beta}\cdot\overline{\mathbf{Q}}^e(\boldsymbol{\beta},\omega)/2 = \mathbf{P}^e_0(\boldsymbol{\beta},\omega) - i\boldsymbol{\beta}\cdot\overline{\mathbf{Q}}^e_0(\boldsymbol{\beta},\omega)/2 + O(|\boldsymbol{\beta}d|^2) \tag{13.34b}$$

and

$$\mathbf{M}^e(\boldsymbol{\beta},\omega) + \mathbf{M}(\boldsymbol{\beta},\omega) = \mathbf{M}^e_0(\boldsymbol{\beta},\omega) + \mathbf{M}_0(\boldsymbol{\beta},\omega) + O(|\boldsymbol{\beta}d|) \tag{13.34c}$$

where the ordinary (continuum) electric and magnetic dipole-moment densities, and the ordinary electric quadrupole-moment density in the unit cell containing the origin of the position vector $\mathbf{r}$ are given by

$$\mathbf{P}_0^e(\boldsymbol{\beta},\omega)=\frac{1}{d^3}\int\limits_{V_c}\rho_\omega^p(\mathbf{r})\mathbf{r}d^3r=\frac{1}{d^3}\int\limits_{V_c}[\rho_\omega(\mathbf{r})\mathbf{r}+\boldsymbol{\mathcal{P}}_\omega(\mathbf{r})]d^3r \tag{13.35a}$$

$$\mathbf{M}_0^e(\boldsymbol{\beta},\omega)=\frac{1}{2d^3}\int\limits_{V_c}\mathbf{r}\times\boldsymbol{\mathcal{J}}_\omega^p(\mathbf{r})d^3r,\quad \mathbf{M}_0(\boldsymbol{\beta},\omega)=\frac{1}{d^3}\int\limits_{V_c}\boldsymbol{\mathcal{M}}_\omega(\mathbf{r})d^3r \tag{13.35b}$$

$$\overline{\mathbf{Q}}_0^e(\boldsymbol{\beta},\omega)=-\frac{1}{i\omega d^3}\int\limits_{V_c}[\boldsymbol{\mathcal{J}}_\omega^p(\mathbf{r})\mathbf{r}+\mathbf{r}\boldsymbol{\mathcal{J}}_\omega^p(\mathbf{r})]d^3r=\frac{1}{d^3}\int\limits_{V_c}\rho_\omega^p(\mathbf{r})\mathbf{r}\mathbf{r}d^3r \tag{13.35c}$$

with the second equality in (13.35a) proven with the help of the identity $\int_{V_c}(\nabla\cdot\boldsymbol{\mathcal{P}}_\omega)\mathbf{r}d^3r=-\int_{V_c}\boldsymbol{\mathcal{P}}_\omega d^3r$, and the second equality in (13.35c) for the ordinary electric quadrupole-moment density proven in several textbooks such as [29, pp. 82–83]. Using the results in (13.34), the average polarization densities in (13.33f) and (13.33d) can be expressed in terms of the ordinary average electric, magnetic, and electric quadrupolar moments of the continuum; specifically

$$\begin{aligned}\mathbf{P}_{\text{ave}}^e(\mathbf{r},t)&\approx[\mathbf{P}_0^e(\boldsymbol{\beta},\omega)-i\boldsymbol{\beta}\cdot\overline{\mathbf{Q}}_0^e(\boldsymbol{\beta},\omega)/2]e^{i(\boldsymbol{\beta}\cdot\mathbf{r}-\omega t)}\\&=\mathbf{P}_{0\text{ave}}^e(\mathbf{r},t)-i\boldsymbol{\beta}\cdot\overline{\mathbf{Q}}_{0\text{ave}}^e(\mathbf{r},t)/2\end{aligned} \tag{13.36a}$$

$$\begin{aligned}\mathbf{M}_{\text{ave}}^e(\mathbf{r},t)+\mathbf{M}_{\text{ave}}(\mathbf{r},t)&\approx[\mathbf{M}_0^e(\boldsymbol{\beta},\omega)+\mathbf{M}_0(\boldsymbol{\beta},\omega)]e^{i(\boldsymbol{\beta}\cdot\mathbf{r}-\omega t)}\\&=\mathbf{M}_{0\text{ave}}^e(\mathbf{r},t)+\mathbf{M}_{0\text{ave}}(\mathbf{r},t)\end{aligned} \tag{13.36b}$$

Multiplying Eqs. (13.28–13.29) by $e^{i(\boldsymbol{\beta}\cdot\mathbf{r}-\omega t)}$, then inserting the expressions in (13.33–13.36) for the fields and polarization densities into these equations, and lastly taking the four-fold $(\boldsymbol{\beta},\omega)$ Fourier transform shows that to first order in $|\boldsymbol{\beta}d|$ the macroscopic fields of the continuum array satisfy the following Maxwell macroscopic space-time continuum equations

$$\nabla\times\boldsymbol{\mathcal{E}}_{\text{ave}}(\mathbf{r},t)+\frac{\partial\boldsymbol{\mathcal{B}}_{\text{ave}}(\mathbf{r},t)}{\partial t}=0 \tag{13.37a}$$

$$\nabla\times\boldsymbol{\mathcal{H}}_{\text{ave}}(\mathbf{r},t)-\frac{\partial\boldsymbol{\mathcal{D}}_{\text{ave}}(\mathbf{r},t)}{\partial t}=\boldsymbol{\mathcal{J}}^a(\mathbf{r},t) \tag{13.37b}$$

$$\nabla\cdot\boldsymbol{\mathcal{B}}_{\text{ave}}(\mathbf{r},t)=0 \tag{13.37c}$$

$$\nabla\cdot\boldsymbol{\mathcal{D}}_{\text{ave}}(\mathbf{r},t)=\rho^a(\mathbf{r},t) \tag{13.37d}$$

with

$$\mathcal{D}_{\text{ave}}(\mathbf{r},t) \approx \epsilon_0 \mathcal{E}_{\text{ave}}(\mathbf{r},t) + \mathcal{P}^e_{0\text{ave}}(\mathbf{r},t) - \frac{1}{2}\nabla \cdot \overline{\mathcal{Q}}^e_{0\text{ave}}(\mathbf{r},t) \tag{13.38a}$$

$$\mathcal{H}_{\text{ave}}(\mathbf{r},t) \approx \mathcal{B}_{\text{ave}}(\mathbf{r},t)/\mu_0 - \mathcal{M}^e_{0\text{ave}}(\mathbf{r},t) - \mathcal{M}_{0\text{ave}}(\mathbf{r},t) \tag{13.38b}$$

for $\mathcal{J}^a(\mathbf{r},t)$ (see (13.10a)) within the spatial and temporal bandwidths ($\Delta\boldsymbol{\beta}$ and $\Delta\omega$) of the largest sufficiently small $|\boldsymbol{\beta}d|$ and $|k_0 d|$ for the approximations in (13.32–13.33) to hold and all multipole polarization densities of higher order than $\mathcal{P}^e_{0\text{ave}}(\mathbf{r},t)$, $\mathcal{M}^e_{0\text{ave}}(\mathbf{r},t) + \mathcal{M}_{0\text{ave}}(\mathbf{r},t)$, and $\overline{\mathcal{Q}}^e_{0\text{ave}}(\mathbf{r},t)$ (the ordinary electric-dipole, magnetic-dipole, and electric-quadrupole space-time polarization densities) to be negligible, where from (13.33) we have

$$\mathcal{E}_{\text{ave}}(\mathbf{r},t) = \int_{-\Delta\omega}^{+\Delta\omega} \int_{-\Delta\beta_z}^{+\Delta\beta_z} \int_{-\Delta\beta_y}^{+\Delta\beta_y} \int_{-\Delta\beta_x}^{+\Delta\beta_x} \mathbf{E}(\boldsymbol{\beta},\omega) e^{i(\boldsymbol{\beta}\cdot\mathbf{r}-\omega t)} d^3\beta \mathrm{d}\omega \tag{13.39}$$

and similarly for the other space-time averages. If the multipole polarization densities of higher order than $\mathcal{P}^e_{0\text{ave}}(\mathbf{r},t)$, $\mathcal{M}^e_{0\text{ave}}(\mathbf{r},t) + \mathcal{M}_{0\text{ave}}(\mathbf{r},t)$, and $\overline{\mathcal{Q}}^e_{0\text{ave}}(\mathbf{r},t)$ are not all negligible over the continuum bandwidths ($\Delta\boldsymbol{\beta}$ and $\Delta\omega$), then the integrals in (13.23) could be further expanded as in (13.34) beyond the first-order $|\boldsymbol{\beta}d|$ terms, similarly to what is done in [23], to obtain ordinary multipole densities in (13.38) of higher order than the dipolar and electric quadrupolar polarization densities. In other words, one retains only the multipole moments of the induced sources that contribute significantly to the E-electric and B-magnetic primary fields with their continuum bandwidths $\Delta\boldsymbol{\beta}$ and $\Delta\omega$. Furthermore, if desirable, the individual contributions from each of these multipole polarizations to the macroscopic permittivity $\overline{\epsilon}(\boldsymbol{\beta},\omega)$ and permeability $\overline{\mu}_{\text{tt}}(\boldsymbol{\beta},\omega)$ defined in Sect. 13.3 can be used to determine separate multipole susceptibilities for small $|\boldsymbol{\beta}d|$ and all temporal frequencies ω. These multipole susceptibilities at each fixed value of $\boldsymbol{\beta}$, unlike the conventional multipole susceptibilities that are functions of ω only, will be causal functions of ω by the same arguments used in Sect. 13.4.4. Fortunately, as explained next, multipole moments higher order than dipoles (or sometimes, electric quadrupoles) are seldom required within the continuum bandwidths.

With the expressions in (13.34–13.35) substituted into (13.30), the total current is given to first order in $\boldsymbol{\beta}$ as

$$\begin{aligned}&\mathbf{J}^{\text{tot}}(\boldsymbol{\beta},\omega) = \\ &-i\omega\mathbf{P}^e_0(\boldsymbol{\beta},\omega) - \omega\boldsymbol{\beta}\cdot\overline{\mathbf{Q}}^e_0(\boldsymbol{\beta},\omega)/2 + i\boldsymbol{\beta}\times\left[\mathbf{M}^e_0(\boldsymbol{\beta},\omega) + \mathbf{M}_0(\boldsymbol{\beta},\omega)\right] + O(|\boldsymbol{\beta}d|^2)\,.\end{aligned} \tag{13.40}$$

Because the microscopic current and charge densities, $\mathcal{J}^p_\omega(\mathbf{r})$ and $\rho^p_\omega(\mathbf{r})$, induced on polarizable or perfectly conducting inclusions are absolutely integrable (so that all the multipole-moment densities are finite), we see from (13.34a) that for $|\boldsymbol{\beta}d|$ small enough the electric quadrupole-moment density contributes negligibly to the

electric polarization and both the electric and magnetic polarizations in (13.28) become equal to the ordinary electric and magnetic dipole moments per unit-cell volume. Higher order multipole moments do not have to be taken into account in order to determine the macroscopic permittivity for $|\boldsymbol{\beta} d|$ sufficiently small (unless the electric dipole polarization $\mathbf{P}_0^e(\boldsymbol{\beta}, \omega)$ is negligible for $|\boldsymbol{\beta} d|$ less than some finite value).

However, both the electric quadrupole-moment density and magnetic dipole-moment density contribute to order $\boldsymbol{\beta}$ in (13.40) as $\boldsymbol{\beta} \to 0$ and thus generally both have to be taken into account (at higher temporal frequencies ω) in determining the macroscopic permeability as $\boldsymbol{\beta} \to 0$ [25, 30, p. 61]. However, as $\boldsymbol{\beta} \to 0$, the permeability does not explicitly reveal the contribution to the fields from the electric-quadrupole polarization for an applied magnetic field; see Problem 2 in Sect. 13.5.1. Nonetheless, for $|k_0 d| = |\omega d/c|$ sufficiently small, we see from (13.40) that the contribution of the electric quadrupole-moment density becomes negligible compared to that of a nonzero magnetic dipole-moment density. (Even though $\mathbf{B} = \boldsymbol{\beta} \times \mathbf{E}/\omega \to 0$ in (13.29a) as $\boldsymbol{\beta}/\omega \to 0$, the value of the permeability remains finite as $\boldsymbol{\beta}/\omega \to 0$; see Footnote 6, and the examples in Sect. 13.5.)

In summary, as both $|\boldsymbol{\beta} d|$ and $|k_0 d|$ become small, the enforced and free-space wavelengths become much larger than the separation distance d between the inclusions, and the anisotropic formulation for the fundamental Floquet mode approaches that of an anisotropic continuum with ordinary electric-dipole, magnetic-dipole, and electric quadrupole polarization densities. *In addition, we have shown that a metamaterial array with inclusions having nonzero electric and/or magnetic dipole moments at low spatial and temporal frequencies (that is, for* $|\boldsymbol{\beta} d|$ *and* $|k_0 d|$ *sufficiently small) can be represented by an anisotropic dipolar continuum with negligible higher-order multipole-moment densities.* Since most molecules can be modeled by polarizable or perfectly conducting inclusions, this result also holds for most natural materials with electrically isolated molecules at sufficiently low spatial and temporal frequencies [31, p. 111]. The fields of the dipolar continuum satisfy the space-time Maxwellian equations in (13.37–13.38) with the electric quadrupole density $\overline{\mathcal{Q}}_{0\text{ave}}^e(\mathbf{r}, t) = 0$.

If the induced macroscopic sources of the continuum are electric and magnetic dipole moments with negligible higher-order multipole moments, then the changes in the electric and magnetic fields at a point in a cavity produced by removal of the inclusions inside a specified shaped electrically small macroscopic volume containing many inclusions (holding fixed the induced microscopic sources on the remaining inclusions) will be given approximately by the depolarizing dyadic for that point and shaped macroscopic volume [1, Chap. 2; 26, Sect. 3.28; 32, Articles 60, 395–400; 33]. This result can be demonstrated most easily in the frequency (ω) domain for an approximately spherical macroscopic volume by averaging the quasi-static fields of the dipolar inclusions contained inside the removed spherical volume over that spherical volume (centered at $\mathbf{r}$) to obtain the depolarizing E-electric and B-magnetic fields equal to $\mathcal{P}_{0\text{ave}}^e(\mathbf{r}, \omega)/(3\epsilon_0)$ and $-2\mu_0[\mathcal{M}_{0\text{ave}}^e(\mathbf{r}, \omega) + \mathcal{M}_{0\text{ave}}(\mathbf{r}, \omega)]/3$, respectively [34, Eqs. (4.18) and (5.62)—the μ_0

in Eq. (5.63) should be 4π]. The applicability of the same form of Maxwell's equations to both hypothetical dipolar continuous media and actual material composed of ensembles of discrete dipolar inclusions or molecules for $|\boldsymbol{\beta}d|$ and $|k_0 d|$ sufficiently <1 is one of the remarkable fundamental results of classical electromagnetic theory.

Before leaving this section, we note that the continuum criterion for the average fields of the array to be well approximated by the fundamental Floquet mode does not imply that the power flow in the higher-order modes of the array continuum must be negligible compared to the power flow in the fundamental Floquet mode (especially if there is strong spatial dispersion) [35, 36].

13.2.1.1 Boundary Conditions for Electric Quadrupolar Continua

The Maxwellian macroscopic space-time continuum equations in (13.37–13.38) hold for applied current excitations with spatial and temporal bandwidths ($\Delta\boldsymbol{\beta}$ and $\Delta\omega$) determined by small enough $|\boldsymbol{\beta}d|$ and $|k_0 d|$, respectively, for the approximations in (13.32–13.36) to be sufficiently accurate that ordinary macroscopic averaging applies over macroscopic volumes ΔV containing many inclusions. These Eqs. (13.37–13.38) were derived for infinite periodic arrays of separated inclusions with small enough $|\boldsymbol{\beta}d|$ and $|k_0 d|$ that all multipole-moment polarization densities of higher order than ordinary dipolar and electric quadrupolar polarization densities are negligible. In this subsection, we want to terminate the infinite array in a surface S that is effectively planar in the sense that any subsurface S_p of S extending a distance less than several lattice distances d is approximately planar. The surface S is assumed to be an interface between the array and free space or another array and we want to determine the boundary conditions across this interface.

The termination of the array(s) by the surface S introduces strong spatial variations of the fields and induced sources in the vicinity of S that invalidates the approximations in (13.32) and (13.33). Although averages of the microscopic fields and induced sources can still be performed using macroscopic volumes ΔV throughout all space, the resulting macroscopic fields will not generally satisfy (13.37–13.38) in a transition layer [37, p. 271] containing the interface surface S. For the original infinite continuum arrays characterized by $|\Delta\boldsymbol{\beta}d| \ll 1$ and $|\Delta k_0 d| = |\Delta\omega d/c| \ll 1$, the thickness δ of the transition layer is much smaller than the free-space and $2\pi/|\boldsymbol{\beta}|$ wavelengths; see discussion of evanescent eigenmodes in the previous section. The effect of this transition layer can be represented in Eq. (13.37) by additional transition-layer electric and magnetic current and charge densities on the right-hand sides of the Eq. (13.37). For example, (13.37a) and (13.37b) become

$$\nabla \times \boldsymbol{\mathcal{E}}_{\text{ave}}(\mathbf{r}, t) + \frac{\partial \boldsymbol{\mathcal{B}}_{\text{ave}}(\mathbf{r}, t)}{\partial t} = -\boldsymbol{\mathcal{K}}_{\delta}(\mathbf{r}, t) \tag{13.41a}$$

$$\nabla \times \boldsymbol{\mathcal{H}}_{\text{ave}}(\mathbf{r},t) - \frac{\partial \boldsymbol{\mathcal{D}}_{\text{ave}}(\mathbf{r},t)}{\partial t} = \boldsymbol{\mathcal{J}}^{a}(\mathbf{r},t) + \boldsymbol{\mathcal{J}}_{\delta}(\mathbf{r},t) \tag{13.41b}$$

where $\boldsymbol{\mathcal{J}}_{\delta}(\mathbf{r},t)$ and $\boldsymbol{\mathcal{K}}_{\delta}(\mathbf{r},t)$ are transition-layer macroscopic electric and magnetic current densities, respectively, that are zero everywhere except within the transition layer of thickness δ. These equations in (13.41), along with the constitutive equations in (13.38), now hold throughout all space. The two divergence equations associated with (13.41) can be obtained by taking the divergence of the equations in (13.41). Note from (13.38a) that $\boldsymbol{\mathcal{P}}^{e}_{\text{ave}}(\mathbf{r},t)$ effectively contains a delta function across the thin transition layer if the electric quadrupole density is not negligible and differs in value on either side of the transition layer; specifically

$$\begin{aligned}\boldsymbol{\mathcal{P}}^{e}_{\text{ave}}(\mathbf{r},t) &= \boldsymbol{\mathcal{P}}^{e}_{0\text{ave}}(\mathbf{r},t) - \frac{1}{2}\nabla\cdot\overline{\boldsymbol{\mathcal{Q}}}^{e}_{0\text{ave}}(\mathbf{r},t)\\ &= \boldsymbol{\mathcal{P}}^{e}_{0\text{ave}}(\mathbf{r},t) - \frac{1}{2}\left[\nabla\cdot\overline{\boldsymbol{\mathcal{Q}}}^{e}_{0\text{ave}}(\mathbf{r},t)\right]_{\text{dfr}} - \frac{1}{2}\hat{\mathbf{n}}\cdot(\overline{\boldsymbol{\mathcal{Q}}}^{e2}_{0\text{ave}} - \overline{\boldsymbol{\mathcal{Q}}}^{e1}_{0\text{ave}})\delta(n)\end{aligned} \tag{13.42}$$

in which $\hat{\mathbf{n}}$ is the unit normal to the surface S pointing from the side "1" to side "2" of the transition layer, and $\delta(n)$ is the delta function in the normal coordinate n. The subscript "dfr" means "delta function removed" from the divergence of the electric quadrupole dyadic, so that $\left[\nabla\cdot\overline{\boldsymbol{\mathcal{Q}}}^{e}_{0\text{ave}}(\mathbf{r},t)\right]_{\text{dfr}}$ can be discontinuous but otherwise nonsingular across the thin transition layer. We are assuming that there are no effective delta functions in the macroscopic dipolar and electric quadrupolar polarization densities, $\boldsymbol{\mathcal{P}}^{e}_{0\text{ave}}(\mathbf{r},t)$, $\boldsymbol{\mathcal{M}}^{e}_{0\text{ave}}(\mathbf{r},t) + \boldsymbol{\mathcal{M}}_{0\text{ave}}(\mathbf{r},t)$, and $\overline{\boldsymbol{\mathcal{Q}}}^{e}_{0\text{ave}}(\mathbf{r},t)$, represented by $\boldsymbol{\mathcal{J}}_{\delta}(\mathbf{r},t)$ and $\boldsymbol{\mathcal{K}}_{\delta}(\mathbf{r},t)$ within the thin transition layer.[13]

Boundary conditions on the tangential components of the macroscopic $\boldsymbol{\mathcal{E}}_{\text{ave}}$ and $\boldsymbol{\mathcal{H}}_{\text{ave}}$ fields and on the normal components of the macroscopic $\boldsymbol{\mathcal{D}}_{\text{ave}}$ and $\boldsymbol{\mathcal{B}}_{\text{ave}}$ fields across the transition layer can be determined by applying the integral forms of (13.41) and the corresponding divergence equations to thin rectangular closed curves and closed surfaces (pillboxes) with their long dimensions of length ℓ on either side of the transition layer so that their short sides are of width $\delta \ll \ell$ (taking into account the effective delta functions in $\nabla\cdot\overline{\boldsymbol{\mathcal{Q}}}^{e}_{0\text{ave}}$ across the transition layer). Although $\ell \gg \delta$, it is assumed that ℓ is short enough that the macroscopic fields and sources along the length of ℓ do not change appreciably. This determination of boundary conditions for the equations in (13.41) with the constitutive relations in

[13] Delta functions $\delta(n)$ and their derivatives in the polarizations as represented by $\boldsymbol{\mathcal{J}}_{\delta}(\mathbf{r},t)$ and $\boldsymbol{\mathcal{K}}_{\delta}(\mathbf{r},t)$ may exist if these polarizations are proportional to unusually high spatial derivatives of the fields, that is, if they display strong enough spatial dispersion. In that case, the boundary conditions in (13.43) may have to be modified. However, significant polarization proportional to unusually high spatial derivatives of the fields generally indicates the presence of higher-order multipoles. For example, $\boldsymbol{\mathcal{P}}^{e}_{0\text{ave}}$ proportional to the second spatial derivative of $\boldsymbol{\mathcal{E}}_{\text{ave}}$ would indicate the presence of magnetic dipoles or electric quadrupoles. Similarly, $\boldsymbol{\mathcal{M}}^{e}_{0\text{ave}}$ or $\overline{\boldsymbol{\mathcal{Q}}}^{e}_{0\text{ave}}$ proportional to the second or third spatial derivatives of $\boldsymbol{\mathcal{B}}_{\text{ave}}$ or $\boldsymbol{\mathcal{E}}_{\text{ave}}$ respectively, would indicate the presence of octopoles.

(13.38) and (13.42) has been done in [38] but without the transition current densities, $\mathcal{J}_\delta(\mathbf{r},t)$ and $\mathcal{K}_\delta(\mathbf{r},t)$. However, the additional integrals over $\mathcal{J}_\delta(\mathbf{r},t)$ and $\mathcal{K}_\delta(\mathbf{r},t)$ become insignificant for δ sufficiently small, or equivalently, for $|\Delta\boldsymbol{\beta}d|$ and $|\Delta k_0 d|$ sufficiently small, provided, as discussed in Footnote 13, that $\mathcal{J}_\delta(\mathbf{r},t)$ and $\mathcal{K}_\delta(\mathbf{r},t)$ do not contain delta functions in the polarization densities. Thus, we can apply the boundary conditions derived in [38][14] with the surface polarization $\mathbf{P}^\delta$ in [38] replaced by $-\hat{\mathbf{n}}\cdot(\overline{\mathcal{Q}}^{e2}_{0\text{ave}}-\overline{\mathcal{Q}}^{e1}_{0\text{ave}})/2$ given in (13.42), to get

$$\boldsymbol{\mathcal{E}}^{2s}_{\text{ave}}-\boldsymbol{\mathcal{E}}^{1s}_{\text{ave}}\approx\frac{1}{2\epsilon_0}\nabla_s\left[\hat{\mathbf{n}}\cdot(\overline{\mathcal{Q}}^{e2}_{0\text{ave}}-\overline{\mathcal{Q}}^{e1}_{0\text{ave}})\cdot\hat{\mathbf{n}}\right] \tag{13.43a}$$

$$\boldsymbol{\mathcal{H}}^{2s}_{\text{ave}}-\boldsymbol{\mathcal{H}}^{1s}_{\text{ave}}\approx\frac{1}{2}\hat{\mathbf{n}}\times\left[\partial(\hat{\mathbf{n}}\cdot\overline{\mathcal{Q}}^{e2}_{0\text{ave}})^s/\partial t-\partial(\hat{\mathbf{n}}\cdot\overline{\mathcal{Q}}^{e1}_{0\text{ave}})^s/\partial t\right] \tag{13.43b}$$

$$\mathcal{D}^{2n}_{\text{ave}}-\mathcal{D}^{1n}_{\text{ave}}\approx\frac{1}{2}\nabla_s\cdot\left[(\hat{\mathbf{n}}\cdot\overline{\mathcal{Q}}^{e2}_{0\text{ave}})^s-(\hat{\mathbf{n}}\cdot\overline{\mathcal{Q}}^{e1}_{0\text{ave}})^s\right] \tag{13.43c}$$

$$\mathcal{B}^{2n}_{\text{ave}}-\mathcal{B}^{1n}_{\text{ave}}\approx 0 \tag{13.43d}$$

where the superscripts "s" and "n" refer to vector components tangential and normal to the surface S, respectively, and we note that $\overline{\mathcal{Q}}^{e}_{0\text{ave}}(\mathbf{r},t)$ is a symmetric dyadic because $\overline{\mathbf{Q}}^{e}_{0}(\boldsymbol{\beta},\omega)$ is a symmetric dyadic. These boundary conditions show that the change in electric quadrupole density across the thin transition layer produces discontinuities in the tangential components of $\boldsymbol{\mathcal{E}}_{\text{ave}}$ and $\boldsymbol{\mathcal{H}}_{\text{ave}}$ and in the normal component of $\boldsymbol{\mathcal{D}}_{\text{ave}}$. They agree with the boundary conditions of Raab and De Lange [25, Eqs. (6.69–6.74)] if a term $\epsilon_0^{-1}\partial Q_{zz}/\partial z/2$ is added to the right-hand side of [25, Eq. (6.71)]. In a private communication, Raab and De Lange have confirmed the necessity of this added term. Our expressions in (13.43) have also been confirmed in an unpublished independent derivation by M.G. Silveirinha using transverse averaging and assuming no delta-function contributions, as discussed in Footnote 13, from the effective polarizations in the transition layer [39]. In [38] we also prove that $\mathcal{E}^{n}_{\text{ave}}$ has a delta function in the transition layer equal to $\hat{\mathbf{n}}\cdot(\overline{\mathcal{Q}}^{2}_{0\text{ave}}-\overline{\mathcal{Q}}^{1}_{0\text{ave}})\cdot\hat{\mathbf{n}}\delta(n)/(2\epsilon_0)$.

The results of several analyses and simulations of periodic arrays, for example those in [39–41], indicate that the effect of the boundary layer becomes negligible for spatial and temporal bandwidths, $|\Delta\boldsymbol{\beta}d|$ and $|\Delta k_0 d|$, less than about 0.1. Thus, one would also expect that the boundary conditions in (13.43) are reliable approximations for $|\Delta\boldsymbol{\beta}d|$ and $|\Delta k_0 d|$ less than about 0.1. If, as discussed in the previous section, these spatial and temporal bandwidths are small enough for the electric quadrupole density to be negligible compared to the dipolar polarization densities, then the electric quadrupole terms in (13.43) can be neglected and (13.43) predicts the usual continuity of the tangential $\boldsymbol{\mathcal{E}}_{\text{ave}}$ and $\boldsymbol{\mathcal{H}}_{\text{ave}}$ fields and the

[14] The field symbols on the left-hand sides of Eqs. (13), (15), and (16) in [38] should be boldface, and the ∇ symbol one line below Eq. (12) of [38] should be ∇_s.

normal $\mathcal{D}_{\text{ave}}$ field (as well as the normal $\mathcal{B}_{\text{ave}}$ field) across the thin transition layer. Lastly, we mention the need for more analysis and simulations to investigate the possibility of additional delta functions, as discussed in Footnote 13, in the polarizations of more strongly spatially dispersive arrays and to determine additional boundary conditions (ABCs) for these arrays [13, 18].

13.3 Anisotropic Constitutive Relations

To formulate an anisotropic description of the fundamental Floquet modes on 3D periodic arrays, we note that for linear inclusion material all the field vectors in (13.29) are linearly related to the applied electric current vector $\mathbf{J}_a(\boldsymbol{\beta}, \omega)$ and, thus, we can express $\mathbf{D}$ and $\mathbf{E}$ as

$$\mathbf{D}(\boldsymbol{\beta}, \omega) = \overline{\mathbf{d}}(\boldsymbol{\beta}, \omega) \cdot \mathbf{J}_a(\boldsymbol{\beta}, \omega) \tag{13.44a}$$

$$\mathbf{E}(\boldsymbol{\beta}, \omega) = \overline{\mathbf{e}}(\boldsymbol{\beta}, \omega) \cdot \mathbf{J}_a(\boldsymbol{\beta}, \omega)\,. \tag{13.44b}$$

The linear relationship in (13.44b) can be inverted to give $\mathbf{J}_a(\boldsymbol{\beta}, \omega)$ in terms of $\mathbf{E}(\boldsymbol{\beta}, \omega)$ as

$$\mathbf{J}_a(\boldsymbol{\beta}, \omega) = \overline{\mathbf{e}}^{-1}(\boldsymbol{\beta}, \omega) \cdot \mathbf{E}(\boldsymbol{\beta}, \omega)\,. \tag{13.44c}$$

Substitution of $\mathbf{J}_a(\boldsymbol{\beta}, \omega)$ from (13.44c) into (13.44a) yields the desired anisotropic electric constitutive relation

$$\mathbf{D}(\boldsymbol{\beta}, \omega) = \overline{\boldsymbol{\epsilon}}_e(\boldsymbol{\beta}, \omega) \cdot \mathbf{E}(\boldsymbol{\beta}, \omega) \tag{13.45}$$

with the permittivity dyadic $\overline{\boldsymbol{\epsilon}}_e(\boldsymbol{\beta}, \omega)$.

It is somewhat more involved to obtain a viable constitutive relation between the secondary magnetic field $\mathbf{H}$ and the primary magnetic field $\mathbf{B}$ because (13.29a) shows that the longitudinal (parallel to the propagation vector $\boldsymbol{\beta}$) component of $\mathbf{B}$ is zero ($\boldsymbol{\beta} \cdot \mathbf{B} = 0$); that is, denoting longitudinal components by the subscript "$_\mathsf{l}$", we have $\mathbf{B}_\mathsf{l} = \mu_0(\mathbf{H}_\mathsf{l} + \mathbf{M}_\mathsf{l}^e + \mathbf{M}_\mathsf{l}) = 0$, and $\mathbf{H}$ cannot be expressed in terms of only the two independent components of $\mathbf{B} = \mathbf{B}_\mathsf{t}$ where the subscript "$_\mathsf{t}$" denotes components transverse to the propagation vector $\boldsymbol{\beta}$. In other words, we can express $\mathbf{H}$ and $\mathbf{B}$ in terms of $\mathbf{J}_a$ as

$$\mathbf{H}(\boldsymbol{\beta}, \omega) = \overline{\mathbf{h}}(\boldsymbol{\beta}, \omega) \cdot \mathbf{J}_a(\boldsymbol{\beta}, \omega) \tag{13.46a}$$

$$\mathbf{B}(\boldsymbol{\beta}, \omega) = \overline{\mathbf{b}}(\boldsymbol{\beta}, \omega) \cdot \mathbf{J}_a(\boldsymbol{\beta}, \omega) \tag{13.46b}$$

but $\mathbf{H}$ in (13.46a) cannot generally be expressed in terms of $\mathbf{B}$ by substituting $\mathbf{J}_a$ from (13.46b) because (13.46b) cannot be inverted to get the three linearly independent components of $\mathbf{J}_a$ in terms of the two linearly independent components of $\mathbf{B}$. Nonetheless, it is permissible to linearly relate $\mathbf{H}$ to any three

independent components of the primary fields. In particular, choosing $(\mathbf{B}, \mathbf{E}_l)$ as these three primary components, the $\mathbf{H} = \mathbf{H}_t + \mathbf{H}_l$ field can be expressed as

$$\mathbf{H}_l(\boldsymbol{\beta}, \omega) = -\mathbf{M}_l^e(\boldsymbol{\beta}, \omega) - \mathbf{M}_l(\boldsymbol{\beta}, \omega) \tag{13.47}$$

$$\mathbf{H}_t(\boldsymbol{\beta}, \omega) = \overline{\boldsymbol{\mu}}_{tt}^{-1}(\boldsymbol{\beta}, \omega) \cdot \mathbf{B}(\boldsymbol{\beta}, \omega) + \overline{\boldsymbol{v}}_{tl}(\boldsymbol{\beta}, \omega) \cdot \mathbf{E}_l(\boldsymbol{\beta}, \omega) \tag{13.48}$$

where $\overline{\boldsymbol{\mu}}_{tt}(\boldsymbol{\beta}, \omega)$ is a transverse permeability dyadic and $\overline{\boldsymbol{v}}_{tl}(\boldsymbol{\beta}, \omega)$ is a magnetoelectric dyadic. In a rectangular (x, y, z) coordinate system with $\boldsymbol{\beta}$ aligned with one of the axes, $\overline{\boldsymbol{\mu}}_{tt}(\boldsymbol{\beta}, \omega)$ and its inverse $\overline{\boldsymbol{\mu}}_{tt}^{-1}(\boldsymbol{\beta}, \omega)$ are 2×2 dyadics and $\overline{\boldsymbol{v}}_{tl}(\boldsymbol{\beta}, \omega)$ is a 2×1 dyadic. (For $\boldsymbol{\beta}$ in directions other than either the x, y, or z direction, the dyadic $\overline{\boldsymbol{\mu}}_{tt}(\boldsymbol{\beta}, \omega)$ has nine elements but only four are independent because $\boldsymbol{\beta} \cdot \overline{\boldsymbol{\mu}}_{tt}(\boldsymbol{\beta}, \omega) = \overline{\boldsymbol{\mu}}_{tt}(\boldsymbol{\beta}, \omega) \cdot \boldsymbol{\beta} = 0$, which gives six homogeneous equations from which five of the elements can be written in terms of the other four elements.)

We could also express $\mathbf{H}_l$ in (13.47) as $\overline{\boldsymbol{\mu}}_{lt}^{-1} \cdot \mathbf{B} + \overline{\boldsymbol{v}}_{ll} \cdot \mathbf{E}_l$, then solve for $\mathbf{E}_l$ to eliminate $\mathbf{E}_l$ from (13.48), and finally solve for $\mathbf{B}$ in (13.48) in terms of $\mathbf{H}$ to get $\mathbf{B}(\boldsymbol{\beta}, \omega) = \overline{\boldsymbol{\mu}}_h(\boldsymbol{\beta}, \omega) \cdot \mathbf{H}(\boldsymbol{\beta}, \omega)$. However, the inverse of $\overline{\boldsymbol{\mu}}_h(\boldsymbol{\beta}, \omega)$ does not exist (because $\mathbf{H}$ has three linearly independent components and $\mathbf{B}$ only two) and thus it proves advantageous to work with $\overline{\boldsymbol{\mu}}_{tt}^{-1}(\boldsymbol{\beta}, \omega)$ in (13.48). The magnetic constitutive parameters $(\overline{\boldsymbol{\mu}}_{tt}^{-1}, \overline{\boldsymbol{v}}_{tl})$ have a total of six independent elements, the same number of independent elements as a single 2×3 dyadic. In Eqs. (13.49–13.51a) below, the magnetoelectric dyadic in (13.48) is assimilated into the permittivity dyadic to maintain a purely anisotropic representation of the array.

With the constitutive relations inserted from (13.45) and (13.48) into (13.29), the fundamental Floquet-mode equations in (13.29) can be recast in the form of the traditional Maxwellian macroscopic equations in an anisotropic medium with primary fields $\mathbf{E}(\boldsymbol{\beta}, \omega)$ and $\mathbf{B}(\boldsymbol{\beta}, \omega)$, namely

$$i\boldsymbol{\beta} \times \mathbf{E}(\boldsymbol{\beta}, \omega) - i\omega \mathbf{B}(\boldsymbol{\beta}, \omega) = 0 \tag{13.49a}$$

$$i\boldsymbol{\beta} \times \overline{\boldsymbol{\mu}}_{tt}^{-1}(\boldsymbol{\beta}, \omega) \cdot \mathbf{B}(\boldsymbol{\beta}, \omega) + i\omega \overline{\boldsymbol{\epsilon}}(\boldsymbol{\beta}, \omega) \cdot \mathbf{E}(\boldsymbol{\beta}, \omega) = \mathbf{J}_a(\boldsymbol{\beta}, \omega) \tag{13.49b}$$

where

$$\overline{\boldsymbol{\epsilon}} \equiv \overline{\boldsymbol{\epsilon}}_e + \boldsymbol{\beta} \times \overline{\boldsymbol{v}}_{tl}/\omega \tag{13.50}$$

defines an effective displacement vector

$$\mathbf{D}^{\text{eff}} = \overline{\boldsymbol{\epsilon}} \cdot \mathbf{E} = \epsilon_0 \mathbf{E} + \mathbf{P}^e + \boldsymbol{\beta} \times \overline{\boldsymbol{v}}_{tl} \cdot \mathbf{E}_l/\omega = \mathbf{D} + \boldsymbol{\beta} \times \overline{\boldsymbol{v}}_{tl} \cdot \mathbf{E}/\omega \tag{13.51a}$$

and we can define an effective transverse H-field as

$$\mathbf{H}_t^{\text{eff}} = \overline{\boldsymbol{\mu}}_{tt}^{-1} \cdot \mathbf{B} = \mathbf{B}/\mu_0 - \mathbf{M}_t^e - \mathbf{M}_t - \overline{\boldsymbol{v}}_{tl} \cdot \mathbf{E}_l = \mathbf{H}_t - \overline{\boldsymbol{v}}_{tl} \cdot \mathbf{E}_l \tag{13.51b}$$

with $\mathbf{H}^{\text{eff}} = \mathbf{H}_t^{\text{eff}} - \mathbf{M}_l^e - \mathbf{M}_l$. Note that, as $\boldsymbol{\beta}/\omega \to 0$, the values of the effective displacement vector $\mathbf{D}^{\text{eff}}$ and permittivity dyadic $\overline{\boldsymbol{\epsilon}}$ become equal to their traditional values (that is, $\mathbf{D}^{\text{eff}} = \mathbf{D}$ and $\overline{\boldsymbol{\epsilon}} = \overline{\boldsymbol{\epsilon}}_e$). Also, for nonbianisotropic inclusions,

$\overline{\boldsymbol{v}}_{\mathrm{tl}}(\boldsymbol{\beta},\omega)$ becomes negligible at low spatial or temporal frequencies (approaching zero as $\boldsymbol{\beta}\to 0$ or $\omega\to 0$; see Footnote 6) and $\mathbf{H}^{\mathrm{eff}}=\mathbf{H}$.

As $\boldsymbol{\beta}\to 0$, it is emphasized that the elements of a transverse dyadic, in particular, the transverse permeability dyadic $\overline{\boldsymbol{\mu}}_{\mathrm{tt}}$ (or $\overline{\boldsymbol{\mu}}_{\mathrm{tt}}^{-1}$), in an (x,y,z) coordinate system fixed in the array, unlike the elements of a complete dyadic such as the permittivity dyadic $\overline{\boldsymbol{\epsilon}}$ (or $\overline{\boldsymbol{\epsilon}}_e$) as $\boldsymbol{\beta}\to 0$, are functions of the direction of $\boldsymbol{\beta}$. Nonetheless, as we explain next, for $\boldsymbol{\beta}\to 0$ the transverse dyadic $\overline{\boldsymbol{\mu}}_{\mathrm{tt}}$ can be used to determine a complete permeability dyadic $\overline{\boldsymbol{\mu}}_b$ that relates a $\mathbf{B}_b$ field with three linearly independent components to a corresponding $\mathbf{H}_b$ field.

Consider for the moment the array excited by both applied plane-wave magnetic and electric current densities such that three linearly independent components of the primary fields $\mathbf{E}_b$ and $\mathbf{B}_b$ are generated. The three components of $\mathbf{H}_b$ can be bianisotropically related to the three components of the $\mathbf{E}_b$ and $\mathbf{B}_b$ fields by a complete permeability dyadic $\overline{\boldsymbol{\mu}}_b^{-1}$ and a complete magnetoelectric dyadic $\overline{\boldsymbol{\nu}}_b$; that is

$$\mathbf{H}_b(\boldsymbol{\beta},\omega)=\overline{\boldsymbol{\mu}}_b^{-1}(\boldsymbol{\beta},\omega)\cdot\mathbf{B}_b(\boldsymbol{\beta},\omega)+\overline{\boldsymbol{\nu}}_b(\boldsymbol{\beta},\omega)\cdot\mathbf{E}_b(\boldsymbol{\beta},\omega)\,. \tag{13.52}$$

[Note that for $\boldsymbol{\beta}\to 0$, applied magnetic currents can be avoided altogether by assuming that electric current sources at infinity illuminate the linear array with spatially uniform incident E-electric and B-magnetic fields in order to obtain the complete fields in (13.52)]. The nine-element permeability dyadic $\overline{\boldsymbol{\mu}}_b$ can be written in an (x,y,z) coordinate system fixed in the 3D periodic array as

$$\overline{\boldsymbol{\mu}}_b=\begin{bmatrix}\mu_{bxx} & \mu_{bxy} & \mu_{bxz}\\ \mu_{byx} & \mu_{byy} & \mu_{byz}\\ \mu_{bzx} & \mu_{bzy} & \mu_{bzz}\end{bmatrix}. \tag{13.53}$$

Setting the applied magnetic current equal to zero, leaving just the applied electric current $\mathbf{J}_a e^{i\boldsymbol{\beta}\cdot\mathbf{r}}$, we have $\mathbf{E}_b=\mathbf{E}$, $\mathbf{B}_b=\mathbf{B}=\mathbf{B}_{\mathrm{t}}$ and $\mathbf{H}_b=\mathbf{H}$ so that the transverse part of (13.52) becomes

$$\mathbf{H}_{\mathrm{t}}=\overline{\boldsymbol{\mu}}_{b\mathrm{tt}}^{-1}\cdot\mathbf{B}+(\overline{\boldsymbol{\nu}}_b\cdot\mathbf{E})_{\mathrm{t}} \tag{13.54a}$$

or because $\mathbf{E}_{\mathrm{t}}=-\omega\boldsymbol{\beta}\times\mathbf{B}/|\boldsymbol{\beta}|^2=-\omega\overline{\boldsymbol{\beta}}\cdot\mathbf{B}/|\boldsymbol{\beta}|^2$; see (13.75)

$$\mathbf{H}_{\mathrm{t}}=\left[\overline{\boldsymbol{\mu}}_{b\mathrm{tt}}^{-1}-\omega\overline{\boldsymbol{\nu}}_{b\mathrm{tt}}\cdot\overline{\boldsymbol{\beta}}/|\boldsymbol{\beta}|^2\right]\cdot\mathbf{B}+\overline{\boldsymbol{\nu}}_{b\mathrm{tl}}\cdot\mathbf{E}_{\mathrm{l}}\,. \tag{13.54b}$$

Comparing (13.54b) with (13.48), we see that

$$\overline{\boldsymbol{\mu}}_{b\mathrm{tt}}^{-1}-\omega\overline{\boldsymbol{\nu}}_{b\mathrm{tt}}\cdot\overline{\boldsymbol{\beta}}/|\boldsymbol{\beta}|^2=\overline{\boldsymbol{\mu}}_{\mathrm{tt}}^{-1} \tag{13.55a}$$

$$\overline{\boldsymbol{\nu}}_{b\mathrm{tl}}=\overline{\boldsymbol{\nu}}_{\mathrm{tl}}\,. \tag{13.55b}$$

The bianisotropic term $\omega\overline{\boldsymbol{\nu}}_{b\mathrm{tt}}/|\boldsymbol{\beta}|$ in (13.55a) is negligible at the lower frequencies ω as $\boldsymbol{\beta}/\omega\to 0$ if the inclusion material does not exhibit bianisotropy; see Footnote

6. At higher frequencies ω, the lattice bianisotropy mentioned in Footnote 6 and which is $O(\boldsymbol{\beta})$ as $\boldsymbol{\beta} \to 0$ can give a finite value to $\omega \overline{\mathbf{v}}_{b\mathrm{tt}}/|\boldsymbol{\beta}|$ as $\boldsymbol{\beta} \to 0$. This finite value can be incorporated into $\overline{\boldsymbol{\mu}}_{b\mathrm{tt}}(\boldsymbol{\beta} \to 0, \omega)$ in (13.55a) and is of little consequence because it approaches zero at the lower frequencies ω where the array behaves as a continuum. Thus, for nonbianisotropic inclusions at lower values of ω and $\boldsymbol{\beta} \to 0$, (13.55a) reduces to

$$\overline{\boldsymbol{\mu}}_{b\mathrm{tt}}^{-1}(\boldsymbol{\beta} \to 0, \omega) = \overline{\boldsymbol{\mu}}_{\mathrm{tt}}^{-1}(\boldsymbol{\beta} \to 0, \omega) \tag{13.56a}$$

or

$$\overline{\boldsymbol{\mu}}_{b\mathrm{tt}}(\boldsymbol{\beta} \to 0, \omega) = \overline{\boldsymbol{\mu}}_{\mathrm{tt}}(\boldsymbol{\beta} \to 0, \omega)\,. \tag{13.56b}$$

If we choose the propagation vector $\boldsymbol{\beta}$ in the $\hat{\mathbf{z}}$ direction, the transverse permeability dyadic $\overline{\boldsymbol{\mu}}_{\mathrm{tt}}$ can be written as a 2×2 matrix

$$\overline{\boldsymbol{\mu}}_{\mathrm{tt}}(\beta_z, \omega) = \begin{bmatrix} \mu_{xx}(\beta_z, \omega) & \mu_{xy}(\beta_z, \omega) \\ \mu_{yx}(\beta_z, \omega) & \mu_{yy}(\beta_z, \omega) \end{bmatrix}. \tag{13.57a}$$

Similarly, if we choose the propagation vector $\boldsymbol{\beta}$ in the $\hat{\mathbf{x}}$ and $\hat{\mathbf{y}}$ directions, we have

$$\overline{\boldsymbol{\mu}}_{\mathrm{tt}}(\beta_x, \omega) = \begin{bmatrix} \mu_{yy}(\beta_x, \omega) & \mu_{yz}(\beta_x, \omega) \\ \mu_{zy}(\beta_x, \omega) & \mu_{zz}(\beta_x, \omega) \end{bmatrix} \tag{13.57b}$$

and

$$\overline{\boldsymbol{\mu}}_{\mathrm{tt}}(\beta_y, \omega) = \begin{bmatrix} \mu_{xx}(\beta_y, \omega) & \mu_{xz}(\beta_y, \omega) \\ \mu_{zx}(\beta_y, \omega) & \mu_{zz}(\beta_y, \omega) \end{bmatrix}. \tag{13.57c}$$

Thus, in view of (13.56), we have

$$\mu_{bxx}(0, \omega) = \mu_{xx}(\beta_z, \omega) = \mu_{xx}(\beta_y, \omega), \quad \mu_{bxy}(0, \omega) = \mu_{xy}(\beta_z, \omega) \tag{13.58a}$$

$$\mu_{byy}(0, \omega) = \mu_{yy}(\beta_z, \omega) = \mu_{yy}(\beta_x, \omega), \ \mu_{byx}(0, \omega) = \mu_{yx}(\beta_z, \omega) \tag{13.58b}$$

$$\mu_{byz}(0, \omega) = \mu_{yz}(\beta_x, \omega), \quad \mu_{bzy}(0, \omega) = \mu_{zy}(\beta_x, \omega) \tag{13.58c}$$

$$\mu_{bzz}(0, \omega) = \mu_{zz}(\beta_x, \omega) = \mu_{zz}(\beta_y, \omega) \tag{13.58d}$$

$$\mu_{bzx}(0, \omega) = \mu_{zx}(\beta_y, \omega), \quad \mu_{bxz}(0, \omega) = \mu_{xz}(\beta_y, \omega) \tag{13.58e}$$

in which $\beta_x \to 0$, $\beta_y \to 0$, and $\beta_z \to 0$. The results in (13.58) reveal that, for nonbianisotropic inclusions at low values of ω, the complete permeability dyadic $\overline{\boldsymbol{\mu}}_b(0, \omega)$ of the array, which is independent of the propagation vector $\boldsymbol{\beta}$ (that is, the nine elements of $\overline{\boldsymbol{\mu}}_b(0, \omega)$ do not change with the direction of $\boldsymbol{\beta}$ in an (x, y, z) coordinate system fixed in the array), can be expressed in terms of the transverse propagation-direction dependent permeability dyadic $\overline{\boldsymbol{\mu}}_{\mathrm{tt}}(\boldsymbol{\beta} \to 0, \omega)$ in three

orthogonal directions (for example, the three principal directions), where $\overline{\boldsymbol{\mu}}_{\rm tt}(\boldsymbol{\beta} \to 0, \omega)$ is determined by solving the microscopic equations for the macroscopic fields of the fundamental Floquet-mode of the 3D array. If $|k_0 d|$ is sufficiently small (and $\boldsymbol{\beta} \to 0$), the array behaves as a continuum and the complete dyadic $\overline{\boldsymbol{\mu}}_b(0, \omega)$ is the $\boldsymbol{\beta} = 0$ continuum permeability dyadic which gives the three-component continuum $\mathbf{H}_b$ field in terms of the three components of the continuum $\mathbf{B}_b$ field by means of the constitutive relationship in (13.52), provided the inclusion material is not bianisotropic for small $|k_0 d|$ as $\boldsymbol{\beta} \to 0$; see Footnote 6. Also, the permeability often varies by a small amount with $\boldsymbol{\beta}$ for $|\boldsymbol{\beta} d| \ll 1$ and then the relationships in (13.58) hold approximately over the bandwidths of $|\boldsymbol{\beta} d| \ll 1$ and $|k_0 d| \ll 1$.

For the permittivity dyadics, the equations analogous to (13.58) can be used to determine $\overline{\boldsymbol{\epsilon}}_b(0, \omega)$ exactly for all ω, even for bianisotropic inclusions, from $\overline{\boldsymbol{\epsilon}}_{\rm tt}(\boldsymbol{\beta} \to 0, \omega) = \overline{\boldsymbol{\epsilon}}_{e\rm tt}(\boldsymbol{\beta} \to 0, \omega)$ (and approximately for $|\boldsymbol{\beta} d| \ll 1$).

13.4 Reality Conditions, Reciprocity Relations, Passivity Conditions, and Causality Relations for the Spatially Dispersive Constitutive Parameters

The definitions of the spatially dispersive macroscopic fields and constitutive parameters for the fundamental Floquet modes are similar though not identical to those in a spatially nondispersive continuum. Consequently, we find in this section that the reality conditions, reciprocity relations, passivity conditions, and causality relations for the fundamental Floquet modes also differ from their corresponding spatially nondispersive continuum relationships. Nevertheless, as the spatial and temporal frequencies, $\boldsymbol{\beta}$ and ω, become sufficiently small for the arrays to approximate continua, then the reality conditions, reciprocity relations, and passivity conditions become essentially the same as those of a spatially nondispersive dipolar continuum.

13.4.1 Reality Conditions

The reality conditions for the fundamental Floquet modes of an array can be derived by returning to the applied current density in (13.7). Although the space-time fields and sources associated with (13.4–13.6) are real, we have assumed a complex plane-wave source in (13.7). Thus, an unstated assumption in (13.7) is that corresponding to each plane wave there is another plane wave $\mathbf{J}_a(-\boldsymbol{\beta}, -\omega) e^{-i(\boldsymbol{\beta}\cdot\mathbf{r} - \omega t)}$ such that

$$\mathbf{J}_a(\boldsymbol{\beta}, \omega) e^{i(\boldsymbol{\beta}\cdot\mathbf{r} - \omega t)} + \mathbf{J}_a(-\boldsymbol{\beta}, -\omega) e^{-i(\boldsymbol{\beta}\cdot\mathbf{r} - \omega t)} \tag{13.59}$$

is a real valued current-density function of $\mathbf{r}$ and t. Since this space-time vector is real valued, taking the complex conjugate of (13.59) does not change its value. It follows that

$$\mathbf{J}_a(-\boldsymbol{\beta}, -\omega) = \mathbf{J}_a^*(\boldsymbol{\beta}, \omega) \tag{13.60}$$

and similarly for the other fundamental Floquet-mode source and field vectors in (13.49, 13.51); in particular

$$\mathbf{E}(-\boldsymbol{\beta}, -\omega) = \mathbf{E}^*(\boldsymbol{\beta}, \omega) \tag{13.61a}$$

$$\mathbf{B}(-\boldsymbol{\beta}, -\omega) = \mathbf{B}^*(\boldsymbol{\beta}, \omega) \tag{13.61b}$$

$$\mathbf{D}^{\text{eff}}(-\boldsymbol{\beta}, -\omega) = \mathbf{D}^{\text{eff}*}(\boldsymbol{\beta}, \omega) \tag{13.61c}$$

$$\mathbf{D}(-\boldsymbol{\beta}, -\omega) = \mathbf{D}^*(\boldsymbol{\beta}, \omega) \tag{13.61d}$$

$$\mathbf{H}(-\boldsymbol{\beta}, -\omega) = \mathbf{H}^*(\boldsymbol{\beta}, \omega)\,. \tag{13.61e}$$

Also, it follows from (13.61) and the constitutive relations in (13.45), (13.48), and (13.51a) that

$$\overline{\boldsymbol{\epsilon}}_e(-\boldsymbol{\beta}, -\omega) = \overline{\boldsymbol{\epsilon}}_e^*(\boldsymbol{\beta}, \omega) \tag{13.62a}$$

$$\overline{\boldsymbol{\epsilon}}(-\boldsymbol{\beta}, -\omega) = \overline{\boldsymbol{\epsilon}}^*(\boldsymbol{\beta}, \omega) \tag{13.62b}$$

$$\overline{\boldsymbol{\mu}}_{\text{tt}}(-\boldsymbol{\beta}, -\omega) = \overline{\boldsymbol{\mu}}_{\text{tt}}^*(\boldsymbol{\beta}, \omega)\,. \tag{13.62c}$$

The anisotropic constitutive parameters satisfy the same kind of reality relation as the fields.

13.4.2 Reciprocity Relations

To derive general reciprocity relations for the spatially dispersive constitutive parameters of the fundamental Floquet modes, begin by rewriting the Maxwell space-frequency domain equations in (13.4a) and (13.4b) for an array of lossy or lossless polarizable inclusions with applied electric current density given in (13.7)

$$\nabla \times \boldsymbol{\mathcal{E}}_\omega(\mathbf{r}) - i\omega \boldsymbol{\mathcal{B}}_\omega(\mathbf{r}) = 0 \tag{13.63a}$$

$$\frac{1}{\mu_0} \nabla \times \boldsymbol{\mathcal{B}}_\omega(\mathbf{r}) + i\omega\epsilon_0 \boldsymbol{\mathcal{E}}_\omega(\mathbf{r}) - \boldsymbol{\mathcal{J}}_\omega^p(\mathbf{r}) - \nabla \times \boldsymbol{\mathcal{M}}_\omega(\mathbf{r}) = \mathbf{J}_a(\boldsymbol{\beta}, \omega) e^{i\boldsymbol{\beta}\cdot\mathbf{r}}\,. \tag{13.63b}$$

The same equations but with $-\boldsymbol{\beta}$ replacing $\boldsymbol{\beta}$ are given by

$$\nabla \times \boldsymbol{\mathcal{E}}_{\omega}^{-}(\mathbf{r}) - i\omega \boldsymbol{\mathcal{B}}_{\omega}^{-}(\mathbf{r}) = 0 \tag{13.64a}$$

$$\frac{1}{\mu_0}\nabla \times \boldsymbol{\mathcal{B}}_{\omega}^{-}(\mathbf{r}) + i\omega\epsilon_0 \boldsymbol{\mathcal{E}}_{\omega}^{-}(\mathbf{r}) - \boldsymbol{\mathcal{J}}_{\omega}^{p-}(\mathbf{r}) - \nabla \times \boldsymbol{\mathcal{M}}_{\omega}^{-}(\mathbf{r}) = \mathbf{J}_a(-\boldsymbol{\beta}, \omega)e^{-i\boldsymbol{\beta}\cdot\mathbf{r}}\,. \tag{13.64b}$$

Take the dot product of $\boldsymbol{\mathcal{B}}_{\omega}^{-}(\mathbf{r})/\mu_0$ and $\boldsymbol{\mathcal{E}}_{\omega}^{-}(\mathbf{r})$ with (13.63a) and (13.63b), respectively, and the dot product of $\boldsymbol{\mathcal{B}}_{\omega}(\mathbf{r})/\mu_0$ and $\boldsymbol{\mathcal{E}}_{\omega}(\mathbf{r})$ with (13.64a) and (13.64b), respectively. Then subtract the sum of Eqs. (13.64a) and (13.64b) from the sum of Eqs. (13.63a) and (13.63b) to get

$$\begin{aligned}
&\frac{1}{\mu_0}\nabla \cdot \left[\boldsymbol{\mathcal{E}}_{\omega}(\mathbf{r}) \times \boldsymbol{\mathcal{B}}_{\omega}^{-}(\mathbf{r}) - \boldsymbol{\mathcal{E}}_{\omega}^{-}(\mathbf{r}) \times \boldsymbol{\mathcal{B}}_{\omega}(\mathbf{r})\right] \\
&= \left[\mathbf{J}_a(\boldsymbol{\beta}, \omega) \cdot \boldsymbol{\mathcal{E}}_{\omega}^{-}(\mathbf{r})e^{i\boldsymbol{\beta}\cdot\mathbf{r}} - \mathbf{J}_a(-\boldsymbol{\beta}, \omega) \cdot \boldsymbol{\mathcal{E}}_{\omega}(\mathbf{r})e^{-i\boldsymbol{\beta}\cdot\mathbf{r}}\right] \\
&\quad + \left[\boldsymbol{\mathcal{J}}_{\omega}^{p}(\mathbf{r}) \cdot \boldsymbol{\mathcal{E}}_{\omega}^{-}(\mathbf{r}) - \boldsymbol{\mathcal{J}}_{\omega}^{p-}(\mathbf{r}) \cdot \boldsymbol{\mathcal{E}}_{\omega}(\mathbf{r})\right] \\
&\quad + \left[\nabla \times \boldsymbol{\mathcal{M}}_{\omega}(\mathbf{r}) \cdot \boldsymbol{\mathcal{E}}_{\omega}^{-}(\mathbf{r}) - \nabla \times \boldsymbol{\mathcal{M}}_{\omega}^{-}(\mathbf{r}) \cdot \boldsymbol{\mathcal{E}}_{\omega}(\mathbf{r})\right]
\end{aligned} \tag{13.65}$$

or, after applying the divergence of a cross product identity to the terms containing $\boldsymbol{\mathcal{M}}_{\omega}$ and using (13.63a) and (13.64a), we have

$$\begin{aligned}
&\frac{1}{\mu_0}\nabla \cdot \left\{\left[\boldsymbol{\mathcal{E}}_{\omega}(\mathbf{r}) \times \boldsymbol{\mathcal{B}}_{\omega}^{-}(\mathbf{r}) - \boldsymbol{\mathcal{E}}_{\omega}^{-}(\mathbf{r}) \times \boldsymbol{\mathcal{B}}_{\omega}(\mathbf{r})\right]\right. \\
&\quad \left. - \left[\boldsymbol{\mathcal{E}}_{\omega}(\mathbf{r}) \times \boldsymbol{\mathcal{M}}_{\omega}^{-}(\mathbf{r}) - \boldsymbol{\mathcal{E}}_{\omega}^{-}(\mathbf{r}) \times \boldsymbol{\mathcal{M}}_{\omega}(\mathbf{r})\right]\right\} \\
&= \left[\mathbf{J}_a(\boldsymbol{\beta}, \omega) \cdot \boldsymbol{\mathcal{E}}_{\omega}^{-}(\mathbf{r})e^{i\boldsymbol{\beta}\cdot\mathbf{r}} - \mathbf{J}_a(-\boldsymbol{\beta}, \omega) \cdot \boldsymbol{\mathcal{E}}_{\omega}(\mathbf{r})e^{-i\boldsymbol{\beta}\cdot\mathbf{r}}\right] \\
&\quad + \left[\boldsymbol{\mathcal{J}}_{\omega}^{p}(\mathbf{r}) \cdot \boldsymbol{\mathcal{E}}_{\omega}^{-}(\mathbf{r}) - \boldsymbol{\mathcal{J}}_{\omega}^{p-}(\mathbf{r}) \cdot \boldsymbol{\mathcal{E}}_{\omega}(\mathbf{r})\right] \\
&\quad + i\omega\left[\boldsymbol{\mathcal{M}}_{\omega}(\mathbf{r}) \cdot \boldsymbol{\mathcal{B}}_{\omega}^{-}(\mathbf{r}) - \boldsymbol{\mathcal{M}}_{\omega}^{-}(\mathbf{r}) \cdot \boldsymbol{\mathcal{B}}_{\omega}(\mathbf{r})\right].
\end{aligned} \tag{13.66}$$

Each of the ω subscripted vectors can be expanded in Floquet modes as given in (13.8) for the electric field. Inserting these expansions into (13.66), integrating over a unit cell, and using the divergence theorem to show that the divergence term is zero, reduces (13.66) to

$$\begin{aligned}
0 = &\left[\mathbf{J}_a(\boldsymbol{\beta}, \omega) \cdot \mathbf{E}(-\boldsymbol{\beta}, \omega) - \mathbf{J}_a(-\boldsymbol{\beta}, \omega) \cdot \mathbf{E}(\boldsymbol{\beta}, \omega)\right] \\
&+ \frac{1}{d^3}\int_{V_c} \left\{\left[\boldsymbol{\mathcal{J}}_{\omega}^{p}(\mathbf{r}) \cdot \boldsymbol{\mathcal{E}}_{\omega}^{-}(\mathbf{r}) - \boldsymbol{\mathcal{J}}_{\omega}^{p-}(\mathbf{r}) \cdot \boldsymbol{\mathcal{E}}_{\omega}(\mathbf{r})\right]\right. \\
&\quad \left. + i\omega\left[\boldsymbol{\mathcal{M}}_{\omega}(\mathbf{r}) \cdot \boldsymbol{\mathcal{B}}_{\omega}^{-}(\mathbf{r}) - \boldsymbol{\mathcal{M}}_{\omega}^{-}(\mathbf{r}) \cdot \boldsymbol{\mathcal{B}}_{\omega}(\mathbf{r})\right]\right\} d^3r\,.
\end{aligned} \tag{13.67}$$

The next step in determining the reciprocity relations for the constitutive parameters is to prove that the integral in (13.67) is zero for arrays with lossy or lossless polarizable inclusions made of linear reciprocal material. Assuming a general linear bianisotropic relationship between $[\boldsymbol{\mathcal{J}}_{\omega}^{p}(\mathbf{r}), \boldsymbol{\mathcal{M}}_{\omega}(\mathbf{r})]$ and $[\boldsymbol{\mathcal{E}}_{\omega}(\mathbf{r}), \boldsymbol{\mathcal{B}}_{\omega}(\mathbf{r})]$ for the inclusions of the array, one can write

$$\mathcal{J}_\omega^p(\mathbf{r}) = \int_{V_c} [\overline{\boldsymbol{\sigma}}_\omega^e(\mathbf{r},\mathbf{r}') \cdot \mathcal{E}_\omega(\mathbf{r}') + \overline{\boldsymbol{\sigma}}_\omega^{em}(\mathbf{r},\mathbf{r}') \cdot \mathcal{B}_\omega(\mathbf{r}')] d^3r' \tag{13.68a}$$

$$\mathcal{M}_\omega(\mathbf{r}) = \int_{V_c} [\overline{\boldsymbol{\sigma}}_\omega^m(\mathbf{r},\mathbf{r}') \cdot \mathcal{B}_\omega(\mathbf{r}') + \overline{\boldsymbol{\sigma}}_\omega^{me}(\mathbf{r},\mathbf{r}') \cdot \mathcal{E}_\omega(\mathbf{r}')] d^3r' \tag{13.68b}$$

and similarly for the $-\boldsymbol{\beta}$ fields

$$\mathcal{J}_\omega^{p-}(\mathbf{r}) = \int_{V_c} [\overline{\boldsymbol{\sigma}}_\omega^e(\mathbf{r},\mathbf{r}') \cdot \mathcal{E}_\omega^-(\mathbf{r}') + \overline{\boldsymbol{\sigma}}_\omega^{em}(\mathbf{r},\mathbf{r}') \cdot \mathcal{B}_\omega^-(\mathbf{r}')] d^3r' \tag{13.69a}$$

$$\mathcal{M}_\omega^-(\mathbf{r}) = \int_{V_c} [\overline{\boldsymbol{\sigma}}_\omega^m(\mathbf{r},\mathbf{r}') \cdot \mathcal{B}_\omega^-(\mathbf{r}') + \overline{\boldsymbol{\sigma}}_\omega^{me}(\mathbf{r},\mathbf{r}') \cdot \mathcal{E}_\omega^-(\mathbf{r}')] d^3r' \tag{13.69b}$$

in which the integration need cover only the unit cell because of the periodicity of the fields, and the spatially dispersive microscopic "conductivity" dyadics, $\overline{\boldsymbol{\sigma}}_\omega^e(\mathbf{r},\mathbf{r}')$, $\overline{\boldsymbol{\sigma}}_\omega^m(\mathbf{r},\mathbf{r}')$, $\overline{\boldsymbol{\sigma}}_\omega^{em}(\mathbf{r},\mathbf{r}')$, and $\overline{\boldsymbol{\sigma}}_\omega^{me}(\mathbf{r},\mathbf{r}')$, are zero for $\mathbf{r}$ or $\mathbf{r}'$ outside the material of the inclusion. In the case of simply "conducting" inclusions, $\overline{\boldsymbol{\sigma}}_\omega^{\,e} = \sigma^e \overline{\mathbf{I}}$, $\overline{\boldsymbol{\sigma}}_\omega^m = \sigma^m \overline{\mathbf{I}}$, and $\overline{\boldsymbol{\sigma}}_\omega^{em} = \overline{\boldsymbol{\sigma}}_\omega^{me} = 0$, where σ^e and σ^m are scalar constants.

Insertion of the fields from (13.68–13.69) into the integral of (13.67) yields

$$\begin{aligned}
&\frac{1}{d^3}\int_{V_c} \Big\{ \big[\mathcal{J}_\omega^p(\mathbf{r}) \cdot \mathcal{E}_\omega^-(\mathbf{r}) - \mathcal{J}_\omega^{p-}(\mathbf{r}) \cdot \mathcal{E}_\omega(\mathbf{r})\big] \\
&\quad + i\omega \big[\mathcal{M}_\omega(\mathbf{r}) \cdot \mathcal{B}_\omega^-(\mathbf{r}) - \mathcal{M}_\omega^-(\mathbf{r}) \cdot \mathcal{B}_\omega(\mathbf{r})\big] \Big\} d^3r \\
&= \int_{V_c}\int_{V_c} \Big\{ \mathcal{E}_w^-(\mathbf{r}) \cdot \big[\overline{\boldsymbol{\sigma}}_\omega^{\,e}(\mathbf{r},\mathbf{r}') - \overline{\boldsymbol{\sigma}}_\omega^{\,eT}(\mathbf{r}',\mathbf{r})\big] \cdot \mathcal{E}_\omega(\mathbf{r}') \\
&\quad + \mathcal{B}_w^-(\mathbf{r}) \cdot \big[\overline{\boldsymbol{\sigma}}_\omega^m(\mathbf{r},\mathbf{r}') - \overline{\boldsymbol{\sigma}}_\omega^{mT}(\mathbf{r}',\mathbf{r})\big] \cdot \mathcal{B}_\omega(\mathbf{r}') \\
&\quad + \mathcal{E}_w^-(\mathbf{r}) \cdot \big[\overline{\boldsymbol{\sigma}}_\omega^{em}(\mathbf{r},\mathbf{r}') - \overline{\boldsymbol{\sigma}}_\omega^{meT}(\mathbf{r}',\mathbf{r})\big] \cdot \mathcal{B}_\omega(\mathbf{r}') \\
&\quad + \mathcal{B}_w^-(\mathbf{r}) \cdot \big[\overline{\boldsymbol{\sigma}}_\omega^{me}(\mathbf{r},\mathbf{r}') - \overline{\boldsymbol{\sigma}}_\omega^{emT}(\mathbf{r}',\mathbf{r})\big] \cdot \mathcal{E}_\omega(\mathbf{r}') \Big\} d^3r d^3r'
\end{aligned} \tag{13.70}$$

where the superscript "T" denotes the transpose of a dyadic. By definition, the array of linear bianisotropic inclusions is reciprocal if

$$\overline{\boldsymbol{\sigma}}_\omega^{\,e}(\mathbf{r},\mathbf{r}') = \overline{\boldsymbol{\sigma}}_\omega^{\,eT}(\mathbf{r}',\mathbf{r}) \tag{13.71a}$$

$$\overline{\boldsymbol{\sigma}}_\omega^m(\mathbf{r},\mathbf{r}') = \overline{\boldsymbol{\sigma}}_\omega^{mT}(\mathbf{r}',\mathbf{r}) \tag{13.71b}$$

$$\overline{\boldsymbol{\sigma}}_\omega^{em}(\mathbf{r},\mathbf{r}') = \overline{\boldsymbol{\sigma}}_\omega^{meT}(\mathbf{r}',\mathbf{r}) \tag{13.71c}$$

in which case the right-hand side of (13.70) is zero and we have from (13.67) that

$$\frac{1}{d^3}\int_{V_c}\Big\{\big[\mathcal{J}^{p}_{\omega}(\mathbf{r})\cdot\mathcal{E}^{-}_{\omega}(\mathbf{r})-\mathcal{J}^{p-}_{\omega}(\mathbf{r})\cdot\mathcal{E}_{\omega}(\mathbf{r})\big] + i\omega\big[\mathcal{M}_{\omega}(\mathbf{r})\cdot\mathcal{B}^{-}_{\omega}(\mathbf{r})-\mathcal{M}^{-}_{\omega}(\mathbf{r})\cdot\mathcal{B}_{\omega}(\mathbf{r})\big]\Big\}d^3r = -[\mathbf{J}_a(\boldsymbol{\beta},\omega)\cdot\mathbf{E}(-\boldsymbol{\beta},\omega)-\mathbf{J}_a(-\boldsymbol{\beta},\omega)\cdot\mathbf{E}(\boldsymbol{\beta},\omega)]=0. \tag{13.72}$$

Concentrating on the last equation in (13.72), namely

$$\mathbf{J}_a(\boldsymbol{\beta},\omega)\cdot\mathbf{E}(-\boldsymbol{\beta},\omega)-\mathbf{J}_a(-\boldsymbol{\beta},\omega)\cdot\mathbf{E}(\boldsymbol{\beta},\omega)=0 \tag{13.73}$$

insert $\mathbf{J}_a(\boldsymbol{\beta},\omega)$ and $\mathbf{J}_a(-\boldsymbol{\beta},\omega)$ from (13.49b) into (13.73) and substitute $\mathbf{B}(\boldsymbol{\beta},\omega)$ and $\mathbf{B}(-\boldsymbol{\beta},\omega)$ from (13.49a) to obtain

$$\mathbf{E}(-\boldsymbol{\beta},\omega)\cdot\left\{\left[\overline{\boldsymbol{\epsilon}}(\boldsymbol{\beta},\omega)+\frac{1}{\omega^2}\overline{\boldsymbol{\beta}}\cdot\overline{\boldsymbol{\mu}}^{-1}_{\mathrm{tt}}(\boldsymbol{\beta},\omega)\cdot\overline{\boldsymbol{\beta}}\right]-\left[\overline{\boldsymbol{\epsilon}}(-\boldsymbol{\beta},\omega)+\frac{1}{\omega^2}\overline{\boldsymbol{\beta}}\cdot\overline{\boldsymbol{\mu}}^{-1}_{\mathrm{tt}}(-\boldsymbol{\beta},\omega)\cdot\overline{\boldsymbol{\beta}}\right]^{T}\right\}\cdot\mathbf{E}(\boldsymbol{\beta},\omega)=0\,. \tag{13.74}$$

The antisymmetric dyadic $\overline{\boldsymbol{\beta}}$ is used to replace $\boldsymbol{\beta}\times$; that is, $\overline{\boldsymbol{\beta}}\cdot\mathbf{V}=-\mathbf{V}\cdot\overline{\boldsymbol{\beta}}=\boldsymbol{\beta}\times\mathbf{V}=-\mathbf{V}\times\boldsymbol{\beta}$ for any vector $\mathbf{V}$; specifically

$$\overline{\boldsymbol{\beta}}=\begin{Bmatrix}0&-\beta_z&\beta_y\\ \beta_z&0&-\beta_x\\ -\beta_y&\beta_x&0\end{Bmatrix}. \tag{13.75}$$

The bilinear form in (13.74) has to be zero for all values of $\mathbf{E}(\boldsymbol{\beta},\omega)$ and $\mathbf{E}(-\boldsymbol{\beta},\omega)$. Thus, we find the following reciprocity relation for the anisotropic constitutive dyadics of 3D arrays of linear, reciprocal bianisotropic lossy or lossless polarizable inclusions at all real values of $(\boldsymbol{\beta},\omega)$

$$\left[\overline{\boldsymbol{\epsilon}}(\boldsymbol{\beta},\omega)+\frac{1}{\omega^2}\overline{\boldsymbol{\beta}}\cdot\overline{\boldsymbol{\mu}}^{-1}_{\mathrm{tt}}(\boldsymbol{\beta},\omega)\cdot\overline{\boldsymbol{\beta}}\right]=\left[\overline{\boldsymbol{\epsilon}}(-\boldsymbol{\beta},\omega)+\frac{1}{\omega^2}\overline{\boldsymbol{\beta}}\cdot\overline{\boldsymbol{\mu}}^{-1}_{\mathrm{tt}}(-\boldsymbol{\beta},\omega)\cdot\overline{\boldsymbol{\beta}}\right]^{T}. \tag{13.76}$$

If we had applied the Landau–Lifshitz single polarization formulation [5, 16–19] discussed in the Introduction to the fundamental Floquet modes, $i\omega\mathbf{D}$ in (13.29b) would include $-i\boldsymbol{\beta}\times(\mathbf{M}^{e}+\mathbf{M})$ so that $\mathbf{H}=\mathbf{B}/\mu_0$ and $\mathbf{D}=\overline{\boldsymbol{\epsilon}}_L\cdot\mathbf{E}$, where

$$\overline{\boldsymbol{\epsilon}}_L(\boldsymbol{\beta},\omega)=\overline{\boldsymbol{\epsilon}}(\boldsymbol{\beta},\omega)+\frac{1}{\omega^2}\overline{\boldsymbol{\beta}}\cdot\left[\overline{\boldsymbol{\mu}}^{-1}_{\mathrm{tt}}(\boldsymbol{\beta},\omega)-\mu_0^{-1}\overline{\mathbf{I}}\right]\cdot\overline{\boldsymbol{\beta}}\,. \tag{13.77}$$

Then we see that (13.76) expresses the single-polarization reciprocity relation [5, 16–19]

$$\overline{\boldsymbol{\epsilon}}_L(\boldsymbol{\beta},\omega)=\overline{\boldsymbol{\epsilon}}^{T}_L(-\boldsymbol{\beta},\omega) \tag{13.78}$$

which, except for the $-\boldsymbol{\beta}$, has the form of the conventional permittivity reciprocity relation in spatially nondispersive continuous media [24, p. 403]. Note, however, that for the fundamental Floquet modal equations, the proof of the reciprocity relations in (13.76) and (13.78) has required returning to the basic definition of reciprocity in the microscopic Maxwellian equations describing the material of the inclusions of the array. Although the Landau–Lifshitz single constitutive dyadic $\overline{\boldsymbol{\epsilon}}_L(\boldsymbol{\beta},\omega)$ for a continuum can be formally expressed as in (13.77) in terms of effective multipole-moment permittivity and permeability dyadics for the continuum [42], the continuum formulation does not provide microscopic expressions as in (13.23) needed to determine $\overline{\boldsymbol{\epsilon}}(\boldsymbol{\beta},\omega)$ and $\overline{\boldsymbol{\mu}}_{\rm tt}(\boldsymbol{\beta},\omega)$.

Letting $\boldsymbol{\beta}\to 0$ in (13.76) reveals that

$$\overline{\boldsymbol{\epsilon}}(0,\omega)=\overline{\boldsymbol{\epsilon}}^{T}(0,\omega) \tag{13.79a}$$

or more generally

$$\overline{\boldsymbol{\epsilon}}(\boldsymbol{\beta},\omega)\approx\overline{\boldsymbol{\epsilon}}^{T}(-\boldsymbol{\beta},\omega),\quad |\boldsymbol{\beta}d|\ll 1\,. \tag{13.79b}$$

It does not necessarily follow from (13.76) that the permeability $\overline{\boldsymbol{\mu}}_{\rm tt}(\boldsymbol{\beta}\to 0,\omega)$ satisfies the same reciprocity relation as $\overline{\boldsymbol{\epsilon}}(0,\omega)$ in (13.79). However, for both $|\boldsymbol{\beta}d|\ll 1$ and $|k_0 d|\ll 1$, the permittivity and inverse permeability dyadics are finite continuous functions of $\boldsymbol{\beta}$ and ω for nonbianisotropic inclusions, and the inverse permeability varies as $\omega/|\boldsymbol{\beta}|$ for bianisotropic inclusions (see Footnote 6). Thus by varying the ratio of $\boldsymbol{\beta}/\omega$ in (13.74), the $\overline{\boldsymbol{\epsilon}}$ and $\overline{\boldsymbol{\mu}}_{\rm tt}^{-1}$ terms have to obey (13.74) separately to give from the $\overline{\boldsymbol{\mu}}_{\rm tt}^{-1}$ term

$$\overline{\boldsymbol{\mu}}_{\rm tt}^{-1}(\boldsymbol{\beta},\omega)\approx\overline{\boldsymbol{\mu}}_{\rm tt}^{-1T}(-\boldsymbol{\beta},\omega),\quad (|\boldsymbol{\beta}d|\ll 1, |k_0 d|\ll 1) \tag{13.80a}$$

or

$$\overline{\boldsymbol{\mu}}_{\rm tt}(\boldsymbol{\beta},\omega)\approx\overline{\boldsymbol{\mu}}_{\rm tt}^{T}(-\boldsymbol{\beta},\omega),\quad (|\boldsymbol{\beta}d|\ll 1, |k_0 d|\ll 1) \tag{13.80b}$$

for reciprocal arrays and $\boldsymbol{\beta}/\omega\neq 0$ in (13.80a) if the inclusions are bianisotropic at the low spatial and temporal frequencies. Unlike the complete dyadics, $\overline{\boldsymbol{\epsilon}}(0,\omega)$ and $\overline{\boldsymbol{\mu}}_b(0,\omega)$, the elements of the transverse dyadic $\overline{\boldsymbol{\mu}}_{\rm tt}(\boldsymbol{\beta}\to 0,\omega)$ can depend on the direction of $\boldsymbol{\beta}$ as $\boldsymbol{\beta}\to 0$. The complete permeability dyadic $\overline{\boldsymbol{\mu}}_b(0,\omega)$ is given in terms of the transverse dyadic $\overline{\boldsymbol{\mu}}_{\rm tt}(\boldsymbol{\beta}\to 0,\omega)$ in (13.58) except possibly for bianisotropic inclusions, which yield a singular $\overline{\boldsymbol{\mu}}_{\rm tt}^{-1}(\boldsymbol{\beta},\omega)$ as $\boldsymbol{\beta}/\omega\to 0$; see Footnote 6. Thus, as explained in the Introduction, a bianisotropic formulation [21, 23] of metamaterials comprised of bianisotropic inclusions may be more suitable than an anisotropic formulation especially for small values of $\boldsymbol{\beta}$ and ω.

13.4.3 Passivity Conditions

Passivity conditions obeyed by the permittivity and permeability constitutive dyadics of the fundamental Floquet modes of passive (no internal sources of power within the material of the inclusions) 3D arrays can be found from the expression for the time-average power supplied by the microscopic electric field $\boldsymbol{\mathcal{E}}_\omega(\mathbf{r})$ to the applied electric current density of (13.7) in each unit cell. This time-average power has to be equal to or less than zero or else average power could be extracted from the passive array; specifically

$$\frac{1}{2}\mathrm{Re}\int_{V_c}\mathbf{J}_a(\boldsymbol{\beta},\omega)\cdot\boldsymbol{\mathcal{E}}^*_\omega(\mathbf{r})e^{i\boldsymbol{\beta}\cdot\mathbf{r}}d^3r\le 0 \tag{13.81}$$

where, as usual, the superscript "*" denotes the complex conjugate. The inequality in (13.81) holds for lossy inclusion material, while the equality holds for lossless inclusion material. Insertion of $\boldsymbol{\mathcal{E}}^*_\omega(\mathbf{r})$ from (13.8) re-expresses (13.81) in terms of the fundamental Floquet modal spectra as

$$\mathrm{Re}[\mathbf{J}_a(\boldsymbol{\beta},\omega)\cdot\mathbf{E}^*(\boldsymbol{\beta},\omega)]\le 0 \tag{13.82}$$

in which the superfluous factor $d^3/2$ has been omitted. (This equation shows that all the power supplied by the applied electric current density can be expressed in terms of the fundamental Floquet modal spectra $\mathbf{J}_a$ and $\mathbf{E}$. Higher order Floquet modal spectra are not required.)

With $\mathbf{J}_a$ substituted from (13.49b) into (13.82), then $\mathbf{B}$ substituted from (13.49a), we find

$$\omega\mathrm{Im}\left\{\mathbf{E}^*(\boldsymbol{\beta},\omega)\cdot\left[\overline{\boldsymbol{\epsilon}}(\boldsymbol{\beta},\omega)+\frac{1}{\omega^2}\overline{\boldsymbol{\beta}}\cdot\overline{\boldsymbol{\mu}}_{\mathrm{tt}}^{-1}(\boldsymbol{\beta},\omega)\cdot\overline{\boldsymbol{\beta}}\right]\cdot\mathbf{E}(\boldsymbol{\beta},\omega)\right\}\ge 0 \tag{13.83a}$$

or

$$\begin{aligned}-i\omega\Bigg\{\mathbf{E}^*(\boldsymbol{\beta},\omega)\cdot\Bigg[&\left(\overline{\boldsymbol{\epsilon}}(\boldsymbol{\beta},\omega)+\frac{1}{\omega^2}\overline{\boldsymbol{\beta}}\cdot\overline{\boldsymbol{\mu}}_{\mathrm{tt}}^{-1}(\boldsymbol{\beta},\omega)\cdot\overline{\boldsymbol{\beta}}\right)\\&-\left(\overline{\boldsymbol{\epsilon}}(\boldsymbol{\beta},\omega)+\frac{1}{\omega^2}\overline{\boldsymbol{\beta}}\cdot\overline{\boldsymbol{\mu}}_{\mathrm{tt}}^{-1}(\boldsymbol{\beta},\omega)\cdot\overline{\boldsymbol{\beta}}\right)^{*T}\Bigg]\cdot\mathbf{E}(\boldsymbol{\beta},\omega)\Bigg\}\ge 0\,.\end{aligned} \tag{13.83b}$$

Since (13.83) has to hold for all values of $\mathbf{E}$, the array is passive and lossy, or passive and lossless, if and only if its associated Hermitian loss matrix is positive definite (PD) or zero [43], respectively; that is

$$-i\omega\left[\left(\overline{\boldsymbol{\epsilon}}(\boldsymbol{\beta},\omega)+\frac{1}{\omega^2}\overline{\boldsymbol{\beta}}\cdot\overline{\boldsymbol{\mu}}_{\mathrm{tt}}^{-1}(\boldsymbol{\beta},\omega)\cdot\overline{\boldsymbol{\beta}}\right)-\left(\overline{\boldsymbol{\epsilon}}(\boldsymbol{\beta},\omega)+\frac{1}{\omega^2}\overline{\boldsymbol{\beta}}\cdot\overline{\boldsymbol{\mu}}_{\mathrm{tt}}^{-1}(\boldsymbol{\beta},\omega)\cdot\overline{\boldsymbol{\beta}}\right)^{*T}\right]=\mathrm{PD} \tag{13.84a}$$

for lossy material, and[15]

$$\left[\overline{\boldsymbol{\epsilon}}(\boldsymbol{\beta},\omega)+\frac{1}{\omega^2}\overline{\boldsymbol{\beta}}\cdot\overline{\boldsymbol{\mu}}_{\mathrm{tt}}^{-1}(\boldsymbol{\beta},\omega)\cdot\overline{\boldsymbol{\beta}}\right]=\left[\overline{\boldsymbol{\epsilon}}(\boldsymbol{\beta},\omega)+\frac{1}{\omega^2}\overline{\boldsymbol{\beta}}\cdot\overline{\boldsymbol{\mu}}_{\mathrm{tt}}^{-1}(\boldsymbol{\beta},\omega)\cdot\overline{\boldsymbol{\beta}}\right]^{*T},\quad \omega\neq\omega_{\mathrm{uc}} \tag{13.84b}$$

for lossless material. For scalar permittivity and permeability transverse to $\boldsymbol{\beta}$ (that is, $\overline{\boldsymbol{\epsilon}}=\epsilon\overline{\mathbf{I}}_{\mathrm{tt}}$ and $\overline{\boldsymbol{\mu}}_{\mathrm{tt}}=\mu\overline{\mathbf{I}}_{\mathrm{tt}}$), (13.84) reduce to

$$\omega\mathrm{Im}\left[\epsilon(\boldsymbol{\beta},\omega)-\frac{|\boldsymbol{\beta}|^2}{\omega^2\mu(\boldsymbol{\beta},\omega)}\right]=\omega\mathrm{Im}\left[\epsilon(\boldsymbol{\beta},\omega)+\frac{|\boldsymbol{\beta}|^2\mu(\boldsymbol{\beta},\omega)}{\omega^2|\mu(\boldsymbol{\beta},\omega)|^2}\right]>0 \tag{13.85a}$$

$$\mathrm{Im}\left[\epsilon(\boldsymbol{\beta},\omega)-\frac{|\boldsymbol{\beta}|^2}{\omega^2\mu(\boldsymbol{\beta},\omega)}\right]=\mathrm{Im}\left[\epsilon(\boldsymbol{\beta},\omega)+\frac{|\boldsymbol{\beta}|^2\mu(\boldsymbol{\beta},\omega)}{\omega^2|\mu(\boldsymbol{\beta},\omega)|^2}\right]=0,\quad \omega\neq\omega_{\mathrm{uc}} \tag{13.85b}$$

in lossy and lossless inclusion material, respectively. These conditions do not necessarily imply that the imaginary parts of ϵ and μ are equal to or greater than zero, or even that the imaginary parts of ϵ and μ are zero in lossless arrays. In general, (13.85b) shows only that the imaginary parts of ϵ and μ have opposite signs in lossless arrays such that the total power dissipated by the array is zero.

From (13.77) it is seen that in terms of the Landau–Lifshitz single polarization formulation [5, 16–19], the lossy and lossless conditions in (13.84) reduce, respectively, to

$$-i\omega\left[\overline{\boldsymbol{\epsilon}}_L(\boldsymbol{\beta},\omega)-\overline{\boldsymbol{\epsilon}}_L^{*T}(\boldsymbol{\beta},\omega)\right]=\mathrm{PD}\quad(\text{lossy}) \tag{13.86a}$$

and

$$\overline{\boldsymbol{\epsilon}}_L(\boldsymbol{\beta},\omega)=\overline{\boldsymbol{\epsilon}}_L^{*T}(\boldsymbol{\beta},\omega),\quad \omega\neq\omega_{\mathrm{uc}}\quad(\text{lossless})\,. \tag{13.86b}$$

[15] At unit-cell resonant frequencies ($\omega=\omega_{\mathrm{uc}}(\boldsymbol{\beta})$) of lossless arrays, the $\mathbf{E}(\boldsymbol{\beta},\omega_{\mathrm{uc}})$ and $\mathbf{B}(\boldsymbol{\beta},\omega_{\mathrm{uc}})$ can be zero and the permittivity and inverse permeability can have poles. Thus, (13.84b) does not necessarily hold at these unit-cell resonant frequencies. These unit-cell singularities disappear for real values of $\boldsymbol{\beta}$ and ω if a small loss is inserted into the material of the array inclusions.

As with the reciprocity relations for the fundamental Floquet modal equations, the proof of these lossy-lossless conditions has required returning to the basic definition of loss and losslessness in the microscopic Maxwellian equations describing the material of the inclusions of the array. Also, as mentioned in Sect. 13.4.2, although the Landau–Lifshitz single constitutive dyadic $\overline{\boldsymbol{\epsilon}}_L(\boldsymbol{\beta},\omega)$ for a continuum can be formally expressed as in (13.77) in terms of effective multipole-moment permittivity and permeability dyadics for the continuum [42], the continuum formulation does not provide microscopic expressions as in (13.23) needed to determine $\overline{\boldsymbol{\epsilon}}(\boldsymbol{\beta},\omega)$ and $\overline{\boldsymbol{\mu}}_{\rm tt}(\boldsymbol{\beta},\omega)$.

Letting $\boldsymbol{\beta}\to 0$ in (13.84) reveals that

$$-i\omega\left[\overline{\boldsymbol{\epsilon}}(0,\omega)-\overline{\boldsymbol{\epsilon}}^{*T}(0,\omega)\right]=\text{PD}\quad\text{(lossy)} \tag{13.87a}$$

$$\overline{\boldsymbol{\epsilon}}(0,\omega)=\overline{\boldsymbol{\epsilon}}^{*T}(0,\omega),\quad \omega\neq\omega_{\rm uc}\quad\text{(lossless)} \tag{13.87b}$$

for lossy and lossless arrays, respectively. These equations imply

$$\omega\text{Im}[\epsilon_{jj}(0,\omega)]>0\quad\text{(lossy)} \tag{13.87c}$$

$$\epsilon_{jk}(0,\omega)=\epsilon^*_{kj}(0,\omega),\quad \omega\neq\omega_{\rm uc}\quad\text{(lossless)} \tag{13.87d}$$

for lossy and lossless arrays, respectively. The lossy-lossless passivity conditions in (13.87) have the same form as the lossy-lossless passivity conditions on permittivity in a spatially nondispersive dipolar continuum. They also hold approximately for $|\boldsymbol{\beta}d|\ll 1$.

It does not necessarily follow from (13.84) that $\overline{\boldsymbol{\mu}}_{\rm tt}(\boldsymbol{\beta}\to 0,\omega)$ satisfies the same passivity conditions as $\overline{\boldsymbol{\epsilon}}(0,\omega)$ in (13.87). However, for both $|\boldsymbol{\beta}d|\ll 1$ and $|k_0d|\ll 1$, the permittivity and inverse permeability dyadics are finite continuous functions of $\boldsymbol{\beta}$ and ω for nonbianisotropic inclusions, and the inverse permeability varies as $\boldsymbol{\beta}/\omega$ for bianisotropic inclusions (see Footnote 6). Thus, by varying the ratio of $\boldsymbol{\beta}/\omega$ in (13.83b), the $\overline{\boldsymbol{\epsilon}}$ and $\overline{\boldsymbol{\mu}}_{\rm tt}^{-1}$ terms have to obey (13.83b) independently to give for the $\overline{\boldsymbol{\mu}}_{\rm tt}^{-1}$ term (noting that $\mathbf{E}\cdot\boldsymbol{\beta}=-\boldsymbol{\beta}\cdot\mathbf{E}$)

$$i\omega[\mathbf{E}(\boldsymbol{\beta},\omega)\cdot\overline{\boldsymbol{\beta}}]^*\cdot\left[\overline{\boldsymbol{\mu}}_{\rm tt}^{-1}(\boldsymbol{\beta},\omega)-\overline{\boldsymbol{\mu}}_{\rm tt}^{-1*T}(\boldsymbol{\beta},\omega)\right]\cdot[\mathbf{E}(\boldsymbol{\beta},\omega)\cdot\boldsymbol{\beta}]\geq 0 \tag{13.88}$$

which implies

$$i\omega\left[\overline{\boldsymbol{\mu}}_{\rm tt}^{-1}(\boldsymbol{\beta},\omega)-\overline{\boldsymbol{\mu}}_{\rm tt}^{-1*T}(\boldsymbol{\beta},\omega)\right]=\text{PD},\quad(|\boldsymbol{\beta}d|\ll 1,|k_0d|\ll 1)\quad\text{(lossy)} \tag{13.89a}$$

$$\overline{\boldsymbol{\mu}}_{\rm tt}(\boldsymbol{\beta},\omega)\approx\overline{\boldsymbol{\mu}}^{*T}_{\rm tt}(\boldsymbol{\beta},\omega),\quad(|\boldsymbol{\beta}d|\ll 1,|k_0d|)\ll 1\quad\text{(lossless)} \tag{13.89b}$$

$$\omega\text{Im}[\mu_{{\rm tt}jj}(\boldsymbol{\beta},\omega)]>0,\quad(|\boldsymbol{\beta}d|\ll 1,|k_0d|\ll 1)\quad\text{(lossy)} \tag{13.89c}$$

$$\mu_{{\rm tt}jk}(\boldsymbol{\beta},\omega)=\mu^*_{{\rm tt}kj}(\boldsymbol{\beta},\omega),\quad(|\boldsymbol{\beta}d|\ll 1,|k_0d|\ll 1)\quad\text{(lossless)} \tag{13.89d}$$

for passive inclusions and $\boldsymbol{\beta}/\omega\neq 0$ in (13.89a) if the inclusions are bianisotropic at the low spatial and temporal frequencies. Unlike $\overline{\boldsymbol{\epsilon}}(0,\omega)$, the permeability

dyadic $\overline{\boldsymbol{\mu}}_{tt}(\boldsymbol{\beta} \to 0, \omega)$ does not necessarily satisfy these passivity conditions for lossy or lossless arrays if $|k_0 d| \ll 1$. Also, unlike the complete dyadics, $\overline{\boldsymbol{\epsilon}}(0, \omega)$ and $\overline{\boldsymbol{\mu}}_b(0, \omega)$, the elements of the transverse dyadic $\overline{\boldsymbol{\mu}}_{tt}(\boldsymbol{\beta} \to 0, \omega)$ can depend on the direction of $\boldsymbol{\beta}$ as $\boldsymbol{\beta} \to 0$. The complete permeability dyadic $\overline{\boldsymbol{\mu}}_b(0, \omega)$ is given in terms of the transverse dyadic $\overline{\boldsymbol{\mu}}_{tt}(\boldsymbol{\beta} \to 0, \omega)$ in (13.58) except possibly for bianisotropic inclusions, which yield a singular $\overline{\boldsymbol{\mu}}_{tt}^{-1}(\boldsymbol{\beta}, \omega)$ as $\boldsymbol{\beta}/\omega \to 0$; see Footnote 6. Thus, as explained in the Introduction, a bianisotropic formulation [21, 23] of metamaterials comprised of bianisotropic inclusions may be more suitable than an anisotropic formulation especially for small values of $\boldsymbol{\beta}$ and ω.

13.4.4 Causality Relations

To discuss the causality of the macroscopic permittivity and inverse-permeability dyadics, $\overline{\boldsymbol{\epsilon}}(\boldsymbol{\beta}, \omega)$ and $\overline{\boldsymbol{\mu}}_{tt}^{-1}(\boldsymbol{\beta}, \omega)$, begin by taking the four-fold $(\boldsymbol{\beta}, \omega)$ Fourier transform of the fundamental Floquet-mode constitutive relation in (13.45) and use the convolution theorem to obtain

$$\mathcal{D}_0(\mathbf{r}, t) = \frac{1}{(2\pi)^4} \int_{-\infty}^{+\infty} \int_{-\infty}^{+\infty} \int_{-\infty}^{+\infty} \int_{-\infty}^{+\infty} \overline{\boldsymbol{\xi}}_0(\mathbf{r}', t') \cdot \mathcal{E}_0(\mathbf{r} - \mathbf{r}', t - t') d^3 r' \mathrm{d}t' \quad (13.90)$$

in which the time-domain functions are the inverse Fourier transforms of the corresponding frequency-domain functions; in particular

$$\overline{\boldsymbol{\xi}}_0(\mathbf{r}, t) = \int_{-\infty}^{+\infty} \int_{-\infty}^{+\infty} \int_{-\infty}^{+\infty} \int_{-\infty}^{+\infty} \overline{\boldsymbol{\epsilon}}_e(\boldsymbol{\beta}, \omega) e^{i(\boldsymbol{\beta} \cdot \mathbf{r} - \omega t)} d^3 \beta \, \mathrm{d}\omega \,. \quad (13.91)$$

The functions of $(\mathbf{r}, t)$ in (13.90–13.91) are real because of the reality conditions in (13.61–13.62) satisfied by the spectra.

The function $\mathcal{E}_0(\mathbf{r}, t)$ is the total time-domain electric field of the fundamental Floquet mode, which is excited by time-domain externally applied electric current density $\mathcal{J}^a(\mathbf{r}, t)$ that we shall stipulate turns on at $t = 0$. Assuming that the material of the inclusions is causal or, more precisely, that the linear constitutive parameters of the inclusion material are causal, the induced fields in the inclusions cannot begin before the applied current and thus the total electric field (induced plus applied) begins at $t = 0$.[16] Since the generalized time-domain displacement

[16] One could conjecture that the induced fundamental Floquet-mode electric field could cancel the applied electric field (for all applied current excitations) such that $\mathcal{E}_0(\mathbf{r}, t) = 0$ for $t < t_0$ where $t_0 > 0$. Then $\mathcal{D}_0(\mathbf{r}, t)$ would begin before $\mathcal{E}_0(\mathbf{r}, t)$ and $\overline{\boldsymbol{\epsilon}}_e(\boldsymbol{\beta}, \omega)$ would not be causal. To see that such a cancellation is not possible, consider an applied field with the time dependence of a delta function at $t = 0$ (uniform frequency spectrum). If there is any loss in the inclusions, the frequency spectrum of the induced fields will decay as $|\omega| \to \infty$ and thus the induced

vector $\mathcal{D}_0(\mathbf{r},t)$ is a linear combination of the total electric field of the fundamental Floquet mode and the induced generalized electric polarization as given in (13.28a), and this induced polarization cannot begin before the applied electric field begins at $t=0$, it follows that $\mathcal{D}_0(\mathbf{r},t)$ must be zero for $t<0$. This implies from (13.90) that $\overline{\boldsymbol{\varepsilon}}_0(\mathbf{r},t)=0$ for $t<0$, so that we have from (13.91)

$$\overline{\boldsymbol{\varepsilon}}_0(\mathbf{r},t)=\int_{-\infty}^{+\infty}\int_{-\infty}^{+\infty}\int_{-\infty}^{+\infty}\int_{-\infty}^{+\infty}\overline{\boldsymbol{\epsilon}}_e(\boldsymbol{\beta},\omega)e^{i(\boldsymbol{\beta}\cdot\mathbf{r}-\omega t)}d^3\beta\,\mathrm{d}\omega=0,\quad t<0\,. \tag{13.92}$$

Taking the three $\boldsymbol{\beta}$ Fourier transforms of (13.92) yields the following fundamental causality relation on $\overline{\boldsymbol{\epsilon}}_e(\boldsymbol{\beta},\omega)$ for each real value of $\boldsymbol{\beta}$

$$\int_{-\infty}^{+\infty}\overline{\boldsymbol{\epsilon}}_e(\boldsymbol{\beta},\omega)e^{-i\omega t}\,\mathrm{d}\omega=\int_{0}^{+\infty}\left[\overline{\boldsymbol{\epsilon}}_e(\boldsymbol{\beta},\omega)e^{-i\omega t}+\overline{\boldsymbol{\epsilon}}_e^{*}(-\boldsymbol{\beta},\omega)e^{i\omega t}\right]\mathrm{d}\omega=0,\quad t<0 \tag{13.93a}$$

where the first equality follows from the reality condition in (13.62a).

A similar argument beginning with (13.48) instead of (13.45), and noting that $\mathbf{B}$ and $\mathbf{E}_\mathrm{I}$ in (13.48) are primary fields that can be chosen independently (see Footnote 16), yields the analogous causality relation for the inverse permeability $\overline{\boldsymbol{\mu}}_{\mathrm{tt}}^{-1}(\boldsymbol{\beta},\omega)$

$$\int_{-\infty}^{+\infty}\overline{\boldsymbol{\mu}}_{\mathrm{tt}}^{-1}(\boldsymbol{\beta},\omega)e^{-i\omega t}\,\mathrm{d}\omega=\int_{0}^{+\infty}\left[\overline{\boldsymbol{\mu}}_{\mathrm{tt}}^{-1}(\boldsymbol{\beta},\omega)e^{-i\omega t}+\overline{\boldsymbol{\mu}}_{\mathrm{tt}}^{-1*}(-\boldsymbol{\beta},\omega)e^{i\omega t}\right]\mathrm{d}\omega=0,\quad t<0 \tag{13.93b}$$

and the analogous causality relation for the magnetoelectric constitutive parameter $\overline{\boldsymbol{\nu}}_{\mathrm{tl}}(\boldsymbol{\beta},\omega)$ in (13.48). Having obtained the causality of $\overline{\boldsymbol{\epsilon}}_e(\boldsymbol{\beta},\omega)$ and $\overline{\boldsymbol{\nu}}_{\mathrm{tl}}(\boldsymbol{\beta},\omega)$, it follows from (13.50) that $\overline{\boldsymbol{\epsilon}}(\boldsymbol{\beta},\omega)$ is also a causal function satisfying

$$\int_{-\infty}^{+\infty}\overline{\boldsymbol{\epsilon}}(\boldsymbol{\beta},\omega)e^{-i\omega t}\,\mathrm{d}\omega=\int_{0}^{+\infty}\left[\overline{\boldsymbol{\epsilon}}(\boldsymbol{\beta},\omega)e^{-i\omega t}+\overline{\boldsymbol{\epsilon}}^{*}(-\boldsymbol{\beta},\omega)e^{i\omega t}\right]\mathrm{d}\omega=0,\quad t<0\,. \tag{13.93c}$$

(Footnote 16 continued)
time-domain fields will be finite for all time including $t=0$ and unable to cancel the delta function in the applied fields. Even if the inclusions are lossless and a delta function in the induced fields exactly canceled the applied-field delta function (an extraordinarily unlikely occurrence), the reactance of the inclusions would not allow the induced fields to be zero in the finite interval $0<t<t_0$. A similar argument shows that the total time-domain fundamental Floquet-mode magnetic field $\mathcal{B}_0(\mathbf{r},t)$ turns on with the applied magnetic field.

An especially attractive feature of the Floquet modal representation developed here is that the above argument for causality holds because none of the integrally defined generalized electric and magnetic polarization densities for the fundamental Floquet mode are approximations. This stands in contrast, for example, to conventional formulations using electric and magnetic dipole approximations, which have been shown to be inherently noncausal, and thus do not satisfy either the basic causality relations in (13.93) or the Kramers–Kronig relations in (13.94) below; see [28].

Also, the causality relations for $\overline{\boldsymbol{\epsilon}}(\boldsymbol{\beta},\omega)$ and $\overline{\boldsymbol{\mu}}_{\rm tt}^{-1}(\boldsymbol{\beta},\omega)$ in (13.93) always hold as long as the integrals in (13.93) exist (converge) since $\overline{\boldsymbol{\epsilon}}(\boldsymbol{\beta},\omega)$ and $\overline{\boldsymbol{\mu}}_{\rm tt}^{-1}(\boldsymbol{\beta},\omega)$ are well defined at each fixed $\boldsymbol{\beta}$ for all ω; see Footnote 15. (If $\overline{\boldsymbol{\epsilon}}(\boldsymbol{\beta},\omega)$ and $\overline{\boldsymbol{\mu}}_{\rm tt}^{-1}(\boldsymbol{\beta},\omega)$ approach constants $\overline{\boldsymbol{\epsilon}}_{\infty}(\boldsymbol{\beta})$ and $\overline{\boldsymbol{\mu}}_{\rm tt\infty}^{-1}(\boldsymbol{\beta})$ as $\omega\to\infty$, then these constants can be subtracted from $\overline{\boldsymbol{\epsilon}}(\boldsymbol{\beta},\omega)$ and $\overline{\boldsymbol{\mu}}_{\rm tt}^{-1}(\boldsymbol{\beta},\omega)$ in (13.93c) and (13.93b), respectively, as in (13.94) below, to ensure that the causality integrals converge).

This universal causality does not necessarily hold for the constitutive parameters of the source-free (no applied current density) fundamental eigenmodes of arrays for which $\boldsymbol{\beta}$ is a function of ω because, even for a single eigenmode, $\boldsymbol{\beta}(\omega)$ may not be a single-valued function of ω for all ω and there may be frequency bands where the eigenmode ceases to exist. In addition, $\boldsymbol{\beta}(\omega)$ for an eigenmode is not generally a real function of ω for all ω even if the inclusions of the array are lossless [27], and it becomes problematic to define field and polarization integrals that produce constitutive parameters consistent with the complex $\boldsymbol{\beta}(\omega)$. Also, for source-free eigenmodes, it often proves advantageous to define anisotropic permittivity and permeability in terms of their relationships to the propagation constants and field impedances of each eigenmode [8, 27, 44] rather than in terms of the field and polarization integrals (weighted averages) as in (13.15) and (13.23), and thus one array would have multiply defined constitutive parameters, none of which would necessarily be causal.

As a consequence of the causality relations in (13.93), the permittivity and inverse permeability dyadics satisfy the Kramers–Kronig causality equations for each fixed $\boldsymbol{\beta}$. The familiar Kramers–Kronig relations can be found by taking the real and imaginary parts of their compact complex version given as [1, p. 98]

$$\overline{\boldsymbol{\epsilon}}(\boldsymbol{\beta},\omega)-\overline{\boldsymbol{\epsilon}}_{\infty}(\boldsymbol{\beta})=\frac{i}{\pi}\,\text{⨍}\!\!\!\!\!\!-\!\!\int_{-\infty}^{+\infty}\frac{\overline{\boldsymbol{\epsilon}}(\boldsymbol{\beta},\nu)-\overline{\boldsymbol{\epsilon}}_{\infty}(\boldsymbol{\beta})}{\omega-\nu}\,\mathrm{d}\nu \tag{13.94a}$$

$$\overline{\boldsymbol{\mu}}_{\rm tt}^{-1}(\boldsymbol{\beta},\omega)-\overline{\boldsymbol{\mu}}_{\rm tt\infty}^{-1}(\boldsymbol{\beta})=\frac{i}{\pi}\,\text{⨍}\!\!\!\!\!\!-\!\!\int_{-\infty}^{+\infty}\frac{\overline{\boldsymbol{\mu}}_{\rm tt}^{-1}(\boldsymbol{\beta},\nu)-\overline{\boldsymbol{\mu}}_{\rm tt\infty}^{-1}(\boldsymbol{\beta})}{\omega-\nu}\,\mathrm{d}\nu \tag{13.94b}$$

where the lines through the integrals denote principal value integrations. These Kramers–Kronig causality relations assume that for a fixed value of $\boldsymbol{\beta}$

$$\lim_{|\omega|\to\infty} \overline{\boldsymbol{\epsilon}}(\boldsymbol{\beta},\omega) = \overline{\boldsymbol{\epsilon}}_\infty(\boldsymbol{\beta}) \tag{13.95a}$$

$$\lim_{|\omega|\to\infty} \overline{\boldsymbol{\mu}}_{\rm tt}^{-1}(\boldsymbol{\beta},\omega) = \overline{\boldsymbol{\mu}}_{\rm tt\infty}^{-1}(\boldsymbol{\beta}) \tag{13.95b}$$

and that $\overline{\boldsymbol{\epsilon}}(\boldsymbol{\beta},\omega) - \overline{\boldsymbol{\epsilon}}_\infty(\boldsymbol{\beta})$ and $\overline{\boldsymbol{\mu}}_{\rm tt}^{-1}(\boldsymbol{\beta},\omega) - \overline{\boldsymbol{\mu}}_{\rm tt\infty}^{-1}(\boldsymbol{\beta})$ approach zero fast enough as $|\omega| \to \infty$ for the integrals in (13.94) to exist. A sufficient condition for the principal value integrals to be well defined for all real ω is that $\overline{\boldsymbol{\epsilon}}(\boldsymbol{\beta},\omega) - \overline{\boldsymbol{\epsilon}}_\infty(\boldsymbol{\beta})$ and $\overline{\boldsymbol{\mu}}_{\rm tt}^{-1}(\boldsymbol{\beta},\omega) - \overline{\boldsymbol{\mu}}_{\rm tt\infty}^{-1}(\boldsymbol{\beta})$ be Hölder continuous [2, Chap. 1]; see Footnote 1.

In Sect. 13.4.3 it was found that passivity of the inclusion material did not necessarily imply that the imaginary parts of the diagonal elements of the macroscopic permittivity and permeability dyadics are greater than zero at every $(\boldsymbol{\beta},\omega)$. Moreover, lossless inclusions do not necessarily imply that the imaginary parts of the diagonal elements of the macroscopic permittivity and permeability dyadics are zero at every $(\boldsymbol{\beta},\omega)$. However, it was proven, as expressed in (13.87d), that as $\boldsymbol{\beta} \to 0$ the imaginary parts of the permittivity diagonal elements, $\mathrm{Im}[\epsilon_{jj}(0,\omega)]$, were equal to zero for lossless inclusions except at the unit-cell resonant frequencies where insertion of a small loss shows from (13.87c) that $\omega\mathrm{Im}[\epsilon_{jj}(0,\omega)]$ is greater than zero. Consequently, the Kramers–Kronig relation in (13.94a) can be used to prove for lossless arrays [5, Sect. 84] and $\boldsymbol{\beta} \to 0$ that except at the unit-cell resonant frequencies, the diagonal elements of the permittivity dyadic satisfy the inequalities

$$\frac{\partial}{\partial\omega}[\omega\epsilon_{jj}(0,\omega)] - \epsilon_{jj\,\infty}(0) \geq \frac{1}{2}\omega\frac{\partial}{\partial\omega}\epsilon_{jj}(0,\omega) \geq 0, \quad \omega \neq \omega_{\rm uc}\,. \tag{13.96}$$

These same inequalities for $\mu_{{\rm tt}jj}(\boldsymbol{\beta} \to 0,\omega)$ do not necessarily hold because, as explained in the context of Eq. (13.89), the $\omega\mathrm{Im}[\mu_{{\rm tt}jj}(\boldsymbol{\beta} \to 0,\omega)]$ may be <0 for $|k_0 d| \not\ll 1$.

Lastly, we mention that the causality of an $\epsilon_{jj}(0,\omega) - \epsilon_{jj\,\infty}(0)$ expressed in (13.94a), coupled with the passivity condition in (13.87c), implies by means of the theorem proven in the Appendix that $\epsilon_{jj}^{-1}(0,\omega) - \epsilon_{jj\,\infty}^{-1}(0)$ is also a causal function. However, the causality of a $\mu_{{\rm tt}jj}^{-1}(\boldsymbol{\beta} \to 0,\omega) - \mu_{{\rm tt}jj\infty}^{-1}(\boldsymbol{\beta} \to 0)$ expressed in (13.94b) does not imply, by means of the theorem in the Appendix, the causality of $\mu_{{\rm tt}jj}(\boldsymbol{\beta} \to 0,\omega) - \mu_{{\rm tt}jj\infty}(\boldsymbol{\beta} \to 0)$ because $\mu_{{\rm tt}jj}^{-1}(\boldsymbol{\beta} \to 0,\omega)$ does not necessarily satisfy the passivity condition in (13.89c) (with $\mu_{{\rm tt}jj}^{-1}$ replacing $\mu_{{\rm tt}jj}$ and ">" replacing "<") for all $k_0 d$, that is, for all ω. In Sect. 13.5.2, we show a specific example of an exact solution (within numerical computational accuracy) to an array having $\mu^{-1}(0,\omega) - \mu_\infty^{-1}(0)$ causal, whereas $\mu(0,\omega) - \mu_\infty(0)$ is not causal.

13.5 Specific Examples

Ideally, it would be illuminating to determine the permittivity and permeability dyadics of a specific 3D periodic array of inclusions, such as lossy dielectric spheres centered in the unit cells of a cubic lattice array, by solving for the microscopic fields in (13.63), then integrating these microscopic fields over a unit cell as shown in (13.15) and (13.23) to get $\mathbf{E}$, $\mathbf{B}$, $\mathbf{P}^e$, and $\mathbf{M}^e$, which yield $\mathbf{D}^{\text{eff}}(\boldsymbol{\beta}, \omega)$ and $\mathbf{H}(\boldsymbol{\beta}, \omega)$ from (13.28) and (13.51a), and finally determining $\overline{\boldsymbol{\epsilon}}(\boldsymbol{\beta}, \omega)$ and $\overline{\boldsymbol{\mu}}_{\text{tt}}(\boldsymbol{\beta}, \omega)$ from (13.51a) and (13.48). However, since, we do not presently have access to a computer code for obtaining an accurate numerical solution to the exact equations of such a 3D array, in the next subsection we will perform the simpler 3D calculation of the electric and magnetic polarizabilities of a lossy dielectric sphere illuminated by an incident plane wave with $e^{i(\boldsymbol{\beta}\cdot\mathbf{r}-\omega t)}$ space-time dependence to show that their associated Clausius–Mossotti susceptibilities are causal (unlike the Clausius–Mossotti susceptibilities associated with the electric and magnetic polarizabilities for the usual dipole approximations [28]). The calculation will be further simplified by letting the propagation vector $\boldsymbol{\beta} \to 0$.

In Sect. 13.5.2 we numerically solve the exact equations for a 2D array of dielectric cylinders by means of a 2D finite-difference frequency-domain (FDFD) computer code.

13.5.1 Polarizabilities of the Lossy (or Lossless) Dielectric Sphere

To find the electric and magnetic polarizabilities of a dielectric sphere as $\boldsymbol{\beta} \to 0$ in the context of the rigorous anisotropic representation developed in the previous sections, we begin by finding expressions for the applied (incident) fields, which obey Maxwell's equations in free space (see Footnote 8), namely

$$\nabla \times \boldsymbol{\mathcal{E}}_{a\omega}(\mathbf{r}) - i\omega \boldsymbol{\mathcal{B}}_{a\omega}(\mathbf{r}) = 0 \tag{13.97a}$$

$$\frac{1}{\mu_0}\nabla \times \boldsymbol{\mathcal{B}}_{a\omega}(\mathbf{r}) + i\omega\epsilon_0 \boldsymbol{\mathcal{E}}_{a\omega}(\mathbf{r}) = \mathbf{J}_{\text{t}}(\boldsymbol{\beta}, \omega) e^{i\boldsymbol{\beta}\cdot\mathbf{r}} \tag{13.97b}$$

where we shall consider only the transverse solution produced by $\mathbf{J}_a = \mathbf{J}_{\text{t}}$ such that $\boldsymbol{\beta} \cdot \mathbf{J}_{\text{t}} = 0$. Since these equations hold throughout all space, the $e^{i\boldsymbol{\beta}\cdot\mathbf{r}}$ spatial dependence of the source current $\mathbf{J}_a(\boldsymbol{\beta}, \omega) = \mathbf{J}_{\text{t}}(\boldsymbol{\beta}, \omega)$ demands that the applied electric and magnetic fields also have this same spatial dependence, that is

$$\boldsymbol{\mathcal{E}}_{a\omega}(\mathbf{r}) = \mathbf{E}_a(\boldsymbol{\beta}, \omega) e^{i\boldsymbol{\beta}\cdot\mathbf{r}} \tag{13.98a}$$

$$\boldsymbol{\mathcal{B}}_{a\omega}(\mathbf{r}) = \mathbf{B}_a(\boldsymbol{\beta}, \omega) e^{i\boldsymbol{\beta}\cdot\mathbf{r}}\,. \tag{13.98b}$$

Insertion of these fields into (13.97) gives

$$i\boldsymbol{\beta} \times \mathbf{E}_a - i\omega \mathbf{B}_a = 0 \tag{13.99a}$$

$$\frac{1}{\mu_0} i\boldsymbol{\beta} \times \mathbf{B}_\mathbf{a} + i\omega\epsilon_0 \mathbf{E}_a = \mathbf{J}_\mathrm{t}\,. \tag{13.99b}$$

Eliminating $\mathbf{B}_a$ from (13.99) shows that for $\boldsymbol{\beta} = \beta\hat{\mathbf{z}} \to 0$, and $\mathbf{J}_\mathrm{t} = J_\mathrm{t}\hat{\mathbf{x}}$

$$\mathbf{E}_a = E_a\hat{\mathbf{x}} = i\omega\mu_0 \mathbf{J}_\mathrm{t}/(k_0^2 - \beta^2) = \mathbf{J}_\mathrm{t}/(i\omega\epsilon_0) + O(\beta^2) = J_\mathrm{t}\hat{\mathbf{x}}/(i\omega\epsilon_0) + O(\beta^2) \tag{13.100a}$$

which can be inserted into (13.99a) to give

$$\mathbf{B}_a = B_a\hat{\mathbf{y}} = \boldsymbol{\beta} \times \mathbf{E}_a/\omega = \beta E_a\hat{\mathbf{y}}/\omega = \beta J_\mathrm{t}\hat{\mathbf{y}}/(i\omega^2\epsilon_0)\,. \tag{13.100b}$$

Substitution of $\mathbf{E}_a$ and $\mathbf{B}_a$ from (13.100) into (13.98) produces

$$\boldsymbol{\mathcal{E}}_{a\omega}(\mathbf{r}) = E_a(1 + i\beta z)\hat{\mathbf{x}} + O(\beta^2) \tag{13.101a}$$

$$\boldsymbol{\mathcal{B}}_{a\omega}(\mathbf{r}) = \beta E_a\hat{\mathbf{y}}/\omega + O(\beta^2) \tag{13.101b}$$

which can be rewritten as

$$\boldsymbol{\mathcal{E}}_{a\omega}(\mathbf{r}) = (E_a + i\omega B_a z)\hat{\mathbf{x}} + O(\beta^2) \tag{13.102a}$$

$$\boldsymbol{\mathcal{B}}_{a\omega}(\mathbf{r}) = B_a\hat{\mathbf{y}} + O(\beta^2)\,. \tag{13.102b}$$

The equations in (13.102) reveal that, as $\boldsymbol{\beta} \to 0$, the solution to the dielectric sphere decouples into two problems; the determination of the fields of an incident $E_a\hat{\mathbf{x}}$ electric field, and the determination of the fields of an incident $B_a\hat{\mathbf{y}}$ magnetic field (with its accompanying $i\omega B_a z\hat{\mathbf{x}}$ electric field). Since the unit vectors $\hat{\mathbf{x}}$ and $\hat{\mathbf{y}}$ have the angular dependences of electric and magnetic dipole fields on the surface of the sphere, respectively, and the $\omega B_a z\hat{\mathbf{x}}$ vector contains the angular dependence of an electric quadrupole field as well, the two uncoupled problems involve electric dipole fields, and magnetic dipole plus electric quadrupole fields, respectively. The boundary conditions of continuous tangential electric and magnetic fields at the surface of the dielectric sphere require that the scattered fields are also those of an electric dipole, and a magnetic dipole plus electric quadrupole, respectively. Thus, the fields of the electric dipole problem (label it as problem 1) can be found by solving a spherical boundary-value problem using first-order spherical Bessel/Hankel functions. The fields of the magnetic dipole plus electric quadrupole problem (label it problem 2) can be found by solving a spherical boundary-value problem using both first-order and second-order spherical Bessel/Hankel functions.

For the electric dipole problem (problem 1), we have the incident fields with $\beta = 0$ given by

$$\mathcal{B}_{a\omega}^{(1)}(\mathbf{r}) = 0 \tag{13.103a}$$

$$i\omega\epsilon_0 \mathcal{E}_{a\omega}^{(1)}(\mathbf{r}) = \mathbf{J}_{\mathrm{t}}(0,\omega) = i\omega\epsilon_0 E_a \hat{\mathbf{x}} \tag{13.103b}$$

and thus the total fields are given by

$$\nabla \times \mathcal{E}_{\omega}^{(1)}(\mathbf{r}) - i\omega \mathcal{B}_{\omega}^{(1)}(\mathbf{r}) = 0 \tag{13.104a}$$

$$\frac{1}{\mu_0}\nabla \times \mathcal{B}_{\omega}^{(1)}(\mathbf{r}) + i\omega\epsilon_0 \left\{ \begin{matrix} \epsilon_r \\ 1 \end{matrix} \right\} \mathcal{E}_{\omega}^{(1)}(\mathbf{r}) = i\omega\epsilon_0 E_a \hat{\mathbf{x}}, \quad \left\{ \begin{matrix} r<a \\ r>a \end{matrix} \right\} \tag{13.104b}$$

where a is the radius and ϵ_r is the relative complex dielectric constant of the sphere, with the imaginary part of ϵ_r containing both the dielectric and conductive losses.

Solving Eqs. (13.103–13.104) for the particular and homogeneous spherical wave solutions, we find $\mathcal{E}_{\omega}^{(1)}(\mathbf{r})$ from which we determine $\mathcal{P}_{\omega}^{(1)}(\mathbf{r}) = \epsilon_0(\epsilon_{\mathrm{r}} - 1)\mathcal{E}_{\omega}^{(1)}(\mathbf{r})$ and the electric dipole moment $\mathbf{p}$ of each sphere from

$$\mathbf{p} = \int_{\text{sphere}} \mathcal{P}_{\omega}^{(1)}(\mathbf{r}) d^3 r \tag{13.105}$$

or specifically

$$\mathbf{p} = \epsilon_0 E_a \alpha_e \hat{\mathbf{x}} = p\hat{\mathbf{x}} \tag{13.106}$$

where the $\boldsymbol{\beta} = 0$ electric polarizability α_e is given by

$$\alpha_e \equiv \frac{p}{\epsilon_0 E_a} = \frac{4\pi a^3}{3}\frac{(\epsilon_{\mathrm{r}} - 1)}{\epsilon_{\mathrm{r}}}(1 + b_1) \tag{13.107a}$$

with

$$b_1 = \frac{2(\epsilon_{\mathrm{r}} - 1)h_1^{(1)}(k_0 a) j_1(ka)}{\{h_1^{(1)}(k_0 a)[kaj_1(ka)]' - \epsilon_{\mathrm{r}} j_1(ka)[k_0 a h_1^{(1)}(k_0 a)]'\}} . \tag{13.107b}$$

The prime superscripts denote differentiation with respect to the dimensionless arguments with $k_0 = \omega\sqrt{\mu_0\epsilon_0}$, $k = k_0\sqrt{\epsilon_r}$, and the first-order Bessel function and the first-order Hankel function of the first kind denoted by j_1 and $h_1^{(1)}$, respectively.

As ϵ_r is allowed to approach ∞, we find the $\boldsymbol{\beta} = 0$ electric polarizability of the PEC sphere, namely

$$\alpha_e^{\mathrm{PEC}} = \frac{4\pi a^3}{3}\left\{ 1 - \frac{2h_1^{(1)}(k_0 a)}{[k_0 a\, h_1^{(1)}(k_0 a)]'} \right\} . \tag{13.108}$$

For the magnetic dipole plus electric quadrupole problem (problem 2), we have the incident fields with $\beta \to 0$ given by

$$\boldsymbol{\mathcal{B}}^{(2)}_{a\omega}(\mathbf{r}) = B_a\hat{\mathbf{y}} \tag{13.109a}$$

$$\boldsymbol{\mathcal{E}}^{(2)}_{a\omega}(\mathbf{r}) = i\omega B_a z\hat{\mathbf{x}} \tag{13.109b}$$

and thus the total fields are given by

$$\nabla \times \boldsymbol{\mathcal{E}}^{(2)}_{\omega}(\mathbf{r}) - i\omega\boldsymbol{\mathcal{B}}^{(2)}_{\omega}(\mathbf{r}) = 0 \tag{13.110a}$$

$$\frac{1}{\mu_0}\nabla \times \boldsymbol{\mathcal{B}}^{(2)}_{\omega}(\mathbf{r}) + i\omega\epsilon_0\left\{\begin{array}{c}\epsilon_r\\ 1\end{array}\right\}\boldsymbol{\mathcal{E}}^{(2)}_{\omega}(\mathbf{r}) = -\omega^2\epsilon_0 B_a z\hat{\mathbf{x}}, \quad \left\{\begin{array}{c}r<a\\ r>a\end{array}\right\}. \tag{13.110b}$$

Solving Eqs. (13.109–13.110) for the particular and homogeneous spherical wave solutions, we find $\boldsymbol{\mathcal{E}}^{(2)}_{\omega}(\mathbf{r})$ from which we determine $\boldsymbol{\mathcal{P}}^{(2)}_{\omega}(\mathbf{r}) = \epsilon_0(\epsilon_r - 1)\boldsymbol{\mathcal{E}}^{(2)}_{\omega}(\mathbf{r})$ and the magnetic dipole moment $\mathbf{m}$ of each sphere from

$$\mathbf{m} = -\frac{i\omega}{2}\int_{\text{sphere}} \mathbf{r} \times \boldsymbol{\mathcal{P}}^{(2)}_{\omega}(\mathbf{r})d^3r \tag{13.111}$$

or specifically

$$\mathbf{m} = \frac{1}{\mu_0}B_a\alpha_m\hat{\mathbf{y}} = m\hat{\mathbf{y}} \tag{13.112}$$

where the $\boldsymbol{\beta} \to 0$ magnetic polarizability α_m is given by

$$\alpha_m \equiv \frac{\mu_0 m}{B_a} = \frac{4\pi a^3}{3}\frac{(\epsilon_r - 1)}{\epsilon_r}\left[\frac{(k_0a)^2}{10} + b_2\right] \tag{13.113a}$$

with

$$b_2 = \frac{(\epsilon_r - 1)}{2\epsilon_r(ka)^2} \times \frac{\{[k_0ah_1^{(1)}(k_0a)]' - 2h_1^{(1)}(k_0a)\}\{[(3-(ka)^2]\sin ka - 3ka\cos ka\}}{j_1(ka)\{[k_0ah_1^{(1)}(k_0a)]' - 2h_1^{(1)}(k_0a)\} - h_1^{(1)}(k_0a)\{[kaj_1(ka)]' - 2j_1(ka)\}}. \tag{13.113b}$$

The electric quadrupole density for this problem 2, determined from (13.23c), does not contribute to the electric polarization density $\mathbf{P}^e(0,\omega)$ in (13.27) because $\boldsymbol{\beta}\cdot\overline{\mathbf{Q}}^e \to 0$ as $\boldsymbol{\beta} \to 0$ and $\mathbf{P}^e_\rho(0,\omega) = \mathbf{p}/d^3$, where $\mathbf{p}$ is given in (13.106–13.107). Moreover, as $k_0a \to 0$, that is, $\omega \to 0$ as well as $\boldsymbol{\beta} \to 0$, and the array behaves as a continuum, the electric-quadrupole-density contribution to the fields also becomes negligible compared to the magnetic polarization (magnetic-dipole-density contribution) (see (13.109b) and (13.34) ff.). However, as $\boldsymbol{\beta} \to 0$ and $\omega \not\to 0$, neither the permittivity nor the permeability reveals the contribution to the fields from the

electric-quadrupolar polarization for an applied magnetic field $\mathbf{B}_a$; see discussion in Sect. 13.2.1.

It should also be noted that the electric polarization producing the magnetic dipole moment of problem 2 does not contribute to the electric dipole moment of problem 1, and the electric polarization producing the electric dipole moment of problem 1 does not contribute to the magnetic dipole moment of problem 2, provided the position vector $\mathbf{r}$ is defined with respect to the center of the sphere; see Footnote 6.

As ϵ_r is allowed to approach ∞, we find the $\boldsymbol{\beta} \to 0$ magnetic polarizability of the PEC sphere, namely

$$\alpha_m^{\text{PEC}} = -\frac{4\pi a^3}{3}\left\{1 - \frac{(k_0 a)^2}{10} - \frac{[k_0 a\, h_1^{(1)}(k_0 a)]'}{2h_1^{(1)}(k_0 a)}\right\}. \tag{13.114}$$

As $|k_0 a| \to \infty$, the $\beta \to 0$ electric and magnetic polarizabilities of the PEC sphere become

$$\alpha_e^{\text{PEC}} \overset{|k_0 a|\to\infty}{\sim} \frac{4\pi a^3}{3}\left\{1 + \frac{2i}{k_0 a} + O\left[1/(k_0 a)^3\right]\right\} \tag{13.115a}$$

$$\alpha_m^{\text{PEC}} \overset{|k_0 a|\to\infty}{\sim} -\frac{4\pi a^3}{3}\left\{-\frac{(k_0 a)^2}{10} - \frac{ik_0 a}{2} + 1 + \frac{i}{2k_0 a} + O\left[1/(k_0 a)^2\right]\right\}. \tag{13.115b}$$

The result in (13.115b) reveals that the real and imaginary parts of α_m^{PEC} approach ∞ as $|k_0 a| \to \infty$.

For the other extreme, $k_0 a \to 0$, we find $h_1^{(1)}(k_0 a)/[k_0 a\, h_1^{(1)}(k_0 a)]' \to -1$, so that

$$\alpha_e^{\text{PEC}} \overset{k_0 a\to 0}{\sim} 4\pi a^3 \tag{13.116a}$$

$$\alpha_m^{\text{PEC}} \overset{k_0 a\to 0}{\sim} -2\pi a^3 \tag{13.116b}$$

which confirms, as one's physical intuition would expect, that the PEC sphere behaves both as a dielectric and as a diamagnetic inclusion (artificial molecule) [7, Sect. 9.5; 8, Fig. 8].

The polarizabilities in (13.108) and (13.114) can be used in the Clausius–Mossotti/Maxwell-Garnett formula [28][17] to obtain approximate susceptibilities for a 3D periodic cubic-lattice array of PEC spheres, namely

$$\chi_{e\text{CM}}^{\text{PEC}}(0, k_0 a) = \epsilon_{\text{CM}}^{\text{PEC}}(0, k_0 a)/\epsilon_0 - 1 = \frac{1}{d^3/\alpha_e^{\text{PEC}} - 1/3} \tag{13.117a}$$

[17] Some authors reserve the name "Clausius–Mossotti" for the formulas with quasi-static polarizabilities and use the name "Maxwell-Garnett" for the formulas with polarizabilities that are functions of frequency ω. In the rest of the section, we shall omit the label "Maxwell-Garnett" and simply refer to these formulas by the name "Clausius–Mossotti."

$$\chi_{m\mathrm{CM}}^{\mathrm{PEC}}(0,k_0a)=\mu_{\mathrm{CM}}^{\mathrm{PEC}}(0,k_0a)/\mu_0-1=\frac{1}{d^3/\alpha_m^{\mathrm{PEC}}-1/3}\,. \tag{13.117b}$$

These Clausius–Mossotti susceptibilities are reasonable approximations to the exact fundamental Floquet-mode susceptibilities of the array for $|k_0d|\lesssim 1$. It is a simple matter to prove that the imaginary parts of $\chi_{e\mathrm{CM}}^{\mathrm{PEC}}(0,k_0a)$ and $\chi_{m\mathrm{CM}}^{\mathrm{PEC}}(0,k_0a)$, like the imaginary parts of the corresponding α_e^{PEC} and α_m^{PEC}, are greater than zero for all values of k_0a.

The equations in (13.87d) and (13.89d) predict that the imaginary parts of the *exact* fundamental Floquet-mode electric and magnetic susceptibilities of the lossless PEC array satisfy for $\boldsymbol{\beta}=0$

$$\mathrm{Im}[\epsilon(0,\omega)]=\mathrm{Im}[\chi_e(0,\omega)]=0,\quad \omega\neq\omega_{uc} \tag{13.118a}$$

$$\mathrm{Im}[\mu(0,\omega)]=\mathrm{Im}[\chi_m(0,\omega)]=0,\quad |k_0d|\ll 1\,. \tag{13.118b}$$

The Clausius–Mossotti PEC susceptibilities also have zero imaginary parts as $k_0a\to 0$ [see (13.121)], as would be expected, since the exact and Clausius–Mossotti susceptibilities become equal in value as ($\boldsymbol{\beta}\to 0,\omega\to 0$).

As $|k_0a|\to\infty$

$$\chi_{e\mathrm{CM}}^{\mathrm{PEC}}(0,k_0a)\overset{|k_0a|\to\infty}{\sim}\frac{12\pi(a/d)^3}{9-4\pi(a/d)^3}+O(1/k_0a) \tag{13.119a}$$

$$\chi_{m\mathrm{CM}}^{\mathrm{PEC}}(0,k_0a)\overset{|k_0a|\to\infty}{\sim}-3+O(1/k_0a) \tag{13.119b}$$

where $a/d\leq 0.5$ since the sphere diameter ($2a$) cannot be larger than the side length (d) of the cubic unit cell. Thus, for the PEC sphere array the Clausius–Mossotti electric susceptibility always approaches a real value greater than zero as $|\omega|\to\infty$ and the Clausius–Mossotti magnetic susceptibility always approaches the negative real value of -3 as $|\omega|\to\infty$; that is

$$\chi_{e\mathrm{CM}\infty}^{\mathrm{PEC}}=\frac{12\pi(a/d)^3}{9-4\pi(a/d)^3} \tag{13.120a}$$

$$\chi_{m\mathrm{CM}\infty}^{\mathrm{PEC}}=-3\,. \tag{13.120b}$$

As $k_0a\to 0$

$$\chi_{e\mathrm{CM}}^{\mathrm{PEC}}(0,k_0a)\overset{k_0a\to 0}{\sim}\frac{12\pi(a/d)^3}{3-4\pi(a/d)^3} \tag{13.121a}$$

$$\chi_{m\mathrm{CM}}^{\mathrm{PEC}}(0,k_0a)\overset{k_0a\to 0}{\sim}-\frac{6\pi(a/d)^3}{3+2\pi(a/d)^3} \tag{13.121b}$$

which shows that the values of the PEC susceptibilities, $\chi_{e\mathrm{CM}}^{\mathrm{PEC}}(0,k_0a)$ and $\chi_{m\mathrm{CM}}^{\mathrm{PEC}}(0,k_0a)$, and the corresponding permittivity and permeability, at $k_0a=0$ are real and always greater than their respective values at $|k_0a|=\infty$.

The Clausius–Mossotti electric and magnetic susceptibilities in (13.117) for the PEC sphere array have no poles in the upper half of the complex ω plane and thus with their values in (13.119) at infinity subtracted, they, as well as their corresponding permittivity and permeability functions, satisfy the causality relations similar to those in (13.93) and the Kramers–Kronig relations similar to those in (13.94); specifically

$$\epsilon_{\mathrm{CM}}^{\mathrm{PEC}}(0,\omega)-\epsilon_{\mathrm{CM}\infty}^{\mathrm{PEC}}=\frac{i}{\pi}\int_{-\infty}^{+\infty}\frac{\epsilon_{\mathrm{CM}}^{\mathrm{PEC}}(0,v)-\epsilon_{\mathrm{CM}\infty}^{\mathrm{PEC}}}{\omega-v}\,\mathrm{d}v \tag{13.122a}$$

$$\mu_{\mathrm{CM}}^{\mathrm{PEC}}(0,\omega)-\mu_{\mathrm{CM}\infty}^{\mathrm{PEC}}=\frac{i}{\pi}\int_{-\infty}^{+\infty}\frac{\mu_{\mathrm{CM}}^{\mathrm{PEC}}(0,v)-\mu_{\mathrm{CM}\infty}^{\mathrm{PEC}}}{\omega-v}\,\mathrm{d}v\,. \tag{13.122b}$$

This is an especially noteworthy result for the diamagnetic permeability, even within the Clausius–Mossotti approximation, because, as explained in the Introduction, diamagnetic permeability has hitherto eluded a consistent causal description. The causality of the Clausius–Mossotti permittivity and permeability is a direct consequence of the causality of the fixed-$\boldsymbol{\beta}$, integrally defined polarizabilities. Although the derivation will not be given here, it can be shown that the Clausius–Mossotti permittivity and permeability functions determined from polarizabilities with free-space incident plane waves (rather than fixed-$\boldsymbol{\beta}$ plane waves) or with dipole moments defined in terms of the fields exterior to the sphere (rather than from their integral definitions) are *not* causal and thus do not satisfy the Kramers–Kronig relations in (13.122).

Because the imaginary parts of the Clausius–Mossotti susceptibilities, $\chi_{\mathrm{eCM}}^{\mathrm{PEC}}(0,k_0a)$ and $\chi_{m\mathrm{CM}}^{\mathrm{PEC}}(0,k_0a)$, are positive for $k_0a>0$, the theorem in the Appendix implies that the functions

$$\xi_{e\mathrm{CM}}^{\mathrm{PEC}}=\frac{1}{\chi_{e\mathrm{CM}}^{\mathrm{PEC}}(0,k_0a)-\chi_{e\mathrm{CM}\infty}^{\mathrm{PEC}}+1}-1 \tag{13.123a}$$

$$\xi_{m\mathrm{CM}}^{\mathrm{PEC}}=\frac{1}{\chi_{m\mathrm{CM}}^{\mathrm{PEC}}(0,k_0a)-\chi_{m\mathrm{CM}\infty}^{\mathrm{PEC}}+1}-1 \tag{13.123b}$$

are also causal and satisfy the Kramers–Kronig relations. However, it does not necessarily follow that the inverse permittivity and permeability functions

$$\frac{1}{\epsilon_{\mathrm{CM}\infty}^{\mathrm{PEC}}}\left[\frac{1}{\epsilon_{\mathrm{CM}}^{\mathrm{PEC}}(0,k_0a)/\epsilon_{\mathrm{CM}\infty}^{\mathrm{PEC}}}-1\right] \tag{13.124a}$$

$$\frac{1}{\mu^{\mathrm{PEC}}_{\mathrm{CM}\infty}}\left[\frac{1}{\mu^{\mathrm{PEC}}_{\mathrm{CM}}(0,k_0a)/\mu^{\mathrm{PEC}}_{\mathrm{CM}\infty}}-1\right] \tag{13.124b}$$

are causal and satisfy the Kramers–Kronig relations. Nonetheless, since the value of $\epsilon^{\mathrm{PEC}}_{\mathrm{CM}}(0,0)/\epsilon^{\mathrm{PEC}}_{\mathrm{CM}\infty}=[8\pi(a/d)^3+3][9-4\pi(a/d)^3][8\pi(a/d)^3+9]^{-1}[3-4\pi(a/d)^3]^{-1}$ is greater than zero, the theorem in the Appendix implies that the inverse permittivity in (13.124a) is causal and satisfies the Kramers–Kronig relations. In contrast, the value of $\mu^{\mathrm{PEC}}_{\mathrm{CM}}(0,0)/\mu^{\mathrm{PEC}}_{\mathrm{CM}\infty}=[2\pi(a/d)^3+3]^{-1}[4\pi(a/d)^3-3]/2$ is less than zero, thus the theorem in the Appendix no longer applies, and the Clausius–Mossotti inverse permeability in (13.124b) is not causal and does not satisfy the Kramers–Kronig relations. These causality results are confirmed by the numerical computations in the next section.

Interestingly, these approximate (Clausius–Mossotti) permeability and inverse permeability are causal and noncausal, respectively, whereas the exact fundamental Floquet-mode permeability and inverse permeability are noncausal and causal, respectively, as we proved in Sect. 13.4.4. The causality of the Clausius–Mossotti permittivity and permeability is a direct consequence of the causality of the fixed-$\boldsymbol{\beta}$, integrally defined polarizabilities. The causality or noncausality of these approximate constitutive parameters need not comply with the causality or noncausality of the corresponding exact constitutive parameters, which take into account the exact interaction of all the inclusions at all frequencies.

13.5.1.1 Numerical Results for the PEC Sphere

The real and imaginary parts of the approximate Clausius–Mossotti susceptibilities, $\chi^{\mathrm{PEC}}_{e\mathrm{CM}}(0,k_0a)$ and $\chi^{\mathrm{PEC}}_{m\mathrm{CM}}(0,k_0a)$, of the 3D PEC sphere array were computed by inserting α^{PEC}_e and α^{PEC}_m from (13.108) and (13.114) into (13.117) and they are plotted in Figs. 13.1, 13.2, 13.3, 13.4. The ratio of the radius of the sphere to the side length of the cubic cell is chosen to be $a/d=0.45$. The asymptotic values of $\chi^{\mathrm{PEC}}_{e\mathrm{CM}}(0,k_0a)$ and $\chi^{\mathrm{PEC}}_{m\mathrm{CM}}(0,k_0a)$ given in (13.119) and (13.121) are verified by the numerical computations and the plots in Figs. 13.1–13.4. The imaginary parts of $\chi^{\mathrm{PEC}}_{e\mathrm{CM}}(0,k_0a)$ and $\chi^{\mathrm{PEC}}_{m\mathrm{CM}}(0,k_0a)$ are positive for $k_0a>0$, whereas the real part of $\chi^{\mathrm{PEC}}_{e\mathrm{CM}}(0,k_0a)$ is positive for $k_0a>0$ and the real part of $\chi^{\mathrm{PEC}}_{m\mathrm{CM}}(0,k_0a)$ is negative for $k_0a>0$ except in the range of $3.8<k_0a<7.7$. In particular, the Clausius–Mossotti expressions for the PEC spheres with a separation $a/d=0.45$ produce a positive macroscopic electric susceptibility and a predominantly negative (diamagnetic) magnetic susceptibility [7, Sect. 9.5; 8, Fig. 8] whose values begin at 1.85 and -0.48, respectively, at $k_0a=0$ and approach 0.44 and -3.0, respectively, as $k_0a\to\infty$. It is noteworthy that these values of 1.85 and -0.48 for the real parts of the electric and magnetic susceptibilities, respectively, as $k_0a\to 0$ with $\boldsymbol{\beta}=0$ in the applied current excitation are very close (within less than 1 %) to the values of the electric and magnetic susceptibilities computed for the

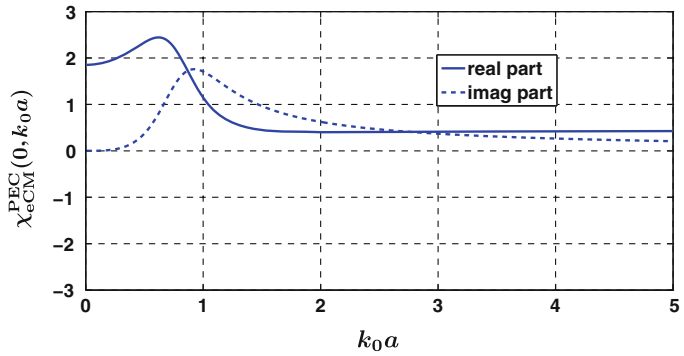

Fig. 13.1 Clausius–Mossotti electric susceptibility for 3D array of PEC spheres ($a/d = 0.45$)

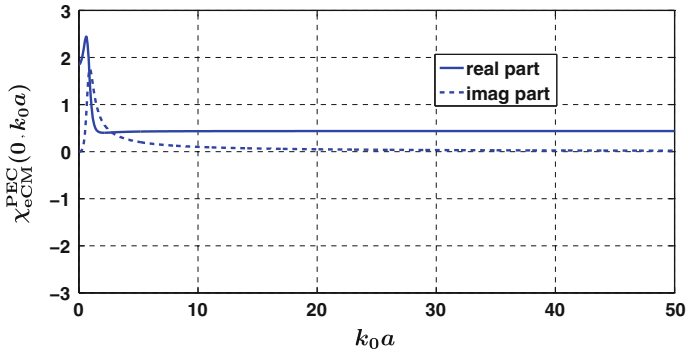

Fig. 13.2 Clausius–Mossotti electric susceptibility for 3D array of PEC spheres ($a/d = 0.45$): larger values of $k_0 a$

source-free eigenmode of the PEC-sphere array in [8, Fig. 8] for $\beta d \ll 1$ and $k_0 d \ll 1$. This dipolar continuum behavior of the macroscopic constitutive parameters for $\beta d \ll 1$ and $k_0 d \ll 1$ can also be found in the bianisotropic homogenization work of Alù [23]. These similar values in the applied-current and source-free macroscopic susceptibilities for $\beta d \ll 1$ and $k_0 d \ll 1$ are expected because the derivation leading to the Clausius–Mossotti dipolar continuum relations in source-free arrays also holds for the same arrays excited by an applied plane-wave electric current density and the Clausius–Mossotti relations are very accurate for $\beta d \ll 1$ and $k_0 d \ll 1$.

We have also computed the fundamental time-domain causality integrals as in (13.93) but for the Clausius–Mossotti PEC-sphere-array electric and magnetic susceptibilities with their asymptotic values in (13.120) subtracted, namely

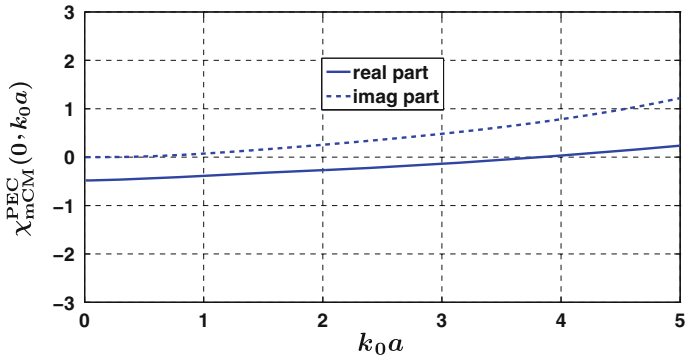

Fig. 13.3 Clausius–Mossotti magnetic susceptibility for 3D array of PEC spheres ($a/d = 0.45$)

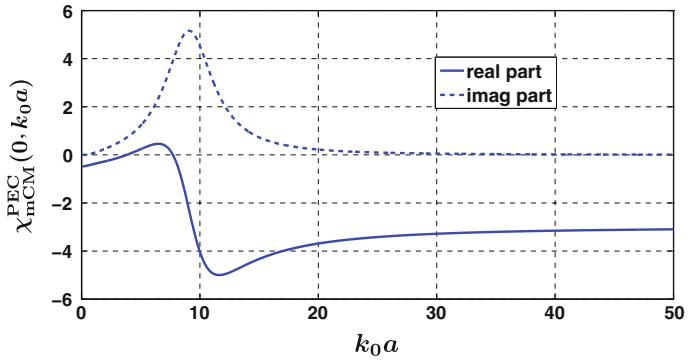

Fig. 13.4 Clausius–Mossotti magnetic susceptibility for 3D array of PEC spheres ($a/d = 0.45$): larger values of $k_0 a$

$$\chi_{e\mathrm{CM}}^{\mathrm{PEC}}(\tau) = 2\mathrm{Re}\int_0^{+\infty} \left[\chi_{e\mathrm{CM}}^{\mathrm{PEC}}(0, k_0 a) - \chi_{e\mathrm{CM}_\infty}^{\mathrm{PEC}}\right] e^{-ik_0 a\tau}\, \mathrm{d}(k_0 a) \tag{13.125a}$$

$$\chi_{m\mathrm{CM}}^{\mathrm{PEC}}(\tau) = 2\mathrm{Re}\int_0^{+\infty} \left[\chi_{m\mathrm{CM}}^{\mathrm{PEC}}(0, k_0 a) - \chi_{m\mathrm{CM}_\infty}^{\mathrm{PEC}}\right] e^{-ik_0 a\tau}\, \mathrm{d}(k_0 a) \tag{13.125b}$$

in which $\tau = ct/a$.

As one sees in Figs. 13.5 and 13.6, the time-domain Clausius–Mossotti susceptibilities for the 3D PEC sphere array defined with the polarizabilities in (13.108) and (13.114), which are determined with a constant $\boldsymbol{\beta} = 0$ and the integral definitions of electric and magnetic polarizations in (13.106–13.107) and (13.112–13.113), derived from (13.23a) and (13.23b), are zero for $t < 0$. Thus, these Clausius–Mossotti susceptibilities, although approximate, are causal and satisfy

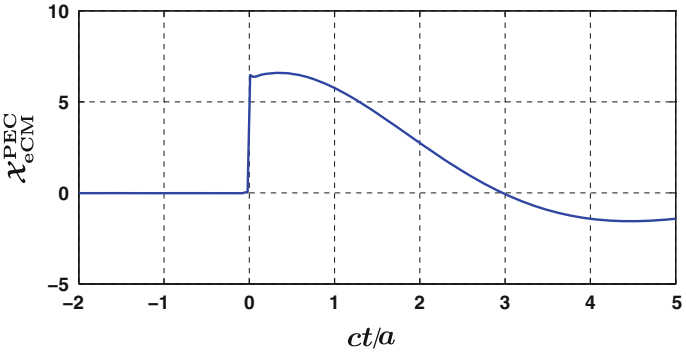

Fig. 13.5 Causality of time-domain Clausius–Mossotti electric susceptibility for 3D array of PEC spheres ($a/d = 0.45$)

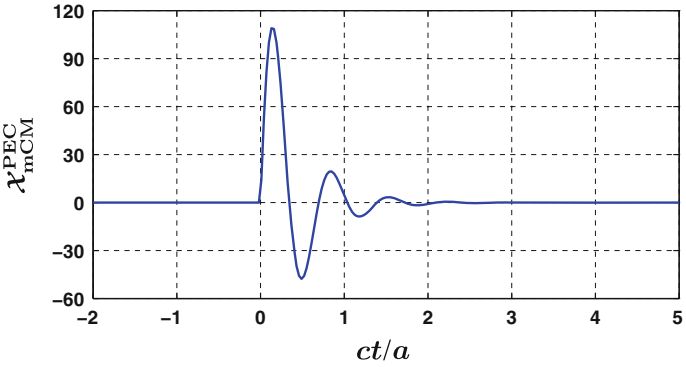

Fig. 13.6 Causality of time-domain Clausius–Mossotti magnetic susceptibility for 3D array of PEC spheres ($a/d = 0.45$)

the Kramers–Kronig relations similar to those in (13.122). This demonstrated causality of the Clausius–Mossotti constitutive parameters defined in terms of electric current integrals at a fixed $\boldsymbol{\beta}$ stands in distinct contrast to the noncausality of the conventional Clausius–Mossotti electric and magnetic susceptibilities defined in terms of the electric and magnetic dipole scattering coefficients of the inclusions, specifically in this case, the Mie dipole scattering coefficients for PEC spheres [28].

Lastly, we verified numerically that the Clausius–Mossotti inverse susceptibility functions in (13.123) as well as the Clausius–Mossotti inverse permittivity function in (13.124a) were indeed causal (their Fourier transforms were zero for $t < 0$), whereas the inverse permeability function in (13.124b) was not causal, its Fourier transform not being zero for $t < 0$. (For brevity, these numerical results are not displayed in figures.) Interestingly, as mentioned at the end of Sect. 13.5.1,

these approximate (Clausius–Mossotti) permeability and inverse permeability are causal and noncausal, respectively, whereas the exact fundamental Floquet-mode permeability and inverse permeability are noncausal and causal, respectively, as we proved in Sect. 13.4.4 and confirm in the example of the next section.

13.5.2 FDFD Solution for a 2D Array of Dielectric Circular Cylinders

As a final example, we determine the macroscopic permittivity and permeability of a 2D metamaterial array, consisting of uniformly spaced, infinitely long dielectric circular cylinders, computed from a finite-difference frequency-domain (FDFD) solution to the rigorous equations derived in Sects. 13.2–13.4. We limit the computations to $\boldsymbol{\beta} \to 0$ for the transverse solution with $\boldsymbol{\beta} = \beta\hat{\mathbf{z}}$ in a principal propagation direction z and the applied transverse electric current density $\mathbf{J}_t = J_t\hat{\mathbf{x}}$ normal to the plane formed by the principal propagation direction and the axial direction ($\hat{\mathbf{y}}$) of the cylinders. We choose a homogeneous, isotropic, causal, microscopic, Drude-model [37, Chap. V], relative complex dielectric constant for each of the cylinders given by

$$\epsilon_{\mathrm{D}} = 1 - \frac{(k_p d)^2}{k_0 d(k_0 d + ik_c d)} \tag{13.126}$$

where d is the separation distance between the center of the circular cylinders located in free space on a square lattice, $k_0 = \omega/c$, $k_p d = 1.5$, $k_c = 0.05k_p$, and the radius a of each circular cylinder is chosen to be such that $a/d = 0.40$. As $|\omega| \to \infty$, this relative complex dielectric constant approaches 1, and as $\omega \to 0$, it approaches $1 + ik_p^2/(k_0 k_c)$, the relative complex dielectric constant of an electrical conductor.

Based on the numerical method reported in [45], we numerically solve for the microscopic fields in (13.63) as $\beta \to 0$, then integrate these microscopic fields over a unit cell as shown in (13.15) and (13.23) to find $\mathbf{D}(0, k_0 d)$ and $\mathbf{H}(0, k_0 d)$ from (13.28), and finally determine $\overline{\boldsymbol{\epsilon}}(0, k_0 d)$ and $\overline{\boldsymbol{\mu}}_{\mathrm{tt}}(\boldsymbol{\beta} \to 0, k_0 d)$ from (13.45) and (13.48). For propagation in the principal direction z of the array with the given applied electric current density in the $\hat{\mathbf{x}}$ direction, the vectors $\mathbf{E}(0, k_0 d)$ and $\mathbf{D}(0, k_0 d)$ are in the $\hat{\mathbf{x}}$ direction, and the vectors $\mathbf{B}(0, k_0 d)$ and $\mathbf{H}(0, k_0 d)$ are in the $\hat{\mathbf{y}}$ direction (along the axis of the cylinders). Thus the permittivity and permeability reduce to scalars, $\epsilon(0, k_0 d)$ and $\mu(0, k_0 d)$, and the magnetoelectric dyadic $\bar{\nu}_{\mathrm{tt}} = 0$. As $\beta \to 0$ the only required integrations in (13.23) for the 2D cylinders reduce to

$$\mathbf{P}_\rho^e(0, \omega) = -\frac{1}{d^2} \int_{A_c} \nabla \cdot \mathcal{P}_\omega(\mathbf{r}) \mathbf{r} d^2 r = \frac{1}{d^2} \int_{\text{cylinder}} \mathcal{P}_\omega(\mathbf{r}) d^2 r \tag{13.127a}$$

for the electric polarization, and

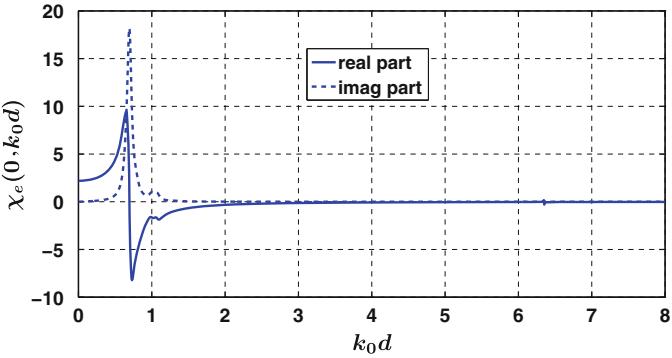

Fig. 13.7 Exact (to within computational accuracy) fundamental Floquet-mode macroscopic electric susceptibility for 2D array of dielectric circular cylinders ($a/d = 0.40$)

$$\mathbf{M}^e(\beta \to 0, \omega) = -\frac{i\omega}{2d^2} \int_{\text{cylinder}} \mathbf{r} \times \boldsymbol{\mathcal{P}}_\omega(\mathbf{r}) d^2 r \tag{13.127b}$$

for the magnetic polarization.

Figure 13.7 shows the real and imaginary parts of the exact (to within computational errors) fundamental Floquet-mode macroscopic electric susceptibility $\chi_e(0, k_0 d) = [\epsilon(0, k_0 d)/\epsilon_0 - 1]$ versus the electrical separation distance $k_0 d$. An enlargement of the second resonance region near $k_0 d = 6.35$ is shown in Fig. 13.8. Each of the resonances resembles a Lorentz resonance. As predicted in Eq. (13.87c) the imaginary part of $\chi_e(0, k_0 d)$ is greater than zero for $\omega > 0$ (that is, for $k_0 d > 0$). The imaginary part remains quite small except near the resonances where it increases in value dramatically.

The real part of the electric susceptibility continuously increases from a positive value of about 2.2 at $k_0 d = 0$ until it reaches the first resonance where it decreases rapidly to a negative value before increasing toward a value of zero and higher near the second resonance where the behavior is repeated. For $k_0 d \ll 1$ the behavior of the real and imaginary parts of the exact fundamental Floquet-mode macroscopic electric susceptibility shown in Fig. 13.7 for the 2D array of conductive dielectric cylinders is similar to the behavior of the Clausius–Mossotti electric susceptibility shown in Fig. 13.1 for the 3D array of PEC spheres.

As determined by (13.93c), the exact fundamental Floquet-mode macroscopic permittivity and thus the macroscopic electric susceptibility of the 2D array of circular cylinders is a causal function satisfying

$$\chi_e(\tau) = 2\text{Re} \int_0^{+\infty} \chi_e(0, k_0 d) e^{-ik_0 d\tau} d(k_0 d) = 0, \quad \tau = ct/d < 0\,. \tag{13.128}$$

Figure 13.9, which shows the plot of $\chi_e(\tau)$ numerically computed from the integral in (13.128) using the $\chi_e(0, k_0 d)$ data shown in Fig. 13.7, confirms the causality of

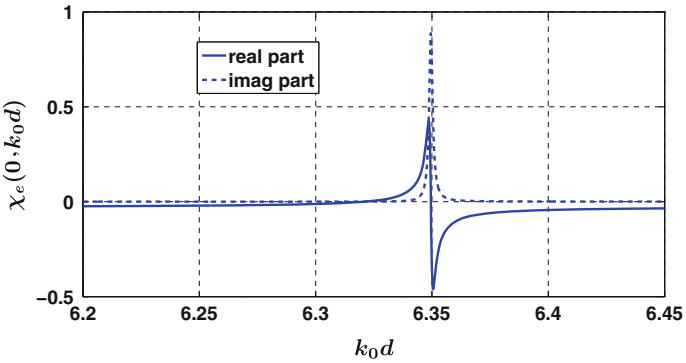

Fig. 13.8 Exact (to within computational accuracy) fundamental Floquet-mode macroscopic electric susceptibility for 2D array of dielectric circular cylinders ($a/d = 0.40$): Enlargement of resonance near $k_0 d = 6.35$

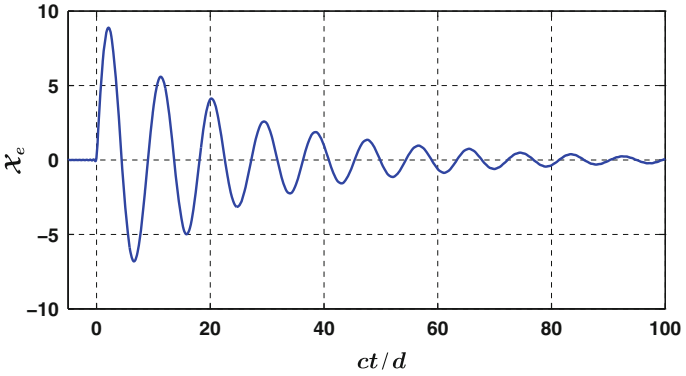

Fig. 13.9 Causality of numerically computed time-domain exact fundamental Floquet-mode electric susceptibility for 2D array of conductive dielectric circular cylinders ($a/d = 0.40$)

this numerically computed exact electric susceptibility. (Using $\chi_e(0, k_0 d)$ data for a maximum $k_0 d$ lying about half way between two resonances produces an effectively causal $\chi_e(\tau)$.) Moreover, as discussed at the end of Sect. 13.4.4, since the macroscopic permittivity $\epsilon(0, k_0 d)$ approaches 1 as $k_0 d \to \infty$ and the imaginary part of $\epsilon(0, k_0 d)$ is greater than zero for $k_0 d > 0$, the theorem in the Appendix predicts that the inverse electric susceptibility defined as $\chi_e^{\text{inv}}(0, k_0 d) = [\epsilon_0/\epsilon(0, k_0 d) - 1]$ is also a causal function; specifically

$$\chi_e^{\text{inv}}(\tau) = 2\text{Re} \int_0^{+\infty} \chi_e^{\text{inv}}(0, k_0 d) e^{-ik_0 d\tau} d(k_0 d) = 0, \quad \tau = ct/d < 0\,. \tag{13.129}$$

This causality of the inverse electric susceptibility is confirmed numerically by computing the integral in (13.129) and plotting the results in Fig. 13.10.

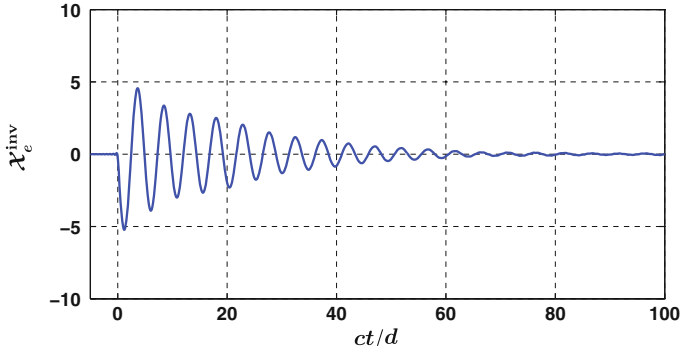

Fig. 13.10 Causality of numerically computed time-domain exact fundamental Floquet-mode *inverse* electric susceptibility for 2D array of conductive dielectric circular cylinders ($a/d = 0.40$)

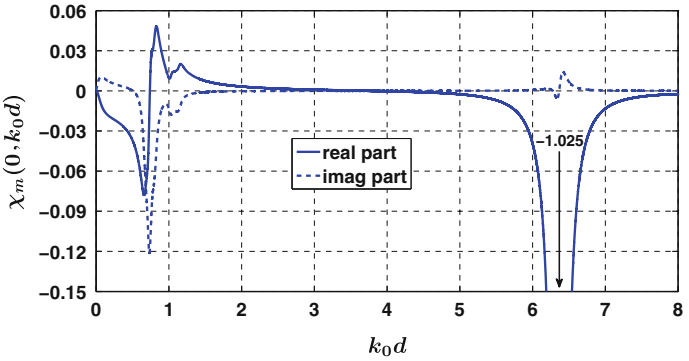

Fig. 13.11 Exact (to within computational accuracy) fundamental Floquet-mode macroscopic magnetic susceptibility for 2D array of dielectric circular cylinders ($a/d = 0.40$)

Next, we show in Fig. 13.11 the real and imaginary parts of the exact (to within computational errors) fundamental Floquet-mode macroscopic magnetic susceptibility $\chi_m(0, k_0 d) = [\mu(0, k_0 d)/\mu_0 - 1]$ versus the electrical separation distance $k_0 d$. This $\chi_m(0, k_0 d)$ is computed from the magnetization in (13.127b) and the average (macroscopic) magnetic field $\mathbf{H}$ in the unit cell. As predicted by (13.89c), the imaginary part of the magnetic susceptibility is greater than zero for $k_0 d \ll 1$ and yet becomes less than zero at larger values of $k_0 d$ as a result of the resonant response of the inclusions.

The real part of the exact fundamental Floquet-mode macroscopic magnetic susceptibility is negative at the lower frequencies because the conductivity of the inclusion material produces a diamagnetic effect at the lower frequencies. (For the loss constant $k_c = 0$ in the Drude-model relative dielectric constant (13.126), the macroscopic magnetic susceptibility equals -0.0206 as $k_0 d \to 0$ and the macroscopic electric susceptibility equals 2.1944 as $k_0 d \to 0$.) The diamagnetism

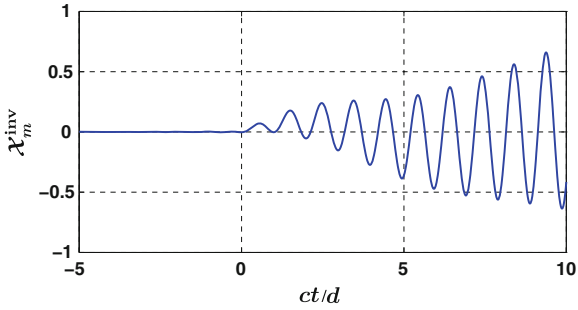

Fig. 13.12 Causality of numerically computed time-domain exact fundamental Floquet-mode *inverse* magnetic susceptibility for 2D array of conductive dielectric circular cylinders ($a/d = 0.40$)

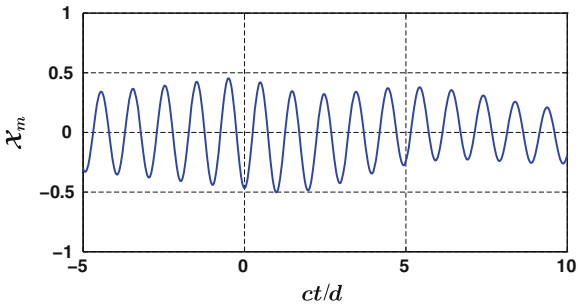

Fig. 13.13 Noncausality of numerically computed time-domain exact fundamental Floquet-mode magnetic susceptibility for 2D array of conductive dielectric circular cylinders ($a/d = 0.40$)

increases until the first resonance is reached where the real part rapidly increases to a positive value and stays positive until encountering the beginning of a second resonance where the real part of the magnetic susceptibility becomes strongly diamagnetic again. The first resonance in the magnetic susceptibility approximates the negative of a Lorentz permittivity resonance. The second resonance shows very unusual behavior in that it somewhat imitates the negative of a Lorentz permittivity resonance but with the roles of the real and imaginary parts of the susceptibility reversed. For $k_0 d \ll 1$ the negative real and positive imaginary parts of the exact fundamental Floquet-mode macroscopic magnetic susceptibility shown in Fig. 13.11 for the 2D array of conductive dielectric cylinders is consistent with the negative real and positive imaginary parts of the Clausius–Mossotti magnetic susceptibility shown in Fig. 13.3 for the 3D array of PEC spheres. (Although not obvious from Fig. 13.11, the imaginary part of the susceptibility $\chi_m(0, k_0 d) \to 0$ as $k_0 d \to 0$.)

The theory of causality in Sect. 13.4.4 predicts in (13.93b) that the exact fundamental Floquet-mode macroscopic *inverse* permeability and thus the macroscopic inverse magnetic susceptibility defined as $\chi_m^{\text{inv}}(0, k_0 d) = [\mu_0/\mu(0, k_0 d) - 1]$ for the 2D array of circular cylinders is a causal function satisfying

$$\chi_m^{\text{inv}}(\tau) = 2\text{Re} \int_0^{+\infty} \chi_m^{\text{inv}}(0, k_0 d) e^{-ik_0 d\tau} \, \mathrm{d}(k_0 d) = 0, \quad \tau = ct/d < 0 \,. \tag{13.130}$$

Figure 13.12, which shows the plot of $\chi_m^{\text{inv}}(\tau)$ numerically computed from the integral in (13.130) using the $\chi_m(0, k_0 d)$ data shown in Fig. 13.11, confirms the causality of this numerically computed exact inverse magnetic susceptibility. (Using $\chi_m(0, k_0 d)$ data for a maximum $k_0 d$ lying about half way between two resonances produces an effectively causal $\chi_m^{\text{inv}}(\tau)$.) However, as discussed at the end of Sect. 13.4.4, since the imaginary part of $\mu(0, k_0 d)$, and thus $1/\mu(0, k_0 d)$, does not maintain the same sign for all $k_0 d > 0$, the theorem in the Appendix cannot be used to predict that the magnetic susceptibility $\chi_m(0, k_0 d)$ is a causal function. Indeed, the computation of

$$\chi_m(\tau) = 2\text{Re} \int_0^{+\infty} \chi_m(0, k_0 d) e^{-ik_0 d\tau} \, \text{d}(k_0 d) \tag{13.131}$$

plotted in Fig. 13.13 using the $\chi_m(0, k_0 d)$ data shown in Fig. 13.11 verifies that the exact fundamental Floquet-mode macroscopic magnetic susceptibility is definitely not causal.

13.6 Conclusion

At high enough frequencies ω, every natural material or artificial material (metamaterial) no longer behaves as a continuum satisfying the traditional time-harmonic dipolar macroscopic Maxwell equations with spatially nondispersive constitutive parameters. Although this departure from a continuum behavior at high frequencies can often be ignored with impunity for the electric and para/ferro(i)magnetic polarization of materials and metamaterials, we show in the Introduction that it is mathematically impossible to characterize a material or metamaterial that is diamagnetic and lossless at low frequencies ω by a causal spatially nondispersive permeability that satisfies continuum passivity conditions and whose value approaches the permeability of free space as the frequency ω approaches infinity. Moreover, this noncausality in the spatially nondispersive dipolar continuum description of diamagnetism is more fundamental than the noncausality, discussed in [28], introduced by the point dipole approximation for scattering from the inclusions (molecules) and is not removed by including higher-order multipole moments in the spatially nondispersive continuum formulation of Maxwell's equations.

In order to characterize metamaterials formed by periodic arrays of polarizable inclusions (separated in free space) in a way that includes diamagnetism and reduces to a continuum description when the enforced and free-space wavelengths in the arrays are large compared to the distance separating the inclusions, we formulate a rigorous spatially ($\boldsymbol{\beta}$) and temporally (ω) dispersive anisotropic representation for these periodic metamaterials. The spatially dispersive anisotropic representation, like the single-polarization description of materials introduced by

Landau and Lifshitz [5], is obtained by exciting the metamaterial arrays with applied electric current densities having $e^{i(\boldsymbol{\beta}\cdot\mathbf{r}-\omega t)}$ plane-wave dependence. Beginning with the microscopic Maxwell's equations for the arrays, it is shown that two constitutive parameters, a spatially dispersive permittivity $\overline{\boldsymbol{\epsilon}}(\boldsymbol{\beta},\omega)$ and a spatially dispersive *inverse* transverse permeability $\overline{\boldsymbol{\mu}}_{\mathrm{tt}}^{-1}(\boldsymbol{\beta},\omega)$, characterize the fundamental Floquet modes of the arrays. These macroscopic permittivities and inverse permeabilities are shown to be causal for each fixed value of the plane-wave propagation vector $\boldsymbol{\beta}$ and to reduce to continuum permittivities and permeabilities at the low spatial and temporal frequencies ($|\boldsymbol{\beta}d|$ and $|k_0 d|$ sufficiently small). The general formulation for spatially dispersive periodic arrays provides convenient equations to express sufficient conditions for the array to approximate a continuum, and to determine boundary conditions for an electric quadrupolar continuum.

The key to this rigorous spatially dispersive anisotropic formulation is the vector decomposition given in (13.20) for the microscopic equivalent electric current density and the resulting generalized dipolar and electric quadrupolar macroscopic polarization densities in (13.23). For both $|\boldsymbol{\beta}d|$ and $|k_0 d|$ sufficiently small, the array behaves as an anisotropic dipolar continuum in which the electric quadrupolar density, and all other higher-order multipoles, are negligible compared with a nonzero dipolar electric and/or magnetic polarization density. This result for an anisotropic continuum is a significant consequence of the rigorous anisotropic representation for spatially dispersive media.

Detailed reality conditions, reciprocity relations, passivity conditions, and causality relations are derived for the macroscopic anisotropic permittivities and permeabilities. Some unusual results emerge from these derivations. Except at the low spatial and temporal frequencies where arrays generally behave as dipolar continua, the reciprocity relations and passivity conditions satisfied by the permittivities and permeabilities are coupled. In particular, the imaginary parts of the diagonal elements of the macroscopic permittivities and permeabilities need not be equal to or greater than zero even though the power dissipated by the passive inclusions is always equal to or greater than zero. This curious result remains true for a diamagnetic permeability even as the spatial propagation constant $\boldsymbol{\beta}$ approaches zero. It is the main reason for the nonexistence of a causal, spatially *nondispersive*, inverse diamagnetic (at low frequencies) permeability that satisfies the usual continuum passivity condition (imaginary parts of the diagonal elements equal to or less than zero) and approaches μ_0^{-1} as $|\omega| \to \infty$.

We also find the rather unusual theoretical result that the exact spatially dispersive permeability for the fundamental Floquet mode, unlike the exact inverse permeability for the fundamental Floquet mode, need not satisfy causality. This result stems from the necessity to use the $\boldsymbol{\mathcal{E}}$ and $\boldsymbol{\mathcal{B}}$ vectors as the primary microscopic fields in the formulation of Maxwell's macroscopic equations for electric charge-current definitions of electric and magnetic polarization.

The anisotropic theory of spatially dispersive periodic arrays is reinforced with a few examples. The initial examples determine the polarizabilities of dielectric

spheres under the generalized integral definitions of dipole moments in a plane-wave field with fixed $\boldsymbol{\beta} \to 0$, that is, the integral definitions used to formulate the spatially dispersive anisotropic theory. These integrally defined, fixed-$\boldsymbol{\beta}$ polarizabilities and their associated Clausius–Mossotti susceptibilities, unlike the point dipole Mie scattering polarizabilities and their associated Clausius–Mossotti susceptibilities [28], are shown to be causal functions that satisfy the Kramers–Kronig relations. However, unlike the exact fundamental Floquet-mode permeability and inverse permeability, which are noncausal and causal, respectively, these approximate Clausius–Mossotti permeability and inverse permeability expressed in terms of integrally defined, fixed-$\boldsymbol{\beta}$ polarizabilities are causal and noncausal, respectively.

Lastly, we numerically solve the derived equations for a 2D periodic array of circular cylinders with Drude-model dielectric inclusions. For a fixed $\boldsymbol{\beta} \to 0$, the computed macroscopic permittivity and permeability confirms the theoretical predictions that the imaginary part of the exact fundamental Floquet-mode permittivity as $\boldsymbol{\beta} \to 0$ satisfies the usual continuum passivity condition of being equal to or greater than zero for all ω, whereas the imaginary part of the exact fundamental Floquet-mode permeability as $\boldsymbol{\beta} \to 0$ satisfies the usual continuum passivity condition only at the lower frequencies but becomes negative at the higher values of ω. Moreover, we confirm that the exact fundamental Floquet-mode permittivity and exact fundamental Floquet-mode inverse permittivity satisfy causality and the Kramers–Kronig relations. In contrast, while the exact fundamental Floquet-mode inverse permeability satisfies causality and the Kramers–Kronig relations, the exact fundamental Floquet-mode permeability itself does not satisfy causality—a result that further confirms the theory.

13.7 Appendix: Causality of the Inverse of a Causal Constitutive Parameter

Consider a susceptibility function $\chi(z)$ that is holomorphic (analytic and single-valued) in the upper half ($y > 0$) of the complex $z = x + iy$ plane (UHP) and has boundary values $\chi(x)$ such that the function $\chi(x)$, which has an even real part and an odd imaginary part, is Hölder continuous and $|\chi(z) - \chi_\infty| \sim 1/|z|^\alpha$, $\alpha > 0$, as $|z| \to \infty$ for $y \geq 0$, where χ_∞ is a finite real (positive, negative or zero) constant such that $\lim_{|x|\to\infty} \chi(x) = \chi_\infty$. Also, assume that $\mathrm{Re}[\chi(0)] > \chi_\infty - 1$ and that either $x\mathrm{Im}[\chi(x)] > 0$ or $x\mathrm{Im}[\chi(x)] < 0$ except at $x = 0$ where $\mathrm{Im}[\chi(0)] = 0$ (or possibly there is a $1/x$ singularity in the $\mathrm{Im}[\chi(x)]$ at $x = 0$). We assume that any resonant singularities in $\chi(x)$ have been eliminated by insertion of a small loss, as explained in Footnote 15 of the main text. These inequalities for the real and imaginary parts of $\chi(x)$ imply that $(\chi(x) - \chi_\infty + 1) \neq 0$ for all x.

As explained in Footnote 1 of the main text, $(\chi(x) - \chi_\infty)$ is a causal function that satisfies the Kramers–Kronig relations (and thus, as explained in the

Introduction, $\chi(0) \geq [\leq] \chi_\infty$ if $x\mathrm{Im}[\chi(x)] \geq [\leq] 0$ and $\chi(\omega)$ is real and continuously differentiable near $\omega = 0$, although these conditions are not required for the proof in this Appendix). In this Appendix, we prove that $(\chi(z) - \chi_\infty + 1)$ has no zeros in the UHP and thus the function

$$\xi(x) = \frac{1}{\chi(x) - \chi_\infty + 1} - 1 \tag{13.132}$$

is also a causal function that satisfies the Kramers–Kronig relations. (For $\chi_\infty = 0$, the function $\xi(x)$ in (13.132) corresponds to the inverse of the traditional continuum relative permittivity or permeability minus 1, and in this case of $\chi_\infty = 0$, a similar result is obtained in [5, Sect. 82] using a proof given by the Russian/Israeli mathematician N. N. Meiman [4, Sect. 123].)

We first note that since the imaginary part of the Hölder continuous function $(\chi(x) - \chi_\infty + 1)$ is nonzero for all x except at $x = 0$ where the real part is greater than zero, the function $\xi(x)$ has no poles on the x axis and is Hölder continuous [2, p. 16]. Like $\chi(x)$, the real part of $\xi(x)$ is even and the imaginary part of $\xi(x)$ is odd. Also, note that since $|\chi(z) - \chi_\infty| \sim 1/|z|^\alpha$, $\alpha > 0$, as $|z| \to \infty$ for $y \geq 0$, it follows that $|\xi(z)| \sim 1/|z|^\alpha$, $\alpha > 0$, as $|z| \to \infty$ for $y \geq 0$. Thus, if it can be proven that the function $(\chi(z) - \chi_\infty + 1)$ has no zeros in the UHP, then $\xi(x)$, like $(\chi(x) - \chi_\infty)$, will be a causal function that satisfies the Kramers–Kronig relations.

To prove that $(\chi(z) - \chi_\infty + 1)$ has no zeros in the UHP, we use the theorem from complex variables that says if a function $f(z)$ be analytic inside a region D enclosed by the contour C and continuous on $D + C$, then

$$N_0 = \frac{1}{2\pi i} \int_C \frac{f'(z)}{f(z)}\, \mathrm{d}z \tag{13.133}$$

where the prime denotes differentiation with respect to the complex variable z and N_0 is the total number of zeros of $f(z)$ inside C, a zero of order m_0 being counted m_0 times [2, Eq. (7.22), p. 76] (see also [46, Sect. 113]). To use (13.133) for our purposes, we choose $f(z) = (\chi(z) - \chi_\infty + 1)$ and the closed contour C as the real line capped by the hemispherical curve in the UHP. Because $|\chi(z) - \chi_\infty| \sim 1/|z|^\alpha$, $\alpha > 0$, as $|z| \to \infty$ for $y \geq 0$, it follows that $|f'(z)/f(z)| \sim 1/|z|^{(1+\alpha)}$, $\alpha > 0$, as $|z| \to \infty$ for $y \geq 0$, and the integral in (13.133) goes to zero on the hemispherical cap, thereby leaving

$$N_0 = \frac{1}{2\pi i} \int_{-\infty}^{+\infty} \frac{f'(x)}{f(x)}\, \mathrm{d}x, \quad f(x) = \chi(x) - \chi_\infty + 1 \tag{13.134}$$

which can be re-expressed as

$$N_0 = \frac{1}{2\pi i}\int_{-\infty}^{+\infty} \ln'[f(x)]\,\mathrm{d}x = \frac{\Delta\phi}{2\pi}, \quad f(x) = \chi(x) - \chi_\infty + 1 \tag{13.135}$$

where $\Delta\phi$ is the change in the number of radians in the continuous angle $\phi = \arg[f(x)]$ as the point x changes from $-\infty$ to $+\infty$ along the real x axis.

Since the imaginary part of $f(x)$ is less [greater] than zero for $x<0$ and equal to zero for $x = 0$, and $\mathrm{Re}[f(0)] > 0$ with $f(-\infty) = 1$, the angle ϕ begins at 0 at $x = -\infty$ and ends at 0 at $x = 0$ while never crossing the real f axis in the complex f plane—thereby ϕ has no total change for the integral over the negative x axis. Similarly, since the imaginary part of $f(x)$ is greater [less] than zero for $x > 0$, and $\mathrm{Re}[f(0)] > 0$ with $f(+\infty) = 1$, the angle ϕ begins at 0 at $x = 0$ and ends at 0 at $x = +\infty$ while never crossing the real f axis in the complex f plane—thereby having no total change for the integral over the positive x axis.[18] Therefore, for the integral over the entire x axis, the change in ϕ is zero; that is, $\Delta\phi = 0$ in (13.135) and $N_0 = 0$. In other words, the number of zeros in the UHP of $\xi(z)$ is zero and thus, given the other properties of $\xi(z)$ discussed above, the function $\xi(x)$ is causal and obeys the Kramers–Kronig relations. Lastly, we observe that the theorem does not hold in general for the function

$$\frac{1}{\chi(x)+1} - \frac{1}{\chi_\infty + 1} \tag{13.137}$$

which corresponds to an inverse relative permittivity or permeability function. For example, the permeability function

$$\mu_{\mathrm{CM}}^{\mathrm{PEC}}(0, k_0 a) - \mu_{\mathrm{CM}\infty}^{\mathrm{PEC}} \tag{13.138}$$

is a causal function defined by (13.117b), whereas the inverse permeability function

$$\frac{1}{\mu_{\mathrm{CM}}^{\mathrm{PEC}}(0, k_0 a)} - \frac{1}{\mu_{\mathrm{CM}\infty}^{\mathrm{PEC}}} = \frac{1}{\mu_{\mathrm{CM}\infty}^{\mathrm{PEC}}}\left[\frac{1}{\mu_{\mathrm{CM}}^{\mathrm{PEC}}(0, k_0 a)/\mu_{\mathrm{CM}\infty}^{\mathrm{PEC}}} - 1\right] \tag{13.139}$$

is not causal because $\mu_{\mathrm{CM}}^{\mathrm{PEC}}(0,0)/\mu_{\mathrm{CM}\infty}^{\mathrm{PEC}}$ is less than zero and thus the foregoing analysis with $\mu_{\mathrm{CM}}^{\mathrm{PEC}}(0,x)/\mu_{\mathrm{CM}\infty}^{\mathrm{PEC}}$ replacing $f(x)$ yields $\Delta\phi = 2\pi$ and $N_0 = 1$ rather than 0.

[18] If the real part of $\chi(x)$ has a $\pm 1/x$ singularity at $x = 0$ the change in ϕ over both the negative and positive x axis is $\mp\pi/2$ to yield a $\Delta\phi = \mp\pi$. However, Eq. (7.22) on page 76 of [2] shows that with a $1/x$ singularity, the formula in (13.133) changes to

$$N_0 \mp \frac{1}{2} = \frac{1}{2\pi i}\int_C \frac{f'(z)}{f(z)}\mathrm{d}z \tag{13.136}$$

and thus we still find $N_0 = 0$.

Acknowledgments This research was supported in part under the U.S. Air Force Office of Scientific Research (AFOSR) grant FA 9550-12-1-0105 through Dr. A. Nachman.

References

1. Hansen TB, Yaghjian AD (1999) Plane-wave theory of time-domain fields: near-field scanning applications. IEEE/Wiley Press, Piscataway
2. Lu JK (1993) Boundary value problems for analytical functions. World Scientific, New York
3. Jeffreys H, Jeffreys BS (1956) Methods of mathematical physics, 3rd edn. Cambridge University Press, Cambridge
4. Landau LD, Lifshitz EM (1980) Statistical physics, 3rd edn, Part 1. Butterworth Heinemann, Oxford
5. Landau LD, Lifshitz EM, Pitaevskii LP (1984) Electrodynamics of continuous media, 2nd edn. Butterworth Heinemann, Oxford
6. Yaghjian AD (2007) Internal energy, Q-energy, Poynting's theorem, and the stress dyadic in dispersive material. IEEE Trans Antennas Propagat 55:1495–1505; Correction. 55:3748
7. Haus HA, Melcher JR (1989) Electromagnetic fields and energy. Prentice Hall, Englewood Cliffs
8. Shore RA, Yaghjian AD (2008) Traveling waves on two- and three-dimensional periodic arrays of lossless scatterers. Radio Science, 42:RS6S21; Correction. 43:RS2S99
9. Vleck JH (1932) The theory of electric and magnetic susceptibilities. Oxford University Press, Oxford
10. Silveirinha MG (2011) Examining the validity of the Kramers–Kronig relations for the magnetic permeability. Phys Rev B 83:165119
11. Yaghjian AD, Best SR (2005) Impedance, bandwidth, and Q of antennas. IEEE Trans Antennas Propagat 53:1298
12. Smith DR, Pendry JB (2006) Homogenization of metamaterials by field averaging. J Opt Soc Am B 23:391
13. Tsukerman I (2011) Effective parameters of metamaterials: a rigorous homogenization theory via Whitney interpolation. J Opt Soc Am B 28:577
14. Vinogradov AP, Aivazyan AV (1999) Scaling theory for homogenization of the Maxwell equations. Phys Rev E 60:987
15. Andryieuski A, Ha S, Sukhorukov AA, Kivshar YS, Lavrinenko AV (2012) Bloch-mode analysis for retrieving effective parameters of metamaterials. Phys Rev B 86:035127
16. Silin VP, Rukhadze AA (1961) Electromagnetic properties of plasmas and plasma-like media. Gosatomizdat, Moscow [in Russian]
17. Agranovich VM, Ginzburg VL (1966) Spatial dispersion in crystal optics and the theory of excitons. Wiley-Interscience, New York; also see 2nd edn (1984), Springer, New York
18. Silveirinha MG (2009) Nonlocal homogenization theory of structured materials. In: Capolino F (ed) Metamaterials handbook: theory and phenomena of metamaterials, Chap 10. CRC Press, Boca Raton
19. Silveirinha MG (2007) Metamaterial homogenization approach with application to the characterization of microstructured composites with negative parameters. Phys Rev B 75:115104
20. Silveirinha MG (2011) Time domain homogenization of metamaterials. Phys Rev B 83:165104
21. Fietz C, Shvets G (2010) Current-driven metamaterial homogenization. Physica B 405:2930
22. Silveirinha MG (2007) Generalized Lorentz-Lorenz formulas for microstructured materials. Phys Rev B 76:245117
23. Alù A (2011) First-principles homogenization theory for periodic metamaterial arrays. Phys Rev B 84:075153

24. Kong JA (1986) Electromagnetic wave theory. Wiley Press, New York
25. Raab RE, De Lange OL (2005) Multipole theory in electromagnetism. Clarendon, Oxford
26. Stratton JA (1941) Electromagnetic theory. McGraw-Hill, New York
27. Shore RA, Yaghjian AD (2012) Complex waves on periodic arrays of lossy and lossless permeable spheres: 1. Theory; and 2. Numerical results. Radio Science, 47:RS2014; and 47:RS2015
28. Alù A, Yaghjian AD, Shore RA, Silveirinha MG (2011) Causality relations in the homogenization of metamaterials. Phys Rev B 84:054305
29. Papas CH (1965) Theory of electromagnetic wave propagation. McGraw-Hill, New York (Dover 1988)
30. Robinson FNH (1973) Macroscopic electromagnetism. Pergamon Press, Oxford
31. Scott WT (1977) The physics of electricity and magnetism, 2nd edn. Robert E. Krieger, Huntington
32. Maxwell JC (1891) A treatise on electricity and magnetism, 3rd edn, vol 1 and 2. Dover (1954), New York
33. Yaghjian AD, (1980) Electric dyadic Green's functions in the source region. Proc IEEE 68:248; see also Yaghjian AD, (1981) Proc IEEE 69:282
34. Jackson JD (1998) Classical electrodynamics, 3rd edn. Wiley, New York
35. Silveirinha MG (2009) Poynting vector, heating rate, and stored energy in structured materials: a first-principles derivation. Phys Rev B 80:235120
36. Silveirinha MG, Costa JT, Alù A (2011) Poynting vector in negative-index metamaterials. Phys Rev B 83:165120
37. Drude P (2005) (1902) The theory of optics. Dover, Longmans, New York
38. Yaghjian AD (2010) Extreme electromagnetic boundary conditions and their manifestation at the inner surfaces of spherical and cylindrical cloaks. Metamaterials 4:70
39. Silveirinha MG, Fernandes CA (2007) Transverse-average field approach for the characterization of thin metamaterial slabs. Phys Rev E 75:036613
40. Simovski CR, Tretyakov SA (2007) Local constitutive parameters of metamaterials from an effective-medium perspective. Phys Rev B 75:195111
41. Scher AD, Kuester EF (2007) Boundary effects in the electromagnetic response of a metamaterial in the case of normal incidence. PIER B 14:341
42. Agranovich VM, Shen YR, Baughman RH, Zakhidov AA (2004) Linear and nonlinear wave propagation in negative refraction metamaterials. Phys Rev B 69:165112
43. Mirsky L (1955) An introduction to linear algebra. Oxford University Press, Oxford
44. Simovsky CR (2008) Analytical-modeling of double-negative composites. Metamaterials 2:169
45. Costa JT, Silveirinha MG, Maslovski SI (2009) Finite-difference frequency-domain method for the extraction of the effective parameters of metamaterials. Phys Rev B 80:235124
46. Churchill RV (1960) Complex variables and applications, 2nd edn. McGraw-Hill, New York

Chapter 14
Transformation Electromagnetics and Non-standard Devices

André de Lustrac, Shah Nawaz Burokur and Paul-Henri Tichit

Abstract The use of transformation electromagnetics for microwave applications is presented. Implementation of non-standard devices such as microwave antennas and waveguide tapers proposed by the Institut d'Electronique Fondamentale at the University of Paris-Sud are reviewed. The operating principle and the respective coordinate transformation of each device is presented and numerical simulations are performed to verify the theoretical formulations. The method to obtain constitutive electromagnetic parameters mimicking the calculated transformed space is detailed and confirmed by full-wave simulations performed using discrete material parameter values and by measurements performed on fabricated metamaterial-based prototypes. The results show that transformation electromagnetics is very interesting for the design and realization of high-performance non-standard devices.

14.1 Introduction

The concept of transformation electromagnetics originally introduced by Pendry [1] and Leonhardt [2] provides a method for designing new electromagnetic systems by controlling the permeability and permittivity distributions. It allows control over the path of electromagnetic waves in the structure in a manner unattainable with natural materials. However, the practical realization of these structures remains a challenge without the use of the extremely successful concept

A. de Lustrac (✉) · S. N. Burokur · P.-H. Tichit
Institut d'Electronique Fondamentale, Univ Paris-Sud,
CNRS UMR 8622 91405 Orsay, France
e-mail: andre.de-lustrac@u-psud.fr

S. N. Burokur
e-mail: shah-nawaz.burokur@u-psud.fr

P.-H. Tichit
e-mail: paul-henri.tichit@u-psud.fr

D. H. Werner and D.-H. Kwon (eds.), *Transformation Electromagnetics and Metamaterials*, DOI: 10.1007/978-1-4471-4996-5_14,

of metamaterials. The first example of this successful merging was the design and experimental characterization of an invisibility cloak in 2006 [3]. Later, other versions of cloaks have been proposed at microwave and optical frequencies. These invisibility cloaking structures [4–12] can serve as benchmark examples for the development of microwave and optical systems based on transformation electromagnetics. In recent years, the combination of transformation optics and metamaterials has led to non-standard electromagnetic systems. Proposals for new devices such as concentrators [13–15], electromagnetic wormholes [16, 17], transitions between waveguides and bends [18–23], and planar antennas [24] have been explored theoretically. Experiments and demonstrations of the space transformation of several devices have later been published [3, 6, 7, 9, 11, 12, 25, 26]. Indeed, practical implementation of transformation optics devices requires the design and use of anisotropic metamaterials with high accuracy as well as trade-offs between theoretical design and realization.

Although the concept was well known for many years [27, 28], the introduction of transformation electromagnetics in 2006 has helped to bring back the correspondence between geometry and materials. In this way, the material can be considered as a new geometry, and information about the coordinate transformation is given by material properties. Based on the reinterpretation of the form-invariance of Maxwell's equations against coordinate transformation, arbitrary control of the electromagnetic field has become possible by introducing a specific coordinate transformation that maps an initial space into another one containing the imagined (or desired) properties. Among the classes of transformations in the literature, several possibilities are available for the design of electromagnetic structures. For example, continuous transformations were introduced by Pendry to realize the first invisibility cloak, which led to anisotropic and inhomogeneous permittivity and permeability tensors. Continuous transformations offer a substantial advantage in their generality of application. The contribution of these transformations was leveraged in many cases as cited above. In parallel, Leonhardt proposed the concept of conformal mappings [2] where transformations obey Fermat's principle and allow the design of devices through the use of isotropic dielectric media [20, 29–31]. The main drawback of these transformations is that their mathematical requirements are often too complex to realize the systems. Following this idea, quasiconformal transformations [6, 8, 9, 11, 12, 32] have emerged, where a slight deformation of the transformation minimizes the anisotropy of the material and allows an approximation of the device with an isotropic medium. Other theoretical works have appeared on space–time transformations [33–36], creating a link with cosmology and celestial mechanics [37–39]. Simultaneously, the concept of finite embedded transformations [13, 21, 22, 40–42] was introduced, which significantly added to design flexibility and enabled steering or focusing electromagnetic waves. Finally, source transformation techniques [43–46] have offered new opportunities for the design of active devices with a source distribution included in the transformed space.

The design stage is very important; first, because the theoretical values of electromagnetic parameters calculated by transformation optics are often too extreme to be practically realized. Therefore, a careful design should allow a simplification of

these values. Moreover, in some cases, the permittivity and permeability tensors have non-diagonal terms that are difficult to implement. To facilitate the realization of structures, it is important to minimize or cancel these terms. In all cases, for a real device, the parameter values should be achievable with available electromagnetic metamaterials. Second, a practical implementation requires a discretization of the theoretical material. This discretization, which is often accompanied by performance degradation, must maintain the degradation to an acceptable level. A trade-off is necessary between the level of discretization and the degradation of structure performance due to this discretization. The space transformation technique can also be used to transform a singular profile of an isotropic material in a regular pattern into an equivalent anisotropic material, leading to a more easily realizable device. For example, dielectric singularities are points where the refractive index n tends toward infinity or zero and electromagnetic waves travel infinitely slow or infinitely fast. Such singularities cannot be realized in practice over a broad spectral range, but the index profile can be transformed into an anisotropic tensor of permittivity and permeability. For example, Ma et al. [47] have succeeded in implementing an omnidirectional retro-reflector through the transformation of a singularity in the index profile into a topological defect. Thus, bounded values of the permittivity and permeability components allowed the realization of the device.

After the discretization of a theoretical profile, the next metamaterial engineering step is to approach and implement the target device. Based on the electric and magnetic resonances, subwavelength metamaterial cells must be properly designed such that the effective electromagnetic parameters can reach desired values.

In the following sections, the transformation electromagnetics technique is applied to four systems: first, the case discussed is of a highly directive antenna by transforming an isotropic one. Then, the case of wave bending in a steerable antenna is addressed. Another antenna application concerning the transformation of a directive emission into an isotropic one is also discussed. Finally, a taper between two waveguides with different widths is proposed and it is shown how it is possible to connect them so as to have a transmission close to unity.

14.2 Highly Directive Antenna

This section deals with the design of a highly directive antenna based on the transformation of an isotropic source radiating in a cylindrical space into a directive antenna radiating in a rectangular space. This begins by deriving the permeability and permittivity tensors of a metamaterial capable of transforming the isotropic source into a compact highly directive antenna in the microwave domain. The aim is to show how a judiciously engineered metamaterial allows the direction of emission of a source to be controlled in order to collect all the energy in a small angular domain around the surface normal, with good impedance matching between the radiating source and the material obtained by transformation optics.

14.2.1 Theoretical Formulation

For the theoretical formulation of the highly directive emission, consider a line source radiating in a cylindrical vacuum space (Fig. 14.1). The line source is placed along the cylindrical axis. Wavefronts represented by cylinders at $r =$ constants and polar coordinates (r, θ) are appropriate to describe such a problem. To transform the cylindrical space, a physical one where lines $\theta =$ constant become horizontal is generated, as illustrated by the schematic principle in Fig. 14.1. Each colored circle of the cylindrical space becomes a vertical line having the same color in the rectangular space, whereas each radial line becomes a horizontal one. Finally, the right half cylinder of diameter d is transformed into a rectangular region with width e and length L. The line source in the center of the cylinder becomes the left black vertical radiating surface in the rectangular space. The transformation can then be expressed as:

$$\begin{cases} x' = \frac{2L}{d}\sqrt{x^2+y^2} \\ y' = \frac{e}{\pi}\arctan\left(\frac{y}{x}\right) \\ z' = z \end{cases} \text{ with } -\frac{\pi}{2} \le \arctan\left(\frac{y}{x}\right) \le \frac{\pi}{2} \tag{14.1}$$

where x', y', and z' are the coordinates in the transformed rectangular space and x, y, and z are those in the initial cylindrical space. Free space is assumed in the cylinder, with isotropic permeability and permittivity tensors ε_0 and μ_0. The following transformations are used to obtain the material parameters of the rectangular space:

$$\varepsilon^{i'j'} = \frac{J_i^{i'} J_j^{j'} \varepsilon_0 \delta^{ij}}{\det(J)} \text{ and } \mu^{i'j'} = \frac{J_i^{i'} J_j^{j'} \mu_0 \delta^{ij}}{\det(J)} \text{ with } J_\alpha^{\alpha'} = \frac{\partial x'^\alpha}{\partial x^\alpha} \tag{14.2}$$

where $J_\alpha^{\alpha'}$ and δ^{ij} are respectively the Jacobian transformation matrix of the transformation of (14.1) and the Kronecker symbol. The Jacobian matrix between the transformed and the original coordinates has four nonzero parameters which depend on the distance from the origin. J_{xx}, J_{yy}, J_{xy} are assumed to be z-independent with $J_{zz} = 1$. The divergence of J_{yy} can be explained by the non-bijection of the initial coordinates y-lines transformation. The inverse transformation is obtained from the initial transformation (14.1) and derived by a substitution method, enabling the metamaterial design which leads to anisotropic permittivity and permeability tensors. Both electromagnetic parameters μ and ε have the same behavior. Also, note that the equality of permittivity and permeability tensors implies a perfect impedance match with no reflection at the interface with vacuum.

By substituting the new coordinate system in the tensor components, and after some simplifications, the following material parameters are derived:

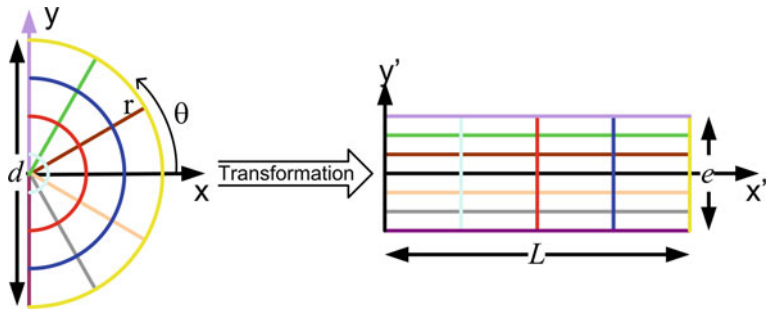

Fig. 14.1 Representation of the transformation of the initial space into the desired space. Each radius line of the cylindrical space is transformed into a horizontal line of the right rectangular space. Each circular line is transformed into a vertical one. Reprinted with permission from Journal of Applied Physics, 2009. 105(10) 104912. Copyright 2009, American Institute of Physics

$$\begin{aligned}\overline{\overline{\varepsilon}} &= \begin{pmatrix} \varepsilon_{xx}(x',y') & 0 & 0 \\ 0 & \varepsilon_{yy}(x',y') & 0 \\ 0 & 0 & \varepsilon_{zz}(x',y') \end{pmatrix} \varepsilon_0 \\ \overline{\overline{\mu}} &= \begin{pmatrix} \mu_{xx}(x',y') & 0 & 0 \\ 0 & \mu_{yy}(x',y') & 0 \\ 0 & 0 & \mu_{zz}(x',y') \end{pmatrix} \mu_0 \end{aligned} \tag{14.3}$$

where

$$\varepsilon_{xx}(x',y') = \mu_{xx}(x',y') = \frac{\pi}{e}x' \quad \varepsilon_{yy}(x',y') = \mu_{yy}(x',y') = \frac{1}{\varepsilon_{xx}(x',y')}$$

$$\varepsilon_{zz} = \mu_{zz} = \frac{d^2\pi}{4eL^2}x'. \tag{14.4}$$

The appropriate choice of the transformation thus assures an absence of non-diagonal components, giving rise to a practical implementation of the device using metamaterials. Figure 14.2 shows the variation of the permittivity tensor components in the transformed rectangular space. The different geometrical dimensions of the initial and transformed space are respectively $d = 15$ cm, $e = 15$ cm, and $L = 5$ cm. Note that the three components of the permittivity depend only on the coordinate x'. This is due to the invariance of the initial space with θ with respect to the distance from the source in the cylindrical space. This distance is represented by x' in the transformed rectangular space.

The divergence of ε_{yy} near $x' = 0$ creates an "electromagnetic wall" with ε_{yy} tending toward infinity on the left side of the rectangular area. This left side also corresponds to the radiating source transformed from the center line source of the cylindrical space. Note the simplicity of the ε_{xx} and ε_{zz} terms that present only a linear variation.

In the transformed rectangular space the confinement of the electromagnetic field can be controlled and increased by the different parameters d, e, and L, and

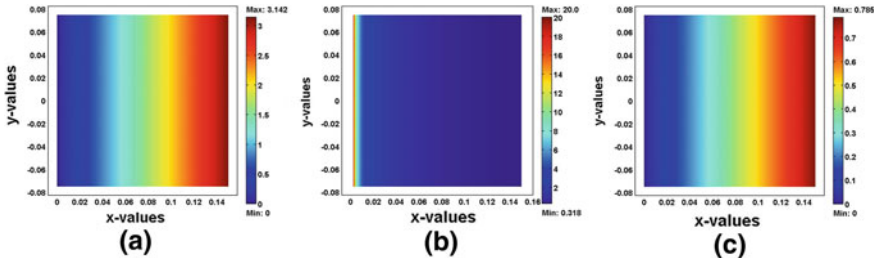

Fig. 14. 2 Variation of the permittivity tensor components: **a** ε_{xx}, **b** ε_{yy}, and **c** ε_{zz}. Reprinted with permission from Journal of Applied Physics, 2009. 105(10) 104912. Copyright 2009, American Institute of Physics

particularly by the ratio $d/2L$. After the transformation, the electromagnetic energy enclosed in the half cylindrical space is confined in the rectangular space. To characterize the emission directivity realized by the radiating source in the rectangular space, the most important parameter is the ratio between the width e of the aperture and the square of the wavelength λ^2 since the maximum directivity of an antenna is given by:

$$D_{\max} = \frac{4\pi A_{\text{eff}}}{\lambda^2} \text{ where } A_{\text{eff}} = \frac{\left|\int_A \int E_a(r)\mathrm{d}S\right|^2}{\int_A |E_a(r)|^2 \mathrm{d}S} \tag{14.5}$$

where A_{eff} is the effective aperture of the antenna and depends on the width e and on the field distribution $E_a(r)$.

14.2.2 Numerical Simulations

Finite Element Method (FEM)-based numerical simulations with Comsol Multiphysics are used to design this transformed directive antenna. As the line source of the right half-cylindrical space becomes a radiating plane in the transformed rectangular space, an excitation is inserted at the left side of the rectangular space as shown in Fig. 14.3a. This space is delimited by metallic boundaries on the upper and lower sides and at the left side of the rectangular space representing the metamaterial having dimensions 15 × 5 cm. The radiating properties of the antenna are calculated and presented in Fig. 14.3.

Three operating frequencies have been considered here; 5, 10, and 40 GHz, corresponding respectively to $e/\lambda = 2.5$, 5 and 20. A directive emission can be observed as illustrated by the magnetic field radiations of the antenna for a TM wave polarization. A very high directivity is noted and can be calculated using the expression given in [48]:

$$D = \frac{41253}{(\theta_1 \theta_2)} \tag{14.6}$$

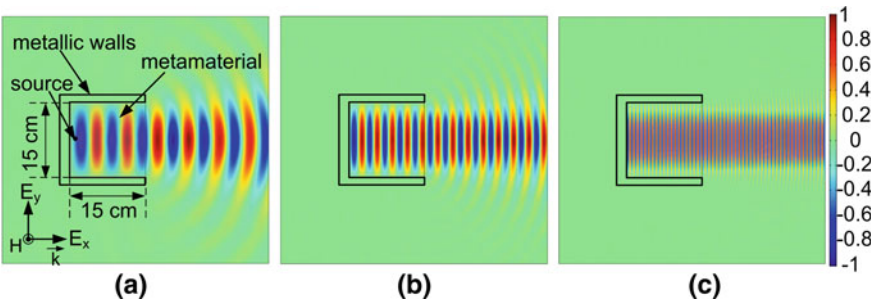

Fig. 14.3 Magnetic field distribution for a TM wave polarization at (**a**) 5 GHz, (**b**) 10 GHz, and (**c**) 40 GHz. Reprinted with permission from Journal of Applied Physics, 2009. 105(10) 104912. Copyright 2009, American Institute of Physics

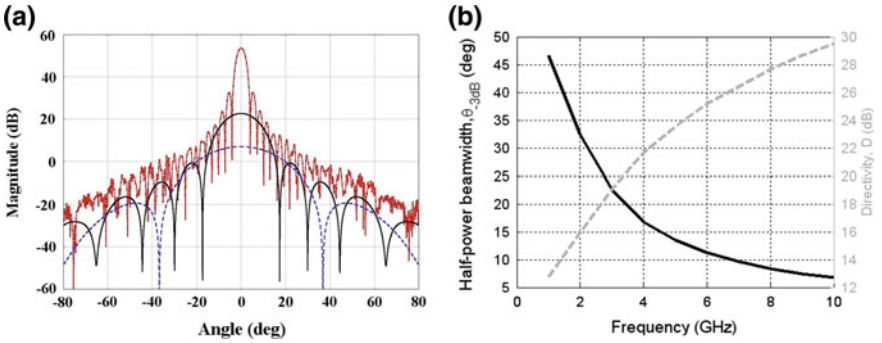

Fig. 14.4 **a** Far-field radiation patterns at 5 GHz (*dashed*), 10 GHz (*continuous*), and 40 GHz (*dashed-dotted*). **b** Half-power beamwidth (*continuous*) and directivity (*dashed*) versus frequency. Reprinted with permission from Journal of Applied Physics, 2009. 105(10) 104912. Copyright 2009, American Institute of Physics

where θ_1 and θ_2 are respectively the half-power beamwidths (in degrees) for the H-plane and E-plane patterns. Here, assume $\theta_1 = \theta_2$. Then for a half-power beamwidth of 13.5° at 10 GHz a directivity of 23.6 dB is obtained, implying a ratio $e/\lambda = 5$. This directivity is comparable with that of a parabolic reflector antenna of the same size [48] and is greater than that of a wideband [2–18 GHz] dual polarized FLANN® horn antenna where the directivity varies from 10 to 23 dB.

The far-field radiation patterns of the antenna are calculated at different frequencies to assess the variation of the directivity. The dimensions of the rectangular box remain the same as above ($e = 15$ cm and $L = 5$ cm). Figure 14.4a shows the radiation patterns for the cases $e/\lambda = 2.5$ (5 GHz), 5 (10 GHz), and 20 (40 GHz). The directivity strongly increases as the frequency increases. It goes from 23.6 dB at 5 GHz to 29.5 dB at 10 GHz and 42 dB at 40 GHz. The directivity enhancement is illustrated by the evolution of the half-power beamwidth versus frequency in Fig. 14.4b.

14.2.3 Parameter Reduction and Discrete Metamaterial Layers

The metamaterial calculated above shows coordinate-dependent electromagnetic parameters following (14.4). This dependency is identical for the permittivity and permeability, allowing an exact impedance matching with vacuum. It is proposed to simplify the calculated parameters of the highly directive antenna for a realistic experimental realization from achievable metamaterial structures. Choosing plane wave solutions for the electric field and magnetic field, with a wave vector $\boldsymbol{k}$ in the x–y plane, and a TM or a TE polarization with respectively the magnetic or electric field polarized along the z-axis, a dispersion equation is obtained:

$$\det(F) = 0 \tag{14.7}$$

with

$$F = \begin{pmatrix} \varepsilon_{xx} - \frac{k_y^2}{\mu_{zz}} & \frac{-k_x k_y}{\mu_{zz}} & 0 \\ \frac{-k_x k_y}{\mu_{zz}} & \varepsilon_{yy} - \frac{k_x^2}{\mu_{zz}} & 0 \\ 0 & 0 & \varepsilon_{zz} - \frac{k_x^2}{\mu_{yy}} - \frac{k_y^2}{\mu_{xx}} \end{pmatrix}. \tag{14.8}$$

The determinant of this equation must be equal to zero. Solving it, one equation is obtained for each polarization. In the TE polarization this equation can be written as

$$\epsilon_{zz} = \frac{k_x^2}{\mu_{yy}} + \frac{k_y^2}{\mu_{xx}} \tag{14.9}$$

whereas in the TM polarization, it becomes:

$$\mu_{zz} = \frac{k_x^2}{\epsilon_{yy}} + \frac{k_y^2}{\epsilon_{xx}}. \tag{14.10}$$

For a possible realization, the dimensions of the semi-cylindrical space must be set so that $d^2/4L^2 = 4$ in order to obtain achievable values for the electromagnetic parameters. An additional simplification arises from the choice of the polarization of the emitted wave. Here, consider a polarized electromagnetic wave with an electric field pointing in the z-direction, which allows for modifying the dispersion equation in order to simplify the electromagnetic parameters without changing Maxwell's equations and propagation in the structure. To obtain these electromagnetic parameters values that are suitable for the manufacturing technology, the same method is used as proposed in [3]. The dispersion equation is multiplied by $xx\mu$ and the metamaterial is thus simply described by:

$$\begin{cases} \mu_{xx} = 1 \\ \mu_{yy} = \frac{1}{\varepsilon_{xx}^2} \\ \varepsilon_{zz} = 4\varepsilon_{xx}^2 \end{cases}. \tag{14.11}$$

Equation (14.11) describes the material parameters that can be achieved with existing metamaterial structures, for example, split ring resonators (SRR) [49] and electric-LC (ELC) resonators [50].

The penalty of the above reduction is an imperfect impedance match at the outer boundary of the metamaterial at $Z = \sqrt{\frac{\mu_{yy}}{\varepsilon_{zz}}}(x = L) = \frac{9}{2\pi^2}$ with $L = 5$ cm and $d = 15$ cm. Thus, the transmission at the outer boundary is calculated classically with$T = \frac{4Z}{(1+Z)^2} = 0.85$ which assures a high level of radiated electromagnetic field. Further simplification consists in discretizing the desired variation of the parameters μ_{yy} and ε_{zz} to secure a practical realization that produces experimental performances close to theory.

Figure 14.5a shows the schematic structure of the directive emission antenna. A microstrip patch antenna on a dielectric substrate constitutes the radiating source. A surrounding material made of alternating electric metamaterial and magnetic metamaterial layers transforms the isotropic emission of the patch antenna into a directive one. The material is composed of five different regions where permittivity and permeability vary according to the profile of Fig. 14.5c. The corresponding reduced magnetic and electric properties of the metamaterial obtained from transformation optics are presented in Fig. 14.5b and c. The distribution of the theoretical material parameters satisfying relation (14.11) is shown in Fig. 14.5b. The distribution in Fig. 14.5c presents the discrete values corresponding to the five regions of the metamaterial used for the experimental validation. To implement the material specifications in Eq. (14.11) using metamaterials, one must choose the overall dimensions, design the appropriate unit cells, and specify their layout. For this implementation, the metamaterial unit cell is not periodic. It is advantageous to optimize the three design elements all at once since common parameters are shared. Equation (14.11) shows that the desired ultra-directive emission will have constant μ_{xx}, with ε_{zz} and μ_{yy} varying longitudinally throughout the structure. The axial permittivity ε_{zz} and permeability μ_{yy} show values ranging from 0.12 to 4.15 and from 1.58 to 15.3, respectively.

As shown by the schematic structure of the antenna in Fig. 14.5a, a square copper patch is printed on a 0.787 mm thick low-loss dielectric substrate (Rogers RT/Duroid 5870^{TM} with 17.5 μm copper cladding, $\varepsilon_r = 2.33$ and $\tan\delta = 0.0012$) and used as the feed source. The metamaterial covers completely the patch feed source to capture the emanating isotropic radiation and transform it into a directive pattern. The metamaterial is a discrete structure composed of alternating layers with anisotropic permeability and permittivity. Figure 14.6 shows photography of the fabricated antenna device. The bulk metamaterial was built from 56 layers of dielectric boards on which subwavelength resonant structures are printed. 28 layers contain artificial magnetic resonators and 28 electric ones. Each layer is made of five regions of metamaterials corresponding to the discretized values of Fig. 14.5c. The layers are mounted two-by-two with a constant air spacing of 2.2 mm between each, in order to best represent the permeability and permittivity characteristics in the different regions. Overall dimensions of the antenna are $15 \times 15 \times 5$ cm.

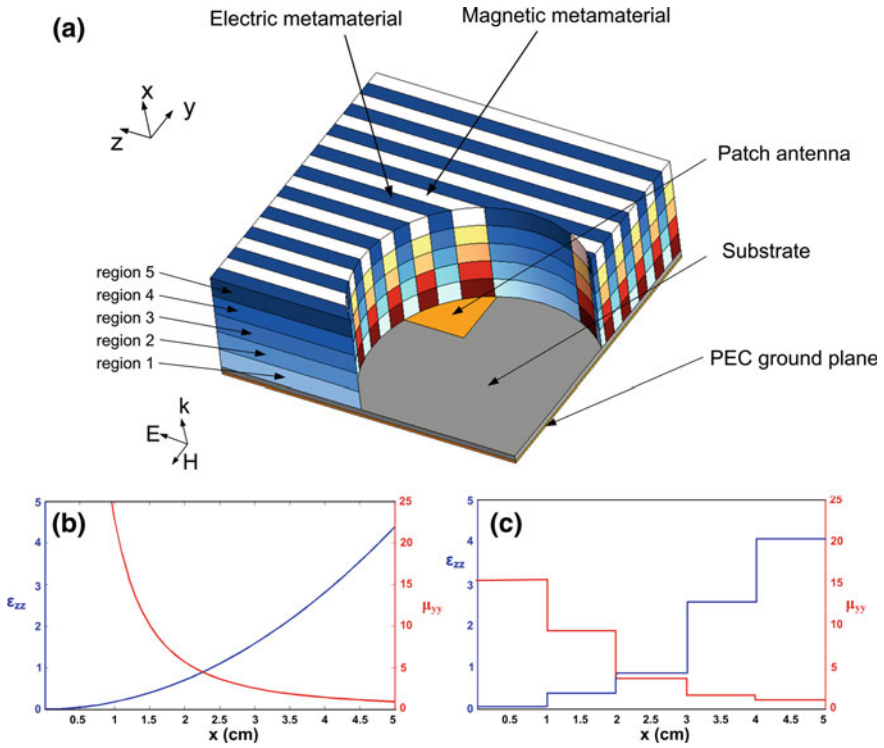

Fig. 14.5 **a** Schematic structure of the proposed antenna with a cylindrical cut to show the internal structure of the material and the radiating source. This source is a microstrip patch antenna on a dielectric substrate. The metamaterial is composed of alternating permittivity and permeability vertical layers. Each layer is made of five different material regions (*pale color* near the patch to *dark color* in the *x*-direction). **b** Theoretical material parameters given by relation (14.11). **c** Discrete values of material parameters used in experimental realization

The details of the metamaterial cells are illustrated in Fig. 14.6. The left and right inserts show the designs of the resonators used in the magnetic (right) and electric (left) metamaterial layers. The layers are divided into five regions in the direction of wave propagation. Each region is composed of three rows of resonators with identical geometry and dimensions. Different resonators are used for electric and magnetic layers. Their schematic drawings are depicted at the bottom of Fig. 14.6.

The permeability (μ_{yy}) and permittivity (ε_{zz}) parameter sets plotted in Fig. 14.5c can be respectively achieved in a composite metamaterial containing SRRs and ELCs, known to provide respectively a magnetic response and an electric response that can be tailored (Fig. 14.6). Because of layout constraints, a rectangular unit cell with dimensions $p_x = p_z = 10/3$ mm was chosen for both resonators. The layout consisted of five regions, each of which was three unit cells long (10 mm). The desired ε_{zz} and μ_{yy} were obtained by tuning the resonators'

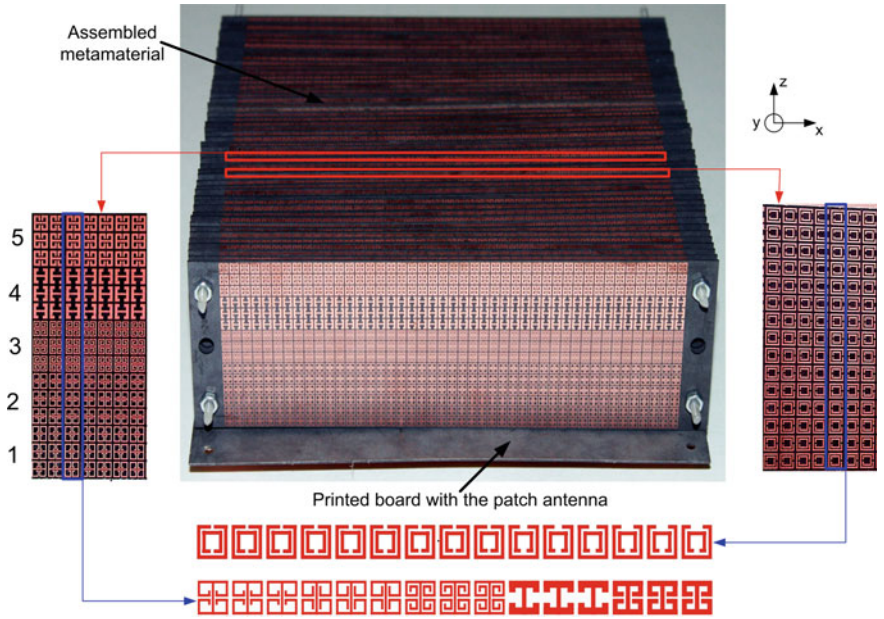

Fig. 14.6 Structure of the antenna: each magnetic and dielectric layer of the metamaterial is divided into five regions to assure the desired variations of electromagnetic parameters along wave propagation direction. The dimensions of the antenna are $15 \times 15 \times 5$ cm. The operating frequency is 10.6 GHz. *Left* and *right* inserts show details of the resonators used in the magnetic (*right*) and electric (*left*) metamaterial layers. Each level is made of three rows of identical resonators

geometric parameters. Using the Ansoft HFSS commercial full-wave finite element simulation software, a series of scattering (S) parameter simulations were performed for the SRR and ELC unit cells separately over a discrete set of the geometric parameters covering the range of interest. A normally incident wave impinging on the unit cell is considered for simulations. Electric and magnetic symmetry planes are applied on the unit cell respectively for the faces normal to the electric and magnetic field vector. By calculating the unit cells separately, there is very low coupling between neighboring ELCs and SRRs. The influence of this coupling is even lower when the electric and magnetic layers are mounted two-by-two. A standard retrieval procedure was then performed to obtain the effective material properties ε_{zz} and μ_{yy} from the S-parameters [51]. The discrete set of simulations and extractions was interpolated to obtain the particular values of the geometric parameters that yielded the desired material properties plotted in Fig. 14.5c. Simulations were also performed using Comsol Multiphysics to assure the functionality of the metamaterial. An operating frequency around 10 GHz was chosen, which yields a reasonable effective medium parameter $\lambda/p_x > 10$, where λ is the free-space wavelength.

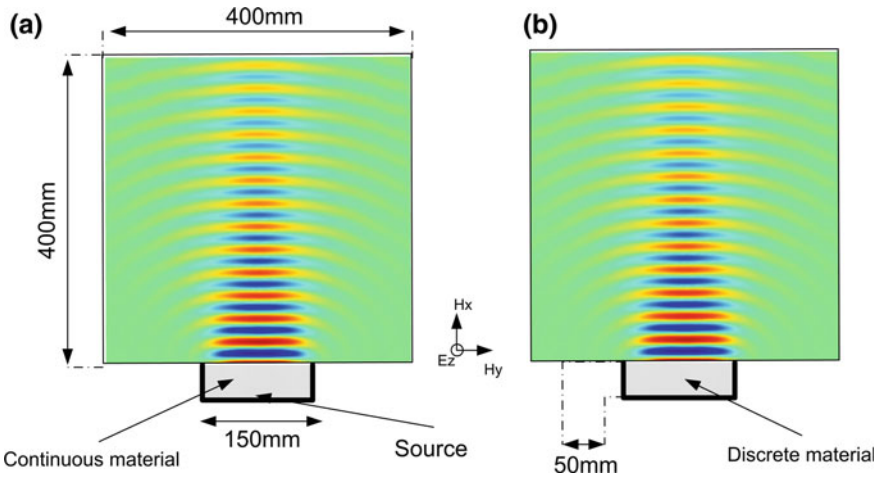

Fig. 14.7 Full-wave finite element simulations of electric fields emitted by the metamaterial antenna. Calculations are performed using the continuous and discrete materials in a 2D configuration using a line source as excitation. **a** Continuous material. **b** Discrete material

In the designs presented in Figs. 14.5 and 14.6, the SRRs and ELCs are used to realize the continuous-material properties required by the directive antenna. To illustrate the equivalence between continuous materials and the actual combination of SRR and ELC metamaterials, simulations were performed of the ideal antenna composed of continuous materials and the experimental antenna composed of SRR and ELC metamaterials, simultaneously and their electromagnetic properties compared. However, full-wave simulation of the experimental antenna is impossible using current computer resources owing to the extremely large memory and computer time required. Instead, full-wave simulations were done using the equivalent discrete material with parameters as shown in Fig. 14.5c. The full-wave simulations have been performed using the finite element method-based commercial software Comsol Multiphysics. Also, the simulations have been made in a 2D configuration using the RF module in a transverse electric (TE) wave propagation mode. A surface current with similar dimensions to the patch feed is used to model the source. The diagram pattern of the antenna is plotted by inserting matched boundaries with far-field conditions. For the metamaterial, values of permittivity and permeability shown in Fig. 14.5 have been introduced in each of the five layers. Figure 14.7 shows simulation results of the electric field emanating from the antenna in both the continuous and discrete material cases. Excellent qualitative agreement is observed from the simulations, indicating that the SRR-ELC combination presents nearly the same electromagnetic parameters as the continuous material. As observed, the intensity of emitted radiation decreases rapidly since the source transformation operates only in the x–y plane.

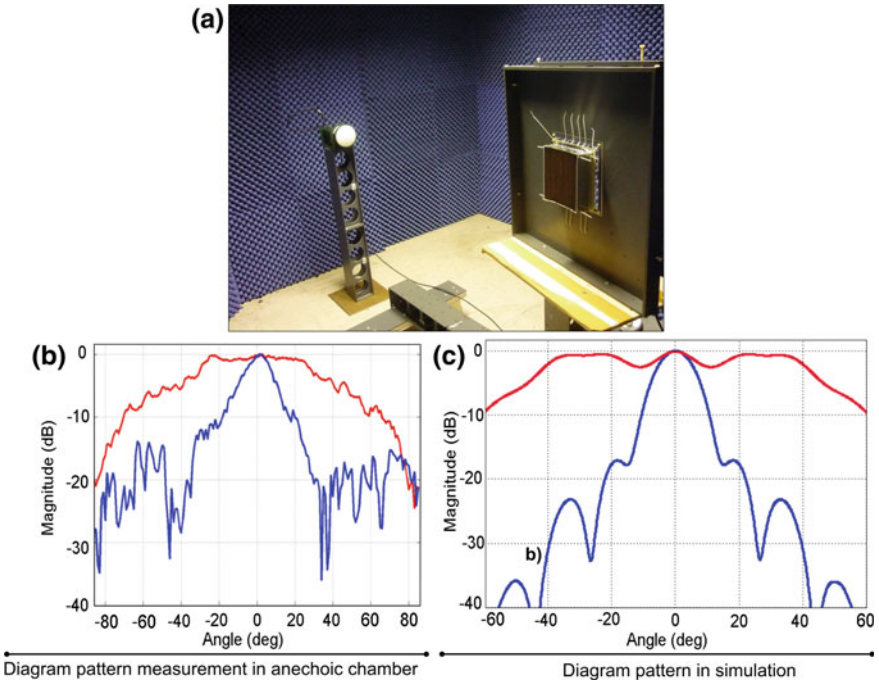

Fig. 14.8 Far-field measurement in an anechoic chamber. **a** Experimental setup. **b** Measurements. **c** Simulations. Radiation patterns of the metamaterial antenna (*blue trace*) and of the feeding microstrip patch antenna alone (*red trace*) are presented at 10.6 GHz

14.2.4 Experimental Measurement of the Ultra-Directive Antenna

To validate the directive emission device performance, two experimental systems are set up to measure the radiated field. The first method consists in measuring the far-field radiation patterns of the antenna in an anechoic chamber. Figure 14.8a shows the far-field measurement system. In such an emission-reception setup, the fabricated metamaterial antenna is used as an emitter and a wideband (2–18 GHz) dual-polarized horn antenna is used as the receiver to measure the radiated power level of the radiating antenna. The measurements are performed for computer-controlled elevation angle varying from −90° to +90°. The microwave source is a vector network analyzer (Agilent 8722 ES) that was also used for detection. The feeding port is connected to the metamaterial antenna by means of a coaxial cable, whereas the detecting port is connected to the horn antenna also by means of a coaxial cable. The measured far-field radiation pattern in the E-plane (plane containing E and k vectors) is presented in Fig. 14.8b.

The antenna presents maximum radiated power at 10.6 GHz with a directive main beam and low parasitic secondary lobes, under −15 dB. The main lobe

presents a 13° half-power beamwidth in the E-plane (x–y plane). This narrow beamwidth is less than that of a parabolic reflector antenna having similar dimensions (diameter equal to 15 cm), where the half-power beamwidth is around 16°. Measurements are found to be consistent with the predicted radiation patterns shown in Fig. 14.8c.

The second experimental setup (Fig. 14.9a) was intended to measure the antenna's near-field microwave radiation. The E-field is scanned by a field-sensing monopole probe connected to the network analyzer by a coaxial cable. The probe was mounted on two orthogonal linear translation stages (computer-controlled Newport MM4006), so that the probe could be translated with respect to the radiation region of the antenna. By stepping the field sensor in small increments and recording the field amplitude and phase at every step, a full 2D spatial field map of the microwave near-field pattern could be acquired in the free-space radiation region.

The total scanning area covers 400 × 400 mm^2 with a lateral step resolution of 2 mm in the dimensions shown by red arrows in Fig. 14.9a. Microwave absorbers are applied around the measurement stage in order to suppress undesired scattered radiations at the boundaries. Figure 14.9 shows the comparison between simulations and experimental results. In Fig. 14.9b, the magnitude of the numerical Poynting vector interpreted as an energy flux for the electromagnetic radiation is plotted for the device and compared to measurements in Fig. 14.9c. As stated earlier, the emission decreases rapidly since only the x–y plane has been considered for the source transformation procedure. A clear directive emission is radiated by the antenna as presented by the numerical simulation in Fig. 14.9d and measurement presented in Fig. 14.9e for the electric near-field mapping of the antenna's radiation. Also, when compared to the radiation of the patch feed alone shown in Fig. 14.9f and g, the narrow beam profile of the proposed device can be seen.

14.3 Azimuthal Antenna

Following the previous example, a two-dimensional coordinate transformation is now proposed which transforms the vertical radiation of a directive plane source into a directive azimuthal emission.

14.3.1 Design Concept

Consider a source radiating in a rectangular space. In theory, the radiation emitted from this source can be transformed into an azimuthal pattern using transformation optics. The transformation procedure is denoted $F(x',y')$ and consists of bending the radiation. Figure 14.10 shows the operating principle of this rotational coordinate transformation. Mathematically, $F(x',y')$ can be expressed as:

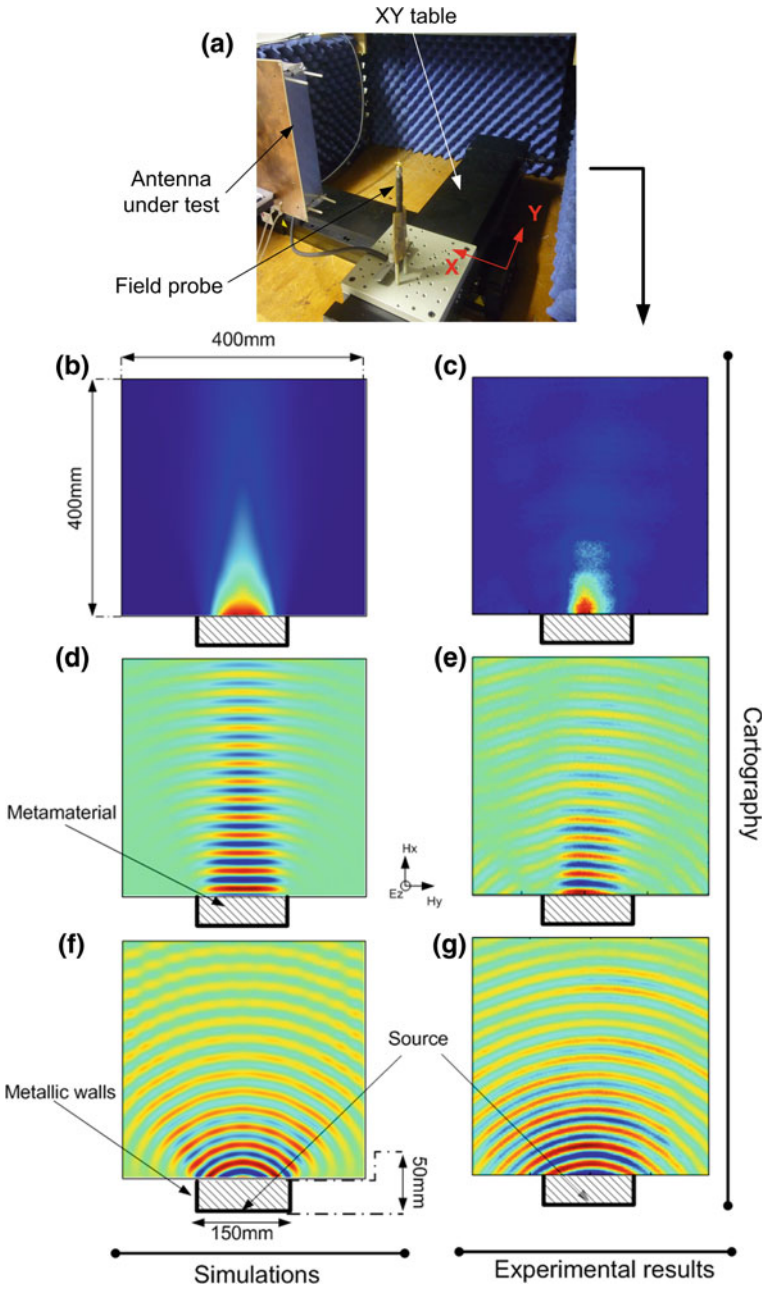

Fig. 14.9 Near-field scanning experiment in comparison with simulations. **a** Experimental setup system. **b** Magnitude of the predicted Poynting vector. **c** Magnitude of the experimental Poynting vector. **d** Magnitude of the predicted near field. **e** Mapping of the near field. **f** Magnitude of the excitation source's predicted near field. **g** Mapping of the excitation source's near field. The mappings are shown at 10.6 GHz

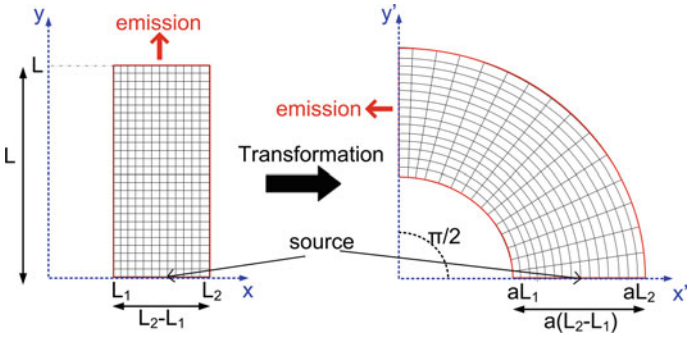

Fig. 14.10 Schematic principle of the 2D rotational coordinate transformation. The emission in a rectangular space is transformed into an azimuthal one

$$\begin{cases} x' = ax\cos(by) \\ y' = ax\sin(by) \\ z' = z \end{cases} \tag{14.12}$$

where x', y', and z' are the coordinates in the bent space, and x, y, and z are those in the initial rectangular space. The initial space is assumed to be free space. L_2, L_1, and L are, respectively, the width and the length of the rectangular space. The rotational transformation of Fig. 14.10 is defined by parameter a considered as an "expansion" parameter and parameter b which controls the rotation angle of the transformation F(x',y'). By substituting the new coordinate system in the tensor components, and after some simplifications, the material parameters are derived. After diagonalization, calculations lead to permeability and permittivity tensors given in the diagonal base by:

$$\begin{aligned} \overline{\overline{\varepsilon}} &= \begin{pmatrix} \psi_{rr} & 0 & 0 \\ 0 & \psi_{\theta\theta} & 0 \\ 0 & 0 & \psi_{zz} \end{pmatrix} \varepsilon_0 \\ \overline{\overline{\mu}} &= \begin{pmatrix} \psi_{rr} & 0 & 0 \\ 0 & \psi_{\theta\theta} & 0 \\ 0 & 0 & \psi_{zz} \end{pmatrix} \mu_0 \end{aligned} \quad \text{with } \psi_{rr} = \frac{a}{br};\ \psi_{\theta\theta} = \frac{a}{b}r;\ \psi_{zz} = \frac{1}{abr} \tag{14.13}$$

14.3.2 Numerical Simulations

The transformation formulation is implemented using the finite element-based commercial solver Comsol Multiphysics. Figure 14.11 shows the comparison of a 2D simulation between a planar source made of current lines in the y–z plane above a limited metallic ground plane (Fig. 14.11a) and the same source surrounded by a metamaterial defined by Eq. (14.13) (Fig. 14.11b). Figure 14.11c and

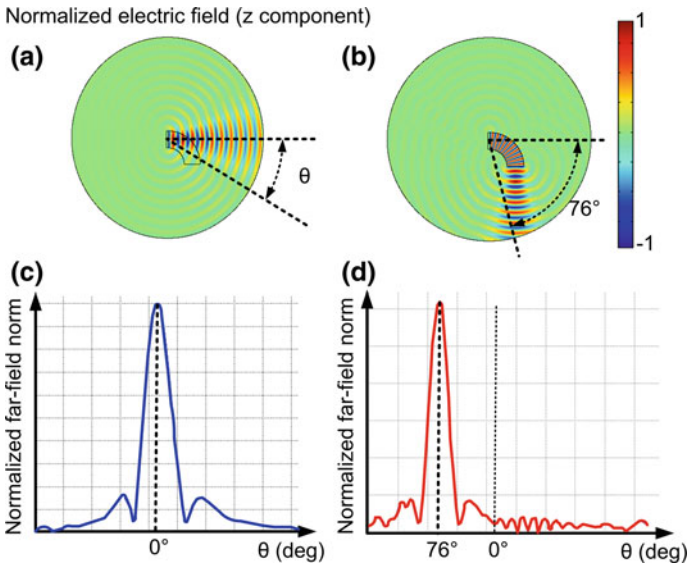

Fig. 14.11 **a–b** Calculated emission of a plane current source above a limited metallic ground plane without and with the metamaterial structure. **c–d** Calculated normalized far field of the antenna without and with metamaterial. A 76° rotation of the radiation is clearly observed

d show, respectively, the far-field patterns of the plane source without and with the metamaterial structure. The left shift of the peak corresponds to a rotation of 76° of the emitted radiation.

For the fabrication of the physical prototype, the calculated material parameters are simplified through a parameter reduction procedure. Then, the polarization of the electromagnetic field is set such that the magnetic field is along the z-direction. In this case, the relevant electromagnetic parameters are μ_{zz}, $\varepsilon_{\theta\theta}$, and ε_{rr}. The terms $\varepsilon_{\theta\theta}$ and μ_{zz} are held constant, leaving the new set of coordinates given by (14.14):

$$\varepsilon_{rr} = \frac{\left(\frac{1}{br}\right)^2}{1.7};\ \varepsilon_{\theta\theta} = 2.8;\ \mu_{zz} = 1.7 \tag{14.14}$$

Setting the physical parameter $b = 6$ allows an optimization of the material parameter ε_{rr}. The profile of the different parameters is presented in Fig. 14.12a. The fabricated prototype is composed of 30 identical layers where each layer is divided into 10 unit cells as illustrated by the single layer in Fig. 14.12b. For the discretization of the material parameters, meta-atoms producing electric resonances are designed on the 0.787 mm thick low loss (tan $\delta = 0.0013$) RO3003™ dielectric substrate. 5 mm rectangular unit cells were chosen for the resonators. The desired ε_{zz} and μ_{yy} were obtained by tuning the resonators' geometric parameters. The 10 cells presented in Fig. 14.12c are designed to constitute the discrete variation of ε_{rr}. Table 14.1 summarizes the corresponding electromagnetic parameters of the cells. The cells are composed of SRRs and ELCs to secure μ_{zz}

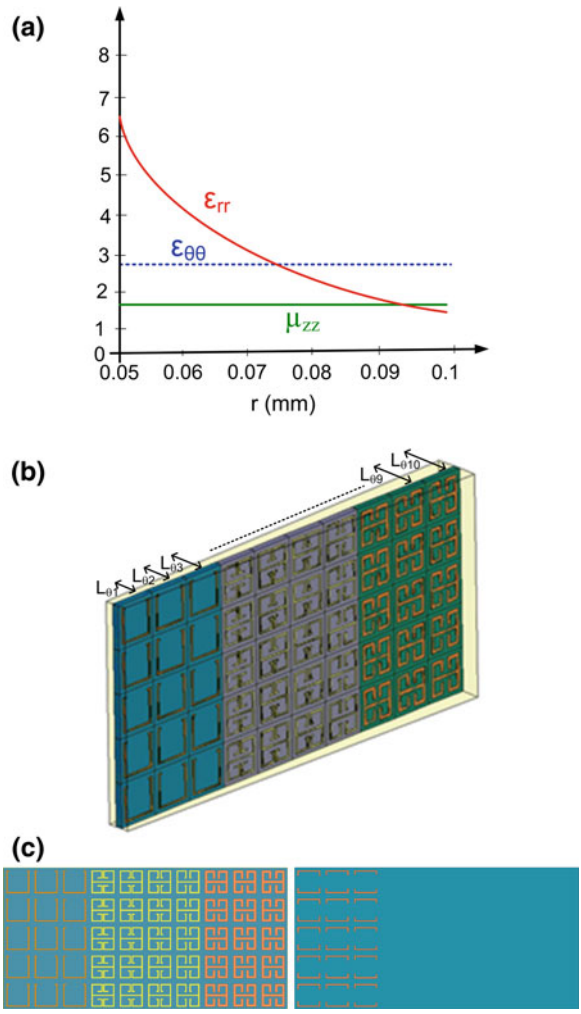

Fig. 14.12 **a** Profile of the material parameters. **b** Single metamaterial layer composed of 10 unit cells providing the material parameters necessary for the coordinate transformation. **c** Front and rear views of the metamaterial cells

and ε_{rr}, respectively. $\varepsilon_{\theta\theta}$ is produced by a host medium, which is a commercially available resin.

For numerical verification of the proposed device performance, a microstrip patch antenna presenting a quasi-omnidirectional radiation pattern is used as the feed source of the metamaterial antenna. This patch source is optimized for a 10 GHz operation. A 3D simulation of the patch antenna and the layered metamaterial is performed using HFSS as illustrated in Fig. 14.13a. Figure 14.13b shows the calculated energy distribution in the middle plane of the layered metamaterial structure. Note that the latter structure first transforms the quasi-omnidirectional radiation of the patch source into a directive pattern and also maintains this highly directive emission after the 76° rotation.

Table 14.1 Electromagnetic parameters μ_{zz}, and ε_{rr} for the 10 cells of the metamaterial layers

Layer	r_i (mm)	$L_{\theta i}$ (mm)	μ_{zz}	ε_{rr}
1	52.5	2.75	1.7	5.8
2	57.5	3.01	1.7	4.842
3	62.5	3.27	1.7	4.096
4	67.5	3.53	1.7	3.504
5	72.5	3.8	1.7	3.04
6	77.5	4.06	1.7	2.664
7	82.5	4.32	1.7	2.35
8	87.5	4.58	1.7	2.09
9	92.5	4.84	1.7	1.87
10	97.5	5.1	1.7	1.68

The length L_θ of each cell is given as a function of its position along the layer

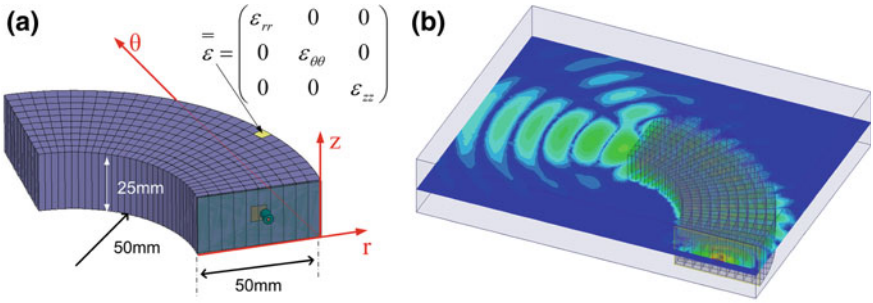

Fig. 14.13 **a** Simulated design consisting of 30 metamaterial layers each composed of 10 cells. **b** Calculated energy distribution at 10 GHz

14.3.3 Experimental Measurements

To validate experimentally the azimuthal directive emission, the device shown in Fig. 14.14a is fabricated. A microstrip square patch antenna printed on a 1 mm thick epoxy dielectric substrate ($\varepsilon_r = 3.9$ and $\tan\delta = 0.02$) is used as the radiating source. The metamaterial is a discrete structure composed of 10 different regions where permittivity and permeability vary according to Eq. (14.14) and to the values of Table 14.1. The bulk metamaterial is assembled using 30 layers of RO3003^{TM} dielectric boards on which subwavelength resonant structures are printed. The layers are mounted one-by-one in a molded matrix with a constant angle of 3° between each. A commercially available liquid resin is then poured into the mold. This resin constitutes the host medium and is an important design parameter closely linked to $\varepsilon_{\theta\theta}$. Its measured permittivity is close to 2.8. The mold is removed after solidification of the resin.

S_{11} parameter measurements are first performed on the fabricated prototype. The measured S_{11} parameter of the metamaterial antenna is compared with the

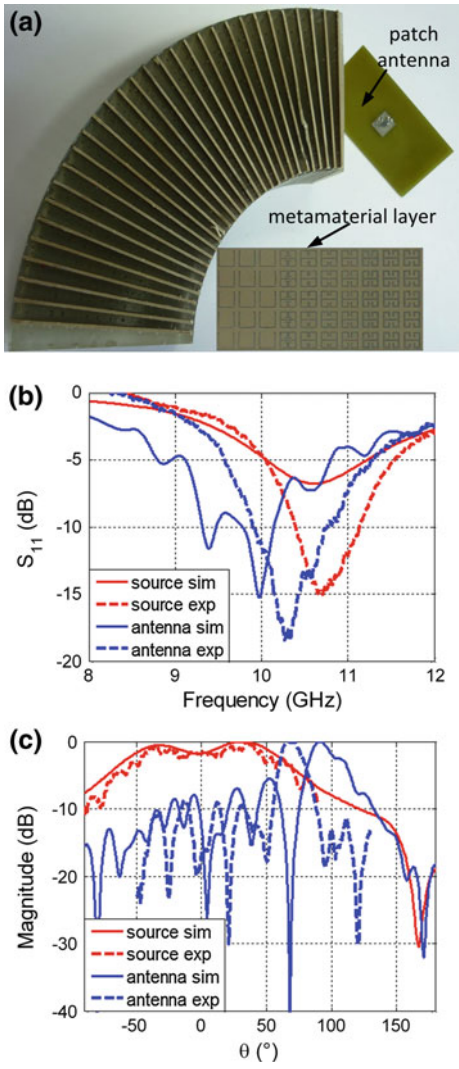

Fig. 14.14 **a** Photograph of the fabricated prototype. **b** Simulated and measured S_{11} parameter of the patch source alone and the metamaterial antenna. **c** Far-field E-plane radiation patterns of the patch source alone and of the metamaterial antenna

HFSS-simulated one in Fig. 14.14b. A good agreement can be observed and return losses reaching 18 dB is observed experimentally at 10.3 GHz compared to 15 dB calculated. This quantity is further compared with that of the feeding patch antenna alone. A better matching can be clearly observed for the metamaterial antenna. The E-plane far-field radiation pattern of the metamaterial antenna is measured in an anechoic chamber. Measurements are performed for the computer-controlled elevation angle varying from −90° to +90°. The measured far-field radiation pattern is presented for the metamaterial device (Fig. 14.14c). From the experiments, it is clearly observed that the transformation of the omnidirectional far-field radiation of the patch antenna into a directive one which is further bent at an angle of 66°, which

is consistent with the 76° predicted by numerical simulations. The difference in bending angle is due to the fabrication tolerances of the meta-atoms providing the gradient radial permittivity and to the positioning of the patch source.

14.4 Isotropic Antenna

In contrast to the first example where a quasi-isotropic emission was transformed into a directive one, here it is described how a coordinate transformation can be applied to transform directive emissions into isotropic ones. It will also be seen how transformation electromagnetics can modify the apparent (electromagnetic) size of a physical object.

14.4.1 Theoretical Design

An intuitive schematic principle to illustrate the proposed method is presented in Fig. 14.15. Consider a source radiating in a circular space as shown in Fig. 14.15a where a circular region bounded by the blue circle around this source limits the radiation zone. Here, a "space stretching" technique is applied. The "space stretching" coordinate transformation consists in stretching exponentially the central zone of this delimited circular region represented by the red circle as illustrated in Fig. 14.15b.

However, a good impedance match must be preserved between the stretched space and the exterior vacuum. Thus, the expansion procedure is followed by a compression of the annular region formed between the red and blue circles so as to secure an impedance match with free space. Figure 14.15c summarizes the exponential form of the coordinate transformation. The diameter of the transformed (generated metamaterial) circular medium is denoted *D*.

Mathematically this transformation is expressed as [52]:

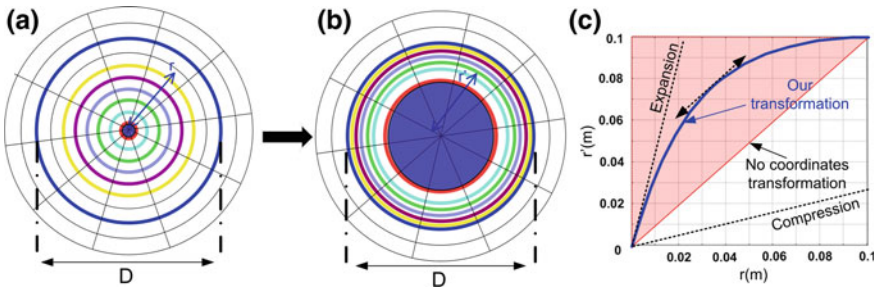

Fig. 14.15 **a** initial space, **b** transformed space, **c** the *blue curve* shows the transformation rule made of an expansion followed by a compression. Reprinted from [52]

$$\begin{cases} r' = \alpha(1 - e^{qr}) \\ \theta' = \theta \\ z' = z \end{cases} \text{ with } \alpha = \frac{D}{2}\frac{1}{1 - e^{\frac{qD}{2}}} \tag{14.15}$$

where r', θ', and z' are the coordinates in the transformed cylindrical space, and r, θ, and z are those in the initial cylindrical space. In the initial space, free-space conditions are assumed with isotropic permittivity and permeability tensors ε_0 and μ_0. Parameter q (in m^{-1}) appearing in Eq. (14.15) must be negative in order to achieve the impedance matching condition. This parameter is an expansion factor which can be physically viewed as the degree of space expansion. A high (negative) value of q means high expansion whereas a low (negative) value of q means nearly zero expansion.

Calculations lead to permeability and permittivity tensors given in the diagonal base by:

$$\overline{\overline{\psi}} = \begin{pmatrix} \psi_{rr} & 0 & 0 \\ 0 & \psi_{\theta\theta} & 0 \\ 0 & 0 & \psi_{zz} \end{pmatrix} = \begin{pmatrix} \frac{qr(r'-\alpha)}{r'} & 0 & 0 \\ 0 & \frac{r'}{qr(r'-\alpha)} & 0 \\ 0 & 0 & \frac{r}{qr'(r'-\alpha)} \end{pmatrix}$$

with

$$r = \frac{\ln\left(1 - {}^{r'}/_{\alpha}\right)}{q} \tag{14.16}$$

The components in the Cartesian coordinate system are calculated and are as follows:

$$\begin{cases} \psi_{xx} = \psi_{rr}\cos^2(\theta) + \psi_{\theta\theta}\sin^2(\theta) \\ \psi_{xy} = \psi_{yx} = (\psi_{rr} - \psi_{\theta\theta})\sin(\theta)\cos(\theta) \\ \psi_{yy} = \psi_{rr}\sin^2(\theta) + \psi_{\theta\theta}\cos^2(\theta) \end{cases} \tag{14.17}$$

The ε and μ tensors components present the same behavior as given in Eq. (14.17).

Figure 14.16 shows the variation of the permittivity and permeability tensor components in the newly generated transformed space. The geometric dimension D is chosen to be 20 cm and parameter q is fixed to -40 m^{-1}. It can be noted that

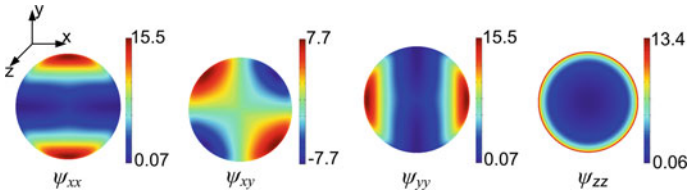

Fig. 14.16 Variation in the permeability and permittivity tensor components of the transformed space for $D = 20$ cm and $q = -40$ m^{-1}. Reprinted from [52]

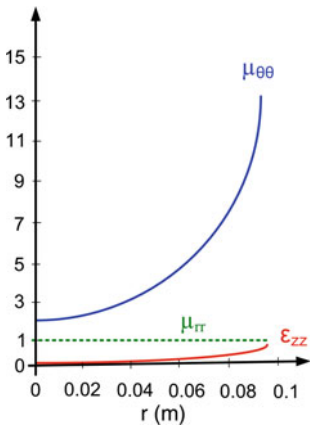

Fig. 14.17 Tailored permittivity and permeability values in a cylindrical configuration. Reprinted from [52]

components ψ_{xx}, ψ_{yy}, and ψ_{zz} present variations and an extrema that are simple to realize with commonly used metamaterials by reducing their inhomogeneous dependence [26]. At the center of the transformed space, ε and μ present very low values ($\ll 1$). Consequently, light velocity and the corresponding wavelength are much higher than in vacuum. The width of the plane source then appears very small compared to wavelength and the source can then be regarded as a radiating wire, which is in fact an isotropic source. The merit of this transformation depends effectively on the expansion factor q value, and more generally, it can be applied to a wide range of electromagnetic objects, where the effective size can be reduced compared to a given wavelength.

By fixing the electric field directed along the z-axis and by adjusting the dispersion equation without changing propagation in the structure, the following reduced parameters can be obtained:

$$\begin{cases} \mu_{rr} = 1 \\ \mu_{\theta\theta} = \left(\frac{r'}{qr(r'-\alpha)}\right)^2 \\ \varepsilon_{zz} = \left(\frac{r}{r'}\right)^2 \end{cases} \tag{14.18}$$

In Eq. (14.18), the parameters present positive values (Fig. 14.17) which can be easily achieved first by discretizing their continuous profile and second by using metamaterial resonators where magnetic and electric responses can be tailored and controlled.

14.4.2 Numerical Verifications

Figure 14.18 presents simulations results of the source radiating in the initial circular space at an operating frequency of 4 GHz for several values of q. The current direction of the source is supposed to be along the z-axis. Simulations are performed in a TE mode with the electric field polarized along the z-direction. The

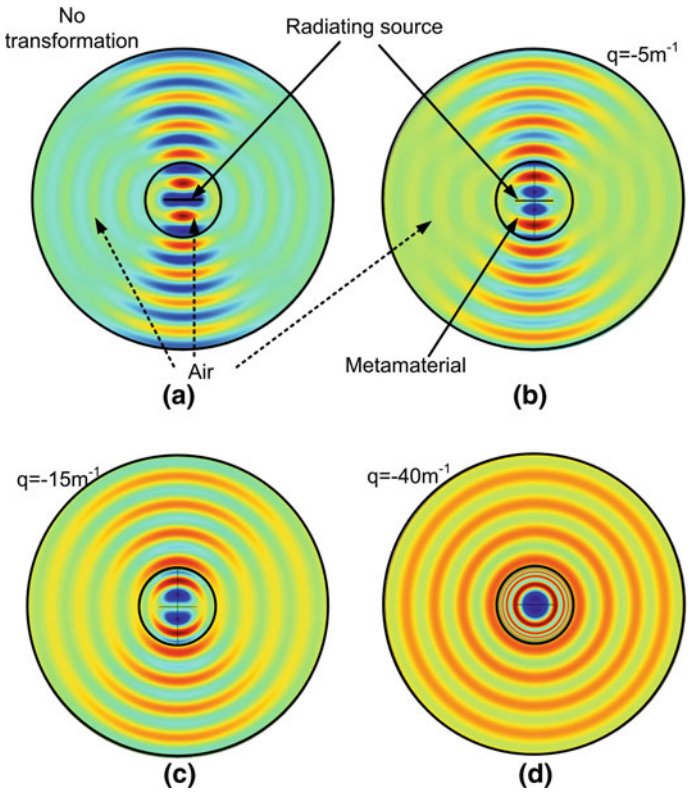

Fig. 14.18 Simulated electric field distribution for a TE wave polarization at 4 GHz. **a** A planar current source is used as the excitation for the transformation. The current direction is perpendicular to the plane of the figure. (**b–d**) Verification of the transformation for different values of expansion factor q. Reprinted from [52]

surface-current source is considered to have a width of 10 cm, which is greater than the 7.5 cm wavelength at 4 GHz. Radiation boundary conditions are placed around the calculation domain in order to plot the radiation properties. Continuity of the field is assured in the interior boundaries. As stated previously and verified from the different electric field distribution patterns, a high negative value of q leads to a quasi-perfect isotropic emission since the space expansion is higher. This phenomenon can be clearly observed in Fig. 14.18d for $q = -40\ \mathrm{m}^{-1}$.

The calculated far-field patterns are shown in Fig. 14.19a. The source alone produces a directive emission, but when it is surrounded by the judiciously engineered coordinate-transformation-based metamaterial, an isotropic emission is produced. Figure 14.19b shows the influence of parameter q on the space expansion in the coordinate transformation. As q becomes highly negative, a greater space expansion is achieved.

To summarize, a directive radiating source with a size greater than the wavelength has been transformed into an isotropic one with a size is much smaller than

the wavelength. This transformation is equivalent to reduce the apparent electromagnetic size of this source. With an opposite transformation the apparent size of the source would have increased. The practical implementation of both transformations is in progress.

14.5 Waveguide Taper

In this last section, the design of a taper is presented to control the flow of light between two waveguides of different cross sections. Three different transformation techniques are presented so as to achieve a reflection less taper between the two waveguides. This example shows the importance of the optimization of the analytical transformation between the initial space and the transformed one to obtain realizable values of electromagnetic parameters. The media obtained from these three methods presents complex anisotropic permittivity and permeability. However, using an exponential transformation leads to the design of a taper from a material with physically achievable material parameters. This application is primarily concerned with the optical frequency regime.

14.5.1 Transformation Formulations

Three different formulations are proposed below to achieve a low-reflection taper between two waveguides of different cross sections. Each waveguide is represented by black lines in its respective space given in Cartesian coordinates as depicted in Fig. 14.20. The aim is to connect the horizontal lines between the spaces to allow transmission of electromagnetic waves. Thus, in the geometric approximation, each ray of light in the first waveguide is guided into the second one by green lines representing the taper. For the first formulation, a linear transformation may be assumed by connecting the two spaces with straight lines as shown in Fig. 14.20a. The second formulation uses a parabolic transformation to achieve the connection (Fig. 14.20b). For the third one, an exponential transformation is defined as shown in Fig. 14.20c. In all three cases, the geometrical properties of the schema under analysis remain unchanged. The widths of the input and output waveguides are denoted a and b, respectively, and the length of the taper in all three cases is taken to be l. Mathematical expressions defining each formulation of the transformation approaches are given in Fig. 14.20. x', y' and z' are the coordinates in the transformed (new) space and x, y, and z are those in the initial space. As can be observed from the mathematical expressions, the different formulations depend on the geometric parameters (a, b, l).

Each transformation leads to a material with specific properties that can play the role of the desired taper. The transformation approach can be summarized into two main points. First, the Jacobian matrix of each transformation formulation is determined so as to obtain the properties of the "taper space".

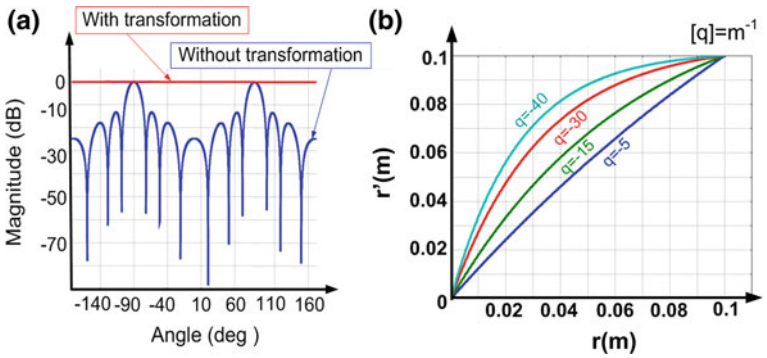

Fig. 14.19 **a** Far-field radiation pattern of the emission with ($q = -40\ \mathrm{m}^{-1}$) and without transformation. **b** Influence of the expansion parameter q on the proposed coordinate transformation. The emitted radiation is more and more isotropic as q tends to high negative values

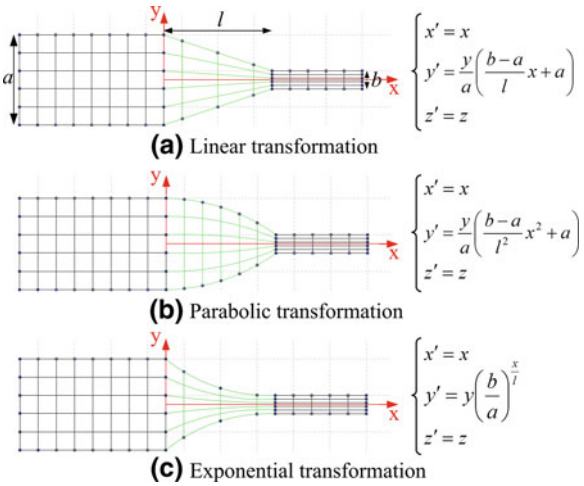

Fig. 14.20 Transformed tapers (*green lines*) between two waveguides (*black lines*) with different cross sections. **a** Linear, **b** parabolic, and **c** exponential transformation formulation. Reprinted from [23]

The second step consists of calculating the new permittivity and permeability tensors in the coordinate system (x', y') so as to mimic the transformed space. At this point, a material has been designed with the specific desired physical properties. This material can then be described by the permeability and permittivity tensors $\overline{\overline{\varepsilon}} = \overline{\overline{\theta}}\varepsilon_0$ and $\overline{\overline{\mu}} = \overline{\overline{\theta}}\mu_0$. In order to simplify the different calculations, take $\frac{J_i^{i'} J_j^{j'} \delta^{ij}}{\det(J)} = \theta^{i'j'}$ with

$$\overline{\overline{\theta}} = \begin{pmatrix} \theta_{xx}(x') & \theta_{xy}(x', y') & 0 \\ \theta_{xy}(x', y') & \theta_{yy}(x', y') & 0 \\ 0 & 0 & \theta_{zz}(x') \end{pmatrix} \tag{14.19}$$

Table 14.2 Components values of $\overline{\overline{\theta}}$ tensor for the three transformations

	$\theta_{xx}(x') = \theta_{zz}(x')$	$\theta_{xy}(x', y')$	$\theta_{yy}(x', y')$
Linear transformation	$\frac{al}{a(l-x')+bx'}$	$\theta_{xx}^2 \frac{b-a}{al} y'$	$\frac{1}{\theta_{xx}} + \frac{\theta_{xy}^2}{\theta_{xx}}$
Parabolic transformation	$\frac{al^2}{(al^2-ax'^2+bx'^2)}$	$\frac{2\theta_{xx}^2(b-a)x'y'}{al^2}$	$\frac{1}{\theta_{xx}} + \frac{\theta_{xy}^2}{\theta_{xx}}$
Exponential transformation	$\left(\frac{b}{a}\right)^{-\frac{x'}{l}}$	$\frac{\theta_{xx}y' \ln\left(\frac{b}{a}\right)}{l}$	$\frac{1}{\theta_{xx}} + \frac{\theta_{xy}^2}{\theta_{xx}}$

The component values of the $\overline{\overline{\theta}}$ tensor are given in Table 14.2 where a non-diagonal term (θ_{xy}) appears. This non-diagonal term is necessary to guide electromagnetic waves in the x–y plane as the case for this taper.

14.5.2 Simulations and Results

To verify the results expressed in the previous section, the finite element-based commercial software Comsol MULTIPHYSICS is used to design the described waveguide taper. Two-dimensional simulations are performed for the validation of the proposed material parameters. Port boundaries are used to excite the first and third transverse electric (TE_1 and TE_3) modes of the input waveguide with the E-field directed along the z-axis to verify the conservation of modes through the taper. The waveguides boundaries are assumed to be Perfect Electric Conductors (PECs) and matched boundaries conditions are applied to the taper. Verifications are done in the microwave domain for a possible future physical prototype based on metamaterials.

The waveguide widths are chosen to be $a = 10$ cm and $b = 2$ cm with 1.5 and 7.5 GHz cutoff frequencies, respectively. The length of the taper is chosen as $l = 5$ cm, thus allowing the generation of the entire spatial dependence of the material parameters $\theta_{xx}(x')$, $\theta_{zz}(x')$, $\theta_{xy}(x',y')$, and $\theta_{yy}(x',y')$ as shown in Fig. 14.21. These distributions are plotted from the expressions given in Table 14.2. Values of permittivity and permeability presented in Fig. 14.21 account for the control of the electromagnetic field in the taper and the conservation of the propagating modes from waveguide 1 to waveguide 2. Although the same spatial distribution profile can be observed for the three different formulations, the parameter values are completely different. For the linear and parabolic transformations, values of μ_{yy} are too high to be physically achievable with existing metamaterials. However, it is clear that the exponential transformation leads to values more easily achievable with metamaterials. Moreover, the physical realization of such a metamaterial taper will be facilitated by the slow variation of the material parameters, implying a gradual variation in the geometric parameters of metamaterial inclusions. Note that the components are calculated in the Cartesian system and obey the following dispersion relation in the TE mode:

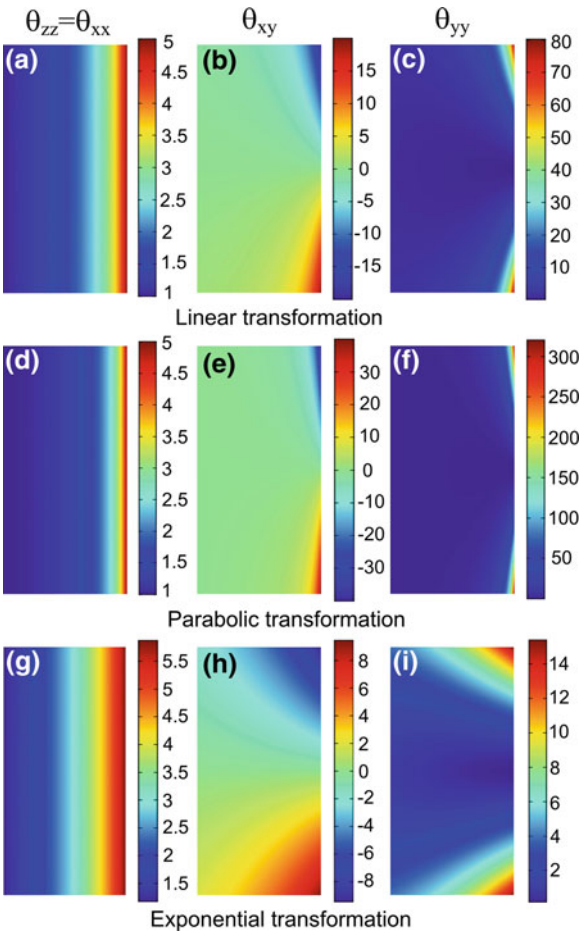

Fig. 14.21 Components of the permittivity and permeability tensors $\overline{\overline{\theta}}$ for the three transformations with $a = 10$ cm, $b = 2$ cm, and $l = 5$ cm. Reprinted from [23]

$$\varepsilon_{zz}\left(\mu_{xy}^2 - \mu_{xx}\mu_{yy}\right) + \mu_{xx}k_x^2 + k_y\left(\mu_{yy}k_y - 2\mu_{xy}k_x\right) = 0 \tag{14.20}$$

This equation is obtained from the propagation equation and describes the control of electromagnetic waves in the material. This relation is also important for a future reduction of parameters, which can be done by simplifying the non-diagonal parameter θ_{xy} to a closed interval near zero when choosing the appropriate length of the taper. For example, by bounding the non-diagonal term of the exponential formulation in Table 14.2, the condition $l > \frac{a^2}{b}\frac{\left|\ln\left(\frac{b}{a}\right)\right|}{2\Delta}$ leads to $-\Delta < \mu_{xy} < \Delta$ where Δ can be very close to zero.

Simulation results for the E-field distribution of the structure under study for all three transformations are presented in Fig. 14.22. The distributions in the tapered waveguides are compared to a non-tapered case at 10 and 30 GHz for the fundamental (TE_1) excitation mode and at 30 GHz for the third (TE_3) excitation

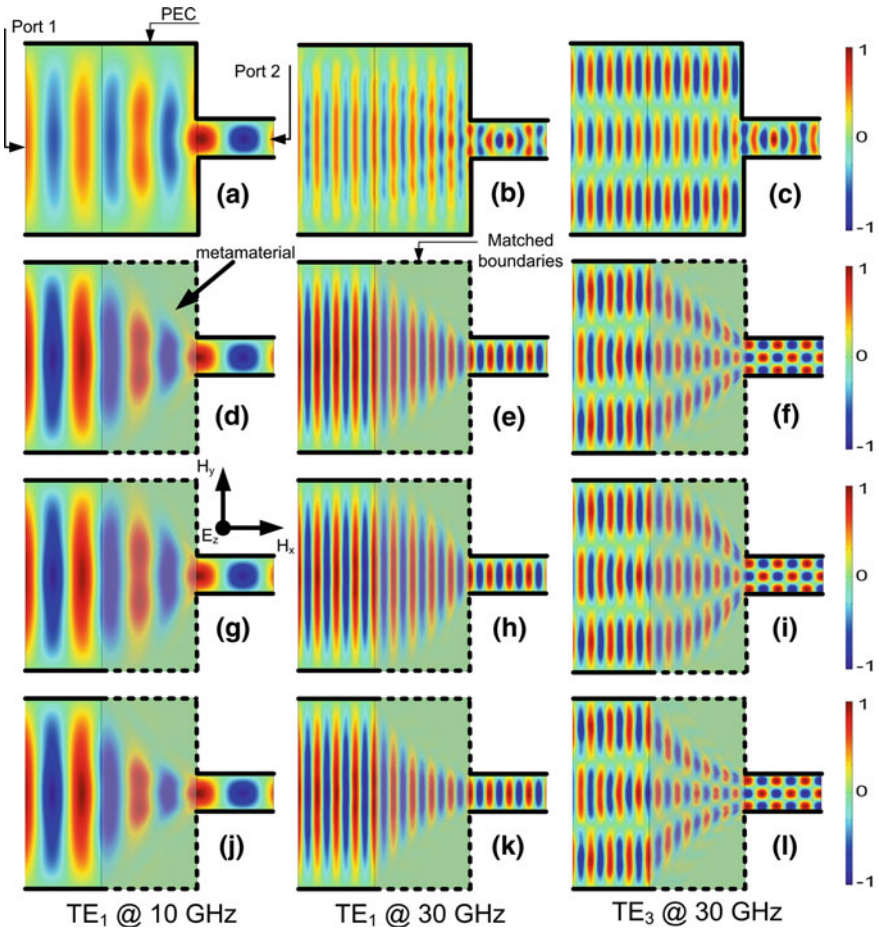

Fig. 14.22 Normalized E-field distribution for TE polarization. **a–c** Non-tapered junction waveguides. **d–f** Tapered junction waveguides with linear transformation. **g–i** Tapered junction waveguides with parabolic transformation. **j–l** Tapered junction waveguides with exponential transformation. Reprinted from [23]

mode. Concerning the non-tapered junction waveguides, phase distortions may be observed due to reflections at the junction from the larger waveguide to the smaller one (Fig. 14.22a–c). These distortions become more severe at higher frequencies (30 GHz). However, simulations performed on the tapered waveguides (Fig. 14.22d–l) illustrate that electromagnetic waves are properly guided from one waveguide to the other without any impact on the guided mode when the transformed medium is embedded between the two waveguides.

The difference in the transformation formulations indicates a change in the path of electromagnetic waves in the tapered section, highlighted by the shaded gray area in Fig. 14.22. Increasing the frequency improves the transmission between the

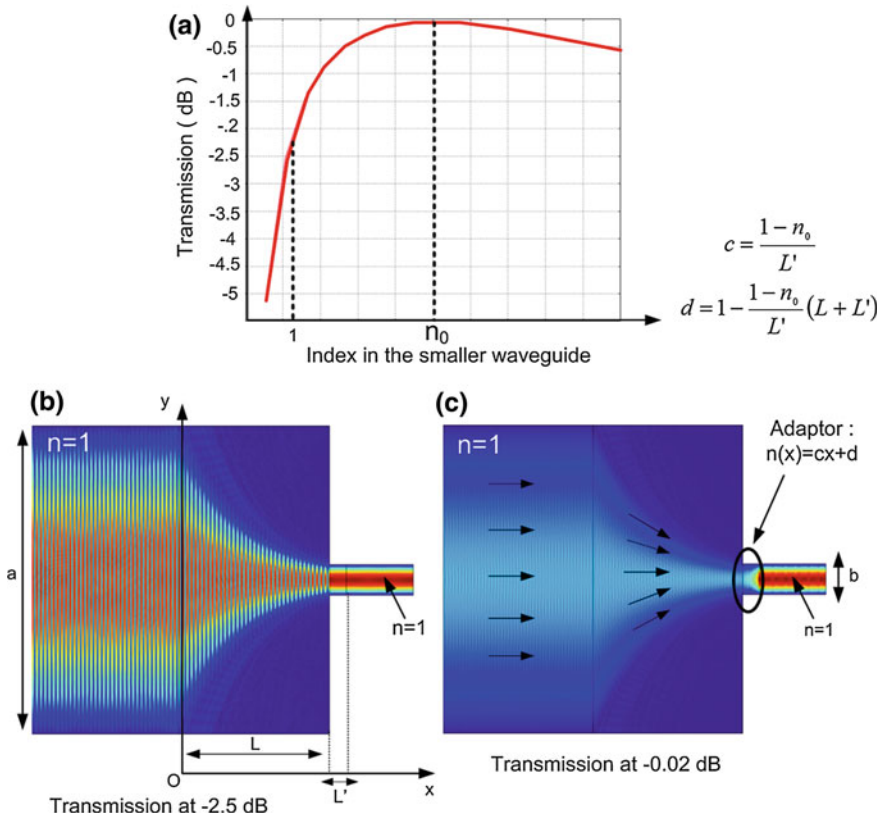

Fig. 14.23 Evolution of the transmission according to the index in the smaller waveguide. Maximum transmission is ensured for n_0. An adaptor is calculated for total transmission between the two waveguides filled with vacuum

two waveguides through the tapered section. This phenomenon can be observed when the E-field distributions are compared at 10 and 30 GHz. At 10 GHz, a slight impedance mismatch between the taper output and the small waveguide input can be observed. This phenomenon decreases at higher frequencies, as illustrated for 30 GHz. It is due to the general rule of coordinate transformations when compressing or expanding space.

To cancel all the reflections and to have a total transmission, it is possible, for example, to create an isotropic gradient index in the second guide. This gradient can be created by choosing a conformal transformation, with a transformation on the x component. Figure 14.23a illustrates the evolution of the transmission coefficient with the index in the small waveguide. Figure 14.23a and b highlights standing waves in the transformation-based material and the large waveguide due to reflections at the entrance of the small waveguide. So, to ensure a quasi-total transmission a material with a gradient index is introduced following the x-axis as presented in Fig. 14.23c. All the energy is then transferred to the smaller

waveguide. The conservation of the energy flow allows us to understand the higher amplitude in the smaller waveguide by a factor $\sqrt{(a/b)}$. Indeed, by denoting π as the norm of the Poynting vector, the relationship is $\pi_1 a = \pi_2 b$; since π is proportional to E^2 in vacuum, the field ratio is equal to $\sqrt{(a/b)}$.

To summarize, compared to an abrupt (non-tapered) junction where phase distortions appear, transformation optics helps to properly guide electromagnetic waves from one waveguide to another without any impact on the guided propagating modes. The implementation of this taper on silicon and glass at 1.5 μm is in progress [53, 54].

14.6 Conclusion

In this chapter, the coordinate transformation theory has been presented as applied to the design of non-standard electromagnetic devices. The coordinate transformation technique does not present any theoretical limit in the design concept, and applications can be scaled to any frequency regime. The ideas of applications can then be extremely varied. The only limit is technological, mainly due to the practical values of electromagnetic parameters achievable with metamaterials. Here, three antenna applications have been proposed in the microwave domain through the use of metamaterials, as well as an optical waveguide taper. The two antenna examples have been practically realized using metamaterials. These metamaterials are periodic structures composed of subwavelength metallic inclusions in a host dielectric matrix. The difficulty in the design of such metamaterials resides in the engineering of the proper inclusions for electric and magnetic resonances. The permittivity and permeability tensors generated by coordinate transformation are often inhomogeneous and anisotropic and it is thus necessary to reduce and discretize these parameters by controlling the dispersion relation of the structure. Thus, a careful choice will make it possible to find an inexpensive and easily realizable material. The drawback of this simplification will then be an impedance mismatch. However, this impedance mismatch can be controlled by an optimization of the parameter simplification.

Acknowledgments The authors thank D. Germain, A. Sellier, X. Wu, and S. Kirouane for their help in the realization and characterization of the prototypes in this study. They also thank the French National Research Agency for its financial support through the METAPHORT, METAVEST, and METAPHOTONIQUE projects.

References

1. Pendry JB, Schurig D, Smith DR (2006) Controlling electromagnetic fields. Science 312:1780–1782
2. Leonhardt U (2006) Optical conformal mapping. Science 312:1777–1780
3. Schurig D, Mock JJ, Justice BJ et al (2006) Metamaterial electromagnetic cloak at microwave frequencies. Science 314:977–980

4. Cai W, Chettiar UK, Kildishev AV et al (2007) Optical cloaking with metamaterials. Nat Photon 1:224–227
5. Kanté B, de Lustrac A, Lourtioz JM et al (2008) Infrared cloaking based on the electric response of split ring resonators. Opt Express 16:9191–9198
6. Gabrielli LH, Cardenas J, Poitras CB et al (2009) Silicon nanostructure cloak operating at optical frequencies. Nat Photon 3:461–463
7. Kanté B, Germain D, de Lustrac A (2009) Experimental demonstration of a nonmagnetic metamaterial cloak at microwave frequencies. Phys Rev B 80:201104
8. Valentine J, Li J, Zentgraf T et al (2009) An optical cloak made of dielectrics. Nat Mater 8:568–571
9. Ergin T, Stenger N, Brenner P et al (2010) Three-dimensional invisibility cloak at optical wavelengths. Science 328:337–339
10. Leonhardt U, Tyc T (2009) Broadband invisibility by non-Euclidean cloaking. Science 323:110–112
11. Li J, Pendry JB (2008) Hiding under the carpet: a new strategy for cloaking. Phys Rev Lett 101:203901
12. Liu R, Ji C, Mock JJ et al (2009) Broadband ground-plane cloak. Science 323:366–369
13. Jiang WX, Cui TJ, Qiang C, Chin JY, Yang XM, Liu R, Smith DR (2008) Design of arbitrarily shaped concentrators based on conformally optical transformation of nonuniform rational B-spline surfaces. Appl Phys Lett 92:264101
14. Luo Y, Chen H, Zhang J, Ran L, Kong JA (2008) Design and analytical full-wave validation of the invisibility cloaks, concentrators, and field rotators created with a general class of transformations. Phys Rev B 77:125127
15. Rahm M, Schurig D, Roberts DA, Cummer SA, Smith DR, Pendry JB (2008) Design of electromagnetic cloaks and concentrators using form-invariant coordinate transformations of Maxwell's equations. Photon Nanostruct Fundam Appl 6:87–95
16. Greenleaf A, Kurylev Y, Lassas M, Uhlmann G (2007) Electromagnetic wormholes and virtual magnetic monopoles from metamaterials. Phys Rev Lett 99:183901
17. Zhang J, Luo Y, Chen H, Huangfu J, Wu BI, Ran L, Kong JA (2009) Guiding waves through an invisible tunnel. Opt Express 17:6203–6208
18. Huangfu J, Xi S, Kong F, Zhang J, Chen H, Wang D, Wu BI, Ran L, Kong JA (2008) Application of coordinate transformation in bent waveguides. J Appl Phys 104:014502
19. Kwon DH, Werner DH (2008) Transformation optical designs for wave collimators, flat lenses and right-angle bends. New J Phys 10:115023
20. Landy NI, Padilla WJ (2009) Guiding light with conformal transformations. Opt Express 17:14872–14879
21. Rahm M, Roberts DA, Pendry JB, Smith DR (2008) Transformation-optical design of adaptive beam bends and beam expanders. Opt Express 16:11555–11567
22. Roberts DA, Rahm M, Pendry JB, Smith DR (2009) Transformation-optical design of sharp waveguide bends and corners. Appl Phys Lett 93:251111
23. Tichit PH, Burokur SN, de Lustrac A (2010) Waveguide taper engineering using coordinate transformation technology. Opt Express 18:767–772
24. Kong F, Wu BI, Kong JA, Huangfu J, Xi S (2007) Planar focusing antenna design by using coordinate transformation technology. Appl Phys Lett 91:253509
25. Chen H, Hou B, Chen S, Ao X, Wen W, Chan CT (2009) Design and experimental realization of a broadband transformation media field rotator at microwave frequencies. Phys Rev Lett 102:183903
26. Tichit PH, Burokur SN, Germain D, de Lustrac A (2011) Design and experimental demonstration of a high-directive emission with transformation optics. Phys Rev B 83:155108
27. Tamm IY (1924) Electrodynamics of an anisotropic medium in the special case of relativity. J Russ Phys Chem Soc 56:248
28. Plebanski J (1960) Electromagnetic waves in gravitational fields. Phys Rev 118:1396–1408

29. Han T, Qiu CW (2010) Isotropic nonmagnetic flat cloaks degenerated from homogeneous anisotropic trapeziform cloaks. Opt Express 18:13038–13043
30. Schmiele M, Varma VS, Rockstuhl C, Lederer F (2010) Designing optical elements from isotropic materials by using transformation optics. Phys Rev A 81:33837
31. Turpin JP, Massoud AT, Jiang ZH, Werner PL, Werner DH (2010) Conformal mappings to achieve simple material parameters for transformation optics devices. Opt Express 18:244–252
32. Chang Z, Zhou X, Hu J, Hu G (2010) Design method for quasi-isotropic transformation materials based on inverse Laplace's equation with sliding boundaries. Opt Express 18:6089–6096
33. Leonhardt U (2000) Space-time geometry of quantum dielectrics. Phys Rev A 62:012111
34. Bergamin L (2008) Generalized transformation optics from triple spacetime metamaterials. Phys Rev A 78:43825
35. Thompson RT, Cummer SA, Frauendiener J (2011) A completely covariant approach to transformation optics. J Opt 13:024008
36. Crudo RA, O'Brien JG (2009) Metric approach to transformation optics. Phys Rev A 80:033824
37. Cheng Q, Cui TJ, Jiang WX, Cai BG (2010) An omnidirectional electromagnetic absorber made of metamaterials. New J Phys 12:063006
38. Narimanov EE, Kildishev AV (2009) Optical black hole: Broadband omnidirectional light absorber. Appl Phys Lett 95:041106
39. Genov DA, Zhang S, Zhang X (2009) Mimicking celestial mechanics in metamaterials. Nat Phys 5:687–692
40. Jiang WX, Cui TJ, Ma HF, Zhou XY, Cheng Q (2008) Cylindrical-to-plane-wave conversion via embedded optical transformation. Appl Phys Lett 92:261903
41. Kundtz N, Smith DR (2009) Extreme-angle broadband metamaterial lens. Nat Mater 9:129–132
42. Rahm M, Cummer SA, Schurig D, Pendry JB, Smith DR (2008) Optical design of reflectionless complex media by finite embedded coordinate transformations. Phys Rev Lett 100:63903
43. Luo Y, Zhang J, Ran L, Chen H, Kong JA (2008) Controlling the emission of electromagnetic source. PIERS Online 4:795–800
44. Luo Y, Zhang J, Ran L, Chen H, Kong JA (2008) New concept conformal antennas utilizing metamaterial and transformation optics. IEEE Antennas Wireless Propag Lett 7:509–512
45. Popa BI, Allen J, Cummer SA (2009) Conformal array design with transformation electromagnetics. Appl Phys Lett 94:244102
46. Allen J, Kundtz N, Roberts DA, Cummer SA, Smith DR (2009) Electromagnetic source transformations using superellipse equations. Appl Phys Lett 94:194101
47. Ma YG, Ong CK, Tyc T, Leonhardt U (2009) An omnidirectional retroreflector based on the transmutation of dielectric singularities. Nat Mater 8:639–642
48. Balanis CA (1997) Antenna theory: analysis and design, 2nd edn. Wiley, New York
49. Pendry JB, Holden AJ, Robbins DJ, Stewart WJ (1999) Magnetism from conductors and enhanced nonlinear phenomena. IEEE Trans Microwave Theory Tech 47:2075–2084
50. Schurig D, Mock JJ, Smith DR (2006) Electric-field-coupled resonators for negative permittivity metamaterials. Appl Phys Lett 88:041109
51. Nicholson AM, Ross GF (1970) Measurement of the intrinsic properties of materials by time-domain techniques. IEEE Trans Instrum Meas 19:377–382
52. Tichit PH, Burokur SN, de Lustrac A (2011) Transformation media producing quasi-perfect isotropic emission. Opt Express 19:20551–20556
53. Ghasemi R, Tichit PH, Degiron A, Lupu A, de Lustrac A (2010) Efficient control of a 3D optical mode using a thin sheet of transformation optical medium. Opt Express 18:20305–20312
54. Lupu A, Dubrovina N, Ghasemi R, Degiron A, de Lustrac A (2011) Metal-dielectric metamaterials for guided wave silicon photonics. Opt Express 19:24746–24761

Index

D. H. Werner and D.-H. Kwon (eds.), *Transformation Electromagnetics and Metamaterials*, DOI: 10.1007/978-1-4471-4996-5, © Springer-Verlag London 2014

C

D